modern aspects of electrochemistry no. 32

Edited by B. E. CONWAY,
J. O'M. BOCKRIS, and RALPH E. WHITE

MODERN ASPECTS OF ELECTROCHEMISTRY

No. 32

LIST OF CONTRIBUTORS

THOMAS Z. FAHIDY
Department of Chemical Engineering
University of Waterloo
Waterloo, Ontario, Canada, N2L 3G1

KATHARINA KRISCHER
Abt. Physikalische Chemie
Fritz-Haber-Institut der Max-Planck-Gesellschaft
Berlin, Germany D-14195

ANDRZEJ LASIA
Department of Chemistry
University of Sherbrooke
Sherbrooke, Quebec, Canada J1K 2R1

MARK C. LEFEBVRE
Department of Chemistry
University of Ottawa
Ottawa, Ontario, Canada K1N 6N5

VIJAY MODI
Department of Mechanical Engineering
Columbia University
New York, New York 10027

ASHOK K. VIJH
Electrochemistry Section
Hydro-Quebec Research Institute
Varennes, Quebec, Canada J3X 1S1

ALAN C. WEST
Department of Chemical Engineering and Applied Chemistry
Columbia University
New York, New York 10027

J. DELIANG YANG
Department of Chemical Engineering and Applied Chemistry
Columbia University
New York, New York 10027

MODERN ASPECTS OF ELECTROCHEMISTRY

No. 32

Edited by

B. E. CONWAY
University of Ottawa
Ottawa, Ontario, Canada

J. O'M. BOCKRIS
Molecular Green Technology
College Station, Texas

and

RALPH E. WHITE
University of South Carolina, Columbia
Columbia, South Carolina

KLUWER ACADEMIC PUBLISHERS
NEW YORK, BOSTON, DORDRECHT, LONDON, MOSCOW

eBook ISBN 0-306-46916-2
Print ISBN 0-306-45964-7

Created in the United States of America

Visit Kluwer Online at: http://www.kluweronline.com
and Kluwer's eBookstore at: http://www.ebooks.kluweronline.com

Preface

This volume is composed of six chapters covering both fundamental and applied electrochemistry, as in previous monographs in this series.

The first chapter, by Krischer, provides a detailed analysis of oscillatory processes that arise in the kinetics of certain electrode processes, for example, in active to passive transitions involving oxide films and in H_2 and small organic molecule oxidations. The origin of such periodic phenomena in electrochemistry has remained obscure for some time. (Why are steady states not simply attained?) The author gives a thorough and mathematical treatment of the conditions required for onset of oscillations, including, it is important to note, coupling with resistive elements of experimental circuits and diffusion. Her review encompasses broader aspects of periodic phenomena such as those currently being considered in theories of transition between "order" and "chaos," part of a new paradigm in biology and cosmology.

Lasia, in the second chapter, offers a much-needed comprehensive treatment of ac impedance ("impedance spectroscopy") as applied to the study of kinetics and mechanisms of electrode processes. He starts out with the elements and fundamentals of the subject and develops case studies for treatment of progressively more complex processes involving coupling between activation and diffusion-controlled faradaic reactions, also including pseudo-capacitative elements in parallel relations with the ubiquitous double-layer capacitance. An extension to the study of electrochemical sorption of hydrogen into host cathode metals is also usefully given. In a forthcoming volume, a second part of this review will be published, covering practical applications, for example, in corrosion, industrial electrolytic processes and battery electrochemistry.

Continuing on the fundamental side, Lefebvre, in Chapter 3, revisits the problem of the significance of stoichiometric numbers in analysis of mechanisms of multistep electrode processes. He considers both forward

and backward directions of multi- (two or three) electron-transfer reactions (e.g., as in Al deposition), and the participation of the associated intermediates. This chapter illustrates the complexity of interpretations of determined stoichiometric numbers and the limitations that arise in their application to mechanism analysis.

Chapter 4 by Vijh is on the environmentally related topic of electro-osmotic dewatering of clays. This subject encompasses interfacial electrochemical and colloid science, and has important applications in washing clay and sand, the treatment of ores and tailings, and dewatering of brown coal and peat, as well as in dealing with liquors and wastes from the electroplating and metal-finishing industries. Geotechnical applications also arise, for example, in the stabilization of soils in locations where mudslides occur. Electrochemistry is involved through the high-area double layers at colloid interfaces and in the provision of the high voltages at the electrodes that drive the processes of electro-osmosis involved in the "dewatering" phenomenon.

Magnetic effects in electrolytic processes have always held a special if somewhat distant interest for electrochemists. In Chapter 5, by Fahidy, an excellent account is given of the fundamentals of this topic and its applications, through magnetohydrodynamics, to electrodeposition and corrosion. Also treated is the basis of the electrolytic Hall effect, which is essential for understanding how electrohydrodynamic forces act on moving ions in a magnetic field.

In industrial electrolytic processes, including metal electrodeposition and preparation reactions, mass transfer and fluid flow are usually of central importance, especially in scaleup from laboratory-scale experimentation. In the final chapter of this volume, West and co-authors give the essential aspects of computer analysis and modeling of such processes in terms of fluid dynamics and mass transfer.

B. E. Conway, University of Ottawa

J. O'M. Bockris, Molecular Green Technology

Ralph E. White, University of South Carolina

Contents

Chapter 2

ELECTROCHEMICAL IMPEDANCE SPECTROSCOPY AND ITS APPLICATIONS

Andrzej Lasia

Chapter 3

ESTABLISHING THE LINK BETWEEN MULTISTEP ELECTROCHEMICAL REACTION MECHANISMS AND EXPERIMENTAL TAFEL SLOPES

Mark C. Lefebvre

Chapter 4

ELECTRO-OSMOTIC DEWATERING OF CLAYS, SOILS, AND SUSPENSIONS

Ashok K. Vijh

Chapter 5

THE EFFECT OF MAGNETIC FIELDS ON ELECTROCHEMICAL PROCESSES

Thomas Z. Fahidy

Chapter 6

ANALYSIS OF MASS TRANSFER AND FLUID FLOW FOR ELECTROCHEMICAL PROCESSES

J. Deliang Yang, Vijay Modi, and Alan C. West

This page intentionally left blank

MODERN ASPECTS OF ELECTROCHEMISTRY

No. 32

This page intentionally left blank

1

Principles of Temporal and Spatial Pattern Formation in Electrochemical Systems

Katharina Krischer

Abt. Physikalische Chemie, Fritz-Haber-Institut der Max-Planck-Gesellschaft, Faradayweg 4 - 6, D-14195 Berlin, Germany

I. INTRODUCTION

The vast body of literature on electrochemical oscillations has revealed a quite surprising fact: dynamic instabilities, manifesting themselves, for example, in bistable or oscillatory reaction rates, occur in nearly every electrochemical reaction under appropriate conditions. An impressive compilation of all the relevant papers up to 1993 can be found in a review article by Hudson and Tsotsis.[1] This finding naturally raises the question of whether there are common principles governing pattern formation in electrochemical systems. In other words, are there universal mechanisms leading to self-organization phenomena in systems with completely different chemical compositions, and thus also distinct rate laws?

Modern Aspects of Electrochemistry, Number 32, edited by B. E. Conway *et al.* Kluwer Academic / Plenum Publishers, New York, 1999.

In general terms, the occurrence of self-organization phenomena is tied to two conditions: The system has to be far from thermodynamic equilibrium, and appropriate feedback mechanisms have to be present.

Obviously, in electrochemical experiments, the first condition is almost always fulfilled. However, the requirement of appropriate feedback mechanisms (i.e., appropriate nonlinear evolution laws) seems to constitute a severe restriction on the possible reaction mechanisms that give rise to pattern formation. From this point of view, it is astonishing that nearly all electrochemical systems exhibit dynamic instabilities.

The progress achieved in understanding oscillatory behavior in various electrochemical systems during the past decade has brought a common framework to light. In most systems the occurrence of dynamic instabilities is linked to the interplay of electrode kinetics, transport processes occurring in the electrolyte, and the electrical circuit. Only the first one of these "ingredients" of the oscillation mechanism depends on the elementary reaction steps occurring at the interface. In contrast, the other two are determined by potentiostatic or galvanostatic control and cell design. Thus, any attempt to understand the physical origin of the instability has to take into consideration the *complete* electrochemical system. The interfacial phenomena themselves have only limited effect on whether the system has dynamic instability.

The important role that electric circuit plays in dynamic instabilities was recognized a long time ago, and lately since the famous and much-cited review article by Wojtowicz[2] appeared, electrochemical oscillators have been divided into two categories: those described by "chemical models" and those described by "electrical models." In systems belonging to the latter class, self-organization phenomena arise owing to the properties of all elements of the circuit, while in chemical models they are caused exclusively by the properties of the electrode/electrolyte interface. Thus, chemical models result from mass balance only, and hence the variables are the concentrations of the reacting species and possibly the state of the electrode. Electrochemical oscillators belonging to this class can be described in exactly the same framework as oscillations in heterogeneous catalysis*: The rate equations are derived from transport processes of the

*Exceptions here seem to be some metal dissolution reactions; see e.g., Ref. 3.

reactants to (and possibly also from) the electrode; adsorption, reaction, and desorption steps; as well as possible changes in the state of the electrode surface. The electrode potential is kept fixed and thus reduces to a parameter.

Frequently encountered mechanisms leading to the spontaneous occurrence of time-dependent reaction rates in heterogeneous catalysis can be found in other review articles.[4–7] However, the relevance of chemical models for explaining the physical mechanism of electrochemical oscillators has been overestimated for a long time, and the hope of learning much from heterogeneous catalysis about how oscillations arise in electrochemical systems has not been fulfilled. In most cases where chemical models were proposed in order to explain the temporal behavior of the system, they were later proved wrong. At present, there are only a few systems in which experimental results strongly suggest that the instability is of chemical origin. Among these are iron dissolution from nitric acid [8,9] and the electrodeposition of Zn.[10] Still debated is whether also the oxidation of Si in acid fluoride solution falls into this category.[11–14] However, with one possible exception,[3] the reaction mechanisms are not yet understood for any of the possible candidates in this class.

In electrical models, the instability results from the interaction of the characteristics of the electrode/electrolyte interface (i.e., the faradaic impedance) with the additional "external" elements of the electric circuit (i.e., electrode capacity, electrolyte) and the control device (i.e., a potentiostat or galvanostat). Consequently, the differential equations governing the temporal evolution of these systems are derived from charge as well as mass balance. The double-layer potential thus constitutes a variable evolving in time. All oscillators belonging to this class (which, as it seems, is the overwhelming majority of the electrochemical oscillators) possess a negative real faradaic impedance in a certain parameter region. That a negative slope in the stationary current-potential curve can destabilize an electrochemical system had been known for many decades.[8] However, it is only recently and mainly due to work by Koper, partly in collaboration with Sluyters and Gaspard, that the interplay of this electrical instability with slow reaction steps or transport processes has been elaborated.[15–17] Through this work, a simple model that accounts for surprisingly many electrochemical oscillators revealed an unexpected wealth of different dynamic behaviors. Meanwhile, a consistent picture of why and when

electrochemical systems oscillate has been developed, which naturally leads to a further division of electrical models into two subcategories, according to the nature of the slow feedback process.[18–20]

However, in spatially extended systems, self-organization in time is, in general, accompanied by pattern formation in space. An understanding of dynamic behavior is not possible without taking into account the spatial degrees of freedom. The first hint that spatial structures may develop at the electrode/electrolyte interface goes back as far as 1844,[21] and intense research on wave phenomena in electrochemical systems was carried out during the first half of this century. It was initiated by Ostwald, who recognized a close relation between electrochemical waves and nerve impulse propagation.[22] As we know today, at a certain level nerve impulse propagation and chemical waves are in fact described by mathematically equivalent equations.[23] Bonhoeffer and Franck continued Ostwald's work.[24–31] They mainly studied activation pulses on iron wires. In view of the fact that the modern concepts of nonlinear dynamics were not yet developed, these remarkable experiments were ahead of their time. Progress in understanding spatial pattern formation had to await the formulation of a theory for temporal self-organization and the development of new techniques that imaged the electrode/electrolyte interface. Both have been achieved only recently. Thus, at present, we are in a position to elucidate the basic mechanism of spatial pattern formation.

The aim of this chapter is to provide a concise discussion of the current understanding of basic principles governing temporal and spatial behavior in electrochemical systems exhibiting dynamic instabilities. The emphasis is on deriving a coherent picture of the theoretical description. In doing so, a hierarchy is built up of models that successively describe more complex behavior, starting with bistability in spatially uniform systems and ending with complex spatiotemporal dynamics. Only electrical models are considered. Furthermore, experimental examples were chosen for detailed discussion only where the relation between experiment and model is unambiguous.

Such an approach is neither compatible with a compilation of the different dynamic behaviors found in one system, because for different dynamic regimes different levels of the theoretical description are adequate, nor can it cover all the different systems that exhibit instabilities. Readers interested in an overview of oscillating systems are referred to the exhaustive review article by Hudson and Tsotsis[1] or an even more recent review article, which is not as comprehensive, by Fahidy and Gu.[32]

Another contemporary and noteworthy review article by Koper follows yet another concept. [20] Koper first stresses the importance of the electric circuit by evaluating, in a rigorous way, the stability of electrochemical systems by frequency response methods. He then thoroughly discusses the dynamics of selected examples, including some semiconductor systems, which are not included in this chapter, with special emphasis on how they relate to the frequency response theory.

The organization of this chapter can be summarized as follows: Section II treats temporal models, which are adequate whenever the system is uniformly parallel to the electrode. It starts with a description of how bistable behavior arises in electrochemical systems. This constitutes a comparatively old result. It is, however, thoroughly explained because it forms the basis of the rest of the chapter. In Sections II.2 and II.3, two distinct mechanisms are discussed that give rise to simple periodic behavior. In each case, a prototype model is first introduced, which can be regarded as a minimal model exhibiting the essential features of oscillators of the respective class. Then, experimental examples that follow this model are reviewed. Since the second type of oscillators is more complex, the analysis of the experimental examples includes a discussion of more realistic models as well as an analysis of the connection of the individual terms of these "physical models" with the terms in the prototype model. Section II.3 summarizes the extent of our knowledge for more complex oscillations, which typically arise in any system belonging to one of these two categories for certain parameter values.

Section III deals with spatial phenomena. The current state of theoretical description is given in Section III.1, and experimental results are compiled in Section III.2. The organization of these two parts is analogous to Section II, that is, first waves in bistable media are discussed and then pattern formation in oscillatory media. Because the investigations of spatial self-organization are still in their infancy, not all theoretical predictions have yet been experimentally verified, and many experiments cannot yet be understood in terms of the underlying physical mechanisms. Hence this section represents a first approach toward a coherent understanding of spatial structures, and a series of open questions is listed at the end.

In the final section, a summary of what has been achieved so far in the understanding of electrochemical self-organization is given.

II. PRINCIPLES OF TEMPORAL PATTERN FORMATION

1. Bistability

As mentioned in the introduction, the electrical nature of a majority of electrochemical oscillators turns out to be decisive for the occurrence of dynamic instabilities. Hence any description of dynamic behavior has to take into consideration *all* elements of the electric circuit. A useful starting point for investigating the dynamic behavior of electrochemical systems is the equivalent circuit of an electrochemical cell as reproduced in Fig. 1. The parallel connection between the capacitor and the faradaic impedance accounts for the two current pathways through the electrode/electrolyte interface: the faradaic and the capacitive "routes." The ohmic resistor in series with this interface circuit comprises the electrolyte resistance between working and reference electrodes and possible additional ohmic resistors in the external circuit. The voltage drops across the interface and the series resistance are kept constant, which is generally achieved by means of a potentiostat.

The current balance of the equivalent circuit readily leads to the general differential equation for that kind of circuitry:

$$CA\frac{d\phi_{\mathrm{DL}}}{dt} + I_{\mathrm{read}}(\phi_{\mathrm{DL}}) = \frac{U-\phi_{\mathrm{DL}}}{R_e}, \tag{1}$$

where C is the (double-layer) capacitance per unit area, A is the area of the capacitor (electrode), and R_e is the sum of all (external) ohmic resistances in series to the working electrode. ϕ_{DL} denotes the potential drop across the double layer, and U is the externally applied voltage. The two terms on the left-hand side (lhs) arise from the two current pathways

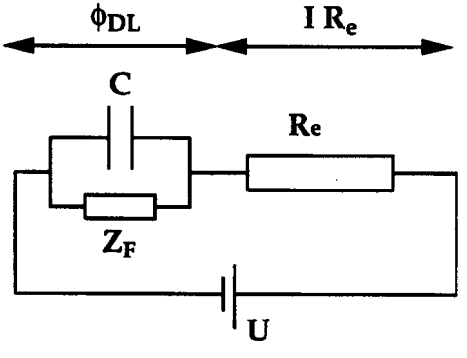

Figure 1. General equivalent circuit of an electrochemical cell with double-layer capacitance C, faradaic impedance Z_F, series resistance (comprising ohmic cell resistance and external resistances) R_e. U is the externally fixed voltage and ϕ_{DL} the potential drop across the double layer.

through the electrode; the right-hand side (rhs) represents the current through R_e, which is equal to the total current through the cell.

The steady states of Eq. (1) [i.e., the solutions of Eq. (1) with $d\phi_{DL}/dt = 0$] can be easily obtained graphically by plotting the characteristics of the external circuit, the load line, and the current-potential characteristics of the electrode/electrolyte interface in one graph [Fig. 2(a)]. Obviously, intersections of both curves are steady states or fixed points of the system, and from Fig. 2(a) it becomes immediately clear that whenever the interfacial characteristic is N-shaped, Eq. (1) possesses three stationary states in a certain range of U and R_e.

When analyzing the stability of the steady states of the circuit, one finds that a steady state, ϕ_{DL}^0, is stable, unless

$$Z_F < 0 \text{ and } R_e > |Z_F|, \text{ with } Z_F^{-1} = \left.\frac{dI_{reac}}{d\phi_{DL}}\right|_{\phi=\phi_{DL}^0}, \tag{2}$$

where Z_F denotes the (zero frequency) faradaic impedance. These conditions have been known for a long time and are often discussed in the literature.[8,15,30,33] The first inequality expresses the fact that any unstable stationary state has to lie on a branch with a negative differential resistance (NDR) of the current-potential curve. The second inequality implies that a steady state can only become unstable if the ohmic resistance of the circuit is larger than the absolute value of the faradaic impedance of the reaction.

Applying these stability criteria to the situation shown in Fig. 2(a), it becomes apparent that whenever the middle branch is unstable (i.e., $R_e > |Z_F|$), there are three fixed points, the two outer ones being necessarily stable (because they lie on a branch with a positive slope). Hence a small perturbation of the middle steady state will drive the system, depending on the direction in which the perturbation occurred, to one of the outer stationary states. This bistability manifests itself in a hysteresis when the external voltage is varied [Fig. 2(b)]. The border of the bistable region is formed by saddle-node bifurcations. In general, a bifurcation occurs if the dynamic behavior of the system changes *qualitatively*. This is, for example, the case if the number or the stability of stationary states or oscillatory solutions changes. At a saddle-node bifurcation, the first of these cases applies: two stationary states merge at the bifurcation point, disappearing when the parameter is changed in one direction and separating when it is changed in the other direction. In Fig. 2(a), a saddle-node bifurcation

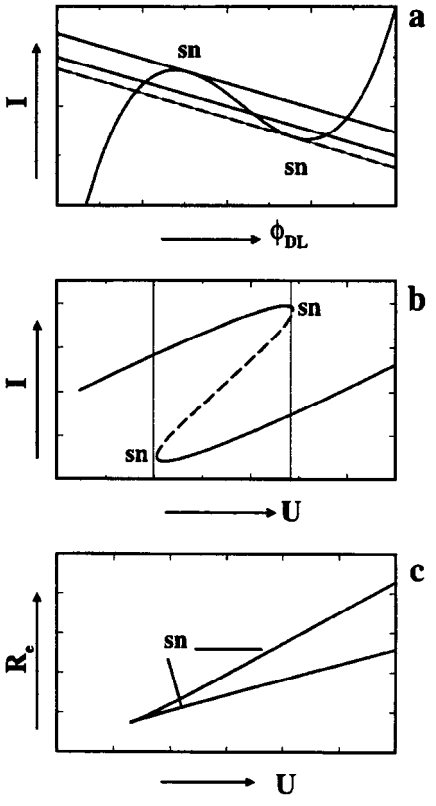

Figure 2. (a) N-shaped current-potential curve and load lines (resulting from the external circuit) for three different values of the external voltage U. The intersections of both curves are steady states. The two outer load lines mark the border of the bistable regime. (b) Bistable region in a current vs. external voltage plot referring to the situation shown in (a). (c) Location of the saddle-node bifurcation (separating monostable and bistable regions) in the U/R_e parameter plane. (sn = saddle-node bifurcation)

corresponds to the degenerate case where the load line and current-potential characteristic coincide at *two* points, and the number of fixed points changes from one to three.

For a given N-shaped current-potential characteristic, there are two parameters that determine the bistable region, R_e and U. In the U/R_e parameter diagram, this region becomes broader while shifting toward larger values of U for increasing R_e, irrespective of the electrochemical reaction [Fig. 2(c)]. Below we will see that this feature is also encountered in all more complicated electrical models that describe simple or complex oscillatory behavior since all of them require an N-shaped polarization curve.

At this point, it appears to be useful to compile the assumptions that have been implicitly made and which enable us to describe the dynamics of the system by the evolution equation of the double-layer potential only.

First, it has been supposed that the faradaic current instantaneously adjusts to a change in the double-layer potential. This means that all other quantities that affect the current, such as concentration of the reactive species and the coverage of adsorbates, are assumed to vary on a time scale that is much shorter than the time scale on which typical variations of the potential occur. In other words, all other quantities are assumed to adjust immediately to their equilibrium values and can be adiabatically eliminated. Second, chemical instabilities have been excluded. In the presence of chemical instabilities, the current is no longer a unique function of ϕ_{DL}, and the state of the system is only defined when taking into account another variable. The absence of chemical instability also implies that a negative differential resistance can only be realized if the current-potential characteristics of the interface exhibit the shape of an N (or multiple Ns) as shown in Fig. 2(a). In contrast, an S-shaped characteristic, being just one example of another characteristic possessing an NDR, would require the existence of a chemical instability.

We now review the possible origins of N-shaped interfacial characteristics that are, as we have seen, essential for the occurrence of instabilities in Eq. (1) and also, as will be demonstrated below, in all other electrical models. Several mechanisms leading to an N-shaped polarization curve have been discussed in various places in the literature. They were collected in a concise way by Koper,[15] whose representation we follow here.

Generally, the reaction current can be expressed as

$$I_{reac}(\phi_{DL}) = n\,F\,A\,k(\phi_{DL})\,c$$

where n is the number of electrons involved in the charge-transfer process, F is Faraday's constant, A is the available electrode area, k is the rate constant, and c is the concentration of the reacting species at the electrode (i.e., at the location of the reaction).* From the expression for the faradaic impedance,

$$Z_F^{-1} = \frac{dI_{reac}(\phi_{DL})}{d\phi_{DL}} = nF\left(ck(\phi_{DL})\frac{dA}{d\phi_{DL}} + Ac\frac{dk(\phi_{DL})}{d\phi_{DL}} + Ak(\phi_{DL})\frac{dc}{d\phi_{DL}}\right)$$

*We use the convention that reduction currents are taken to be negative and oxidation currents positive.

three origins for a negative differential impedance are possible: (1) $dA/d\phi_{DL} < 0$, (2) $dk/d\phi_{DL} < 0$, and (3) $dc/d\phi_{DL} < 0$. All three cases occur in many examples in the literature.

1. *The available electrode area decreases with increasing polarization* if a potential-dependent adsorption of a species occurs that completely inhibits the reaction and the extent of the adsorption increases with increasing overpotential for the reaction. The most prominent example of such an "electrode poisoning" is the formation of oxide layers in many metal dissolution reactions. [34]

2. *The decrease of the electron transfer rate with increasing polarization* can have two different origins: It can be caused by adsorbates that do not totally inhibit a reaction (in which case 1 would apply) but increase the activation energy for the reaction. Extensively studied examples are the reduction reaction of metal ions in the presence of organic agents.[35–37] The negative sign of the potential dependence of the rate constant can also be the result of the potential-dependent desorption of a catalyst. Examples exhibiting this type of negative resistance are certain irreversible reduction reactions at Hg that are made reversible in the presence of halides or halidelike anions such as thiocyanate. [38–42] In these reactions, the role of the anions is to considerably shift the polarographic wave toward the reversible half-wave potential. The catalytic effect of these specifically adsorbing halides is attributed to a surface reaction, such as complexation, that assists electron transfer. For sufficiently negative potentials, the anions become desorbed from the electrode, and the catalytic effect is lost. In this context, the best-studied reactions are the reduction reactions of In^{3+} and Ni^{2+} to metallic In or Ni, respectively.

3. *The decrease of the concentration of the electroactive species with increasing potential* has to be attributed to double-layer effects. As first pointed out by Frumkin,[43] in dilute solutions the electron transfer rate is affected by variations of the potential in the double layer in two ways. The potential in the outer Helmholtz plane, ϕ_2, is due to the extension of the double layer not identical to the potential in the solution (at the end of the double layer), ϕ_{DL}, so that the effective driving force of the reaction is $\phi_{DL} - \phi_2$. Furthermore, the concentration of ionic reactants in the reaction plane, c, is influenced by electrostatic effects and differs from the concentration just outside the double layer, c_0, by a Boltzmann term:

$$c = c_0 \exp(-zF\phi_2/RT) \tag{3}$$

where z is the (signed) charge number of the electroactive species. Hence, $dc/d\phi_{DL}$ can become negative if cations (positive z) are oxidized positive to the point-of-zero charge (pzc) (i.e., if the electrode is charged positively) or anions are reduced negative to the point-of-zero charge at low ionic strength. (For high ionic strength, ϕ_2 becomes negligible.) There are numerous examples of a negative differential resistance during anion reduction and cation oxidation in the literature, many of which are compiled in Ref. 44. The best known of these reactions is perhaps the reduction of peroxodisulfate, studied primarily by Frumkin and his school. [45,46]

Although they appear evident, two points that are essential for the further considerations are explicitly mentioned here. First, the finite series resistance that is necessary to destabilize a steady state implies that the double-layer potential (in this chapter always denoted as ϕ_{DL}) differs considerably from the externally fixed voltage U. We denote as *potentiostatic conditions* operating conditions under which U is fixed but ϕ_{DL}, as well as the current, may evolve in time. Systems in which the external resistance can be neglected (and hence $U \equiv \phi_{DL}$) are called *strictly potentiostatic*. [Obviously, in a strictly potentiostatic system, the double-layer potential does not represent a variable that can vary with time according to Eq. (1) but reduces to a parameter, and any instability in a strictly potentiostatic system is of a chemical nature.] Second, recall that the equivalent circuit describes a galvanostatic system for $R_e \to \infty$ and $U \to \infty$, and thus galvanostatic systems are naturally included in the analysis.

Finally, before discussing oscillatory behavior, it is worth noting that a circuit equivalent to that shown in Fig. 1 also arises in semiconductor physics where a semiconductor device takes on the role of the faradaic impedance and the other elements of the circuit are electronic elements. [47,48] Thus interesting parallels can be drawn between the dynamics of electrochemical and semiconductor systems. Furthermore, stability criteria derived for the latter can be directly applied to electrochemical systems. This is especially interesting for the interaction of S- or Z- shaped current-potential curves with the external circuit, which are not considered here owing to the presence of chemical instabilities. [49]

2. Simple Periodic Oscillations of Type I: Negative Differential Resistance Oscillators

(i) Prototype Model and Bifurcation Behavior

So far, it has been assumed that the dynamic behavior of the electrochemical system is determined by the temporal evolution of the double-layer potential only. All other processes affecting the reaction rate were considered to always be in equilibrium. However, oscillatory behavior requires at least one additional degree of freedom. In the early literature on electrochemical oscillations it was conjectured that slow transport of electroactive species leads to slow variations in their double-layer concentration, and that the latter thus provides the second variable, which in connection with an N-shaped polarization curve, is sufficient to cause oscillations of the current density. This suggestion has been corroborated for cases in which mass transport is dominated by diffusion.[39,42,50–56] It was elaborated for a chemical model by Wojtowicz and Conway,[53] who treated the case of coupling between a diffusion-controlled process with an electrosorption-oxidation reaction. A general mathematical formulation of the electrical model and a detailed analysis of the dynamic behavior are given by Koper.[15] In this article, oscillators complying with this mechanism are called *negative differential resistance* (NDR) oscillators. First the prototype model of NDR oscillators and its dynamic properties are introduced, and then some example experiments in which the characteristics of the oscillator are clearly recognizable are discussed.

We consider here a situation where the mass transport of the electroactive species may become rate determining, but all other processes which control the current-potential characteristics can still adjust rapidly. Thus, the concentration of the electroactive species, c, becomes time dependent. Since we allow only for diffusion, its temporal evolution is given by Fick's second law [i.e., in the case of a planar electrode, by $\partial c/\partial t = D \cdot (\partial^2 c/\partial z^2)$, with the diffusion coefficient D, and z the spatial coordinate perpendicular to the electrode]. At the electrode ($z = WE$), the concentration obeys Fick's first law, $(\partial c/\partial z)\,|_{z=WE} = i_{\text{reac}}/(nF)$. At a certain distance from the electrode, it is assumed that the concentration is at a constant value, c^b, its bulk value (constituting the second boundary condition). The concept of the Nernst diffusion layer underlies this idea.

Obviously, we have to deal with a partial differential equation coupled to our ordinary differential equation [Eq. (1)]. It can be easily shown that

all stationary states are characterized by a linear concentration profile, but all other solutions can only be obtained through tedious numerical calculations. However, the basic physical mechanism giving rise to the first oscillatory instability is maintained when it is assumed that a linear concentration profile across the diffusion layer adjusts instantaneously (i.e., that the concentration profile rapidly relaxes to its steady-state profile). In this case, the partial differential equation reduces to an ordinary differential equation for the concentration at the electrode surface, and the prototype equations for NDR oscillators read

$$C\frac{d\phi_{DL}}{dt} = -nF\,ck(\phi_{DL}) + \frac{U-\phi_{DL}}{R_e A} \tag{4a}$$

and

$$\frac{dc}{dt} = -\frac{2}{\delta}\,ck(\phi_{DL}) + \frac{2D}{\delta^2}\left(c^b - c\right) \tag{4b}$$

where c now denotes the concentration at the electrode, D is the diffusion constant, c^b is the bulk concentration, δ is the thickness of the Nernst diffusion layer, and the other symbols have the same meaning as earlier. Equation (4a) is identical to Eq. (1). The two terms on the rhs of Eq. (4b) describe the decrease in the concentration at the surface of the electrode owing to the reaction, and its increase owing to diffusion from the bulk, respectively. Note that the reaction term is proportional to $1/\delta$, while the diffusion term is proportional to $1/\delta^2$. Hence, for thin diffusion layers, which can be realized, for example, by high rotation rates when working with rotating disk electrodes, replenishing of the concentration becomes much faster than the consumption through the reaction; in this case, the concentration in the double layer takes on its bulk value, and we are back to the bistable system.

For further analysis of Eq. (4), it is advantageous to write the equations in dimensionless form. Transforming the variables according to

$$\frac{c}{c^b} \to c,\ \frac{nF}{RT}\phi_{DL} \to \phi_{DL},\ \frac{2D}{\delta^2}t \to t$$

where R is the gas constant and T the absolute temperature, we obtain the following differential equations:

$$\varepsilon \frac{d\phi_{DL}}{dt} = -ck(\phi_{DL}) + \frac{U - \phi_{DL}}{\rho} \tag{5a}$$

and

$$\frac{dc}{dt} = -ck(\phi_{DL}) + 1 - c \tag{5b}$$

$$\text{with } \varepsilon = \frac{2CRT}{c^b n^2 F^2 \delta} \rho = \frac{c^b D n^2 F^2 R_e A}{\delta RT} \text{ and } U \frac{nF}{RT} \to U,\ k(\phi_{DL}) \frac{\delta}{D} \to k(\phi_{DL})$$

For a given $k(\phi_{DL})$, there are three parameters that determine the dynamic behavior: ε, which describes the ratio of the time scales of potential and concentration changes; *U,* the dimensionless external voltage; and ρ, the dimensionless external resistance. If $k(\phi_{DL}) >> 1$, diffusion is the rate-limiting step while $k(\phi_{DL}) << 1$ indicates reaction control.

Conveniently, an investigation of the dynamic behavior of a set of differential equations starts out with the determination of the fixed points and their stability. The latter is studied by linearizing the system's equation about the steady state and then evaluating the temporal evolution of small perturbations. Denoting the perturbations by $\delta\phi_{DL}$ and δc, in our case the equations read:

$$\begin{pmatrix} \frac{d\delta\phi_{DL}}{dt} \\ \frac{d\delta c}{dt} \end{pmatrix} = \left\{ \begin{matrix} \varepsilon^{-1}\left[-c\frac{dk(\phi_{DL})}{d\phi_{DL}} - \frac{1}{\rho}\right] & -\varepsilon^{-1}k(\phi_{DL}) \\ -c\frac{dk(\phi_{DL})}{d\phi_{DL}} & -k(\phi_{DL}) - 1 \end{matrix} \right\}_{(\phi_{DL}^{ss}, c^{ss})} \begin{pmatrix} \delta\phi_{DL} \\ \delta c \end{pmatrix} = J \begin{pmatrix} \delta\phi_{DL} \\ \delta c \end{pmatrix} \tag{6}$$

whereby the fixed point is at (ϕ_{DL}^{ss}, c^{ss}). Solving a linear set of differential equations is equivalent to calculating the eigenvalues and eigenvectors of the Jacobian matrix *J.* The stability of the fixed point is then uniquely determined by the signs of the eigenvalues of *J.* It is stable if all eigenvalues are negative, and unstable if at least one eigenvalue is positive.

Generally, the eigenvalues depend on the system's parameter and may change their sign when a parameter is varied. Hence, a vanishing eigenvalue indicates a stability change in the stationary state (i.e., a bifurcation). In this context, two bifurcations are of particular importance. At a *saddle-node* (sn) bifurcation, one real eigenvalue becomes 0, and therefore also the determinant of *J.* As mentioned in Section II.1, a saddle-node bifurca-

tion is associated with the merging of two stationary states (a saddle and a node) and hence signifies a multiplicity of steady states.

The second important bifurcation that is connected with a stability change in a stationary state is the *Hopf* bifurcation. At a Hopf bifurcation, the real parts of two conjugate complex eigenvalues of J vanish, and as Hopf's theorem[57] ensures, a periodic orbit or limit cycle is born. A limit cycle is a closed loop in phase space toward which neighboring points (of the kinetic representation) are attracted or from which they are repelled. If all neighboring points are attracted to the limit cycle, it is stable; otherwise it is unstable (see Ref. 57). The periodic orbit emerging from a Hopf bifurcation can be stable or unstable and the existence of a Hopf bifurcation cannot be deduced from the mere fact that a system exhibits oscillatory behavior. Still, in a system with a sufficient number of parameters, the presence or absence of a Hopf bifurcation is indicative of the presence or absence of stable oscillations.

The most important results of the linear stability analysis, Eq. (5), are compiled. First, consider under what conditions the fixed points (ϕ_{DL}^{ss}, c^{ss}) of Eq. (5) are stable. A steady state is stable if Tr $(J) < 0$ and Det $(J) > 0$, where Tr (J) is the trace and Det (J) the determinant of J, and thus in our case if

$$\mathrm{Tr}(J) < 0 \quad \Leftrightarrow \quad -\frac{dk(\phi_{DL}^{ss})}{d\phi_{DL}} < \frac{1}{c_{ss} \cdot \rho} + \frac{\varepsilon}{c_{ss}}\left[1 + k\left(\phi_{DL}^{ss}\right)\right] \tag{7a}$$

and

$$\mathrm{Det}(J) > 0 \quad \Leftrightarrow \quad -\frac{dk(\phi_{DL}^{ss})}{d\phi_{DL}} < \frac{\left[1 + k\left(\phi_{DL}^{ss}\right)\right]}{\rho}\frac{1}{c^{ss}} \tag{7b}$$

The right-hand sides of both inequalities are always positive irrespective of the values of the parameters [as $k(\phi_{DL}) > 0$]. Hence, a steady state (ss) with a positive slope in the current-potential characteristic, $dk(\phi_{DL}^{ss})/d\phi_{DL} > 0$, is stable, independent of the value of the parameters.

On the other hand, depending on the resistance ρ and the ratios of the time scales ε, steady states with a negative faradaic impedance can become unstable. If Det $(J) < 0$, the stationary state is always a saddle point. From Eq. (7b) it is evident that provided $dk(\phi_{DL}^{ss})/d\phi_{DL} < 0$, the determinant is negative if the resistance ρ exceeds a critical value, ρ_{cr}. At this critical value, Det $(J) = 0$, which is the condition for a saddle-node bifurcation.

Hence, and not surprisingly, just as for the one-dimensional system (Eq. 1), Eq. (5) predicts a bistable behavior for a sufficiently large series resistance.

However, Eq. (7) reveals that a steady state of the NDR oscillator [Eq. (5)] can also undergo a Hopf bifurcation, which occurs if $\mathrm{Tr}\,(J) = 0$ and $\mathrm{Det}\,(J) > 0$. These conditions can be fulfilled if ρ is not too large [otherwise $\mathrm{Det}\,(J) < 0$] and ε is sufficiently small. Clearly, the first condition excludes a Hopf bifurcation under galvanostatic conditions and in fact as becomes clear later, oscillatory behavior is not possible under these conditions. As mentioned, a small value of ε means that upon a perturbation of the steady state, the potential reacts faster than the concentration.

The existence of oscillations can be illustrated in the $\phi_{DL} - c$ phase plane (Fig. 3). The two lines represent the nullclines, that is, the solutions of $d\phi_{DL}/dt = 0$ (the ϕ_{DL} nullcline) and $dc/dt = 0$ (the c nullcline). Any intersection of the nullclines is a steady state. If the ϕ_{DL} nullcline possesses a negative slope at the steady state, as in Fig. 3, the vector component that

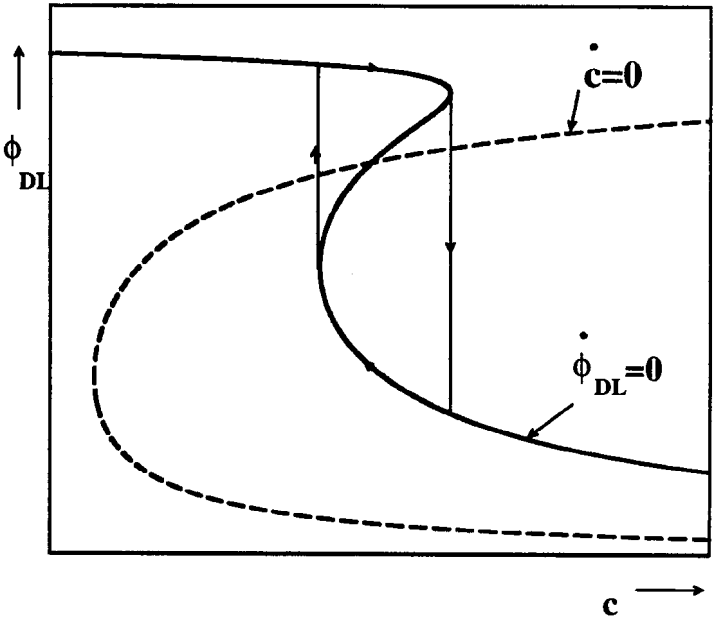

Figure 3. Nullclines of Eq. (5) for a parameter value at which a stable limit cycle exists.

defines the direction in which ϕ_{DL} changes in the neighborhood of the steady state points away from it ($d\phi_{DL}/dt > 0$ to the left of the ϕ_{DL} nullcline and $d\phi_{DL}/dt < 0$ to the right of it). In contrast, the corresponding vector component, defining the direction of concentration change, points toward the steady state ($dc/dt > 0$ to the left of the c nullcline and $dc/dt < 0$ to the right of it). For small ε, the change of ϕ_{DL} is much faster than that of c, and it is easy to see that the destabilizing dynamics of ϕ_{DL}, together with a small ε, result in oscillations. Starting close to (but not at) the steady state, ϕ_{DL} rapidly increases at a nearly constant concentration until the system has reached a point on the ϕ_{DL} nullcline. Now c slowly increases (as on this part of the ϕ_{DL} nullcline $dc/dt > 0$) until the state of the system reaches the end of the high-potential branch. Here a fast change of the ϕ_{DL} dynamics sets in again, quickly leading the system to the low-potential branch of the ϕ_{DL} nullcline on which c slowly decreases. Thus, the system evolves toward the end of this branch, triggering a fast increase of ϕ_{DL}.

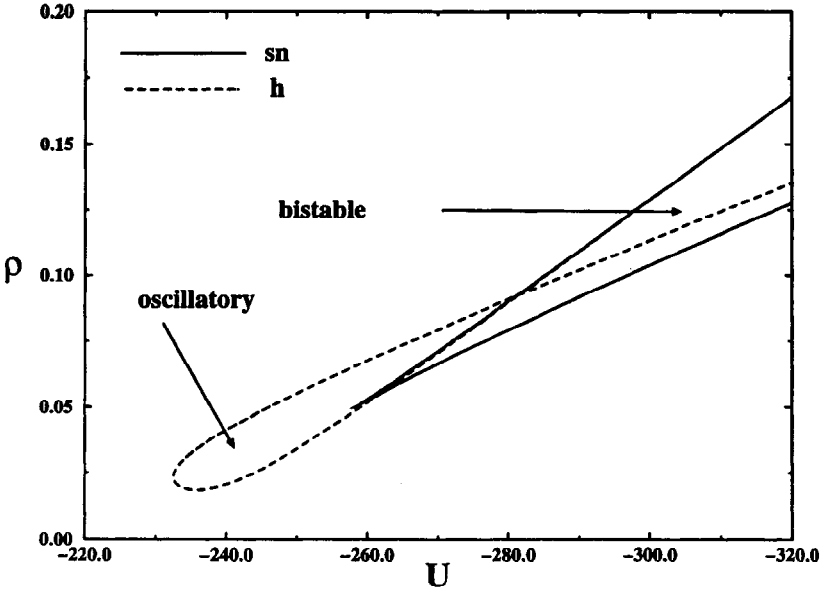

Figure 4. Two-parameter skeleton bifurcation diagram of the NDR oscillator model [Eq. (5)] in the U/ρ parameter plane. Roughly, the locations of saddle-node (sn) and Hopf (h) bifurcations divide the parameter plane into regions with monostable, bistable, and oscillatory behavior, respectively.

Consequently, the system again acquires a state on the upper branch, and the game starts over.

The results discussed can be found in Fig. 4, where the oscillatory and bistable parameter regions of Eq. (7) are depicted in the ρ/U parameter plane. The bistable region, enclosed by saddle-node bifurcations, possesses exactly the same characteristics as the one-variable model: It has a V-shaped form that opens toward high values of ρ and U [see Fig. 2(c)]. The curve of Hopf bifurcations encircling the oscillatory region loops around the tip of the saddle-node V, extending toward values of ρ and U lower than those of the bistable regime. At the left side of the V, the Hopf bifurcation line runs very close to the saddle-node curve. In fact, the Hopf curve ends at a point in the saddle-node curve where both bifurcations coalesce. At this point, the Jacobian matrix possesses two eigenvalues with a vanishing real and a vanishing imaginary part, representing a doubly degenerate situation which is known as a Takens–Bogdanov (TB) bifurcation.

The interesting aspect of such higher degenerated bifurcations is that in general, they possess universal dynamic behavior in their neighborhood, which also involves global bifurcations that cannot be detected with a simple linear stability analysis. The existence of global bifurcations can be deduced from knowledge of the existence of a higher degenerate bifurcation. For instance, the existence of a TB point ensures, besides the existence of a saddle node and a Hopf bifurcation, the existence of a so-called saddle-loop bifurcation. At this global bifurcation, there exists one curve in phase space that starts and ends in a saddle point. The formation of such a "homoclinic loop" generates or destroys a limit cycle. Thus the complete two-parameter bifurcation diagram is much more complex than Fig. 4 suggests. A detailed analysis[15] revealed that it exhibits qualitatively the same fine structure as the cross-shaped phase diagram that is often found in chemical oscillators.[58] As was shown by Guckenheimer,[59] its complete bifurcation structure is very intricate. However, many bifurcations occur in a tiny parameter region so that it appears to be very unlikely that the fine structure of the bifurcation diagram can be resolved experimentally. From this point of view, the skeleton structure shown in Fig. 4 contains the most important information.

At this point, it is worth noting that besides slow mass transfer, there are other mechanisms conceivable that lead mathematically to equivalent equations, and thus can be understood within the same framework. The common feature of these mechanisms is that in the expression for the

reaction current there appears a time-dependent quantity that *does not depend on the electrode potential.* For example, consider a reaction that takes place via an adsorbed state and let the adsorption process be slow[17] but the mass transfer sufficiently fast that the concentration in front of the electrode is nearly constant. A simple model complying with this mechanism is described by the following dimensionless equations:

$$C\frac{d\phi_{DL}}{dt} = -nFk(\phi_{DL})\,\theta + \frac{U - \phi_{DL}}{R_e A} \tag{8a}$$

and

$$\frac{d\theta}{dt} = k_a(1-\theta) - k_d\,\theta - k(\phi_{DL})\,\theta \tag{8b}$$

where θ is the coverage of the adsorbate and k_a and k_d denote the rate constants for adsorption and desorption, respectively. All other symbols have the same meaning as before. If desorption can be neglected, the mathematical structure of Eq. (8) is equivalent to Eq. (5), yielding the same bifurcation diagram.

(ii) Experimental Examples

It was pointed out earlier that oscillations in NDR oscillators are linked to three features of the electrochemical system: (1) an N-shaped steady-state polarization curve; (2) a resistance in series with the working electrode, which must not be too large; and (3) a slow recovery of the electroactive species, in most cases due to slow mass transport. Hence, for every system that was discussed in the context of the possible origin of N-shaped characteristics, conditions can be established under which stable limit cycles exist, and for most of the systems mentioned, oscillations were in fact observed. This unifying approach was first put forth by Koper and Sluyters, and numerous experimental examples of electrochemical oscillations that can be deduced according to this mechanism are discussed in Ref. 60.

Here only a few examples are mentioned. There are many systems described in the literature in which oscillations are connected with the inhibition of a reaction by a (mostly organic) adsorbate.[35–37,60–62] An impressive systematic study of oscillations during the reduction of Cu^{2+} on Hg in the presence of homologous alcohols, phosphonium halides,

Table 1
Parameters of Current Oscillations Based on the Inhibited Charge Transfer of Cu^{2+}/Cu^{0} (Hg) in the Presence of Different Types of Inhibitors

Inhibitor	$-E_{tr}$ without R (mV)	$-E_{tr}$ with R (mV)	(di/dE) without R (μA/V)	External R (kΩ)	f (s^{-1})	$c_{inhibitor}$ (mol·dm^{-3})
C_4H_9OH	112	152	–5.9	30	1	0.3 c_s [a]
$C_5H_{11}OH$	285	320	–2.4	30	3	0.1 c_s
$C_6H_{13}OH$	250	270	–7.8	30	1	0.2 c_s
$C_7H_{15}OH$	250	306	–2.8	30	1.3	$7\cdot10$
$C_8H_{17}OH$	240	291	–4.0	30	0.2–0.3	$2\cdot10^{-4}$
$[(C_6H_5)_3\cdot CH_3\cdot P]ClO_4$	350	438		100	0.3–0.5	$2\cdot10^{-4}$
		400	–8.55	80		$2\cdot10^{-4}$
		330		40		$4\cdot10^{-4}$
$[(C_6H_5)_3\cdot C_2H_5\cdot P]\ ClO_4$	350	430	–7.85	100	0.3–0.5	$2\cdot10^{-4}$
		390		70		
$[(C_4H_9)_4\cdot P]\ ClO_4$	250	400	–20.35	40	1	$2\cdot10^{-4}$
		350		30	1	
$[(C_4H_9)_4\cdot N\ ClO_4$	300	410	–18.5	70	0.3	$2\cdot10^{-4}$
		410		60	1	
$[(C_6H_5)_3\cdot C_2H_5\cdot P]Br$	1300	1340	–36	50	0.15	$2\cdot10^{-4}$
$(C_6H_5)_2\cdot C_2H_5\cdot PO$	250	300	–15.99	50	0.2	$2\cdot10^{-4}$
		300		40	0.2	
		317		30	0.25	
$(C_3H_7)_2\cdot C_6H_5\cdot PO$	285	350	–20	70	0.2	$2\cdot10^{-4}$
$(C_4H_8)_2\cdot C_6H_5\cdot PO$	130	200	–98	60	0.2	$2\cdot10^{-4}$
$(C_2H_5)_2\cdot C_6H_5\cdot PO$	280	322	–3.97	30	1	$4.6\cdot10^{-3}$
$(C_8H_{17})_3\cdot(CH_3)_2\cdot PO$	250	291	–4.6	30	0.25...0.33	10^{-4}
Camphor $(C_{10}H_{16})O$	375	425	–33	30	0.25	$2\cdot10^{-4}$

Source: After H.-D. Dörfler, *Nova Acta Leopoldina,* NF **61** (268) 25–49 (1989), with permission of the author and Leopoldina.

Notes: Transition potentials E_{tr} with and without external resistance, increase di/dE of the dc polarographic i/E curves in the potential region $di/dE < 0$, oscillation frequency f, inhibitor concentration c. Acting inhibitors: alcohols, phosphonium salts, phosphine oxides, and camphor. Supporting electrolyte: 0.1 mol l^{-1} H_2SO_4.

[a] c_s = concentration of saturation in mol·dm^{-3}.

phosphine oxides, and camphor was published by Dörfler.[61] A list of conditions under which these inhibitors induce oscillations is reproduced in Table 1.[61] Though at the time the table was published, the connection between an N-shaped current-potential characteristic, mass transport, and the involvement of a series resistor was not yet clearly established, Dörfler emphasizes that all of the systems exhibit a negative polarization slope and that a series resistance is necessary for oscillatory behavior. Hence it can be assumed that the oscillations follow exactly the mechanism outlined above.

For two systems, the reduction of $S_2O_8^{2-}$ and the reduction of In^{3+} in the presence of SCN^- at Hg, investigations of the dynamic behaviors of the systems are detailed enough to allow a rough comparison of experimental and predicted bifurcation behavior. Coinciding bifurcation diagrams are a much better indicator of whether a model correctly captures the essential mechanistic steps than a comparison of the dynamic behavior at isolated points in parameter space or of oscillation forms. These systems are set out in more detail below.

(a) Reduction of peroxodisulfate

Current oscillations during the reduction of multiply charged anions for which the formation of passivating films could be excluded, such as

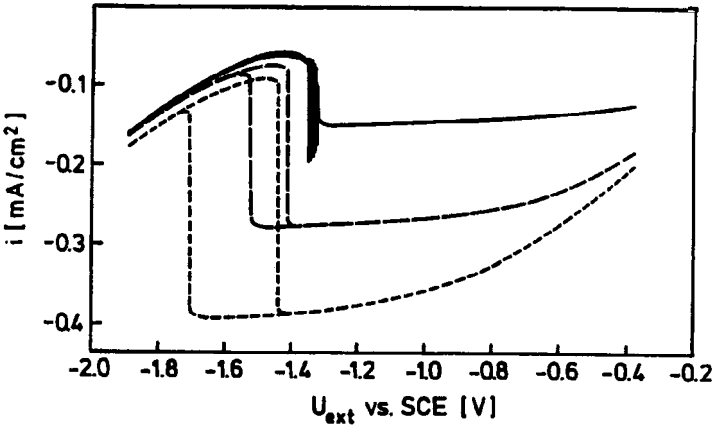

Figure 5. Current-voltage curves of a rotating Ag electrode in a solution containing 1 mM $Na_2S_2O_8$ and 0.5 mM Na_2SO_4 (pH 5) at three different rotation rates, f, of the electrode: solid line, f = 5 Hz; long dashed line, f = 20 Hz; short dashed line, f = 40 Hz. (After Flätgen and Krischer.[149])

$S_2O_8^{2-}$, $PtCl_4^{3-}$, CrO_4^{2-}, $Fe(CN)_6^{3-}$, and $S_4O_6^{2-}$ at low ionic strength, became famous through the work of Frumkin and his school.[45,46,63] Negative to the point-of-zero charge, the anions are electrostatically repelled. As explained earlier, at low ionic strength, this gives rise to a negative differential resistance. In accordance with the fact that this phenomenon should be independent of the electrode material, oscillations were observed for a variety of metal electrodes, such as Hg, Cu, Au, Pt, and Ag. In a semiquantitative model based on equations such as Eq. (4), where the potential ϕ_2 [see Eq. (3)] was determined from the double-layer charge density, the negative faradaic impedance according to Frumkin's correction (see above) was indeed obtained and oscillatory as well as bistable regions determined.[56,64]

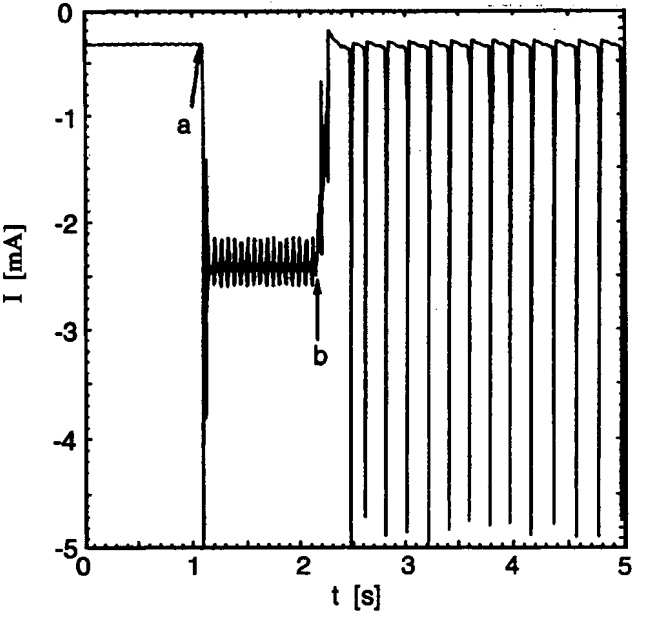

Figure 6. Coexistence of stationary behavior (between 0 and 1.1 s) and oscillations (from 2.4 s on) during the reduction of $S_2O_8^{2-}$ at a rotating Pt electrode, rotation rate f = 20 Hz. Between points a and b the system was perturbed by enhancing the rotation frequency to about 150 Hz, triggering the transition from the fixed point to the limit cycle. (After Wolf *et al.*[56] with the kind permission of VCH Publishers.)

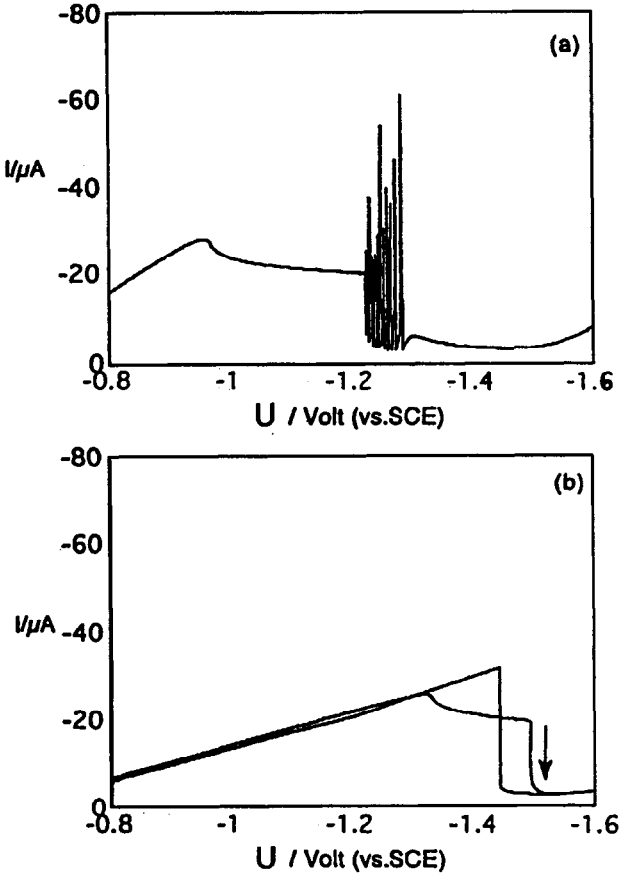

Figure 7. Voltammograms of the In^{3+} reduction on an HMDE from SCN^- solution in the presence of an external resistor R_e. (a) R_e = 10 kΩ, (b) R_e = 30 kΩ (Electrolyte: 9 mM In^{3+}, 5 M NaSCN, pH 2.9, T = 25 °C.) (From M. T. M. Koper, in *Advances in Chemical Physics,* Vol. XCII, I. Prigogine and S. A. Rice, eds., Vol. 161, 1996. Copyright 1996, John Wiley & Sons, Inc. Reprinted by permission of John Wiley & Sons, Inc.)

Figure 5 shows experimental cyclic voltammograms of the reduction of $S_2O_8^{2-}$ at a rotating Ag electrode for three different rotation rates. For high rotation rates, which correspond to a thin diffusion layer and hence to a small value of δ in Eq. (4b), the system exhibits bistable behavior. The

width of the bistable region becomes smaller and shifts toward more positive voltages for decreasing rotation rates. Finally, for the slowest mass transport, the system exhibits oscillations around the branch that has a negative polarization slope. The dependence of dynamic behavior on the rotation rate confirms the essential role of mass transfer in the emergence of oscillatory instability. Furthermore, the experimental δ/U phase diagram was reproduced in the above-mentioned model calculations.[64]

One of the rare experimental examples demonstrating the coexistence of a periodic and a stationary solution is reproduced in Fig. 6. The data were obtained during the reduction of $S_2O_8^{2-}$ at a rotating Pt electrode.[56] Again, the results are in agreement with model calculations.[56]

(b) Reduction of In^{3+} in the presence of SCN^-

The prototype model [Eq. (4)] was originally formulated for the reduction of In^{3+} in the presence of SCN^- on Hg,[33] a system whose dynamic behavior was thoroughly investigated, first by Tamamushi *et al.*[65,66] and de Levie,[39] and later in much detail by Koper, Sluyters, and

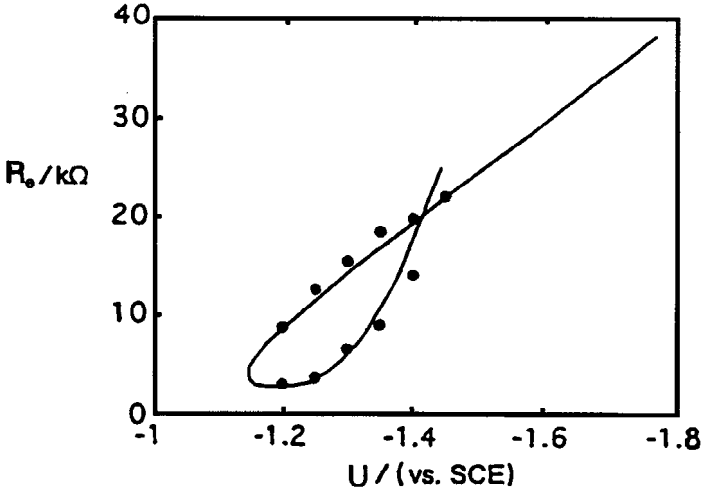

Figure 8. Line of Hopf bifurcations in the R_e/U parameter plane for the In^{3+} reduction on an HMDE from SCN^- solution. (Reprinted from M. T. M. Koper, *J. Electroanal. Chem.* **409**, 175–182, 1996, with kind permission from Elsevier Science, Lausanne, Switzerland.)

Gaspard.[42,60,67,68] In Fig. 7 two cyclic voltammograms of the In^{3+}/SCN^- system are displayed. The two curves manifest the influence of the series resistance discussed: The upper voltammogram, in which a small external resistance is connected in series to the working electrode, exhibits oscillatory behavior. Note that the oscillations again occur on the negative branch of the current-voltage curve, as is typical for NDR oscillators. If a larger series resistance is used, the oscillations become transformed into bistable behavior [Fig. 7(b)]. Figure 8 displays the experimentally determined location of the Hopf bifurcation in the R_e/U parameter plane. The Hopf bifurcations lie on a loop whose orientation closely resembles that of the calculated bifurcation diagram (see Fig. 4).

3. Simple Periodic Oscillations of Type II: Hidden Negative Differential Resistance Oscillators

(i) Prototype Model and Bifurcation Behavior

As discussed in the preceding section, a characteristic feature of NDR oscillators is that they possess only one potential-dependent process, the electron transfer reaction. Systems of this class oscillate under potentiostatic but not under galvanostatic conditions. When a sufficiently large series resistance is present, the oscillations occur in the current-voltage curve around a branch with a negative slope in the steady-state polarization curve. Another class of electrochemical oscillators is known whose mechanism involves two different potential-dependent processes. These systems also oscillate under galvanostatic conditions, and the oscillations appear around a branch of the steady-state polarization curve having a positive slope. However, it turns out that under certain conditions, also in this type of oscillator, the charge-transfer rate, $k(\phi_{DL})$, decreases with increasing potential, and hence $dk(\phi_{DL})/d\phi_{DL} < 0$. The presence of the second potential-dependent process ensures that the slope of the steady-state polarization curve in the region where the oscillations occur becomes positive. Koper and Sluyters[17] used the expression "hidden" negative charge-transfer resistance to characterize the faradaic impedance behavior. In this chapter we use this term and name this class of oscillators *hidden negative differential resistance* (HNDR) oscillators.

First a prototype model of HNDR oscillators is introduced in which special emphasis is put on the essential mechanistic features of such oscillators. Thereafter, emphasis is transferred to two especially transpar-

ent experimental examples—the oxidation of hydrogen in the presence of certain electrosorbing cations and anions, and the oxidation of formic acid.

In order to derive the prototype model, consider the following situation. Assume that an electrolyte contains two species, the electroactive species, E, which is either oxidized or reduced, and a second species, P, with a potential-dependent adsorption isotherm. Furthermore, suppose that the isotherm of P is such that the coverage decreases with increasing overpotential for the conversion of E, and that the reaction rate of E decreases with increasing coverage of P. For the moment, this mechanism might appear somewhat artificial, but in fact as is demonstrated later, there are many electrochemical oscillators that operate in an analogous way. The following set of equations represents the simplest formulation of this mechanism:

$$C\frac{d\phi_{DL}}{dt} = -nFk_E(\phi_{DL})(1-\theta) + \frac{U-\phi_{DL}}{R_e A} \tag{9a}$$

and

$$\frac{d\theta}{dt} = k_P\left[\theta_0(\phi_{DL}) - \theta\right] \tag{9b}$$

where θ denotes the coverage of species P and $\theta_0(\phi_{DL})$ the potential-dependent equilibrium value of θ. Thus the term $[\theta_0(\phi_{DL}) - \theta]$ represents the deviation of the actual coverage from its equilibrium value, and the rate constant k_P determines how fast the coverage relaxes to its equilibrium value. Equation (9a) coincides with Eq. (4a) with one exception: The reaction current is proportional to the (time-dependent) free adsorption sites per unit area $(1 - \theta)$. Note that $k(\phi_{DL})$ in Eq. (4a) has been termed $k_E(\phi_{DL})$ here.

For further analysis, we rewrite the equation in a dimensionless form. Using the following transformations, $k_P t \rightarrow t$, $(nF/RT)\phi_{DL} \rightarrow \phi_{DL}$, $(nF/RT)U \rightarrow U$, the equations read:

$$\varepsilon\frac{d\phi_{DL}}{dt} = -k(\phi_{DL})(1-\theta) + \frac{U-\phi_{DL}}{\rho} \tag{10a}$$

and

$$\frac{d\theta}{dt} = \theta_0(\phi_{DL}) - \theta \tag{10b}$$

with the ratio of the time scales $\varepsilon = (CRTk_p)/(n^2F^2k_0)$ and the dimensionless resistance $\rho = (A\,n^2\,F^2\,R_e\,k_0)/(RT)$ where $k_E(\phi_{DL})$ has been written as $k_E(\phi_{DL}) = k_0 k(\phi_{DL})$, $k(\phi_{DL})$ (denoting the dimensionless, potential-dependent part of the reaction rate, the dimension being incorporated in the nonvariable part, k_0.

We are interested in the oscillatory solutions of Eq. (10). Hence we start the analysis of the dynamic behavior of the model by deriving the conditions for a Hopf bifurcation [Tr $(J) = 0$ and Det $(J) > 0$, J being the Jacobian matrix]:

$$\mathrm{Tr}(J) = 0 \rightarrow -\frac{dk(\phi_{DL}^{ss})}{d\phi_{DL}} = \left(\varepsilon + \frac{1}{\rho}\right)\left(1 - \theta_0^{ss}\right)^{-1} \tag{11a}$$

and

$$\mathrm{Det}(J) > 0 \rightarrow \frac{dk(\phi_{DL}^{ss})}{d\phi_{DL}}(1 - \theta^{ss}) + \frac{1}{\rho} > \frac{d\theta_0^{ss}}{d\phi_{DL}}k(\phi_{DL}^{ss}) \tag{11b}$$

(The superscript ss indicates that the derivatives are taken at the steady state.) The first equation requires that $dk/d\phi_{DL} < 0$; that is, also in this class of oscillators, a Hopf bifurcation is linked to a real negative impedance. Since we assume that the coverage decreases with increasing electrode potential, $d\theta/d\phi_{DL} < 0$, the second condition can be simultaneously fulfilled, depending on the other parameter values. Two of them are worth discussing. First it can be seen that ε has to be sufficiently small. In physical terms this means that for oscillations to occur, the adjustment of the equilibrium coverage θ_0 has to take place on a slower time scale than the changes of the potential. This implies that the zero-frequency impedance becomes positive, and the negative current-potential characteristic of the fast process manifests itself in a real negative impedance for nonzero perturbation frequencies.[19] From a dynamic point of view, this condition is equivalent to the requirement that the destabilizing process has to be faster than the stabilizing one.* Second, in contrast to the NDR model, there exists no upper threshold of ρ, and thus this mechanism also allows oscillations to arise under galvanostatic conditions.

The way in which the main ingredients of the model—the N-shaped current-potential characteristics of the · charge transfer process and the

*This requirement was illustrated for NDR oscillators with the help of nullclines (see Fig. 3).

inhibition of the reaction through adsorption of another species—interact is illustrated in Fig. 9. Figure 9(a) displays an example of a combination of a steady-state polarization curve in the absence of species P (dashed curve) and an equilibrium coverage of P (solid curve) that admits a Hopf bifurcation. The crucial feature is that the inhibitor coverage decreases in a potential region where the polarization slope of the inhibitor-free system is negative. Figure 9(b) shows how the stationary current-potential curve is modified in the presence of the inhibitor. The reaction sets in only if the equilibrium coverage of the inhibitor decreases. Hence, part of the negative differential resistance of $k(\phi_{DL})$ is hidden; only if most of the inhibitor has become desorbed does the effect of the negative faradaic impedance become distinguishable.

The dashed line in Fig. 9(b) denotes stationary states that are unstable under galvanostatic control, and the bars indicate the potential region in which oscillations occur. The oscillatory region is bordered by a Hopf bifurcation at low current densities and a saddle-loop bifurcation at high current densities. At a saddle-loop bifurcation, a limit cycle is destroyed through a collision with a saddle point, and it is preceded by progressively prolonged oscillation periods that diverge upon the collision with the saddle point.

As can be seen from Fig. 9(b), the limit cycle coexists with a stationary state at high over-potentials. The latter is the only attractor after the saddle-loop bifurcation. Hence, when the current density is increased above the value of the saddle-loop bifurcation, the potential jumps to a steady state far in the anodic region. Once the system has acquired the anodic steady state, it will stay on this branch as the current density is lowered until the stationary state disappears in a saddle-node bifurcation. Although, of course, the sequence of bifurcations depends on the remaining parameters, it is the most frequently observed scenario, usually persisting in a wide range of parameters.

To summarize the typical features of HNDR oscillators, they exhibit oscillatory behavior on a branch with a positive characteristic under galvanostatic as well as potentiostatic conditions when a sufficiently large series resistance is involved. At low current densities, the oscillations characteristically set in through a Hopf bifurcation; they are predominantly destroyed by a saddle-loop bifurcation at high current densities; and they coexist with a stable stationary state at much more anodic values and hence are associated with a hysteresis.

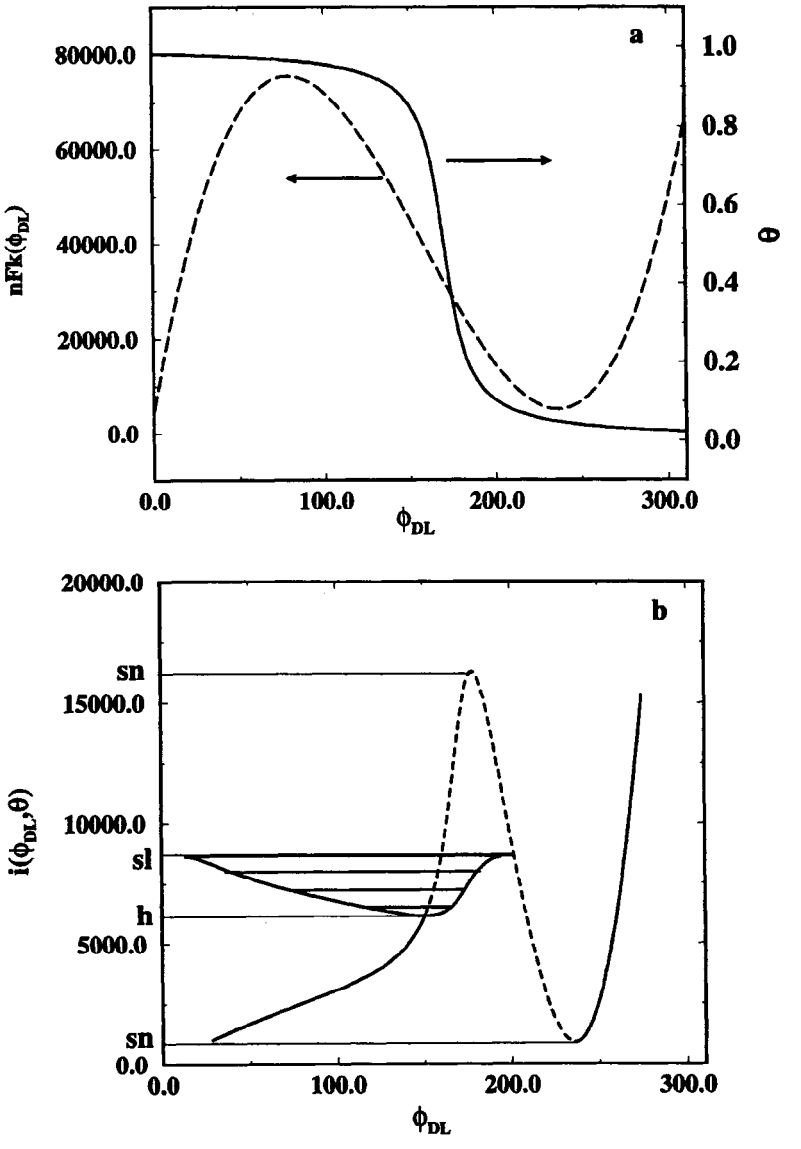

Figure 9. (a) Example of a combination of reaction current $k(\phi_{DL})$ (dashed curve) in the absence of an inhibiting species [Eq. (10a), $\theta = 0$] and an equilibrium coverage $\theta_0(\phi_{DL})$ that admits a Hopf bifurcation (solid curve). (b) Stationary polarization curve of Eq. (10). The dashed line indicates where the stationary state becomes unstable under galvanostatic conditions. The vertical bars display the amplitudes of the oscillations. sn, saddle node bifurcation; sl, saddle loop bifurcation; h, Hopf bifurcation.

In an experiment, not all of the features might be clearly visible. In particular, the increase in period close to the saddle-loop bifurcation often occurs in such a brief interval that it is easily missed. Furthermore, the stationary state at high overpotentials commonly lies at such positive values that undesired side reactions, such as oxidation of the electrode, take place. Thus, often an experimentalist will avoid crossing the saddle-loop bifurcation and only investigate the first branch of the diagram.

Just as a negative differential resistance can have different chemical origins, there are different reaction schemes possible that possess the characteristic features of HNDR oscillators. Another hypothetical mechanism discussed in the literature [17,19] is the potential-dependent adsorption of the reactant, that is, the following reaction steps are considered:

$$X_{sol} \rightarrow X_{ads} \rightarrow P + ne^-$$

where X_{sol} denotes the species in front of the electrode and X_{ads} the adsorbed species, which react to form the product P from the adsorbed state. This mechanism is described by the following equations:

$$\varepsilon \frac{d\phi_{DL}}{dt} = -k(\phi_{DL})\,\theta + \frac{U - \phi_{DL}}{\rho} \tag{12a}$$

and

$$\frac{d\theta}{dt} = k_a(\phi_{DL})\,(1-\theta) - k(\phi_{DL})\,\theta \tag{12b}$$

where k_a is the rate constant for adsorption. Since the reaction requires adsorbed species, oscillations become possible if the adsorption constant k_a increases with potential so that the adsorption takes on significant rates only at potentials at which the rate constant $k(\phi_{DL})$ exhibits a negative slope with respect to potential. In the following paragraphs, two experimental examples with a very transparent mechanism are discussed in detail.

(ii) Experimental Examples

(a) H_2 oxidation in the presence of electrosorbing metals and halides

The oxidation of H_2 on Pt in the presence of electrosorbing metals, such as Cu^{2+}, Ag^+, Cd^{2+}, or Bi^{3+}, and strongly adsorbing anions, such as

Cl^- or Br^-, constitutes the first experimental example where the importance of the hidden negative differential resistance for oscillatory behavior was recognized. [69,70] Furthermore, the individual steps of the oscillation mechanism can easily be studied separately, allowing assignment of the essential features of the mechanism. This system therefore represents an ideal experimental model for illustrating the properties of HNDR oscillators.

Oscillations during H_2 oxidation have been observed under various conditions since the early 1930s[71–74] and have been thought for a long time to be linked to oxide formation or dissolution of H into the electrode material. Horanyi and Visy[71] were the first to deliberately add different electrosorbing cations to the electrolyte. They demonstrated that in the presence of such metal ions, the oscillations are associated with the underpotential deposition of the corresponding metals. Kodera and coworkers used the system some years later and proposed a mechanism for the oscillations that is based on a chemical instability, namely a bistable adsorption isotherm that is due to attractive interactions between the deposited metal atoms.[7 5] However, from extensive studies on the underpotential deposition of various metals on Pt, the existence of a bistable isotherm can meanwhile be excluded. Thus the model has to be rejected. A convincing mechanism giving rise to the oscillations was proposed recently by Krischer *et al.,*[69,70] and their argument is presented below.

First, consider the behavior of H_2 oxidation under potentiostatic conditions in a solution with high conductivity, that is, with almost vanishing ohmic resistance. Figure 10 displays three cyclic voltammograms obtained at a comparatively slow scan rate in three different electrolytes: (1) H_2-saturated sulfuric acid, (2) H_2-saturated sulfuric acid containing a small amount of Cl^-ions, and (3) H_2-saturated sulfuric acid containing small amounts of $Cl^-$and Cu^{2+} ions. In pure sulfuric acid (curve a), the hydrogen oxidation current is practically independent of potential, reflecting the large rate constant of H_2 oxidation on Pt, which leads to diffusion-controlled reaction rates at a relatively low overpotential. As can be seen in curve b, the addition of Cl^- causes a considerable decrease in the current with increasing potential. This negative polarization slope is attributed to the inhibition of H_2 oxidation by specifically adsorbed Cl^- ions. Owing to the negligible catalytic activity of Cu for H_2 oxidation, the additional presence of Cu^{2+} ions (curve c) finally leads to a nearly complete suppression of the H_2current cathodic to potentials at which the underpotential deposition of Cu^{2+} is completed, that is cathodic to about

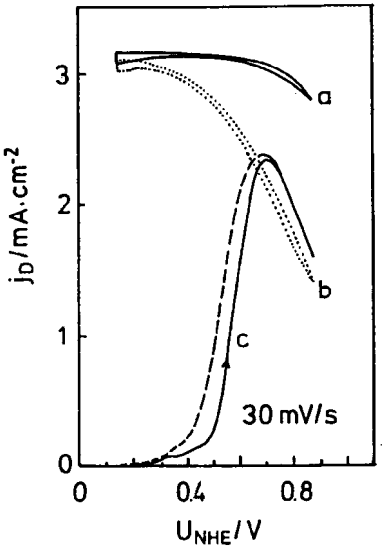

Figure 10. Cyclic voltammograms of a rotating Pt disk in three different electrolytes and a comparatively slow scan rate (30 mV/s): (a) 0.5 M H_2SO_4, H_2 sat.; (b) 0.5 M H_2SO_4, H_2 sat., 10^{-2} M Cl^-; (c) 0.5 M H_2SO_4, H_2 sat., 10^{-2} M Cl^-, 5×10^{-5} M Cu^{2+}. (After Krischer *et al.*[69])

400 mV for the conditions of Fig. 10(c). The increase in the hydrogen current marks the beginning of desorption of the Cu layer, and the current takes on the value for the Cu-free solution (curve b) if all the Cu has been desorbed from the electrode. The small hysteresis in the anodic and cathodic scan in curve c is due to the slow formation of the Cu monolayer and thus is of a kinetic nature.

When comparing curves b and c in Fig. 10, we recognize two features which, as discussed earlier, are essential parts of the mechanisms of HNDR oscillators. (1) The system $H_2/Cl^-/H_2SO_4$ possesses a negative faradaic impedance caused by Cl^- adsorption. (2) This negative impedance is hidden at cathodic potentials due to Cu underpotential deposition, which provides a second potential-dependent process that affects the reaction rate. A third requirement for oscillations to occur is that the process leading to the negative impedance occurs on a faster time scale than the potential-dependent step that hides the negative faradaic impedance. Applied to our example, this means that Cl^- adsorption and desorption should be much faster than Cu deposition and dissolution. Figure 11 nicely illustrates that this is in fact the case.

The three current-potential curves in Fig. 11 were obtained for the same solutions as in Fig. 10, but at a much faster scan rate. Curves a and

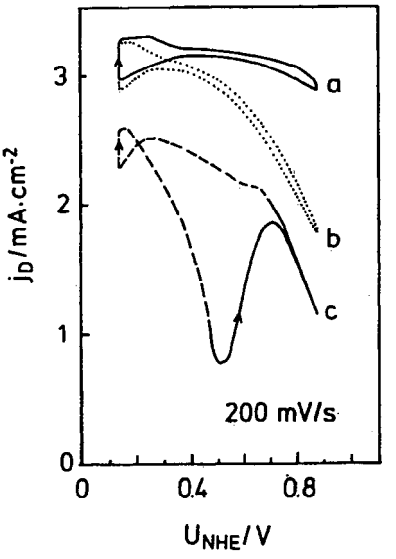

Figure 11. Cyclic voltammograms of a rotating Pt disk in three different electrolytes and a comparatively fast scan rate (200 mV/s). (a)–(c) same as in Fig. 10. (After Krischer *et al.*[69])

b, corresponding to the H_2 saturated electrolyte without and with Cl^- ions, respectively, are unchanged, compared with the corresponding ones in Fig. 10, except for a larger contribution of the capacitive current. This suggests that the relaxation of the Cl^- coverage to its equilibrium value can still follow the change in potential. However, the voltammogram obtained in the Cu^{2+}-containing electrolyte changed drastically. During the cathodic scan, the current-potential curve exhibited a negative slope over nearly the entire potential range. This means that the area active for hydrogen oxidation also increased at potentials at which Cu was deposited on the electrode (indicated by the dashed line). Thus the rate of Cl^- desorption has to be much faster than that of Cu^{2+} deposition. Note also that when Cu stripping has set in, the current decreases a little further, which should again be attributed to the faster dynamics of Cl^-, this time to the fast adsorption.

When the system is operated under galvanostatic conditions or when a sufficiently large series resistance is added, pronounced oscillations are observed around the positively sloped branch in the steady-state polarization curve. A cyclic voltammogram exhibiting current oscillations is reproduced in Fig. 12. Typical time series under galvanostatic control, close to the onset of oscillatory behavior, are shown in Fig. 13(A). Their

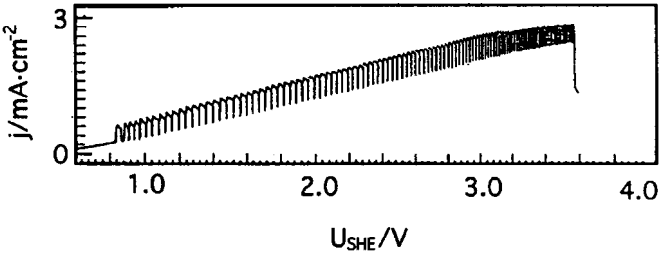

Figure 12. Positive potential scan with $R_e A = 1062\ \Omega\ cm^2$, H_2 saturated 0.5 M H_2SO_4, $[Cu^{2+}] = 10^{-5}$ M, $[Cl^-] = 3 \times 10^{-4}$ M, scan rate = 2 mV s^{-1}. (After Wolf *et al.*[18])

harmonic nature and increasing amplitudes suggest that the oscillations emerge through a supercritical Hopf bifurcation. Figure 13(B) displays time series at the high current-density end of the oscillatory region which, as the progressively longer periods of the oscillations indicate, is an example of a saddle-loop bifurcation.[76*]

Figure 14(a) shows simultaneous measurements of electrode potential and changes in Cu coverage, and Fig. 14(b) shows electrode potential and changes in the H_2 current during oscillations. Cu coverage and H_2 current were obtained from rotating ring-disk measurements. [69] As one expects for the slow variable of a dynamic system, the Cu coverage changes gradually, whereas the potential oscillations possess a relaxation-like character with steep slopes. In Fig. 14(b) it can be seen that the phase relation between potential and H_2 current can be quite complicated. This measurement provided key information when the oscillation mechanism was uncovered. The H_2 current exhibits a minimum when the potential increases steeply (i.e., in parallel with the dissolution of Cu), and a maximum close to the abrupt decrease in potential (i.e., in parallel with the deposition of Cu). However, the hydrogen current should be a monotonic function of the free Pt surface. From this response it follows that anion coverage is essential for the oscillatory mechanism. These two examples show how valuable phase information on different variables is for the elucidation of an oscillatory mechanism. For example, the phase relations measured are in contrast to those in the model by Kodera *et al.*[75]

*Note that from the figure alone, the saddle-loop bifurcation cannot be distinguished from another infinite period bifurcation, a saddle node with infinite period.[57]

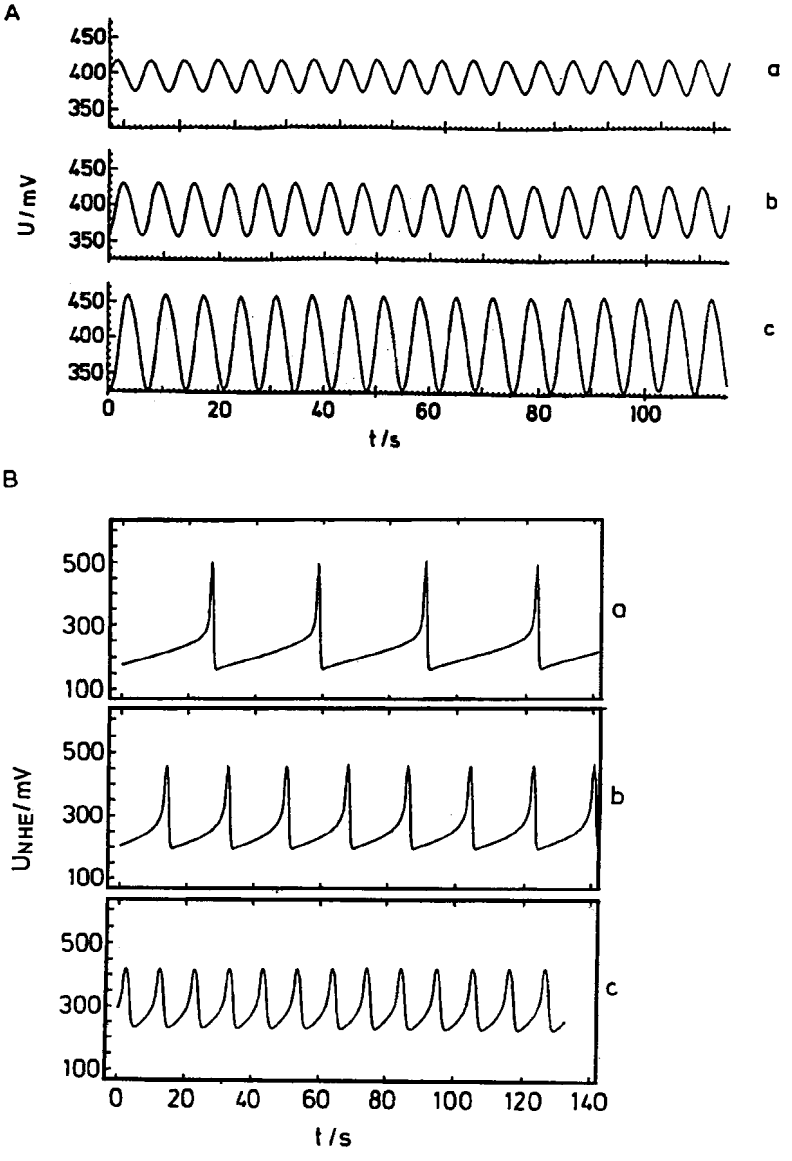

Figure 13. (A) Sinusoidal, small-amplitude potential oscillations close to the onset of oscillations at low current densities during the galvanostatic oxidation of H_2. (a) 50 $\mu A/cm^2$; (b) 52.5 $\mu A/cm^2$; (c) 60 $\mu A/cm^2$. (B) Large-amplitude relaxation oscillations close to the end of the oscillatory region at high current densities during the galvanostatic oxidation of H_2. (a) 120 $\mu A/cm^2$; (b) 200 $\mu A/cm^2$; (c) 300 $\mu A/cm^2$ (potential given vs. SHE). (After Krischer *et al.*[76])

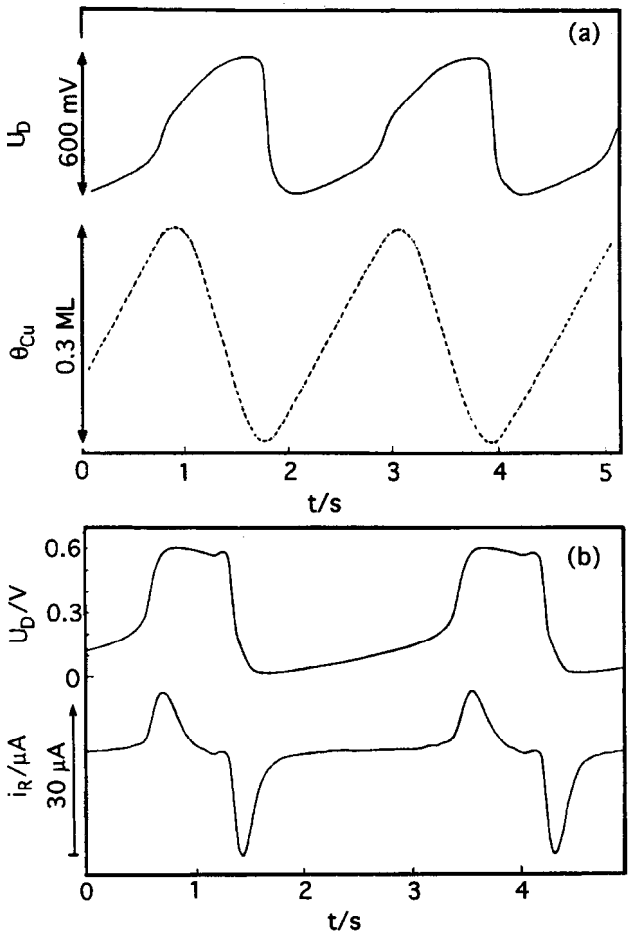

Figure 14. (a) Potential oscillations (top) and oscillations of the copper coverage (bottom) during the galvanostatic oxidation of H_2 (5×10^{-5} M Cu^{2+}, 3×10^{-2} M Cl^-, 1440 μA/cm^2. (b) Potential oscillations at a Pt disk (top) and oscillations of the hydrogen current at a Pt ring (bottom) during the galvanostatic oxidation of H_2 at a rotating ring-disk electrode. Note that the hydrogen current at the disk is low if the ring current is high and vice versa (5×10^{-5} M Cu^{2+}, 5×10^{-3} M Cl^-, 1600 μA/cm). (After Krischer *et al.*[69])

and thus present further evidence that their model does not represent the correct mechanism.

Another important test for the validity of a model is its capability to reproduce phase diagrams in the parameter plane. Here one has to distinguish between phase diagrams in a parameter plane spanned by parameters of the external circuit and those spanned by parameters affecting the chemical steps. The first type of bifurcation diagram is universal for all oscillators belonging to one of the two categories discussed in this section (NDR or HNDR oscillators). Hence they are useful only for categorizing the oscillator type; they do not provide any information on which chemical species are essential for the occurrence of oscillations. A phase diagram of our H_2 oxidation system spanned by the external circuit parameters R_e/U is displayed in Fig. 15. In region A, a single stable stationary state is found; in region B, two stable states coexist; region C marks the coexistence of oscillations with the stationary state; and in region D, only oscillations exist. It can be seen that there is a minimum value of R_e needed

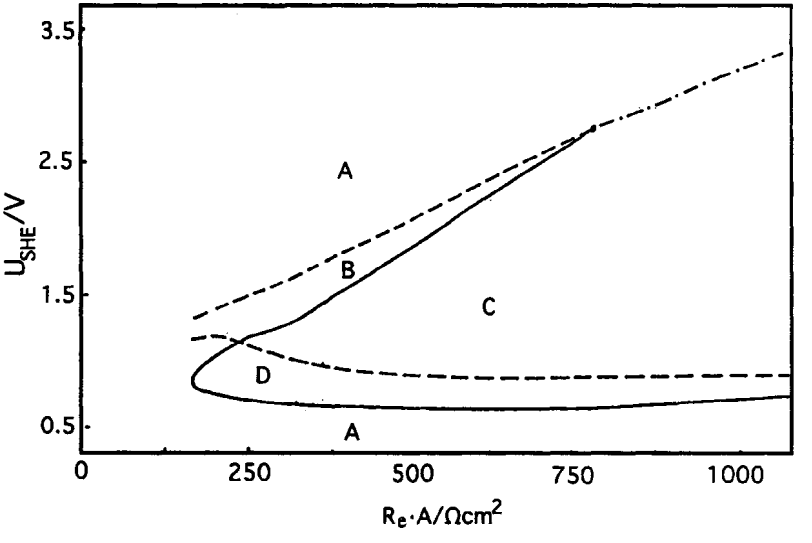

Figure 15. Regions of different dynamic behavior of H_2 oxidation in the U/R_e parameter plane; 1×10^{-5} M Cu^{2+}, 3×10^{-4} M Cl^-; (A) a stable stationary state; (B) coexistence between a stable stationary state at high currents and one at low currents; (C) coexistence of oscillations at high currents and a stationary state at low currents; (D) oscillations. (After Wolf *et al.*[18])

to obtain oscillations. The region where oscillatory behavior coexists with a stationary state broadens with increasing resistance, allowing oscillations to arise under galvanostatic conditions. Hence, compared with NDR oscillators (cf. Fig. 4), the parameter region in which oscillations are found is much larger.

Dynamic behavior has been studied under galvanostatic conditions as a function of the preset current and the bulk concentrations of Cu^{2+}, Cl^-, and Br^-. Since the latter parameters act on the kinetics of the reaction, these bifurcation diagrams are useful when trying to identify the chemical steps of the model. The phase diagrams in the halide concentration/current-density plane are reproduced in Fig. 16. It can be seen that the critical current density for the onset of oscillatory behavior increases with decreasing halide concentration. In the Cu^{2+}concentration/current-density plane, the opposite trend was found. Note also that the Br^- concentration

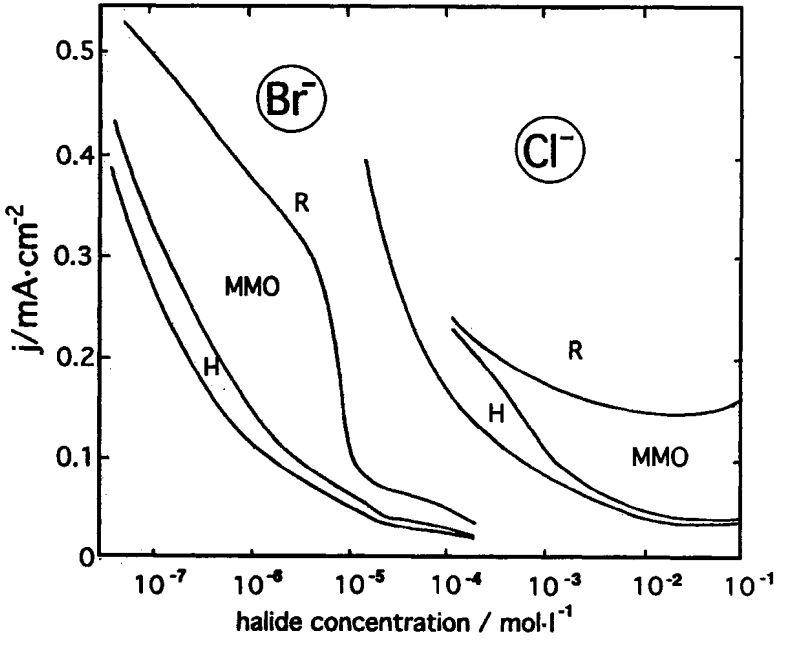

Figure 16. Regions of different dynamic behaviors during the galvanostatic oxidation of H_2 in the current density–halide concentration plane. H, small harmonic oscillations; MMO, mixed-mode oscillations (see Section II.4); R, large-amplitude relaxation oscillations. (After Wolf *et al.*[70])

necessary to establish oscillations is 10^3 times smaller than in the case of Cl^-. This reflects the different adsorption behaviors of these two anions; Br^- is generally adsorbed more strongly and hence up to more cathodic potentials than Cl^-. A correlation of adsorption isotherms of halides and dynamic behavior was found in single-crystal experiments.[69,77] In the case of Cl^- adsorption on three low-index Pt single-crystal surfaces, the interaction between Cl^- and Pt was strongest on Pt(100), less pronounced in the case of Pt(111), and weakest in the case of Pt(110).[78,79] In the last case, no oscillations could be found, whereas single periodic behavior was observed at Pt(111) and more complex behavior in the case of Pt(100).*

On the basis of these experiments, Wolf *et al.*[70] formulated a model that reproduces the qualitative features of the system. The variables of the model are the electrode potential, ϕ_{DL}, and the coverage of the electrode with metal, θ_m, and anions, θ_x, respectively. The change in the potential follows again from a current balance (where it was assumed that the current due to anion ad- or desorption is negligible). The temporal evolution of the coverages is described by the phenomenological rate laws of the adsorption and desorption of metal ions and anions, respectively:

$$C\frac{d\phi_{DL}}{dt} = -i_{H_2} - i_m + \frac{U - \phi_{DL}}{R_e \cdot A} \tag{13a}$$

$$\frac{d\theta_m}{dt} = \upsilon_m^{ads} - \upsilon_m^{des} \tag{13b}$$

and

$$\frac{d\theta_x}{dt} = \upsilon_x^{ads} - \upsilon_x^{des} \tag{13c}$$

where

$$\upsilon_m^{ads} = k_m c_m (1 - \theta_m - \theta_x) \exp\left[-a_m(\phi_{DL} - \phi_{DL}^{m0})\right]$$

$$\upsilon_m^{des} = k_m \theta_m \exp\left[a_m(\phi_{DL} - \phi_{DL}^{m0})\right]$$

*The missing oscillations of the Pt(110)/Cu^{2+}/Cl^- system are clearly linked to the adsorption behavior of Cl^-. The extent to which the different behavior found with Pt(111) and Pt(100) is due to the different adsorption properties of Cl^- has still to be examined.

$$v_x^{\text{ads}} = k_x c_x (1 - \theta_m - \theta_x) \exp\left[a_x(\phi_{\text{DL}} - \phi_{\text{DL}}^{x0})\right]$$

and

$$v_x^{\text{des}} = k_x\, \theta_x \exp\left[-a_x\left(\phi_{\text{DL}} - \phi_{\text{DL}}^{x0}\right)\right]$$

The bulk concentrations c_m and c_x are normalized to the standard concentration 1 M, and a_m, a_x symbolize the exponential terms 0.5 n_m *F/RT* and 0.5 n_x *F/RT,* respectively, with n_m and n_x the number of electrons transferred during metal and halide adsorption, respectively. The respective (potential-independent) rate constants are denoted by k_m and k_x.

The equation for the hydrogen current, i_{H_2}, was derived by the following considerations: At high anodic overpotentials, the dissociative adsorption of H_2 onto the available free sites is the rate-determining step, and thus i_{H_2} can be expressed as

$$i_{\text{H}_2} = k_{\text{H}_2}^{\text{ads}}\, c_{\text{H}_2}^{s}\, (1 - \theta_m - \theta_x)^2$$

where $c_{\text{H}_2}^{s}$ denotes the surface H_2 concentration and $k_{\text{H}_2}^{\text{ads}}$ the rate constant of adsorption. Assuming that the rate of replenishment of $c_{\text{H}_2}^{s}$ by diffusion is equal to its consumption through the reaction (i.e., that the temporal change in $c_{\text{H}_2}^{s}$ can be neglected), the H_2 current is also given by

$$i_{\text{H}_2} = k_{\text{H}_2}^{\text{diff}}\, (c_{\text{H}_2}^{b} - c_{\text{H}_2}^{s})$$

where $c_{\text{H}_2}^{b}$ is the H_2 bulk concentration. Combining both equations, one obtains

$$i_{\text{H}_2} = \frac{k_{\text{H}_2}^{\text{ads}}\, c_{\text{H}_2}^{b}\, (1 - \theta_m - \theta_x)^2}{1 + \dfrac{k_{\text{H}_2}^{\text{ads}}}{k_{\text{H}_2}^{\text{diff}}}\, (1 - \theta_m - \theta_x)^2} \tag{14}$$

The current density associated with the underpotential deposition of a monolayer metal, i_m, is obtained from the charge flowing during the deposition of 1 ML, q_{mono}:

$$i_m = q_{\text{mono}} \frac{d\theta_m}{dt}$$

In order to simulate the behavior of galvanostatic systems, the expression $(U - \phi_{\text{DL}})/(R_e A)$ has to be replaced by the applied current density.

Solving for the simultaneous zeros of Eqs. (13b) and (13c) as a function of the electrode potential, ϕ_{DL}, yields the adsorption isotherms of metal and anions. These are shown together with the total steady-state coverage in Fig. 17(a). In Fig. 17(b) the resulting stationary hydrogen current and a calculated cyclic voltammogram at a low scan rate are reproduced. The qualitative features of the corresponding experiments (i.e., the complete inhibition of hydrogen oxidation at potentials negative to 0.4 V), the decrease in the oxidation current positive to 0.5 V, and the occurrence of a kinetic hysteresis are well represented [see Fig. 10(c)].

The model contains all the general features of HNDR oscillators. Therefore it is not surprising that oscillations are obtained when an anodic voltage scan is calculated in the presence of a sufficiently large series resistance [Fig. 18(a)]. Nor is it astonishing that the universal skeleton bifurcation diagram of HNDR oscillators in the U/R_e parameter plane is reproduced [Fig. 18(b)]. On the other hand, the qualitative agreement of the location of the bifurcations as a function of current density and metal ion or anion concentration (Fig. 19) strongly supports the view that the electrode processes that cause the negative differential charge-transfer resistance and the slow potential-dependent process are correctly identified. Observe especially that in the model as well as in the experiment, the current density necessary to produce sustained potential oscillations is shifted toward higher values with increasing metal ion concentration and toward lower values with increasing anion concentration (see Fig. 16). Furthermore, as is to be expected from the proposed mechanistic role of metal ions and anions, Eq. (13) possesses only oscillatory solutions if the anion dynamics are faster than those of the cations, that is, $k_x > k_m$.[64]

(b) Formic acid oxidation

Another example for an HNDR oscillator is formic acid oxidation. Formic acid is one of the simplest organic molecules, and very likely it is an intermediate product during the oxidation of many organic molecules that are intensively studied in connection with their possible use in fuel cells. Thus, the oxidation of formic acid has been a "hot topic" for decades. Oscillatory behavior during formic acid oxidation was observed as early as the 1920s.[80,81] Today, there is a large body of literature devoted to temporal oscillations in this system. There has been controversial debate on the origin of the dynamic instability, although up to the very recent work by Strasser *et al.*,[82,83] all authors seemed to agree that the autocata-

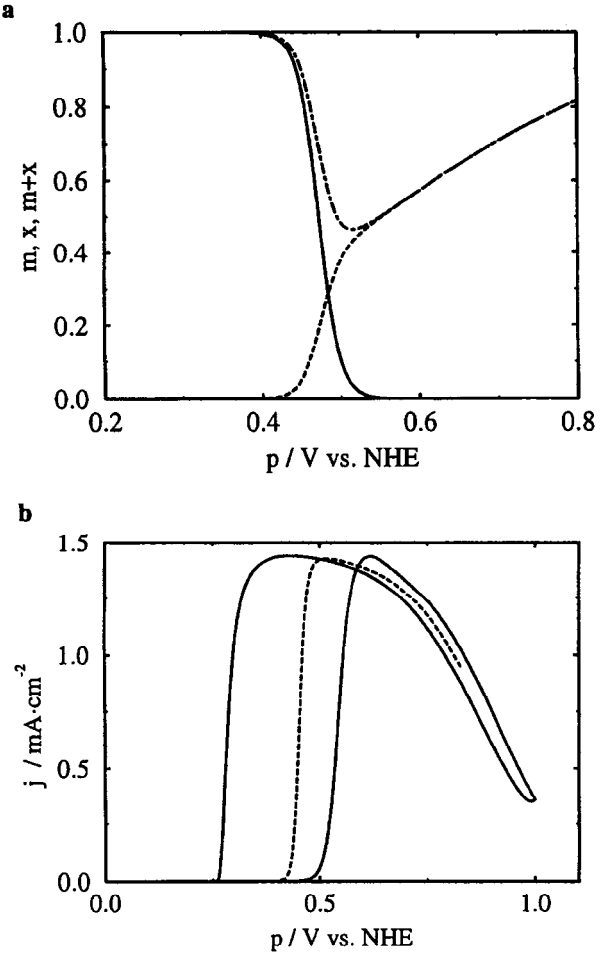

Figure 17. (a) From Eqs. (13 b and c) calculated steady-state coverages of the metal (solid line), anion (short-dashed line), and total coverage (dot-dashed line) vs. potential. (b) The resulting stationary hydrogen current density (dashed line) vs. potential and the calculated cyclic voltammogram. The hysteresis is due to slow ad- and desorption of copper. (After Wolf *et al.*[70])

lytic step is of a chemical nature.[84–92] However, it appears that most authors were not aware of the essential role the external circuit can play, and so none of the studies give the impression that the utmost was done to exclude an electrochemical instability, that is, the presence of an ohmic

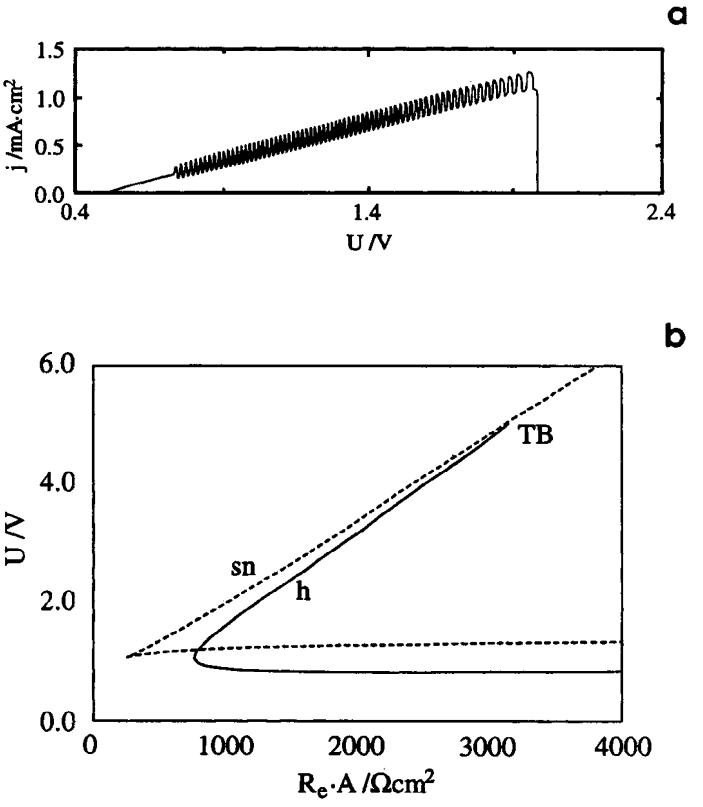

Figure 18. (a) Calculated positive potential scan for $R_eA = 1062\ \Omega\ cm^2$ using Eqs. (13a–13c). (b) Calculated locations of Hopf (h) and saddle-node (sn) bifurcations in the U/R_e parameter plane. (After Wolf *et al.* [18])

potential drop in the control circuit. On the other hand, Strasser *et al.* provided evidence that an external resistor is indeed needed for oscillations to occur under their experimental conditions. At the same time, they ruled out most of the chemical instabilities proposed as sources for the oscillatory dynamics by studying a simpler subsystem of formic acid oxidation. In the author's opinion, the experiments and conclusions discussed in Refs. 82, 83, which have many points in common with another recently proposed model,[92] are so convincing that in spite of the diverse mechanisms proposed in the literature, one can confidently classify the formic acid oscillator as an HNDR type.

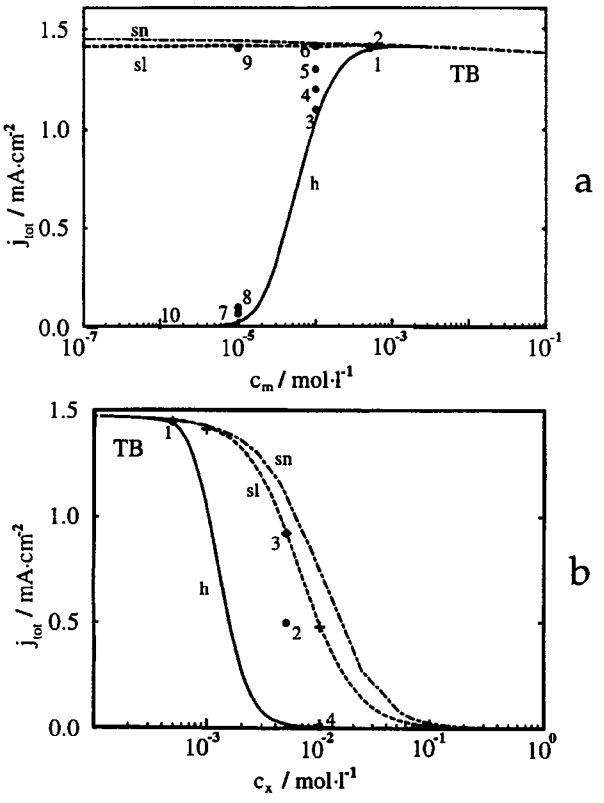

Figure 19. Calculated locations of Hopf (h), saddle-node (sn), and saddle-loop (sl) bifurcations in the (a) current density–copper concentration and (b) current density–halide concentration parameter planes using the galvanostatic variant of Eqs. (13a–13c); i.e. $(u - \phi_{DL})/(R_e A) \rightarrow j_{tot}$. (After Wolf *et al.* [70])

Both above-mentioned models [83,92] are based on the now widely accepted dual-path mechanism, first proposed by Capon and Parsons [93]

$$HCOOH + * \rightleftharpoons$$

$$HCOOH_{ad} \begin{cases} \rightarrow {\bullet}COOH_{ad} + H^+ + e^- \xrightarrow{fast} CO_2 + * + 2H^+ + 2e^- & \text{(F1)} \\ \rightarrow CO_{ad} + H_2O, & \text{(F2)} \end{cases}$$

where * denotes a free adsorption site. The first path (F1) represents the direct oxidation of formic acid where adsorbed HCOOH is oxidized to a

reactive intermediate, most likely $\bullet COOH_{ad}$, which is immediately further oxidized to the final product, CO_2. The indirect path is associated with the heterogeneously catalyzed dissociation of formic acid to water and adsorbed CO, which blocks the surface sites for further adsorption of HCOOH. The removal of the "poison" CO proceeds via an electrochemical surface reaction with a second species.[84] An important property of the species is that it also blocks surface sites for HCOOH oxidation. Strasser *et al.* suppose that this species is adsorbed OH, which is formed and reacts according to the following steps*:

$$H_2O + * \rightleftharpoons OH_{ad} + H^+ + e^- \tag{F3}$$

$$OH_{ad} + CO_{ad} \rightarrow CO_2 + H^+ + 2* + e^- \tag{F4}$$

Okamoto *et al.*[92] proposed that the second species is water adsorbed adjacent to CO and that preadsorbed CO is necessary for the adsorption of the second species. This seems to be a questionable interpretation that is not taken up in further discussion, although with the exception of the adsorption term for species 2, the resulting model seems to be mathematically equivalent to a subset of three equations derived by Strasser *et al.*[83] and discussed later [Eqs. (15b)–(15d)].

The mechanistic counterparts can be easily recognized by comparing the reaction scheme (F1)–(F4) with the one for H_2 oxidation discussed in the last section. The direct oxidation path (F1) accounts for most of the oxidation current and thus corresponds to the H_2 oxidation current. At potentials cathodic to OH adsorption, CO slowly poisons the surface according to (F2); it is removed in reaction (F4). Hence, (F2) and (F4) play the role of ad- and desorption of the metal ions, respectively. Neglecting the indirect path for a moment, the adsorption of OH (F3), being a fast process, will lead to a decrease in the oxidation current stemming from the direct path, and induce a negative slope in the polarization curve, just

*Note that in 1968 Wojtowicz *et al.*[84] were able to directly measure the buildup of OH or O coverage on a Pd electrode in a single oscillatory cycle and correlate it with the periodic process. Moreover, they proposed in their chemical model that the electrosorbed OH (or O), as well as an intermediate product of H.COOH oxidation that is adsorbed at the electrode, are essential for producing oscillations.

as the halide ions do in the case of the H_2 system. When relating the system to the prototype model [Eq. (10)], (F1) and (F3) give rise to the N-shaped polarization curve $k(\phi_{DL})$ in Eq. (10a). (F2) and (F4) act like the poisoning species P [Eq. (10b)]. With this information in the back of one's mind, the familiar features of HNDR oscillators are more easily identified.

Consider first a cyclic voltammogram of the oxidation of HCOOH on Pt(100) in a solution of high conductivity and thus almost vanishing ohmic resistance (Fig. 20). Starting at the cathodic limit point, the surface is mainly poisoned by CO for potentials up to about 0.5 V and direct oxidation is efficiently impeded, leading to a low oxidation current. In parallel with the onset of OH adsorption, the poison is oxidized and the current increases owing to the larger electrode area accessible for the direct oxidation of formic acid. Once CO is removed, an OH coverage builds up that also acts as a poison for HCOOH oxidation. In the cathodic scan, a pronounced increase in current is observed at potentials at which OH desorbs, giving way to a nearly free surface. The subsequent decrease in current density is partly a consequence of the slow indirect path building up the CO coverage and partly due to the decreasing overpotential for formic acid oxidation. Note that the hysteresis in the cyclic voltammogram is of a kinetic nature. Strasser *et al.* report a reversible stationary polarization curve exhibiting a maximum at about 0.5 V.

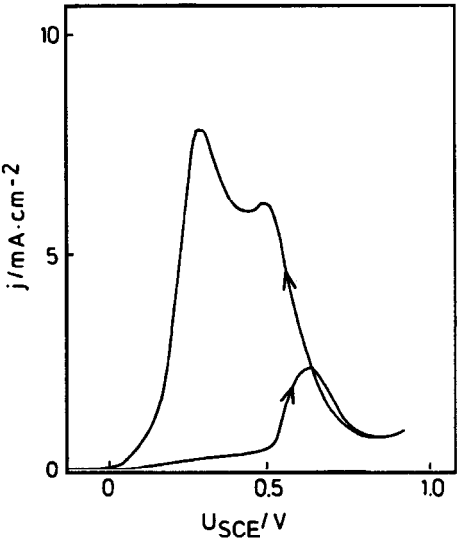

Figure 20. Current-voltage characteristic of the oxidation of formic acid on Pt(100). Electrolyte: 1 M HCOONa, 0.5 MH_2SO_4, pH 2.6. Scan rate: 10 mV/s. (Reprinted with permission from P. Strasser, M. Lübke, F. Raspel, M. Eiswirth and G. Ertl, *J. Chem. Phys.* **107,** 979–990, 1997. Copyright 1997 American Institute of Physics.)

When a sufficiently large external resistor is connected in series, the current oscillates on the branch with the positive polarization slope, though in a region where OH adsorption takes place (Fig. 21). (Recall that OH adsorption is the fast process that is responsible for a negative real impedance in an interval of nonzero frequencies.) The first three time series shown in Fig. 21(b) were obtained on the anodic scan, the last two

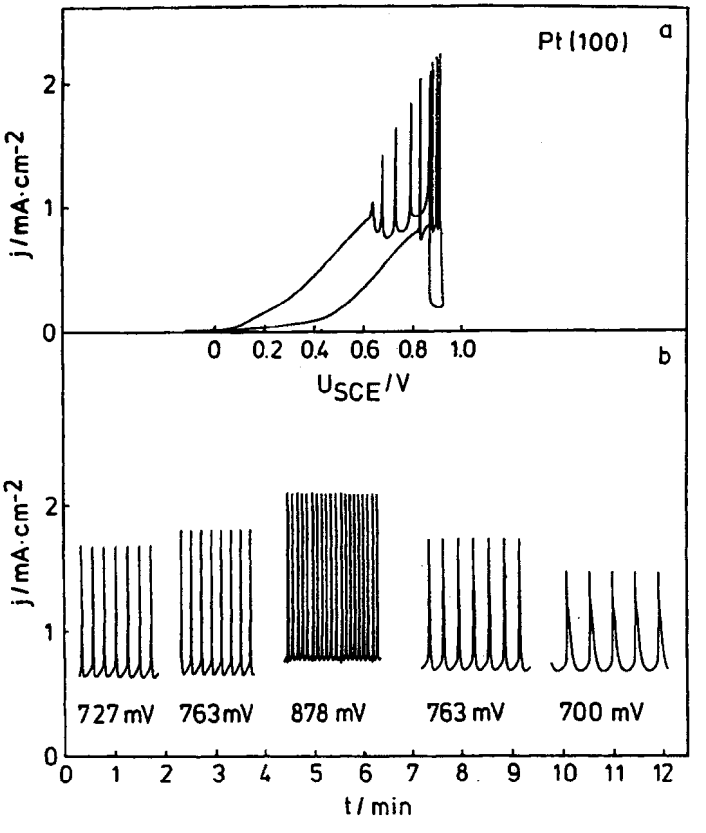

Figure 21. (a) Cyclic voltammogram of formic acid oxidation on Pt(100) with external resistance ($R_e = 600\,\Omega$). Electrolyte: 0.05 M HCOOH, 10^{-3} M $HClO_4$; scan rate: 5 mV/s. (b) Current oscillations after holding the scan at different potentials U. The frost three time series (from left to right) were obtained when the potential was stopped during the anodic scan; the remaining two when it was stopped on the cathodic scan. (Reprinted with permission from P. Strasser, M. Lübke, F. Raspel, M. Eiswirth and G. Ertl, *J. Chem. Phys.* **107,** 979–990, 1997. Copyright 1997 American Institute of Physics.)

on the cathodic scan. The resemblance of the two sets suggests that the apparent hysteresis of the branches with the positive characteristics in the cyclic voltammogram is again of a kinetic nature. In contrast, the hysteresis close to the anodic turning point is connected with a true bistability between a low-current steady state and sustained oscillations.

The chemical reaction scheme (F1)–(F4) was translated into a mathematical model. [83] The variables of the model are formic acid concentration in the reaction plane, c_{FA}, the coverages of the electrode with carbon monoxide, θ_{CO}, and with OH, θ_{OH}, and the electrode potential, ϕ_{DL}. In contrast to some previously proposed models, the pH in the reaction plane was assumed to be constant and entered only the reaction constants for a given bulk solution acidity. The concentration of the radical species $\bullet COOH_{ad}$ was adiabatically eliminated because its oxidation is by far the fastest process of the scheme. The resulting equations read:

$$\frac{dc_{FA}}{dt} = -\frac{2a}{\delta}(\nu_{direct} + \nu_{poison}) + \frac{2D_{FA}}{\delta^2}(c_{FA}^b - c_{FA}) \tag{15a}$$

$$\frac{d\theta_{OH}}{dt} = k_{OH}^{ads} \exp\left(\frac{\alpha F}{RT}\phi_{DL}\right)(1 - \theta_{OH} - \theta_{CO}) - k_r \exp\left(\frac{\alpha F}{RT}\phi_{DL}\right)\theta_{CO}\theta_{OH} - k_{OH}^{des} \exp\left[\frac{-(1-\alpha)F}{RT}\phi_{DL}\right]_{\theta_{OH}} \tag{15b}$$

$$\frac{d\theta_{CO}}{dt} = \nu_{poison} - k_r \exp\left(\frac{\alpha F}{RT}\phi_{DL}\right)\theta_{CO}\theta_{OH} - k_{CO}^{des}\,\theta_{CO} \tag{15c}$$

and

$$C_{DL}\frac{d\phi_{DL}}{dt} = (j_{tot} - j_{direct} - j_{OH}^{ads} - j_r + j_{des}^{OH}) \tag{15d}$$

The temporal evolution of formic acid in the double layer [Eq. (15a)] is governed by the rate of the oxidation of formic acid via the direct (ν_{direct}) and indirect (ν_{poison}) paths and its replenishment by diffusion. For the latter it was again assumed that the concentration profile across the diffusion layer relaxes instantaneously to a linear profile. δ denotes the diffusion-layer thickness (which is assumed to be constant), D_{FA} the diffusion constant of formic acid, and c_{FA}^b the bulk concentration of formic acid. A

proportional constant resulting from the units chosen for c_{FA} and the rates v_i (see Ref. 83) is defined as *a*.

The rate for the direct oxidation of formic acid was described by the following expression where the adsorbed formic acid ($HCOOH_{ad}$) was adiabatically eliminated:

$$v_{direct} = \frac{k_d \exp\left(\frac{\alpha F}{RT}\phi_{DL}\right) k_{ads}^{FA} c_{FA}}{k_d \exp\left(\frac{\alpha F}{RT}\phi_{DL}\right) + k_{ads}^{FA} c_{FA}} (1 - f\theta_{OH} - \theta_{CO})$$

where k_d and k_{ads} denote the rate constants of reaction and adsorption, respectively, and α is the symmetry factor. The empirical factor f was introduced to take into account the observed incomplete blockage of formic acid oxidation at anodic potentials (see Fig. 20).

The poisoning rate, v_{poison}, was assumed to be proportional to the number of free surface sites and the formic acid concentration in the double layer:

$$v_{poison} = k_{poison}\, c_{FA}(1 - \theta_{CO} - \theta_{OH})$$

where k_{poison} is the corresponding rate constant.

The time variation of the OH coverage [Eq. (15b)] is given by adsorption and desorption of OH (first and last term, respectively), and the reaction with CO (second term). α is the transfer coefficient. Changes in the CO coverage [Eq. (15c)] are caused by the poisoning reaction, the reaction with CO, and desorption of CO. The temporal evolution of the electrode potential [Eq. (15d)] results from charge conservation. The faradaic current densities, j_i, are connected with the reaction rates, v_i, by $j_i = nFS_{tot}v_i$, where n is the number of electrons exchanged in the reaction and S_{tot} is the total number of surface sites per unit area. The total current j_{tot} is either a parameter (if galvanostatic conditions are used) or it is given by $j_{tot} = (U - \phi_{DL})/R_e A$, with the usual meaning of U, R_e, and A.

For sufficiently high series resistance, the model possesses stable oscillatory solutions. A calculated cyclic voltammogram is displayed in Fig. 22(a) together with the stationary polarization slope (dashed line). Clearly, on the one hand, the cyclic voltammogram exhibits the characteristic attributes of self-poisoning oxidation reactions of small organic molecules. The most important features are a slowly increasing current for $U > 0.5$ V, owing to the reactive removal of the poisoning CO in parallel

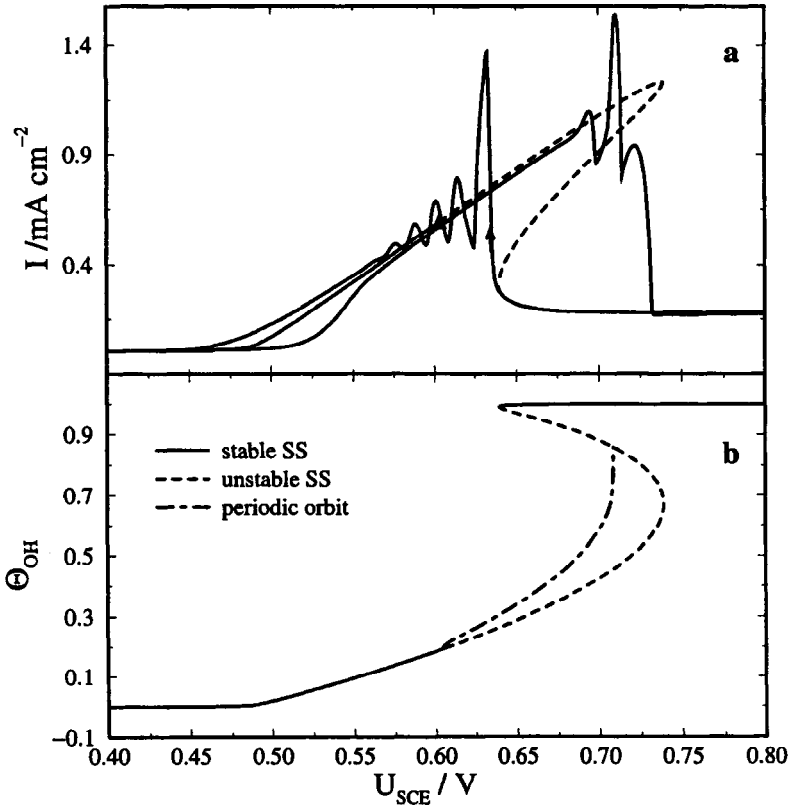

Figure 22. (a) Calculated cyclic voltammograms and stationary *I/U* curve for the formic acid oxidation model [Eq. (15)]. The anodic and cathodic scans are indicated by arrows. The dashed line shows the portion of the stationary state curve that corresponds to unstable steady states. The triangle at $U = 0.6$ V marks the location of the Hopf bifurcation. (b) Calculated one-parameter bifurcation diagram of the formic acid model: steady-state coverage of OH, θ_{OH}, vs. applied voltage *U*. Solid line indicates a stable steady state (SS), the dashed line an unstable steady state, and the dot-dashed line shows the maximum amplitude of stable oscillations. (Reprinted with permission from P. Strasser, M. Eiswirth and G. Ertl, *J. Chem. Phys.* **107,** 991–1003, 1997. Copyright 1997 American Institute of Physics.)

to the onset of OH adsorption at about 0.5 V, and the occurrence of kinetic hysteresis in the cathodic region, owing to the small rate of the poisoning reaction. On the other hand, the typical features of HNDR oscillators can be recognized. Oscillations occur on the positive branch of the polarization curve. They emerge at anodic potentials through a Hopf bifurcation and

are destroyed through the collision with a saddle point (dashed line), that is, in a saddle-loop bifurcation [Fig. 22(b)]. These two bifurcations, as well as the saddle-node bifurcations [which occur at the end of the multivalued steady-state curve in Fig. 22(b)], are plotted in a bifurcation diagram in the U/R_e parameter plane (Fig. 23). Note the agreement with the diagrams shown in Fig. 15 and Fig. 18(b), as well as the necessity of a finite-series resistance to observe oscillatory solutions.

Several groups have emphasized that the dynamic behavior of formic acid oxidation on low-index single-crystal planes exhibits structural effects.[86,87,91,94] According to these studies, current oscillations were easily observed on Pt(100); seemed to exist in only a small parameter interval on Pt(110); and proved to be even more difficult to detect on Pt(111). Furthermore, on Pt(100), current spikes appeared in the cyclic voltammogram, predominantly on the cathodic scan. In contrast, on Pt(110) they showed up mainly on the anodic scan, and were often absent on Pt(111), although oscillations emerged under stationary conditions. Strasser *et al.* point out that these differences are in accord with the above-discussed model.[82,83]

There is experimental evidence that the affinity of the individual crystal planes toward CO varies remarkably, Pt(111) exhibiting the lowest affinity. This fact is reflected in widely differing rate constants of the

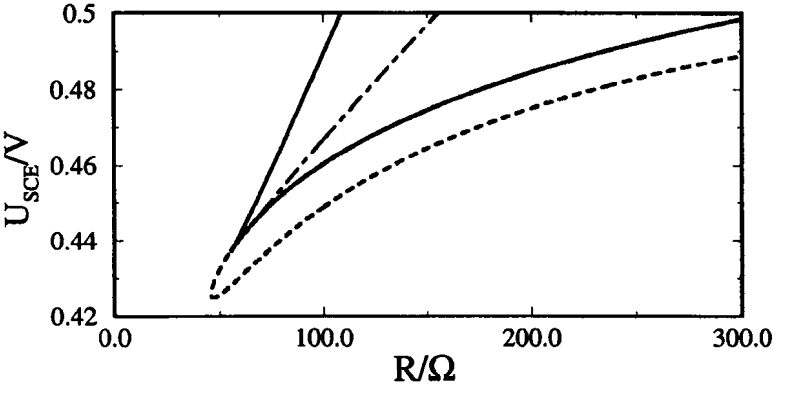

Figure 23. A calculated two-parameter bifurcation diagram for the formic acid model [Eq. (15)] showing the locations of the saddle-node (solid line), Hopf (dashed line), and saddle-loop bifurcations (dotted-dashed line). All three curves meet in a Takens–Bogdanov point close to the cusp. (Reprinted with permission from P. Strasser, M. Eiswirth and G. Ertl, *J. Chem. Phys.* **107,** 991–1003, 1997. Copyright 1997 American Institute of Physics.)

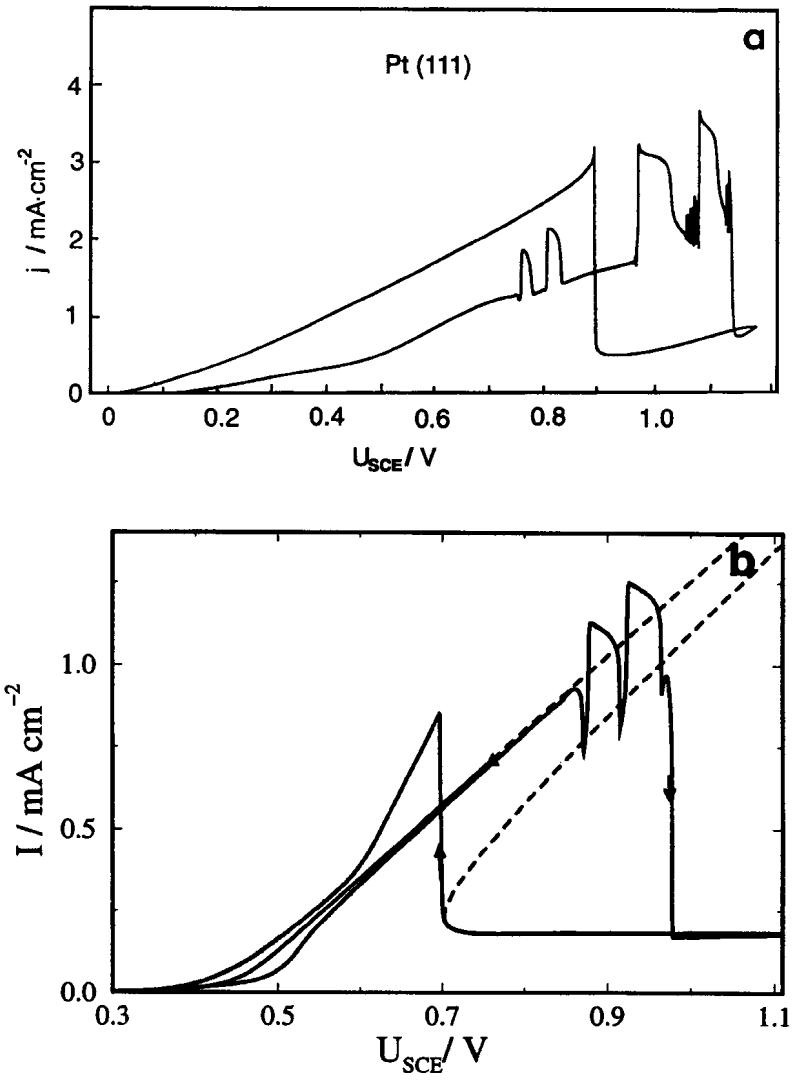

Figure 24. (a) Experimental cyclic voltammogram of formic acid oxidation on Pt (111) with external resistance $R_e = 430\ \Omega$. Electrolyte: 0.05 M HCOOH, 10^{-3} M $HClO_4$. Scan rate: 5 mV/s. (After Strasser *et al.* [82]) (b) Calculated cyclic voltammogram and stationary current-voltage curve for the formic acid model [Eq. (15)]. A smaller k_{poison} was chosen than the one used in Fig. 22(a). The anodic and cathodic scans are indicated by arrows. The dashed line shows the portion of the stationary state curve that corresponds to unstable steady states. (After Strasser *et al.* [83] with permission of the authors.)

poisoning reaction (F2), and, indeed, when the rate constant of the indirect path (k_{poison}) is varied, the different experimental findings on the three low-indexed Pt surfaces can be reproduced. [83] A comparison of an experimental cyclic voltammogram recorded with a Pt(111) electrode and a calculated *I/U* curve with a k_{poison} smaller than that used in Fig. 22 is reproduced in Fig. 24(b).

4. Mixed-Mode Oscillations

In the last section we focused on mechanistic requirements that give rise to simple periodic oscillations. The statement that more complex dynamic behaviors have been observed for all electrochemical oscillators is hardly exaggerated, however. The expression "more complex dynamics" includes all phenomena whose mathematical description requires at least three variables. Perhaps the most popular complex behavior is deterministic chaos, of which there are numerous clear-cut examples for oscillating electrochemical systems in the literature. [67,68,76,90,95–108] More unusual dynamics have also been found, a spectacular example of which is the period doubling of a torus. [109] However, in the majority of experimental studies, and often together with chaotic behavior, the occurrence of mixed-mode wave forms has been described. [42,67,76,82,85,88,95–97,102,103,110–120] The latter denotes time series that are composed of alternating small- and large-amplitude oscillations. Typically, an individual mixed-mode wave form is stable over only a small parameter region, and when an experimentally controlled quantity is changed, intricate bifurcation sequences are observed. [67,96,97,103] These experimental investigations provided valuable insight into the bifurcation structures of a certain class of dynamic systems and led to several theoretical studies. [121,122]

In this chapter, the experimentally observed wave forms are not reviewed from the point of view of dynamic systems theory. Rather, we focus on the physical mechanisms that cause complex oscillatory behavior. In general, the phenomena considered require the presence of autocatalysis and two negative feedback loops. Recall that simple oscillations are caused by the interaction of an autocatalytic variable and one negative feedback variable. Thus it is plausible to look for an additional variable that introduces a second negative feedback loop into the two mechanisms considered in the last section.

We discuss an extension of NDR oscillators as studied by Koper and Gaspard. This mechanism accounts for most of the mixed-mode oscilla-

tions (MMOs) observed in this class of oscillators. HNDR oscillators do not seem to possess similarly standardized bifurcation fine structures, pointing to the different origins of the complex behavior; most of this behavior is not yet understood from the mechanistic viewpoint. Nevertheless, there are some important hints on general features that give rise to MMOs in HNDR oscillators; these are discussed in Section II.4.(ii). While an attempt was made to avoid expressions originating from the theory of nonlinear dynamics, at some places technical terms are inevitable. Explaining all of them would have resulted in lengthy definitions. Readers not familiar with them can find easily understandable explanations in the books by Scott [123] or Strogatz, [57] and in the review ref. 2.

(i) Mixed-Mode Oscillations in NDR Oscillators

(a) A general model

In Section II.2.(i), NDR oscillators are described by two variables: the electrode potential, which constitutes the positive feedback variable; and the concentration of the electroactive species in the reaction plane, *c,* which is assumed to vary due to the charge-transfer reaction and diffusion from the bulk electrolyte. In deriving the temporal evolution equation for *c,* a steady-state approximation was made for the concentration profile across the diffusion layer. This latter assumption of a fast-relaxing diffusion layer and, for this reason, a concentration profile that is at all times linear, represents a questionable simplification. Under oscillatory conditions, the reaction rate has mixed diffusion and reaction control; curved concentration profiles will be established owing to a delayed response of the diffusion layer to concentration changes at the electrode. Thus, though Eq. (5) correctly predicts the occurrence of oscillations as well as the qualitative location of oscillatory and bistable regions in the parameter plane, it does not completely represent the qualitative dynamic behavior obtained when the original partial differential equation is taken into account. This important fact was recognized by Koper and Gaspard, who relaxed the assumption of a linear profile by allowing for another degree of freedom in the diffusion layer. [16,124] They divided the electrolyte into three parts: a semi-infinite layer for $z > \delta$ (with z the coordinate perpendicular to the electrode), where the concentration is equal to its bulk value c^b; a first layer between $z = \delta$ and $z = \delta/2$ with the concentration c^z; and a second layer between $z = \delta/2$ and $z = 0$ (the location of the electrode) with

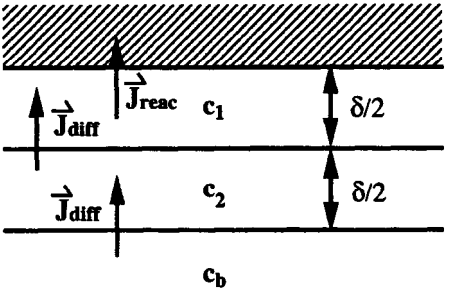

Figure 25. Geometry of the two diffusion-layer models for a planar electrode.

the concentration c^1 (Fig. 25). The differential equations for c^1 and c^2 result from diffusion and reaction fluxes, which are indicated in Fig. 25. Of course, this concept is not restricted to a planar electrode. Rather, the equations were first derived for a hanging mercury drop electrode (HMDE) and thus spherical electrode geometry (and for this reason also spherical electrolyte layers). Furthermore, using Nernst's model of a steady-state diffusion layer, the same equations can also be used to simulate mass transport to a rotating disk electrode.[16] The general set of equations reads:

$$C\frac{d\phi_{DL}}{dt} = -nFk(\phi_{DL})c^1 + \frac{U-\phi_{DL}}{R_eA} \tag{16a}$$

$$\frac{dc^1}{dt} = a_1k(\phi_{DL})c^1 + a_2D(c^2 - c^1) \tag{16b}$$

and

$$\frac{dc^2}{dt} = a_3D(c^b - a_4c^2 + a_5c^1) \tag{16c}$$

where the parameters have the same meaning as before and the coefficients a_i are uniquely determined by mass transport and electrode geometry.

A linear stability diagram of the steady states of Eq. (16) in the U/ρ parameter plane is shown in Fig. 26.* Observe the similarity of the locations of the Hopf and saddle-node bifurcations in this diagram and in the corresponding figure of the two-variable version of the NDR oscillator (see Fig. 4). The dashed lines in Fig. 26 mark the transitions of a node to

*The diagram was calculated for a dimensionless version of Eqs. (16). ρ is, as in Eqs. (5), the dimensionless resistance.

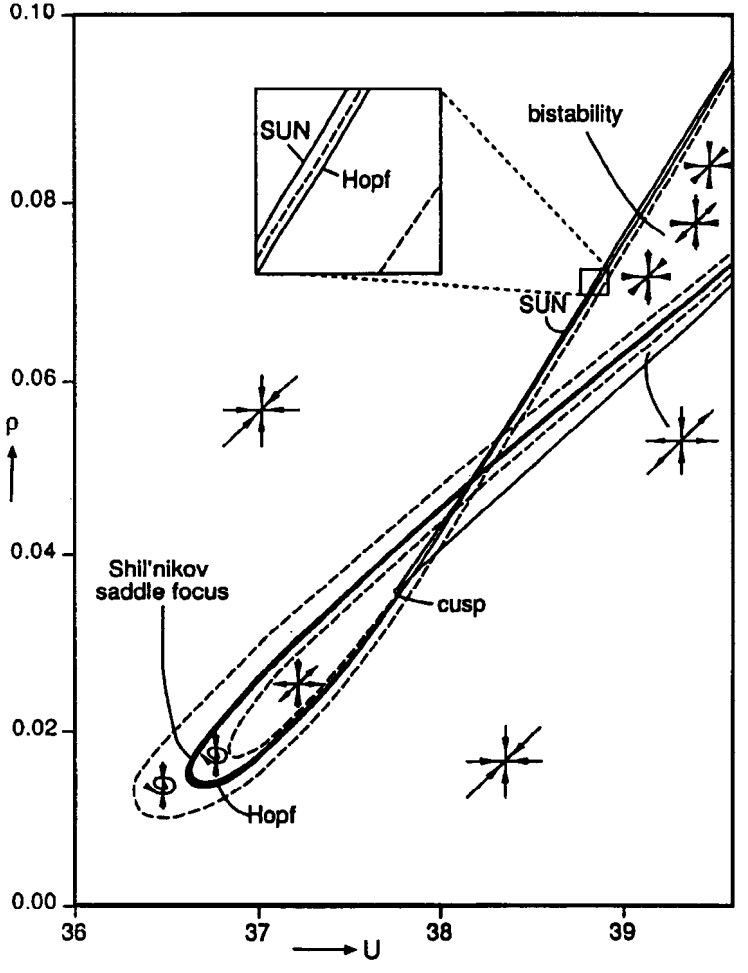

Figure 26. Skeleton bifurcation diagram in the U-ρ parameter plane for the model equation (16). Shown are Hopf and saddle-node bifurcations (SUN = saddle-unstable-node bifurcation) as well as the border of the focus-node transition (dashed line); mixed-mode wave forms exist close to the dark region (which marks the region where a fixed point is a Shil'nikov saddle focus). The phase portraits sketch the linear stability of the fixed point(s). (Reprinted with permission from M. T. M. Koper and P. Gaspard, *J. Chem. Phys.* **96,** 7797, 1992. Copyright 1992, American Institute of Physics.)

a focus, that is, they show where a pair of eigenvalues of the Jacobian matrix of Eq. (16) becomes imaginary. The dashed region sketches domains where the occurrence of complex dynamics is favored [more precisely, where Shil'nikov's condition (see Ref. 16) is fulfilled]. A more detailed study of the dynamics defined by Eq. (16) indeed reveals very intricate sequences of higher bifurcations giving rise to MMOs as shown in Figs. 27 and 28. The time series show how the dynamic behavior changes when ρ is increased at $U = 37$. Coming from low resistances, the steady state undergoes a Hopf bifurcation, giving way to small-amplitude oscillations. Raising ρ further, relaxation spikes suddenly appear, creating the fast MMOs, and a further increase in ρ changes the number of large- and small-amplitude oscillations during one period.

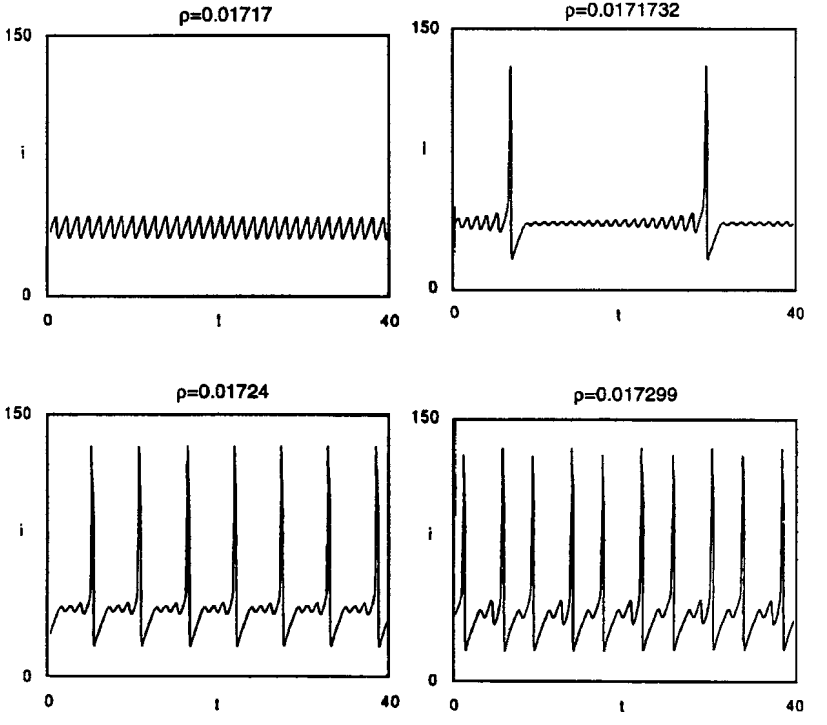

Figure 27. Typical oscillatory time series for the current *i* for low values of the resistance (first MMO regime) obtained for Eq. (16). Depicted are a small-amplitude time series, an MMO state 1^{19}, an MMO state 1^3, and a $1^1\,1^2$ state. (Reprinted with permission from M. T. M. Koper and P. Gaspard, *J. Phys . Chem.* **95**, 4945, 1991. Copyright 1991, American Chemical Society.)

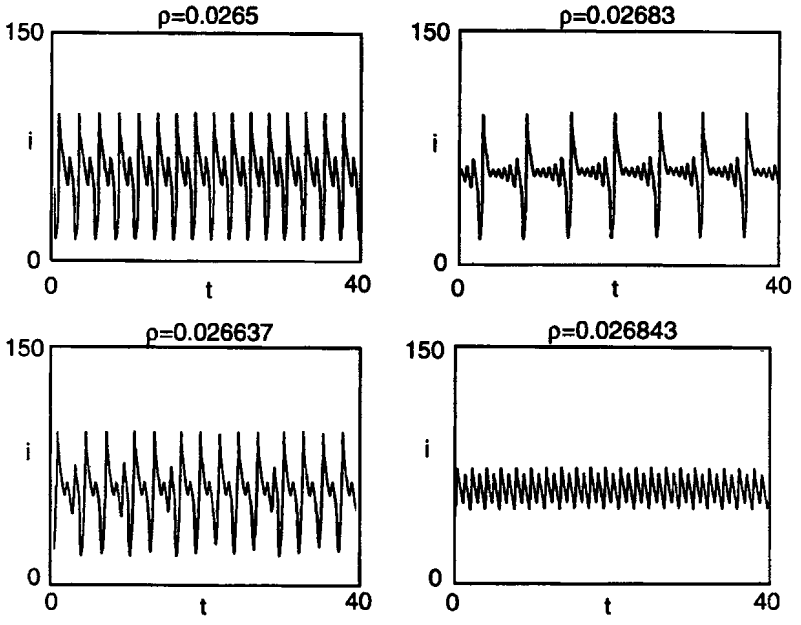

Figure 28. Typical oscillatory time series for the current i for higher values of the resistance (second MMO regime) obtained for Eq. (16). Depicted are the MMO states 1^1, 1^5, a chaotic state situated between the periodic states 1^1 and 1^2, and a period-doubled, small-amplitude oscillation. (Reprinted with permission from M. T. M. Koper and P. Gaspard, *J.Phys. Chem.* **95,** 4945, 1991. Copyright 1991, American Chemical Society.)

Conveniently, MMOs are characterized by a symbolic notation L^S where L denotes the number of large and S the number of small oscillations during one period. Thus, the MMOs depicted in Fig. 27 are designated as 1^{19}, 1^3, and 1^11^2 states. In the notation of the latter state, it is indicated that one period is built up from concatenated principal states. In fact, in the simulations, many such concatenated states were found; for example, between the 1^3 and the 1^2 state, $1^3(1^2)^n$ states with n going from 1 to 10 were observed. These sequences are called *Farey sequences* because a one-to-one correspondence of successive MMO states and the ordering of the rational numbers, which is conveniently represented in a Farey tree* (see Fig. 31), can be established. In general, at low values of the resistance, the sequences of MMOs obey an incomplete Farey arithmetic.[125]

*A Farey tree arises in number theory as a scheme for the generation of all the rational numbers between a given pair of rationals. This proceeds by the so-called Farey addition of two rationals p/q and r/s which is equal to $(p + q)/(r + s)$.

This Farey-sequence MMO regime is separated from a second MMO regime by a large parameter interval of intermediate ρ values where simple relaxation oscillations (1^0 states) exist. A sequence of the latter is shown in Fig. 28. In this second MMO regime, the transitions between two periodic mixed-mode states are distinct from the first one. Here, a periodic state undergoes a period doubling cascade to become chaotic. The transition from this chaotic state back to the next periodic MMO can either follow an inverse period doubling sequence or occur through a tangent bifurcation.[57] The third time series in Fig. 28 is an example of a chaotic state existing between the periodic states 1^1 and 1^2.

In concluding this discussion of modeling of MMOs in NDR oscillators, it is worth emphasizing two points: First, MMOs in the model arise from the coupling of the Hopf bifurcation (present in the two-variable system) to a slow mode of transport. Hence neither an additional chemical species nor any chemical or electrochemical reaction step was introduced. As a consequence, all electrochemical oscillators categorized as NDR oscillators should, for appropriate parameter values, display MMOs. This conjecture was verified by Koper and Sluyters for many NDR oscillators on an HMDE.[60] Second, one might wonder how far the dynamics of this still very crude truncation are representative of the dynamics of the original partial differential equation. According to Koper and Gaspard,[124] exactly the same qualitative behavior was observed in spatially well-discretized numerical solutions of the full problem.

(b) Comparison with experiments

Among the large variety of MMOs found in experimental systems, we focus here on two examples. In the systems chosen, extensive studies of the dependence of the wave forms on the parameters were carried out, and the bifurcation sequences obtained displayed a nearly perfect agreement with the predictions of the model.

Equation (16) was originally derived to model the reduction of In^{3+} from SCN^- solution on the HMDE. The bifurcation behavior of this system is summarized in the two-parameter bifurcation diagram in Fig. 29.[67] Most remarkably, the two distinct MMO sequences of the model also show up in the experiment. Farey sequences were observed close to the Hopf bifurcation at low values of the series resistance, whereas at the high resistance end of the oscillatory regime, periodic-chaotic mixed-mode sequences were found. Owing to this good agreement of the bifurcation

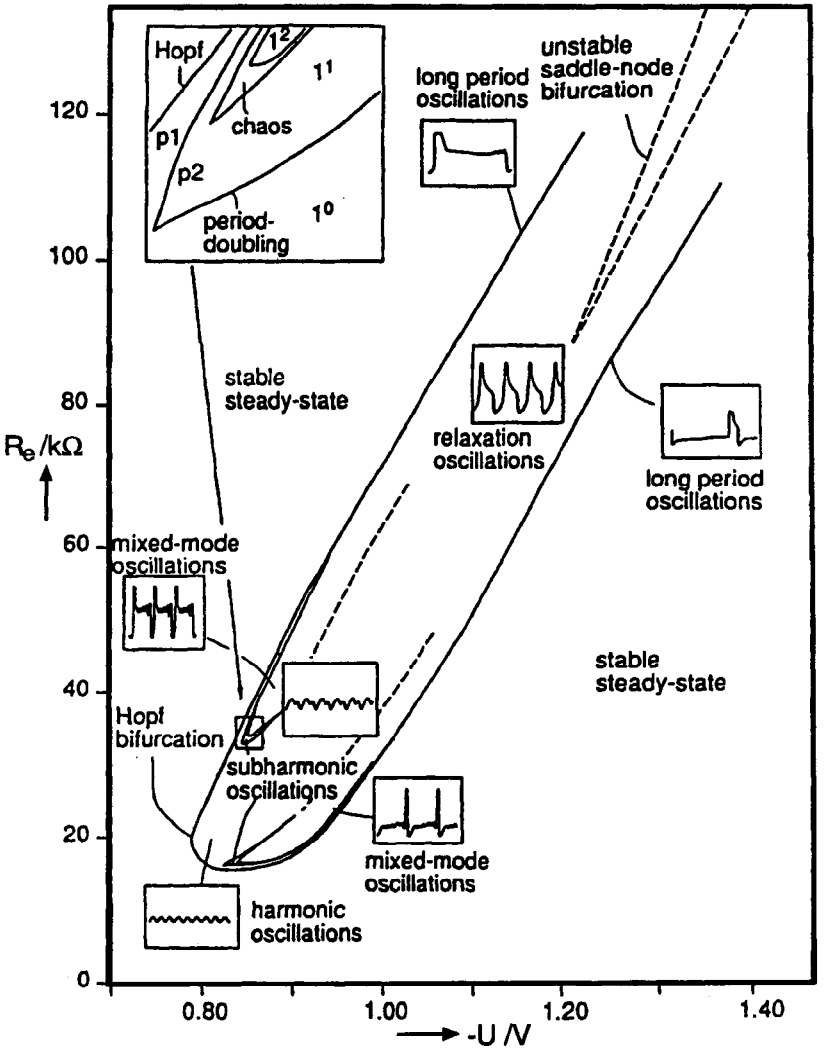

Figure 29. Experimentally determined bifurcation diagram for the In^{3+}/SCN^{-} system showing regions of stationary, oscillatory, or complex behavior in the V-R plane. The two regions where the two types of MMOs occur can be seen at the low resistance and high resistance end of the "oscillation tongue," respectively. (Reprinted with permission from M. T. M. Koper, P. Gaspard, and J. H. Sluyters, *J. Chem. Phys.* **97,** 8250, 1992. Copyright 1992, American Institute of Physics.)

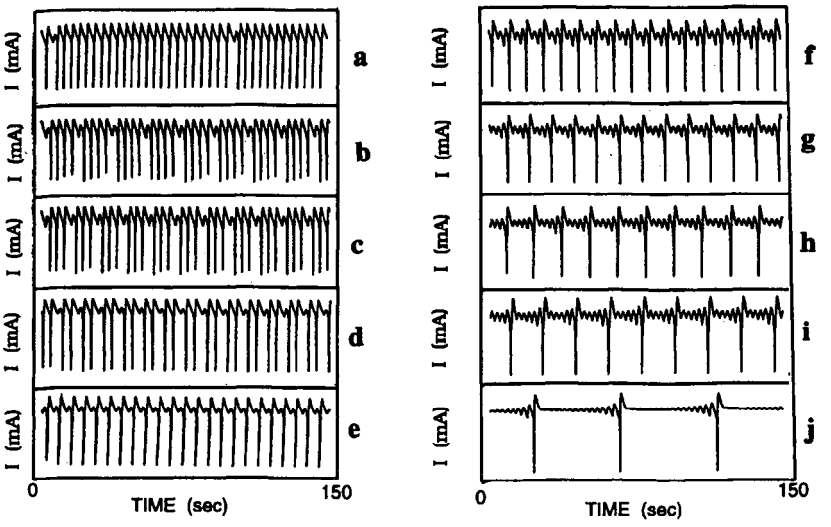

Figure 30. A sequence of MMOs measured during the electrodissolution of copper in phosphoric acid. From (a) to (j) the applied potential was increased in small steps. The continuous increase in the number of small oscillations relative to the number of large oscillations during one period is evident. (a) Close to the limiting 1^0 state, (b) a 4^1 state, (c) a 3^1 state, (d) a 2^1 state, (e) the 1^1 state, (f) the 1^2 state, (g) the 1^3 state, (h) a 1^4 state, (i) a 1^5 state, and (j) an MMO state close to the end of the sequence (the 0^1 state). (Reprinted with permission from F. N. Albahadily, J. Ringland, and M. Schell, *J. Chem. Phys.* **90,** 813, 1989. Copyright 1989, American Institute of Physics.)

behavior, the experimental time series, not surprisingly, closely resemble those of Figs. 27 and 28.[67] These results strongly support the idea that the complex wave forms observed in NDR oscillators arise because of slow mass transport.

Another most remarkable experimental study in which the two types of mixed-mode sequences were also observed was carried out by Albahadily *et al.*,[96,97] who studied the electrodissolution of copper in phosphoric acid from a rotating disk. Figure 30 shows a series of Farey states observed in this system, and in Fig. 31, the experimentally observed mixed-mode states are listed in the structure of a Farey tree. On the high rotation-rate end of the 1^0 state, alternating periodic and chaotic behavior appeared. The first period-doubled oscillation arising from the 1^2 parent state is reproduced in Fig. 32 together with the 1^2 parent state. In Fig. 33, a two-parameter bifurcation diagram is depicted in which the succession

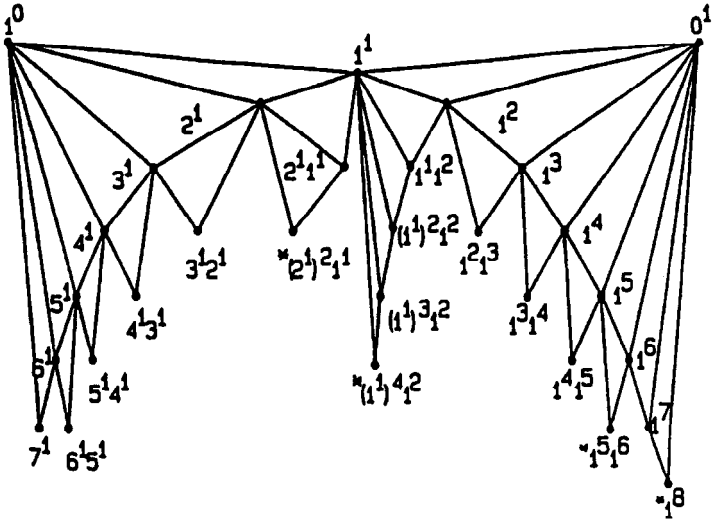

Figure 31. A portion of the Farey tree constructed from observed states. States marked with an asterisk were observed for only four to six cycles. Most of the states were observed for many more cycles. (Reprinted with permission from F. N. Albahadily, J. Ringland, and M. Schell, *J. Chem. Phys.* **90**, 813, 1989. Copyright 1989, American Institute of Physics.)

of periodic and chaotic states that is characteristic for the periodic-chaotic sequences of the second MMO regime is clearly visible.

At this point, it should be emphasized that in contrast to the In^{3+}/SCN^{-} system in which the physicochemical mechanism is very likely described by the reaction scheme underlying Eq. (16), the individual reaction steps that cause the oscillations during Cu dissolution are far from being

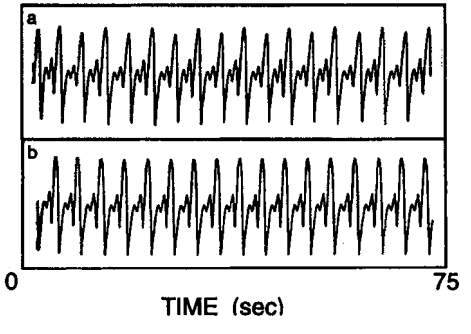

Figure 32. Wave forms measured during the dissolution of copper in phosphoric acid. (a) The subharmonic (period doubled) of the 1^2 state. (b) The 1^2 state. (Reprinted with permission from M. Schell and F. N. Albahadily, *J. Chem. Phys.* **90**, 822, 1989. Copyright 1989, American Institute of Physics.)

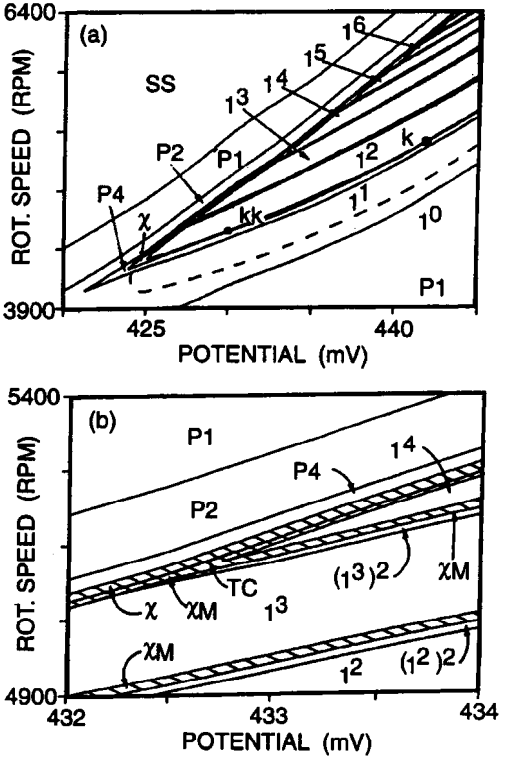

Figure 33. (a) Experimentally determined phase diagram (during the dissolution of copper in phosphoric acid) depicting the regions in the parameter plane rotation speed of the working electrode vs. the potential set at the working electrode, for which different behaviors were observed. (b) An enlargement of a region in (a). L^S, periodic mixed-mode state, L = 1, S = 1, 2, . . . 6; $(L^S)^2$, subharmonic of a mixed-mode state; χM, chaotic mixed-mode state; SS, stationary state; P1, small-amplitude periodic oscillations; P2, subharmonic of P1 ; P4, second subharmonic of P1; χ, chaotic state with small-amplitude oscillations; TC, approximate location of the curve at which the transition from small-amplitude chaos to chaotic MMOs occurred. (Reprinted with permission from M. Schell and F. N. Albahadily, *J. Chem. Phys.* **90,** 822, 1989. Copyright 1989, American Institute of Physics.)

understood. Hence the impression should not be created that there is any established connection between the mechanism of Cu dissolution and the individual terms in Eq. (16). However, whatever the "true equations" describing the dissolution of Cu might be, the agreement between the experimentally determined and the calculated bifurcation structures tells us that the mathematical structure of the resulting equations will be very similar. From this respect we can learn much about the underlying dynamics or phase-space properties of Cu dissolution from Eq. (16).

(c) Mixed-mode oscillations in HNDR Oscillators

Experimental studies of HNDR oscillators exhibit an even richer spectrum of different transitions between complex wave forms than NDR oscillators. However, their physical origin is for the most part unknown, and, accordingly, up to now their modeling has remained an open challenge. Nevertheless, there are some aspects that are worth discussing in this context.

Upon deriving the prototype model of HNDR oscillators, it was assumed that mass transport was fast and thus that the concentration of the electroactive species in the reaction plane was independent of time. Whenever this assumption does not hold and mass transport is incorporated into the mathematical description, the resulting set of equations contains both oscillator types, the NDR and the HNDR. Consider, for example, the following extension of the abstract HNDR model (Eq. 10):

$$\varepsilon \frac{d\phi_{DL}}{dt} = -ck(\phi_{DL})(1-\theta) + \frac{U-\phi_{DL}}{\rho} \tag{17a}$$

$$\frac{d\theta}{dt} = \theta_0(\phi_{DL}) - \theta \tag{17b}$$

and

$$\mu \frac{dc}{dt} = -ck(\phi_{DL})(1-\theta) + 1 - c \tag{17c}$$

Equation (17c) describes concentration changes of the current-carrying species that are due to reaction and diffusion. It has again been assumed that the steady-state concentration profile becomes adjusted immediately. μ is a parameter of O (1) (i.e., the characteristic times of the two slow

variables, θ and *c,* are of comparable magnitude). Obviously, Eqs. (17a) and (17c) are (for θ = 0) equal to the NDR prototype model, whereas Eqs. (17a) and (17b) describe the HNDR oscillator.

In general, the interaction of two feedback loops constitutes the basis for complex dynamics. Hence also in HNDR oscillators, slow transport should be taken into account as a possible source of complex oscillatory phenomena. However, this mechanism should operate only in parameter regimes in which, or close to which, both suboscillators possess oscillatory solutions.

Actually, Eq. (15) describing formic acid oxidation allows for a delayed transport of formic acid (Eq. 15a), and Strasser *et al.*[83] stress the existence of both oscillator types in their model. They also present simulations of MMOs that appeared in parameter space close to the line where the NDR suboscillator [which is obtained when the indirect pathway of formic acid oxidation, (F2), (F4) is neglected] exhibits a Hopf bifurcation. These model calculations are reproduced in Fig. 34. The experimentally observed MMOs are sensitive to the strength of stirring (which was done with a magnetic stirrer).[82] This gives a strong hint that in

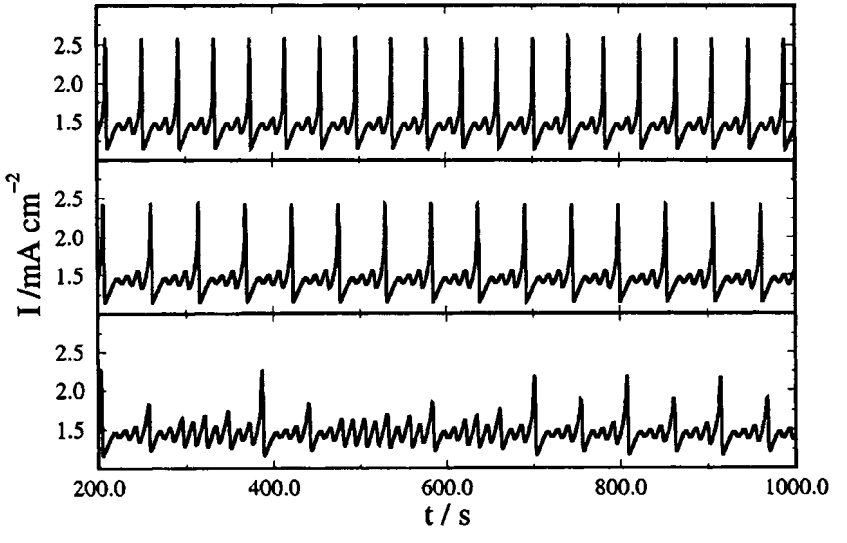

Figure 34. From the formic acid model [Eq. (15)] calculated mixed-mode time series for different values of *U*. (After Strasser *et al.*[83] with permission of the authors.)

this case the mechanism sketched above does hold. However, since it is only expected to generate MMOs close to conditions under which both suboscillators exhibit instabilities, it does not apply to the variety of MMOs observed under galvanostatic conditions. No convincing physical mechanism has been offered so far for these examples.

At the end of this section, two illustrations are given of interesting, though from the physical mechanistic side, still puzzling, experimentally obtained bifurcation sequences. Figure 35 shows a typical series of oscillations as observed during the galvanostatic oxidation of H_2 in the presence of Cu^{2+} and Cl^- ions. When the current density is increased from a low initial value, the system exhibits a Hopf bifurcation. The emerging

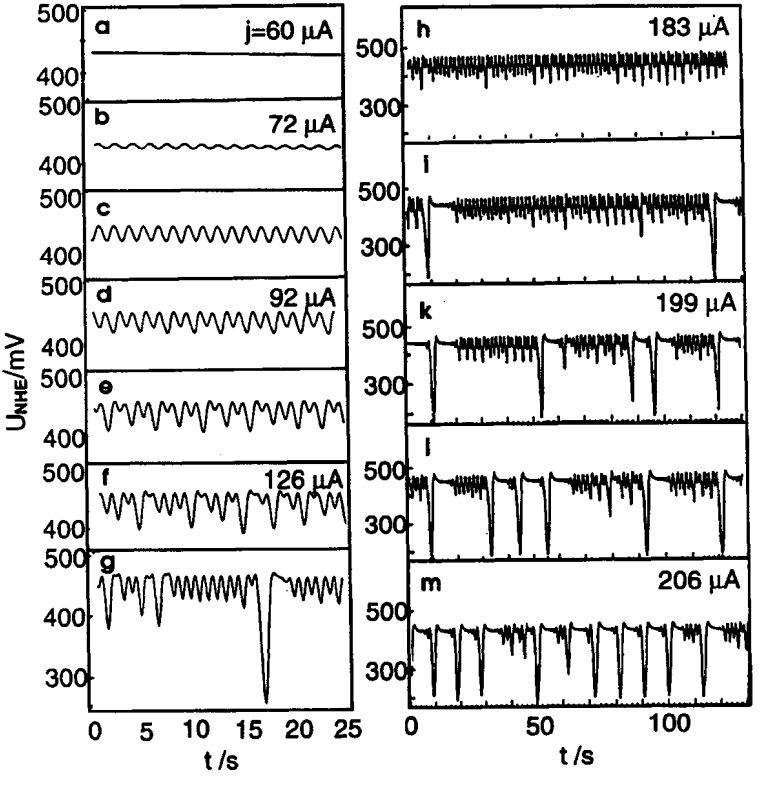

Figure 35. Time series observed during the oxidation of H_2 under galvanostatic conditions for increasing values of the current density. Electrolyte: (a)–(g) 1 M $HClO_4$, 1.5×10^{-4} M Cu^{2+}, 5×10^{-5} M Cl^-, H_2 sat.; (h)–(m) 1 M $HClO_4$, 3×10^{-5} M Cu^{2+}, 3×10^{-5} M Cl^-, H_2 sat. (After Krischer *et al.* [76])

small-amplitude oscillations [Fig. 35(b)] do not continuously grow if the current density is increased further, but undergo a sequence of period doublings to small-amplitude chaos [Fig. 35(d–f)]. From this chaotic state, a transition to MMOs occurs when the current density is increased even further. The MMOs manifest themselves by large-amplitude bursts between the irregular small-amplitude oscillations [Fig. 35(g) and (i)]. These bursts occur in irregular intervals in which the average time between two bursts continuously shortens with further increases in j [Fig. 35(k–m)]. As can be seen from Fig. 36, this sequence or related ones were

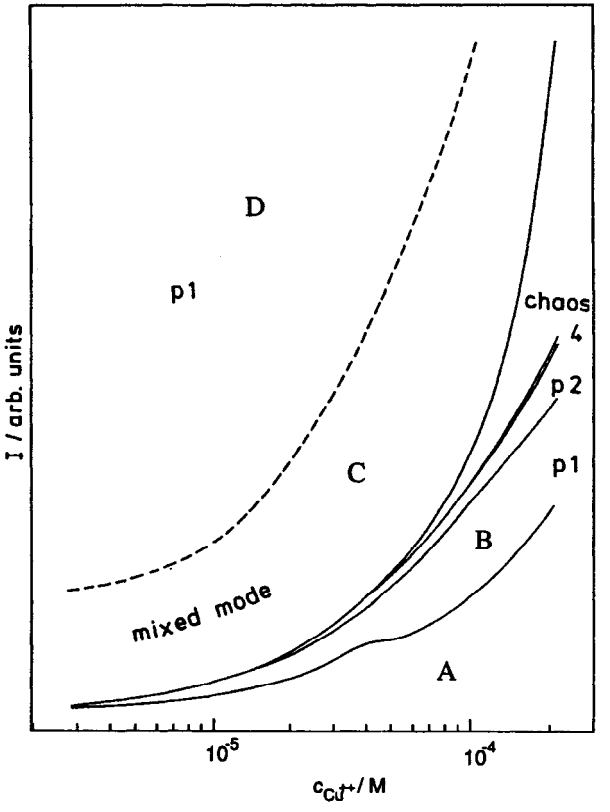

Figure 36. Experimental bifurcation diagram of the existence regions of different oscillation forms during galvanostatic H_2 oxidation on Pt as a function of the Cu^{2+} concentration. pN, period-N oscillation. (A) one stable steady state; (B) small-amplitude oscillations; (C) mixed-mode oscillations; (D) large-amplitude period-1 oscillations. (After Krischer *et al.*[103])

observed over the whole Cu concentration region in which oscillatory behavior existed. Krischer *et al.*[76,103] classify this scenario as an "interior crisis." This is a general term for a global bifurcation in which a small chaotic attractor touches the inset of a coexisting saddle point or orbit and in which a new attractor containing the locus of the former one is generated.[126,127]

The second example is again taken from formic acid oxidation. In Ref. 88 two sequences of mixed-mode oscillations are described which were found when formic acid was oxidized at an elevated temperature (50 ºC) at a rotating platinum electrode. The interesting aspect here is that the large amplitudes in the first sequence are as large as the small amplitudes in the second sequence. Hence, the period-l state that separates the two sequences corresponds to the 1^0 state of the first sequence and the 0^1 state of the second one.

It seems to be questionable whether these two distinct sequences can be described by the model discussed earlier. At this point, the reader should be reminded that although the mechanisms discussed are believed to represent essential features of the individual systems, all of them are simplified caricatures of the "true" system. The validity of the simplifications, of course, changes with the operating parameters, and thus the potential of a certain model to predict experimental observations depends on the experimental conditions. In the case of the last example, it was proposed[20] that a second negative differential charge-transfer resistance, owing to the formation of higher oxides, plays a role in the second MMO sequence. Obviously, such a mechanism is not captured in the model (and also has not yet been experimentally verified).

5. Concluding Remarks

The best-known examples of electrochemical oscillators are reactions involving the anodic dissolution of a metal in acidic solution. With the exception of the complex bifurcation scenarios observed during Cu dissolution, they have not yet been discussed in this chapter. This is because their kinetics are much more complicated than those of the examples reviewed. Thus, despite the fact that oscillatory metal dissolution reactions have been an intense subject of research over decades, there does not seem to be a single example where the reaction mechanism is identified unambiguously and understood in depth. This is for the most part due to complicated passivation and reactivation kinetics which involve the for-

mation and dissolution of macroscopic films. Nevertheless, there are quite a few examples where evidence, or at least strong hints, exist that in these cases also the origin of the oscillations is of an electrical nature.

A clear-cut example of oscillatory dissolution of a metal that belongs to the HNDR type of oscillators is Ni dissolution in sulfuric acid. Early studies of the current-voltage characteristics under both potentiostatic and galvanostatic control by Osterwald[128,129] as well as very detailed investigations of bifurcation behavior by Lev *et al.,*[100,101] exhibit exactly the characteristic features of HNDR oscillators, the most important of them being oscillations around a branch with a positive slope in the polarization curve and a homoclinic bifurcation at the high-current end of the oscillatory regime (when measured under galvanostatic conditions). Haim *et al.*[130] propose a kinetic model for this system which reproduces the qualitative features of the experimental phase diagram. However, the chemical steps underlying their model are somewhat discrepant in relation to a mechanism suggested by Keddam *et al.*[131] For a final clarification of the detailed chemical mechanism, this controversy must be solved. For a discussion of the differences between both models see also Ref. 20.

For Co electrodissolution in phosphoric acid, Sazou and Pagitsas[132,133] carried out a systematic study of the dynamic behavior in the voltage/external resistance parameter plane. The skeleton bifurcation diagram they found is typical for an NDR oscillator; that is, bistability between stationary states occurs at high values of ohmic resistance, whereas oscillations are observed at relatively low values of the external resistance. However, from a chemical point of view, Co dissolution seems to be among the most complicated metal electrodissolution reactions because quite a number of different oxide species are involved. Explanations of the dynamics hardly go further than a general statement that the instabilities are due to the formation of a passive film in combination with an IR drop.

In the case of the electrodissolution of Cu in phosphoric acid, the situation is similar. The dynamic behavior was clearly shown to be a result of a negative slope of the polarization curve in connection with the ohmic potential drop,[134] but a detailed mechanistic model is not available. However, important steps in this direction were made by Tsitsopoulos *et al.,*[135,136] who identified the chemical composition of different oxides being formed under oscillatory conditions, using surface science techniques.

Finally, in this context, Fe dissolution in sulfuric acid should be mentioned. For this system, Russel and Newman[137] presented data that clearly show that under their experimental conditions, bistability is caused by the IR drop in the electrolyte. However, there remains a slight uncertainty because Epelboin *et al.* found a Z-shaped polarization curve, even after correcting for the ohmic drop.[138]

This confronts us with two further points: first, how to determine the category to which an oscillator belongs, and second, how to proceed in order to elucidate the essential mechanistic steps. Concerning the first point, one should always start by doing the utmost to test whether the instability is of a chemical or of an electrical nature; that is, by reducing the ohmic resistance as far as possible. Once this has been done for the electrical oscillators, the bifurcation behavior as a function of the applied voltage and external resistance for potentiostatic control can be used as a criterion for assigning a system to one of the two oscillator types.* Alternatively, as demonstrated by Koper,[19,20] stability studies and categorization of electrochemical oscillators can be performed by impedance spectroscopy. The theoretical foundations as well as the practical approach of this elegant strategy can be found in Refs. 19 and 20. An example in which the oscillator type was identified by impedance measurements is the oxidation of formaldehyde.[19,114] However, the strength of this method, namely, allowing a classification of oscillators without a mechanistic model, also shows its limits: This method is not any better than the bifurcation diagrams spanned by the electrical parameters in providing information on chemical species involved in the oscillations.

The second task of uncovering the essential chemical steps determining the dynamic behavior is a very difficult problem that cannot be solved according to a general strategy. If it is possible to measure the time series of various physical quantities, the phase relation between them can often be useful. This has been nicely demonstrated in the case of H_2 oxidation [Section II.3.(ii)], where oscillations of potential, copper coverage, and hydrogen current were measured concurrently. The copper coverage changed much more slowly than the potential, and thus it could be concluded that it is involved in the slow feedback cycle. If, on the other hand, a quantity follows without phase shift, or with a phase shift of 180º, the species it probes is, at most, necessary to establish the negative

*Or, as in the case of galvanostatic control, it could be a function of the applied current.

differential resistance in the polarization slope (provided the model is an electrical one), but it might not be essential[139] at all for the oscillations to occur. Hence, just because the concentration of a species oscillates, it does not mean that this species is important for the oscillation mechanism.

Besides ring-disk measurements [see Section II.3.(ii).(a)], several other methods have proved useful for the simultaneous recording of current (or potential) and a second quantity (e.g., by means of electrochemical quartz crystal microbalance measurements,[114,117,140,141] electroreflectivity measurements,[142] probe beam deflection studies,[143] differential electrochemical mass spectroscopy,[144] or excess microwave reflectivity[145]). In view of the variety of methods that can be used to study electrochemical oscillations, on the one hand, and the present knowledge about basic mechanisms leading to oscillatory behavior, on the other, the author is quite confident that the number of oscillators whose oscillatory mechanism is understood in some depth will rapidly increase in the near future. This is especially true for oscillating electro-oxidation reactions,* where recent progress in the understanding of the formic acid system should be of much help.

III. PRINCIPLES OF SPATIAL PATTERN FORMATION

Throughout Section II, lumped (i.e., spatially homogeneous) systems were considered which are based on the idea that different locations of an electrode react synchronously; that is, any spatial variations in concentration or potential parallel to the electrode were neglected. This assumption is a suitable working hypothesis for understanding the conditions under which a system exhibits temporal instabilities. However, any complete description also has to incorporate transport processes that may occur parallel to the electrode and thus represent a spatial coupling. The resulting partial differential equation may be regarded as being composed of two parts: the reaction part or local part† that comprises the spatially inde-

*For a survey of oscillating electro-oxidation reactions, see, for example, Table 1 in Ref. 146.

† The expression "reaction part" comes from the analogy with models of homogeneous chemically active media where the temporal changes result from the reaction kinetics only. The alternative name "local part" indicates that at a position x_0 this part contributes only to the temporal evolution at x_0 but not to that at any other positions, x_i.

pendent dynamics (i.e., those terms defining the lumped system), and the spatial coupling terms, originating from transport processes parallel to the electrode. The interplay of both parts often results in the formation of spatial patterns, which may be stationary or vary in time. Therefore, the considerations from the previous section form only a basis for understanding dynamic instabilities in electrochemical systems. Any attempt to obtain a qualitative picture of the dynamic behavior has to take into account the spatial degrees of freedom. Progress made during the past 5 years has led to important insights into rules governing spatial pattern formation in electrochemical systems, and these are the topic of this section.

Section III.1 is concerned with spatiotemporal models, which represent an extension of the temporal models discussed in Section II. In the basic model, the electrode is characterized by one spatial dimension, leading in connection with the electrolyte to a spatially two-dimensional domain. The emphasis is on the nature of the spatial coupling [Section III.1.(i)] as well as the impact of the control mode on the spatiotemporal dynamics [Section III.1.(ii)]. Since both aspects can be seen most clearly in the spatiotemporal variant of the one-variable model [Eq.(1)], the main body of Section III.1 deals with bistable systems. Next, spatial symmetry breaking in NDR oscillators in electrolytes exhibiting an (approximately) uniform conductivity is considered [Section III.1.(iii)]. The complications arising in solutions in which conductivity has to be described by a location-dependent quantity are indicated in Section III.1.(iv). In this section, the shortcomings of predecessor models are also addressed. Pattern formation in electrochemical systems is complicated in many situations in which a parameter of the lumped system becomes a function of position, and thus homogeneous solutions do not exist at all. This is the case, for example, whenever an electrode is embedded in an insulator. This aspect is dealt with for disk electrodes in Section III.1.(v), without, however, providing a mathematical treatment.

The experimental results are compiled in Section III.2, which starts with a short description of the methods used to visualize (potential) patterns at electrode surfaces. First wave phenomena in the bistable regime and then in the oscillatory regime are reviewed, with the focal point being on how they fit into the theoretical picture developed in Section III.1.

1. Models

(i) Bistable Systems under Potentiostatic Control: The Nature of Spatial Coupling

In all electrical models discussed in Section II, the double-layer potential is the autocatalytic variable. Hence, any spatial patterns in these systems should be associated with an inhomogeneous distribution of the double-layer potential and, for this reason, also with an electric field component parallel to the electrode in the electrolyte. Thus, different locations of the electrode are coupled together through migration currents parallel to the electrode. In other words, if the double-layer potential changes at one location, migration currents in the electrolyte make this change felt at other locations across the electrode. Therefore, migration currents provide the system with the ability to exchange information between different positions in space. The mechanism by which migration affects the dynamics can be seen best when considering a bistable system where all concentrations in the cell can be assumed to be constant in space and time, and the dynamic behavior can be described by a single variable.

Before deriving the spatiotemporal model, it is worthwhile to develop a qualitative picture of the effect of the migration currents on front propagation. Consider a situation in the bistable regime where part of the electrode is in one steady state and part of it in the other (Fig. 37). The electric field component parallel to the electrode that exists in the interfacial region induces migration currents parallel to the electrode. These cross currents cause a broadening of the interface that alone would lead in the end to a flat distribution. However, the reaction part tries to drive the potential back to the steady state. All positions where the value of the double-layer potential is above that of the unstable fixed point [indicated by the dashed line in Fig. 37; see also Fig. 2(a,b)] are driven toward the upper steady state and all states below this "separatrix" to the lower one. Hence, the overall effect caused by the interplay of migration and reaction is the motion of the interface, and the more stable of the two stationary states (the lower one in Fig. 37) expands at the expense of the other (metastable) one.

The equivalent circuit of the basic, spatially extended, system as introduced in Ref. 147 is shown in Fig. 38. The electrochemical cell is approximated by a one-dimensional electrode with periodic boundary conditions, while the electrolyte is a two-dimensional, electroneutral

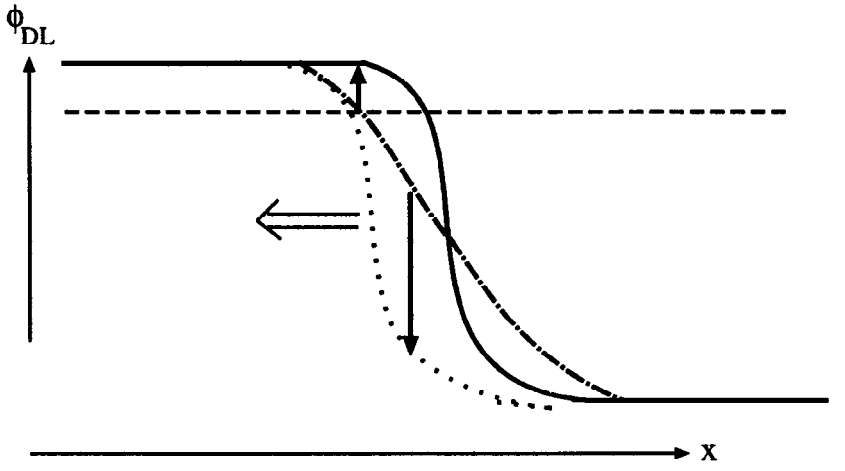

Figure 37. Development of a potential front from the interplay of local dynamics and spatial coupling. The solid line is the original profile. The dot-dashed line indicates the homogenizing effect of the migration currents on the initial spatial profile. The arrows indicate the reestablishment of the spatial profiles (dotted line) by the local dynamics. The dashed line indicates the saddle fixed point. Both effects result in the motion of the interface to the left.

medium with conductivity σ. This is a slightly idealized description of a ring electrode whose circumference is large compared with its width. Each infinitesimal segment of the electrode, or more precisely of the electrode/electrolyte interface, is described by a parallel connection of a capacitor with the specific double-layer capacitance C_{DL} and a resistor having a specific faradaic impedance Z_F.

Before studying the properties of the full equivalent circuit, let us consider the potential distribution in the electrolyte separately. From the electroneutrality condition and uniformity of concentrations, it follows that the potential in the electrolyte, ϕ, obeys Laplace's equation. Furthermore, according to the equivalent circuit, there is an equipotential plane at some distance from the working electrode. The physical picture behind this boundary condition is that either the distance between the working and reference electrodes is so large that all potential inhomogeneities that might exist at the working electrode have faded away at the distance where the reference electrode is located, or, in the case of shorter distances, that the equipotential plane is established at the end of the double layer of the

*Of course, in order to obtain an equipotential plane in this case, the reaction taking place at the counter-electrode must have a large reaction constant.

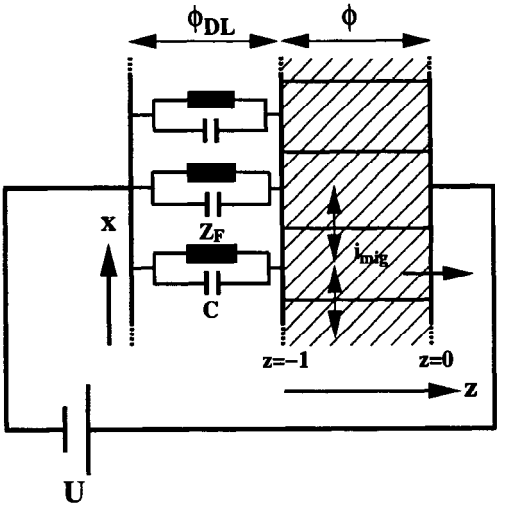

Figure 38. Equivalent circuit of the basic spatially extended system. x, direction parallel to the electrode; z, direction perpendicular to the electrode.

counter-electrode.* In any case, the potential difference between the working electrode and the equipotential plane is kept constant, and thus the equipotential plane can be regarded as the location of the reference electrode. Note that situations in which the reference electrode is placed very close to the working electrode by means of a Luggin–Haber capillary are not included in such a description. Here the potential at a point in the electrolyte rather than in a plane has a constant difference with respect to the working electrode potential, and different boundary conditions have to be used.

In dimensionless quantities, Laplace's equation reads

$$\frac{\partial^2\phi}{\partial z^2} = -\beta^2 \frac{\partial^2\phi}{\partial x^2}, \quad x \in [0,2\pi) \text{ and } z \in [-1,0] \tag{18a}$$

with $\beta = (2\pi w/L)$ where ϕ is the potential in the electrolyte and β is a geometrical parameter denoting the ratio of the distance between the working and reference electrodes, w, to the circumference of the working electrode, L. The direction parallel to the electrode is x, and z represents the direction perpendicular to the electrode ($z = -1$* is located at the

*This choice of coordinates turns out to be advantageous in all spatially extended models. Note that it is different from the one in Section II, where the electrode is located at $z = 0$.

electrode surface). Equation (18a) is subject to the following boundary conditions:

$$\phi(x, z, t) = \phi(x + 2\pi, z, t) \tag{18b}$$

$$\phi(x, z = 0, t) = 0 \tag{18c}$$

and

$$\phi(x, z = -1, t = 0) = \phi^0 \tag{18d}$$

which corresponds to periodic boundary conditions in x (18b), an equipotential plane at $z = 0$ (18c), and some given potential distribution at the electrode (18d).

Mazouz *et al.* [148] elaborated on the importance of the cell geometry for potential distribution in the electrolyte [i.e., for the solution of Eq. (18)], which controls the dynamics of the system. ϕ is given by the following series:

$$\phi(x,z,t) = \sum_{n=1}^{\infty} \{[A_n(t) \cdot \cos(nx) + B_n(t) \cdot \sin(nx)] \cdot \sinh(n \cdot \beta \cdot z)\} + A_0(t) \cdot z \tag{19}$$

that is, a Fourier series (in the direction parallel to the electrode) whose coefficients decrease with progressively larger distances from the electrode, proportional to sinh ($n\beta z$). Thus the coefficients depend on three quantities: the wave number n, the distance from the electrode, z, and the geometrical parameter, β. Accordingly, any inhomogeneous potential distribution at the electrode (i.e., at $z = -1$) is damped into the electrolyte (i.e., decreases for $|z| < 1$). Furthermore, the damping is more efficient for short wavelengths (large n) than for large wavelengths (small n), leading to the delocalization of a structure localized at the electrode. Finally, the amount of the delocalization depends on the electrode arrangement, which is characterized by β. These three points are illustrated in Fig. 39, in which potential profiles at four equally spaced distances from the working electrode are shown. The potential distribution at the electrode, also shown in Fig. 39, was chosen as representative of a possible situation in a bistable regime. It exhibited two levels (corresponding to the two stable states) that are connected by a narrow interfacial region. Consider first Fig. 39(a), where the potential distribution was obtained for a large value of β. In this case, the height of the nucleus drops off strongly into the electrolyte, its

width expanding significantly at the same time. Both effects are less pronounced for smaller β, that is, a smaller distance between the working and reference electrodes [Fig. 39(b)]. For vanishing β, they asymptotically approach a linear decrease of the potential between the working and reference electrodes without any spreading of the potential inhomogeneity in the x-direction [Fig. 39(c)].

The electric field components in the x-direction cause migration currents parallel to the electrode, which leads to a recharging of the double layer. Thus, the time dependence comes into play through the boundary condition (18d). The equation governing the temporal evolution of the double-layer potential results from the charge balance through a "slice," $w \times dx$, of the electrolyte as indicated in Fig. 38[147]:

$$\frac{\partial \phi_{DL}}{\partial t} + i_{reac}(\phi_{DL}) = -\sigma \left(\beta \int_{z=-1}^{0} \frac{\partial^2 \phi}{\partial x^2} dz + \frac{1}{\beta} \left. \frac{\partial \phi}{\partial z} \right|_{z=0} \right) \tag{20}$$

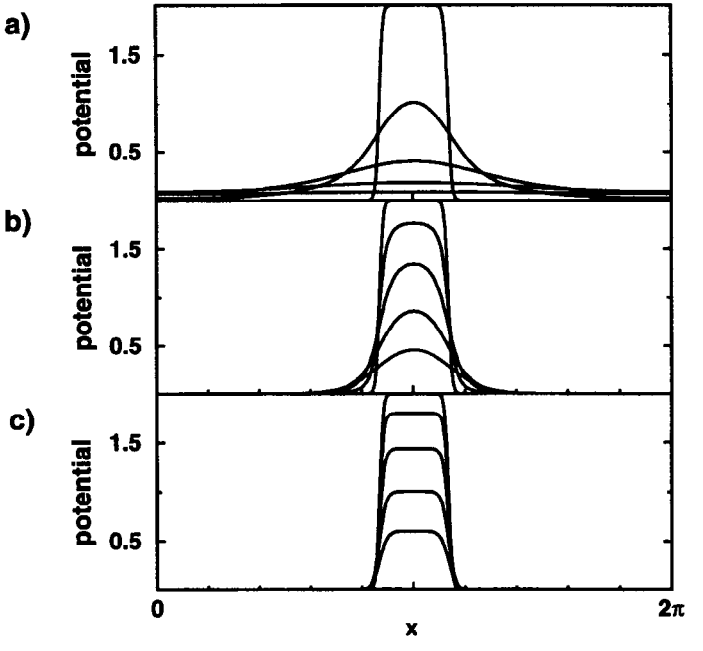

Figure 39. Potential distribution as a function of x for five locations z_i in the electrolyte, and three values of β. (a) β = 4, (b) β = 0.5, (c) β = 0.1, (z_i = –1, –0.9, –0.8, –0.7, and –0.6 (note that z_i = –1 is at the electrode, i.e., the potential distribution chosen). (After Mazouz *et al.*[148])

where σ symbolizes the (dimensionless) specific conductivity of the electrolyte. The lhs of Eq. (20) describes the capacitive and faradaic current densities through the interface, and the two terms on the rhs comprise the migration currents through the three remaining sides of the slice. The double-layer potential, $\phi_{DL}(x)$, and the electrolyte potential at the location of the electrode, $\phi(x,z=-1)$, are related by

$$U = \phi_{DL}(x) + \phi(x)\big|_{z=-1} \tag{21}$$

which results from conditions of potentiostatic control. As above, U stands for the externally applied voltage.

Using Laplace's equation, Eq. (20) can be further simplified to

$$\frac{\partial \phi_{DL}}{\partial t} = -i_{reac}(\phi_{DL}) - \frac{\sigma}{\beta} \cdot \left.\frac{\partial \phi}{\partial z}\right|_{z=-1} \tag{22}$$

and hence the full problem is defined by Eqs. (18), (21), and (22).

As discussed earlier, the equations describing the dynamics of spatially distributed systems are composed of a "reaction part" that defines the spatially homogeneous solutions and is equal to the equation governing the lumped system, and a part that defines the spatial coupling between different parts of the electrode. When comparing the equation describing the dynamics of the lumped one-variable system [Eq. (1)] with that describing the dynamics of the double-layer potential of the spatially distributed system [Eq. (22)], it becomes apparent that the second term on the rhs of Eq. (22), which takes into account all migration currents in the electrolyte, contains two contributions: the current flowing through the electrolyte in a homogeneous situation where the potential varies linearly with z and is thus equal to $(\sigma/\beta)\cdot(U - \phi_{DL}) = (\sigma/\beta)\cdot\phi(z=-1)$, and the contribution of the cross currents defining the spatial coupling.* Thus it is useful to reformulate Eq. (22) in the following way:

$$\frac{\partial \phi_{DL}}{\partial t} = -i_{reac}(\phi_{DL}) - \frac{\sigma}{\beta}\phi|_{z=-1} + \frac{\sigma}{\beta}\left(\phi|_{z=-1} - \left.\frac{\partial \sigma}{\partial z}\right|_{z=-1}\right) \tag{23a}$$

*Note that $\sigma/\beta = 1/\rho$ in the notation used in Section II [see, e.g., Eq. (5)]. Here, ρ is expressed through the specific conductivity σ and the geometric parameter β because these two parameters define different attributes of spatial coupling.

$$= g(\phi_{DL}) + \frac{\sigma}{\beta}\left(\phi|_{z=-1} - \left.\frac{\partial\phi}{\partial z}\right|_{z=-1}\right) \tag{23b}$$

where the second term of Eq. (22) is split into two parts and the "reaction part" is lumped into the function g. Therefore the second term in Eq. (23b) describes the spatial coupling.

In general, the spatial coupling of a system is characterized by two attributes: its range and its strength. The range of the coupling is a measure of the characteristic distance over which a change in the state at a particular position instantaneously affects neighboring parts. The coupling strength defines the ratio of the characteristic times of the local dynamics and the spatial coupling. In electrochemical systems, the range of the coupling is determined by the geometric parameter β, whereas the specific conductivity σ determines the coupling strength (for a given characteristic time of the reaction).[148] As first emphasized in Ref. 149, under many experimental conditions (if $\beta > 1$) the coupling in electrochemical systems is long range or nonlocal. Thus it differs from diffusive coupling, which is the dominant coupling type in other chemical systems (e.g., in the Belousov–Zhabotinsky reaction or in heterogeneously catalyzed surface reactions).[150] Diffusive coupling is local or short range in the sense that, instantaneously, only the nearest neighbors are noticeably affected by a local change in the state of the system. The consequences of nonlocal coupling on dynamic behavior have been the subject of recent intense studies and are reviewed below.

For the moment, the properties of Eq. (23) will be examined in more detail according to Ref. 148. The range of coupling is the result of an interplay of the potential distribution in the electrolyte and the time dependence of the double-layer potential. This can be rationalized by means of Fig. 40, in which the spatial coupling term normalized to unit strength,

$$\frac{1}{\beta}\left(\phi|_{z=-1} - \left.\frac{\partial\phi}{\partial z}\right|_{z=-1}\right),$$

is plotted against position for a rectangular potential profile at the electrode. This potential distribution again leads to a situation in the bistable regime where a large part of the electrode acquires one of the two steady

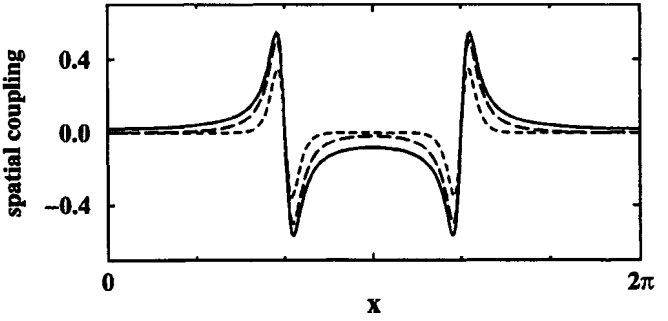

Figure 40. Spatial coupling term in Eq. (23) for three values of β corresponding to the three potential distributions in the electrolyte shown in Fig. 39. Solid line, β = 4; long-dashed line, β = 0.5; dashed line, β = 0.1). (After Mazouz *et al.*[148])

states and a small part the other one, both parts being connected by a sharp interface.

The three curves in Fig. 40 correspond to three different values of β. The solid curve, obtained for the largest value of β, does not fall off to 0, even for positions farthest from the interface. Earlier, it was explained that for large values of β, a structure localized at the electrode strongly broadens out with progressively larger separations from the electrode. Hence, far from the electrode (close to the equipotential plane), the electric field possesses a component parallel to the electrode even at x positions that are remote from the inhomogeneity at the electrode. Taking into account that the integral over all cross currents flowing between the working and reference electrode at a certain position of x, say x_0, is decisive for the recharging of the electrode at x_0, it is understandable why the spatial coupling in electrochemical systems is usually long range. For smaller values of β, the broadening of the potential distribution into the electrolyte becomes less pronounced and thus the coupling range decreases, leading in the limit of vanishing β to local or diffusive coupling (the short- and long-dashed curves in Fig. 40). Since β is an experimentally accessible parameter, the coupling range can be deliberately tuned; this is a singular property of electrochemical systems.

Unfortunately, another peculiar property of electrochemical systems is that the parameters determining the spatial coupling, σ and β, also affect the reaction part. This fact impedes a straightforward examination of the repercussion of the coupling range and strength on dynamic behavior. The influence of σ and β on local dynamics and spatial coupling can be seen

in Eq. (23), but it becomes even more transparent when rewriting the time dependence of the double-layer potential in terms of the evolution equations of the coefficients of its Fourier series expansion:

$$\phi_{DL}(x,t) = \sum_{n=1}^{\infty} \{[a_n(t) \cdot \cos(nx) + b_n(t) \cdot \sin(nx)]\} + a_0(t) \qquad (24)$$

The Fourier coefficients of ϕ_{DL} and those of $\phi|_{z=-1}$ [Eq. (19)] are connected by the potentiostatic constraint [Eq. (21)]:

$$a_0 = U + A_0, \text{ and } a_n = \sinh(n\beta)A_n$$

Calculating the derivative

$$\left.\frac{\partial\phi}{\partial z}\right|_{z=-1}$$

in Eq. (23b) by using Eq. (19), and inserting the corresponding Fourier series for ϕ_{DL} and

$$\left.\frac{\partial\phi}{\partial z}\right|_{z=-1}$$

in Eq. (23), allows us to write the differential equations for the Fourier coefficients of Eq. (23) as

$$\frac{da_0}{dt} = -f_0(a_i, b_i) - \frac{\sigma}{\beta} \cdot a_0 =: g_0(a_i, b_i) \qquad (25a)$$

and

$$\frac{da_n}{dt} = -f_n(a_i, b_i) - \sigma \cdot n \cdot \coth(n\cdot\beta) \cdot a_n$$

$$= g_n(a_i, b_i) - \sigma \left(n \cdot \coth(n\cdot\beta) - \frac{1}{\beta}\right) a_n \qquad (25b)$$

Here the terms $f_j(a_i, b_i)$ $(i, j = 0, \ldots, \infty)$ are the Fourier components of the reaction current density, i_{reac}. Owing to the symmetry of the problem, the equations for the coefficients of the sine modes, b_n, are analogous to those of the cosine modes, a_n. Therefore, here as well as in the mode equations given below, they are not listed separately. The "reaction part"

(the dynamics of the homogeneous system) was lumped again into the function *g*. In this way, the term defining the spatial coupling [the last term in Eq. (25b)] is easily discernible. Note that in this formulation, the different roles that σ and β play are clear: σ only influences the relative time scales of coupling and homogeneous kinetics and thus defines the coupling strength. On the other hand, β influences the ratio of the damping terms of the different modes and thus varying β changes the range of the coupling Furthermore, it becomes clear that the spatial coupling as a function of position (see Fig. 40) converges toward a characteristic function, with a maximum range for large values of β as

$$\lim_{\beta\to\infty}\left(n\cdot\coth(n\beta)-\frac{1}{\beta}\right)=n.$$

From $\beta = 3$, the maximum range is attained (see the solid curve in Fig. 40), which means that in typical electrochemical experiments that are not carried out with a Luggin–Haber capillary, the coupling range is nearly maximum.*

In order to analyze the impact of range and strength on pattern formation, Mazouz *et al.*[148] carried out a computer simulation in which the dependence of the reaction part *g* on σ and β was disregarded and only σ and β in the spatial coupling term were changed. The outcome of this approach can be seen in Fig. 41. The nine images display *x-t* plots of transitions in the bistable regime. The reaction dynamics [the functions *g* in Eq. (25)] as well as the initial conditions were identical in each case. The latter were chosen so that a small portion of the electrode was set in the high-current steady state and the remaining electrode fraction in the low-current steady state. Within a column, the coupling strength decreases from top to bottom and within a row, the range increases from left to right.

First, it is noticeable that in all cases the transition occurs via sharp interfaces that propagate in time across the electrode. Furthermore, it can be seen that the coupling strength has a pronounced effect on the width of the interface as well as on the velocity of the fronts, the interface being broader and the transition faster for large values of σ. However, the qualitative shape of the *x-t* plots remains unaffected within one row. On the other hand and very remarkably, the coupling range determines the qualitative behavior of the transition. For small values of β, [i.e., for nearly diffusive coupling (first column)], the fronts move with constant velocity,

*For the transformation of β into physical quantities, see Eq. [18(a)].

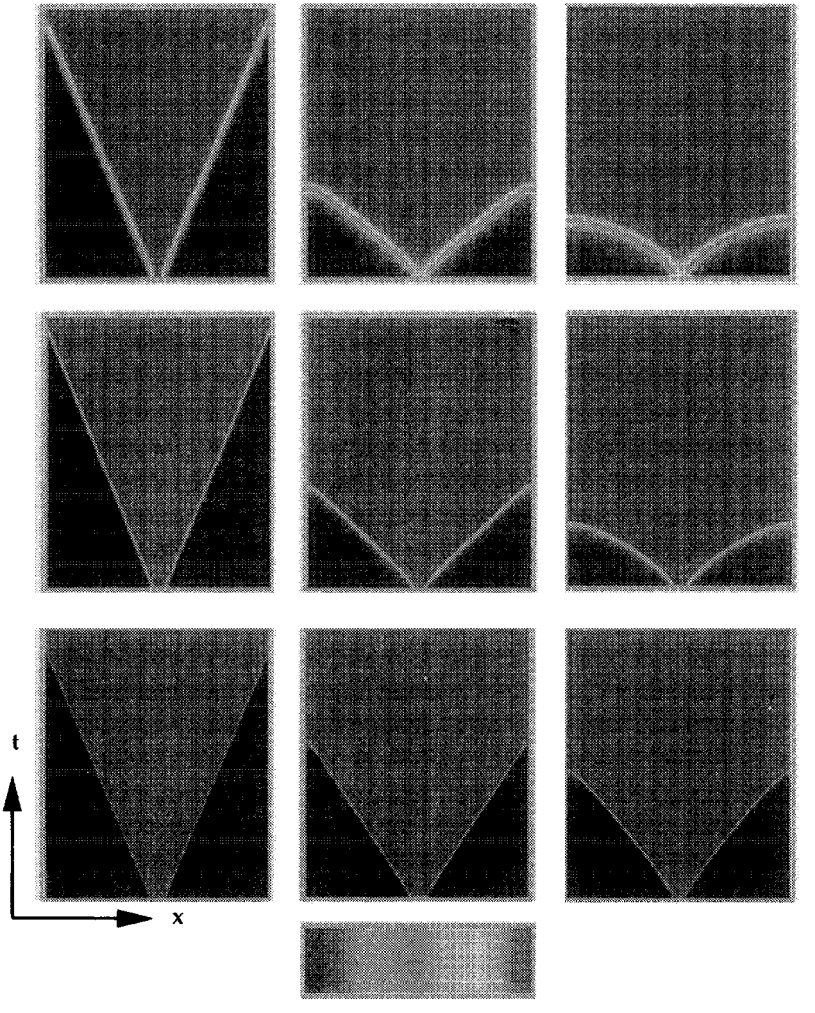

Figure 41. Gray-scale representation of the spatiotemporal evolution of the potential at the electrode ($z = -1$) for different values of coupling strength and coupling range. The "reaction part" g was kept constant and identical in all nine cases. The coupling strength decreases from top to bottom (top row, $\sigma = 0.565$; middle row, $\sigma = 0.0565$; and bottom row, $\sigma = 0.00565$). The coupling range increases from left to right (left column, $\beta = 0.1$; middle column, $\beta = 1$; and right column, $\beta = 10$). The gray scale given at the bottom was chosen nonmonotonically for clarity. (After Mazouz *et al.*[148])

as is known for fronts in reaction-diffusion equations.[151,152] An increase in the range causes an accelerated movement of the fronts and, as will be discussed below, accelerated waves are the outstanding feature of experimentally observed electrochemical waves. The influence of the coupling range on the width of the interface is comparatively small, and the average velocity, though of course being larger in the case of the accelerated fronts, is not affected significantly when β varies.

As explained, in reality a change of the conductivity, σ, or the geometric parameter, β, would also alter the homogeneous steady state [see Eq. (25a) or (23a)], making it impossible to verify through experimentation the prediction of the influence of coupling strength and range. However, it is conceivable for σ and β to be changed simultaneously so that their ratio and hence the homogeneous steady state is kept constant. In this case, one would expect to see a superimposition of both the effects discussed above. This is shown in Fig. 42, where again *x-t* plots of transitions in the bistable regime are depicted together with the global current. When going from left to right, strength and range were increased so that their ratio was kept constant. For small values of σ and β, the interface is sharp and propagates with constant velocity. This gives rise to a linear increase in the global current. For intermediate values of σ and β [Fig. 42(b) and (c)], the effects of both increased coupling range and coupling strength manifest themselves in accelerated front motion, faster transitions, and broader interfaces. In the total current, the accelerated motion is reflected by a faster than linear increase in the current. As the coupling range converges to a maximum value for increasing values of β, the influence of the increased strength dominates the behavior at large values of the coupling parameters. Figure 42(d) nicely demonstrates that large values of the coupling strength oppose pattern formation. The initial inhomogeneity spreads quickly across the whole electrode. The further evolution toward the steady state occurs nearly simultaneously over the whole electrode. In this case, the behavior of the total current is determined by the autocatalytic reaction component. Examples where conclusions about spatial structures were drawn from the global current are discussed in Ref. 153.

To summarize, the important feature of coupling through the electrolyte in electrochemical systems is that the spatial coupling is nonlocal or long range if the reference electrode is further away than about half of the length of the electrode. The range decreases when an equipotential plane (e.g., the counter-electrode) is brought close to the working electrode. A

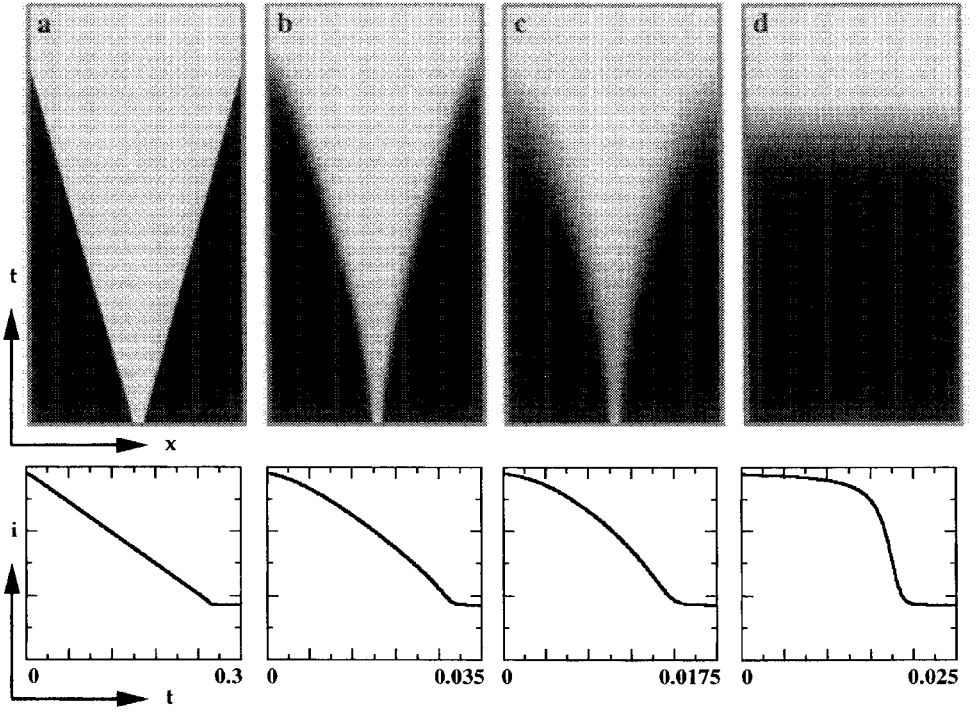

Figure 42. Gray-scale representation of the spatiotemporal evolution of the potential at the electrode (top row) and time series of the global current (bottom row) for four different values of σ/β. (a) σ/β = 0.477/0.0477; (b) σ/β = 4.77/0.477; (c) σ/β = 15.957/1.5957; (d) σ/β = 159.57/15.957. (After Mazouz *et al.*[148])

consequence of long-range coupling is the occurrence of accelerated fronts, which become asymptotic towards constantly moving fronts with decreasing coupling range. Increasing the conductivity of the electrolyte yields, on the one hand, broader spatial structures up to the complete synchronization of the electrode, and on the other, faster wave movement.

(ii) Bistable Systems under Galvanostatic Control or, with an External Resistor, under Potentiostatic Control: The Impact of an Additional Global Coupling

For the homogeneous steady state, it makes no difference whether the ohmic resistance in the external circuit arises from the electrolyte resistance or from an external resistor deliberately introduced into the circuit. In a spatially extended system, however, these two sources of ohmic resistance have to be distinguished. This topic was studied by Mazouz *et al.,* [154] and their main results are summarized here.

From the appropriate equivalent circuit for a system with an external resistor, as displayed in Fig. 43, it becomes apparent that a change in the

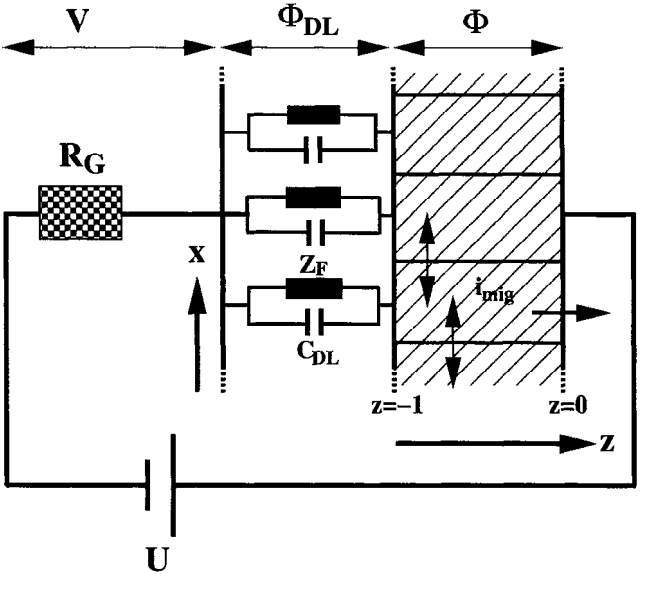

Figure 43. Equivalent circuit for the basic, spatially one-dimensional system with an external resistor.

voltage drop across the external resistor affects all locations of the electrode equally. If the current density increases at a certain location of the electrode, the larger potential drop across the external resistor makes this local change in current density felt at every position on the electrode *with the same intensity.* This kind of coupling is a global coupling.

Hence, in the presence of an external resistor or under galvanostatic control, the total spatial coupling is composed of a global coupling contribution originating from the external resistor, and a nonlocal coupling contribution arising from the electrolyte. The complex interplay of global and nonlocal coupling can be elucidated from the equations governing the enlarged equivalent circuit. The potentiostatic constraint then reads

$$U = V + \phi_{\mathrm{DL}}(x) + \phi(x)\big|_{z=-1} \tag{26a}$$

where V is the potential drop across the external resistor and U, ϕ_{DL}, and ϕ symbolize, as above, the externally applied voltage, the double-layer potential, and the potential drop in the electrolyte, respectively. The hitherto undefined quantity V is given by

$$V = I \cdot R_G = -R_G \cdot \frac{\sigma}{\beta} \cdot \int_0^{2\pi} \frac{\partial \phi}{\partial z}\bigg|_{z=-1} dx =: \frac{\gamma}{2\pi} \int_0^{2\pi} \frac{\partial \phi}{\partial z}\bigg|_{z=-1} dx = \gamma \langle \phi|_{z=-1} \rangle \tag{26b}$$

Here γ is a measure of the ratio of the external resistance, R_G, and the electrolyte resistance per unit area, β/σ; I is the total current. Equations (18) and (22) remain unaffected by the presence of the external resistor and hence the complete system is described by Eqs. (18), (22), and (26). The interaction of the two coupling channels can again be seen better when these equations are transformed into Fourier space:

$$\begin{aligned} \frac{da_0}{dt} &= -f_0(a_i, b_i) - \frac{\sigma}{\beta} \cdot (a_0 - U) + \frac{\sigma}{\beta} \cdot \frac{\gamma}{(\gamma + 1)} \cdot (a_0 - U) \\ &=: g_0(a_i, b_i) + \frac{\sigma}{\beta} \cdot \frac{\gamma}{(\gamma + 1)} \cdot a_0 \end{aligned} \tag{27a}$$

$$\begin{aligned} \frac{da_n}{dt} &= -f_n(a_i, b_i) - \sigma \cdot n \cdot \coth(n \cdot \beta) \cdot a_n \\ &=: g_n(a_i, b_i) - \sigma \left[n \cdot \coth(n \cdot \beta) - \frac{1}{\beta} \right] a_n \end{aligned} \tag{27b}$$

A comparison between Eqs. (25) and (27) allows us to identify the term originating from the global coupling with $(\sigma/\beta)[\gamma/(\gamma+1)] \cdot a_0$. Note that as the integral over all nontrivial Fourier modes in Eq. (26b) vanishes, the global coupling only contributes to the dynamics of the homogeneous mode. The limit of $\gamma \to \infty$ corresponds to the galvanostatic control mode. In this limit the global coupling term becomes maximum, namely $(\sigma/\beta) \cdot a_0$. Hence, galvanostatic control introduces a global coupling into the system that is given by the product of the electrolyte resistance and the average double-layer potential, a_0. Varying the external resistance between 0 (corresponding to potentiostatic control without an external resistor) and ∞ changes the strength of the global coupling continuously between 0 and σ/β.

Since both types of coupling, that through the electrolyte as well as the global coupling originating from the external resistor, depend on σ and β, the total coupling depends in a complex manner on these two parameters. This is elucidated in Fig. 44, where the contribution of the total coupling to the capacitive charging of the double-layer potential is shown as a function of position for a rectangularlike potential profile at the electrode. Figures 44(a–c) correspond to three different values of β. This value is smallest in Fig. 44(a) and largest in Fig. 44(c). For each value of β, the quantity of the spatial coupling terms was calculated for four different values of γ. The solid lines were obtained for $\gamma = 0$ (i.e., the potentiostatic case); the long dashed lines were obtained for $\gamma = 1$ (i.e., a case where the electrolyte resistance and global resistance are equal); and finally, the dotted curve was obtained for $\gamma = 10$ as well as for $\gamma = 100{,}000$ [i.e., the (asymptotically) galvanostatic case]. Since σ enters linearly into both the nonlocal as well as the global coupling term, its variation would lead to a rescaling of the y-axis for the other parameters given. Hence it was kept constant at a value of 1.

The implication from Figs. 44(a–c) is that the global coupling has an impact on pattern formation only if β (i.e., the distance between the working and reference electrodes) is small, or more quantitatively, if $\beta < 1$. For values of β at which the range of the nonlocal coupling through the electrolyte has almost attained its maximum value the presence of an external resistor has virtually no effect on the dynamics.

The consequences of a variation in β on the dynamic behavior of a galvanostatically controlled system are illustrated in Fig. 45. Shown again are transitions in the bistable region for two different values of σ. For small σ (first row) and small β (left column), the influences of the two coupling

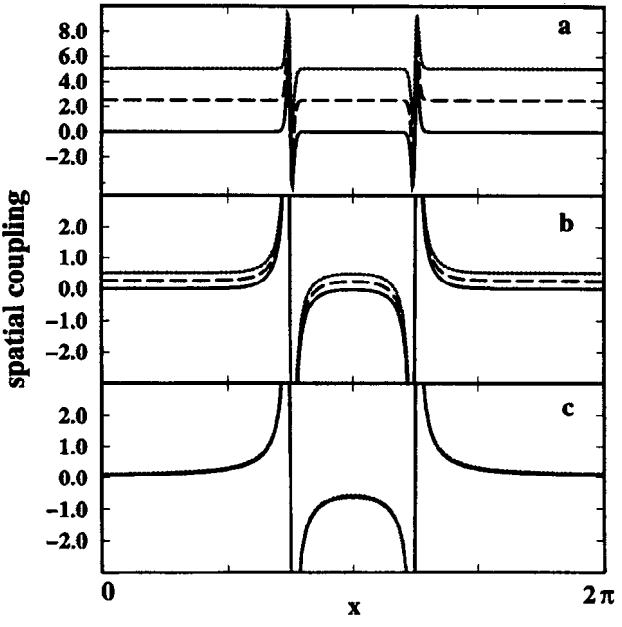

Figure 44. Spatial coupling term (see text) in Eq. (27) calculated for a rectangular double-layer potential distribution for three different cell geometries: (a) $\beta = 0.05$, (b) $\beta = 0.5$ and (c) $\beta = 5$. In each figure the spatial coupling has been calculated for four values of γ: $\gamma = 0$ (solid line), $\gamma = 1$ (dashed line), $\gamma = 10$ (dotted line) and $\gamma = 100{,}000$ (dotted line). In all three cases, the curves for the two larger values of γ are indistinguishable. (After Mazouz *et al.* [154])

types can be clearly distinguished. The nonlocal coupling alone would lead to a front propagating with a constant velocity. As the velocity increases with σ, and σ is comparatively small in this case, the front moves slowly. Owing to the presence of the global coupling, the front propagation is accompanied by a homogeneous variation in the electrode. This causes a homogeneous transition of a part of the electrode to the high-current state when the front has propagated over only a short distance. With progressively larger β, the strength of the global coupling decreases. As a result, instead of causing a homogeneous transition, the global coupling leads to accelerating fronts at values of β at which the potentiostatic system would still exhibit fronts traveling with nearly constant velocity. For large values of β, finally, the behavior is identical to that in the potentiostatic case. For a value of σ that is ten times larger (second row), the global

coupling becomes so pronounced for small values of β that the initial inhomogeneity quickly spreads over the whole electrode and the transition occurs over the whole electrode at the same time. Fronts become discernible only for larger values of β, although, owing to the high value of the coupling strength, they possess a broad interface.

An important consequence of the different parameter dependencies of global and nonlocal coupling is that a variation in β has opposite effects in galvanostatically and potentiostatically controlled systems: With a lowering of β in a galvanostatic system, the increase in the strength of the global coupling tends to synchronize behavior at different parts of the electrode and thus pattern formation becomes less likely for small values of β than for large ones. As is evident from Fig. 45, this trend is accompanied by faster changes in dynamic behavior. When β is decreased in potentiostatic systems, on the other hand, the smaller coupling range leads to an enhanced tendency for pattern formation. Taking into account that

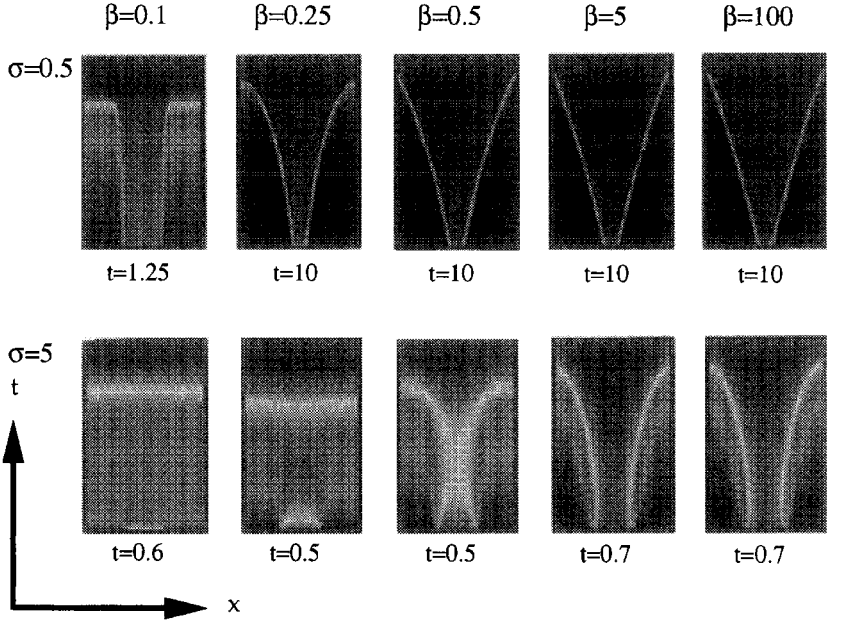

Figure 45. Gray-scale representation of the spatiotemporal evolution of the double layer potential in a galvanostatically controlled bistable system for different values of σ and β. The total time of integration is given below each image. The gray scale is the same as in Fig. 41. (After Mazouz *et al.*[154])

for large values of β, the coupling becomes indistinguishable under both operational modes, Mazouz *et al.*[154] conclude that under galvanostatic control, the parameter region in which patterns emerge is smaller than that under potentiostatic control. However, they also point out that the differences in the pattern-forming properties of both operational modes vanish with vanishing σ.

(iii) Waves in NDR Oscillators

As we have seen earlier, spatial coupling in bistable systems, which can be described in terms of the double-layer potential only, has been thoroughly investigated, and the properties that determine dynamic behavior seem to be understood. In comparison, an understanding of the spatial dynamics of oscillatory electrochemical reactions is still in its infancy. Mazouz *et al.* presented the first theoretical results.[155] They apply to the special situation when the conductivity of the electrolyte can be assumed to be uniform in space and time. This is a restriction, because in the oscillatory regime, the concentrations of the reacting species are generally a function not only of time but also of space. Thus the hypothesis of uniform conductivity is justified only if the transference numbers of the educts and products negligible (i.e., in the presence of a large excess of supporting electrolyte).

In this case, Laplace's equation still represents a good description of the potential distribution in the electrolyte, and all results discussed in Section III.1 remain valid. Furthermore, the change of concentration caused by migration currents of the reacting species can be neglected, and the appropriate equations (first derived by Flätgen and Krischer[147]) on which the calculations are based, read in dimensionless form for the potential:

$$\frac{\partial^2 \phi}{\partial z^2} = -\beta^2 \cdot \frac{\partial^2 \phi}{\partial x^2} \quad \text{for } x \in [0,2\pi) \text{ and } z \in [-1,0] \tag{28a}$$

$$\phi(x,z,t) = \phi(x + 2\pi,z,t) \tag{28b}$$

$$\phi(x,z = 0,t) = 0 \tag{28b}$$

$$\phi(x,z = -1, t = 0) = \phi^0 \tag{28d}$$

$$U = \phi_{DL}(x) + \phi(x)\big|_{z=-1} \tag{28e}$$

$$\frac{\partial \phi_{DL}}{\partial t} = -i_{reac}(\phi_{DL}, c) - \frac{\sigma}{\beta} \cdot \frac{\partial \phi}{\partial z}\bigg|_{z=-1} \tag{28f}$$

and for the concentration

$$c = c\big|_{z=-1} + (1 - c\big|_{z=-1}) \cdot (z+1)\frac{w}{\delta} \qquad \text{for } -1 < z \le -1 + \frac{\delta}{w} \tag{28g}$$

$$c = 1 \qquad \text{for } -1 + \frac{\delta}{w} \le z \le 0 \tag{28h}$$

$$c(x + 2\pi, z, t) = c(x, z, t) \tag{28i}$$

and

$$\frac{\partial c}{\partial t}\bigg|_{z=-1} = -|i_{reac}(\phi_{DL}, c)| + 1 - c|_{z=-1} + \alpha \frac{\partial^2 c}{\partial x^2} \tag{28j}$$

with

$$\alpha = \frac{4\pi^2 \delta^2}{L^2}$$

Equations (28a)–(28f) are exactly the same as those discussed in the previous section, the only difference being that the concentration at or near the electrode, $c|_{z=-1}$, enters the reaction current, i_{reac}, in Eq. (28f) as a variable. In the equations for the concentration (28g)–(28j), the prototype equation of the spatially homogeneous NDR oscillator Equation (4a–b) can be easily recognized. Equations (28g) and (28h) describe at all times linear concentration profiles across the diffusion layer δ/w, and Eq. (28*i*) represents periodic boundary conditions parallel to the electrode. Again, the time dependence enters the problem only through the boundary condition at the electrode [Eq. (28j)]. The reaction part of this equation, being composed of the reaction current, i_{reac}, and diffusion from the end of the diffusion layer to the electrode (i.e., perpendicular to the electrode), is familiar from the spatially homogeneous model. The last term represents an additional spatial coupling, diffusion parallel to the electrode. However, an estimate by Flätgen[156] shows that the diffusion parallel to the electrode

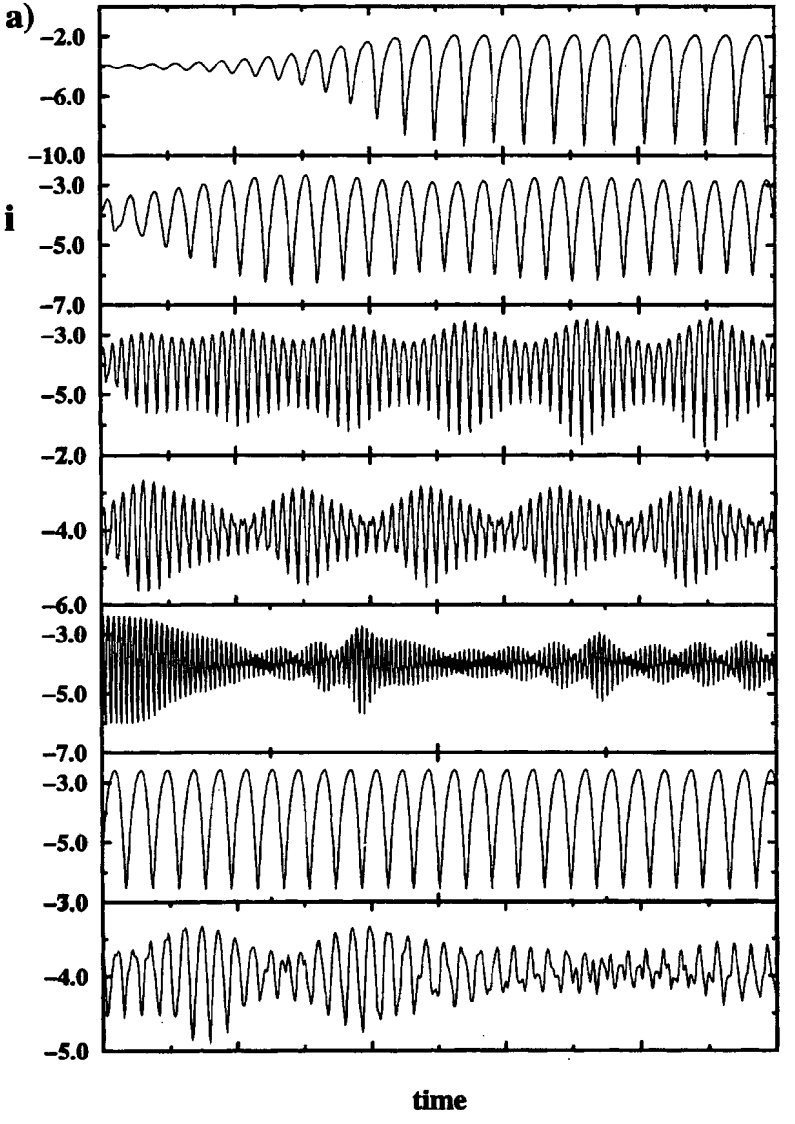

Figure 46. (a) Time series of the global current for increasing electrode length L. (L enters σ and β so that σ/β remains constant). Top to bottom, $L = 0.1884$, 0.314, 0.3454, 0.4082, 0.4396, 0.5652, 6.28 ($w = 0.03$). Total time shown: $t = 20$, $t = 50$, $t = 100$, $t = 20$, $t = 30$. (b) Gray-scale representation of the spatiotemporal evolution of the potential at the electrode corresponding to the first two and last three cases of (a). [In (b) only a section of (a) is shown.] (After Mazouz *et al.*[155])

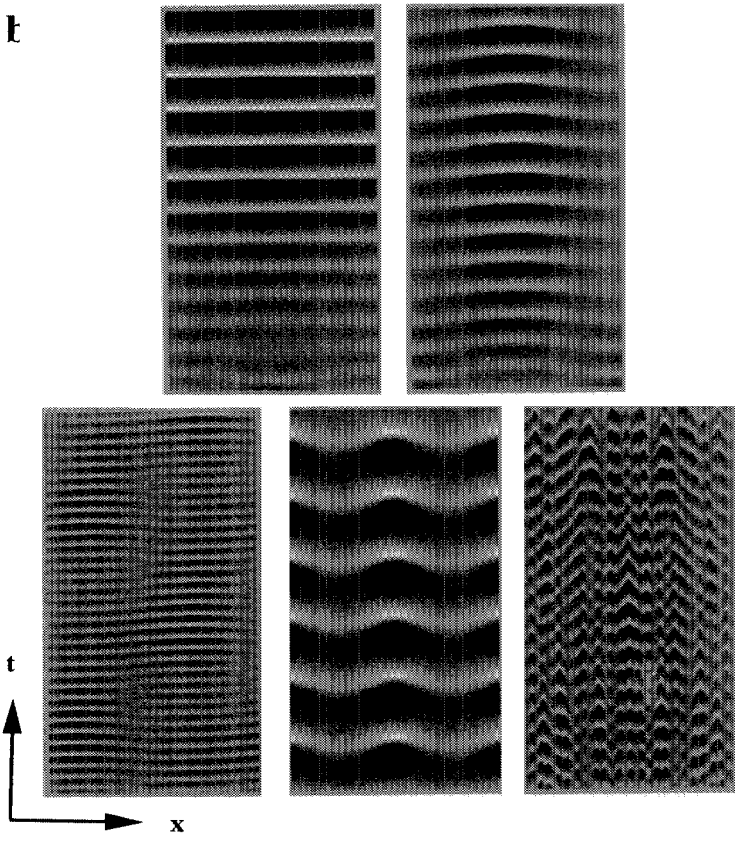

Figure 46. Continued.

is by far the slowest process in the case of rotating electrodes where a small diffusion-layer thickness makes diffusional transport to the electrode very efficient. Hence, when considering pattern formation at rotating ring electrodes, as experimentally investigated by Flätgen and Krischer,[149,153] diffusional coupling should not significantly influence the dynamics. Calculations by Mazouz *et al.*[155] confirmed this conjecture, and in the simulations discussed below, the last term in Eq. (28j) was not taken into account.

Figure 46 depicts the results of a series of calculations that were obtained for different values of the electrode length in the oscillatory

regime close to the Hopf bifurcation. Note that in the dimensionless equations, the electrode length, L, enters the parameters σ and β so that the ratio σ/β is independent of L. Furthermore, β was chosen so that the coupling was almost diffusive. In this parameter regime, a change of L has a significant impact only on the coupling strength, not on its range. First consider the time series of the global current depicted in Fig. 46(a). Here the coupling strength was decreased (the electrode length increased) from top to bottom. Obviously, in only three cases, the first two time series and the sixth one, does the current exhibit simple periodic behavior. In all other cases, more complex oscillations occur. Hence, complex temporal dynamics can be observed in systems with only two variables if spatial instabilities are present.

For the first two and the last three time series of Fig. 46(a), the corresponding position-time plots are shown in Fig. 46(b). The first two images demonstrate how the first instability manifests itself, leading to spatial structures. In both cases, initially a small sinusoidal perturbation was added at a certain instant of the oscillatory cycle. Clearly, in the first case, the initial perturbation is damped out and the system relaxes to the homogeneous oscillation. The second image depicts spatiotemporal behavior after the homogeneous solution has just become unstable. The long-term dynamics can be characterized by a homogeneous oscillation onto which is superimposed a standing wave. Note that this spatial instability does not manifest itself in a measurement of the global current. A further decrease in the coupling strength results in an intricate sequence of periodic and aperiodic patterns. The third and the last image represent examples of spatially aperiodic behavior, the fourth one being an example of a regular pattern with wave number two.

The preliminary results discussed in Ref. 155 indicate that the variety of patterns becomes less pronounced for parameter values farther away from the Hopf bifurcation. This seems to be especially true in the region where the time series possesses a pronounced relaxationlike character. However, as shown in Fig. 47(b), here all homogeneous solutions also might become unstable, so that frontlike structures emerge during an oscillatory cycle. The oscillation of the global current is characterized by a fast increase in current density followed by a slower relaxation to a quasi-stationary low current-density state where the system remains some time before the next cycle starts. A comparison with the spatiotemporal plot reveals that during the fast increase of the current the spatial picture closely resembles that obtained in the bistable regime (i.e., an apparent

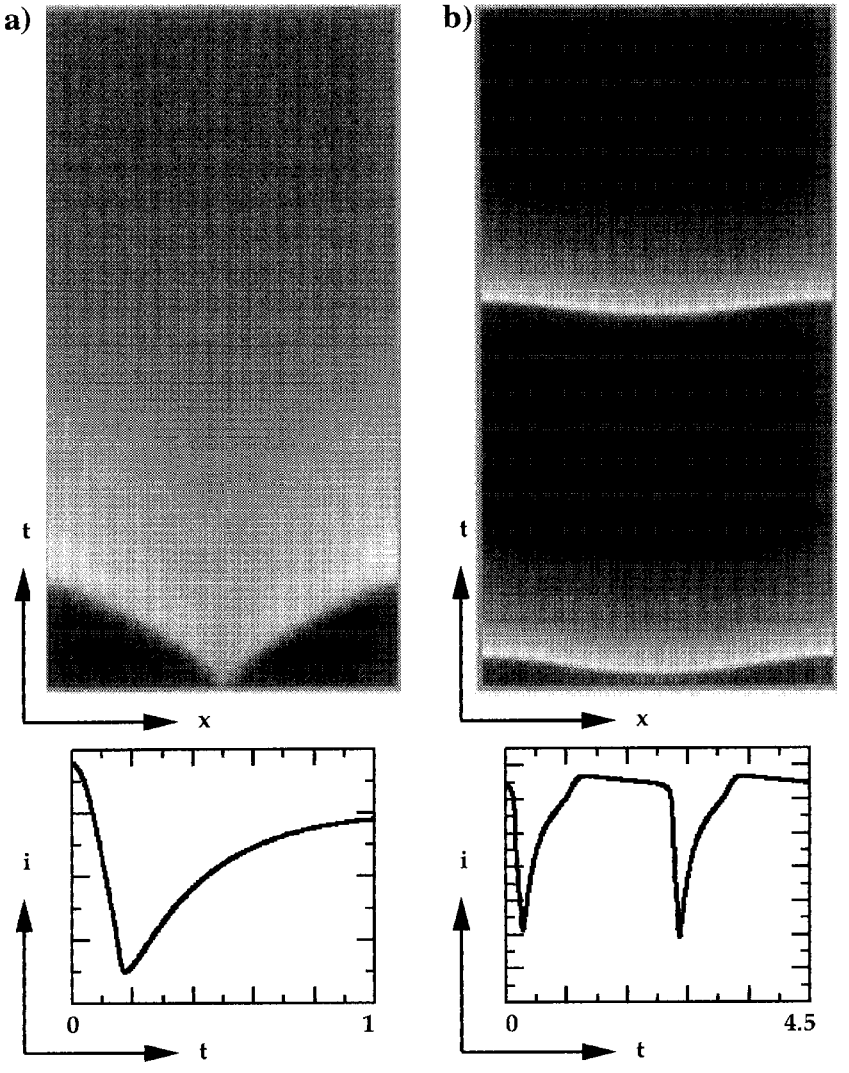

Figure 47. Gray-scale representation of the spatiotemporal evolution of the potential at the electrode (top) and time series of the global current (bottom) in the (a) bistable and (b) oscillatory regime. (After Mazouz *et al.*[155])

front propagates across the electrode, and the velocity of the front increases with time). During the rest of the cycle, the electrode acquires a nearly uniform potential distribution that evolves slowly over time. In comparison, a transition in the bistable regime is depicted in Fig. 47(a).

This transition differs from the one discussed in Section III.1.(i) insofar as one of the steady states is a focus (which is, of course, only possible in a two-variable system), and the current does not monotonically increase but overshoots its stationary value, toward which it slowly relaxes. Also, here the increase in current density is accompanied by an accelerated front, whereas the delayed relaxation of the steady state occurs on a spatially quasi-homogeneous electrode.

(iv) Extensions of the Model and Alternative Models

Before the model discussed above was published, there were three other suggestions of how to model spatiotemporal dynamics in electrochemical systems. The first attempt at a theoretical description of electrochemical pattern formation came from Jorne.[157] His model is based on a chemical instability in the reaction mechanism and only takes into account the concentrations of the reacting species as dependent variables, not the potential. This, of course, means that the model is not applicable to any of the systems exhibiting an electrical instability. This includes the examples treated by Jorne,[157] namely, anion reduction reactions or cation reduction in the presence of SCN^-. Meanwhile, both oscillators are unanimously classified as NDR oscillators [see Section II.2.(ii)] and hence their spatiotemporal description requires a different approach.

The other two models, proposed by Haim *et al.*[158] and Koper and Sluyters,[159] become reduced to electrical models in the spatially homogeneous case. Hence the double-layer potential is a dependent variable, and the models contain elements that are also included in the model by Flätgen and Krischer.[147] In this respect, these two models can be viewed as predecessors of the one presented above. However, each of them contains physically unreasonable assumptions that lead to results contradictory to those obtained with the above-discussed model.

Haim *et al.*[158] aim at a description of waves that were observed during the electrodissolution of an Ni wire in sulfuric acid.[160,161] Their starting point is a lumped system, the behavior of which they had previously treated in order to simulate the global dynamics of Ni dissolution.[130] This model falls into the category of HNDR oscillators,[20] with the variables being the double-layer potential and the degree of surface modification. The latter is assumed to be local, and migration currents provide the only communication channel. The potential distribution in the electrolyte is presumed to obey Laplace's equation. Haim *et al.,* however, missed

including the capacitive fluxes in the charge balance from which they derive their boundary condition at the electrode. As a consequence, subsequently derived equations are also incorrect, and the conclusions drawn in Ref. 158 remain questionable in spite of the apparent agreement between simulated and experimental results. Obvious discrepancies between the model by Haim *et al.* and that discussed above concern the effect of the control mode on pattern formation. Haim *et al.* found that the larger the external resistor, the more pronounced the spatial patterns, whereas Mazouz *et al.*[154] argue that an external resistor has a synchronizing effect and thus opposes pattern formation.

Koper and Sluyters' approach to a general formulation of wave propagation in systems belonging to the NDR type of oscillators starts with the current balance between the working electrode and an equipotential plane at the location x_0. Upon deriving the corresponding equation, they assume a homogeneous current distribution at the equipotential plane. This is a reasonable assumption only for large distances between the working electrode and the equipotential plane, but it is not adequate for shorter distances. In the latter case, the potential distribution at the electrode does not appreciably widen into the electrolyte [see Fig. 39(c)], and therefore the current densities are not uniform at the equipotential plane. In the opinion of the author, however, the main point of criticism concerns the description of the potential distribution in the electrolyte. The latter is assumed to vary linearly between the working electrode and the equipotential plane. As shown earlier, the linear potential profile leads to a spatially local coupling, mathematically resulting in a formal diffusion term. Hence this model does not capture the nonlocal nature of the spatial coupling that proved to be characteristic for spatiotemporal dynamics in electrochemical systems. In addition, Koper and Sluyters assume that an equipotential plane exists at the end of the diffusion layer and beyond. In experiments, potential inhomogeneities are still measured at a distance on the order of millimeters. In a stirred electrolyte or when a rotating electrode is used, the diffusion layer has an extension only on the order of several tens of micrometers. In these cases, besides the failure to describe the nonlocal nature of the spatial coupling, the coupling strength is underestimated.

The spatiotemporal model and the simulations discussed so far provide important insights into the qualitative properties governing the formation of spatial structures in electrochemical systems. However, they are restricted to a certain geometry, namely, "quasi one-dimensional" ring

electrodes, and to a uniform conductivity in the electrolyte. When systems in which the last assumption does not hold are considered, the equations become much more complicated. The potential distribution can no longer be derived by Laplace's equation, and terms involving mixed partial derivatives, such as $(\partial c_i/\partial x)(\partial\phi/\partial x)$, add to the complexity of the boundary condition at the electrode. The derivation of the set of partial differential equations governing the dynamics under these not so favorable conditions (from a mathematical point of view) are given in Ref. 147. To date, simulations with this more complicated set of equations have not been carried out. It is therefore not clear whether the additional terms give rise to qualitatively new dynamic behaviors, or whether they yield only quantitative differences. This question is especially important for understanding pattern formation in metal dissolution reactions, where the high current density leads to a large excess of metal ions close to the electrode, and for this matter, also to a nonuniform conductivity. In the next section, an attempt is made to interpret some of the phenomena observed during metal dissolution reactions using the simple model discussed in this section. One should, however, bear in mind that this interpretation is based on the expectation that the most dominant features of the model will be retained also in more complicated environments. Thus, it might turn out that this picture has to be corrected.

(v) Some Considerations on Pattern Formation at Disk Electrodes

Several experimental studies, most of which will be discussed below, were carried out with disk electrodes embedded in an insulating material. In these cases, the dynamics seem to be strongly influenced by the edge of the electrode. These effects cannot be understood by a straightforward extension of the one-dimensional case discussed earlier.

From a mathematical point of view, the treatment of spatiotemporal dynamics on disk electrodes is considerably more difficult than that of the (infinitesimally thin) ring electrode. Of course, on the one hand this is due to the additional spatial dimension. Since the direction into the electrolyte has also to be considered, the problem is spatially three-dimensional. However, even if this complication is neglected by considering, in a first step, only the radial and axial directions (i.e., neglecting possible structures in the azimuthal direction), solving the resulting partial differential equations is still a challenging task. This is due to the mixed boundary

condition at the electrode end of the domain, which is sketched in Fig. 48(a). At the insulator, the current density in the axial direction is zero, and thus

$$\left.\frac{\partial \phi}{\partial z}\right|_{z=-1} = 0.$$

At the electrode, the current flux at a certain position r_1 is given by the sum of capacitive and faradaic current densities. A thorough mathematical analysis of this problem was carried out by Christoph *et al.*[162] The following discussion concentrates on the illustration of one qualitative point that seems to be significant for any wave phenomenon at disk electrodes.

An important result regarding current and potential distributions at disk electrodes, pointed out by Newman,[163–165] is that owing to the ohmic potential drop, a uniform current density and a uniform double-layer potential cannot coexist. First, consider the primary potential and current distribution where the electrolyte potential at the electrode constitutes an equipotential surface. The primary current density is given[165] by

$$\frac{i(r)}{i_{\mathrm{avg}}} = \frac{0.5}{\sqrt{1 - \dfrac{r^2}{r_0^2}}}$$

where i_{avg} is the average current density, r is the radial coordinate, and r_0 is the radius of the disk. The origin of r is at the center of the disk. Thus the primary current distribution diverges at the rim of the electrode [Fig. 48(b), solid line].

Newman further showed that when slow reaction kinetics are taken into account, the distribution of the potential at the electrode becomes nonuniform. The resulting current distribution, also called *secondary current distribution,* becomes more uniform than the primary current distribution [Fig. 48(b), dashed line]. The discontinuity at the end of the electrode is eliminated.

The higher current density at the rim of the electrode is to be attributed to the current flow through the solution beyond the electrode. This can also be phrased differently: The *effective* solution resistance at a specific location of the electrode is a function of the radius.[162] At the end of the

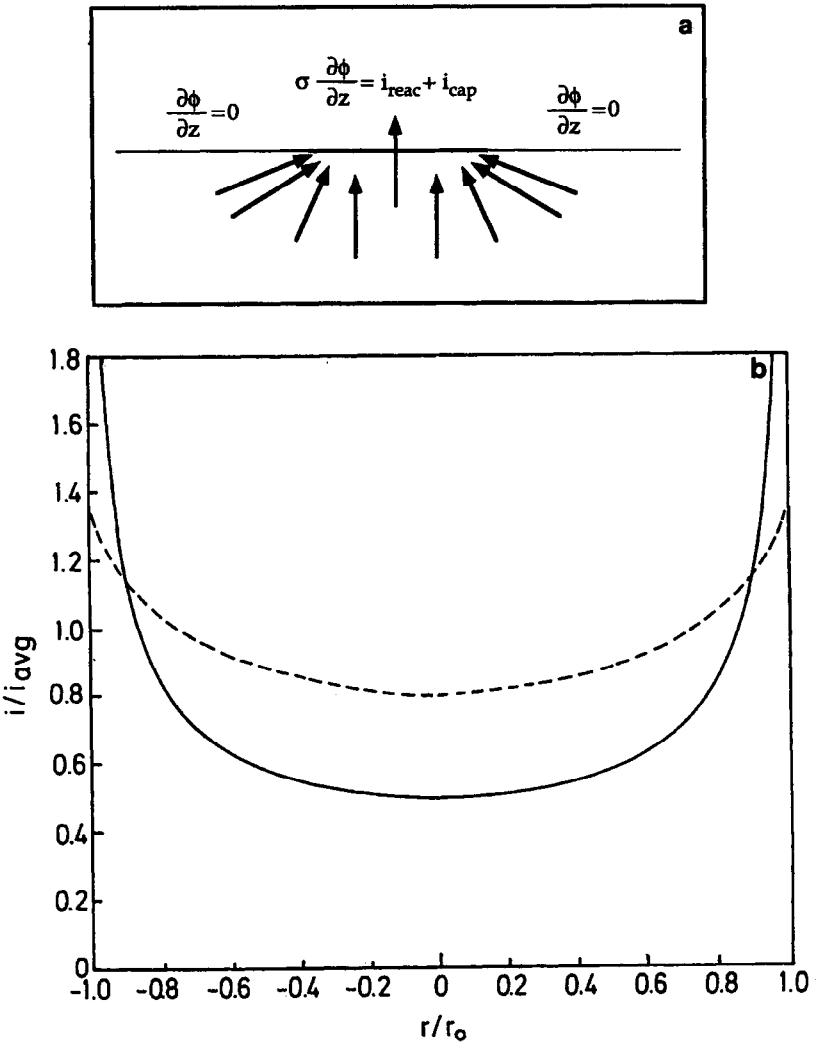

Figure 48. (a) Boundary condition at the electrode end of the spatial domain in the case of a disk electrode embedded in an insulator. The arrows indicate current flow in the electrolyte. (b) Primary (solid line) and a secondary (dashed line) current distribution as a function of the radial position.

disk ($r = 1$), the effective solution resistance is at a minimum, whereas it is at a maximum at the center of the disk.

With this knowledge one can construct a simplified picture of how location-dependent resistance affects dynamic behavior.[162] Neglecting the spatial coupling through the electrolyte, the differential equation for the double-layer potential depends on the radial position according to

$$C\frac{d\phi_{DL}}{dt} = -i_{reac}(\phi_{DL}) + \frac{U - \phi_{DL}}{A \cdot R_e(r)}$$

With this equation the effect of the location-dependent resistance on the steady states in the bistable regime can be seen easily. The stationary solutions as a function of the radial position are illustrated in Fig. 49(a),

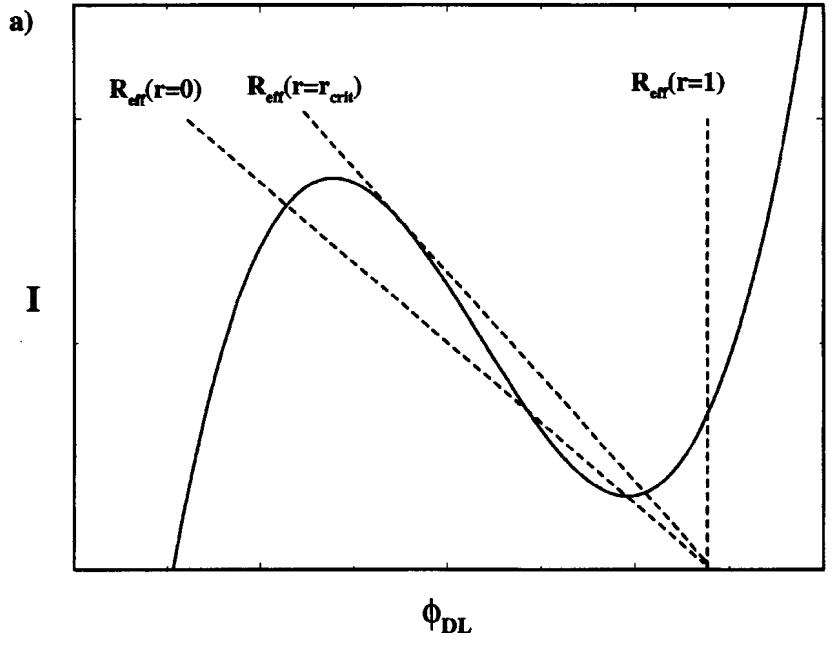

Figure 49. (a) N-shaped steady-state polarization curve and different load lines referring to the different effective local electrolyte resistances. The intersections between the polarization curve and load line are stationary states at a certain radial position when the spatial coupling vanishes. (b) Coexisting radial profiles of the double-layer potential at a disk electrode for an electrochemical system with a bistable "reaction part."

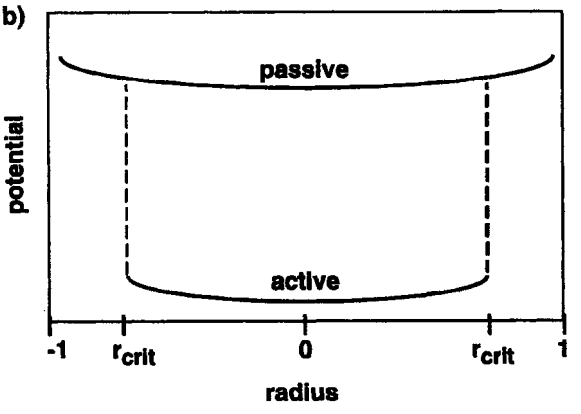

Figure 49. Continued.

where again the reaction current, i_{reac}, is assumed to possess an N-shaped polarization curve. At the rim of the electrode ($r = 1$), the effective electrolyte resistance becomes so small that it can be neglected altogether. Hence, at the rim of the electrode, the system is strictly potentiostatic ($U = \phi_{DL}$). Consequently, it is always monostable. With increasing distance from the electrode, the slope of the load line becomes smaller, and from a critical distance on, three steady states exist. Thus, in the central part of the disk the reaction dynamics are bistable. Putting the uncoupled positions together results in the two spatial profiles shown in Fig. 49(b). Each state in the bistable regime is characterized by a spatially inhomogeneous profile.

The profile in which all positions take on a state on the low current density branch exhibits only weak spatial variations. The other one possesses two steep steps that connect the passive states at the rim with the active states in the central part of the electrode. For the uncoupled system, the transition from the active to the passive state can occur anywhere between $r = 0$ and $r = r_{crit}$ (i.e., a whole family of such spatial profiles exists). When allowing for a finite (but still weak) coupling, only one of these profiles exists, namely that where relative stability of passive and active states is equal. It is reminiscent of the interfaces that form during a transition in the bistable regime on a ring electrode as discussed earlier. Those, however, are moving in time and hence are only transient phenomena; the long-term behavior always exhibits a homogeneous steady state.

At disk electrodes, in contrast, profiles connecting steady states on the active and passive branch constitute, at least in the limit of very weak spatial coupling, stationary structures.

2. Experiments

(i) Experimental techniques

From this discussion we have seen that the main pattern-forming variable is the potential. Furthermore, the dynamics are crucially determined by transport processes and cell geometry. Consequently, experimental studies rely on the availability of methods that do not interfere with transport processes. Ideally, they probe the potential distribution in the electrolyte close to the electrode or the double-layer potential. To date, three methods have been employed in the study of patterns in electrochemistry: potential probe measurements, surface plasmon microscopy, and visible light microscopy.

The major advantage of potential probes is that they directly measure the local potential in the electrolyte and allow a straightforward and quantitative interpretation of the data. Besides, they are easy to operate and inexpensive. Their obvious disadvantage is that they readily hinder the transport of the reacting species and/or shield the electric field. This has restricted their use to one-dimensional geometries.[24,28,30,149,160,161,166,167] In many applications, spatial resolution was achieved with several stationary indicator electrodes. The number of potential probes varied between two and sixteen, yielding a poor spatial resolution of several millimeters to several centimeters. In contrast, the temporal resolution is only restricted by the response time of the probes, which can be easily adjusted down to the microsecond regime (see later discussion).

In an elegant setup, stationary potential probes were used in combination with rotating ring electrodes (Fig. 50). This setup has the advantage that the transport of the reacting species is well defined and can be optimally controlled (as is the case for any rotating electrode). The spatial resolution is simply achieved by measuring as many points as desired during one rotation of the electrode. Hence, in this arrangement, the spatial resolution is restricted by the diameter of the potential probe, which can be as small as a few micrometers. However, the price for this greatly improved spatial resolution is a longer response time of the potential probe (see later discussion). The temporal resolution at a certain location along

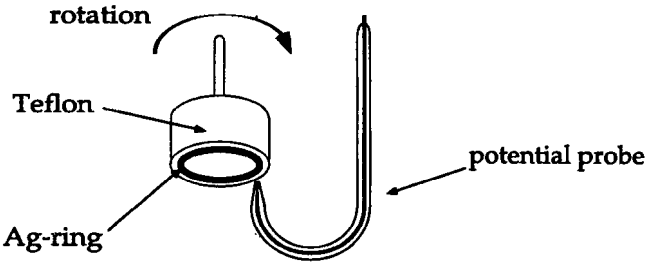

Figure 50. Experimental setup for measuring spatiotemporal pattern formation on a rotating ring electrode with a stationary potential probe. (After Flätgen and Krischer.[149])

the ring is obviously limited by the rotation rate of the electrode. Since the rotation rate also determines the dynamic behavior, the temporal resolution cannot be chosen independently from the dynamic regime. This might especially become a problem in the oscillatory regime, which typically occurs at lower rotation rates than the bistable regime.

The potential probes employed so far have all consisted of glass tubes that were pulled out to a capillary at the tip and contained a reference electrode inside the tube. As mentioned earlier, the diameter of the tip restricts the spatial resolution in the second setup. With the patch clamp technique,[168,169] it is possible to produce capillaries with openings as small as 0.1 μm in diameter. Ideally, the capillary can be viewed as a parallel connection of a capacitor and a resistor where the capacitor symbolizes the glass and the resistor is the solution inside the capillary.[156] Hence, the response time of the probe τ can be roughly estimated by $\tau = R_{\text{probe}}\ C_{\text{probe}}$. For a fast response time, a rapid broadening of the thin tip is necessary as well as high conductivity of the solution inside the capillary. This can be achieved by filling the tip with agar-agar gel saturated with a salt of high solubility such as NaCl or Na_2SO_4. The agar-agar gel prevents the electrolyte from being contaminated by the solution inside the tip. In this way, response times of 10 μs were achieved for a 200-μm probe. In comparison, a 1 mM electrolyte yields a 0.3-s response time.[156]

Surface plasmon microscopy[170] allows the recording of two-dimensional images of the potential distribution at the electrode and combines high temporal and spatial resolution with a nonperturbing nature. These properties, which are optimal for spatiotemporal dynamics studies, are confronted with two restraints. A quantitative analysis of the data is more

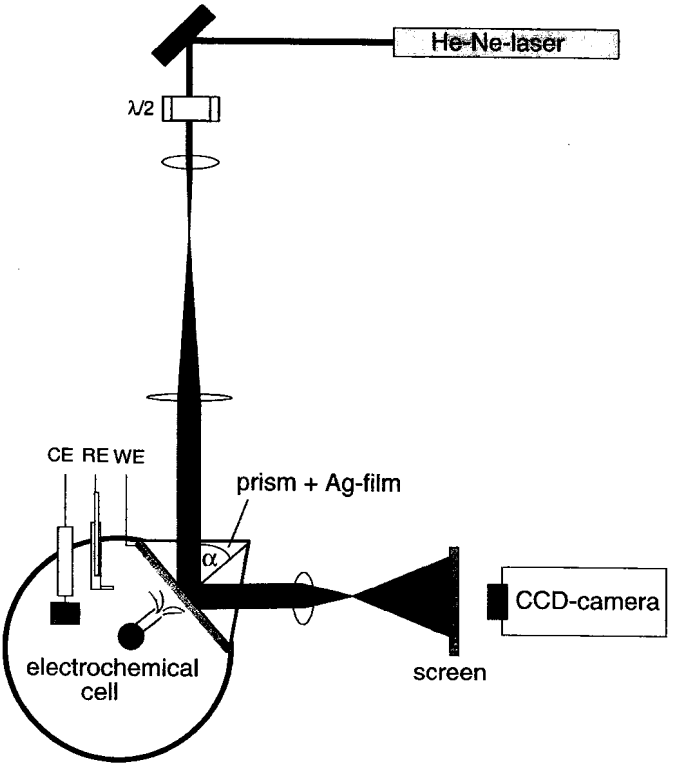

Figure 51. Experimental setup for studying spatiotemporal patterns by means of SP microscopy. WE, working electrode; RE, reference electrode; CE, counter-electrode; and J, impinging jet. (After Flätgen *et al.*[170])

difficult than in the case of potential probes, and the working electrode material is restricted to certain metals.

An experimental setup of an SP microscope suitable for spatiotemporal measurements in an electrochemical environment is depicted in Fig. 51. The working electrode consists of an Ag or Au film of about 50-nm thickness that is evaporated onto a glass prism having a high refractive index. The glass prism permits the excitation of surface plasmons by

*Tadjeddine and Hadjadj[171,172] showed that a $Pt_x Al_{1-x}$ alloy, which behaves electrochemically in a way identical to Pt, can also be optically excited and thus is also applicable to SPM studies.

p-polarized laser light, which is passed through the prism onto the metal film at a certain angle of incidence. This arrangement has become known as the Kretschmann configuration.[173] The excitation of SPs occurs in a narrow interval of the angle of incidence at which the energy and momentum of the incoming photons and SPs match. The SP excitation manifests itself as a strong decrease in intensity of the reflected laser beam. In an electrochemical environment, the dispersion relation of the SPs changes with the potential applied in a certain potential range.

Figure 52 displays two typical resonance curves obtained at two values of the potential. The curves are clearly shifted relative to each other. Obviously, if the potential drop is different at two different locations at the electrode, the intensity of the reflected laser beam at a certain angle of incidence should be different. Hence, spatially resolved pictures of the potential distribution along the electrode can be obtained if the laser beam is broadened and the irradiated part of the electrode is imaged onto a screen, which can be recorded with any charge-coupled device (CCD).

The fast dynamics of oscillatory electrochemical reactions often require a temporal resolution considerably better than video frequency. In the studies discussed in the next section, cameras with a full-frame transfer architecture that allows the recording of about 1000 frames per second were used. The spatial resolution is limited by the propagation length of

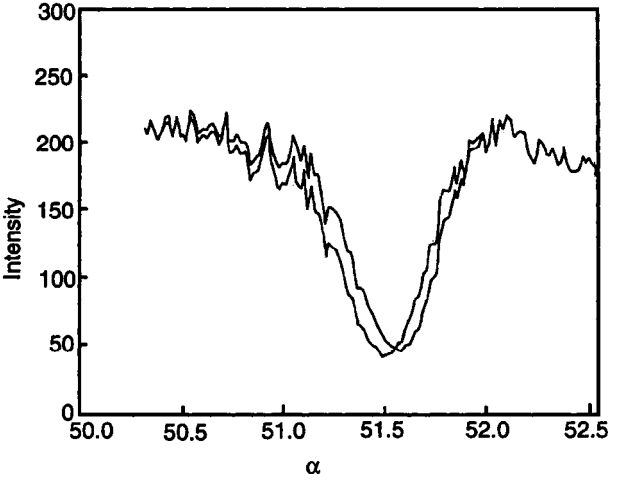

Figure 52. Reflectivity vs. angle of incidence for two values of the applied potential. (After Flätgen *et al.* [178])

SPs and thus depends on the frequency of the exciting laser light. For example, for an He-Ne laser (632 nm), it is about 20 μm.[174] The electrode is freely accessible, and a defined convection can be achieved by means of an impinging jet.

The direct observation of waves on electrode surfaces with video cameras is often possible in metal dissolution reactions where, in general, different double-layer potentials are connected with distinct thicknesses of salt or oxide layers. The latter are so pronounced that they possess visible contrast in the reflectivity. Obviously, this direct imaging is restricted to reactions that are accompanied by drastic changes of the electrode morphology. Hence, the reactions that are mechanistically the most difficult ones to understand are the easiest ones to study from an experimental point of view.

(ii) Fronts in the Bistable Regime

(a) Reduction of peroxodisulfate

Extensive investigations of front propagation in a bistable regime under potentiostatic control were carried out for the reduction of $S_2O_8^{2-}$ by Flätgen and Krischer.[149,153] These studies, being the first ones of electrochemical waves that are not linked to metal dissolution reactions, provided ample evidence that (1) spatial coupling occurs through migration currents in the electrolyte, and (2) the coupling is nonlocal in nature. These are the coupling attributes that in later theoretical studies proved to be decisive in accounting for pattern formation in electrochemical systems (see Section III.1). In this context, it is important to note that in all experiments carried out so far with this system, no external resistor was used. Furthermore, the distance between the working and reference electrodes was considerably larger than the circumference of the electrode, resulting in a maximum in the nonlocality of the coupling.

A typical transition from the passive to the active state, as measured with a potential probe and a rotating Ag ring electrode, is reproduced in Fig. 53. The accelerated motion of the interface immediately leaps to the eye. It is, according to the explanation given in Section III.1, a consequence of nonlocal coupling. Accelerated fronts were found to be the characteristic feature in all passive to active transitions. By contrast, during the much slower transitions from the active to the passive state, often only faint spatial variations were observed, but no sharp interfaces between

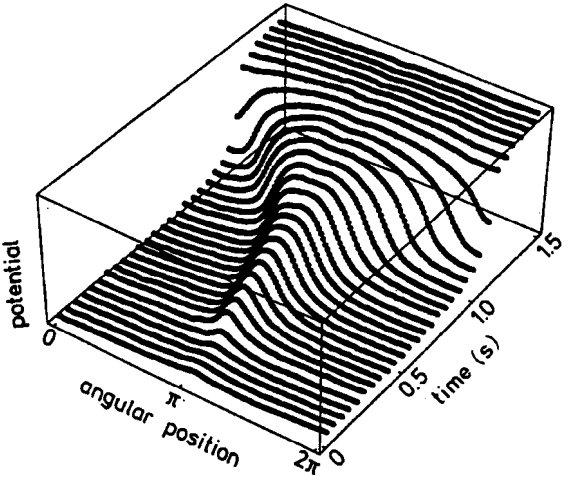

Figure 53. Spatiotemporal plot of the local potential during a transition from the passive (low current density) to the active (high current density) state in the bistable regime of the reduction of peroxodisulfate. Circumference of the electrode, 3.46 cm. (After Flätgen and Krischer.[149])

these states.[153] The fact that the active to passive transition is slower suggests that the reaction dynamics are slower than in the passive to active transitions. This, in turn, means that the coupling strength is larger, or, in other words, the synchronizing effect of the spatial coupling is more pronounced. Recall that the coupling strength is roughly determined by the ratio of the characteristic times of local dynamics and spatial coupling.

The average front velocity of the passive to active transitions has been examined as a function of a series of parameters.[149] The most important result of these studies is that the average velocity was found to increase approximately linearly with the conductivity (Fig. 54), but did not notably depend on the concentration of $S_2O_8^{2-}$ at constant conductivity. From these experiments it could be concluded that diffusion has no influence on spatial coupling. An increase in the front velocity with increasing conductivity was also found much earlier for metal dissolution reactions by Bonhoeffer and Renneberg[24] and also by Franck.[28] In all three studies, the average velocity of the fronts was found to range between a few cm s^{-1} and m s^{-1}.

Passive to active transitions, as imaged with the surface plasmon microscope, are depicted in Figs. 55 and 56 (color plate following page 112). In the first example, the working electrode consisted of an Ag ring having a

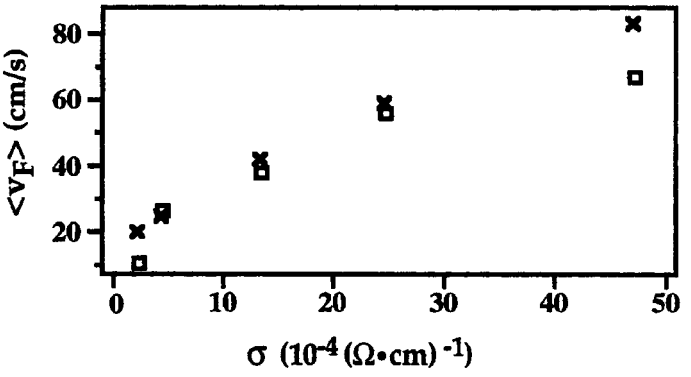

Figure 54. Average front velocity as a function of the electrolyte conductivity σ. (After Flätgen and Krischer.[149])

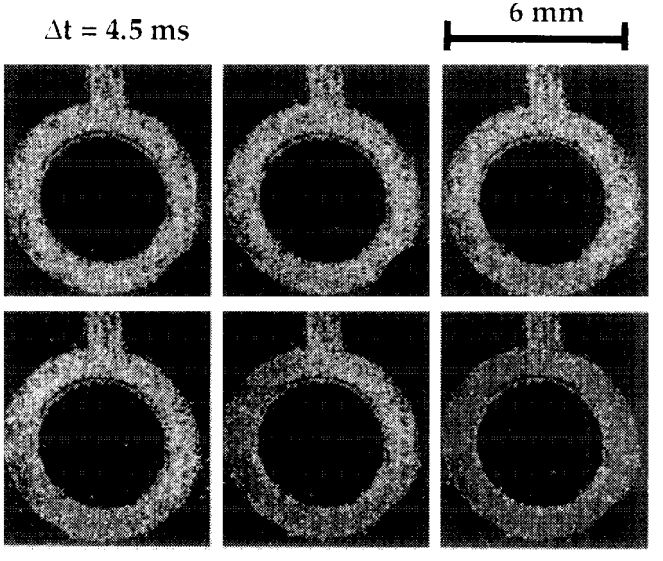

Figure 55. SP microscope images of a potential wave on an Ag ring electrode during the reduction of peroxodisulfate (elapsed time between the images, 4.5 s). (After Flätgen *et al.*[170]) A color representation of this figure can be found following page 112.

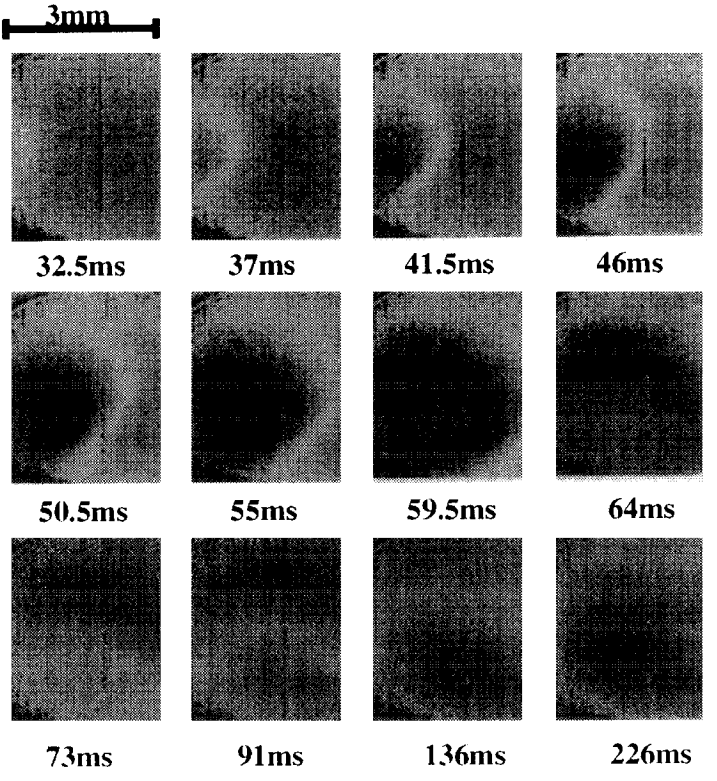

Figure 56. SP microscope images of a potential wave on an Ag disk electrode during the reduction of peroxodisulfate. (After Flätgen *et al.*[170]) A color representation of this figure can be found following page 112.

comparatively substantial width. The images shown were recorded in equidistant time intervals and quite clearly, also in this case where the electrode can no longer be viewed as quasi one-dimensional, the front motion is accelerated (Fig. 55).

In the second example, a disk electrode was evaporated onto the prism (Fig. 56). Here, as well as in all other studies carried out with disk electrodes, the active phase nucleated at some location along the rim of the electrode, from where it spread across the surface. In view of the consideration discussed in Section III.1.(v), this is surprising, because the electrode rim should always be more passive than the center of the electrode. Therefore, one would expect that the active phase forms easiest in the center of the disk, which was also found in simulations.[162]

(b) Co electrodissolution

Another system for which Otterstedt *et al.* have recently carried out many studies on spatial pattern formation is the electrodissolution of Co in acidic phosphate solutions.[167,175–177] As for most electrodissolution reactions of metals in acidic solution, when the potential is varied in the anodic direction, there is a well-known critical potential, the Flade potential, at which a sudden decrease in current density to nearly 0 occurs. This active to passive transition is attributed to the formation of an oxide film that prevents further dissolution of the metal. In potentiostatic experiments, depending on the other control parameters, bistability or oscillations are observed in the vicinity of the Flade potential. For all metal dissolution reactions, complicating factors, such as convection induced by density gradients due to the high current densities involved and the complicated kinetics of salt and oxide film formation, come into play. However, many of the phenomena observed are analogous to that predicted by the simple spatiotemporal model described earlier. Thus, Otterstedt *et al.* interpret their results by invoking the spatial coupling mechanism through the electric field as given in Eqs. (18), (20), and (21).

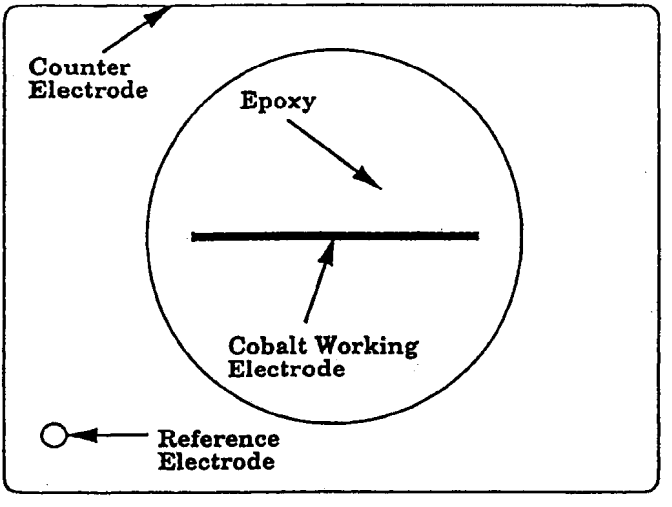

Figure 57. Top view of the experimental setup used to study waves on quasi-one-dimensional Co electrodes. (Reprinted with permission from R. D. Otterstedt, P. J. Plath, N. I. Jaeger, and J. L. Hudson, *Phys. Rev. E* **54,** 3744, 1996. Copyright 1996, American Physical Society.)

These authors [176] obtained a quasi one-dimensional electrode geometry by embedding a Co foil in an epoxy resin so that an area 50×0.5 mm was exposed to the electrolyte (Fig. 57). The counter-electrode was bent into a rectangle 150×100 mm located in the same plane as that of the working electrode. The reference electrode was placed close to a corner of the counter-electrode.

Front propagation was studied by initiating transitions from the passive to the active state by scratching the passive Co electrode slightly at one end with a glass rod and monitoring the spatial changes with a video camera. The characteristic behavior turned out to closely resemble that of the electrocatalytic reaction; that is, the fronts traveled across the electrode with increasing velocity (Fig. 58).[176] Furthermore, the width of the interface increased with time. In Ref. 176, the authors stress the importance of long-range coupling for the occurrence of acceleration. However, they argue that this effect acted in conjunction with a second mechanism that also caused an acceleration. During the transition, the total current increased, leading to a more cathodic potential everywhere along the electrode. This effect in turn resulted in an enhanced rate of dissolution of the

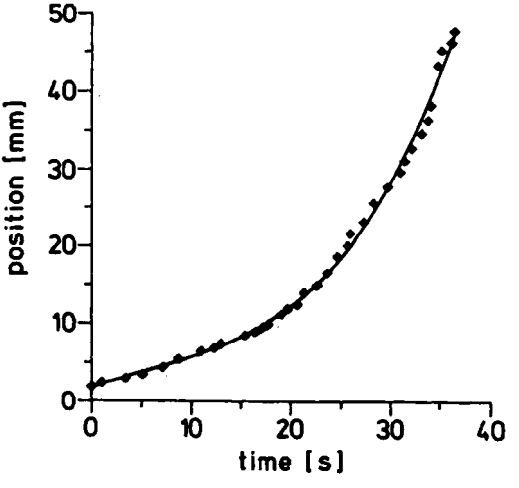

Figure 58. Position-time plot of an accelerating front in the bistable regime of Co dissolution. (Reprinted from R. D. Otterstedt, P. J. Plath, N. I. Jaeger, J. C. Sayer, and J. L. Hudson, *Chem. Eng. Sci.* **51,** 1747, 1996 with kind permission of Elsevier Science Ltd., Kidlington, UK.)

oxide layer, which again had an accelerating effect on the front motion. To the best of the present author's understanding, the fact that the potential becomes more positive *everywhere along the electrode* is nothing more than a consequence of the basic long-range coupling and therefore does not represent an additional mechanism.

(c) Other metal dissolution reactions

Finally, some old results from the schools of Bonhoeffer and Franck, mainly on activation waves on passive iron wires, will be discussed. In these early studies, very long metal wires with lengths of up to 1 m served as working electrodes, and again, fronts during the passive to active transition were investigated. The spatial profiles were recorded with potential probes. In some studies, the activation front was followed by a repassivation wave, a behavior that today we know occurs in the excitable regime.[23] A stationary state is excitable if, upon a small perturbation of the steady state, the system is first driven away from it and only after some time does it return to the original state.

Regarding the results discussed above, the interesting aspect of these experiments is that the front velocities took on a constant value. Some data can be seen in Fig. 59. The first three examples show activation fronts in the bistable regime of Fe, Au, and Zn dissolution, respectively; the last two curves display examples of pulses in an excitable regime, again for metal dissolution reactions. In all examples, two stationary electrodes were used to probe the local potential. The velocity of the fronts or pulses were extracted from the time difference at which the transitions were measured at the two probes. In all five examples, the readings of the two probes seem to be just time-shifted versions of each other. This indicates that the structures propagate with constant shape and velocity.

A characteristic property of the model presented above is that the coupling range changes with the ratio of the length of the electrode, L, and

Figure 59. Potential-time curves measured at two different positions along a metal wire during (a) Fe dissolution in 1 N H_2SO_4, (b) Au corrosion in 1 N HCl/2 N NaCl, (c) Zn dissolution in 4 N NaOH, (d) Activity wave of Fe in 12 N HNO_3 with successive repassivation; and (e) passivation wave during Co dissolution in 1.3 M CrO_3 + 1 N HCl with successive reactivation. The distance between the potential probes corresponds to the distance given under each curve. (After Franck,[30] reprinted with permission from VCH Publishers.)

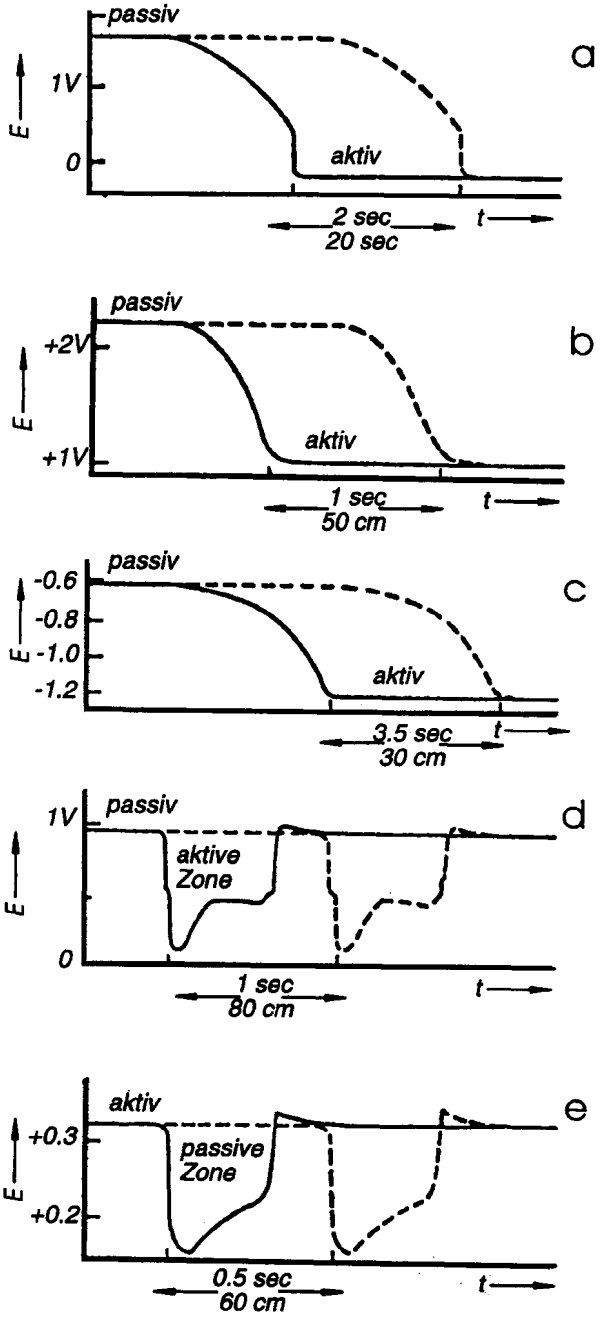
passiv
1V
E
0
aktiv
2 sec
20 sec
t
a
passiv
+2V
E
+1V
aktiv
1 sec
50 cm
t
b
passiv
-0.6
-0.8
E -1.0
-1.2
aktiv
3.5 sec
30 cm
t
c
1V
passiv
aktive
Zone
E
0
1 sec
80 cm
t
d
aktiv
+0.3
passive
Zone
E
+0.2
0.5 sec
60 cm
t
e

the distance between the working and reference electrodes, w. The larger the electrode for a given distance between the working and reference electrodes, the shorter the coupling range. Thus, the coupling becomes local for large values of L/w, and the resulting waves are typical reaction diffusion waves, propagating with constant shape and velocity. In view of the length of the electrode used in the experiments cited above, it is tempting to interpret the results as confirmation of the predictions of the model. However, such a conclusion has to be regarded with caution for several reasons. On the one hand, the exact cell geometry that is decisive for spatial coupling cannot be reconstructed. On the other hand, although the authors present evidence that spatial coupling occurs through the electric field, at least one of the systems, namely, Fe dissolution in nitric acid and most likely also Co dissolution in CrO_3 and HCl, does *not* belong to the class of electrical models, and hence it cannot be expected that it can be described in terms of the model equations (18), (21), (22), or (28). Finally, as for all metal dissolution reactions, other coupling mechanisms such as convection or surface tension cannot be excluded a priori.

(iii) Waves in the Oscillatory Regime

(a) Reduction of peroxodisulfate

In Section III.1.(iii), spatial patterns of NDR oscillators in two different parameter regimes in the oscillatory region were discussed, one close to the Hopf bifurcation, at parameter values where the system possesses one steady state and the other in the multistationary regime at parameter values where the oscillations take on a typical relaxation character. So far, for $S_2O_8^{2-}$ reduction, there are experiments covering only the second parameter regime. They were recorded with an SP microscope, and an example is depicted in Fig. 60 (color plate following page 112). The global current, shown in Fig. 60(a), clearly resembles the calculated one of Fig. 47(b): An oscillatory period is characterized by a sharp increase in current density, a slow relaxation to the original low level, and a quasi-stationary phase. When relating the spatial behavior shown in Fig. 60(b) to the global current shown in Fig. 60(a), it can be seen that a wave emerges at the right lower rim of the electrode as soon as the current starts to rise, and propagates across the whole electrode during the fast part of the oscillation period where the current increases. By contrast, the slow recovery of the current to the initial low value is

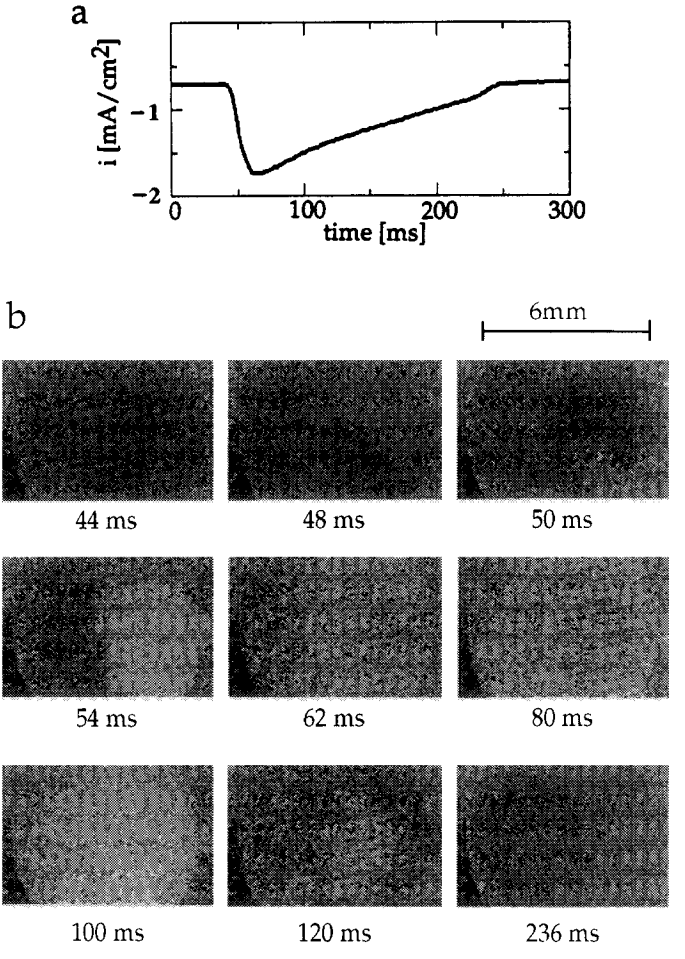

Figure 60. (a) Time trace of the global current during an oscillation (oscillation frequency was about 2 Hz). (b) SP microscope images of the electrode during the oscillation. Electrolyte: 2 mM $Na_2S_2O_8$, 0.1 mM Na_2SO_4, and 0.01 M NaOH. (After Flätgen *et al.*[178]) A color representation of this figure can be found following page 112.

accompanied by only faint spatial variations that can hardly be identified owing to the comparatively high noise level of the data.

Qualitatively analogous behavior, corresponding to the calculated spatiotemporal pictures of Fig. 47(a), can be found in a regime where the system is still bistable, but one of the stationary states has become a focus.* In this case, during the passive to active transition, the current overshoots its stationary value toward which it relaxes from high current densities [Fig. 61(a) and the color plate following page 112]. The sharp rise in current is accompanied by traveling potential waves exhibiting a pronounced interface, whereas during the subsequent relaxation of the current, only smooth, radially symmetric spatial structures can be discerned [Fig. 61(b)]. Hence the characteristic feature of the simulations, namely, frontlike waves that occur in parallel with the fast increase in current, and only weak spatial variations during the remaining part of the oscillation period, are found again in the experiment. However, obviously, the patterns are influenced by the presence of the boundary, and any deeper analysis of the dynamics has to take into account its effect. In this context, it again remains unclear why the activation waves start at the rim of the electrode and not at its center.[162]

Flätgen *et al.*[178] discuss typical time and length scales in the peroxodisulfate system. The fast dynamic of the potential determines the width of the fronts that accompany the rapid increase in current density. The latter occurs on the order of 10 ms, and typical interface widths range between 0.1 and 0.5 mm. The slower changes in concentration determine the overall period of the oscillation (10–0.5 Hz) as well as the total length of a wave train. The latter is on the order of centimeters, which is larger than the diameter of the electrode and causes a quasi-homogeneous appearance of the electrode during most of the oscillation period.

(b) Co electrodissolution

Otterstedt *et al.*[167,176] also studied waves in the oscillatory regime during Co dissolution. The oscillations possess a relaxationlike character, which is typical for oscillations between the active and the passive state of metal dissolution reactions. They are characterized by long, quasi-stationary periods of vanishing current density, followed by a sharp

*At these parameter values, the dynamics cannot be described with one variable anymore and for this reason the example is presented here rather than in the previous section.

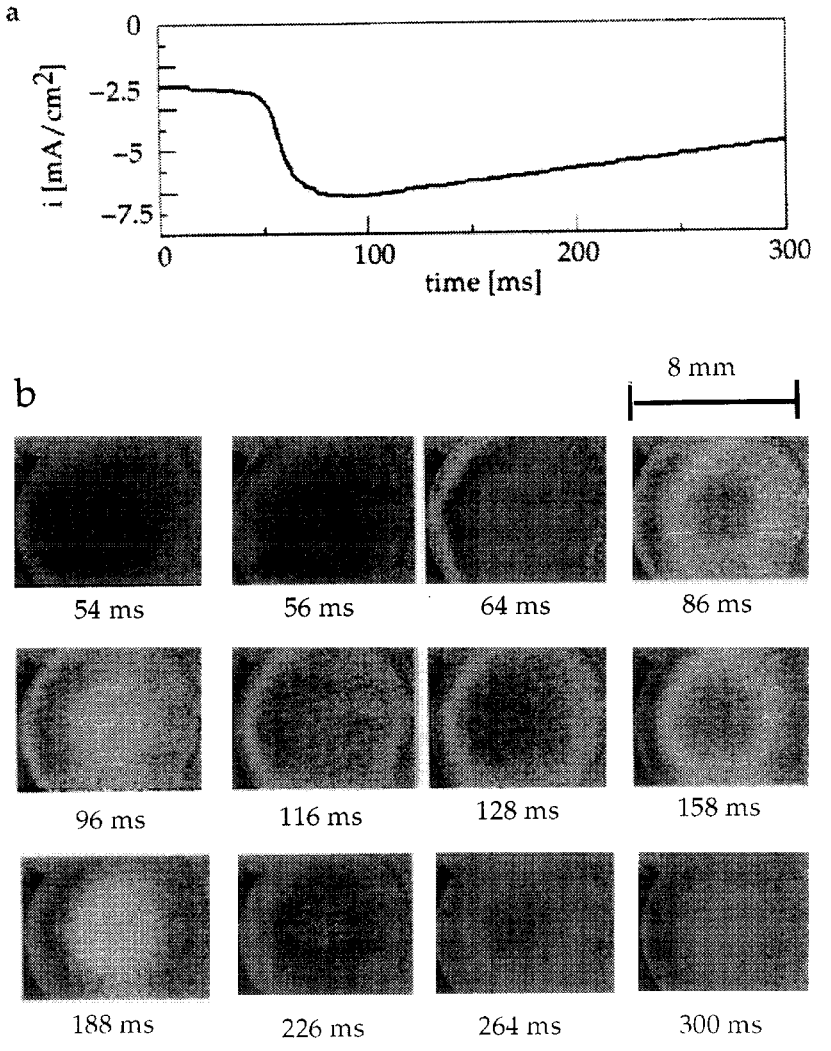

Figure 61. (a) Time trace of the global current during a transition in the bistable regime at parameter values close to the oscillatory regime (note that the relaxation to the active state is not completely shown). (b) SP microscope images of the electrode during the transition. Electrolyte: 1 mM $Na_2S_2O_8$, 0.1 mM Na_2SO_4, and 0.01 M NaOH. (After Flätgen *et al.*[178]) A color representation of this figure can be found following page 112.

increase in current and a slower relaxation back to the passive state [Fig. 62(a)]. The spatial picture resembles that of $S_2O_8^{2-}$ reduction shown in Fig. 60 where the oscillation also exhibited a relaxationlike character. A sharp activation front propagates across the surface in parallel with the increase in current density, while the electrode surface is nearly homogeneous during the remaining part of the oscillatory cycle.

When a quasi-one-dimensional ribbon was used as the working electrode (see Fig. 57), the activation waves emerged at the same time at the two edges of the ribbon and increased their velocity while traveling toward the center. The positions of the leading fronts as a function of time are shown in Fig. 62(b).

When the applied potential was moved close to the Flade potential, surprising changes occurred in the temporal and spatial behavior. An oscillation in the total current density exhibited small-amplitude oscillations that were superimposed on the decreasing part of the oscillatory cycle [Fig. 63(a)]. Considering spatial behavior, we first note that again an active region traveled with increasing velocity across the electrode [Fig. 63(b)]. However, the velocity of the front was much slower, so that repassivation occurred in its wake and a pulselike structure was formed. Whenever a modulation in the current density occurred, the trailing edge of the active region accelerated in the reverse direction, that is, into the repassivated region. In this way, the velocity of the trailing edge was found to be larger than that of the leading edge. However, the trailing edge did not travel up to the end of the electrode but died out before the next modulation occurred. Thus one could also view this complex motion as the accelerated propagation of an active area that pulsates in width. Close to the Flade potential, the electrode was activated more easily. Otterstedt *et al.* establish a connection between the more favorable conditions for the reactivation of the electrode and the occurrence of these modulated waves.[167] Finally, it should be noted that all phenomena described here for the Co ribbon were also found at Co disks.[175]

An important result of the theoretical description of the electrochemical patterns discussed above was that the distance between the working electrode and the equipotential surface has an important impact on the pattern formation, or more precisely, on the range of the spatial coupling. In view of this knowledge, it is to be expected that electrode configurations different from this parallel arrangement of two equipotential surfaces affect the dynamics in a different way. An experimental setup often employed in electrochemical experiments is the use of a Haber–Luggin

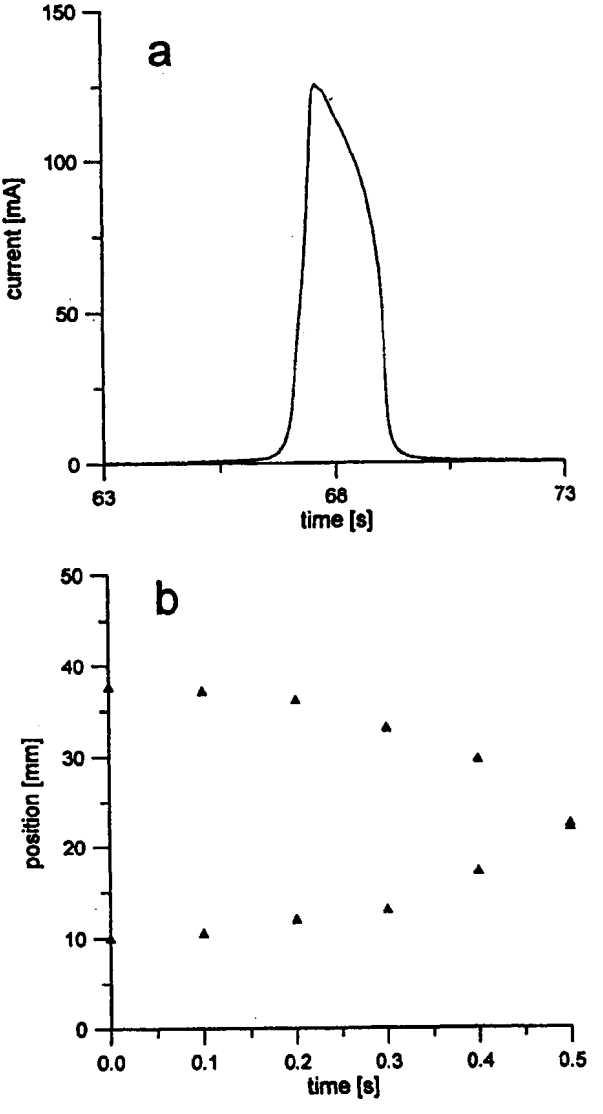

Figure 62. Single autonomous oscillation during Co dissolution. (a) Total current vs. time. (b) Position of the leading edges of the activation waves vs. time. (Reprinted with permission from R. D. Otterstedt, P. J. Plath, N. I. Jaeger, and J. L. Hudson, *Phys. Rev. E* **54,** 3744, 1996. Copyright 1996, American Physical Society.)

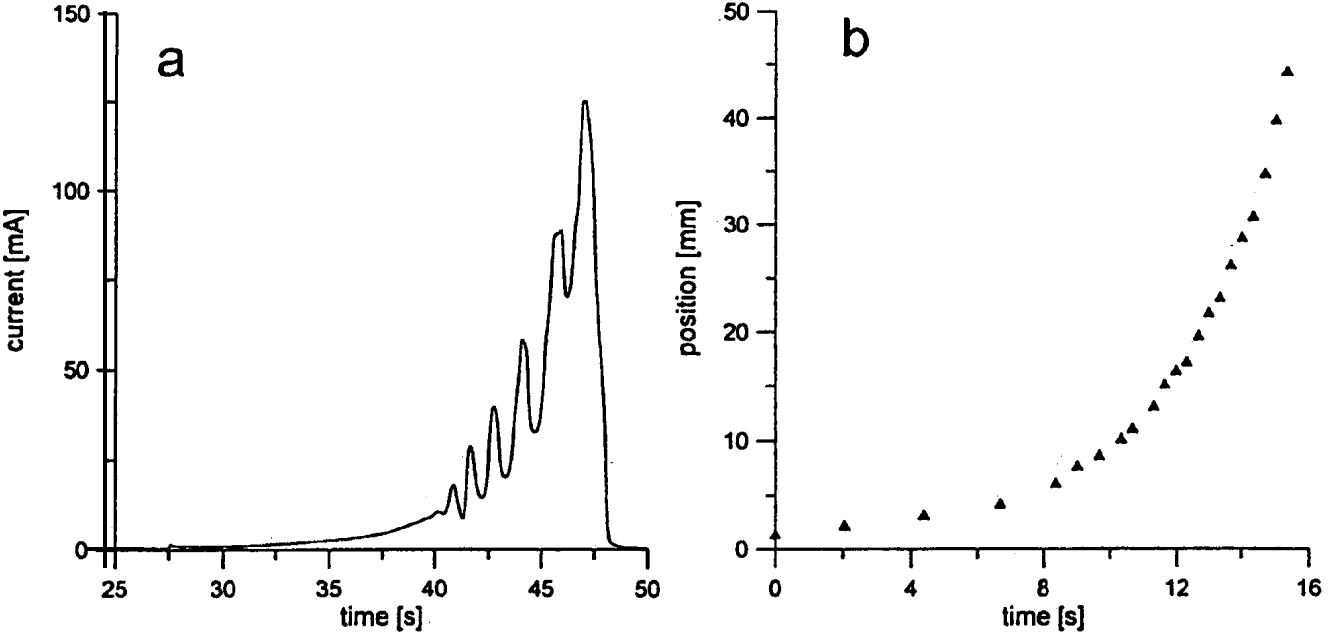

Figure 63. Single autonomous oscillation with modulation during Co dissolution. (a) Total current vs. time. (b) Position of the leading edges of the activation wave vs. time. (Reprinted with permission from R. D. Otterstedt, P. J. Plath, N. I. Jaeger, and J. L. Hudson, *Phys. Rev. E* **54**, 3744, 1996. Copyright 1996, American Physical Society.)

capillary so that the difference in potential between a point close to the working electrode and the potential of the working electrode is controlled. Otterstedt *et al.* demonstrated that the use of a Haber–Luggin capillary indeed gives rise to wave phenomena that are different from those described above, where an equipotential surface parallel to the Co wire can be assumed to exist at the location of the reference electrode.[177]

In the experiments described in this paragraph, the Haber–Luggin capillary was located at the center of a disk or ring electrode, close to its surface (Fig. 64). With this arrangement, a rotating wave consisting of an active area in an otherwise passive region was typically observed. The wave constantly moved around the center of the disk, thereby keeping a steady shape [Fig. 65(A)]. Thus, the global current density remains approximately constant [Fig. 65(B)], while at a point close to the rim of the electrode, the potential regularly oscillates with an amplitude of about 1 V [Fig. 65(C)]. Similar results were obtained with a ring electrode.[167]

Closer to the Flade potential, the width of the active area started to oscillate or breathe in a way similar to that of the modulated waves described in the above experiments. The difference between these two types of modulated waves is that here the wave constantly rotates around the center and possesses a localized structure, while in the above experiments it traveled once across the whole electrode and reappeared only after some time.

Finally, with the reference electrode close to the working electrode, stationary patterns also formed under certain conditions. They consisted of an active area in the center of the disk surrounded by a passive ring. The

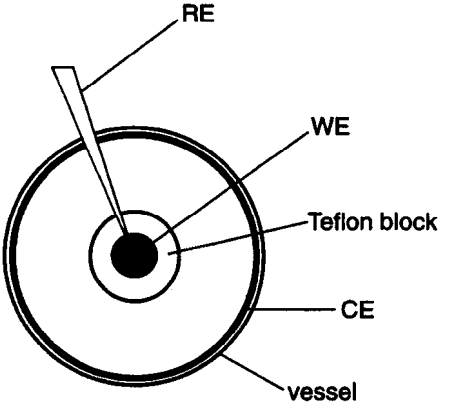

Figure 64. Experimental setup with the reference electrode at the center of a disk (or ring) electrode close to the surface. RE, reference electrode; WE, working electrode; CE, counter-electrode. (After Otterstedt *et al.*[177] Reproduced by permission of the Royal Society of Chemistry.)

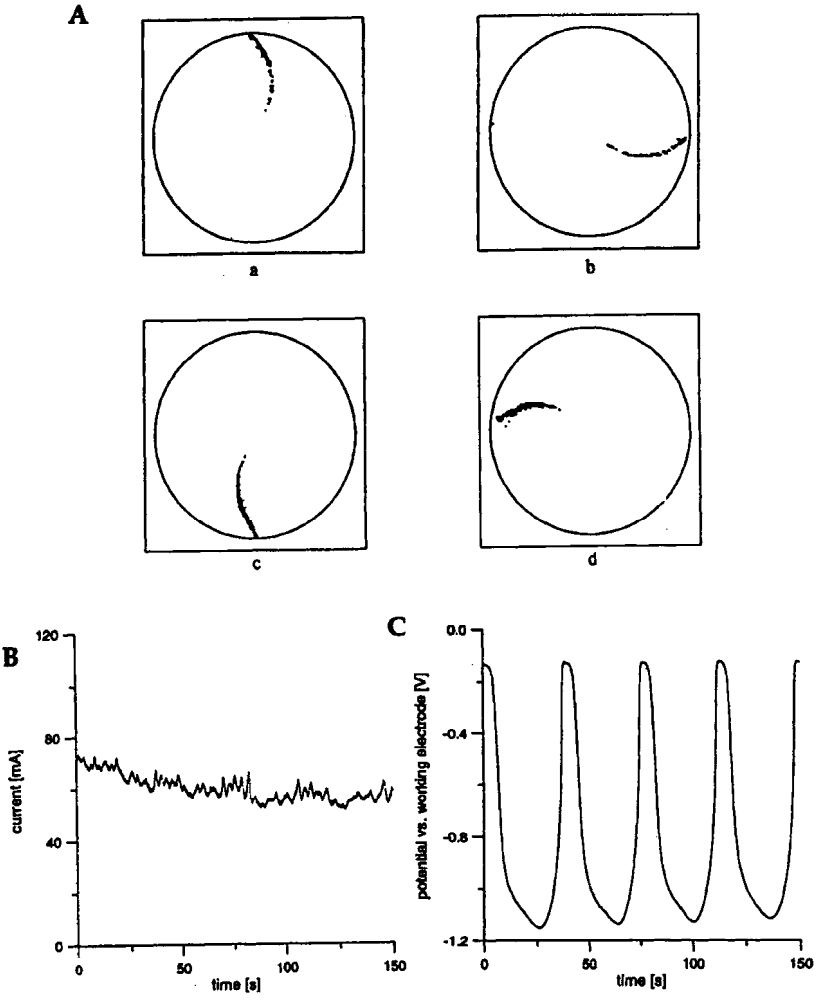

Figure 65. (A) Video images of a clockwise rotating wave during Co dissolution. (B) Total current vs. time. (C) Potential between the working electrode and an additional reference electrode with a capillary placed at the rim of the working electrode ca. 1 mm away from the surface. (After Otterstedt *et al.*[177] Reproduced by permission of the Royal Society of Chemistry.)

three patterns described were observed when the Flade potential was approached from the cathodic side.

The key to understanding the occurrence of these rotating waves lies in the interplay of the shift in potential of the counter-electrode when the active area increases, and the radial dependence of the IR drop between the reference electrode and different positions of the working electrode.[177] However, a complete explanation of the phenomenon has to await the results of the theoretical treatment of the problem currently being investigated by Christoph *et al.*[162*]

(c) Ni electrodissolution

A much-quoted experiment on pattern formation in electrochemical systems was carried out by Lev *et al.*,[160,161] while investigating the anodic dissolution of Ni. In these experiments, the working and counter-electrodes consisted of 10 to 20-cm-long Ni wires that were arranged in parallel 6 to 12 mm apart. The reference electrode was placed 40 mm behind the counter-electrode. The local current distribution was recorded with 16 equispaced microreference electrodes, and the spatiotemporal dynamics were investigated during four types of global behavior.

During galvanostatic oscillations, the current in one part of the electrode was always found to be shifted by 180° relative to the other part of the electrode. This behavior was maintained down to the smallest electrodes tested, which had a length of 1 cm. An example of these antiphase oscillations, also referred to as standing waves, is shown in Fig. 66.

When the electrodes are covered with only a thin layer of solution, a potential gradient along the working electrode can arise, which leads to chaotic potential oscillations under galvanostatic conditions. In this chaotic regime, the current distribution still exhibited the general features of the antiphase oscillations, but the maximum local amplitude as well as the period of the oscillations varied from one oscillation cycle to the next.

When an external resistor was incorporated between the working and reference electrodes, and the system was operated *under potentiostatic conditions,* the antiphase oscillations became transformed into traveling pulses with velocities of about 4.5 m s^{-1}.

*Added in proof: Very recently it was demonstrated that when the reference electrode is located close to the working electrode a *negative* global coupling is introduced into the system that favors pattern formation. (P. Grauel, J. Christoph, G. Flätgen and K. Krischer, *J. Phys. Chem. B* **102** (1998) 10264.

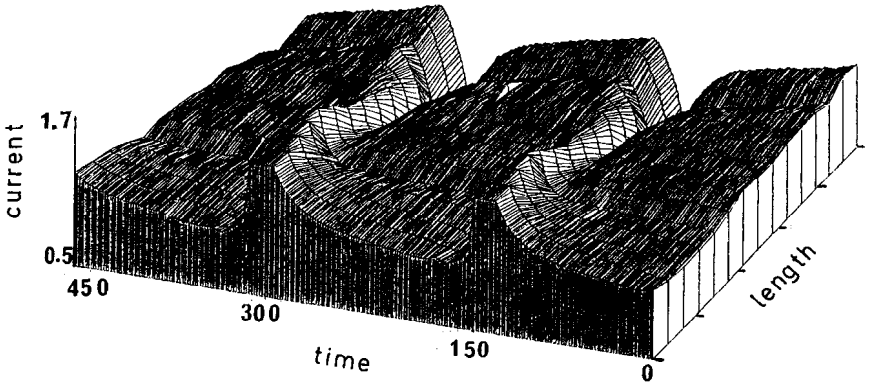

Figure 66. Local current distribution of antiphase oscillations during the dissolution of Ni under galvanostatic control. (Reprinted with permission of *Nature* from O. Lev, M. Sheintuch, L. M. Pismen, and C. Yarnitzky, *Nature* **336,** 488, 1988. Copyright 1988, Macmillan Magazines Ltd.)

Finally, transitions in the bistable regime from a stable oscillatory state to a stationary state were investigated under galvanostatic conditions (Fig. 67). Quite astonishingly, the transition was not accompanied by a moving front as in all the other examples discussed so far. Rather, it occurred with a few enlarging oscillations followed by a huge, long-lasting modulation of the current. The relatively active side of the electrode first

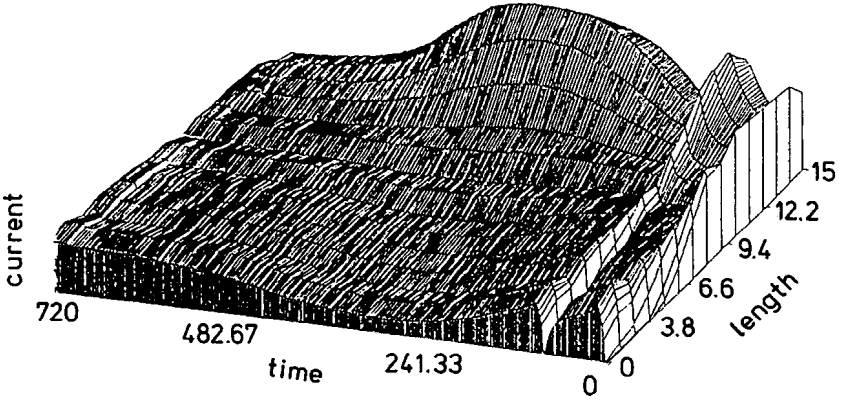

Figure 67. Local current distribution during the transition from an oscillatory state in the transpassive region to a state in the oxygen evolution region measured under potentiostatic operation. (Reprinted from O. Lev, M. Sheintuch, H. Yarnitsky, and L. M. Pismen, *Chem. Eng. Sci.* **45,** 839, 1990. Copyright 1990 with kind permission from Elsevier Science Ltd., Kidlington, U.K.)

becomes more active, while the other side matches this behavior by a corresponding decrease of current, followed by a gradual approach to the new steady state.

This constitutes a very interesting sequence of observations. As mentioned, Haim *et al.*[158] reproduced this sequence in a model they proposed in order to model the spatiotemporal dynamics of Ni dissolution. Unfortunately, to the best of the present author's understanding, there is a problem with the boundary condition at the electrode and thus a definite explanation is not possible at this stage.

(d) Fe electrodissolution in H_2SO_4

The most clear-cut examples of the influence of an insulating boundary on spatiotemporal dynamics come from experiments on the dissolution of iron. In 1969, Pigeau and Kirkpatrick[179] presented a sequence of images in which a wave could be seen that emerged at the rim of a disk-shaped electrode and propagated toward the center. These radially symmetric waves constituted passivation waves accompanying the decrease in current density during typical relaxation oscillations.

This system was used by Hudson *et al.*,[180] who demonstrated that the spatiotemporal picture can become more complex when the applied potential is fixed closer to the Flade potential. The first series of studies was carried out with disk electrodes embedded in an insulating Teflon sheet. In Ref. 180, the authors present two series of experiments. In the first, they reproduced the dynamics of the base oscillatory state as described by Pigeau and Kirkpatrick. The time series corresponding to this state is shown in Fig. 68(A), and difference images of a video sequence are reproduced in Fig. 69. The activation of the surface, being so fast that it cannot be resolved in time with a video camera, occurred between images a and b. Shortly after this, repassivation sets in (image d), starting from the rim of the electrode and progressing inward in a fairly uniform manner (images e–h). Up to the next activation, no visible changes on the surface are discernible. Note that in Fig. 69 as well as in the three successive figures, difference images are displayed, and thus only the newly passivated parts can be seen.

Closer to the Flade potential, the radial symmetry is broken, and the spatiotemporal picture shown in Fig. 70 is obtained. This time, only about half of the electrode (the lower left-hand side in image a) is activated, and front formation and propagation occur only on this half of the electrode.

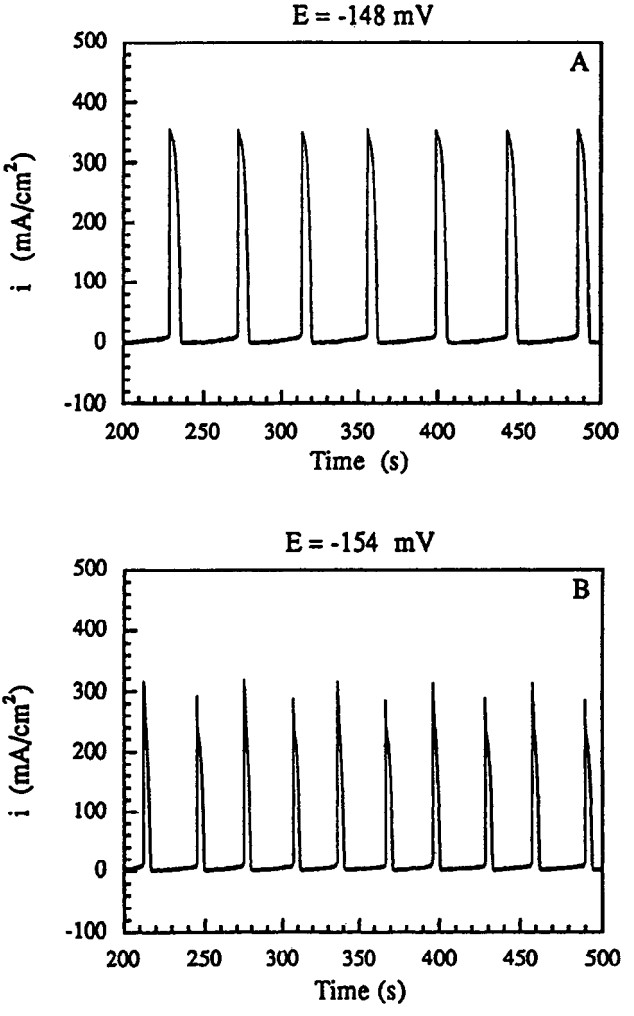

Figure 68. Current oscillations during anodic dissolution of iron at (A) –148 mV and (B) –154 mV vs. Hg/Hg_2SO_4. (After Hudson et *al.* [180])

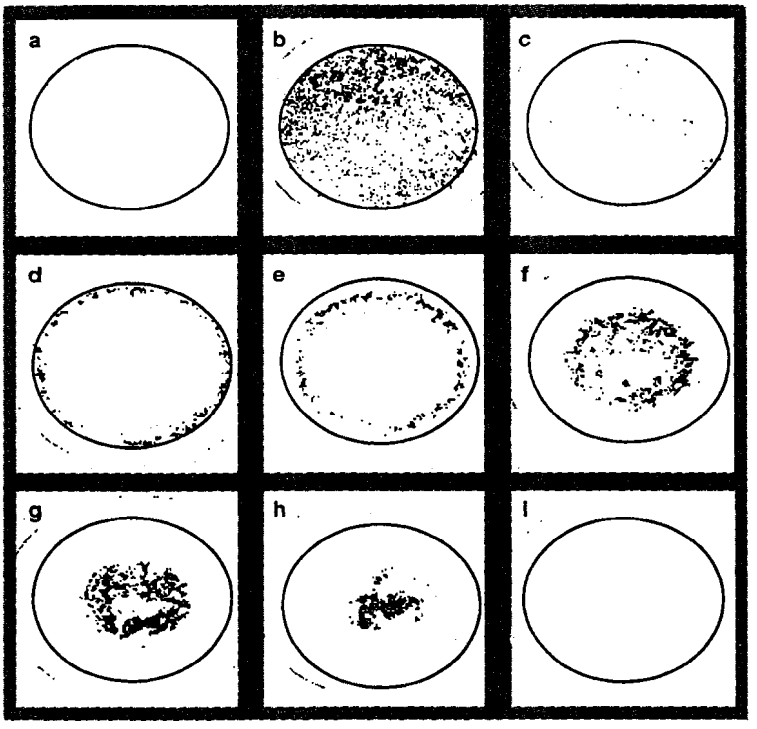

Figure 69. Difference images of successive snapshots of the Fe surface (a) during the passive state, (b) during the passive to active transition, (c) immediately after the transition to the active state, (d)–(i) during gradual relaxation to the passive state for the oscillations shown in Fig. 68(A). The superimposed solid circle marks the boundary of the iron electrode. Changes outside this boundary are associated with noise. (After Hudson *et al.* [180])

During the second oscillation in time, activation and film growth take place on the complementary portion of the surface. Thus the time trace of the complete cycle consists of two current peaks in the time series shown in Fig. 68(B).*

An analogous behavior was found on ring electrodes.[181] Far from the Flade potential, the complete ring was activated between two images of the video, and the subsequent repassivation wave formed at the outer and inner border of the ring; in this way the outer wave appeared slightly before

*In Fig. 68(B), these two peaks have slightly different amplitudes, which is, however, attributed to heterogeneities of the electrode surface and not to an intrinsic property of the dynamics because the two halves of the disk should theoretically be exactly symmetrical.

the inner one. The latter behavior is again most likely a result of the inhomogeneous potential distribution, which arises as a result of the metal/insulator boundary. Closer to the Flade potential, a spatiotemporal period-doubling bifurcation, corresponding to the one described above, was observed. In every other oscillation of the current density, one half of the ring participated in the activation-passivation cycle and the other half in the remaining oscillations (Fig. 71). In these studies, the authors succeeded in observing yet another spatiotemporal behavior while still lowering the potential toward the Flade potential. Subtracted images of

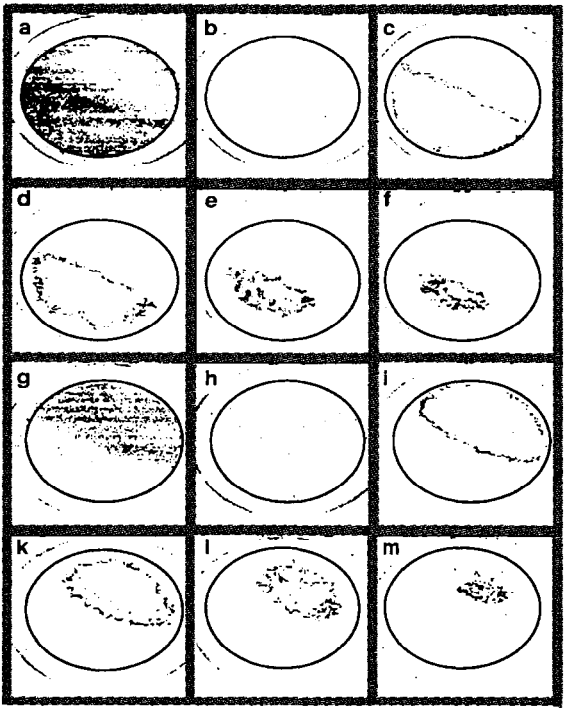

Figure 70. Differences of successive snapshots of the Fe surface corresponding to the oscillations shown in Fig. 68(B). One period consists now of two activation-passivation cycles that occur on symmetric parts of the electrode. The superimposed solid circle marks the boundary of the iron electrode. Changes outside this boundary are associated with noise. (After Hudson *et al.* [180])

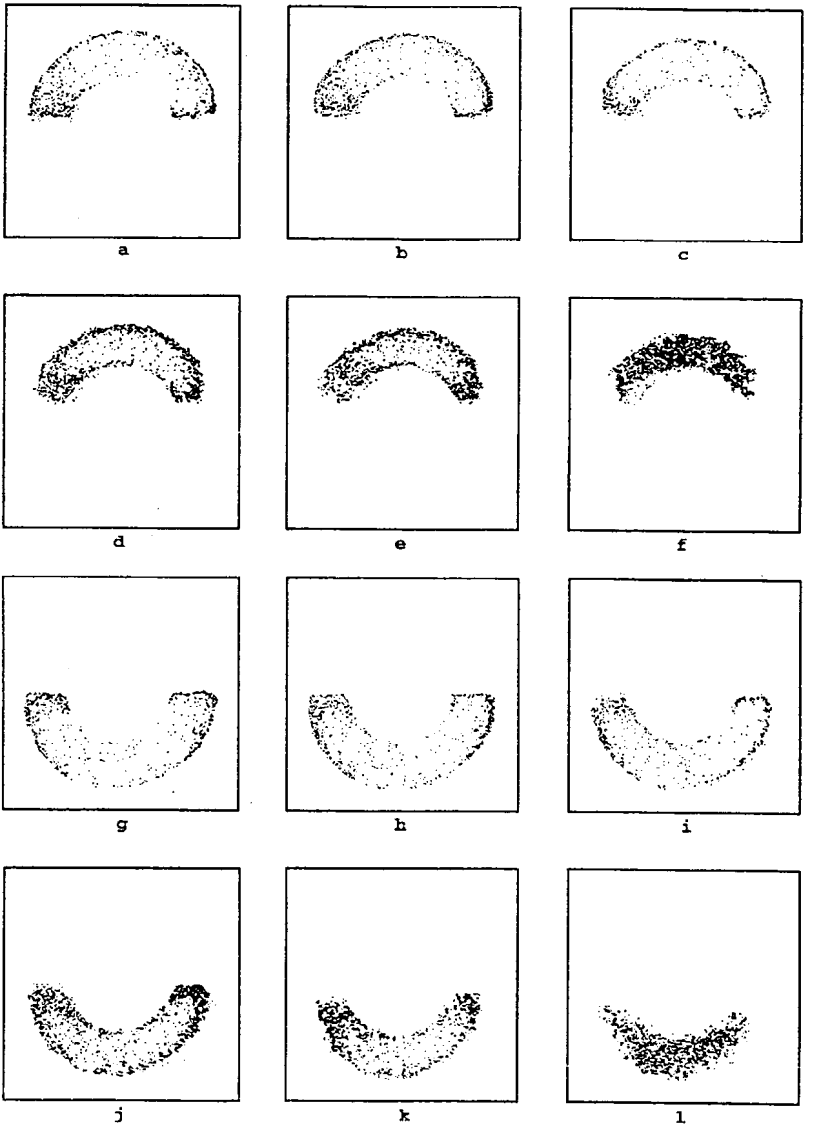

Figure 71. Differences of successive snapshots of the surface during passivation phases of two successive current oscillations of a period-2 state of the potentiostatic dissolution of an iron ring electrode. (Reprinted with permission from J. C. Sayer and J. L. Hudson, *Ind. Eng. Chem.* **Res. 34**, 3246, 1995. Copyright 1995, American Chemical Society.)

the subsequent passivation phases are shown in Fig. 72. During the first current peak in the time series, the activation to passivation proceeds firstly on two oppositely placed quadrants; this is followed by an activation to passivation cycle on the other two quadrants.

The last series of experiments that will be described in this chapter were carried out with arrays of small circular Fe electrodes embedded in an insulator.[182] The small electrodes were closely packed in different geometries. The idea behind this setup was that the electrode array should behave similarly to one large electrode of the same size and geometry. However, the advantage of using several small electrodes is that a spatiotemporal picture can be obtained by measuring the currents at the small electrodes. This can be done much faster than with video frequency, and hence the activation waves could also be spatially resolved. It is interesting that the activation waves always start in the center of the electrode array, whereas the passivation waves start, as found with disk electrodes, at the rim of the array. This behavior is in accordance with the simple picture developed in Section III.1.(v) for the local dynamics of disk electrodes embedded in an insulator. There it was argued that the boundary of the disk is always more passive than the center, and thus the activation waves should be more likely to start in the center, whereas passivation waves can be expected to originate at the rim. Also, for array configurations, which cannot be viewed as a caricature of a disk, Fei *et al.*[182] qualitatively observed the same behavior. Among these configurations was, for example, a quasi-one-dimensional arrangement consisting of 2×8 electrodes. Here the activation waves emerged from the two central electrodes, whereas passivation started again at the ends. Finally, we note that the period-doubled states were also found in electrode arrays of various configurations. Obviously, this bifurcation is a robust phenomenon.

To summarize this section on pattern formation during iron dissolution, two types of phenomena were consistently observed. First, the principal propagation of activation and passivation waves seems to be dictated by the nonuniform potential distribution that arises as a result of the transition from the conducting electrode to an insulating material. Second, close to the Flade potential, spatiotemporal period doubling is observed. In the case of disk or ring electrodes, this bifurcation breaks the radial symmetry of the electrodes. It remains a challenging task to elucidate the origin of this spatial bifurcation.

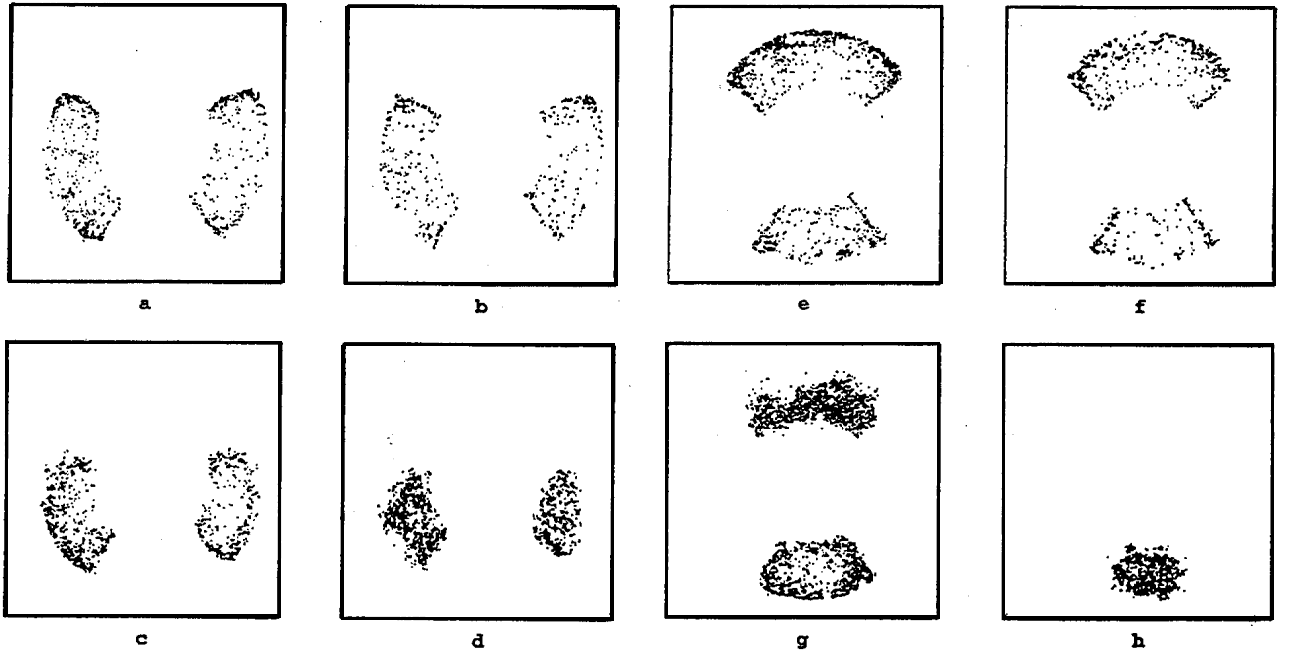

Figure 72. Differences of successive snapshots of the surface during passivation phases of two successive current oscillations of a second period-2 state of the potentiostatic dissolution of an iron ring electrode. (Reprinted with permission from J. C. Sayer and J. L. Hudson, *Ind. Eng. Chem. Res.* **34**, 3246, 1995. Copyright 1995, American Chemical Society.)

3. Concluding Remarks

The discussion of the experimental results in Section III.2 shows that a fundamental understanding of pattern formation in electrochemical systems has been achieved. However, it also demonstrates that the present state represents just a first step toward a complete picture of possible dynamic behaviors. There are many observations that cannot yet be explained, for example, the spatiotemporal period-doubling bifurcation detected during the electrodissolution of iron, the occurrence of antiphase oscillations during Ni electrodissolution, or the emergence of modulated waves during the electrodissolution of Co. Nevertheless, these phenomena seem to be understandable through an extension of the models introduced in Section III.1.

However, the reader should be aware that there are many other systems in which different types of patterns have been observed that result from a qualitatively different kind of coupling. Hence they also require fundamentally different models from that considered in this chapter. This first includes convection-induced patterns. These might arise from large concentration gradients in the solutions or different surface tensions as found, for example, under certain conditions for anodic metal dissolution[183,184] or for some inhibited charge-transfer processes at Hg electrodes.[185] A theoretical analysis of hydrodynamic dissipative structures can be found in Refs. 186–188. However, growth patterns emerging during electrodeposition[189–198] also have to be mentioned in this context. In many of these cited examples, fractal structures were observed.

Another type of pattern was found during the electrochemical codeposition of Ag and In or Ag and Sb. As early as 1938, Raub and Schall[199] reported spiral formation during the deposition of an Ag/In alloy. Almost 50 years later, the related Ag/Sb system was studied by Krastev *et al.*,[200–203] revealing, besides spiral waves, the occurrence of target patterns and moving bands. A prime condition for these patterns to develop seems to be the existence of a convective flow along the working electrode. Phenomenologically, the patterns closely resemble those found in heterogeneous catalysis. Thus the wavelength of the spiral waves is on the order of 10 μm and the wave speed is a few μm s^{-1}. Recall that the patterns discussed above, which emerge as a result of migration, possess characteristic wave speeds of cm s^{-1} to m s^{-1} and characteristic lengths on the order of several millimeters to several centimeters.

IV. SUMMARY

Starting from the knowledge that in most electrochemical systems, oscillations, or more generally speaking, dynamic instabilities, originate from the electrical nature of the systems, common principles that govern their spatiotemporal dynamics have been reviewed. The complexity of the dynamic behavior was chosen as the organizational tool. This approach naturally distinguishes between spatially homogeneous systems, which possess a finite number of degrees of freedom, and spatially structured systems, which are characterized by an infinite number of degrees of freedom. Within one group, the minimal number of dependent variables necessary to describe a certain type of behavior serves as a measure of the complexity of the dynamics.

The simplest manifestation of self-organization in a reacting system is the occurrence of bistability, that is, the coexistence of two locally stable homogeneous states. In all electrical models, bistable behavior results from the interaction of an N-shaped stationary polarization curve with a sufficiently large ohmic resistor in the external circuit. These two features also represent the backbone for all more complex forms of self-organization where, owing to exactly these two properties of the system, the double-layer potential takes on the role of the autocatalytic variable.

Simple periodic, spatially homogeneous oscillations may emerge as a result of two distinct feedback mechanisms. In NDR oscillators, the feedback loop does not contain an additional potential-dependent process. Often the feedback process is due to slow transport of the electroactive species, which is predominantly diffusion. The oscillations appear in a region where the stationary current-potential curve exhibits a negative slope, and they require an ohmic series resistance of suitable magnitude in the circuit. If the resistance is too large, the system exhibits bistability between two stationary states, and thus systems belonging to this class do not oscillate under galvanostatic conditions.

In HNDR oscillators, the feedback loop contains a slow, potential-dependent process that acts on the rate of the main charge-transfer reaction. Oscillations occur around a branch of the stationary polarization curve with a positive slope, under potentiostatic conditions in the presence of a sufficiently large series ohmic resistor, as well as under galvanostatic conditions. The destabilization is again due to a fast negative impedance process. However, the negative slope is hidden in the stationary current-potential curve. This is because the slope of the polarization curve is

dominated by the slow feedback process, which possesses a positive impedance. Systems in this class exhibit a bistability between a stable limit cycle and a stationary steady state for large ohmic resistance.

More complex oscillations arise in many cases owing to slow transport processes. For NDR oscillators it was shown that owing to the delayed relaxation of the diffusion layer upon changes in the concentration at the electrode, diffusion of the electroactive species introduces two distinct feedback modes into the system. Also in HNDR oscillators, the occurrence of more complex oscillations can be coupled to the slow diffusion of electroactive species. In this case, the enlarged model consists of two subsystems, one of the NDR type and one of the HNDR type, the complex behavior arising from their interactions. However, since NDR oscillators do not oscillate under galvanostatic conditions, this mechanism cannot account for mixed-mode oscillations or any other complex wave forms observed under constant current load. To date, no explanation has been given for the complex temporal behavior encountered under galvanostatic conditions.

This hierarchy of temporal models that assume uniformity parallel to the electrode forms the basis for describing the spatiotemporal dynamics of electrochemical systems. The new elements entering the picture when spatial degrees of freedom are allowed for are migration currents parallel to the electrode that, as shown experimentally and substantiated theoretically, constitute the spatial coupling in the kinds of electrochemical systems considered here. Since the migration currents depend on the distribution of potential in the entire electrochemical cell, cell geometry and especially the arrangement of the electrodes play a decisive role in spatiotemporal dynamics. Furthermore, the strength of the spatial coupling is proportional to the specific conductivity of the electrolyte and thus the average propagation velocity of potential waves increases with conductivity.

So far, only a few basic electrode configurations have been investigated in detail. Spatial coupling is long range or nonlocal if the reference and counter-electrodes are “sufficiently far away” from the working electrode so that there is an equipotential surface parallel to the working electrode at the location of the reference electrode. This means that a change in the state of the system at a particular position on the electrode has a finite effect instantaneously over a finite characteristic distance from this position, the coupling range. A consequence of nonlocal coupling is

the occurrence of accelerated waves in the bistable and oscillatory regimes, as evidenced by many experimental examples.

"Sufficiently far away" has been quantified theoretically for one-dimensional electrodes, where it was shown that, roughly speaking, the ratio of the length of the working electrode to the distance between the working and reference electrode has to be larger than 1. If there exists an equipotential surface closer to the electrode (provided, e.g., by the counter-electrode), the coupling range becomes progressively smaller, asymptotically approaching local, that is, diffusive coupling.

In galvanostatic systems, or more generally, in systems with an external resistor connected in series with the working electrode, in addition to the spatial coupling through the electrolyte, there is a global coupling which has a synchronizing effect on pattern formation. The strength of this global coupling depends on the total cell resistance, that is, again on the electrode arrangement.

Typical wave velocities arising from the spatial coupling through the electric field are on the order of cm s^{-1} to m s^{-1}, and characteristic wavelengths are on the order of centimeters. Hence, in most experiments, one wave train at a time propagates across the surface.

The purpose of this chapter has been to illustrate that considerable progress has been made in the understanding of temporal instabilities and of spatial structures, such as the accelerated motion of fronts, and characteristic wave velocities and wavelengths. However, there remain many open questions, among them bifurcations of the basic patterns in the oscillatory regime, which are encountered, for example, during Fe electrodissolution or Co electrodissolution, as well as the influence of different electrode geometries and arrangements on pattern formation. Their solutions represent a challenge for future studies. In this respect, the possibility of deliberately influencing the patterns by choosing a certain cell design, electrode geometry, or conductivity is an especially interesting prospect.

ACKNOWLEDGMENTS

Thanks are due to Nadia Mazouz and Jan Christoph for critical comments on the manuscript and to many colleagues for fruitful discussions over recent years. Professor Gerhard Ertl's continuous, encouraging interest and generous support of this work is gratefully acknowledged. I am indebted to Dr. Dan Bizzotto for improving my "international English,"

to Ingeborg Reinhardt for careful reading and word processing, and I appreciate the help of Waruno Mahdi and Margot Lübke in preparing many of the figures. I acknowledge all the authors who have made some of their figures available to me.

REFERENCES

[1] J. L. Hudson and T. T. Tsotsis, *Chem. Eng. Sci.* **49** (1994) 1493.
[2] J. Wojtowicz, in *Modern Aspects of Electrochemistry* **8,** J. O' M. Bockris and B. E. Conway, eds., Plenum, New York, 1973, p. 47.
[3] A. J. Pearlstein, H. P. Lee, and K. Nobe, *J. Electrochem. Soc.* **132** (1985) 2159.
[4] F. Schüth, B. E. Henry, and L. D. Schmidt, *Adv. Catal.* **39** (1993) 51.
[5] R. Imbihl and G. Ertl, *Chem. Rev.* **95** (1995) 697.
[6] M. Eiswirth and G. Ertl, in *Chemical Waves and Patterns,* R. Kapral and K. Showalter, eds., Kluwer, Dordrecht, 1995, p. 447.
[7] M. Eiswirth, J. Bürger, P. Strasser, and G. Ertl, *J. Phys. Chem.* **100** (1996) 19118.
[8] K. J. Vetter, *Electrochemical Kinetics,* Academic Press, London, 1967.
[9] C. Gabrielli, M. Keddam, E. Strupinek-Lissac, and H. Takenouti, *Electrochim. Acta* **21** (1976) 757.
[10] I. Epelboin, M. Ksouri, E. Lejay, and R. Wiart, *Electrochim. Acta* **20** (1975) 603.
[11] J. N. Chazalviel and F. Ozanam, *J. Electrochem. Soc.* **139** (1992) 2501.
[12] F. Ozanam, J. N. Chazalviel, A. Radi, and M. Etman, *J. Electrochem. Soc.* **139** (1992) 2491.
[13] M. Aggour, doctoral thesis, Technical University Berlin, 1994.
[14] H. J. Lewerenz and S. Rauscher, personal communication.
[15] M. T. M. Koper, *Electrochim. Acta* **37** (1992) 1771.
[16] M. T. M. Koper and P. Gaspard, *J. Chem. Phys.* **96** (1992) 7797.
[17] M. T. M. Koper and J. H. Sluyters, *J. Electroanal. Chem.* **371** (1994) 149.
[18] W. Wolf, M. Lübke, M. T. M. Koper, K. Krischer, M. Eiswirth, and G. Ertl, *J. Electroanal. Chem.* **399** (1995) 185.
[19] M. T. M. Koper, *J. Electroanal. Chem.* **409** (1996) 175.
[20] M. T. M. Koper, *Adv. Chem. Phys.* **92** (1996) 161.
[21] J. P. Joule, *Philos. Mag.* **24** (1844) 106.
[22] H. L. Heathcote, *Z. Phys. Chem.* **37** (1901) 368.
[23] V. S. Zykov, *Simulation of Wave Processes in Excitable Media,* Manchester University Press, Manchester, 1987.
[24] K. F. Bonhoeffer and W. Renneberg, *Z. Phys.* **118** (1941) 389.
[25] K. F. Bonhoeffer, *Z. Elektrochem.* **47** (1941) 147.
[26] K. F. Bonhoeffer and G. Vollheim, *Z. Naturforsch.* **8b** (1953) 406.
[27] U. F. Franck, *Z. Naturforsch.* **4a** (1949) 378.
[28] U. F. Franck, *Z. Elektrochem.* **55** (1951) 154.
[29] U. F. Franck and L. Meunier, *Z. Naturforsch.* **8b** (1953) 396.
[30] U. F. Franck, *Z. Elektrochem.* **62** (1958) 649.
[31] U. F. Franck and R. FitzHugh, *Z. Elektrochem.* **65** (1961) 156.
[32] T. Z. Fahidy and Z. H. Gu, in *Modern Aspects of Electrochemistry* **27,** R. E. White, B. E. Conway, and J. O'M. Bockris, eds., Plenum, New York, 1995, p. 383.
[33] M. T. M. Koper and J. H. Sluyters, *J. Electroanal. Chem.* **308** (1991) 151.
[34] H. Kaesche, *Die Korrosion der Metalle,* Springer, Berlin, 1990.
[35] H. Jehring and U. Kürschner, *J. Electroanal. Chem.* **75** (1977) 799.

[36]H. Jehring, N. V. Huyen, T. X. Gian, E. Horn, and C. Hirche, *J. Electroanal. Chem.* **135** (1979) 37.
[37]H.-D. Dörfler and E. Müller, *J. Electroanal. Chem.* **135** (1982) 37.
[38]R. de Levie and A. A. Husovsky, *J. Electroanal. Chem.* **22** (1969) 29.
[39]R. de Levie, *J. Electroanal. Chem.* **25** (1970) 257.
[40]J. Heyrovsky and J. Kuta, *Principles of Polarography,* Academic Press, New York, 1966.
[41]L. Pospisil and R. de Levie, *J. Electroanal. Chem.* **25** (1970) 245.
[42]M. T. M. Koper and J. H. Sluyters, *J. Electroanal. Chem.* **303** (1991) 73.
[43]A. N. Frumkin, *Z. Elektrochem.* **59** (1955) 807.
[44]L. E. Gierst, in *Transactions of the Symposium on Electrode Processes,* E. Yeager, ed., Wiley, New York, 1961, p. 109.
[45]A. Frumkin, O. Petrii, and N. Nicolaeva-Fedorovich, *Dokl. Akad. Nauk SSSR* **136** (1961) 1158.
[46]A. Gokhshtein and A. Frumkin, *Dokl. Akad. Nauk SSSR* **132** (1960) 388.
[47]E. Schöll, *Nonequilibrium Phase Transitions in Semiconductors,* Springer, Berlin, 1987.
[48]F.-J. Niedernostheide, ed., *Nonlinear Dynamics and Pattern Formation in Semiconductors and Devices,* Springer, Berlin, 1995.
[49]A. Wacker and E. Schöll, *J. Appl. Phys.* **78** (1995) 7352.
[50]Y. A. Chizmadzhev, *Dokl. Akad. Nauk SSSR* **133** (1960) 745.
[51]A. Y. Gokhshtein, *Dokl. Akad. Nauk SSSR* **140** (1961) 1114.
[52]A. Y. Gokhshtein, *Dokl. Akad. Nauk SSSR* **149** (1963) 880 and **148** (1963) 136.
[53]J. Wojtowicz and B. E. Conway, *J. Chem. Phys.* **52** (1970) 1407.
[54]H. Degn, *Trans. Faraday Soc.* **64** (1968) 1348.
[55]J. Keizer and D. Scherson, *J. Phys. Chem.* **84** (1980) 2025.
[56]W. Wolf, J. Ye, M. Purgand, M. Eiswirth, and K. Doblhofer, *Ber. Bunsenges. Phys. Chem.* **96** (1992) 1797.
[57]S. H. Strogatz, *Nonlinear Dynamics and Chaos,* Addison Wesley, Reading, MA, 1994.
[58]P. De Kepper and J. Boissonade, in *Oscillations and Travelling Waves in Chemical Systems,* R. J. Field and M. Burger, eds., Wiley, New York, 1985, p. 223.
[59]J. Guckenheimer, *Physica D* **20** (1986) 1.
[60]M. T. M. Koper and J. H. Sluyters, *J. Electroanal. Chem.* **352** (1993) 51.
[61]H.-D. Dörfler, *Nova Acta Leopoldina* **61** (1989) 25.
[62]H.-D. Dörfler and E. Müller, *J. Electroanal. Chem.* **135** (1982) 37.
[63]A. Gokhshtein, *Dokl. Akad. Nauk SSSR* **149** (1962) 880.
[64]W. Wolf, doctoral thesis, Free University of Berlin, 1994.
[65]R. Tamamushi, *J. Electroanal. Chem.* **11** (1965) 65.
[66]R. Tamamushi and K. Matsuda, *J. Electroanal. Chem.* **12** (1966) 436.
[67]M. T. M. Koper, P. Gaspard, and J. H. Sluyters, *J. Chem. Phys.* **97** (1992) 8250.
[68]M. T. M. Koper, P. Gaspard, and J. H. Sluyters, *J. Phys. Chem.* **96** (1992) 5674.
[69]K. Krischer, M. Lübke, W. Wolf, M. Eiswirth, and G. Ertl, *Electrochim. Acta* **40** (1995) 69.
[70]W. Wolf, K. Krischer, M. Lübke, M. Eiswirth, and G. Ertl, *J. Electroanal. Chem.* **385** (1995) 85.
[71]G. Horány and C. Visy, *J. Electroanal. Chem.* **103** (1979) 353.
[72]G. Armstrong and J. A. V. Butler, *Disc. Faraday Soc.* **1** (1947) 122.
[73]M. Thalinger and M. Volmer, *Z. Phys. Chem.* **150** (1930) 401.
[74]D. T. Sawyer and E. T. Seo, *J. Electroanal. Chem.* **5** (1963) 23.
[75]T. Kodera, T. Yamazaki, M. Masuda, and R. Ohnishi, *Electrochim. Acta* **33** (1988) 537.
[76]K. Krischer, M. Lübke, W. Wolf, M. Eiswirth, and G. Ertl, *Ber. Bunsenges. Phys. Chem.* **95** (1991) 820.
[77]M. Eiswirth, M. Lübke, K. Krischer, W. Wolf, J. L. Hudson, and G. Ertl, *Chem. Phys. Lett.* **192** (1992) 254.

[78] N. Markovic and P. N. Ross, *Langmuir* **9** (1993) 580.
[79] M.-S. Zei, personal communication.
[80] E. Müller, Z. *Elektrochem.* **29** (1923) 264.
[81] E. Müller and S. Tanaka, *Z. Elektrochem.* **34** (1928) 256.
[82] P. Strasser, M. Lübke, F. Raspel, M. Eiswirth, and G. Ertl, *J. Chem. Phys.* **107** (1997) 979.
[83] P. Strasser, M. Eiswirth, and G. Ertl, *J. Chem. Phys.* **107** (1997) 997.
[84] J. Wojtowicz, N. Marincic, and B. E. Conway, *J. Chem. Phys.* **48** (1968) 4333.
[85] M. Schell, F. N. Albahadily, J. Safar, and Y. Xu, *J. Phys. Chem.* **93** (1989) 4806.
[86] F. Raspel, R. J. Nichols, and D. M. Kolb, *J. Electroanal. Chem.* **286** (1990) 279.
[87] F. Raspel and M. Eiswirth, *J. Phys. Chem.* **98** (1994) 7613.
[88] F. N. Albahadily and M. Schell, *J. Electroanal. Chem.* **308** (199 1) 151.
[89] X. Cai and M. Schell, *Electrochim. Acta* **37** (1990) 673.
[90] Y. Xu and M. Schell, *J. Phys. Chem.* **94** (1990) 7137.
[91] N. Markovic and P. N. Ross, *J. Phys. Chem.* **97** (1993) 9771.
[92] H. Okamoto, N. Tanaka, and M. Naito, *Chem. Phys. Lett.* **248** (1996) 289.
[93] A. Capon and R. Parsons, *J. Electroanal. Chem.* **44** (1973) 239.
[94] A. Tripkovic, K. Popovic, and R. R. Adzic, *J. Chim. Phys.* **88** (1991) 1635.
[95] F. N. Albahadily and M. Schell, *J. Chem. Phys.* **88** (1988) 4312.
[96] M. Schell and F. N. Albahadily, *J. Chem. Phys.* **90** (1989) 822.
[97] N. Albahadily, J. Ringland, and M. Schell, *J. Chem. Phys.* **90** (1989) 813.
[98] M. R. Bassett and J. L. Hudson, *J. Phys. Chem.* **92** (1988) 6963.
[99] M. R. Bassett and J. L. Hudson, *J. Phys. Chem.* **93** (1989) 2731.
[100] O. Lev, A. Wolffberg, A. Sheintuch, and L. M. Pismen, *Chem. Eng. Sci.* **43** (1988) 1339.
[101] O. Lev, A. Sheintuch, L. M. Pismen, and A. Wolffberg, *J. Phys. Chem.* **93** (1989) 1661.
[102] F. Argoul, J. Huth, P. Merzeau, A. Arneodo, and L. Swinney, Physica D 62 (1993) 170.
[103] K. Krischer, M. Lübke, M. Eiswirth, W. Wolf, J. L. Hudson, and G. Ertl, *Physica D* **62** (1993) 123.
[104] H. D. Dewald, P. Parmananda, and R. W. Rollins, *J. Electrochem. Soc.* **140** (1993) 1969.
[105] Y. Wang and J. L. Hudson, *AIChE J.* **37** (1991) 1833.
[106] H. Okamoto, N. Tanaka, and M. Naito, *Electrochim. Acta* **39** (1994) 2471.
[107] W. Li, K. Nobe, and A. J. Pearlstein, *J. Electrochem. Soc.* **140** (1993) 721.
[108] M. U. Kleinke, *J. Phys. Chem.* **99** (1995) 17403.
[109] M. R. Bassett and J. L. Hudson, *Physica D* **35** (1989) 289.
[110] D. Sazou, M. Pagitsas, and C. Georgolios, *Electrochim. Acta* **37** (1992) 2067.
[111] D. Sazou, M. Pagitsas, and C. Georgolios, *Electrochim. Acta* **38** (1993) 2321.
[112] M. T. M. Koper, E. A. Meulenkamp, and D. Vanmaekelbergh, *J. Phys. Chem.* **97** (1993) 7337.
[113] M. T. M. Koper, *Ber. Bunsenges. Phys. Chem.* **100** (1996) 497.
[114] M. T. M. Koper, M. Hachkar, and B. Beden, *J. Chem. Soc., Faraday Trans.* **92** (1996) 3975.
[115] N. Fetner and J. L. Hudson, *J. Phys. Chem.* **94** (1990) 6506.
[116] T. G. J. vanVenrooij and M. T. M. Koper, *Electrochim. Acta* **40** (1995) 1689.
[117] G. Inzelt and V. Kertesz, *Electrochim. Acta* **40** (1995) 221.
[118] Y. H. Xu, H. H. Wu, H. P. Dai, and S. M. Zhou, *Prog. Nat. Sci.* **4** (1994) 248.
[119] M. Krausa and W. Vielstich, *J. Electroanal. Chem.* **399** (1995) 7.
[120] G. Neher, L. Pohlmann, and H. Tributsch, *J. Phys. Chem.* **99** (1995) 17763.
[121] J. Ringland, N. Issa, and M. Schell, *Phys. Rev. A* **41** (1990) 4223.
[122] M. T. M. Koper, *Physica D* **80** (1995) 72.
[123] S. K. Scott, *Chemical Chaos,* Clarendon Press, Oxford, 1991.
[124] M. T. M. Koper and P. Gaspard, *J. Phys. Chem.* **95** (1991) 4945.
[125] J. Maselko and H. L. Swinney, *J. Chem. Phys.* **85** (1986) 6430.
[126] C. Grebogi, E. Ott, and J. A. Yorke, *Physica D* **7** (1983) 181.

[127] J. M. T. Thompson and H. B. Stewart, *Nonlinear Dynamics and Chaos,* Wiley, Chichester, 1987.
[128] J. Osterwald and H. G. Fellner, *J. Electrochem. Soc.* **107** (1960) 473.
[129] J. Osterwald, *Electrochim. Acta* **7** (1962) 523.
[130] D. Haim, O. Lev, L. M. Pismen, and M. Sheintuch, *J. Phys. Chem.* **96** (1992) 2676.
[131] M. Keddam, H. Takenouti, and N. Yu, *J. Electrochem. Soc.* **132** (1985) 2561.
[132] D. Sazou and M. Pagitsas, *J. Electroanal. Chem.* **323** (1992) 247.
[133] M. Pagitsas and D. Sazou, *J. Electroanal. Chem.* **334** (1992) 81.
[134] S. H. Glarum and J. H. Marshall, *J. Electrochem. Soc.* **132** (1985) 2872.
[135] L. T. Tsitsopoulos, I. A. Webster, and T. T. Tsotsis, *Surf. Sci.* **220** (1989) 391.
[136] L. T. Tsitsopoulos, T. T. Tsotsis, and I. A. Webster, *Surf. Sci.* **191** (1987) 225.
[137] P. Russell and J. Newman, *J. Electrochem. Soc.* **130** (1983) 547.
[138] I. Epelboin, C. Gabrielli, M. Keddam, and H. Takenouti, *Electrochim Acta* **20** (1975) 913.
[139] M. Eiswirth, A. Freund, and J. Ross, *Adv. Chem. Phys.* **80** (1991) 127.
[140] G. Inzelt, V. Kertesz, and G. Láng, *J. Phys. Chem.* **97** (1993) 6104.
[141] G. Inzelt and V. Kertesz, *Electrochim. Acta* **38** (1993) 2385.
[142] M. Hachkar, M. M. de Choy, A. Rakotondrainibe, B. Beden, and C. Lamy, *Phys. Rev. A* **43** (1991) 2480.
[143] V. Kertesz, G. Inzelt, C. Barbero, R. Koetz, and O. Haas, *J. Electroanal. Chem.* **392** (1995) 91.
[144] L. Pohlmann, G. Neher, and H. Tributsch, *J. Phys. Chem.* **98** (1994) 11007.
[145] H. J. Lewerenz and G. Schlichthoerl, *J. Electroanal. Chem.* **327** (1992) 85.
[146] M. Hachkar, B. Beden, and C. Lamy, *J. Electroanal. Chem.* **287** (1990) 81.
[147] G. Flätgen and K. Krischer, *J. Chem. Phys.* **103** (1995) 5428.
[148] N. Mazouz, G. Flätgen, and K. Krischer, *Phys. Rev. E* **55** (1997) 2260.
[149] G. Flätgen and K. Krischer, *Phys. Rev. E* **51** (1995) 3997.
[150] R. Kapral and K. Showalter, eds., *Chemical Waves and Patterns,* Kluwer, Dordrecht, 1995.
[151] J. D. Murray, *Mathematical Biology,* Springer, Berlin, 1990.
[152] A. S. Mikhailov, *Foundations of Synergetics I,* 2nd ed., Springer, Berlin, 1994.
[153] G. Flätgen, K. Krischer, and G. Ertl, *Z. Naturforsch.* **50a** (1995) 1097.
[154] N. Mazouz, G. Flätgen, K. Krischer, and I. G. Kevrekidis, *J. Electrochem. Soc.* **145** (1998) 2404.
[155] N. Mazouz, K. Krischer, G. Flätgen, and G. Ertl, *J. Phys. Chem.* **101** (1997) 2403.
[156] G. Flätgen, doctoral thesis, Free University of Berlin, 1995.
[157] J. Jorne, *Electrochim. Acta* **28** (1983) 1713.
[158] D. Haim, O. Lev, L. M. Pismen, and M. Sheintuch, *Chem. Eng. Sci.* **47** (1992) 3907.
[159] M. T. M. Koper and J. H. Sluyters, *Electrochim. Acta* **38** (1993) 1535.
[160] O. Lev, M. Sheintuch, L. M. Pismen, and C. Yarnitzky, *Nature* **336** (1988) 488.
[161] O. Lev, M. Sheintuch, H. Yarnitsky, and L. M. Pismen, *Chem. Eng. Sci.* **45** (1990) 839.
[162] J. Christoph, M. Eiswirth, and K. Krischer, *in preparation.*
[163] J. Newman, *J. Electrochem. Soc.* **113** (1966) 501.
[164] J. Newman, *J. Electrochem. Soc.* **113** (1966) 1235.
[165] J. Newman, *Electrochemical Systems,* 2nd ed., Prentice-Hall, Englewood Cliffs, NJ, 1991.
[166] R. Suzuki, *Adv. Biophys.* **9** (1976) 115.
[167] R. D. Otterstedt, P. J. Plath, N. I. Jaeger, and J. L. Hudson, *Phys. Rev. E* **54** (1996) 3744.
[168] E. Nehrer and B. Sakmann, *Nature* **260** (1976) 799.
[169] E. Nehrer and B. Sakmann, *Spektrum der Wissenschaft* **5** (1992) 48.
[170] G. Flätgen, K. Krischer, B. Pettinger, K. Doblhofer, H. Junkes, and G. Ertl, *Science* **269** (1995) 668.
[171] A. Tadjeddine and A. Hadjadj, *J. Electroanal. Chem.* **246** (1988) 43.
[172] A. Hadjadj, A. Tadjeddine, and G. Hincelin, *J. Electroanal. Chem.* **228** (1987) 251.
[173] E. Kretschmann, *Opt. Commun.* **6** (1972) 185.

[174] H. E. de Bruijn, R. P. H. Kooymann, and J. Greve, *Appl. Optics* **32** (1993) 2426.
[175] R. D. Otterstedt, N. I. Jaeger, and P. J. Plath, *Int. J. Bifurcation and Chaos* **4** (1994) 1265.
[176] R. D. Otterstedt, P. J. Plath, N. I. Jaeger, J. C. Sayer, and J. L. Hudson, *Chem. Eng. Sci.* **51** (1996) 1747.
[177] R. D. Otterstedt, P. J. Plath, N. I. Jaeger, and J. L. Hudson, *J. Chem. Soc., Faraday Trans.* **92** (1996) 2933.
[178] G. Flätgen, K. Krischer, and G. Ertl, *J. Electroanal. Chem.* **409** (1996) 183.
[179] A. Pigeau and H. B. Kirkpatrick, *Corrosion* **25** (1969) 209.
[180] J. L. Hudson, J. Tabora, K. Krischer, and I. G. Kevrekidis, Phys. Lett. A 179 (1993) 355
[181] J. C. Sayer and J. L. Hudson, *Ing. Eng. Chem. Res.* **34** (1995) 3246.
[182] Z. Fei, R. G. Kelly, and J. L. Hudson, *J. Phys. Chem.* **100** (1996) 18986.
[183] M. U. Kleinke, O. Teschke, and M. A. Tenan, *J. Electrochem. Soc.* **138** (1991) 2763.
[184] M. A. Tenan, O. Teschke, M. U. Kleinke, and F. Galembeck, *Langmuir* **6** (1990) 1640.
[185] G. R. Wessler, P. Schwartz, H. Linde, E. Mueller, and H. D. Dörfler, *Z. Phys. Chem. (Leipzig)* **267** (1986) 945.
[186] V. V. Nechiporuk and I. L. Elgurt, *Ukr. Khim. Zh.* (Russ. Ed.) **59** (1993) 388.
[187] V. V. Nechiporuk and O. E. Petrenko, *Ukr. Khim. Zh.* (Russ. Ed.) **61** (1995) 120.
[188] V. V. Nechiporuk, D. P. Babyuk, and V. N. Kapranov, *Russ. J. Electrochem.* (Transl. of Elektrokhimiya) **32** (1996) 758.
[189] G. Marshall, E. Perone, P. Tarela, and P. Mocskos, *Chaos, Solitons & Fractals* **6** (1995) 315.
[190] G. Marshall, S. Tagtachian, and L. Lam, *Chaos, Solitons & Fractals* **6** (1995) 325.
[191] M. Huth, H. L. Swinney, W. D. McCormick, A. Kuhn, and F. Argoul, *Phys. Rev. E* **51** (1995) 3444.
[192] A. Kuhn, F. Argoul, J. F. Muzy, and A. Arneodo, *Phys. Rev. Lett.* **73** (1994) 2998.
[193] F. Argoul, E. Freysz, A. Kuhn, C. Leger, and L. Potin, *Phys. Rev. E* **53** (1996) 1777.
[194] M. Wang and N. Ming, *Phys. Rev. A* **45** (1992) 2493.
[195] R. P. Rastogi, I. Das, A. Pushkarna, and S. Chand, *J. Phys. Chem.* **97** (1993) 4871.
[196] D. L. Piron, I. Nagatsugawa, and C. Fan, *J. Electrochem. Soc.* **138** (1991) 3296.
[197] R. E. Yee and J. Jorne, *J. Electrochem. Soc.* **137** (1990) 2403.
[198] H. Yan, J. Downes, P. J. Boden, and S. J. Harris, *J. Electrochem. Soc.* **143** (1996) 1577.
[199] E. Raub and A. Schall, *Z. f. Metallkunde* **30** (1938) 149.
[200] I. Krastev and M. Nicolova, *J. Appl. Electrochem.* **16** (1986) 875.
[201] I. Krastev, M. Nikolova, and I. Nakada, *Electrochim. Acta* **34** (1989) 1211.
[202] I. Krastev, M. E. Baumgartner, and C. J. Raub, *Metalloberfl.* **46** (1992) 116.
[203] I. Krastev and M. T. M. Koper, *Physica A* **213** (1995) 199.

2

Electrochemical Impedance Spectroscopy and its Applications

Andrzej Lasia

Département de Chimie, Université de Sherbrooke, Sherbrooke, Québec, Canada J1K 2R1

I. INTRODUCTION

Electrochemical impedance spectroscopy (EIS) or ac impedance methods have seen a tremendous increase in popularity in recent years. Initially applied to the determination of the double-layer capacitance[1–4] and in ac polarography,[5–7] they are now used to characterize electrode processes and complex interfaces. This method studies the system response to the application of a periodic small-amplitude ac signal. The measurements are carried out at different ac frequencies and thus the name *impedance spectroscopy* was later adopted. Analysis of the system response contains information about the interface, its structure, and the reactions taking place there. Electrochemical impedance spectroscopy is now described in the general books on electrochemistry,[8–17] specific books[18,19] on EIS, and

Modern Aspects of Electrochemistry, Number 32, edited by B. E. Conway *et al.* Kluwer Academic / Plenum Publishers, New York, 1999.

numerous articles and reviews.[6,20–31] It has become very valuable in research and applied chemistry. The *Chemical Abstracts* database shows about 1500 citations per year of the term "impedance" since 1993, and about 1200 in earlier years, and about 500 citations per year of "electrochemical impedance." Although the term "impedance" may also include nonelectrochemical measurements, and "electrochemical impedance" may not include all the electrochemical studies, the popularity of this technique cannot be denied.

However, EIS is a very sensitive technique and must be used with great care. In addition, it is not always well understood. This may be because it is often difficult for nonspecialists to understand existing reviews on EIS and frequently the articles do not show the complete mathematical development of equations connecting the impedance with the physicochemical parameters. It should be stressed that EIS cannot give all the answers. It is a complementary technique and other methods must also be used to elucidate the interfacial processes. The purpose of this chapter is to fill this gap by presenting a modern and relatively complete review of electrochemical impedance spectroscopy, including the mathematical development of the fundamental equations.

1. Response of Electrical Circuits

(i) Arbitrary Input Signal

Application of an electrical perturbation (current, potential) to an electrical circuit causes a response. In this chapter, the system response to an arbitrary perturbation and later to an ac signal, is discussed. Knowledge of the Laplace transform technique is assumed, but the reader may consult numerous books on the subject if necessary.

First, let us consider application of an arbitrary (but known) potential $E(t)$ to a resistance R. The current $i(t)$ is given as $i(t) = E(t)/R$. When the same potential is applied to the series connection of the resistance R and capacitance C, the total potential difference is the sum of potential drops on each element. Taking into account that for a capacitance $E(t) = Q(t)/C$, where Q is the charge stored in a capacitor, the following equation is obtained:

$$E(t) = i(t)R + \frac{Q(t)}{C} = i(t)R + \frac{1}{C}\int_0^t i(t)dt \tag{1}$$

This equation may be solved using either Laplace transform or differentiation techniques.[32–34] Differentiation gives

$$\frac{di(t)}{dt} + \frac{i(t)}{RC} = \frac{1}{R}\frac{dE(t)}{dt} \tag{2}$$

which may be solved for known $E(t)$ using standard methods for differential equations.

The Laplace transform is an integral transform in which a function of time $f(t)$ is transformed into a new function of a parameter s called *frequency*, $\bar{f}(s)$ or $F(s)$, according to

$$\mathcal{L}[f(t)] = \bar{f}(s) = F(s) = \int_0^\infty F(t)\exp(-st)dt \tag{3}$$

The Laplace transform is often used in the solution of differential and integral equations. In general, the parameter s may be complex, $s = v + j\omega$, where $j = \sqrt{-1}$, but in this chapter only the real transform will be considered, that is $s = v$. Direct application of the Laplace transform to Eq. (1), taking into account that

$$\mathcal{L}\left[\int_0^t i(t)dt\right] = i(s)/s,$$

gives

$$E(s) = i(s)R + \frac{i(s)}{sC} \tag{4}$$

which leads to

$$i(s) = E(s)/\left(R + \frac{1}{sC}\right) \tag{5}$$

The ratio of the Laplace transforms of potential and current, $E(s)/i(s)$, is expressed in units of resistance, Ω, and is called *impedance*, $Z(s)$. In this case

$$Z(s) = \frac{E(s)}{i(s)} = R + \frac{1}{sC} \tag{6}$$

The inverse of impedance is called *admittance,* $Y(s) = 1/Z(s)$. These are *transfer functions* that transform one signal (e.g., applied voltage), into another (e.g., current). Both are called *immittances.* Some other transfer functions are discussed in Refs. 18, 35, and 36. It should be noted that the impedance of a series connection of a resistance and capacitance, Eq. (6), is the sum of the contributions of these two elements: resistance, R, and capacitance, $1/sC$.

For the series connection of a resistance, R, and inductance, L, the total potential difference consists of the potential drop in both elements:

$$E(t) = i(t)R + L\frac{di(t)}{dt} \tag{7}$$

Taking into account that $\mathcal{L}[di(t)/dt] = s\,i(s) - i(0^+)$, and taking $i = 0$ at $t = 0$, one obtains the current response in the Laplace space:

$$i(s) + E(s)/(R + sL) \tag{8}$$

In both cases considered here, the system impedance consists of the sum of two terms, corresponding to two elements: resistance and capacitance or inductance.

In general, one can write contributions to the total impedance corresponding to the resistance as R, the capacitance as $1/sC$, and the inductance as sL. The addition of impedances is analogous to the addition of resistances. Knowledge of the system's impedance allows an easy solution of the problem.

For example, when a constant voltage, E_0, is applied at time zero to a series connection of R and C, the current is described by Eq. (5). Taking into account that the Laplace transform of a constant $\mathcal{L}(E_0) = E_0/s$, one gets:

$$i(s) = \frac{E_0}{s(R + 1/sC)} = \frac{E_0}{R}\frac{1}{s + 1/RC} \tag{9}$$

The inverse transform of (9) gives the current relaxation versus time

$$i(t) = \frac{E_0}{R}\exp(-t/RC) \tag{10}$$

The result obtained shows that after the application of the potential step, current initially equals E_0/R and decreases to 0 as the capacitance is charged to the potential difference E_0.

Similarly, application of the potential step to a series connection of R and L produces a response given by Eq. (8) which, after substitution of $E(s) = E_0/s$, gives

$$i(s) = \frac{E_0}{s(R + sL)} = \frac{E_0}{L}\frac{1}{s(s + R/L)} = \frac{E_0}{R}\left(\frac{1}{s} + \frac{1}{s + R/L}\right) \tag{11}$$

An inverse transform gives the time dependence of the current:

$$i(t) = \frac{E_0}{R}\left[1 - \exp\left(-\frac{Rt}{L}\right)\right] \tag{12}$$

The current starts at 0 because the inductance constitutes infinite resistance at $t = 0$ and increases to E_0/R as the effect of inductance becomes negligible in the steady-state condition.

Other problems of transient system response may be solved in a similar way. More complex examples are presented, for example, in Refs. 33–34. It should be added that an arbitrary signal may be applied to the system and if the Laplace transforms of the potential and current are determined, for example, by numerical transform calculations, the system impedance is determined. In the Laplace space the equations [e.g., Eqs. (9) and (11)] are much simpler than those in the time space [e.g. Eqs. (10) and (12)] and analysis in the frequency space s allows the determination of the system parameters. This analysis is especially important when an ideal potential step cannot be applied to the system because of the bandwidth limitations of the potentiostat.[37] In this case it is sufficient to know $i(t)$ and the real value of the potential applied to the electrodes by the potentiostat, $E(t)$, which allows numerical Laplace transformations to be carried out and the system impedance obtained.

In the cases involving more time constants (i.e., more than one capacitance or inductance in the circuit), the differential equations describing the system are of the second or higher order and the impedances obtained are the second or higher order functions of s.

(ii) Alternating Voltage Input Signal

In EIS we are interested in a system's response to the application of a sinusoidal signal; for example, $E = E_0 \sin(\omega t)$, where E_0 is the signal amplitude, $\omega = 2\pi f$ is the angular frequency, and f is the alternating voltage (av) signal frequency. This problem may be solved in different

ways. First, let us consider application of an av signal to a series R-C connection. Taking into account that the Laplace transform of the sine function $L[\sin(\omega t)] = \omega/(s^2 + \omega^2)$, use of Eq. (5) gives

$$i(s) = \frac{E_0\omega}{s^2+\omega^2}\frac{1}{R+1/sC} = \frac{E_0\omega}{R}\frac{1}{s^2+\omega^2}\frac{1}{s+1/RC} \tag{13}$$

Distribution into simple fractions leads to

$$i(s) = \frac{E_0}{R[\omega^2+(1/RC)^2]}\left[\omega^2\frac{\omega}{s^2+\omega^2} + \frac{\omega}{RC}\frac{s}{s^2+\omega^2} - \frac{\omega}{RC}\frac{1}{s+1/RC}\right] \tag{14}$$

and the inverse Laplace transform, taking $L^{-1}[s/(s^2+\omega^2)] = \cos \omega t$, gives

$$i(t) = \frac{E_0}{R[\omega^2+(1/RC)^2]}\left[\omega^2\sin(\omega t) + \frac{\omega}{RC}\cos(\omega t) - \frac{\omega}{RC}\exp(-t/RC)\right] \tag{15}$$

The third term in Eq. (15) corresponds to a transitory response observed just after application of the av signal and it decreases quickly to 0. The steady-state equation may be rearranged into a simpler form:

$$i(t) = \frac{E_0}{R\left(1+\dfrac{1}{(\omega RC)^2}\right)}\left[\sin(\omega t) + \frac{1}{\omega RC}\cos(\omega t)\right] \tag{16}$$

and by introducing $\tan \varphi = 1/\omega RC$ the following form is found:

$$i(t) = \frac{E_0}{\sqrt{R^2+\dfrac{1}{(\omega C)^2}}}\sin(\omega t + \varphi) = \frac{E_0}{|Z|}\sin(\omega t + \varphi) \tag{17}$$

where φ is the phase angle between current and potential, $\varphi = \text{atan}(1/\omega RC)$. It is obvious that the current has the same frequency as the applied potential but is phase shifted by the angle φ. The value $|Z|$ has units of resistance; it is the length of a vector obtained by the addition of two perpendicular vectors: R and $1/\omega C$.

2. Impedance of Electrical Circuits

In order to simplify the calculations of impedances, the result obtained for the periodic perturbation of an electrical circuit may be represented using complex notation. The system impedance, $Z(j\omega)$, may be represented as

$$Z(j\omega) \equiv \hat{Z} = Z' + jZ'' = R + \frac{1}{j\omega C} = R - j\frac{1}{\omega C} \tag{18}$$

and the real and imaginary parts of the impedance are $Z' = R$ and $Z'' = -1/\omega C$, respectively. It should be noted that the complex impedance $Z(j\omega)$ [Eq. (18)] may be obtained from $Z(s)$ [Eq.(6)], by substitution: $s = j\omega$. In fact, this is the imaginary Laplace transform. The modulus of $Z(j\omega)$ Eq. (17)], equals

$$|Z| = \sqrt{(Z')^2 + (Z'')^2} = \sqrt{R^2 + (1/\omega C)^2} \tag{19}$$

and the phase angle between the imaginary and real impedance equals $\varphi = \arg(\hat{Z}) = \text{atan}(-1/\omega RC)$. It should be noted that the sign of φ between potential and current, described above for the impedances, is different from that found between current and potential, Eq. (17). It may be recalled that in complex notation

$$Z(j\omega) = |Z|\exp(j\varphi) = |Z|[\cos(\varphi) + j\sin(\varphi)] \tag{20}$$

Analysis of Eq. (17) indicates that the current represents a vector of the length $i_0 = E_0/|Z|$, which rotates with the frequency ω. Current and potential are rotating vectors in the time domain, as represented in Figure 1(a). Using complex notation, they may be described by

$$E = E_0 \exp(j\omega t) \text{ and } i = i_0 \exp[j(\omega t + \varphi)] \tag{21}$$

These vectors rotate with a constant frequency ω, and the phase angle φ between them stays constant. Instead of showing rotating vectors in time and space, it is possible to present immobile vectors in the frequency space, separated by the phase angle φ. These vectors are called *phasors*; they are equal to $\tilde{E} = E_0$ and $\tilde{I} = I_0 \exp(j\varphi)$, where the initial phase shift of the potential is assumed to be 0 [see Fig. 1(b)].

In general, the complex impedance may be written for any circuit by taking R for a resistance, $1/j\omega C$ for a capacitance, and $j\omega L$ for an inductance and applying Ohm's and Kirchhoff's laws to the connection of these elements. Several examples of this method are presented in the next section.

(i) Series R-C *Circuit*

In the case of a series connection of the resistance and capacitance, the impedance is given by $Z(j\omega) = R + 1/j\omega C = R - j/\omega C$. The result may be represented graphically using two types of plots: *complex plane* (also

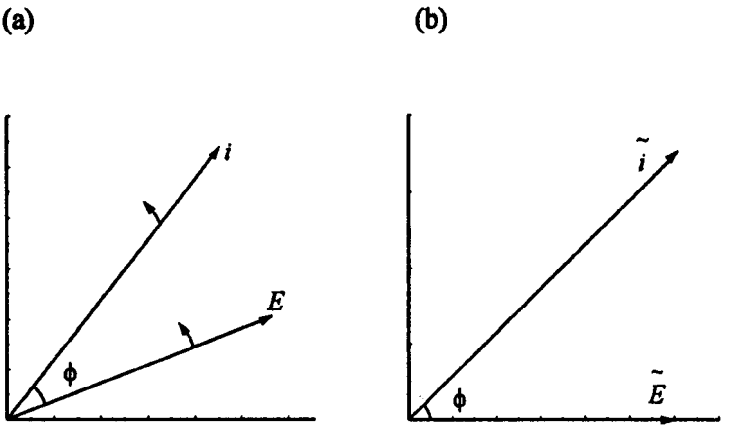

Figure 1. Representation of ac signals: (a) rotating voltage and current vectors in time space and (b) voltage and current phasors in frequency space.

known as *Argand* or *Nyquist plots*) and *Bode plots.* The complex plane plot is a plot of Z'' versus Z', that is, the imaginary versus the real components, plotted for various frequencies. A complex plane plot for a series connection *R-C* ($R = 100\ \Omega$, $C = 2 \times 10^{-5}$ F) circuit is shown in Fig. 2. It consists of a straight line perpendicular to the real axis. Other types of graphs are Bode plots, that is, log $|Z|$ (magnitude) and phase angle φ versus log ω. They are also shown in Fig. 2. The graph of log $|Z|$ versus log ω [Fig. 2(d)] contains one breakpoint or corner frequency. This point corresponds to the system characteristic frequency $\omega = 1/RC = 500\ s^{-1}$ or a time constant $\tau = RC = 0.002$ s. The phase angle changes from 90° at low frequencies to 0 at high frequencies. This circuit corresponds to an ideally polarized electrode in solution, e.g., a mercury electrode-supporting electrolyte solution.

The complex plane plots may also be obtained for admittances. The admittance for the series *R-C* connection equals

$$Y(j\omega) = \frac{1}{Z(j\omega)} = \frac{1}{R - \dfrac{j}{\omega C}} = \frac{R}{R^2 + \dfrac{1}{\omega^2 C^2}} + \frac{j}{\omega C\left(R^2 + \dfrac{1}{\omega^2 C^2}\right)} \tag{22}$$

It represents a semicircle on the complex plane plot [Fig. 2(c)]. It should be stressed that for capacitive circuits the imaginary impedance is always negative and the imaginary admittance is positive.

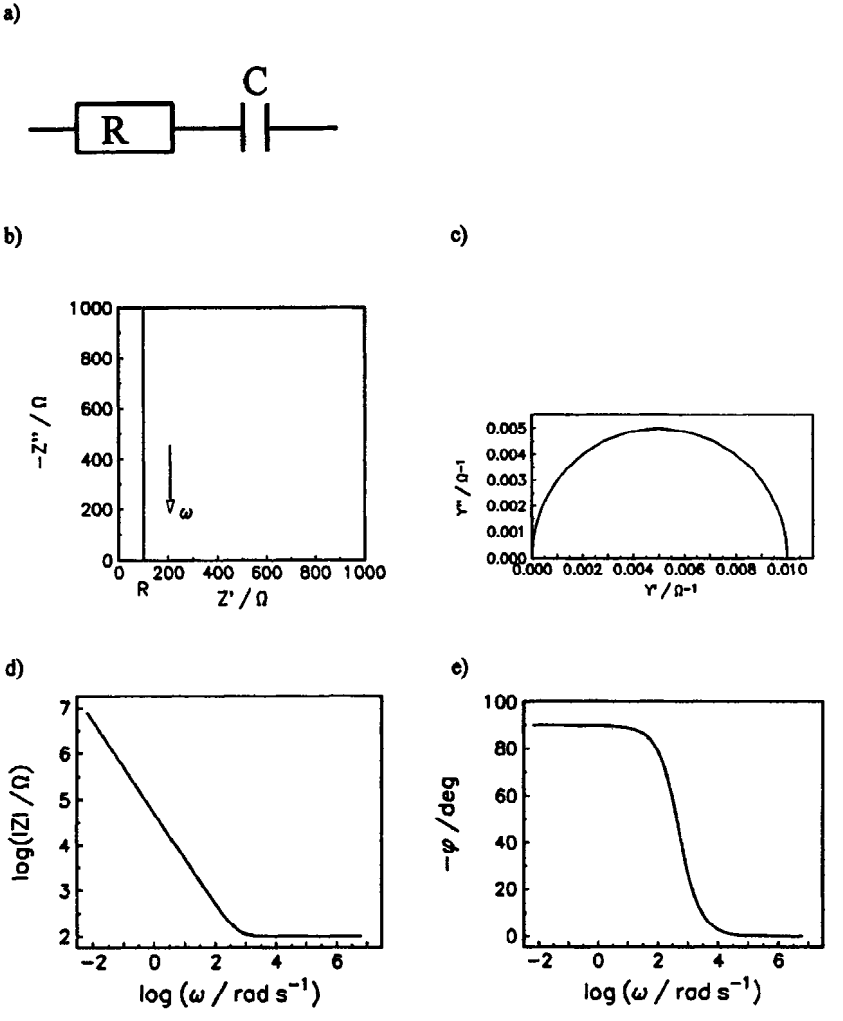

Figure 2. (a) Series connection of a resistance and a capacitance, $R = 100\ \Omega$, $C = 20\ \mu$F. (b), (c) Complex plane and (d), (e) Bode plots for circuit.

(ii) Parallel R-C *Circuit*

For a parallel *R*-*C* connection, the total admittance is $Y(j\omega) = 1/R + j\omega C$ so that

$$Z(j\omega) = \frac{1}{1/R + j\omega C} = \frac{R}{1 + j\omega RC} = \frac{R}{1 + \omega^2 R^2 C^2} - \frac{j\omega R^2 C}{1 + \omega^2 R^2 C^2} \tag{23}$$

There are two limits of the impedance: $\omega = 0$, $\hat{Z} = R$ and $\omega \to \infty$, $\hat{Z} = 0$. The corresponding complex plane and Bode plots for the same values of *R* and *C* elements as those used in the series *R*-*C* model above, are shown in Fig. 3. The Nyquist plot shows a semicircle of radius *R*/2 with the center on the real axis and the frequency at the semicircle maximum equal to: $\omega = 1/RC$. The circuit's characteristic breakpoint frequency (the inverse of the characteristic time constant), as observed in the impedance Bode graph, is the same as for the series and the parallel *R*-*C* circuits. The complex plane admittance plot represents a straight line parallel to the imaginary axis [Fig. 3(c)], which is similar to the impedance complex plane plot for the series *R*-*C* connection.

(iii) Series: R_s *+ Parallel R-C Circuit*

Finally, the impedance of the circuit shown in Fig. 4, consisting of a series connection of the resistance R_s with the parallel connection of R_{ct}-C_{dl}, is given as

$$Z(j\omega) = R_s + \frac{1}{1/R_{ct} + j\omega C_{dl}} \tag{24}$$

The corresponding complex plane and Bode plots are also shown in Fig. 4 for $R_{ct} = 100\,\Omega$, $R_s = 10\,\Omega$, and $C_{dl} = 20\,\mu$F. The main difference between the circuits in Fig. 3 and Fig. 4 is connected with the fact that in the latter circuit, at $\omega \to \infty$, $Z \to R_s$ and $\varphi \to 0$, owing to the presence of R_s, and for $\omega \to 0$ $Z \to R_s + R_{ct}$. The frequency corresponding to the maximum of Z'' is still equal to $\omega = 1/R_{ct}\,C_{dl} = 500\ s^{-1}$. In addition, the Bode log $|Z|$ plot shows that there are two breakpoints (bends). For comparison, the admittance complex plane plot is also shown in Fig. 4(c).

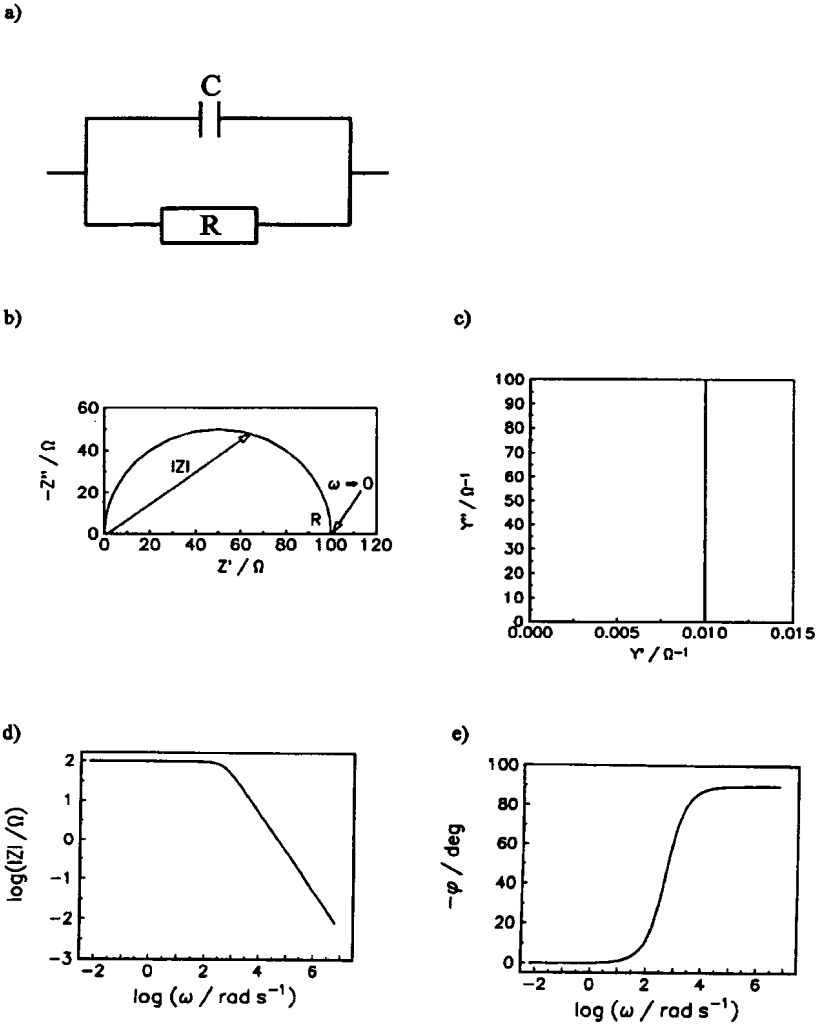

Figure 3. (a) Parallel connection of R and C, $R = 100\ \Omega$, $C = 20\ \mu$F. (b), (c) Complex plane and (d), (e) Bode plots for circuit.

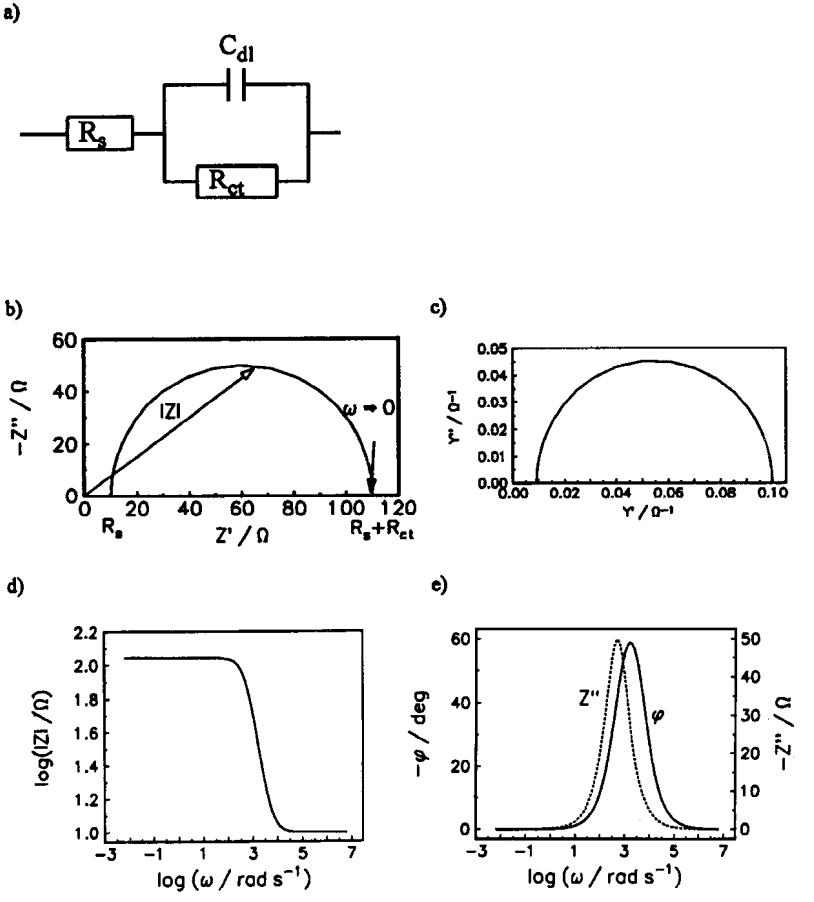

Figure 4. (a) Circuit with $R_s = 10\ \Omega$, $R_{ct} = 100\ \Omega$, $C_{dl} = 20\ \mu$F. (b), (c) Complex plane and (d), (e) Bode plots for the circuit.

3. Interpretation of Complex Plane and Bode Plots

Complex plane (Nyquist) plots are the most often used in the electrochemical literature because they allow an easy prediction of the circuit elements. However, they do not show all details; for example, exactly the same Nyquist impedance plots shown in Fig. 3 and Fig. 4 may be obtained for different values of the capacitance *C*. The only difference between them will be the fact that the points on the semicircle would correspond to different frequencies. Nevertheless, Nyquist plots allow an easy relation

to the electrical model. On the other hand, Bode plots contain all the necessary information. That is why Bode plots are mainly used in circuit analysis. Bode magnitude plots may be easily predicted from the circuit impedance.[33] Let us consider the circuit shown in Fig. 4(a). Its impedance is presented by Eq. (24). This equation may be rearranged into another form:

$$\hat{Z} = (R_s + R_{ct}) \frac{1 + j\omega\left(\frac{R_s R_{ct} C_{dl}}{R_s + R_{ct}}\right)}{1 + j\omega(R_{ct} C_{dl})} = (R_s + R_{ct}) \frac{1 + j\omega\tau_2}{1 + j\omega\tau_1} \qquad (25)$$

where τ_1 and τ_2 are the Bode characteristic time constants. From Eq.(25) log(|Z|) is easily evaluated:

$$\log(|Z|) = \log(|R_s + R_{ct}|) + \log(|1 + j\omega\tau_2|) - \log(|1 + j\omega\tau_1|) \qquad (26)$$

In order to construct asymptotic lines in the Bode magnitude plot, the contribution of each term in Eq. (26) can be considered independently and then their sum may be easily obtained. Each term $\log(|1 + j\omega\tau|)$ has two limits: when $\omega\tau << 1$, i.e., $\omega << 1/\tau$, $\log(|1 + j\omega\tau|) = 0$ and when $\omega\tau >> 1$, $\log(|1 + j\omega\tau|) = \log\tau + \log\omega$, which corresponds to a straight line with a slope of 1 and intercept $\log\omega = -\log\tau$.

The graphs corresponding to these lines are shown in Fig. 5. The breakpoint frequencies in the Bode magnitude plot, Fig 4(d) and Fig. 5, are $\omega_1 = 1/\tau_1 = 500\ s^{-1}$ and $\omega_2 = 1/\tau_2 = 5500\ s^{-1}$. The continuous line is the sum of the three asymptotes. In this way Bode magnitude graphs may be constructed for other circuits.

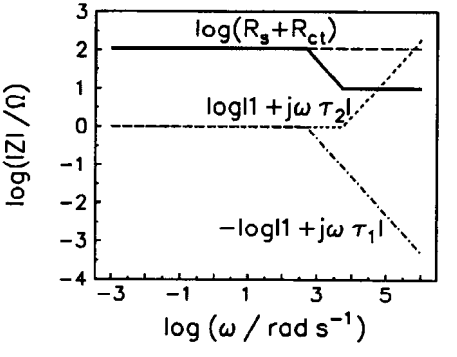

Figure 5. Construction of the Bode magnitude plot for the circuit in Fig. 4(a) using Eq. (26). The solid line is a sum of all three contributions.

The Bode phase-angle graph is shown in Fig. 4(e). The phase angle is described by

$$\varphi = \text{atan}\,(Z''/Z') = \text{atan}\left(\frac{\omega R_{ct}^2 C_{dl}}{R_s + R_{ct} + (\omega R_{ct} C_{dl})^2 R_s}\right) \tag{27}$$

It can be shown that this function has a maximum at

$$\omega = \frac{1}{R_{ct} C_{dl}} \sqrt{\frac{R_S + R_{ct}}{R_S}} \tag{28}$$

which, in this case, equals $\omega = 1658\ s^{-1}$. It should be noted that the maximum of the phase angle is different from the maximum of the imaginary part of the impedance, corresponding to the maximum of the semicircle at $Z' = R_s + R_{ct}/2$ at $\omega = 1/R_{ct}\,C_{dl}$. The plots of Z' and Z'' (or their logarithms) as a function of log ω are also sometimes shown in the literature.

II. IMPEDANCE MEASUREMENTS

The dc transient response of electrochemical systems is usually measured using potentiostats. In the case of EIS, an additional perturbation is added to the dc signal to obtain the frequency response of the system. The system impedance may be measured using various techniques:

- ac bridges
- Lissajous curves
- phase-sensitive detection (PSD)
- frequency response analysis (FRA)
- fast Fourier transform (FFT)

Because older techniques are described in detail in Refs. 18, 19, 26, 28, 30, and 31, this chapter focuses on the last three techniques.

1. ac Bridges

This technique was the first used to measure double-layer parameters (principally of the dropping mercury electrode) and later to measure electrode impedance in the presence of a faradaic reaction to determine the kinetics of electrode processes. The use of ac bridges provides meas-

urements of very good precision. It has been described in detail in Refs. 18, 26, 28, and 38. An ac bridge with potentiostatic control may also be used. Although this method is slow, because bridge compensation must be carried out at each frequency manually, it is still used, principally in precise double-layer measurements.[39–41]

2. Lissajous Curves

Recording the applied av potential and the resulting ac current on a twin-beam oscilloscope produces Lissajous curves (in this case an ellipse),[18,28,30] which may be used to the determine the impedances. Because of its frequency limitations and sensitivity to noise, this technique is not currently used in electrochemical measurements.

3. Phase-Sensitive Detection

Phase-sensitive detection is used in lock-in amplifiers, which are interfaced with potentiostats.[42,43] Only a general idea of these measurements will be presented here. In this method the measured signal, E_1, which is proportional to the ac current from the potentiostat, is

$$E_1 = E_{1,a} \sin(\omega t + \varphi_1) \tag{29}$$

where $E_{1,a}$ is the signal amplitude and φ_1 is the phase shift and is multiplied by a square-wave signal of the same angular frequency ω. The square-wave signal may be represented as a Fourier series:

$$E_2 = \frac{4}{\pi} \sum_{n=0}^{\infty} \frac{1}{2n+1} \sin\left[(2n+1)\omega t + \varphi_2\right] \tag{30}$$

where n is an integer and the amplitude of the square signal is taken as unity. The resulting signal $E_1 \times E_2$ equals

$$E_1 E_2 = \sum_{n=0}^{\infty} \frac{4E_1}{(2n+1)\pi} \sin(\omega t + \varphi_1) \sin\left[(2n+1)\omega t + \varphi_2\right]$$

$$= \sum_{n=0}^{\infty} \frac{2E_1}{(2n+1)\pi} \left\{\cos[-2n\omega t + \varphi_1 - (2n+1)\varphi_2]\right.$$

$$- \cos\left[(2n+2)\omega t + \varphi_1 + (2n+1)\varphi_2\right]\Big\}$$

$$= \frac{2E_1}{\pi}\left\{\begin{array}{l}\cos(\varphi_1 - \varphi_2) - \cos(2\omega t + \varphi_1 + \varphi_2) \\ + \frac{1}{3}\cos(-2\omega t + \varphi_1 - 3\varphi_2) - \frac{1}{3}\cos(4\omega t + \varphi_1 + 3\varphi_2) \\ + \frac{1}{5}\cos(-4\omega t + \varphi_1 - 5\varphi_2) - \frac{1}{5}\cos(6\omega t + \varphi_1 + 5\varphi_2) + \ldots\end{array}\right\} \tag{31}$$

It contains one time-independent component, depending on the phase difference of two signals, and is proportional to the amplitude of the measured ac signal. It reaches a maximum when the phase difference of the two signals being mixed is 0. The output signal is subsequently applied to a low-pass filter that averages the signal components having frequencies above the filter cutoff frequency. It produces a dc signal proportional to the amplitude. Because the average value of periodic functions is equal to 0, the average value of E_1E_2 [Eq. (31)], equals

$$\text{Ave}\,(E_1E_2) = \frac{2E_1}{\pi}\cos(\varphi_1 - \varphi_2) \tag{32}$$

The disadvantage of the lock-in technique is that it retains contributions of the harmonic frequencies $(2n + 1)\,\omega_{\text{ref}}$ if they are present in the input signal (e.g., harmonics, noise), although their influence is attenuated by 1/3, 1/5, 1/7, etc. with increasing *n*. For example, when the frequency in Eq. (29) is three times the reference frequency in Eq. (30), the average signal obtained

$$\text{Ave}\,(E_1E_2) = \frac{2E_1}{3\pi}\cos(\varphi_1 - 3\varphi_2) \tag{33}$$

is attenuated three times. If the reference signal is synchronized with the applied signal (they are both generated from the same source), φ_2 is equal to 0 and the expressions become simplified.

A schematic diagram of a lock-in amplifier is shown in Fig. 6. The measured signal is mixed with the reference square-wave signal of the same frequency and the resulting signal goes through a low-pass filter, producing an average of all components. The phase shifter allows for precise adjustment of the reference phase in order to zero the phase difference $\varphi_1 - \varphi_2$. In two-phase lock-in amplifiers, the measured signal

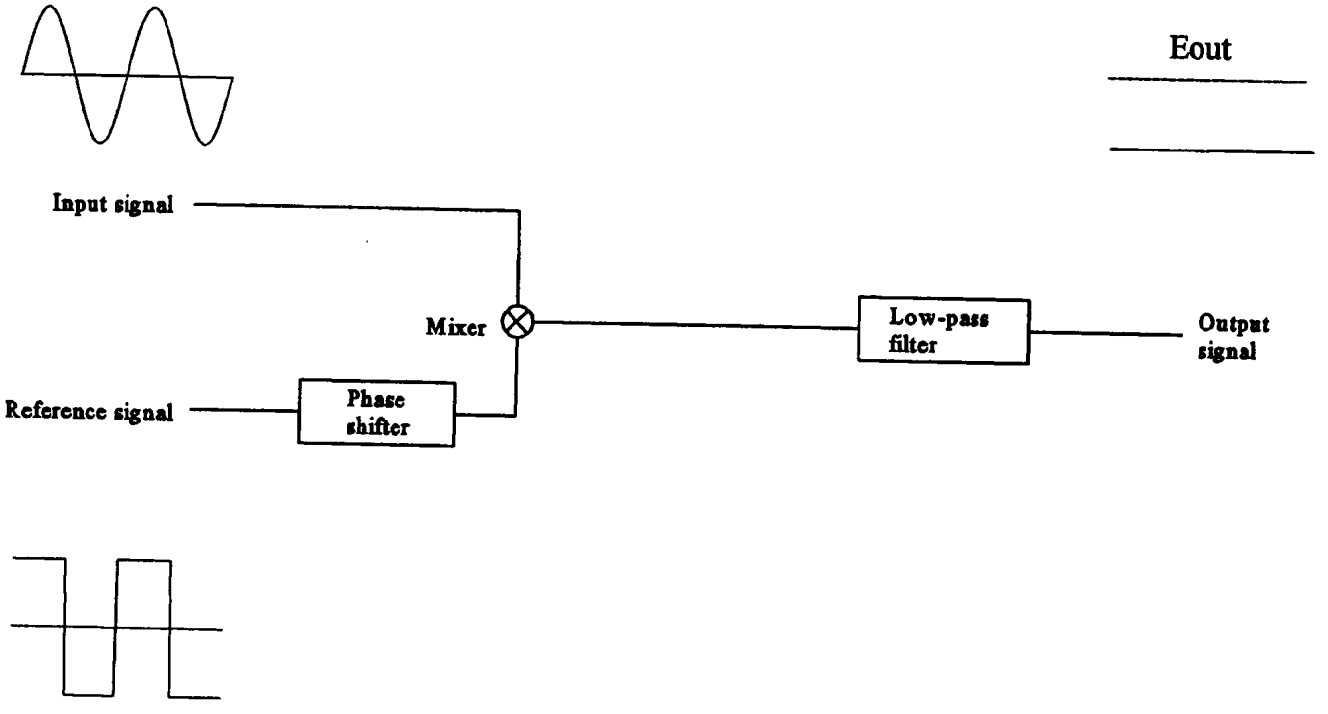

Figure 6. Schematic operation of a lock-in amplifier.

is mixed with the reference signal to obtain the in-phase component and, in addition, with the reference signal shifted by $\pi/2$ to resolve the imaginary component.

Lock-in amplifiers operate in the frequency range from 0.5 (lower limit up to 10 Hz, depending on the manufacturer) to ~ 10^5 Hz, with a precision of 0.1 to 0.2%. Modern lock-in amplifiers are controlled by a microprocessor and permit automated measurements with automatic range selection.

4. Frequency Response Analyzers

Frequency response analyzers are instruments that determine the frequency response of a measured system. Their functioning is different from that of lock-in amplifiers. They are based on the correlation of the studied signal with the reference.[44] The measured signal [Eq. (29)], is multiplied by the sine and cosine of the reference signal of the same frequency and then integrated during one or more wave periods:

$$\mathrm{Re}\,(E_1) = \frac{1}{T}\int_0^T E_{1,a}\sin(\omega t + \varphi_1)\sin(\omega t)dt = \frac{E_{1,a}}{2}\cos(\varphi_1) \qquad (34)$$

and

$$\mathrm{Im}\,(E_1) = \frac{1}{T}\int_0^T E_{1,a}\sin(\omega t + \varphi_1)\cos(\omega t)dt = \frac{E_{1,a}}{2}\sin(\varphi_1) \qquad (35)$$

Such integration recovers the real and imaginary parts of the measured signal. It can also be shown that all the harmonics are strictly rejected, that is, correlation of $\sin(k\omega t + \varphi)$ with $\sin(\omega t)$ or with $\cos(\omega t)$ is equal to 0 for $k > 1$. The advantage of the correlation process is also reduction of noise (of arbitrary frequency), its influence decreasing with an increase of the integration time. Figure 7 shows the attenuation of the output signal as a function of frequency and the number of integration cycles *N*. Modern FRAs carry out all the computations digitally. They have a wide frequency range (12 decades) and high precision.

Recently, Diard *et al.*[45] studied the effects of electrochemical nonlinearities on impedance measurements using an FRA. They derived theoretical expressions for the error in impedance measurements using the odd harmonic test criterion.[46] Measurements of the fundamental and third

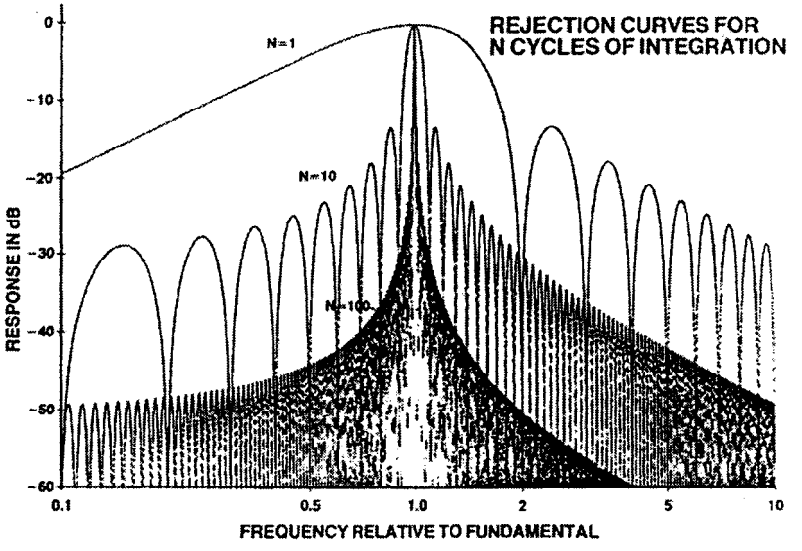

Figure 7. Frequency response of an FRA averaging filter for different numbers of integration cycles.[44]

Table 1
Comparison of PSD and FRA

Lock-in amplifier	FRA
Advantages	Advantages
Very sensitive	Faster analysis
Effectively removes noise	Wide frquency range
Reduces harmonic distortion	Removes harmonic distortion
Supresses dc noise	Direct output to external device
Relatively low cost	Easy stand-alone measurements
Disdavantages	Disadvantages
Limited frequency range	Higher cost
Slower	Limited noise removal
Stand-alone readings difficult	Limited sensitivity

harmonic in the electrode response are sufficient to estimate the impedance error. Evans[47] recently compared PSD and FRA, as shown in Table 1.

5. Fast Fourier Transform

It was shown in Section I. 1(i) that the system impedance is defined as the ratio of Laplace transforms [Eq. (6)], of potential and current. In general, the transformation parameter is complex, $s = v + j\omega$. The imaginary Laplace transform

$$F(j\omega) = \int_0^\infty f(t)e^{-j\omega t}dt \tag{36}$$

is called the *single-sided Fourier transform.* Taking the Fourier transform of the perturbation signal and that of the resulting signal allows determination of the transfer function, for example, the system ac impedance may be obtained from

$$Z(j\omega) = \frac{F[E(t)]}{F[i(t)]} = \frac{E(j\omega)}{i(j\omega)} \tag{37}$$

where F denotes the Fourier transform. The fast Fourier transform provides a fast and efficient algorithm for computation of the Fourier transform.[48] The number of points acquired must be equal to 2^k, where k is an integer.

Certain properties of the FFT technique influence the results.[28,48–50] First the Fourier transform defined by Eq. (36) involves integration to infinity. In practice only data of limited length are transformed, causing broadening of the computed frequency spectrum. This problem is known as *leakage.* It may be minimized by increasing the data record acquired in the time domain. However, it will disappear when the acquisition time is exactly equal to an integer multiple of the wave repetition period. That is, if the data acquisition is terminated at times other than the multiple of the wave period, sharp discontinuities of the signal are introduced (because there is no continuity between the last and the first point of the signal), which causes frequency peak broadening; that is, a distribution of frequencies is obtained instead of discrete values. Therefore, synchronization of the sampling time with the wave period is necessary.

Another problem called *aliasing* is connected with the presence of frequencies larger than half of the time domain sampling frequency. This problem may be easily eliminated by ensuring that the sampling frequency is greater than (or at least equal to) twice the highest frequency present in the measured signal. In some cases the highest frequencies may be filtered out by a low-pass filter. This minimum sampling frequency, which is necessary to get information about the existing signal, is called the *Nyquist sampling rate.*

In general, the perturbing signal may have an arbitrary form. However, in practice, the most often used perturbation signals are[50–52] (1) pulse, (2) noise, and (3) sum of sine waves.

(i) Pulse Perturbation

The Fourier transform of an infinite short pulse function: $h(t) = K\delta(t)$, where $\delta(t)$ is Dirac's delta function, equals $H(j\omega) = K$, that is, it contains all the frequencies with the same amplitude K. Such a function cannot be realized in practice and must be substituted by a pulse of a short duration Δt. However, such a function does not have uniform response in the Fourier (i.e., frequency) space. The Fourier transform of such a function, defined as: $h(t) = 1$ for $t = 0$ to T_0 and $h(t) = 0$ elsewhere, equals

$$H(j\omega) = \int_0^\infty h(t)e^{-j\omega t}dt = \int_0^{T_0} e^{-j\omega t}dt = \frac{1 - e^{-j\omega T_0}}{j\omega} \tag{38}$$

Figure 8 presents a graph of the amplitude of $|H(j\omega)|$ as a function of frequency. It is obvious that the amplitude of the higher frequency signals is attenuated. Therefore, only a limited frequency range may be studied because the higher frequency response is too small. It was shown[50,51] that even low-level noise significantly disturbs the impedance spectra obtained.

(ii) Noise Perturbation

White noise, that is, noise consisting of a continuous spectrum of frequencies (or a computer-generated pseudo-random white noise), may be used as a perturbation signal in practical impedance measurements.[50,51] However, single-frequency components obtained by the FFT have relatively low amplitudes and a long data acquisition time is necessary to

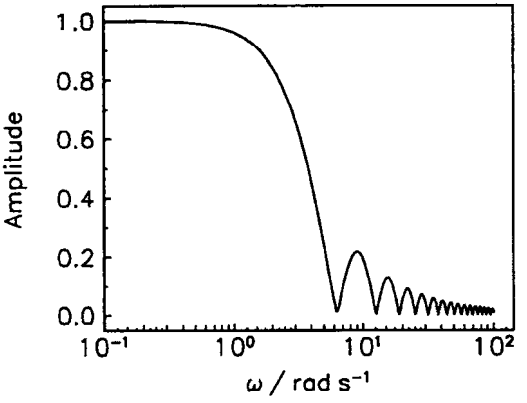

Figure 8. FFT amplitude, $|H(j\omega)|$, of the pulse function [Eq. (38)] of duration $T_0 = 1$ s.

obtain reliable results.[50,51] Even low noise contamination of the measured signal leads to significantly disturbed impedance spectra.

(iii) Sum of Sine Waves

This technique was introduced and used extensively by D. E. Smith and co-workers.[49,50,53,54] In it, the perturbation signal is composed of a sum of selected sinusoids. The applied signal consists of a fundamental harmonic frequency f_0 and a number of odd harmonics $(2n + 1)f_0$. This arrangement is superior to other perturbation wave forms.[50] All these frequencies are applied at the same time and the response to each frequency is found by the FFT. Smith and co-workers used this technique to study electrode kinetics in the frequency range 10 to 500 Hz. It should be mentioned that the technique is used in low-frequency impedance analysis (below 10 Hz) in PAR 273 series potentiostats (software implemented).

Popkirov and Schindler[51] have demonstrated that the measured results may be improved by the appropriate selection of phases and amplitudes of the individual sinusoidal components. First, signal phases may be optimized to minimize the observed peak-to-peak signal amplitude. This also allows the amplitudes of the individual components to be increased by over 30%, maintaining the total amplitude at its initial level and thus increasing the power of the single-frequency components. A decrease in the standard deviation of the impedance by 25% was obtained

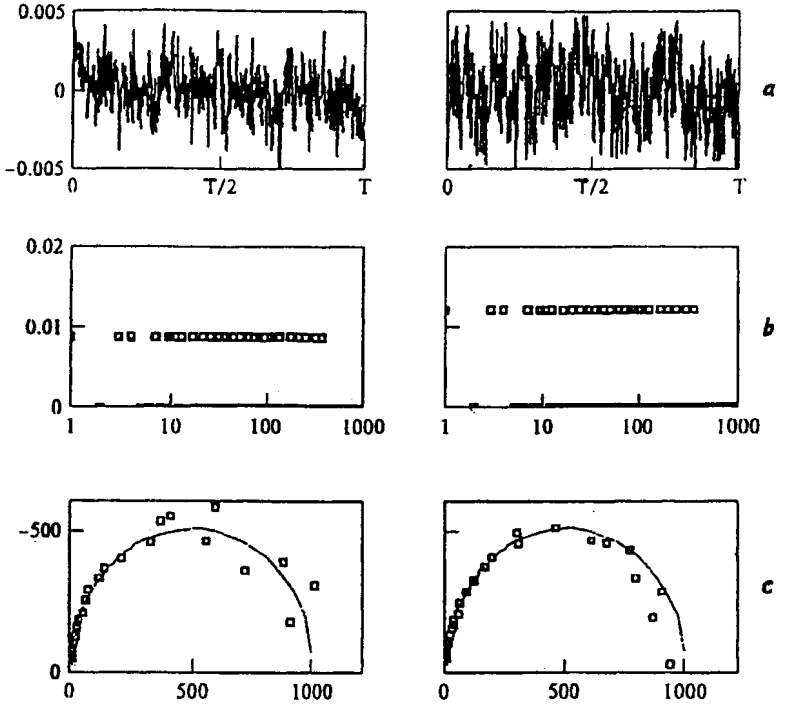

Figure 9. FFT analysis of the sum of sine wave perturbation; left side, no optimization; right side, optimization of phases. (a) Perturbation voltage in the time domain. (b) Perturbation voltage in the frequency domain. (c) Complex plane plots of simulated impedance spectra with 5% noise added to the current response. Solid lines show response without noise.[51]

in that way. The results of such optimization are shown in Fig. 9. An additional possibility is an optimization of the amplitudes. It is known that the response of electrochemical cells is different for different frequencies so that the response is weaker in the low-frequency range and larger at high frequencies. In addition, higher noise is observed at low frequencies (for the same perturbation amplitude). When the amplitudes of different frequencies are optimized, that is, they are selected in such a way that the response remains nearly constant, the response signal is much less sensitive to noise. An example of such optimization is displayed in Fig. 10.

The main advantage of the FFT technique is that the information is obtained quickly; therefore it may be used to study impedances evolving

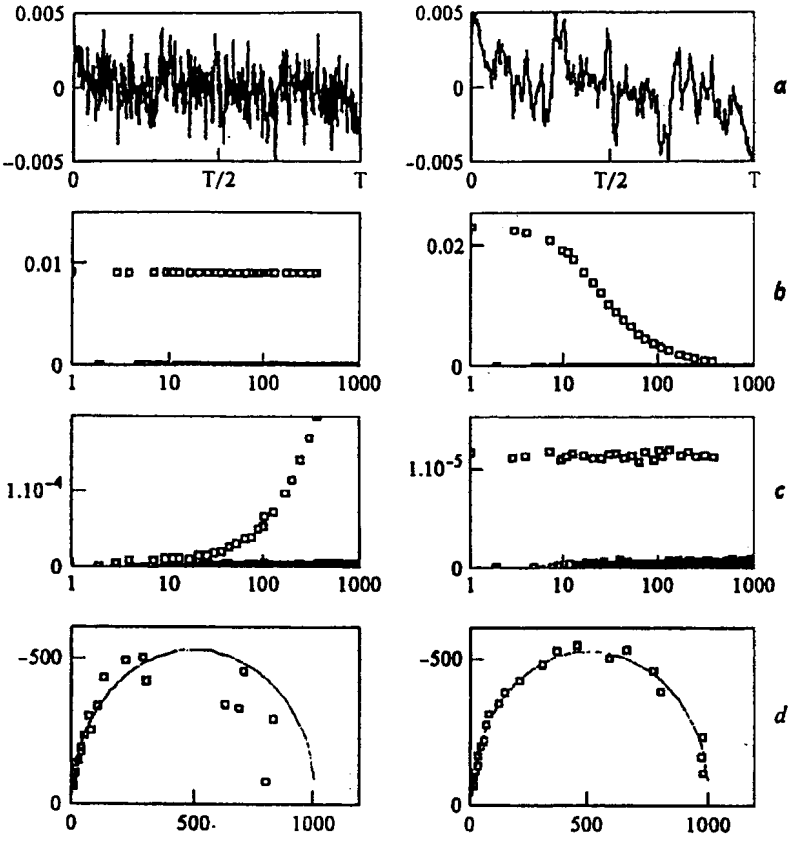

Figure 10. FFT analysis of the sum of sine wave perturbation; left side, no optimization; right side, optimization of amplitudes. (a) Perturbation voltage in the time domain. (b) Perturbation voltage in the frequency domain. (c) Current response with 10% noise added, presented in frequency domain. (d) Complex plane plots of simulated impedance spectra with 10% noise added to the current response. Solid lines show response without noise.[51]

with time (of course, the impedance must be considered constant during the time of measurement). The limitation of the FFT technique is that the response to individual frequencies is usually weaker than that when only one frequency is used. It should be added that other types of analysis of system responses were also used, for example, Laplace transform of the applied perturbation and the response to determine the impedance spectra.[28,55–61]

III. IMPEDANCE OF FARADAIC REACTIONS IN THE PRESENCE OF DIFFUSION

Total electrode impedance consists of the contributions of the electrolyte, the electrode solution interface, and the electrochemical reactions taking place on the electrode. First, we consider the case of an ideally polarizable electrode, followed by semi-infinite diffusion in linear, spherical, and cylindrical geometry and, finally a finite-length diffusion.

1. The Ideally Polarizable Electrode

An ideally polarizable electrode behaves as an ideal capacitor because there is no charge transfer across the solution/electrode boundary. In this case, the equivalent electrical model consists of the solution resistance, R_s, in series with the double-layer capacitance, C_{dl}. An analysis of such a circuit was presented in Section I.2(i).

2. Semi-Infinite Linear Diffusion

In general, it is possible to write the expression for the impedance for any mechanism. The procedure shown below is general and may be applied to other processes involving diffusion. For the reaction:

$$\mathrm{Ox} + ne \rightleftharpoons \mathrm{Red} \tag{39}$$

the current is described by

$$i = nF[k_f C_O(0) - k_b C_R(0)] \tag{40}$$

where k_f and k_b are the potential-dependent rate constants for the forward and backward reactions: $k_f = k_o \exp[-\alpha nf(E - E^0)]$ and $k_b = k_o \exp[(1 - \alpha)nf(E - E^0)]$, k_o and E^0 are the standard rate constant and standard potential, respectively, $C_O(0)$ and $C_R(0)$ are the surface concentrations of the forms Ox and Red, α is the transfer coefficient, n is the number of electrons, and $f = F/RT$. When a small av perturbation signal, $\Delta E = E_0 \exp(j\omega t)$, is applied, the current and concentrations oscillate around steady-state values: $i = i_{dc} + \Delta i$, $C_O = C_{O,dc} + \Delta C_O$, and $C_R = C_{R,dc} + \Delta C_R$, where the subscript *dc* indicates a parameter that changes only slowly with time (i.e., either a steady-state term or one that does not change with ω or its harmonics), and the symbol Δ indicates a parameter oscillat-

ing periodically with time. In general, the oscillating potential and the concentrations may be written as

$$\Delta E = \tilde{E}\exp(j\omega t),\ \Delta i = \tilde{\imath}\exp(j\omega t)\ \Delta C_{\mathrm{O}} = \tilde{C}_{\mathrm{O}}\exp(j\omega t)\ \text{and}\ \Delta C_{\mathrm{R}} = \tilde{C}_{\mathrm{R}}\exp(j\omega t) \tag{41}$$

where $\tilde{E}$, $\tilde{\imath}$, $\tilde{C}_{\mathrm{O}}$, and $\tilde{C}_{\mathrm{R}}$ are the phasors of the voltage, current, and concentrations. Because we are interested in the ac components of these parameters, we can solve equations for ΔE, Δi, ΔC_{O} and ΔC_{R} only. In general, the current is a function of the potential and concentrations [Eq. (40)], and it may be represented as an infinite Taylor series:

$$\begin{aligned}\Delta i = {} & \left(\frac{\partial i}{\partial E}\right)\Delta E + \left(\frac{\partial i}{\partial C_{\mathrm{O}}}\right)\Delta C_{\mathrm{O}} + \left(\frac{\partial i}{\partial C_{\mathrm{R}}}\right)\Delta C_{\mathrm{R}} \\ & + \frac{1}{2}\left(\frac{\partial^2 i}{\partial E^2}\right)(\Delta E)^2 + \frac{1}{2}\left(\frac{\partial^2 i}{\partial C_{\mathrm{O}}^2}\right)(\Delta C_{\mathrm{O}})^2 + \frac{1}{2}\left(\frac{\partial^2 i}{\partial C_{\mathrm{R}}^2}\right)(\Delta C_{\mathrm{R}})^2 \\ & + \left(\frac{\partial^2 i}{\partial E \partial C_{\mathrm{O}}}\right)\Delta E\Delta C_{\mathrm{O}} + \left(\frac{\partial^2 i}{\partial E \partial C_{\mathrm{R}}}\right)\Delta E\Delta C_{\mathrm{R}} + \left(\frac{\partial^2 i}{\partial C_{\mathrm{O}} \partial C_{\mathrm{R}}}\right)\Delta C_{\mathrm{O}}\Delta C_{\mathrm{R}} + \ldots\end{aligned} \tag{42}$$

It can be seen that because Eq. (40) is linear with respect to the concentrations, only first-order derivatives versus concentrations are different from 0. For small perturbations, it is a good approximation to keep only the linear terms. This *linearization is a fundamental property* of EIS; therefore the amplitudes applied must be small, $\Delta E < 8/n$ mV [6] peak-to-peak, where n is the number of electrons exchanged in the reaction. Analysis of higher harmonics has also been described.[6,7,27,62] The derivatives in Eq. (42) correspond to stationary conditions and may be obtained from Eq. (40):

$$\frac{\partial i}{\partial E} = -n^2 F f\left[\alpha k_f C_{\mathrm{O}}(0) + (1-\alpha)k_b C_{\mathrm{R}}(0)\right] \tag{43}$$

$$\frac{\partial i}{\partial C_{\mathrm{O}}} = nFk_f \ \text{and}\ \frac{\partial i}{\partial C_{\mathrm{R}}} = -nFk_b \tag{44}$$

In order to find concentrations, Fick's diffusion equation must be solved for ΔC. For semi-infinite linear diffusion, the following equations must be solved:

$$\frac{\partial \Delta C_O}{\partial t} = D_O \frac{\partial^2 \Delta C_O}{\partial x^2} \text{ and } \frac{\partial \Delta C_R}{\partial t} = D_R \frac{\partial^2 \Delta C_R}{\partial x^2} \tag{45}$$

Taking into account Eq. (41) and

$$\partial \Delta C_O / \partial t = j\omega \tilde{C}_O \exp(j\omega t) \tag{46}$$

Eq. (45) may be rearranged to

$$j\omega \tilde{C}_O = D_O \frac{d^2 \tilde{C}_O}{dx^2} \text{ and } j\omega \tilde{C}_R = D_R \frac{d^2 \tilde{C}_R}{dx^2} \tag{47}$$

with the boundary conditions

$$x = 0: \quad \frac{d\tilde{C}_O}{dx} = \frac{\tilde{i}}{nFD_O}, \quad \frac{d\tilde{C}_R}{dx} = -\frac{\tilde{i}}{nFD_R} \tag{48}$$

$$D_O \frac{d\tilde{C}_O}{dx} + D_R \frac{d\tilde{C}_R}{dx} = 0 \tag{49}$$

$$x \to \infty: \quad \tilde{C}_O \to 0 \text{ and } \tilde{C}_R \to 0 \tag{50}$$

where, at $x \to \infty$, only a dc concentration gradient exists. After further rearrangements one obtains

$$\frac{d^2 \tilde{C}_O}{dx^2} = \left(\frac{j\omega}{D_O}\right) \tilde{C}_O = s_O^2 \, \tilde{C}_O \text{ and } \frac{d^2 \tilde{C}_R}{dx^2} = \left(\frac{j\omega}{D_R}\right) \tilde{C}_R = s_R^2 \, \tilde{C}_R \tag{51}$$

which have the following solutions:

$$\tilde{C}_O(x) = A \exp(-s_O x) + B \exp(s_O x) \text{ and } \tilde{C}_R(x) = A' \exp(-s_R x) + B' \exp(s_R x) \tag{52}$$

For semi-infinite diffusion B and B' are both equal to 0, to fulfill condition (50). In order to determine the constants A and A', the condition at $x = 0$ must be considered:

$$\frac{d\tilde{C}_O}{dx} = -s_O A = \frac{\tilde{i}}{nFD_O} \tag{53}$$

and substituting s_O and s_R [Eq.(50)], one gets

$$A = \tilde{C}_O(0) = -\frac{\tilde{i}}{nF\sqrt{j\omega D_O}} \text{ and } A' = \tilde{C}_R(0) = \frac{\tilde{i}}{nF\sqrt{j\omega D_R}} \tag{54}$$

Now it is possible to make the substitutions into Eq. (42), conserving only linear terms:

$$\tilde{i} = -\frac{n^2F^2}{RT}\left[\alpha k_f C_O(0) + (1-\alpha)k_b C_R(0)\right]\tilde{E} - \frac{\tilde{i}k_f}{\sqrt{j\omega D_O}} - \frac{\tilde{i}k_b}{\sqrt{j\omega D_R}} \tag{55}$$

and the faradaic impedance equals $\hat{Z}_f = -\tilde{E}/\tilde{i}$ (the negative sign arises from the assumed convention in which the cathodic current is positive):

$$\hat{Z}_f = \frac{RT}{n^2F^2}\frac{1 + \dfrac{k_f}{\sqrt{j\omega D_O}} + \dfrac{k_b}{\sqrt{j\omega D_R}}}{\alpha k_f C_O(0) + (1-\alpha)k_b C_R(0)} \tag{56}$$

The total faradaic impedance, $\hat{Z}_f$, consists of three terms: The first one comes from the derivative $\partial i/\partial E$ and is called the *charge-transfer resistance,* R_{ct}; the two others, which are contributions from $\partial i/\partial C_i$, are called *impedances of mass transfer*[63–66] $\hat{Z}_W$; in the case of semi-infinite diffusion it is called a semi-infinite Warburg impedance.

$$\hat{Z}_f = R_{ct} + \hat{Z}_W = R_{ct} + \hat{Z}_{W,O} + \hat{Z}_{W,R} \tag{57}$$

$$R_{ct} = \frac{RT}{n^2F^2}\frac{1}{\alpha k_f C_O(0) + (1-\alpha)k_b C_R(0)} \tag{58}$$

$$\hat{Z}_{W,O} = \frac{RT}{n^2F^2}\frac{k_f}{\sqrt{j\omega D_O}\left[\alpha k_f C_O(0) + (1-\alpha)k_b C_R(0)\right]} \tag{59}$$

$$= \frac{RT}{n^2F^2}\frac{1}{\sqrt{j\omega D_O}\left\{\alpha C_O(0) + (1-\alpha)C_R(0)\exp[nf(E-E^0)]\right\}}$$

$$\hat{Z}_{W,R} = \frac{RT}{n^2F^2}\frac{\exp[nf(E-E^0)]}{\sqrt{j\omega D_R}\left\{\alpha C_O(0) + (1-\alpha)C_R(0)\exp[nf(E-E^0)]\right\}} \tag{60}$$

Assuming that the process is dc reversible, the surface concentrations are described by the Nernst equation: $C_O(0)/C_R(0) = \exp[nf(E-E^0)]$ and Eqs. (59) and (60) may be written as

$$\hat{Z}_W = \hat{Z}_{W,O} + \hat{Z}_{W,R} = \frac{RT}{n^2F^2\sqrt{j\omega}}\left(\frac{1}{\sqrt{D_O}\,C_O(0)} + \frac{1}{\sqrt{D_R}\,C_R(0)}\right) = \frac{\sqrt{2}}{\sqrt{j}}\frac{\sigma}{\sqrt{\omega}} \tag{61}$$

where σ is the mass-transfer coefficient equal to the sum of the contributions of the forms Ox and Red:

$$\sigma = \sigma_O + \sigma_R = \frac{RT}{n^2F^2\sqrt{2}}\left[\frac{1}{\sqrt{D_O}C_O(0)} + \frac{1}{\sqrt{D_R}C_R(0)}\right] \tag{62}$$

Because $1/\sqrt{j} = (1/\sqrt{2})(1-j)$, the mass-transfer impedance may be written as

$$\hat{Z}_W = \sigma\omega^{-1/2} - j\sigma\omega^{-1/2} \tag{63}$$

This equation may be also obtained directly by assuming that the charge-transfer reaction is reversible and calculating the mass-transfer impedance from

$$\hat{Z}_W = \frac{dE}{di} = \sum_{i=O,R}\frac{dE}{dC_i}\frac{\tilde{C}_i}{\tilde{i}} \tag{64}$$

where, from the Nernst equation, one gets:

$$dE/dC_O = RT/nFC_O(0) \text{ and } dE/dC_R = -RT/nFC_R(0) \tag{65}$$

After substitution of Eq. (64) into (65), Eq. (63) is obtained as before. Assuming that only the oxidized form is initially inthe solution (C_O^*), the surface concentrations may be estimated from[11]

$$C_O(0) = C_O^*\frac{\xi\theta}{1+\xi\theta} \text{ and } C_R(0) = C_O^*\frac{\xi}{1+\xi\theta} \tag{66}$$

where $\xi = (D_O/D_R)^{1/2}$ and $\theta = \exp[nf(E - E^0)]$ and $\xi\theta = \exp[nf(E - E_{1/2})]$. Substituting Eq. (66) into (58) the charge-transfer resistance may be expressed as

$$R_{ct} = \frac{RT}{n^2F^2k_bC_O^*}\frac{1+\exp[nf(E-E_{1/2})]}{\xi} = \frac{RT}{n^2F^2k_0C_O^*}\frac{1+\exp[nf(E-E_{1/2})]}{\xi^\alpha\exp[(1-\alpha)nf(E-E_{1/2})]} \tag{67}$$

and it has a minimum at

$$E_s = E_{1/2} + \frac{RT}{nF}\ln\frac{\alpha}{1-\alpha} \tag{68}$$

For the processes for which the transfer coefficient, α, is equal to 0.5, the minimum of R_{ct} is observed at the half-wave potential. Similarly, the mass-transfer impedance equals

$$\hat{Z}_W = \frac{RT}{n^2F^2C_O^*\sqrt{j\omega D_O}} \frac{\left[1 + \exp[nf(E - E_{1/2})]\right]^2}{\exp[nf(E - E_{1/2})]}$$

$$= \frac{4RT}{n^2F^2C_O^*\sqrt{j\omega D_O}} \cosh^2\left[\frac{nf(E - E_{1/2})}{2}\right] \tag{69}$$

The Warburg impedance has a minimum at $E_{1/2}$. The mass-transfer impedance is a vector containing real and imaginary components that are identical, that is, the phase angle $\varphi = \text{atan}(Z''_W/Z'_W) = \text{atan}(-1) = -45°$. The faradaic impedance is shown in Fig. 11(b) (dashed line). On the complex plane plot, it is a straight line with a slope of 1 and intercept R_{ct}. The total electrode impedance consists of the solution resistance, R_s, in series with the parallel connection of the double-layer capacitance, C_{dl},

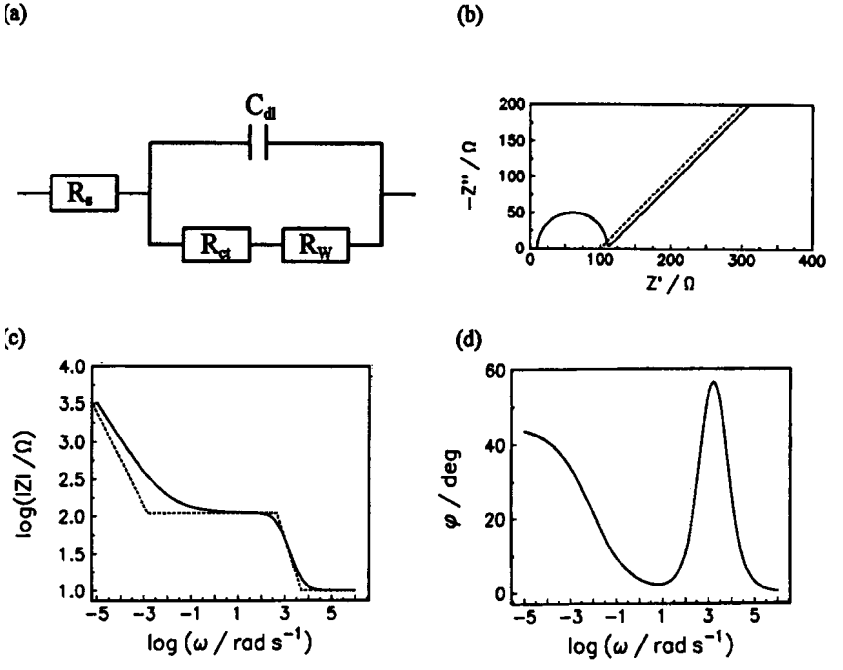

Figure 11. (a) Semi-infinite linear diffusion model, $R_s = 10\,\Omega$, $R_{ct} = 100\,\Omega$, $C_{dl} = 20\,\mu F$, $\sigma = 10\,\Omega\,s^{-1/2}$. (b) Complex plane and (c), (d) Bode plots for the model, continuous line, total impedance; dashed line in (b), faradaic impedance.

and faradaic impedance [Fig. 11(a)]. This is the Randles model.[64,65,67] Figure 11(b–d) also shows complex plane and Bode plots for the total electrode impedance in the presence of slow charge-transfer kinetics. It should be stressed that the Warburg impedance cannot be represented by a connection of simple R and C elements because of the noninteger power of frequency ($\omega^{-1/2}$) and it constitutes a distributed element that can only be approximated by an infinite series of simple electrical elements.

When the surface and bulk concentrations are the same, that is, when the mass-transfer impedance may be neglected, the equivalent circuit corresponds to that in Fig. 4. In this case a semicircle is observed on the complex plane plots. In the other limiting case, when the charge-transfer resistance is neglected (reversible case), a straight line with a slope of 1 is obtained on the complex plane.

The dependence of the mass-transfer and charge-transfer impedances on the electrode potential is displayed in Fig. 12. The charge-transfer and mass-transfer impedances have a minimum at E_s [Eq. (68)] and $E_{1/2}$, respectively, according to Eqs. (67) and (69).

A procedure for assessing nonlinearities in the Randles circuit,[64] based on nonlinear regression analysis, was described recently.[68]

VanderNoot69has studied poorly separated faradaic and diffusional processes. He has found that a complex, nonlinear, least-squares regression is capable of extracting kinetic information from impedance measurements when the ratio of the charge-transfer process time constant $t_f =$

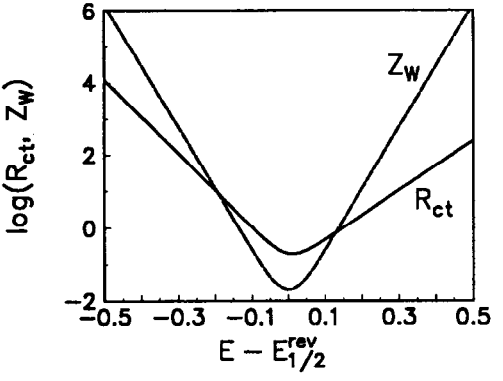

Figure 12. Dependence of logarithms of R_{ct} and $|Z_W|$ on potential for $\alpha = 0.4$.

$R_{ct}C_{dl}$ to the diffusion process time constant $t_d = R_{ct}^2/(2\sigma^2)$, $t_f/t_d = 2\sigma^2 C_{dl}/R_{ct}$, is lower than or equal to 30.

Armstrong and Firman[70] analyzed a mechanism that included two successive electron-transfer reactions. A general approach to multistep mechanisms involving soluble species in semi-infinite diffusion was presented recently by Harrington.[71] It allows determination of the number of breakpoint frequencies on the Bode magnitude plot for an arbitrary mechanism and, in consequence, for the determination of the reaction mechanism and kinetics.

3. Spherical Diffusion

This case arises, for example, when working with dropping or hanging mercury electrodes. Let us consider semi-infinite diffusion to a sphere of radius r_0 with both oxidized and reduced forms soluble in the solution. In this case Eq. (47) should be substituted by[13,14]

$$\frac{\partial \tilde{C}_O}{\partial t} = D_O\left(\frac{\partial^2 \tilde{C}_O}{\partial r^2} + \frac{2}{r}\frac{\partial \tilde{C}_O}{\partial r}\right) \text{ and } \frac{\partial \tilde{C}_R}{\partial t} = D_R\left(\frac{\partial^2 \tilde{C}_R}{\partial r^2} + \frac{2}{r}\frac{\partial \tilde{C}_R}{\partial r}\right) \tag{70}$$

These equations may be rearranged into a simpler form [Eq. (51)] substituting $\tilde{u} = r\tilde{C}_O$ and $\tilde{v} = r\tilde{C}_R$:

$$\frac{d^2\tilde{u}}{dx^2} = s_O^2\tilde{u} \text{ and } \frac{d^2\tilde{v}}{dx^2} = s_R^2\tilde{v} \tag{71}$$

The solution is

$$\tilde{u} = A\exp(-\sqrt{j\omega/D_O}\,r) \text{ and } \tilde{v} = A\exp(-\sqrt{j\omega/D_R}\,r) \tag{72}$$

Taking into account that $d\tilde{u}/dr = \tilde{C}_O + rd\tilde{C}_R/dr$ and that at $r = r_0$ (at the electrode surface), $d\tilde{C}_O/dr = \tilde{\imath}/nFD_O$, the following solutions are obtained:

$$\tilde{C}_O(0) = -\frac{\tilde{\imath}r_0}{nFD_O(1 + r_0\sqrt{j\omega/D_O})} \text{ and } \tilde{C}_R(0) = -\frac{\tilde{\imath}r_0}{nFD_R(1 + r_0\sqrt{j\omega/D_R})} \tag{73}$$

The mass-transfer impedance may be obtained from Eq. (64). Assuming a reversible dc process, one obtains, similar to the case of linear diffusion:

$$\hat{Z}_W = \sum_{i=O,R} \frac{RT}{n^2F^2D_iC_i(0)} \frac{r_0}{\left(1 + r_0\sqrt{\frac{j\omega}{D_i}}\right)} \tag{74}$$

or

$$\hat{Z}_W = \sum_{i=O,R} \sigma_i\omega^{-1/2} \frac{1 + y_i - j}{1 + y_i + 0.5y_i^2} \tag{75}$$

where

$$y_i = \frac{1}{r_0}\sqrt{\frac{2D_i}{\omega}} \tag{76}$$

The influence of the nonlinearity of diffusion on the observed complex plane plots is shown in Fig. 13. Spherical mass transfer causes the formation of a depressed semicircle at low frequencies instead of the linear behavior observed for linear semi-infinite diffusion. For very small electrodes (ultramicroelectrodes) or low frequencies, the mass-transfer impedances become negligible and the dc current becomes stationary. On the Bode phase-angle graph, a maximum is observed at low frequencies.

4. Cylindrical Electrodes

An example of cylindrical diffusion is diffusion toward a conducting wire. Solutions for cylindrical electrodes have been given by Fleischmann *et al.*[72,73] and Jacobsen and West.[74] The methods presented by both groups give the same results; however, the latter is simpler. In this case the diffusion equation is similar to that for spherical diffusion [Eq. (70)]. The solution is shown here for the oxidized form only:

$$\frac{\partial\tilde{C}_O}{\partial t} = D_O\left(\frac{\partial^2\tilde{C}_O}{\partial r^2} + \frac{1}{r}\frac{\partial\tilde{C}_O}{\partial r}\right) \tag{77}$$

Rearrangement for the oscillating concentration, using Eq. (46), leads to

$$\frac{d^2\tilde{C}_O}{dr^2} + \frac{1}{r}\frac{d\tilde{C}_O}{dr} - \left(\frac{j\omega}{D_O}\right)\tilde{C}_O = 0 \tag{78}$$

Substitution of $z = r(j\omega/D_O)^{1/2}$ gives

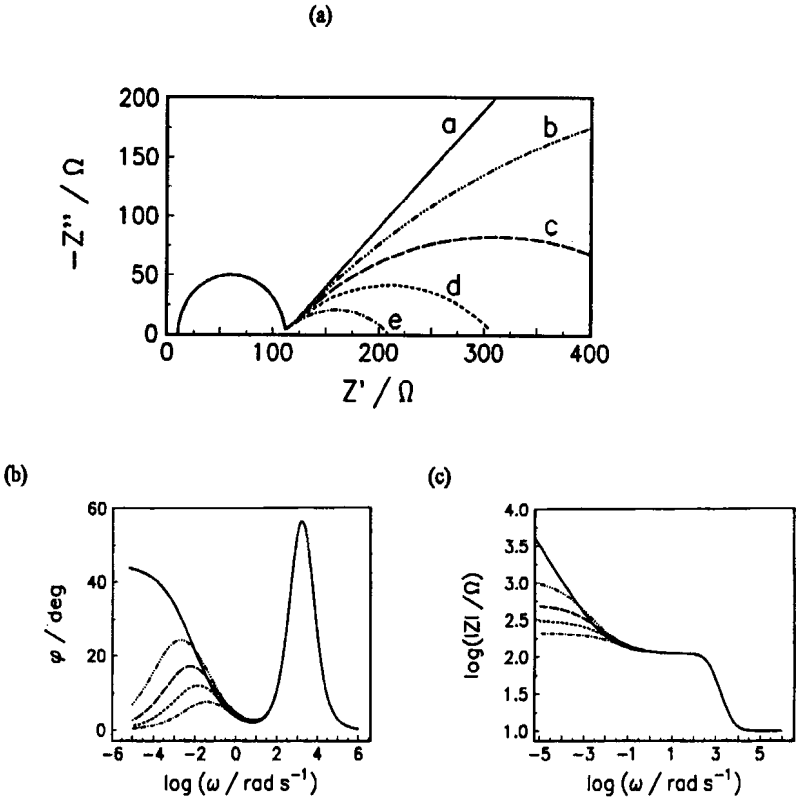

Figure 13. Complex plane (a) and Bode (b), (c) plots for semi-infinite spherical diffusion; sphericity parameter $\sqrt{2D_i}/r_0$: (a) ∞ linear diffusion, (b) 0.02, (c) 0.05, (d) 0.1, (e) 0.2 $s^{-1/2}$; $R_s = 10\ \Omega$, $R_{ct} = 100\ \Omega$.

$$\frac{d^2 \tilde{C}_O}{dz^2} + \frac{1}{z}\frac{d \tilde{C}_O}{dz} - \tilde{C}_O = 0 \tag{79}$$

This is a modified Bessel equation of zero order with the general solution[74]

$$\tilde{C}_O = AI_0[z] + BK_0[z] \tag{80}$$

where A and B are constants and I_0 and K_0 are zero-order modified Bessel functions. Taking into account semi-infinite diffusion conditions, that is $\tilde{C}_0 \to 0$ when $r \to \infty$, leads to $A = 0$. At the electrode surface, $r = r^0$:

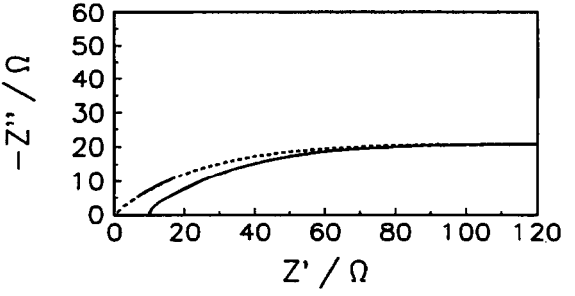

Figure 14. Faradaic (dashed line) and total (continuous line) impedance for a reversible reaction under conditions of semi-infinite cylindrical diffusion. $R_s = 10\ \Omega$.

$$\frac{d\,\tilde{C}_O}{dr} = \sqrt{\frac{j\omega}{D_O}}\,BK_1[z_0] = \frac{\tilde{\imath}}{nFD_O} \tag{81}$$

where $z_0 = r_0(j\omega/D_O)^{1/2}$ and

$$B = \frac{\tilde{\imath}}{nF\sqrt{j\omega D_O}K_1[z_0]} \tag{82}$$

Then, using Eq. (64) one may get

$$\hat{Z}_W = \frac{dE}{dC_O}\frac{\tilde{C}_O}{\tilde{\imath}} = \frac{RT}{n^2F^2D_OC_O^*}\frac{r_0K_0[z_0]}{z_0K_1[z_0]} \tag{83}$$

The function in Eq. (83) may be evaluated using Mathematica, Maple, or specific subroutines for complex modified Bessel functions. The corresponding complex plane plots are shown in Fig. 14. At low frequencies, cylindrical diffusion produces a constant imaginary impedance component.

5. Disk Electrodes

The solution for disk electrodes was presented by Fleischmann et al.[72,73] In this case the differential equation corresponds to diffusion normal and radial (two-dimensional) to the electrode. They obtained the following equations describing the faradaic impedance in the case of a slow charge transfer when only Ox is initially present in the solution, its concentration being C_O^*:

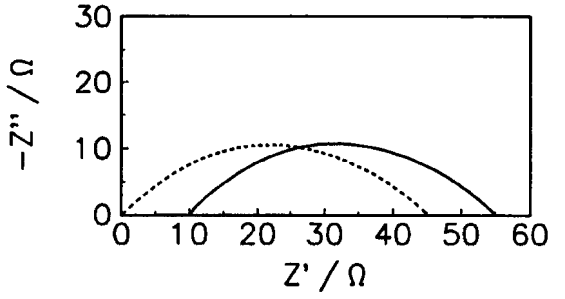

Figure 15. Faradaic (dashed line) and total (continuous line) impedances under conditions of diffusion to a disk and a reversible charge transfer.

$$Z'_f = R_{ct} + \frac{4RT}{n^2F^2D_O^{1/2}\omega^{1/2}C_O^*}\int_0^\infty \left[J_1\left(\beta\frac{a}{l}\right)\right]^2 \frac{\cos(\Theta/2)d\beta}{\beta(1+\beta^4)^{1/4}} \tag{84}$$

$$Z''_f = \frac{4RT}{n^2F^2D_O^{1/2}\omega^{1/2}C_O^*}\int_0^\infty \left[J_1\left(\beta\frac{a}{l}\right)\right]^2 \frac{\sin(\Theta/2)d\beta}{\beta(1+\beta^4)^{1/4}} \tag{85}$$

where a is the disk radius, J_1 is the Bessel function of the first kind and first order, $l^2 = D/\omega$, and $\tan\Theta = 1/\beta^2$. The first term in Z'_f corresponds to the charge-transfer resistance. The integrals in Eqs. (84)–(85) were given in Ref. 73 as the functions Φ_4 and Φ_5 of $(a^2\omega/D)$ and in a different form in Ref. 72. At sufficiently high frequencies, the results are similar to those for linear diffusion whereas at low frequencies, the impedance becomes real as for spherical electrodes. The complex plane plots for diffusion to a disk shown in Fig. 15 exhibit a flattened semicircle. Fleischmann and Pons [72,73,75] also considered diffusion to microring electrodes.

6. Finite-Length Diffusion

In many cases the diffusion is not semi-infinite. This case, for example, is observed for polymer electrodes, for a thin mercury layer deposited on surfaces, and for rotating disk electrodes. In such cases, in Eq. (52) parameters B and B' are not equal to 0. Two cases may be distinguished for finite-length diffusion, depending on the condition at the boundary located at a distance l from the electrode:

1. Transfer of electroactive species is possible at $x = l$, and $C(l) = 0$, but $dC(l)/dx \neq 0$. This is the conducting or transmissive boundary. It is observed, for example, in a rotating disk electrode, where the diffusion layer thickness is determined by the rotation rate.
2. No charge transfer is possible at $x = l$, that is, $dC(l)/dx = 0$. This is the reflecting boundary, observed in conducting polymers.

(i) Transmissive Boundary

In order to determine the constants A, B, A', and B' in Eq. (52), boundary conditions must be used. The concentration gradients at the electrode surface are

$$x = 0: \left.\frac{d\tilde{C}_O}{dx}\right|_{x=0} = -s_O A + s_O B = \frac{\tilde{\imath}}{nFD_O} \text{ and } \left.\frac{d\tilde{C}_R}{dx}\right|_{x=0} = -s_R A' + s_R B' = -\frac{\tilde{\imath}}{nFD_R} \tag{86}$$

$$x = l: \tilde{C}_O = A\exp(-s_O l) + B\exp(s_O l) = 0 \text{ and } \tilde{C}_R = A'\exp(-s_R l) + B'\exp(s_R l) = 0 \tag{87}$$

which leads to

$$A = -\frac{\tilde{\imath}}{nF\sqrt{j\omega D_O}}\frac{\exp(s_O l)}{\exp(s_O l) + \exp(-s_O l)} \text{ and } B = \frac{\tilde{\imath}}{nF\sqrt{j\omega D_O}}\frac{\exp(-s_O l)}{\exp(s_O l) + \exp(-s_O l)} \tag{88}$$

$$A' = \frac{\tilde{\imath}}{nF\sqrt{j\omega D_R}}\frac{\exp(s_R l)}{\exp(s_R l) + \exp(-s_R l)} \text{ and } B' = -\frac{\tilde{\imath}}{nF\sqrt{j\omega D_R}}\frac{\exp(s_R l)}{\exp(s_R l) + \exp(-s_R l)} \tag{89}$$

The surface concentrations are

$$\tilde{C}_O(0) = -\frac{\tilde{\imath}}{nF\sqrt{j\omega D_O}}\tanh\left(\sqrt{\frac{j\omega}{D_O}}\,l\right) \text{ and } \tilde{C}_R(0) = \frac{\tilde{\imath}}{nF\sqrt{j\omega D_R}}\tanh\left(\sqrt{\frac{j\omega}{D_R}}\,l\right) \tag{90}$$

and substitution into Eq. (64) gives the mass-transfer impedances:

$$\hat{Z}_W = \frac{RT}{n^2F^2C_O(0)\sqrt{j\omega D_O}}\tanh\left(\sqrt{\frac{j\omega}{D_O}}\,l\right) + \frac{RT}{n^2F^2C_R(0)\sqrt{j\omega D_R}}\tanh\left(\sqrt{\frac{j\omega}{D_R}}\,l\right) \tag{91}$$

or, assuming that the diffusion coefficients of O and R are the same, this becomes

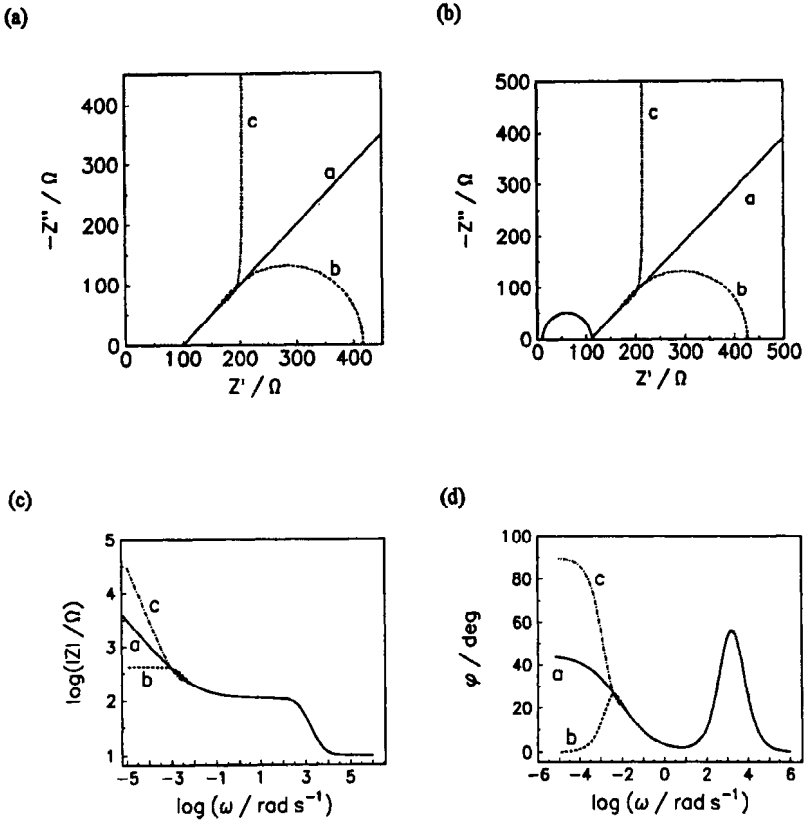

Figure 16. Faradaic (a) and total (b)–(d) impedances for: (a) linear semi-infinite, (b) finite transmissive, and (c) finite reflective boundaries. $R_s = 10\ \Omega$, $R_{ct} = 100\ \Omega$.

$$\hat{Z}_W = \frac{\sigma}{\sqrt{\omega}} \tanh\left(\sqrt{\frac{j\omega}{D}}\, l\right)(1-j) \tag{92}$$

The faradaic impedance is displayed in Fig. 16(a) and the total impedance in Fig. 16(b–d). At low frequencies the function $\tanh(x) \cong x$, and $\hat{Z}_W$ becomes real and frequency independent:

$$\hat{Z}_W(\omega \to 0) = \frac{\sqrt{2}\sigma l}{\sqrt{D}} \tag{93}$$

Therefore the low-frequency limit of the electrode impedance equals

$$\hat{Z} = R_s + R_{ct} + \frac{\sqrt{2}\sigma l}{\sqrt{D}} \tag{94}$$

(ii) Reflective Boundary

In this case the boundary conditions at $x = 0$ are the same as for Eq. (86) but at $x = l$ they are different, the concentration gradient being equal to 0:

$$\frac{d\tilde{C}_O}{dx} = -s_O A \exp(-s_O l) + s_O B \exp(s_O l) = 0 \tag{95}$$

and

$$\frac{d\tilde{C}_R}{dx} = -s_R A' \exp(-s_R l) + s_R B' \exp(s_R l) = 0 \tag{96}$$

They give

$$\tilde{C}_O(0) = -\frac{\tilde{\imath}}{nF\sqrt{j\omega D_O}} \coth\left(\sqrt{\frac{j\omega}{D_O}}\, l\right) \text{ and } \tilde{C}_R(0) = -\frac{\tilde{\imath}}{nF\sqrt{j\omega D_R}} \coth\left(\sqrt{\frac{j\omega}{D_R}}\, l\right) \tag{97}$$

and

$$\hat{Z}_W = \frac{RT}{n^2F^2C_O(0)\sqrt{j\omega D_O}} \coth\left(\sqrt{\frac{j\omega}{D_O}}\, l\right) + \frac{RT}{n^2F^2C_R(0)\sqrt{j\omega D_R}} \coth\left(\sqrt{\frac{j\omega}{D_R}}\, l\right) \tag{98}$$

or assuming equal diffusion coefficients:

$$\hat{Z}_W = \frac{\sigma}{\sqrt{\omega}} \coth\left(\sqrt{\frac{j\omega}{D}}\, l\right)(1 - j) \tag{99}$$

The corresponding faradaic and total electrode impedances are shown in Fig. 16. At low frequencies $\coth(x) \cong 1/x + x/3$ and $\hat{Z}_W$ becomes

$$\hat{Z}_W = \frac{\sqrt{2}\sigma l}{3\sqrt{D}} - j\frac{\sqrt{2D}\sigma}{\omega l} \tag{100}$$

The imaginary part of the impedance goes to infinity and the real part to a constant value, which indicates that no charge transfer occurs at low

frequencies and the electrode behavior is purely capacitive. For these conditions, the Warburg impedance corresponds to a series connection of the resistance $R_W = Z'_W$ and the capacitance $C_W = l/\sqrt{2D}\sigma$. The limiting value of the real part of the total cell impedance equals

$$Z'_t = R_s + R_{ct} + \sqrt{2}\sigma l/3\sqrt{D} \tag{101}$$

The problem of finite-length diffusion in spherical and cylindrical symmetry was solved by Jacobsen and West.[74]

7. Analysis of Impedance Data in the Case of Semi-Infinite Diffusion: Determination of Kinetic Parameters

In the case of a charge transfer to a diffusing species, ac voltammetry or ac polarography is usually used and the impedance curves are determined from a series of ac voltammetric curves registered at different frequencies. The methods of analysis of such curves are described in the following sections.

(i) Randles Analysis[64,65,67]

Experimentally measured ac current or total admittances are functions of the electrode potential. Figure 17 presents the dependence of the total admittances of a process limited by the diffusion of electroactive species to and from the electrode and the kinetics of the charge-transfer process, on the electrode potential. Information on the kinetics of the electrode process is included in the faradaic impedance. It may be simply

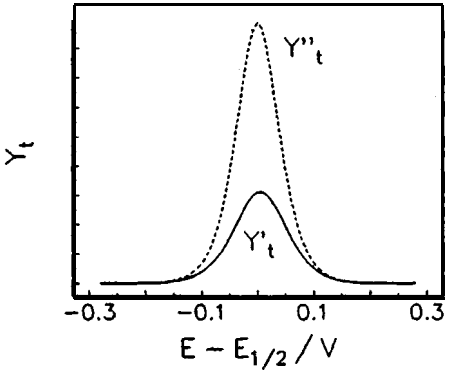

Figure 17. Dependence of real and imaginary admittances for a diffusion-kinetic process on the electrode potential.

determined from the total electrode impedance[64,65]:

$$\frac{1}{\hat{Z}_f} = \hat{Y}_f = \frac{1}{\hat{Z}_t - R_s} - j\omega C_{dl} \tag{102}$$

It should be kept in mind that to calculate the impedances from the admittances, the following equation must be used:

$$Z' = \frac{Y'}{(Y')^2 + (Y'')^2} \text{ and } Z'' = -\frac{Y''}{(Y')^2 + (Y'')^2} \tag{103}$$

The parameters R_s and C_{dl} must be determined in a separate experiment in a solution containing supporting electrolyte only, keeping the same distance between the working electrode and the tip of the Luggin capillary (i.e., to maintain R_s constant). This may be possible when this distance is large or the solution in the cell is exchanged without changing the electrode configuration. The other possibility is to extrapolate the admittance (or impedance) from the range where the faradaic impedance is negligible, that is, from potentials more positive and more negative than the peak potential. Then the real and imaginary components of the faradaic impedance are plotted against $\omega^{-1/2}$. They form two parallel lines with slopes of σ and intercepts of $Z'_f = R_{ct}$ and zero (Fig. 18). The dependence of R_{ct} on potential allows the determination of the standard rate constant and the transfer coefficient.

In order to eliminate the influence of the depolarizer concentration, one can also evaluate the ratio of the slope to the intercept of the Randles plot. Proper rearrangement leads to

$$\frac{\sigma}{R_{ct}} \frac{\exp[nf\frac{a}{b}[E - E_{1/2}]}{1 + \exp[nf[E - E_{1/2}]} = \frac{\xi k_b}{\sqrt{2D_O}} \tag{104}$$

from which the rate constant as a function of the electrode potential may be evaluated. At the reversible half-wave potential, this ratio gives directly the standard rate constant:

$$\left(\frac{\sigma}{R_{ct}}\right)_{E_{1/2}} = \frac{2\xi^{\alpha}}{\sqrt{2D_O}} k_0 \tag{105}$$

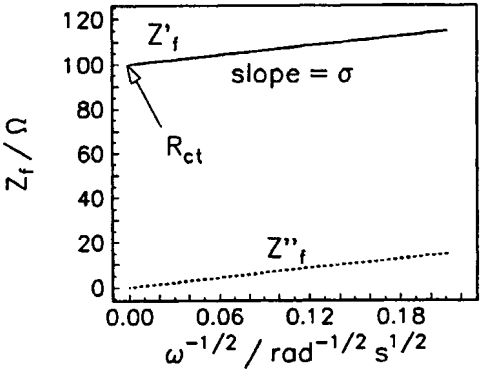

Figure 18. Dependence of real and imaginary parts of the faradaic impedance of a diffusion-kinetic process on $\omega^{-1/2}$ at a constant potential.

(ii) de Levie–Husovsky Analysis

de Levie and Husovsky[76] have proposed a method based on an analysis of faradaic admittances. The faradaic admittance may be easily determined from the total impedance:

$$\hat{Y}_f = \frac{1}{\hat{Z}_t - R_s} - j\omega C_{dl} \tag{106}$$

The ratio of the imaginary to real faradaic admittances equals

$$\frac{Y''_f}{Y'_f} = \frac{\zeta}{1-\zeta} \tag{107}$$

where

$$\zeta = \frac{k_f}{\sqrt{2\omega D_O}} + \frac{k_b}{\sqrt{2\omega D_R}} = \frac{k_f}{\sqrt{2\omega D_O}}\{1 + \exp[nf(E - E_{1/2})]\} \tag{108}$$

The forward rate constant is easily determined from the dependence of $\log[\zeta/\{1 + \exp[1 + nf(E - E_{1/2})]\}]$ versus E.

(iii) Analysis of cot φ

Another type of determination of kinetic parameters is based on the determination of the phase angle of the faradaic impedance. From Eqs. (57), (67), and (69), one may get:

$$\cot\varphi = \frac{Z_f'}{Z_f''} = 1 + \frac{R_{ct}}{\sigma}\omega^{1/2} \tag{109}$$

or after substitution:

$$\cot\varphi = 1 + \frac{\sqrt{2}D_O^{(1-\alpha)/2}D_R^{\alpha/2}\omega^{1/2}}{k_0 \exp[(1-\alpha)f(E-E_{1/2})]\{1+\exp[-nf(E-E_{1/2})]} \tag{110}$$

It is clear that cotφ depends linearly on $\omega^{1/2}$ and on electrode potential. It has a maximum at the potential E_s described by Eq. (58). The difference between the potential of the maximum of cotφ and $E_{1/2}$ allows estimation of the transfer coefficient α. The potential dependence of cotφ is shown in Fig. 19. The maximum value of cotφ is described by

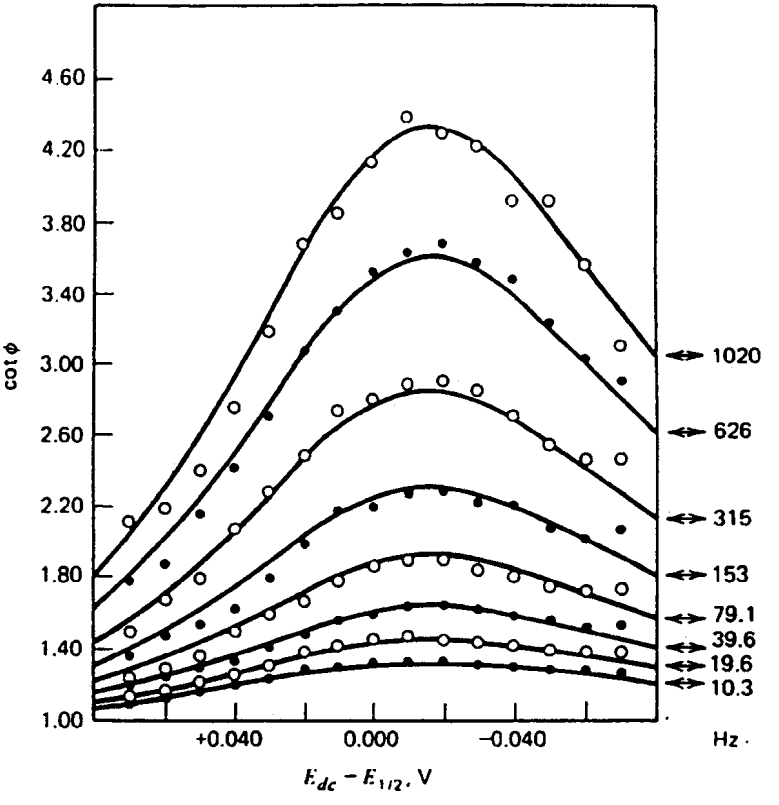

Figure 19. Dependence of cot φ as a function of potential for $TiCl_4$ reduction in an aqueous $H_2C_2O_4$ solution at various frequencies.[77]

$$[\cot\varphi]_{max} = 1 + \frac{\left(2D_O^{1-\alpha}D_R^{\alpha}\right)^{1/2}}{k_0\left[\left(\frac{\alpha}{\beta}\right)^{-\alpha} + \left(\frac{\alpha}{\beta}\right)^{\beta}\right]}\omega^{1/2} \tag{111}$$

while at the half-wave potential it is given by

$$[\cot\varphi]_{E_{1/2}} = 1 + \left(\frac{D_O^{1-\alpha}D_R^{\alpha}}{2}\right)^{1/2}\frac{\omega^{1/2}}{k_0} \tag{112}$$

Analysis of cotφ as a function of $\omega^{1/2}$, illustrated in Fig. 20, gives access to the standard rate constant k_0.

(iv) Sluyter's Analysis

Complex plane plots obtained in the case of a slow charge transfer with semi-infinite diffusion were presented in Fig. 11(a). They represent a semicircle (at high frequencies) followed by a straight line. General

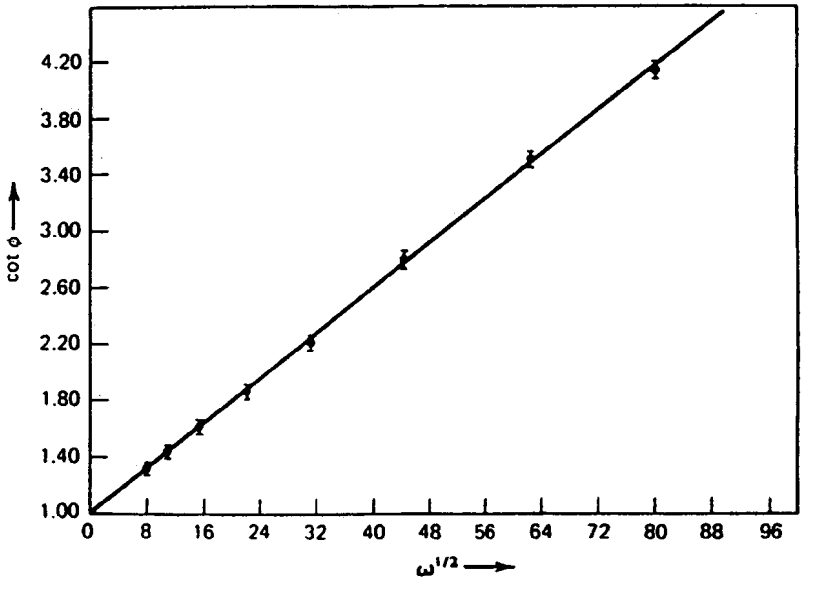

Figure 20. Dependence of cot ϕ vs. $\omega^{1/2}$ for $TiCl_4$ reduction in an aqueous $H_2C_2O_4$ solution. Data from Ref. 77.

equations describing total real and imaginary impedance were analyzed by Sluyters and co-workers.[26,27,78,79] The total electrode impedance is given as

$$\hat{Z}_t = R_s + \frac{1}{\frac{1}{\hat{Z}_f} + j\omega C_{dl}} \tag{113}$$

where the faradaic impedance is described by Eq. (57). This equation leads to rather complicated expressions for the real and imaginary parts of the total impedance:

$$Z' = R_s + \frac{R_{ct} + \sigma\omega^{-1/2}}{\left(\sigma\omega^{1/2}C_{dl} + 1\right)^2 + \omega^2 C_{dl}^2 \left(R_{ct} + \sigma\omega^{-1/2}\right)^2} \tag{114}$$

and

$$Z'' = \frac{\omega C_{dl}\left(R_{ct} + \sigma\omega^{-1/2}\right)^2 + \sigma^2 C_{dl} + \sigma\omega^{-1/2}}{\left(\sigma\omega^{1/2}C_{dl} + 1\right)^2 + \omega^2 C_{dl}^2 \left(R_{ct} + \sigma\omega^{-1/2}\right)^2} \tag{115}$$

A graphic illustration of these equations is presented in Fig. 11(b). Although, in simple cases, the process parameters may be obtained graphically, the best way to analyze the impedances is by the complex nonlinear least-squares approximation technique. The following parameters may be obtained from such fits: R_s, C_{dl}, R_{ct}, and the Warburg coefficient σ.

IV. IMPEDANCE OF A FARADAIC REACTION INVOLVING ADSORPTION OF REACTING SPECIES

In Section III, reactions of charge transfer to diffusing species in solution were considered. In this section, reactions involving adsorbed species in the absence of diffusion limitations will be presented. The latter condition means that the concentration gradient at the electrode surface is negligible, that is, the concentrations in solution are large enough and/or currents are low. Reactions involving one, two and more adsorbed species will be considered subsequently.

1. Faradaic Reaction Involving One Adsorbed Species

Let us consider the following reactions:

$$A_{sol} + e \underset{k_{-1}}{\overset{k_1}{\Leftrightarrow}} B_{ads} \tag{116}$$

$$B_{ads} + e \underset{k_{-2}}{\overset{k_2}{\Leftrightarrow}} C_{sol} \tag{117}$$

where the index sol denotes species in solution and ads an adsorbed species. The rates of these reactions may be written, assuming a Langmuir adsorption isotherm for B, as

$$v_1 = k_1^0 \Gamma_s a_A \exp[-\beta_1 f(E - E_1^0)] - k_1^0 \Gamma_B \exp[(1 - \beta_1) f(E - E_1^0)] \tag{118}$$

and

$$v_2 = k_2^0 \Gamma_B \exp[-\beta_2 f(E - E_2^0)] - k_2^0 \Gamma_s a_C \exp[(1 - \beta_2) f(E - E_2^0)] \tag{119}$$

where k_i^0 are the standard rate constants of these two reactions; β_i are the symmetry coefficients; Γ_A and Γ_S are the surface concentrations of the species A and of free adsorption sites, respectively; a_A and a_C are the surface concentrations of A and C (assumed as equal to the bulk concentrations); and E_i^0 are the standard Red-Ox potentials of these reactions. At the equilibrium potential, E_{eq}, the net rates of both reactions are null and the following relations are obtained:

$$\exp[f(E_{eq} - E_1^0)] = \Gamma_s^0 a_A / \Gamma_A^0 = (1 - \Theta_0) a_A / \Theta_0 \tag{120}$$

$$\exp[f(E_{eq} - E_2^0)] = \Gamma_B^0 / \Gamma_s^0 a_C = \Theta_0 / (1 - \Theta_0) a_C \tag{121}$$

where the index 0 indicates equilibrium conditions, and a relation between surface coverage, Θ, and surface concentration was introduced: $\Gamma_i = \Theta_i \Gamma_\infty$ and Γ_∞ is the maximal surface concentration. The introduction of Eqs. (120) and (121) into (118) and (119), and taking into account that $E - E_i^0 = E - E_{eq} + E_{eq} - E_i^0 = \eta + E_{eq} - E_i^0$, where η is the overpotential, gives

$$v_1 = k_1^0 \Gamma_\infty a_A^{1-\beta_1} (1 - \Theta_0)^{-\beta_1} \Theta_0^{\beta_1} (1 - \Theta) \exp(-\beta_1 f \eta)$$

$$
\begin{aligned}
&- k_1^0 \Gamma_\infty a_A^{1-\beta_1}(1-\Theta_0)^{1-\beta_1}\Theta_0^{-(1-\beta_1)}\Theta \exp[(1-\beta_1)f\eta] \\
&= k_1(1-\Theta)\exp(-\beta_1 f\eta) - k_{-1}\Theta \exp[(1-\beta_1)f\eta] \\
&= \vec{k}_1(1-\Theta) - \overleftarrow{k}_{-1}\Theta
\end{aligned}
\tag{122}
$$

and

$$
\begin{aligned}
v_2 &= k_2^0 \Gamma_\infty a_C^{\beta_2}(1-\Theta_0)^{\beta_2}\Theta_0^{-\beta_2}\Theta \exp(-\beta_2 f\eta) \\
&\quad - k_2^0 \Gamma_\infty a_C^{\beta_2}(1-\Theta_0)^{-(1-\beta_2)}\Theta_0^{1-\beta_2}(1-\Theta)\exp[(1-\beta_1)f\eta] \\
&= k_2\Theta \exp(-\beta_1 f\eta) - k_{-2}(1-\Theta)\exp[(1-\beta_1)f\eta] \\
&= \vec{k}_2\,\Theta - \overleftarrow{k}_{-2}(1-\Theta)
\end{aligned}
\tag{123}
$$

where the following new rate constants were introduced:

$$
k_1 = k_1^0 \Gamma_\infty a_A^{1-\beta_1}\left(\frac{\Theta_0}{1-\Theta_0}\right)^{\beta_1} \qquad k_{-1} = k_1^0 \Gamma_\infty a_A^{1-\beta_1}\left(\frac{1-\Theta_0}{\Theta_0}\right)^{1-\beta_1} \tag{124}
$$

$$
k_2 = k_2^0 \Gamma_\infty a_C^{\beta_2}\left(\frac{1-\Theta_0}{\Theta_0}\right)^{\beta_2} \qquad k_{-2} = k_2^0 \Gamma_\infty a_C^{\beta_2}\left(\frac{\Theta_0}{1-\Theta_0}\right)^{1-\beta_2} \tag{125}
$$

$$
\vec{k}_1 = k_1 \exp(-\beta_1 f\eta), \quad \overleftarrow{k}_{-1}\exp[(1-\beta_1)f\eta],
$$

$$
\vec{k}_2 = k_2 \exp(-\beta_2 f\eta), \quad \vec{k}_{-2} = k_{-2}\exp[(1-\beta_2)f\eta] \tag{126}
$$

The total observed current is

$$
i = F(v_1 + v_2) = Fr_0 \tag{127}
$$

At the equilibrium potential, the rates of reactions (116) and (117) are equal to 0, which implies an additional condition:

$$
\frac{k_1 k_2}{k_{-1}k_{-2}} = 1 \tag{128}
$$

that is, there are only three independent rate constants in the system. Under steady-state conditions, the rate of formation of the adsorbed species B is the same as the rate of their consumption, therefore

$$\frac{d\Gamma_B}{dt} = \Gamma_\infty \frac{d\Theta}{dt} = \frac{\sigma_1}{F}\frac{d\Theta}{dt} = r_1 = \nu_1 - \nu_2 = 0 \tag{129}$$

where $\sigma_1 = F\Gamma\infty$ is the charge necessary for the total surface coverage by B. In order to calculate the reaction faradaic impedance equations describing the current, $i(\eta, \Theta)$ [Eq. (127)] and the rate of formation of absorbed species r_1 (η, Θ) [Eq. (129)] should be linearized, giving:

$$\Delta i = \left(\frac{\partial i}{\partial \eta}\right)_\Theta \Delta\eta + \left(\frac{\partial i}{\partial \Theta}\right)_\eta \Delta\Theta = F\left[\left(\frac{\partial r_0}{\partial \eta}\right)_\Theta \Delta\eta + \left(\frac{\partial r_0}{\partial \Theta}\right)_\eta \Delta\Theta\right] \tag{130}$$

$$\frac{\sigma_1}{F}\frac{d\Delta\Theta}{dt} = \Delta r_1 = \left(\frac{\partial r_1}{\partial \eta}\right)_\Theta \Delta\eta + \left(\frac{\partial r_1}{\partial \Theta}\right)_\eta \Delta\Theta \tag{131}$$

A model containing higher-order term contributions in Eqs. (130)–(131) to fundamental harmonic impedances was recently discussed by Darowicki [80,81] and Diard *et al.*[82] Taking into account that (see Section III.2)

$$\Delta i = \tilde{\imath}\exp(j\omega t), \quad \Delta r_i = \tilde{r}_i \exp(j\omega t) \quad \Delta\eta = \tilde{\eta}\exp(j\omega t) \quad \text{and} \quad \Delta\Theta = \tilde{\Theta}\exp(j\omega t) \tag{132}$$

one obtains

$$\frac{\tilde{\imath}}{F} = \tilde{r}_0 = \left(\frac{\partial r_0}{\partial \eta}\right)_\Theta \tilde{\eta} + \left(\frac{\partial r_0}{\partial \Theta}\right)_\eta \tilde{\Theta} \tag{133}$$

and

$$\frac{\sigma_1}{F} j\omega \tilde{\Theta} = \left(\frac{\partial r_1}{\partial \eta}\right)_\Theta \tilde{\eta} + \left(\frac{\partial r_1}{\partial \Theta}\right)_\eta \tilde{\Theta} \tag{134}$$

Elimination of $\tilde{\Theta}$ from Eqs. (133)–(134) gives the faradaic admittance as

$$\hat{Y}_f = -\frac{\tilde{i}}{\tilde{\eta}} = -F\left(\frac{\partial r_0}{\partial \eta}\right)_\Theta - \frac{\dfrac{F^2}{\sigma_1}\left(\dfrac{\partial r_0}{\partial \Theta}\right)_\eta \left(\dfrac{\partial r_1}{\partial \eta}\right)_\Theta}{j\omega - \dfrac{F}{\sigma_1}\left(\dfrac{\partial r_1}{\partial \Theta}\right)_\eta} = A + \frac{B}{j\omega + C} \tag{135}$$

The first term in Eq. (135) is the inverse of the charge-transfer resistance: $A = 1/R_{ct}$. Knowing the faradaic impedance, the total electrode impedance, may be determined using Eq. (102). The derivatives in Eq. (135) may be easily evaluated from Eqs. (122), (123), (127), and) 129):

$$A = Ff\left\{\beta_1 \vec{k}_1(1-\Theta) + (1-\beta_1)\overleftarrow{k}_{-1}\Theta + \beta_2 \vec{k}_2\Theta + (1-\beta_2)\overleftarrow{k}_{-2}(1-\Theta)\right\} \tag{136}$$

$$B = \frac{F^2 f}{\sigma_1}\left(-\vec{k}_1 - \overleftarrow{k}_{-1} + \vec{k}_2 + \overleftarrow{k}_{-2}\right) \times \left\{\beta_1 \vec{k}_1(1-\Theta) + (1-\beta_1)\overleftarrow{k}_{-1}\Theta - \beta_2 \vec{k}_2\Theta - (1-\beta_2)\overleftarrow{k}_{-2}(1-\Theta)\right\} \tag{137}$$

and

$$C = \frac{F}{\sigma_1}\left(\vec{k}_1 + \overleftarrow{k}_{-1} + \vec{k}_2 + \overleftarrow{k}_{-2}\right) \tag{138}$$

It is evident that parameters A and C are always positive and that B may be positive or negative, depending on the values of the rate constants.

2. Impedance Plots in the Case of One Adsorbed Species

The faradaic admittance of reactions (116) and (117) is described by Eq. (135). Analysis of the complex plane plots in such a case was presented by Cao.[83] Bai and Conway[84] presented three-dimensional plots for such a reaction. Two general cases should be considered, depending on the sign of the parameter B:

1. $B < 0$

In this case the faradaic admittance may be written as

$$\hat{Y}_f = \frac{1}{R_{ct}} - \frac{|B|}{j\omega + C} \tag{139}$$

It changes from R_{ct}^{-1} at very high frequencies to $R_{ct}^{-1} - |B|/C$ at very low frequencies. The faradaic impedance is described as

$$\hat{Z}_f = \frac{1}{\hat{Y}_f} = R_{ct} + \frac{R_{ct}^2|B|}{j\omega + C - R_{ct}|B|}$$

$$= R_{ct} + \frac{R_a}{1 + j\omega R_a C_a} = R_{ct} + \frac{1}{\frac{1}{R_a} + j\omega C_a} \qquad (140)$$

where

$$R_a = \frac{R_{ct}^2|B|}{C - R_{ct}|B|} \quad \text{and} \quad C_a = \frac{1}{R_{ct}^2|B|} \qquad (141)$$

The limit of faradaic impedance at infinite frequency is also called the *transfer impedance,* R_t, while the limit at zero frequency is called the *polarization resistance,* R_p :

$$\lim_{\omega \to 0} (Z_f) = R_p \quad \text{and} \quad \lim_{\omega \to \infty} (Z_f) = R_t \qquad (142)$$

In our case $R_p = R_{ct} + R_{ct}^2 |B|/(C - R_{ct}|B|)$ and $R_t = R_{ct}$. Equation (140) represents a series connection of the charge-transfer resistance with a parallel connection of the resistance R_a and pseudo-capacitance C_a. The complete equivalent circuit in this case is shown in Fig. 21. The observed complex plane plots depend on the sign of the denominator of R_a.

la. $C - R_{ct}|B| > 0$

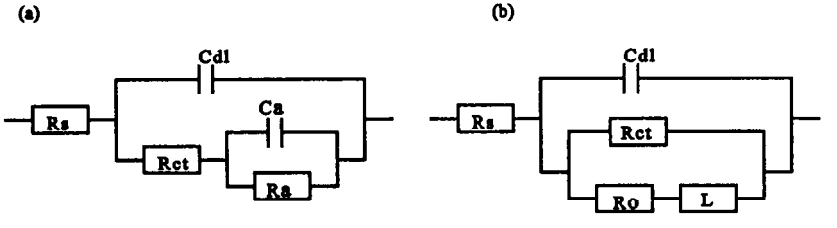

Figure 21. Equivalent circuit for the case of one adsorbed species: (a) for $B < 0$ and (b) B > 0.

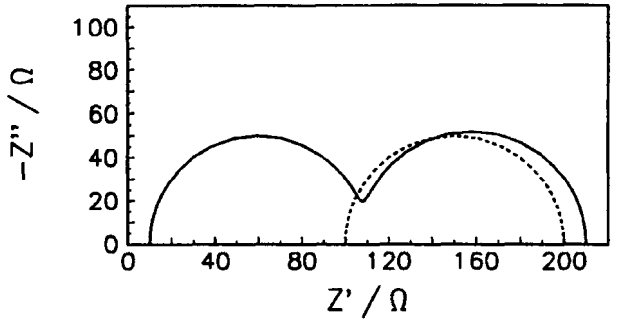

Figure 22. Complex plane plots for the case of one adsorbed species and $B < 0$ [Eqs. (139)–(140)]; continuous line, total impedance; dashed line, faradaic impedance. Parameters used: $R_{ct} = 100\ \Omega$, $R_a = 100\ \Omega$, $C_a = 2 \times 10^{-3}$ F, $C_{dl} = 2 \times 10^{-5}$ F, $R_s = 10\ \Omega$.

In this case all the elements are positive and the faradaic impedance represents one semicircle on the complex plane plots (see Fig. 22). When $C_a >> C_{dl}$, the total impedance represents two semicircles (Fig. 22). When $A >> |B|/C$ the faradaic impedance is equal to R_{ct}. The complex plane plots are analogous to those shown in Fig. 4 and represent one capacitive semicircle.

lb. $C - R_{ct}\,|B| = 0$

In this case the faradaic impedance is

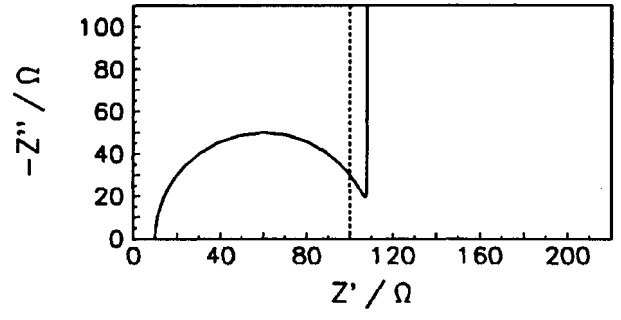

Figure 23. Complex plane plot for the case of one adsorbed species, $B < 0$ and $C - R_{ct}\,|B| = 0$; continuous line, total impedance; dashed line, faradaic impedance. Parameters used: $R_{ct} = 100\ \Omega$, $C_a = 2 \times 10^{-3}$ F, $C_{dl} = 2 \times 10^{-5}$ F, $R_s = 10\ \Omega$.

$$\hat{Z}_f = R_{ct} - j\frac{1}{\omega C_a} \tag{143}$$

which corresponds to a series connection of R_{ct} and C_{dl}. The corresponding complex plane plots are presented in Fig. 23.

1c. $C - R_{ct}|B| < 0$

In this case the parameter R_a is negative and the corresponding complex plane plots are displayed in Fig. 24.

2. $B = 0$

When $B = 0$, the faradaic impedance is real and equals R_{ct}. One semicircle is observed in the complex plane plots (Fig. 4).

3. $B > 0$

In this case the faradaic admittance is given by

$$\hat{Y}_f = \frac{1}{R_{ct}} + \frac{B}{j\omega + C} = \frac{1}{R_{ct}} + \frac{1}{R_o + j\omega L} \tag{144}$$

with

$$R_o = C/B \quad \text{and} \quad L = 1/B \tag{145}$$

and the faradaic impedance by

$$\hat{Z}_f = \frac{1}{\dfrac{1}{R_{ct}} + \dfrac{1}{R_o + j\omega L}} \tag{146}$$

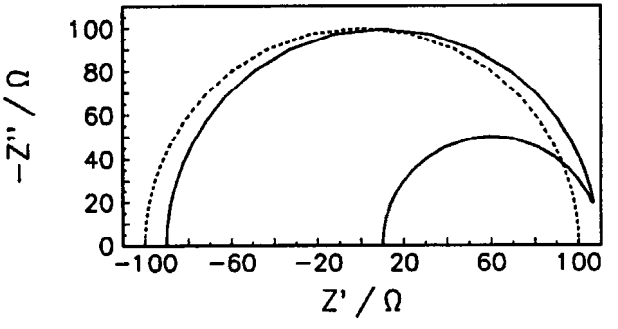

Figure 24. Complex plane plot for the case of one adsorbed species, $B < 0$ and $C - R_{ct}|B| < 0$; continuous line, total impedance; dashed line, faradaic impedance. Parameters used: $R_{ct} = 100\ \Omega$, $R_a = -200\ \Omega$, $C_a = 2 \times 10^{-3}$ F, $C_{dl} = 2 \times 10^{-5}$ F, $R_s = 10\ \Omega$.

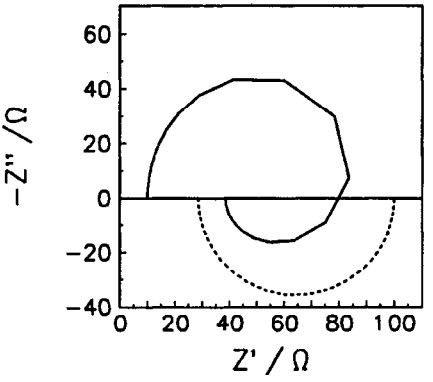

Figure 25. Complex plane plots for the case of one adsorbed species and $B > 0$ [Eqs. (144)–(146)]; continuous line, total impedance; dashed line, faradaic impedance. Parameters used: $R_{ct} = 100\ \Omega$, $R_o = 40\ \Omega$, $L = 0.2$ H, $C_{dl} = 2 \times 10^{-5}$ F, $R_s = 10\ \Omega$.

which corresponds to the parallel connection of the charge-transfer resistance with series connection of the resistance R_o and inductance L [Fig. 21(b)]. In this case $R_p = R_{ct}R_o/(R_{ct} + R_o)$. The equivalent circuit and the corresponding complex plane plots of faradaic and total impedances are shown in Fig. 25. Diard *et al.*[85] determined conditions under which such a low-frequency pseudo-inductive loop may be found.

The above analysis shows that in the simple case of one adsorbed intermediate (according to Langmuirian adsorption), various complex plane plots may be obtained, depending on the relative values of the system parameters. These plots are described by various equivalent circuits, which are only the electrical representations of the interfacial phenomena. In fact, there are no real capacitances, inductances, or resistances in the circuit (faradaic process). These parameters originate from the behavior of the kinetic equations and are functions of the rate constants, transfer coefficients, potential, diffusion coefficients, concentrations, etc. In addition, all these parameters are highly nonlinear, that is, they depend on the electrode potential. It seems that the electrical representation of the faradaic impedance, however useful it may sound, is not necessary in the description of the system. The system may be described in a simpler way directly by the equations describing impedances or admittances (see also Section IV). In

a system following the Frumkin adsorption isotherm, discontinuous impedances may be obtained.[86]

It should be added that for the system involving one adsorbed species described above, there are two sets of kinetic parameters giving the same experimental curves.[87] In fact, permutation of the kinetic parameters: $k_1 \leftrightarrow k_2$, $k_{-1} \leftrightarrow k_{-2}$, and $\beta_1 \leftrightarrow \beta_2$ gives the same values of the dc current, the charge-transfer resistance, and the parameters *B* and *C*. The problem of identifiability and distinguishability of electrode processes was further studied by Bertier *et al.*[88–91]

The impedance of a more complex process involving coupling between adsorption and diffusion was studied by Armstrong and coworkers.[92,93]

3. Faradaic Impedance in the Case Involving Two Adsorbed Species

Typical examples of processes involving two or more adsorbed species are reactions of corrosion or anodic dissolution of metals, oxygen evolution, etc. In the case of two adsorbed species *B* and *C,* the electrochemical reactions may be written as[84,94,95]:

$$A_{sol} + e \underset{k_{-1}}{\overset{k_1}{\Leftrightarrow}} B_{ads} \tag{147}$$

$$B_{ads} + e \underset{k_{-2}}{\overset{k_2}{\Leftrightarrow}} C_{ads} \tag{148}$$

and

$$C_{ads} + \underset{k_{-3}}{\overset{k_3}{\Leftrightarrow}} D_{sol} \tag{149}$$

The rates of Eqs. (147)–(149) may be expressed with respect to the equilibrium potential similarly to Eqs. (122) and (123):

$$v_1 = \vec{k}_1(1 - \Theta_1 - \Theta_2) - \overleftarrow{k}_{-1}\Theta_1 \tag{150}$$

$$v_2 = \vec{k}_2\Theta_1 - \overleftarrow{k}_{-2}\Theta_2 \tag{151}$$

and

$$v_3 = k_3\Theta_2 - k_{-3}(1 - \Theta_1 - \Theta_2) \tag{152}$$

where Θ_1 and Θ_2 are the surface coverages by *B* and *C,* respectively, and rate constants k_3 and k_{-3} are potential independent. From the condition at the equilibrium potential, $v_1 = v_2 = v_3 = 0$, the following condition for the rate constants is obtained (see Eq. 128):

$$\frac{k_1 k_2 k_3}{k_{-1} k_{-2} k_{-3}} = 1 \tag{153}$$

The charge is exchanged in reactions (147) and (148) only; therefore the total current is given as

$$i = F(v_1 + v_2) = Fr_0 \tag{154}$$

The mass balance for Θ_1 and Θ_2 gives, similarly to Eq. (129):

$$\frac{\sigma_1}{F}\frac{d\Theta_1}{dt} = v_1 - v_2 = r_1 \tag{155}$$

$$\frac{\sigma_2}{F}\frac{d\Theta_2}{dt} = v_2 - v_3 = r_2 \tag{156}$$

Taking into account that r_0, r_1, and r_2 are the functions of η, Θ_1, and Θ_2, linearization of Eqs. (154)–(156) and the introduction of phasors gives

$$\tilde{i} = F\left[\left(\frac{\partial r_0}{\partial \eta}\right)_{\Theta_1,\Theta_2} \tilde{\eta} + \left(\frac{\partial r_0}{\partial \Theta_1}\right)_{\eta,\Theta_2} \tilde{\Theta}_1 + \left(\frac{\partial r_0}{\partial \Theta_2}\right)_{\eta,\Theta_1} \tilde{\Theta}_2\right]$$

$$j\omega\frac{\sigma_1}{F}\tilde{\Theta}_1 = \left(\frac{\partial r_1}{\partial \eta}\right)_{\Theta_1,\Theta_2} \tilde{\eta} + \left(\frac{\partial r_1}{\partial \Theta_1}\right)_{\eta,\Theta_2} \tilde{\Theta}_1 + \left(\frac{\partial r_1}{\partial \Theta_2}\right)_{\eta,\Theta_1} \tilde{\Theta}_2 \tag{158}$$

and

$$j\omega\frac{\sigma_1}{F}\tilde{\Theta}_2 = \left(\frac{\partial r_2}{\partial \eta}\right)_{\Theta_1,\Theta_2} \tilde{\eta} + \left(\frac{\partial r_2}{\partial \Theta_1}\right)_{\eta,\Theta_2} \tilde{\Theta}_1 + \left(\frac{\partial r_2}{\partial \Theta_2}\right)_{\eta,\Theta_1} \tilde{\Theta}_2 \tag{159}$$

Equations (157)–(159) present a system of three equations with three unknowns: Θ_1, Θ_2, and $\tilde{i}/\tilde{\eta}$. The faradaic admittance is determined as

$$\hat{Y}_f = \frac{1}{\hat{Z}_f} = \frac{\tilde{i}}{\tilde{\eta}} = A + \frac{B + j\omega C}{j\omega D - \omega^2 + E} \tag{160}$$

where

$$A = \frac{1}{R_{ct}} = -F\left(\frac{\partial r_0}{\partial \eta}\right)_{\Theta_1,\Theta_2} \tag{161}$$

$$B = -\frac{F^3}{\sigma_1\sigma_2}\left\{\begin{array}{l} -\left(\frac{\partial r_0}{\partial \Theta_1}\right)\left(\frac{\partial r_1}{\partial \eta}\right)\left(\frac{\partial r_1}{\partial \Theta_2}\right) + \left(\frac{\partial r_0}{\partial \Theta_1}\right)\left(\frac{\partial r_1}{\partial \Theta_2}\right)\left(\frac{\partial r_2}{\partial \eta}\right) \\ -\left(\frac{\partial r_0}{\partial \Theta_2}\right)\left(\frac{\partial r_1}{\partial \Theta_1}\right)\left(\frac{\partial r_2}{\partial \eta}\right) + \left(\frac{\partial r_0}{\partial \Theta_2}\right)\left(\frac{\partial r_1}{\partial \eta}\right)\left(\frac{\partial r_2}{\partial \Theta_1}\right) \end{array}\right\} \tag{162}$$

$$C = -F^2\left[\frac{1}{\sigma_1}\left(\frac{\partial r_0}{\partial \Theta_1}\right)\left(\frac{\partial r_1}{\partial \eta}\right) + \frac{1}{\sigma_2}\left(\frac{\partial r_0}{\partial \Theta_2}\right)\left(\frac{\partial r_2}{\partial \eta}\right)\right] \tag{163}$$

$$D = -F\left[\frac{1}{\sigma_1}\left(\frac{\partial r_1}{\partial \Theta_1}\right) + \frac{1}{\sigma_2}\left(\frac{\partial r_2}{\partial \Theta_2}\right)\right] \tag{164}$$

and

$$E = \frac{F^2}{\sigma_1\sigma_2}\left[\left(\frac{\partial r_1}{\partial \Theta_1}\right)\left(\frac{\partial r_2}{\partial \Theta_2}\right) - \left(\frac{\partial r_1}{\partial \Theta_2}\right)\left(\frac{\partial r_2}{\partial \Theta_1}\right)\right] \tag{165}$$

where the negative sign before the parameters *A, B,* and *C* originates from the current definition (positive current for reduction). If the reactions (147)–(149) are written as oxidations, this sign should be omitted. Calculation of the derivatives shows that parameters *A, D,* and *E* are always positive and parameters *D* and *E* may be positive or negative.

The faradaic impedance may be obtained from Eq. (160) as

$$\hat{Z}_f = \frac{1}{A} + \frac{B + j\omega C}{A^2\left[(D + B/A) + j\omega(E + C/A) - \omega^2\right]} \tag{166}$$

The polarization resistance is $R_p = R_{ct} + B/[A^2(D + B/A)]$.

4.. Impedance Plots in the Case of Two Adsorbed Species

The second term in Eq. (166) represents a second-order electrochemical impedance,[95] and its denominator may be expressed in the following form:

$$1 + j\omega 2\zeta/\omega_n - (\omega/\omega_n)^2 \tag{167}$$

where ω_n is the undamped natural frequency and ζ is the damping ratio of the system[32] expressed as

$$\omega_n = \sqrt{D + B/A} \quad \text{and} \quad \zeta = \frac{1}{2}\frac{E + C/A}{2\sqrt{D + B/A}} \tag{168}$$

Depending on the value of the parameter ζ, the poles of the second term of Eq. (167) are real or imaginary. Taking into account Eq. (167), there are 54 theoretically different cases of poles and zeros. They were considered systematically in Ref. 95. The faradaic impedance may be represented by many different equivalent circuits, depending on the sign of parameters *B* and *C* and relative values of all the parameters.[94] Its complex plane plots display different forms from two capacitive semicircles through various capacitive and inductive loops to two inductive loops. In order to obtain the total impedance, the double-layer capacitance and solution resistance should be added to the faradaic impedance. Some examples of complex plane plots of faradaic impedances are presented in Fig. 26.

5. Faradaic Impedance for a Process Involving Three or More Adsorbed Species

Similarly to the case of two adsorbed species presented above, more complicated cases may be considered. Such a case is often found in corrosion.[96] Assuming the existence of three adsorbed species, a system of equations similar to Eqs. (157)–(159) may be written:

$$-\frac{\tilde{i}}{F} + \left(\frac{\partial r_0}{\partial \eta}\right)\tilde{\eta} + \left(\frac{\partial r_0}{\partial \Theta_1}\right)\tilde{\Theta}_1 + \left(\frac{\partial r_0}{\partial \Theta_2}\right)\tilde{\Theta}_2 + \left(\frac{\partial r_0}{\partial \Theta_3}\right)\tilde{\Theta}_3 = 0 \tag{169}$$

$$\left(\frac{\partial r_1}{\partial \eta}\right)\tilde{\eta} + \left[\left(\frac{\partial r_1}{\partial \Theta_1}\right) - j\omega\frac{\sigma_1}{F}\right]\tilde{\Theta}_1 + \left(\frac{\partial r_1}{\partial \Theta_2}\right)\tilde{\Theta}_2 + \left(\frac{\partial r_1}{\partial \Theta_3}\right)\tilde{\Theta}_3 = 0 \tag{170}$$

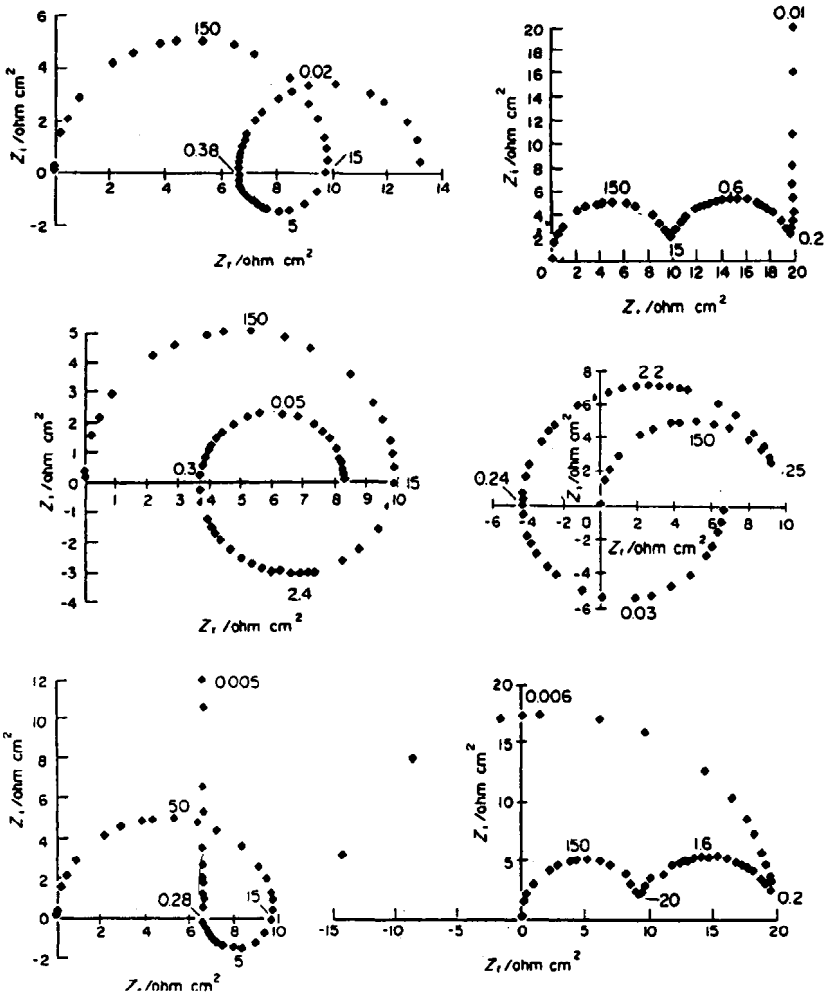

Figure 26. Some examples of the complex plane plots obtained for the case of two adsorbed species.[94]

$$\left(\frac{\partial r_2}{\partial \eta}\right)\tilde{\eta} + \left(\frac{\partial r_2}{\partial \Theta_1}\right)\tilde{\Theta}_1 + \left[\left(\frac{\partial r_2}{\partial \Theta_2}\right) - j\omega\frac{\sigma_2}{F}\right]\tilde{\Theta}_2 + \left(\frac{\partial r_2}{\partial \Theta_3}\right)\tilde{\Theta}_3 = 0 \qquad (171)$$

and

$$\left(\frac{\partial r_3}{\partial \eta}\right)\tilde{\eta} + \left(\frac{\partial r_3}{\partial \Theta_1}\right)\tilde{\Theta}_1 + \left(\frac{\partial r_3}{\partial \Theta_2}\right)\tilde{\Theta}_2 + \left[\left(\frac{\partial r_2}{\partial \Theta_3}\right) - j\omega\frac{\sigma_3}{F}\right]\tilde{\Theta}_3 = 0 \qquad (172)$$

where Θ_i are surface coverages of adsorbed species, σ_i are their charges necessary for monolayer coverage, and r_i are the corresponding mass balances and relations between adsorbed species, as in Eqs. (155)–(156), which may be different for different mechanisms. Equations (169)–(172) are solved using methods for the solution of the system of linear equations (e.g., Crammer's method). In the case of three adsorbed species, very complicated complex plane plots may be obtained. Some examples are presented in Ref. 96.

A general model of a multistep mechanism involving adsorption and diffusion was recently given by Harrington.[97]

V. IMPEDANCE OF SOLID ELECTRODES

1. Frequency Dispersion and Electrode Roughness

The general model of the ideally polarizable electrode presented in Section III.1 [see also Eq. (17) and Fig. 2], and that in the presence of a faradaic reaction [Section III.2, Fig. 4(a)] are found experimentally on liquid electrodes (e.g., mercury, amalgams, and indium-gallium). On solid electrodes,[98] deviations from the ideal behavior are often observed. On ideally polarizable solid electrodes, the electrically equivalent model usually cannot be represented (with the exception of monocrystalline electrodes in the absence of adsorption) as a series connection of the solution resistance and double-layer capacitance. However, on solid electrodes a frequency dispersion is observed; that is, the observed impedances cannot be represented by the connection of simple *R-C-L* elements. The impedance of such systems may be approximated by an infinite series of parallel *R-C* circuits, that is, a transmission line [see Section VI, Fig. 41(b), ladder circuit]. The impedances may often be represented by an equation without simple electrical representation, through distributed elements. The Warburg impedance is an example of a distributed element.

Problems similar to those observed on ideally polarizable solid electrodes also arise in the presence of faradaic reactions at these electrodes. In the next section, various models used to explain solid electrode impedance behavior are presented.

2. Constant Phase Element

Dispersion of the measured complex dielectric constant is known from dielectric relaxation experiments.[18] The complex dielectric constant ε^* may be represented as

$$\frac{\varepsilon^* - \varepsilon_\infty}{\varepsilon_s - \varepsilon_\infty} = \int_0^\infty \frac{G(\tau)}{1 + j\omega\tau}\, d\tau \tag{173}$$

where ε_∞ and ε_s are the dielectric constants determined at $\omega \to \infty$ and $\omega \to 0$, respectively, and $G(\tau)$ is the time constant distribution function. When there is only one relaxation time constant, that is, $G(\tau) = \delta(\tau - \tau_0)$, Eq. (173) simplifies to

$$\frac{\varepsilon^* - \varepsilon_\infty}{\varepsilon_s - \varepsilon_\infty} = \frac{1}{1 + j\omega\tau_0} \tag{174}$$

Cole and Cole[99] described the observed distribution of relaxation times as

$$\frac{\varepsilon^* - \varepsilon_\infty}{\varepsilon_s - \varepsilon_\infty} = \frac{1}{1 + (j\omega\tau_0)^\phi} \tag{175}$$

where ϕ is a constant between 0 and 1. When $\phi = 1$, there is only one time constant in the system (no dispersion) and Eq. (173) reduces to Eq. (174). Equation (175) represents a semicircle rotated by $(1 - \phi)90°$ on the complex plane. This behavior can be explained by Eq. (173) with the distribution function $G(\tau)$ described as

$$G(\tau) = \frac{1}{2\pi\tau} \frac{\sin[(1-\phi)\pi]}{\cosh[\phi \ln(\tau/\tau_0)] - \cos[(1-\phi)\pi]} \tag{176}$$

which represents a lognormal distribution that is a normal distribution of a function of $\ln(\tau/\tau_0)$. An example of such a distribution function is shown in Fig. 27. For $\phi = 1$, the distribution function becomes the Dirac delta function.

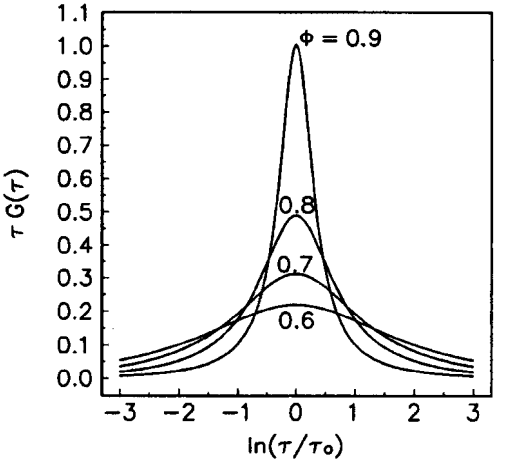

Figure 27. The distribution function $\tau G(\tau)$ versus $\ln(\tau/\tau_0)$ according to Eq. (176).

The impedance of the ideally polarizable electrode may be represented as a series connection of the solution resistance and the double-layer capacitance, which produces a straight line perpendicular to the real axis on the complex plane plots. However, on solid electrodes, a straight line with an angle lower than $\pi/2$ is often observed [Fig. 28(a)]. In order to describe such behavior, a model of distributed time constants, similar to that used by Cole and Cole,[99] was proposed.[100] It was supposed[101] that such a distribution may arise from (1) a microscopic roughness caused by scratches, pits, etc., always present on solid surfaces, which causes coupling of the solution resistance with the surface capacitance; and (2) a capacitance dispersion of interfacial origin, connected with the slow adsorption of ions and chemical inhomogeneities of the surface. In such cases the double-layer capacitance may be expressed in terms of a constant phase element (CPE). Its impedance is given by

$$\hat{Z}_{\mathrm{CPE}} = \frac{1}{T(j\omega)^{\phi}} \tag{177}$$

where T is a constant in F cm^{-2} s$^{\phi-1}$ and ϕ is related to the angle of rotation of a purely capacitive line on the complex plane plots: $\alpha = 90°\ (1 - \phi)$ [Fig. 28(a)]. Equation (177) may also be written as

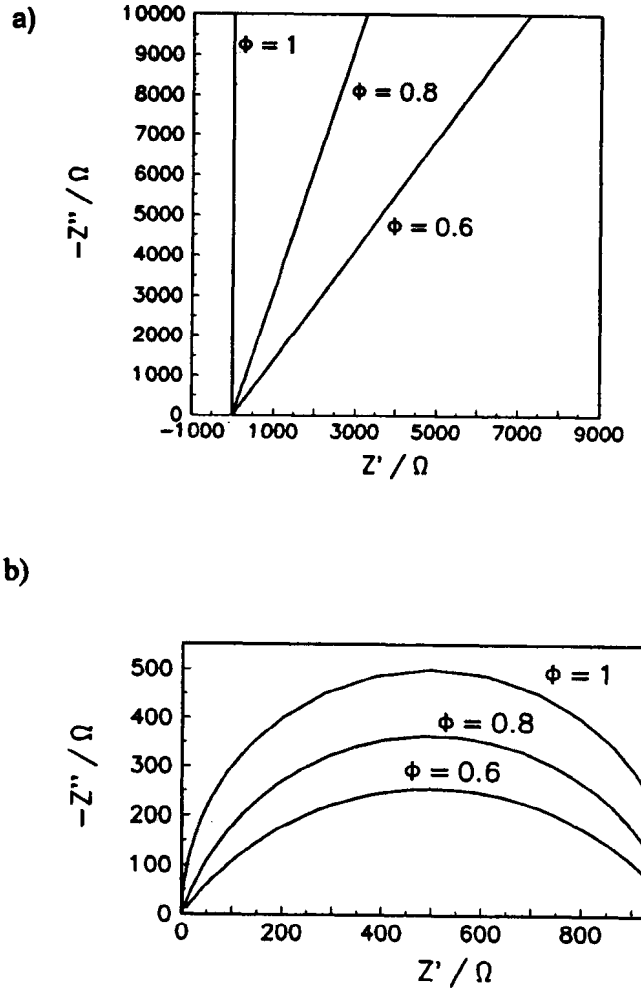

Figure 28. Complex plane plots in the presence of a constant phase element: (a) ideally polarizable electrode and (b) in the presence of a faradaic reaction.

$$\hat{Z}_{\mathrm{CPE}} = \frac{1}{T\omega^{\phi}} [\cos(\phi\pi/2) - j \sin(\phi\pi/2)] \tag{178}$$

and it represents a "leaking" capacitor, which has nonzero real and imaginary components. Only in the case when $\phi = 1$, one gets $T \equiv C_{\mathrm{dl}}$ and purely capacitive behavior obtained. In general, Eq. (177) may represent

pure capacitance for $\phi = 1$, infinite Warburg impedance for $\phi = 0.5$, pure resistance for $\phi = 0$, and pure inductance for $\phi = -1$. Brug *et al.*[100] presented a method for estimating the average double-layer capacitance, $\bar{C}_{dl}$, from the value of T. Assuming that the electrode impedance may be expressed as a sum of the solution resistance and the impedance of the CPE element, and using the Cole–Cole formula for the distributed time constants, the total impedance may be expressed as

$$\hat{Z} = R_s + \frac{1}{(j\omega)^{\phi}T} = R_s\left[1 + \frac{1}{(j\omega)^{\phi}(TR_s)}\right] = R_s\left[1 + \frac{1}{(j\omega\tau_0)^{\phi}}\right] \tag{179}$$

where $\tau_0 = R_s\bar{C}_{dl}$. This leads to

$$T = \bar{C}_{dl}^{\phi} R_s^{-(1-\phi)} \tag{180}$$

which allows the estimation of the average double-layer capacitance in the presence of the CPE element.

In the presence of the faradaic reaction, assuming that the faradaic impedance can be expressed as a simple equivalent resistance, the complex plane plots represent a rotated semicircle [Fig. 28(b)], instead of a semicircle centered on the Z' axis.[102–104] Similarly, the double-layer capacitance in the presence of the faradaic reaction may be obtained as[100]

$$T = \bar{C}_{dl}^{\phi}\left[R_s^{-1} + R_{ct}^{-1}\right]^{1-\phi} \tag{181}$$

An example of the application of Eq. (181) to the reduction of protons and Tris-oxalato ferric ions was presented by Brug *et al.*[100] Lasia and Rami[87] studied the hydrogen evolution reaction on polycrystalline Ni in 1 M NaOH. They obtained rotated semicircles on the complex plane plots, and the values of the parameters T and ϕ were potential dependent; however, the double-layer capacitances estimated from Eq. (181) were constant, equal to ~38 μF cm^{-2}, which is a reasonable value taking into account some surface roughness. Similar results were also obtained on rhodium.[105]

VanderNoot[106] tried to extract the distribution function $G(\tau)$ from the CPE model. He found that the Fourier inversion method is not suitable, but that the maximum entropy deconvolution works relatively well. However, because this is an ill-posed problem, the results obtained are very sensitive to the experimental errors (noise).

Historically, the CPE phenomenon was usually attributed to surface roughness. Pajkossy *et al.*[101,107] recently studied the origins of the CPE.

They found that surface roughness of the order found on polycrystalline metals could lead to the CPE behavior only at much higher frequencies than those observed experimentally. They concluded that an increase in the surface roughness of polycrystalline Pt did not change (even slightly increased) the ϕ parameter. However, it was found that the capacitance dispersion increases markedly with the addition of chloride ions.[101]

Experiments carried out on monocrystalline Au(111) and Au(100) electrodes in the absence of specific adsorption did not show any frequency dispersion.[107] Dispersion was observed, however, in the presence of specific adsorption of halide ions. It was attributed to slow adsorption and diffusion of these ions and phase transitions (reconstructions). In their analysis these authors expressed the electrode impedance as: $\hat{Z} = R_s + (j\omega\hat{C}_{int})^{-1}$ where $\hat{C}_{int}$ is a complex electrode capacitance. In the case of a simple CPE circuit, this parameter is $\hat{C}_{int} = T(j\omega)^{\phi-1}$. However, an analysis of the ac impedance spectra in the presence of specific adsorption revealed that the complex plane capacitance plots (C''_{int} vs. C'_{int}) show the formation of deformed semicircles. Consequently, Pajkossy *et al.* proposed the electrical equivalent model shown in Fig. 29, in which instead of the CPE there is a double-layer capacitance in parallel with a series connection of the adsorption resistance and capacitance, R_{ad} and C_{ad}, and the semi-infinite Warburg impedance connected with the diffusion of the adsorbing species. A comparison of the measured and calculated capacitances (using the model in Fig. 29) for Au(111) in 0.1 M $HClO_4$ in the presence of 0.15 mM NaBr is shown in Fig. 30.

A similar analysis of complex impedances obtained from the frequency dispersion on a passive stainless steel was carried out by Devaux *et al.*[108]

Stoynov[109] has extended the CPE model for finite-thickness diffusion. He introduced a bounded CPE (BCP) impedance or finite constant phase element

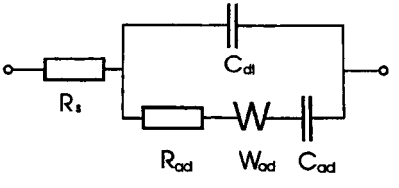

Figure 29. Equivalent-circuit model of the electrode in the presence of adsorption.[107]

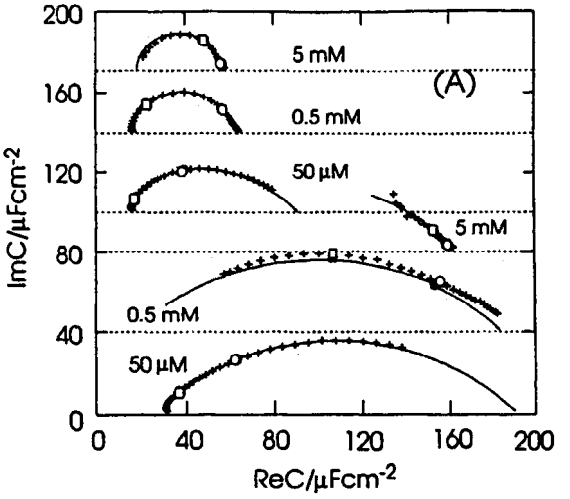

Figure 30. Nyquist plot of complex capacitances for Au(111) in 0.1 M $HClO_4$ in the presence of bromide ions; Br^- concentrations given in the figure; upper three curves at E = 0.3 V; lower three curves at E = 0.1 V vs. SCE.[107]

$$\hat{Z}_{BCP} = \frac{1}{T(j\omega)^{\phi}} \tanh\left[R_s T(j\omega)^{\phi}\right] \tag{182}$$

where R_s is the solution resistance. In fact, at high frequencies, Eq. (182) reduces to a simple CPE [Eq. (177)], and at low frequencies it reduces to R_s. For $\phi = 0.5$, BCP has a form similar to that of the impedance in the case of the finite-length diffusion. Just as the CPE represents infinite diffusion for $\phi = 0.5$, the BCP represents finite-length diffusion for the same value of ϕ. Complex plane plots for the BCP element are presented in Fig. 31. This element has a physical meaning for $\phi < 0.6$.[19]

3. Fractal Model

Solid surfaces are usually irregular and their detailed geometry is not known. In order to describe their geometry, the concept of fractal dimensions was introduced.[110] This concept is based on the self-similarity of surfaces, implying different scaling. The difference between simple and fractal magnification is shown in Fig. 32.[111] Simple magnification only increases the size of the object while fractal magnification reveals self-similarity at different scales. Such a magnification process may continue

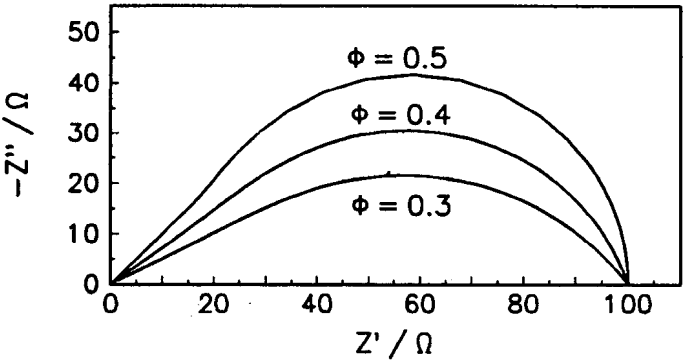

Figure 31. Complex plane plots for the bounded thickness impedance (BCP) for $R_s = 100\ \Omega$, $T = 0.01$ F cm^{-2} s$^{\phi-1}$, and different values of parameter ϕ.

indefinitely. The line enclosing the object in Fig. 32(c) is the von Koch line[112,113]; it is continuous, of infinite length, and is nowhere differentiable. It is interesting to note that the observed (measured) length of the von Koch line is scaled in a complex way: its length depends on the yardstick used to measure it. In the example in Fig. 32, the object is magnified three times and the line length is magnified four times. This leads to the fractal dimension of the von Koch line $D_H = (\ln 4)/(\ln 3) = 1.262$.[111,114] In general, the fractal dimension of the line may be between 1 and 2. Such reasoning may also be used for surfaces for which the fractal dimensions may be between 2 and 3.

Fractal geometry was introduced to electrochemistry by Le Méhauté *et al.*[115] It was shown by Nyikos, Pajkossy, and co-workers[113–114,116–122]

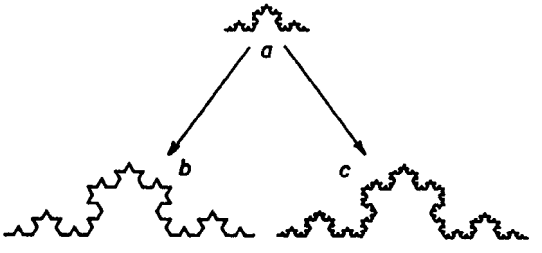

Figure 32. (a) Images with (b) simple and (c) fractal magnifications.[111]

that the fractal geometry of ideally polarizable (i.e., blocking) interfaces generates a CPE behavior described by Eq. (177) in Section V.2. However, it should be stressed that, in general, there is no simple relation between the fractal dimension D_H and the parameter ϕ[123] of the CPE, although higher fractal dimensions lead to smaller values of ϕ.[114] Fractal theory was subsequently extended to irregular or quasi-random surfaces lacking well-defined self-similarity.[119,120] Pajkossy and Nyikos[124] carried out simulations of blocking electrodes with a self-similar spatial capacitance distribution and found that the calculated impedances exhibited the CPE behavior. Fractal theory was also tested experimentally using fractal electrodes prepared by microelectronic techniques.[118]

Subsequently, fractal theory was extended to faradaic processes.[111,114,117,118,125,126] de Levie[111,125] has shown that the impedance of a fractal electrode, in the absence of mass transfer control, is given as

$$\hat{Z} = R_s + \frac{1}{b}\left(\frac{1}{\frac{1}{R_{ct}} + j\omega C_{dl}}\right)^{\phi} \tag{183}$$

where the parameter b is given by

$$b = f_g \rho^{\phi-1} \tag{184}$$

where ρ is the solution resistivity and f_g is a factor depending on the fractal surface geometry,[110] which may be based on von Koch curves,[127] Cantor bars,[128–130] Sierpinski carpets,[131–133] etc.[98] When the surface is flat and homogeneous, $\phi = 1$, $f_g = 1$, $b = 1$ and Eq. (184) reduces to Eq. (112). According to de Levie,[111] Eq. (183) may be applied to fractal electrodes in equilibrium; that is, in the absence of the dc current, which may introduce a local interfacial potential difference. When the exact fractal structure is not known, the parameter b cannot be obtained and the only parameters accessible are

$$C_{exp} = b^{1/\phi} C_{dl} \quad \text{and} \quad R_{ct,exp} = b^{1/\phi} R_{ct} \tag{185}$$

Examples of the complex plane plots obtained for fractal electrodes are presented in Fig. 33. With a decrease in parameter ϕ, the semicircles become deformed (skewed). The complex plane impedance plots obtained from Eq. (183) are formally similar to those found by Davidson and Cole[134] in their dielectric studies. Kinetic analysis of the hydrogen evolution reaction on surfaces displaying fractal ac impedance behavior was

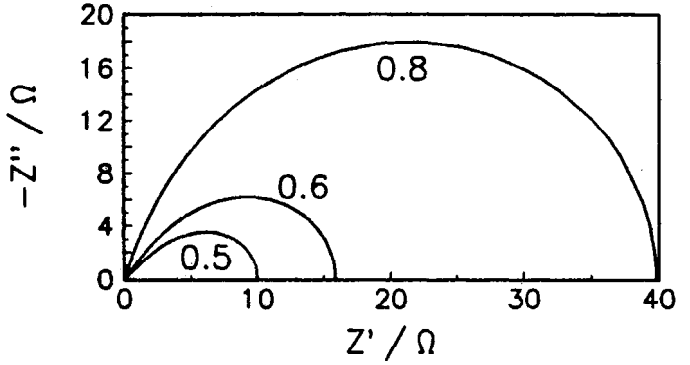

Figure 33. Complex plane plots on fractal electrodes for different values of parameter ϕ.

carried out by Lasia and co-workers,[135–137] who obtained rate constants expressed as $k_{i,\mathrm{exp}} = b^{1/\phi} k_i$. In order to compare the intrinsic activities of such electrodes with that of polycrystalline nickel, the ratio of $k_{i,\mathrm{exp}}/C_{\mathrm{dl,exp}} = k_i/C_{\mathrm{dl}}$ was used. It was found that this ratio has similar values for Raney Ni and polycrystalline Ni; therefore the intrinsic activity of these electrodes is similar and the observed increase in activity of Raney Ni electrodes arises from their very large real surface area.

In general, self-similar fractal surfaces do not exist in the real world. The fractal models may only approximate random surfaces. In addition, Eq. (183) for $\phi = 0.5$ is formally identical with the semi-infinite porous model presented in the next section. The fractal model in the presence of diffusion is discussed in Refs. 111 and 118. Experimental verifications of the fractal model were also carried out for some electrodes.[118,121,138] It was also stated that the fractal dimension of the surface may be found from dc experiments.[114,118,139,140]

4. Porous Electrode Model

In electrocatalysis there is great interest in increasing the real surface area of electrodes. In such cases porous electrodes are used. Because modeling of real electrodes is difficult, a simpler model is usually used in which it is assumed that pores have a cylindrical shape with a length l and a radius r.[24,141–145]

In order to describe the impedance of such electrodes, first a dc solution must be found. Two cases are considered here: (1) porous electrodes in the absence of internal diffusion and (2) in the presence of axial diffusion. It is assumed that the electrical potential and concentration of electroactive species depend on the distance from the pore orifice only and there is always an excess of the supporting electrolyte (i.e., migration can be neglected).

(i) Porous Electrodes in the Absence of Internal Diffusion

In this case it is assumed that the concentration of the electroactive species is independent of the distance along a pore. In the next section we will see when such an assumption is valid. The axially flowing dc current, *I,* which enters the pore, flows toward the walls and its value decreases with the distance x from the pore orifice (Fig. 34). This decrease in the current is proportional to the current flowing to the wall:

$$\frac{dI}{dx} = -\frac{(2\pi r dx)j}{dx} = -2\pi r j \tag{186}$$

where $2\pi r dx$ is the surface area of a pore section dx and j is the current density. Because of Ohm's law, a potential drop along the pore also occurs:

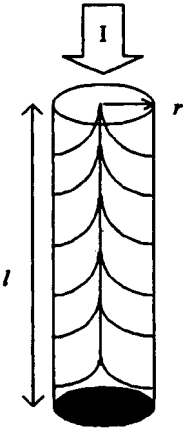

Figure 34. Pore model.

$$\frac{dE}{dx} = -I\left(\frac{\rho dx}{\pi r^2}\right)\frac{1}{dx} = -I\left(\frac{\rho}{\pi r^2}\right) \tag{187}$$

where ρ is the specific solution resistance and $(\rho dx/\pi r^2)$ is the resistance of the section dx of the solution in the pore. The last term in the parentheses in Eq. (187) may be called the solution resistance per unit length of the pore, $R = \rho/\pi r^2$, and is expressed in Ω cm^{-1}. Similarly, the current flowing through an element dx of the surface area, $(2\pi r dx)j$, may be represented as E/Z, where Z is the impedance of pore walls per unit of the pore length, in Ω cm. It can be shown that $Z = Z_{el}/2\pi r$ where Z_{el} is the specific impedance of pore walls in Ω cm^2. Z_{el} consists of the faradaic, Z_f, and the double-layer impedance: $Z_{el} = (1/Z_f + j\omega C_{dl})^{-1}$.

(a) de Levie's treatment

de Levie[146] was the first to describe the impedance of porous electrodes. He presented Eqs. (186) and (187) in the following form:

$$\frac{dI}{dx} = -\frac{E}{\hat{Z}} \tag{188}$$

$$\frac{dE}{dx} = -RI \tag{189}$$

Taking the second derivative of Eq. (189) and substituting Eq. (188), one obtains

$$\frac{d^2E}{dx^2} = -R\frac{dI}{dx} = \left(\frac{R}{\hat{Z}}\right)E \tag{190}$$

This equation describes changes in the electrical potential as a function of pore length. de Levie assumed that the impedance of pore walls is independent of the pore distance (Z is not a function of distance), which implies that there is no net dc current. The solution is

$$E = C_1 \exp(-\sqrt{R/\hat{Z}}x) + C_2 \exp\sqrt{R/\hat{Z}}x) \tag{191}$$

where C_1 and C_2 are the integration constants. Taking into account the boundary conditions

$$x = 0 \qquad E = E_0$$

and

$$x = l \qquad dE/dx = 0$$

where E_0 is the potential at $x = 0$, the dc solution is

$$E = E_0 \frac{\cosh\left[\sqrt{\frac{R}{\hat{Z}}}\,(l-x)\right]}{\cosh\left(\sqrt{\frac{R}{\hat{Z}}}\,l\right)} \tag{192}$$

and

$$\left(\frac{dE}{dx}\right)_{x=0} = -E_0\sqrt{\frac{R}{\hat{Z}}}\,\tanh\left(\sqrt{\frac{R}{\hat{Z}}}\,l\right) = -I_0 R \tag{193}$$

The total pore impedance, $\hat{Z}_{\text{por}}$, is then obtained as

$$\hat{Z}_{\text{por}} = \frac{E_0}{I_0} = \sqrt{R\hat{Z}}\,\coth\left(\sqrt{\frac{R}{\hat{Z}}}\,l\right) \tag{194}$$

This equation may be rearranged into

$$\hat{Z}_{\text{por}} = \frac{R_{\Omega,p}}{\Lambda^{1/2}}\coth\left(\Lambda^{1/2}\right) \tag{195}$$

where $R_{\Omega,p} = \rho l/\pi r^2$ and $\Lambda = (2\rho l^2/r)/\hat{Z}_{\text{el}}$. It is evident that the faradaic impedance of pore walls was assumed to be independent of potential despite the fact that the potential changes with the pore depth. The faradaic impedance may be obtained assuming that the Butler–Volmer equation adequately describes the electrochemical process. Although the original development was carried out using electrode potential E, a more adequate representation of impedance would be with respect to the overpotential η:

$$\frac{1}{\hat{Z}_f} = \frac{1}{R_{\text{ct}}} = \frac{dj}{d\eta} = j_0 nf\left[\alpha\, e^{-\alpha nf\eta} + (1-\alpha)\, e^{(1-\alpha)nf\eta}\right] \tag{196}$$

Of course, under dc conditions, when $\omega = 0, \hat{Z}_{\text{el}} = R_{\text{ct}}$. For the ensemble of n pores and in the presence of the solution resistance outside the pores, the total impedance becomes

$$\hat{Z}_t = R_s + \frac{\hat{Z}_{\text{por}}}{n} \tag{197}$$

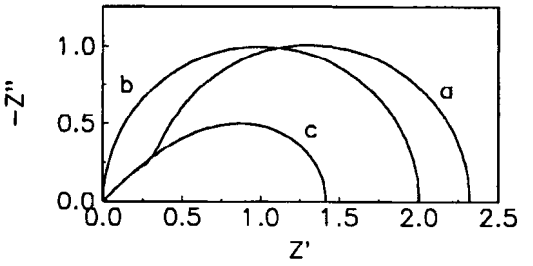

Figure 35. Complex plane plots for a porous electrode according to de Levie's model [Eq. (195)]. (a) General case [Eq. (195)]; (b) limiting case for shallow pores [Eq. (199)]; (c) limiting case for very deep pores [Eq. (200)].

Equation (195) predicts the observation of a straight line at 45° at high frequencies, followed by a semicircle (Fig. 35(a)]. At low frequencies, the impedance becomes real:

$$Z(\omega = 0) = R_p = \sqrt{\frac{\rho R_{ct}}{2\pi^2 r^3}} \coth\left(\sqrt{\frac{2\rho}{rR_{ct}}}\, l\right) \tag{198}$$

The behavior of the porous electrode depends on the *penetration depth,* λ, of the alternating signal into the pore. This parameter is defined as $\Lambda = l/\lambda$, or $\lambda = (r\hat{Z}_{el}/2\rho)^{1/2}$. Equation (195) has two limiting cases. First, when $\lambda >> l$, $\Lambda \to 0$, $\coth(\Lambda^{1/2}) \to \Lambda^{-1/2}$, and the equation becomes

$$\hat{Z}_{por} = \frac{R_{\Omega,p}}{\Lambda} = \frac{1}{2\pi rl}\hat{Z}_{el} \tag{199}$$

where $s = 2\pi rl$ is the total pore surface area. Equation (199) represents simply the impedance of a flat electrode having a surface area *s.* In this case the ac signal penetrates to the bottom of the pore and the electrode behaves as a flat one; then its impedance may be described by a semicircle on the complex plane plot [Fig. 35(b)].

Another limiting case is obtained when the penetration depth is much smaller than the pore length, $\lambda << l$, that is, the pores behave as semi-infinite channels; then $\Lambda \to \infty$, $\coth(\Lambda^{1/2}) \to 1$, and

$$\hat{Z} = \frac{R_{\Omega,p}}{\Lambda^{1/2}} = \left(\frac{\rho}{2\pi^2 r^3}\right)^{1/2} \hat{Z}_{el}^{1/2} \tag{200}$$

In this case the complex plane plot presents a deformed semicircle [Fig. 35(c)]. In such a case, plotting $Z_i = |Z|^2 \sin(2\varphi)$ vs. $Z_r = |Z|^2 \cos(2\varphi)$ gives a perfect semicircle.[146] Equation (200) is formally identical with Eq. (183) for the fractal model with $\phi = 0.5$, and these two models are indistinguishable.

In further work the impedance of the double layer was substituted by the CPE:

$$\hat{Z}_{el} = \left[1/\hat{Z}_f + (j\omega)^{\phi} T \right]^{-1} \tag{201}$$

An example of porous behavior was presented by Los *et al.*[147] for the hydrogen evolution reaction on $LaPO_4$-bonded Ni powder electrodes in 30% NaOH. Examples of the complex plane plots are shown in Fig. 36. Using the complex nonlinear least-squares (CNLS) fit, the parameters R_{ct}, T, and C_{dl} were determined.

(b) Rigorous treatment

It is obvious that de Levie's treatment is an approximation, because $\hat{Z}_f$, and in consequence $\hat{Z}_{el}$, are potential dependent. In a rigorous treatment, Eqs. (186) and (187) should be solved. The second derivative of Eq. (187),

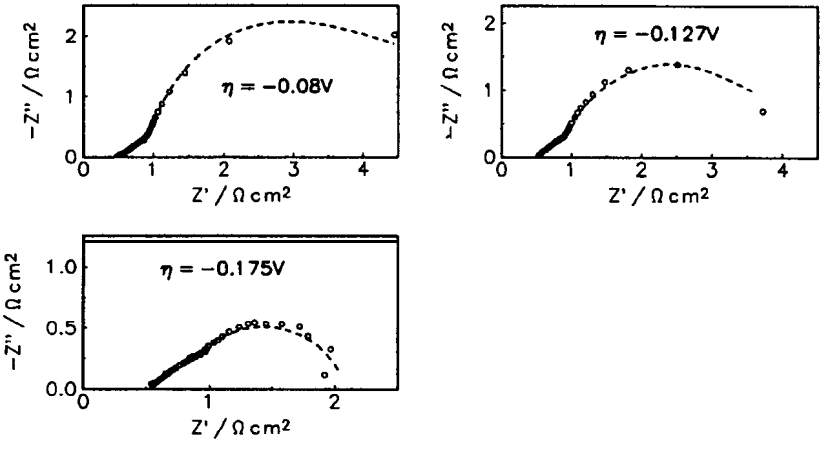

Figure 36. Complex plane plots for $LaPO_4$-bonded Ni powder electrodes during hydrogen evolution in 30% NaOH at 70°C.[147]

written using the Butler–Volmer expression for current and overpotentials, is[148,149]

$$\frac{d^2\eta}{dx^2} = \frac{2\rho}{r} j = \frac{2\rho j_0}{r}\left[e^{\alpha n f \eta} - e^{-(1-\alpha) n f \eta}\right] = \frac{2\rho j_0}{r}\left[e^{b_1 \eta} - e^{-b_2 \eta}\right] \tag{202}$$

Assuming that $\alpha = 0.5$ and $b = 0.5\, nf$, Eq. (202) may be written in a simpler form as

$$\frac{d^2\eta}{dx^2} = \frac{4\rho j_0}{r} \sinh(b\eta) \tag{203}$$

The first integration of Eq. (202) gives, taking into account that at $x = l$, $d\eta/dx = 0$, and $\eta_l = \eta(l)$:

$$\frac{d\eta}{dx} = -\{(4\rho j_0/r)[\exp(b_1\eta)/b_1 + \exp(-b_2\eta)/b_2$$

$$-\exp(b_1\eta_l)/b_1 - \exp(-b_2\eta_l)]\}^{1/2} \tag{204}$$

Equation (204) may be solved analytically only for the case of semi-infinite length of pores and for $\alpha = 1/2$, 1/3, and 2/3.[144] In a general case, it may be solved numerically. Let us consider now the case of semi-infinite pores, that is, when the potential at the bottom of the pore drops to 0, $\eta_l = 0$. In this case Eq. (204) may be rearranged to

$$\frac{d\eta}{dx} = -4\sqrt{\frac{\rho j_0}{r}} \sinh\left(\frac{b\eta}{2}\right) \tag{205}$$

which has a solution:

$$\tanh\left(\frac{b\eta}{4}\right) = \tanh\left(\frac{b\eta_0}{4}\right) \exp\left(-2\sqrt{\frac{\rho j_0 b}{r}}\, x\right) \tag{206}$$

It may be noticed that Eq. (206) is formally identical with that developed for the Gouy–Chapman theory of the double layer. Substitution of Eq. (189) into (205) gives the expression for the steady-state current on porous electrodes:

$$I = 4\pi r \sqrt{\frac{r j_0}{\rho b}} \sinh(b\eta_0/2) \tag{207}$$

which gives, at negative potentials, a Tafel slope of $2\ln(10)/\alpha f = 0.118/\alpha$ V at 25°C. This result indicates that the Tafel slope on porous electrodes is double its normal value.

If the potential distribution in pores is known, the pore impedance may be obtained by numerical summation of the impedances of small sections, Δx, of the pore walls, starting from the bottom of the pore:

$$\hat{Z}_i = \left(\frac{\rho}{\pi r^2}\right)\Delta x + 1/\left[(2\pi r\Delta x)/\hat{Z}_{\mathrm{el},i} + 1/\hat{Z}_{i-1}\right] \tag{208}$$

where $\hat{Z}_{\mathrm{el},i}$ is the specific electrode impedance at the distance x. The solution obtained may be compared with de Levie's solution [Eq. (195)]. Complex plane plots obtained for the same conditions using two different approaches are displayed in Fig. 37.

The analysis of the results indicates that the resistance at $\omega = 0$, R_p obtained using the correct analysis is twice that found from de Levie's equation. In addition, the plot of squared impedances produces a deformed ellipsoid instead of a perfect semicircle. It has been shown[147] that the CNLS fit of the simulated impedances to the de Levie equation (195) is not good, there being systematic differences between these two curves. However, when the CPE is used instead of the double-layer capacitance, the approximation is good. The values obtained for the parameter ϕ are between 0.91 and 0.93.[149] In this case the use of the CPE only hides the inadequacy of the model.

(ii) Porous Electrodes in the Presence of Axial Diffusion

During electrolysis, concentration changes in the pores. This problem has been addressed in numerous papers.[148,150–155] Simplifications such as assuming totally irreversible reaction kinetics, semi-infinite pores, or that the concentration gradient in pores is exponential were usually made. Recently, Lasia[156] solved the problem for a quasi-reversible process and a finite pore length. It was assumed that the electrode process could be described by the current overpotential equation:

$$j = j_0\left(\frac{C_{\mathrm{O}}}{C_{\mathrm{O}}^*}e^{b\eta} - \frac{C_{\mathrm{R}}}{C_{\mathrm{R}}^*}e^{-b\eta}\right) \tag{209}$$

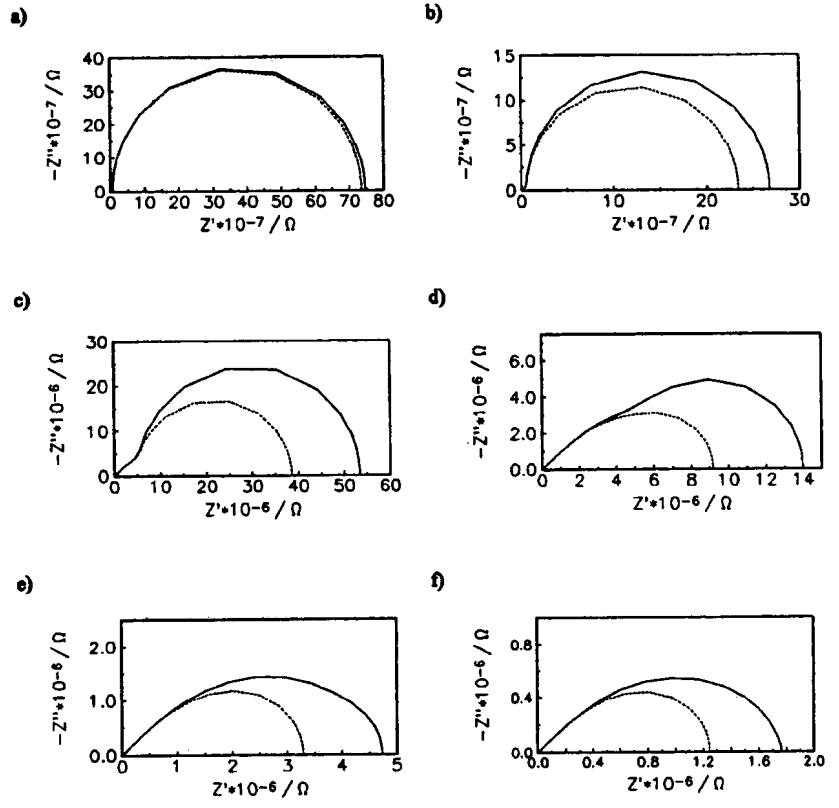

Figure 37. Complex plane plots for a porous electrode at different overpotentials; pore parameters: $l = 0.05$ cm, $r = 10^{-4}$ cm, $\rho = 10\ \Omega$ cm, $j_0 = 10^{-6}$ A cm^{-2}, η_0: (a) 0.025, (b) 0.1, (c) 0.2, (d) 0.3, (e) 0.4, and (f) 0.5 V; continuous lines, simulated; dashed lines, calculated using de Levie's model [Eq. (195)]. [149]

where C_i (i = O or R) and C_i^* represent surface and bulk concentrations of Ox and Red, respectively. Assuming that the diffusion coefficients of the two forms are identical, Eq. (209) can be rearranged into

$$j = j_0\left[a\left(e^{b\eta} + me^{-b\eta}\right) - (m+1)e^{-b\eta}\right] \tag{210}$$

where $a = C_O/C_O^*$ and $m = C_O^*/C_R^*$. The current flowing through the section dx of the pore walls is related to the changes in concentration:

$$j = -\frac{nF}{2\pi r dx}\frac{dN}{dt} = -\frac{nFr}{2}\frac{dC}{dt} \tag{211}$$

or taking into account diffusion:

$$\frac{\partial a}{\partial t} = D\frac{\partial^2 a}{\partial x^2} - \frac{2}{nFrC_O^*}j \tag{212}$$

which, under steady-state conditions, reduces to

$$\frac{d^2 a}{dx^2} - \frac{2}{nFrC_O^*}j = 0 \tag{213}$$

The potential drop in the pore is still described by Eq. (202), with the current given by Eq. (210). Equations (202) and (213) may be combined together as

$$\frac{d^2\eta}{dx^2} = \nu\frac{d^2 a}{dx^2} \quad \text{where} \quad \nu = nFDC_O^*\rho \tag{214}$$

Equation (214) has the analytical solution:

$$\eta - \eta_0 = \nu(a - 1) \tag{215}$$

which allows elimination of one variable from Eqs. (202) and (213). In a general case, the first integration may be carried out analytically and the next numerically. The derived dependence of η and a as functions of distance may be used to calculate the impedance.

The value of the parameter v determines whether the porous behavior is determined by the potential or the concentration drop. When $v << 1$ V, the system behavior is determined principally by the concentration gradient and when $v >> 1$ V, it is determined by the potential drop. For typical conditions, $D = 10^{-5}$ cm^2 s^{-1}, $\rho = 10\ \Omega$ cm, and $C^* = 10^{-3}$ to 10^{-2} M, $v \sim 10^{-5}$ to 10^{-4} V. For these conditions the porous behavior is determined by the concentration gradient and the potential gradient down pores is negligible. Only for extreme conditions where the solvent or the supporting electrolyte (at high concentration) undergoes the Red-Ox reaction may the process be limited by the potential drop in the pores.

In a limiting case when the potential drop in the pores may be neglected, an analytical solution of Eq. (213) may be obtained:

$$a = \gamma + (1-\gamma)\frac{\cosh\left[\sqrt{B}(l-x)\right]}{\cosh\left(\sqrt{B}\,l\right)} \tag{216}$$

where

$$\gamma = \frac{e^{2b\eta_0} + m}{m+1} \quad \text{and} \quad B = \frac{2j_0}{nFrDC_O^*}\left(e^{b\eta_0} + me^{-b\eta_0}\right) \tag{217}$$

If the dc solution is known, the electrode impedance may be calculated. As usual, the current [Eq. (212)], must be linearized:

$$\Delta j = \left(\frac{\partial j}{\partial \eta}\right)_a \Delta\eta + \left(\frac{\partial j}{\partial a}\right)_\eta \Delta a \tag{218}$$

Then the expression for the impedance is obtained as

$$\frac{1}{\hat{Z}_f} = \frac{\tilde{j}}{\tilde{\eta}} = \left(\frac{\partial j}{\partial \eta}\right) + \left(\frac{\partial j}{\partial a}\right)\frac{\tilde{a}}{\tilde{\eta}} \tag{219}$$

In order to find a solution for the oscillating concentration, Eq. (212) must be solved for Δa. Substitution and rearrangement gives

$$\frac{d^2(\tilde{a}/\tilde{\eta})}{dx^2} - \left(\frac{\tilde{a}}{\tilde{\eta}}\right)\left[\frac{j\omega}{D} + \frac{2}{nFrDC_O^*}\left(\frac{dj}{da}\right)\right] - \frac{2}{nFrDC_O^*}\left(\frac{dj}{d\eta}\right) = 0 \tag{220}$$

or

$$\frac{d^2\tilde{y}}{dx^2} - \tilde{y}K - L = 0 \tag{221}$$

where

$$\tilde{y} = \tilde{a}/\tilde{\eta} \quad K = \frac{j\omega}{D} + \frac{2}{nFrDC_O^*}\left(\frac{dj}{da}\right) \quad L = \frac{2}{nFrDC_O^*}\left(\frac{dj}{d\eta}\right) \tag{222}$$

with the boundary conditions:

$$x = 0 \qquad \tilde{y} = 0$$

and

$$x = l \qquad d\tilde{y}/dx = 0$$

The analytical solution of Eq. (221) is

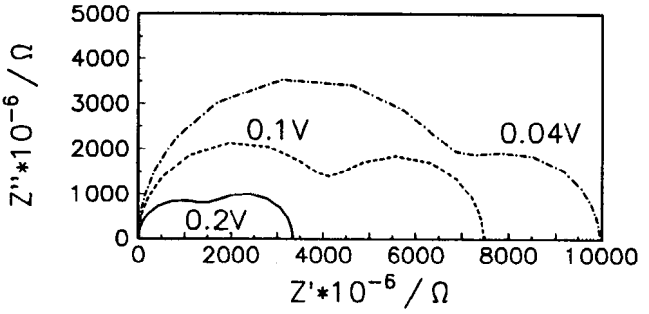

Figure 38. Complex plane plots for a porous electrode in the presence of a concentration gradient at different overpotentials; $l = 0.05$ cm, $r = 10^{-4}$ cm, $\rho = 10\ \Omega$ cm, $D = 10^{-5}$ cm^2 s^{-1}, $m = 1$, $j_0 = 10^{-7}$ A cm^{-2}, $C_O^* = 0.01$ M.

$$\frac{\tilde{a}}{\tilde{\eta}} = \frac{L}{K}\left\{-1 + \frac{\cosh\left[\sqrt{K}\,(l-x)\right]}{\cosh(\sqrt{K}\,l)}\right\} \tag{223}$$

Now, substitution into Eq. (219) gives the faradaic impedance and using Eq. (208), the total impedance may be calculated numerically. The presence of the concentration gradient in the pores produces two potential-dependent semicircles (Figs. 38 and 39). It should be added that at high frequencies a small part of a straight line at the angle of $\pi/4$ may still be observed as in Fig. 39, similarly to that in Figs. 35–37.

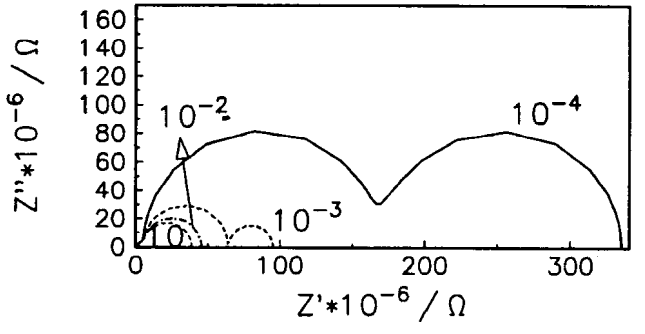

Figure 39. Influence of the depolarizer concentration on the complex plane plots for a porous electrode; $j_0 = 10^{-6}$ A cm^{-2}, $\eta = 0.2$ V; concentrations in mol cm^{-3} are indicated in the figure; other parameters as in Fig. 38.

In real cases, the problem is much more complicated, because various pores are present and in fact the pore size distribution and the exact surface morphology are not known.

(iii) Other Pore Geometries

For pores of a geometry different from the cylindrical, at high frequencies where the impedance is determined by double-layer charging, instead of a straight line, some forms of arc may also be obtained. The impedance of a V-grooved electrode was studied by de Levie.[157] Such surfaces may be prepared, for example, by abrasion. de Levie described the impedance of a groove per unit groove length as

$$\hat{Z} = \frac{\rho}{\tan\beta} \frac{I_0(\lambda)}{\lambda I_1(\lambda)} \tag{224}$$

where ρ is the specific solution resistance, β is the angle between the groove wall and the normal to the surface, I_0 and I_1 are the modified Bessel functions of zero and first order, and

$$\lambda = 2\sqrt{\frac{\rho l}{Z_s \beta}} \tag{225}$$

where l is the groove depth (normal to the surface) and Z_s is the double-layer impedance per unit of true surface area. Equation (225) reduces to the impedance of a perfectly flat surface for β = 90° and to the impedance of a cylindrical porous electrode for β = 0°. Recently, Gunning[158] obtained an exact solution of the de Levie grooved surface in the form of an infinite series. Comparison with the de Levie equation shows that the deviations arise at higher frequencies.

Keiser *et al.* [159] studied the impedance of arbitrarily shaped pores. They simulated the complex plane plots in the absence of a faradaic process (Fig. 40). Instead of a straight line at 45°, observed for cylindrical pores at high frequencies, different forms of plateaus or a semicircle were observed.

Eloot *et al.*[160] suggested a new general matrix method for calculations involving noncylindrical pores, in which the pore is divided into sections and for each section a transmission line model with constant impedances is used. Direct simulations of the impedances for porous electrodes were also carried out using a random walk method.[161,162]

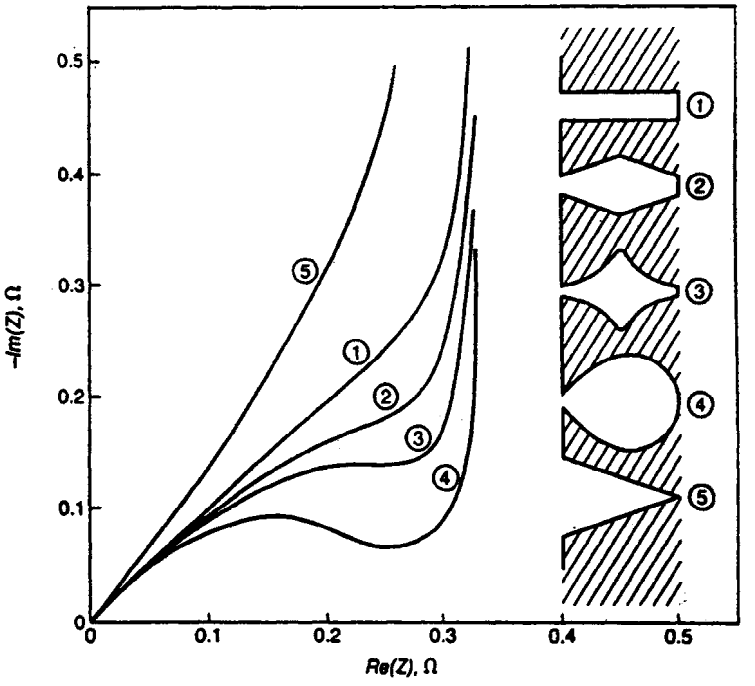

Figure 40. Calculated impedances for various shapes of a single pore blocking electrode. [159]

5. Generalized Warburg Element

Macdonald [18] introduced a generalized finite-length Warburg element described as

$$\hat{Z} = \frac{R_s}{A_0 R_s (j\omega)^{\phi}} \tanh\left[A_0 R_s (j\omega)^{\phi}\right] \tag{226}$$

to describe nonuniform diffusion under finite-length transmission conditions, where R_s is the solution resistance. For $\phi = 0.5$, $A_0 = l/(R_s\sqrt{D})$, which represents a finite-length diffusion. Nonuniform diffusion occurs, for example, when the diffusion coefficient is a function of the distance. This equation is formally identical with Stoynov's finite constant phase element BCP [Eq. (182)]. However, Stoynov[109] stated that Eq. (226)

represents uniform finite-length diffusion and not the nonuniform diffusion case.

A similar equation but containing the function coth was used by Inzelt and Láng [163] to describe the diffusional impedance of conducting polymers under reflective conditions [see Section III.6(ii) and Eq. (99)]. An electrical model containing this element accounted well for the impedance spectra, with a minimum number of free parameters.

Although models including impedance represented by Eq. (226) may well describe some experimental data, the physical significance of the parameter A_0 for $\phi < 0.5$ is not clear.

VI. CONDITIONS FOR "GOOD" IMPEDANCES

1. Linearity, Causality, Stability, Finiteness

The impedance technique is often applied to electrochemical systems that have not been studied before. The complex plane and Bode plots obtained often displayed shapes that had never been encountered previously. Before starting the analysis and modeling of the experimental results, one should be certain that the impedances are valid. There is a general mathematical procedure that allows verification of the impedance data. It was introduced by Kramers [164] and Kronig, [165] further developed by Bode,[166] and later applied to EIS.[18,167–177] During the impedance measurements, a small ac perturbation is applied to the system. The impedance derived is valid provided that the four criteria of linearity, causality, stability, and finiteness are met. [33,169]

- *Linearity*: A system is linear when its response to a sum of individual input signals is equal to the sum of the individual responses. This also implies that the system is described by a system of linear differential equations [see e.g., Eqs. (2) and (7)]. Electrochemical systems are usually highly nonlinear and the impedance is obtained by the linearization of equations [see e.g., Eqs. (42) and (130)] for small amplitudes. For linear systems, the response is independent of the amplitude. It is easy to verify the linearity of the system: if the impedance obtained is the same when the amplitude of the applied ac signal is halved, then the system is

linear. In addition, linear systems cannot exhibit hysteresis in their response at $\omega = 0$.

- *Causality*: The response of the system must be entirely determined by the applied perturbation; that is, the output depends only on the present and past input values. A causal system cannot predict what its future input will be. Causal systems are also called *physically realizable* systems. If the system is at rest and a perturbation is applied at $t = 0$, the response must be 0 for $t < 0$. In the complex plane, the above criterion requires that for $t < 0$, $\omega = 0$. Moreover, the integral on and inside a closed path C of an analytic function (i.e., it has a derivative at each point)[178] must be equal to 0:

$$\oint_C Z(s)ds = 0 \tag{227}$$

If the function $Z(s)$ has singularities, then the sum of the residuals of the poles a_i must equal 0:

$$\frac{1}{2\pi j}\oint_C \frac{Z(s)}{s - a_i} ds = f(a_i) \quad \text{and} \quad \sum_i f(a_i) = 0 \tag{228}$$

Equations (227) and (228) are mathematical forms of causality. The system is causal if it does not have any singularities [Eq. (227)], or the sum of residues is 0 [Eq. (228)]. The physical meaning of these equations is that the system does not generate noise independent of the applied signal.

- *Stability*: The stability of a system is determined by its response to inputs. A stable system remains stable unless it is excited by an external source, and it should return to its original state once the perturbation is removed and the system cannot supply power to the output irrespective of the input. The system is stable if its response to the impulse excitation approaches 0 at long times or when every bounded input produces a bounded output. Mathematically this means that the function does not have any singularities that cannot be avoided. The impedance $Z(s)$ must satisfy the following conditions: $Z(s)$ is real when s is real (that is, when $\omega \to 0$) and $\mathrm{Re}[Z(s)] \geq 0$ when $v \geq 0$ [$s = v + j\omega$, see Section I.1(i)]. This last condition ensures that there are no negative resistances in the system. The impedance measurements must also

be stationary; that is, the measured impedance must not be time dependent. This condition may be easily checked by repetitive recording of the impedance spectra; then the Bode plots obtained should be identical.

- *Finiteness*: The real and imaginary components of the impedance must be finite valued over the entire frequency range $0 < \omega < \infty$. In particular, the impedance must tend to a constant real value for $\omega \to 0$ and $\omega \to \infty$.

2. Kramers–Kronig Transforms

The Kramers–Kronig relations hold provided the four above constraints are satisfied and (1) allow the calculation of the imaginary impedance from the real part:

$$Z''(\omega) = -\left(\frac{2\omega}{\pi}\right)\int_0^\infty \frac{Z'(x) - Z'(\omega)}{x^2 - \omega^2}\,dx \tag{229}$$

(2) the real impedance from the imaginary part, if the high-frequency asymptote for the real part is known:

$$Z'(\omega) = Z'(\infty) + \frac{2}{\pi}\int_0^\infty \frac{zZ''(\omega) - \omega Z''(\omega)}{x^2 - \omega^2}\,dx \tag{230}$$

(3) the real impedance from the imaginary part, if the zero-frequency asymptote of the real part is known:

$$Z'(\omega) = Z'(0) + \left(\frac{2\omega}{\pi}\right)\int_0^\infty \frac{\left(\frac{\omega}{x}\right)Z''(x) - Z''(\omega)}{x^2 - \omega^2}\,dx \tag{231}$$

(4) the polarization resistance R_p from the imaginary part:

$$R_p = Z'(\infty) - Z'(0) = \left(\frac{2}{\pi}\right)\int_0^\infty \frac{Z''(x)}{x}\,dx \tag{232}$$

or (5) the phase angle from the magnitude (modulus):

$$\varphi(\omega) = \left(\frac{2\omega}{\pi}\right)\int_0^\infty \frac{\ln|Z(x)|}{x^2 - \omega^2}\,dx \tag{233}$$

Similar transformations may also be carried out for admittances. Such procedures are important when the impedance goes to infinity at low frequencies (blocking electrodes, CPE, semi-infinite mass transfer, etc.). The major difficulty in applying the Kramers–Kronig relations is that the integration must be performed over the whole frequency range from zero to infinity. However, the impedance results are known only over a finite frequency range. The discrepancies that arise may be attributed to errors of integration or to failure to satisfy the four above conditions.

Kendig and Mansfeld [179] used Eq. (232) and supposed that the imaginary impedance is symmetric. They carried out integration between the frequency corresponding to the maximum of the imaginary impedance and infinity, and multiplied the result by 2. However, their method is limited to systems containing one time constant.

Macdonald *et al.* [167–169] and Dougherty and Smedley [177] used a polynomial approximation of the impedance function, followed by analytical integration of the polynomials. However, extrapolation of polynomials over a large frequency range may be unreliable. Haili [180] extrapolated Z'' as proportional to ω as $\omega \to 0$ and as inversely proportional to ω as $\omega \to \infty$ and $Z' \to R_s$.

Esteban and Orazem [170,171] proposed using Eqs. (230) and (231) simultaneously to calculate the impedance below the lowest measured frequency, ω_{min}, and to continue the integration procedure to three or four decades of smaller frequency, ω_0. The latter parameter is chosen in such a way that the real impedance goes to a constant value while the imaginary impedance goes to 0 at ω_0.

Later, Orazem and co-workers [175,181,182] used an approximation to the experimental impedance by the Voigt model (Fig. 41) followed by a transformation of the model data. To take into account the inductive loops, they proposed using negative resistances. This method was used to approximate the impedance from various circuits containing resistive, capacitive, and inductive elements; Warburg impedance; CPE; etc. Because each parallel *R-C* circuit is transformable, the entire circuit must also be transformable. In this method the explicit Kramers–Kronig integration is replaced by the fit to the Voigt model. If the data cannot be well approxi-

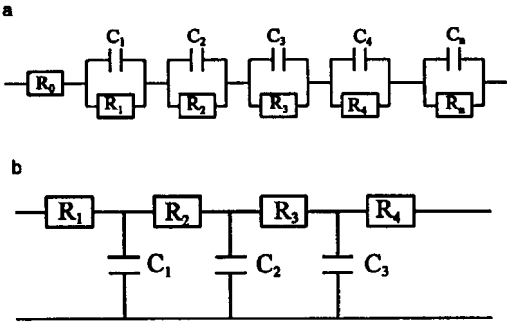

Figure 41. (a) Voigt and (b) ladder models.

mated, it means that they are not transformable. Such an approximation may be written as

$$Z'(\omega) = R_s + \sum_{k=1}^{M} \frac{R_k}{1 + (\omega R_k C_k)^2} = R_s + \sum_{k=1}^{M} \frac{R_k}{1 + (\omega\tau_k)^2} \tag{234}$$

and

$$Z''(\omega) = -\sum_{k=1}^{M} \frac{\omega R_k \tau_k}{1 + (\omega\tau_k)^2} \tag{235}$$

where $\tau_k = R_k C_k$ and M is the number of R-C elements used in the Voigt circuit to approximate the experimental impedance. The problem with this approach is the initial selection of R_k and C_k parameters in the complex nonlinear least-squares approximation, which are unknown. Similarly, Boukamp and Macdonald [183] proposed an approximation of the experimental impedances using a distribution of relaxation times. They represented the function $G(\tau)$ in Eq. (173), written for immittances, as a sum of M discrete delta functions: $G(\tau) = \Sigma_{m=1}^{M} g_m \delta(\tau - \tau_m)$, where g_m are dimensionless weighting coefficients and τ_m are characteristic time constants to be determined.

This method was further modified by Boukamp,[184] who also used the Voigt circuit but with a fixed distribution of time constants τ_k; that is, the time constants were defined and the adjustable parameters were R_k. Parameters τ_k were chosen as equal to the inverse of the experimental

angular frequencies ω_k, which are usually logarithmically distributed (5 to 10 per decade). Under such conditions, Eqs. (234) and (235) become linear in the R_k values and the problem of approximation reduces from iterative nonlinear to a linear single-matrix inversion. The method is quite robust with respect to the choice of the distribution and range of τ_k values. In practice, six to seven time constants per frequency decade ($\tau_k = 1/\omega_k$) should be selected to get a good approximation. Through inspection of the relative residual plots, it is possible to isolate data that do not comply with the Kramers–Kronig transformations. The sign of R_k parameters is not important, but the time constants are always positive (by definition); the negative τ_k could mask some non-Kramers–Kronig transformable behavior.

Macdonald [185] proposed another form of the Kramers–Kronig integrals in which integration to infinity and the poles are avoided. In the case of blocking electrodes, the impedance goes to infinity as $\omega \to 0$. For such electrodes, the admittance Kramers–Kronig transformation could be used. Alternatively, a suitable parallel resistance could be added to the system (in such a system the impedance must always be real and equal to this shunt resistance at $\omega = 0$) and then the transformation of the data obtained [186] can be carried out. In general, Kramers–Kronig transforms constitute a very sensitive criterion of the validity of the ac impedance data. An example of such an analysis is shown in Fig. 42.[177]

It has been shown that instead of Kramers–Kronig transforms, another method involving a coherence function [28,187] could be used to validate the data. The coherence function, γ, is defined as [188,189]

$$\gamma_{xy} = \left(\frac{\overline{S_{xy}}\,\overline{S_{xy}^*}}{\overline{S_{xx}}\,\overline{S_{yy}}} \right)^{1/2} \tag{236}$$

where $\overline{S_{xx}}$ is the average input signal power spectrum, $\overline{S_{yy}}$ is the average output signal power spectrum, $\overline{S_{xy}}$ is the average crosspower spectrum, the symbol * denotes the complex conjugate, and $S_{xx}(\omega)$ is the power spectrum of parameter x as defined by its Fourier transform X:

$$S_{xx}(\omega) = X(\omega)X^*(\omega) \tag{237}$$

The power spectra may be directly obtained using dynamic signal analyzers that measure signals as a function of time and perform the fast Fourier transform. The coherence function takes values betweaen 0 and 1 and characterizes statistical validity of the frequency response measurements:

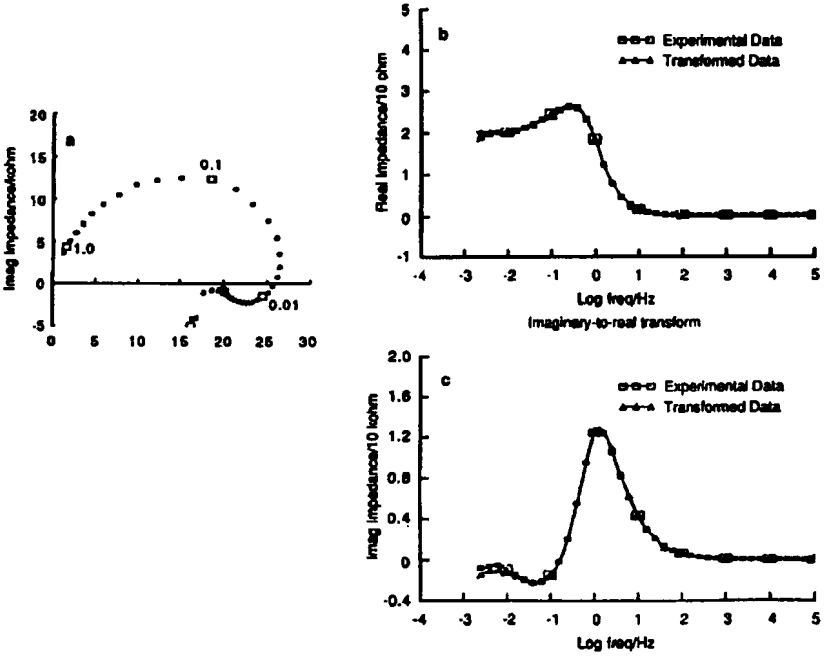

Figure 42. Impedance spectrum for an Al electrode in (a) water and (b), (c) its Kramers–Kronig transforms. [177]

it is equal to 1 when perfect coherence exists. This function may be used when the Fourier-transformed data exist and the Kramers–Kronig transforms are difficult to use (unbounded impedance, truncated data, etc.). [187]

3. Nonstationary Impedances

As mentioned earlier, the measured system should be stationary and should not evolve with time. In practice, such conditions cannot always be met. For example, corrosion processes may continue during the experiment and change the measured impedance. Such measurements should be carried out quickly. However, very often the most interesting features are observed at low frequencies and the experiment may take hours. In such cases it is possible to follow the evolution of impedances with time at one frequency and then repeat the experiment many times at different frequencies. [190] In order to use such a method, the initial conditions must always

be the same. This method was used recently to follow the electrochemical impedance of a guillotined aluminum electrode.[190] Stoynov *et al.*[191–194] introduced a new mathematical method for nonstationary impedances involving four-dimensional analysis and rotating Fourier transforms. Although the simulations were carried out, they were not applied in experimental studies of nonstationary systems.

VII. MODELING OF EXPERIMENTAL DATA

1. Selection of the Model

The objective of analyzing EIS data is to elucidate the electrode process and to derive its characteristic parameters. It should be stressed here that EIS is a very sensitive technique, but it does not provide a direct measure of physical phenomena. Other electrochemical experiments (dc, transients) should also be carried out, together with good physical knowledge of the system (solution and surface composition, thickness, porosity, the presence of various layers, hydrodynamic conditions, etc.). Interpretation of impedance data requires the use of an appropriate model. This is a quite difficult task that must be carried out very carefully.

The modeling may be classified as (1) physicochemical, process,[175,181,195,196] or structural[19,197,198,199] modeling and (2) measurement,[195,196] formal,[19] or mathematical[200,201] modeling. Process modeling links measured impedances with physicochemical parameters of the process (kinetic parameters, concentrations, diffusion coefficients, sample geometry, hydrodynamic conditions, etc.). Measurement modeling explains the experimental impedances in terms of mathematical functions in order to obtain a good fit between the calculated and experimental impedances. In the latter case, the parameters obtained do not necessarily have a clear physicochemical significance.

Ideally, first the measurement modeling should be carried out. The number and the nature of the circuit elements should be identified and then the process modeling should be carried out. Such a procedure is relatively elementary for a circuit containing simple elements: *R, C,* and *L.* It may also be carried out for circuits containing distributed elements that can be described by a closed-form equation: CPE, semi-infinite, finite length, or spherical diffusion, etc. However, many different conditions arise from the numerical calculations (e.g., for correct solution for porous electrodes, for

nonlinear diffusion, whether it is to a disk, cylinder, etc.; or for nonuniform diffusion, nonhomogeneous materials such as conducting polymers). In such cases *a priori* model predictions are difficult or impossible to make. It should be stressed that proper modeling is the most difficult part of the analysis and is often misunderstood and wrongly interpreted.

Usually an equivalent circuit is chosen and the fit to the experimental data is performed using the complex nonlinear least-squares technique. However, the model deduced from the reaction mechanism may have too many adjustable parameters, while the experimental impedance spectrum is simple. For example, a system with one adsorbed species (Section IV.2) may produce two semicircles in the complex plane plots, but experimentally, often only one semicircle is identified. In such a case, approximation to a full model introduces too many free parameters and a simpler model containing one time-constant should be used. Therefore, first the number and nature of parameters should be determined and then the process model should be constructed in consistency with the parameters found and the physicochemical properties of the process.

Another problem of data modeling is connected with the fact that the same data may be represented by different equivalent circuits. [200] For example, a system containing one capacitive loop (Fig. 4) may be exactly described by either of the two equivalent circuits shown in Fig. 43. In fact, the admittance of these two circuits may be written in the general form:

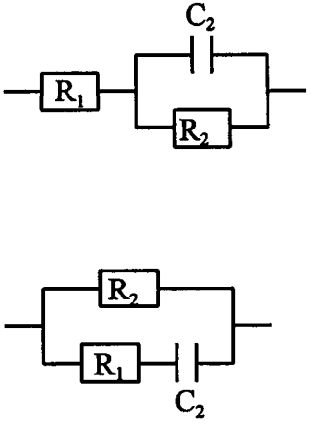

Figure 43. Alternative circuits for the impedance behavior of a system containing one capacitive loop.

$$Y = \frac{a_1 j\omega + a_0}{j\omega + b_0} = a_1 + \frac{a_0 - a_1 b_0}{j\omega + b_0} \tag{238}$$

where

$$a_1 = R_1^{-1},\ a_0 = 1/(C_2 R_1 R_2) \text{ and } b_0 = (R_1^{-1} + R_2^{-1})/C_2 \text{ for circuit (a)} \tag{239}$$

or

$$a_1 = R_1^{-1} + R_2^{-1},\ a_0 = 1/(C_2 R_1 R_2) \text{ and } b_0 = 1/(R_1 C_2) \text{ for circuit (b)}$$

and these two cases are indistinguishable. Equation (238) indicates that there is only one time-constant of the system [see Eq. (25)]. Similarly, a system displaying two capacitive loops (i.e., having two time-constants, Fig. 23), may be adequately described by the three circuits in Fig. 44. Their admittance may be written as

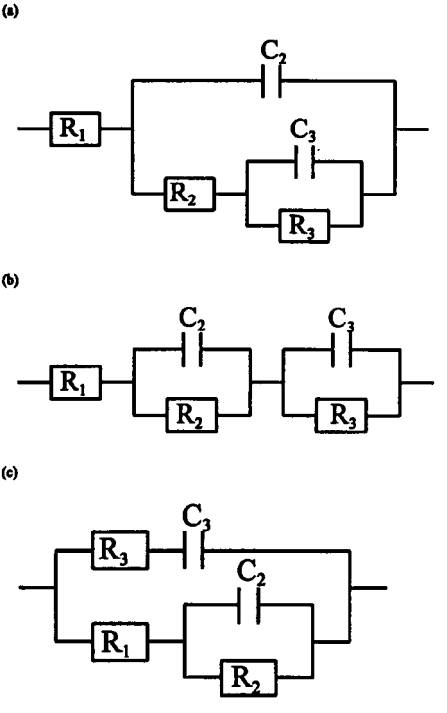

Figure 44. Three circuits describing a system displaying two capacitive loops: (a) ladder, (b) Voigt, and (c) mixed.

$$Y = \frac{a_2(j\omega)^2 + a_1 j\omega + a_0}{(j\omega)^2 + b_1 j\omega + b_0} \tag{240}$$

The behaviors of these three circuits are also indistinguishable; that is, for a proper choice of the parameters, they display the same impedance spectrum at all frequencies.

The circuits most often used in measurement modeling are the Voigt, ladder, and Maxwell circuits, as presented in Fig. 45. Zoltowski[200] proposed using ladder circuits for measurement modeling, substituting circuit resistances and capacitances by the CPE elements.

Very often modeling depends on the errors in the experimental data. Orazem *et al.*[196] studied the approximation of synthetic data corresponding to the impedance response of a single electrochemical reaction on a rotating disk electrode under the conditions of nonuniform current and

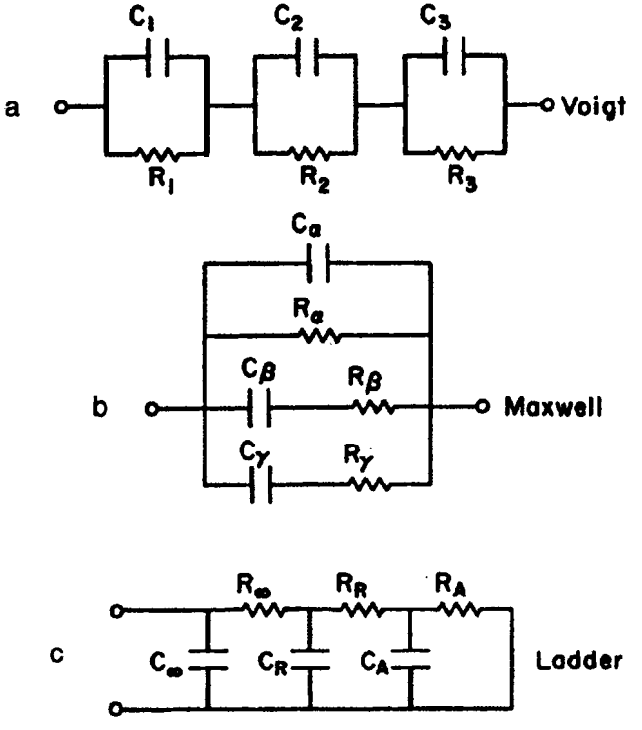

Figure 45. Typical circuits used in ac modeling; they are experimentally indistinguishable: (a) Voigt, (b) Maxwell, and (c) ladder.[18]

potential distribution. The complex plane plot represented a depressed semicircle. The authors found that the input data could be quite well approximated by a circuit consisting of a solution resistance in series with the parallel connection of a resistance and a CPE element (see Fig. 28) and three other circuits containing two time constants (ladder, Voigt, and mixed). These authors also studied a more complex case. They stated that the ambiguity demonstrated above is common to model identification for all electrochemical measurements and presents the greatest challenge for the analysis of impedance data. For example, impedance of a porous electrode may be described by the Voigt circuit with a sufficient number of *R-C* elements or by Eq. (195). Development of a proper model requires knowledge of the chemistry and physics of the system, some prior information about it, and a good understanding of the characteristics of the measured values. Such a model identification procedure should be supported by a series of measurements at different potentials, temperatures, concentrations, disk rotation rates, etc.

Stoynov and collaborators [19,197–199] developed mathematical methods for identifying structures and parameters from impedance data. They also used spectral analysis, which could identify the number and nature of time constants existing in the system.

Direct use of equivalent circuits may lead to analysis of more complex data. For example, for a system containing one adsorbed species, Eq. (139) may be described by the ladder circuit shown in Fig. 21. The parameters R_a and C_a describing the faradaic impedance [Eq. (141)] are complex functions of the parameters *A, B,* and *C;* while direct use of Eq. (135) leads to simpler data analysis (i.e., parameters *A, B,* and *C* are simpler functions of the kinetic parameters than the electric parameters R_a and C_a).

2. CNLS Approximations

(i) CNLS Method

After validated data are obtained, one can proceed with modeling. To do this, a complex nonlinear least-squares (CNLS) program is used.[18,202–204] This is a nonlinear least-squares fit of the real and imaginary parts, or the magnitude and phase angle of the experimental impedance and admittance to a given model. In general, the sum of squares:

$$S = \sum_{i=1}^{N} \left\{ w_i' \left[Z_i' - Z_{i,\mathrm{calc}}' \right]^2 + w_i'' \left[Z_i'' - Z_{i,\mathrm{calc}}'' \right]^2 \right\} \tag{241}$$

must be minimized, where Z'_i and Z''_i are the real and imaginary parts of the experimental impedances at the frequencies ω_i; $Z'_{\mathrm{i,calc}}$ and $Z''_{\mathrm{i,calc}}$ are the values calculated from a given model; w_i' and w_i'' are the statistical weights of the data; and the summation runs over all N experimentally used frequencies. The minimization is most often carried out using the iterative Marquard–Levenberg algorithm.[202,203,205] Because of the iterative nature of the algorithm, the initial choice of the parameters is very important: they must lie relatively close to the real values, otherwise the CNLS method may become divergent. Usually a simpler model is used first; several parameters are determined; then they are kept constant as new parameters are added; and finally, all the parameters are used as adjustable. Such a procedure may be tricky and in some cases local minima are found. In such cases, it is advisable to repeat the approximation starting with different initial parameter values. If the process converges to another minimum, the relative values of the weighted sum of squares or χ^2 should be compared. Sometimes very flat minima are obtained, leading to large values of the relative standard deviations of the measured parameters.

Another problem is connected with the goodness of fit and the number of free parameters used in the approximating function. The identification procedure may give the number and nature of the elements in the circuit. The number of adjustable parameters should be kept to a minimum. Usually the approximation starts with the smallest possible number of parameters; then an additional parameter is added and the decrease in the sum of squares must be compared. Such a decrease must be statistically important. It may be tested using the F-test for the additional parameter.[206] The addition of some elements in the circuit may be connected with the addition of more than one parameter. The F-test of the addition of k parameters to the approximating function is described as

$$F_{\mathrm{exp}} = \frac{[S(N-p) - S(N-p-k)]/k}{S(N-p)/(N-p)} \tag{242}$$

where $S(N-p)$ is the sum of squares [Eq. (241)] for p parameters and N-p degrees of freedom, $S(N-p-k)$ is the sum of squares for $p+k$ free parameters; and N is the number of points. This parameter should be compared with the function $F(k,N-p,\alpha)$ for k and $N-k$ degrees of

freedom, and a level of confidence α, from the statistical tables. If F_{exp} is lower than $F(k,N-k)$, the hypothesis that the function has $p + k$ parameters must be rejected. This test should be used with prudence and always the *smallest possible number of added parameters k* should be used. It may happen that when k parameters are added, only the first one increases the value of $F_{exp} > F(1,N-1,\alpha)$, although for k parameters F_{exp} is also $> F(k,N-k,\alpha)$.

In addition to comparing the sum of squares, the experimental and simulated data should be compared by using complex plane and Bode plots. The phase-angle Bode plot is particularly sensitive in detecting time constants. Boukamp [203] proposed to study the residual sum of squares after subtracting the assumed model values from the total impedance data. If the model is valid, the residuals should behave randomly. If they display regular tendencies, it may mean that the model is not correct and further elements should be added. However, the variations of the residuals should be statistically important.

Macdonald [207] studied precision of the parameters determined by EIS. He added noise to the simulated impedance data and used the CNLS technique to determine the parameters and their standard deviation. Using this technique, it was possible to determine how the impedance errors are transferred to the determined parameters, depending on their relative values. This method allows sensitivity of the parameters to the random noise to be determined.

(ii) Statistical Weights

The choice of statistical weights in the CNLS fit is very important. Because the measured impedances may vary at different frequencies over several orders of magnitude when unitary weights ($w_i = 1$) are used, only the largest impedances contribute to the sum of squares *S*. In such a case, low time constants may be overlooked. In general, several repetitions of the experiment allow the standard deviation of each point (σ'_i and (σ''_i) to be determined, and the statistical weights may be obtained as $w'_i = (\sigma'_i)^{-2}$ and $w''_i = (\sigma''_i)^{-2}$. Although this is the best approach, such a procedure is time-consuming and rarely used in practice. Another alternative proposed by Macdonald [18] was to use proportional weighting, that is, taking weights inversely proportional to the measured or estimated impedances: $w_i = 1/Z_i^2$ or $w_i = 1/Z^2_{i,calc.}$ Such weighting methods mean that the real and imaginary parts of the impedance may be independently determined and

that their precisions are independent. However, in practice, these parameters are often measured using the same sensitivity for both components; therefore a better weighting procedure may be the use of modulus weighting: $w_i = 1/(Z'^2 + Z''^2)$.[203,208]

Orazem and co-worker[195,196,209,210] studied the error structure of the impedances measured using a Solartron frequency-response analysis. They found that the standard deviations of the real and imaginary impedances are identical and may be described by

$$\sigma_i = \alpha|Z_i'| + \beta|Z_i''| + \gamma\frac{|Z_i|^2}{R_m} \tag{243}$$

where α, β, and γ are constant parameters determined for a given instrumental system and R_m is the value of the current-measuring resistor. Such an error structure was verified for solid-state and electrochemical systems under a wide variety of experimental conditions and for errors ranging from milliohms to megaohms and allowed for better determination of system parameters.

(iii) AC Modeling Programs

Several programs for EIS modeling are available:

- J.R. Macdonalds's program,[18,202] written in Fortran, source code is available. It contains various models already predefined, many weighting possibilities, and allows for easy modifications of the subroutines for the model impedance calculations. Fortran is a language that contains intrinsically complex number calculations, which facilitates the programming process. Its disadvantage is a special formatted data input (however, it can be easily corrected).
- Boukamp's program,[203] written in Pascal and distributed with EG&G software, is very popular. Equivalent circuits are constructed from several predefined elements. However, there is no possibility of changing the subroutines or introducing new equations.
- Scribner Associates, Inc. developed a software (Zplot) for data acquisition and analysis. It is based on Macdonald's algorithm and the data analysis has been simplified. It uses a number of predefined circuits without the possibility of modification.

- Sirotech Ltd.[211] developed software that performs a similar task and is able to choose the best equivalent circuit.
- Several software packages (often with very limited modeling capabilities) come with the hardware; for example, from Gamry Instruments, Inc.: EIS900; BAS-Zahner (Thales); Eco Chemie BV: Autolab; Tacussel: ZComputer, etc.
- Some other programs have been developed in the literature without being widely commercialized.[204,212–215]

VIII. INSTRUMENTAL LIMITATIONS

EIS measurements should be carried out over a wide frequency range in order to identify all time-constants in the circuit (usually 10 frequencies per decade). The highest frequency depends on the potentiostat used because it may introduce a phase shift at high frequencies and on the stray capacitance and inductance of the experimental setup (cables, cell, etc.). A typical range in modern systems is 20 to 50 kHz, although they may reach megahertz values. With an increase in sensitivity, the potentiostats tend to slow down and the response on a 10-mA current scale is much faster than that on 10-μA scale. Much higher frequencies up to 10 MHz were used by Barański *et al.*[216,217] but the experiments were carried out on ultramicroelectrodes without a potentiostat. Corrections for slow response of the potentiostat may be made and the increases the effective bandwidth by about one order of magnitude.[218] If the response of the electronic system is linear, the parasitic impedances, $\hat{Z}_{in}$ and $\hat{Z}_{oc}$, together with the complex sensibility, $\hat{S}$ (Fig. 46) may be obtained from

$$\hat{S}\hat{Z}_m = \hat{Z}_{in} + \frac{1}{\frac{1}{\hat{Z}_{el}} + \frac{1}{\hat{Z}_{oc}}} \tag{244}$$

where $\hat{Z}_m$ is the measured impedance and $\hat{Z}_{el}$ is the impedance of the electrochemical cell. Three measurements—one in the open circuit and two with two different resistances instead of $\hat{Z}_{el}$—allow the determination of three unknown complex parameters and further correction of the measured impedance. Such corrections should be repeated at each frequency, and the cable configuration used for calibration should be the same as for the electrochemical measurements. Schöne and Wiesbeck[219]

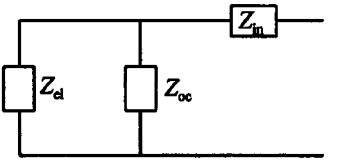

Figure 46. Equivalent circuit for the case of a slow response of the potentiostat.

proposed another method involving two working electrodes for high-frequency (≤ 5 MHz) impedance measurements.

The lowest frequency typically used is 10^{-3} Hz. This limit is connected with the possible changes in the state of the electrode during long-period measurements. At this frequency, measurements averaged over five wave periods take 1 h 23 min. Measurement at all frequencies takes a much longer time. *

The use of FRAs may lead to erroneous results when the frequency is swept too fast. [30,220] The change of frequency may lead to a transient regime. If the measurements are performed during this transient, error is introduced into the results. It depends on the initial phase of the sinusoidal excitation. It can be neglected when 10 cycles of signal integration and at least 5 steps per decade are used in measurements. This error becomes negligible at higher frequencies (> 10 Hz for the Solartron) because of the internal delay of the measurements at each frequency.

It is relatively easy to get measurements of good precision for impedances between 1 and 10^5 Ω at frequencies below 5×10^4 Hz. However, for lower and higher impedances, distortions may be observed. Very high impedances are found, for example, in measurements of protective coatings on metallic surfaces, and very low impedances are found in molten salts. The errors for high-impedance measurements originate from the finite potentiostat input impedance. Such resistance should be at least 100 times larger than the measured impedance; if not, a calibration procedure is necessary.

Another distortion is observed at very low impedances, corresponding to an inductance in series with the electrode impedance. It is observed at high frequencies and leads to large positive imaginary impedances. [221,222] This inductance arises from that of the leads and the current

* Comparison of results from log "up" vs log "down" scans of frequency are then useful for detecting systematic changes of response with time.

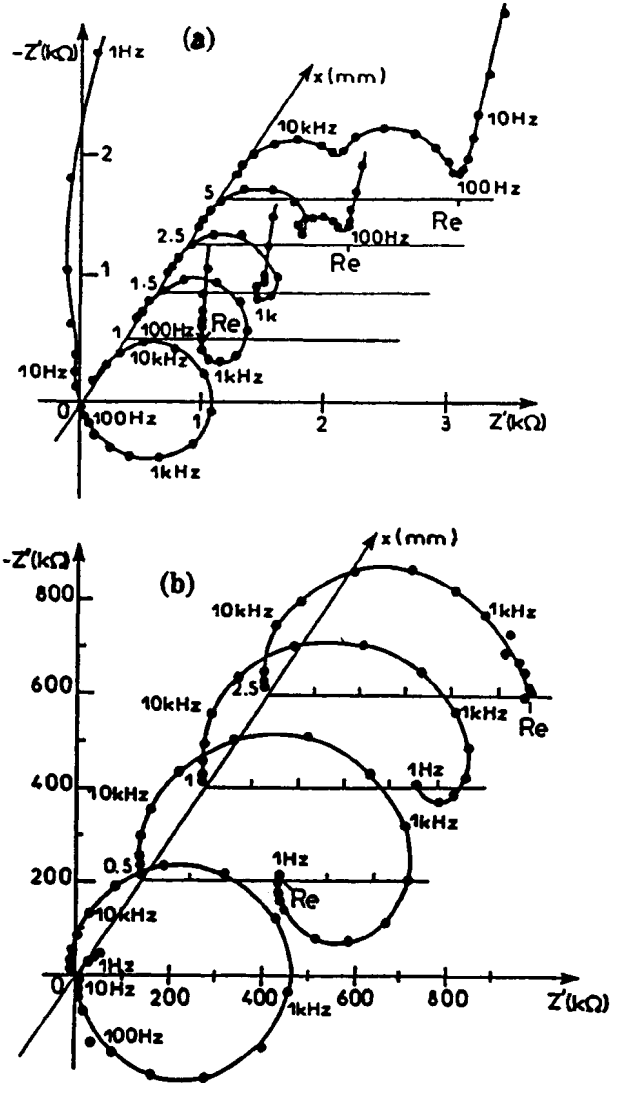

Figure 47. Impedance diagrams for different distances x between the working electrode and the Luggin capillary tip in (a) 80% acetic acid and (b) 100% acetic acid.[223]

measuring resistor. Often, such effects may be minimized by shortening the cables and shielding the reference electrode.

The distance between the working electrode and the Luggin capillary may also affect the impedance measurements and lead to artifacts.[223] In principle, an increase in the distance between the Luggin capillary tip and working electrode should only increase the solution resistance, which shifts the complex plane plot along the real axis. Figure 47 presents examples of the complex plane plots obtained at several distances in acetic acid. Such behavior arises from the contribution of the reference electrode to the measured impedances and it was explained by introducing the resistance and capacitance of the reference electrode and a capacitive coupling between the reference electrode and counter and working electrodes.[223] Similar artifacts, observed at high frequencies, are also observed in highly conducting solutions [224] when the Luggin capillary is located too close to the electrode surface. These artifacts can be minimized by inserting a thin platinum wire into the Luggin capillary and the salt bridge.[224–226]

IX. CONCLUSION

Electrochemical impedance spectroscopy has become a mature and well-understood technique. It is now possible to acquire, validate, and quantitatively interpret the experimental impedances. This chapter has been addressed to understanding the fundamental processes of diffusion and faradaic reaction at electrodes. However, the most difficult problem in EIS is modeling the electrode processes, which is where most of the problems and errors arise. There is an almost infinite variety of different reactions and interfaces that can be studied (corrosion, coatings, conducting polymers, batteries and fuel cells, semiconductors, electrocatalytic reactions, chemical reactions coupled with faradaic processes, etc.) and the main effort is now being applied to understanding and analyzing these processes. These applications will be the subject of a second review in a forthcoming volume in this series.

REFERENCES

[1] D. C. Graham, *Chem. Rev.* **41** (1947) 441.
[2] R. Parsons, in *Modern Aspects of Electrochemistry,* Vol. 1, Plenum, New York, 1954, p. 103.

[3]P. Delahay, *Double Layer and Electrode Kinetics,* Wiley-Interscience, New York, 1965.
[4]D. M. Mohilner, in *Electroanalytical Chemistry,* A. J. Bard, ed., Vol. 1, Marcel Dekker, New York, 1966, p. 241.
[5]B. Breyer and H. H. Bauer, *Alternating Current Polarography and Tensammetry, Chemical Analysis Series,* P. J. Elving and I. M. Kolthoff, eds., Wiley-Interscience, New York, 1963.
[6]D. E. Smith in *Electroanalytical Chemistry,* A. J. Bard, ed., Vol. 1, Marcel Dekker, New York, 1966, p. 1.
[7]A. M. Bond, *Modern Polarographic Techniques in Analytical Chemistry,* Marcel Dekker, New York, 1980.
[8]P. Delahay, *New Instrumental Methods in Electrochemistry,* Interscience, New York, 1954.
[9]K. J. Vetter, *Electrochemical Kinetics,* Academic Press, New York, 1967.
[10]D. D. Macdonald, *Transient Techniques in Electrochemistry,* Plenum, New York, 1977.
[11]A. J. Bard and L. R. Faulkner, *Electrochemical Methods,* Wiley, New York, 1980.
[12]*Instrumental Methods in Electrochemistry,* Southampton Electrochemistry Group, Ellis Horwood, Chichester, UK, 1985.
[13]E. Gileadi, *Electrode Kinetics for Chemists, Engineers, and Material Scientists,* VCH, New York, 1993.
[14]C. M. A. Brett and A. M. Oliveira Brett, *Electrochemistry, Principles, Methods, and Applications,* Oxford, Oxford University Press, 1993.
[15]Z. Galus, *Fundamentals of Electrochemical Analysis,* Ellis Horwood, New York, 1994.
[16]H. B. Oldham and J. C. Myland, *Fundamentals of Electrochemical Science,* Academic Press, San Diego, CA, 1994.
[17]I. Rubinstein, ed., *Physical Electrochemistry, Principles, Methods, and Applications,* Marcel Dekker, New York, 1995.
[18]J. R. Macdonald, *Impedance Spectroscopy Emphasizing Solid Materials and Systems,* Wiley, New York, 1987.
[19]Z. B. Stoynov, B. M. Grafov, B. S. Savova-Stoynova, V. V. Elkin, and B. B. Damaskin, *Electrochemical Impedance,* Nauka, Moscow, 1991 (in Russian).
[20]R. D. Armstrong, M. F. Bell, and A. A. Metcalfe, in *Electrochemistry. A Specialist Periodical Report,* H.R. Thirsk, ed., Vol. 6, Chemical Society, Burlington House, London, 1978, p. 98.
[21]W. I. Archer and R. D. Armstrong, in *Electrochemistry. A Specialist Periodical Report,* H.R. Thirsk, ed., Vol. 7, Chemical Society, Burlington House, London, 1980, p. 157.
[22]D. D. Macdonald, in *Techniques for Characterization of Electrodes and Electrochemical Processes,* R. Varma and J. R. Selman, eds., Wiley, New York, 1991, p. 515.
[23]F. Mansfeld and W. J. Lorenz, in *Techniques for Characterization of Electrodes and Electrochemical Processes,* R. Varma and J. R. Selman, eds., Wiley, New York, 1991, p. 581.
[24]S. Szpak, in *Techniques for Characterization of Electrodes and Electrochemical Processes*, R. Varma and J. R. Selman, eds., Wiley, New York, 1991, p. 677.
[25]J. R. Scully, D. C. Silverman, and M. W. Kendig, eds., *Electrochemical Impedance: Analysis and Interpretation,* American Society for Testing and Materials, Philadelphia, 1993.
[26]M. Sluyters-Rehbach and J. H. Sluyters, in *Analytical Chemistry,* A. J. Bard, ed., Vol. 4, Marcel Dekker, New York, 1970, p. 1.
[27]M. Sluyters-Rehbach and J. H. Sluyters, *Comprehensive Treatise of Electrochemistry,* Vol. 9, Plenum, New York, 1984, p. 177.
[28]D. D. Macdonald and M. C. H. McKurbe, in *Modern Aspects of Electrochemistry,* J. O'M. Bockris, B. E. Conway, and R. E. White, eds., Vol. 14, Plenum, New York, 1982, p. 61.
[29]D. D. Macdonald and M. C. H. McKurbe, in *Electrochemical Corrosion Testing,* ASTM Special Publ. 727, American Society for Testing and Materials, Philadelphia, 1981.

[30]C. Gabrielli, *Identification of Electrochemical Processes by Frequency Response Analysis,* Technical Report No 004, Solartron, Hampshire, UK, 1984.
[31]C. Gabrielli, *Use and Applications of Electrochemical Impedance Techniques,* Technical Report No 24, Solartron, Hampshire, UK, 1990.
[32]G. Doetsch, *Laplace Transformation,* Dover, New York, 1953.
[33]J. J. DiStefano, III, A. R. Stubberud, and I. J. Williams, *Theory and Problems of Feedback and Control Systems,* 2nd. ed., Schaum's Outline Series, McGraw-Hill, New York, 1990.
[34]S. Goldman, *Transformation Calculus and Electrical Transients,* Prentice-Hall, Englewood Cliffs, NJ, 1950.
[35]C. Gabrielli, M. Keddam, and H. Takenouti, *Electrochim. Acta* **35** (1990) 1553.
[36]C. Gabrielli and B. Tribolet, *J. Electrochem. Soc.* **141** (1994) 957.
[37]A. A. Pilla, in *Electrochemistry. Calculations, Simulation and Instrumentation,* J. S. Mattson, H. B. Mark, Jr., and H. C. MacDonald, eds., Marcel Dekker, New York, 1972, p. 139.
[38]R. D. Armstrong, W. P. Race, and H. R. Thirsk, *Electrochim. Acta* **13** (1968) 215.
[39]A. Muszalska and J. Jarzebska, *J. Electroanal. Chem.* **318** (1991) 145.
[40]M. M. Gomez, R. Motilla, and E. Diez, *Electrochim. Acta* **34** (1989) 831.
[41]K. Chandrasekara Pillai, W. E. Waghorne, and O. Wilson, *J. Electroanal. Chem.* **252** (1988) 151.
[42]*A Lock-In Primer,* EG&G, Princeton Applied Research, Princeton, NJ, 1986.
[43]R. de Levie and A. A. Husovsky, *J. Electroanal. Chem.* **20** (1969) 181.
[44]P. E. Wellstead, *Frequency Response Analysis,* Technical Note No. 10, Solartron Instruments, Hampshire, UK.
[45]J.-P. Diard, B. Le Gorrec, and C. Montella, *J. Electroanal. Chem.* **377** (1994) 61.
[46]C. Gabrielli, M. Keddam, and H. Takenouti, in *Electrochemical Methods in Corrosion Research,* M. Duprat, ed., Vol. 8, Materials Science Forum, 1986, p. 417.
[57]N. J. Evans, *Electrochemistry Newsletter,* April 1996, p. 11.
[48]E. O. Birgham, *The Fast Fourier Transform,* Prentice-Hall, Englewood Cliffs, NJ, 1974.
[49]D. E. Smith, *Anal. Chem.* **48** (1976) 221A.
[50]S. C. Creason, J. W. Hayes, and D. E. Smith, *J. Electroanal. Chem.* **47** (1973) 9.
[51]G. S. Popkirov and R. N. Schindler, *Bulgarian Chem. Commun.* **27** (1994) 459.
[52]G. S. Popkirov and R. N. Schindler, *Rev. Sci. Instrum.* **64** (1993) 3111.
[53]R. J. Schwall, A. M. Bond, R. J. Loyd, J. G. Larsen, and D. E. Smith, *Anal. Chem.* **49** (1977) 1797.
[54]A. J. Bond, R. J. Schwall, and D. E. Smith, *J. Electroanal. Chem.* **85** (1977) 231.
[55]A. A. Pilla, *J. Electrochem. Soc.* **117** (1970) 467.
[56]A. A. Pilla, in *Electrochemistry. Calculations, Simulation, and Instrumentation,* J. S. Mattson, H. B. Mark, Jr., and H. C. MacDonald, Jr., eds., Marcel Dekker, New York, 1972, p. 139.
[57]K. Doblhofer and A. A. Pilla, *J. Electroanal. Chem.* **39** (1972) 91.
[58]C. Gabrielli, M. Keddam, and J. F. Lizee, *J. Electroanal. Chem.* **205** (1986) 59.
[59]J. Ye and K. Doblhofer, *J. Electroanal. Chem.* **272** (1989) 11, 29.
[60]M. Neumannspallart and M. Elman, *J. Electroanal. Chem.* **327** (1994) 33.
[61]A. A. Sagüés, S. C. Krans, and E. I. Moreno, *Electrochim. Acta* **41** (1996) 1239, 2661.
[62]J. S. Gill, L. M. Callow, and J. D. Scantlebury, *Corrosion* **39** (1983) 61.
[63]E. Warburg, *Ann. Phys. Chem.* **67** (1899) 493.
[64]J. E. B. Randles, *Disc. Farad. Soc.* **1** (1947) 11.
[65]D. C. Grahame, *J. Electrochem. Soc.* **99** (1952) 370C.
[66]S. R. Taylor and E. Gileadi, *Corr. Sci.* **51** (1995) 664.
[67]J. E. B. Randles, *Transactions of the Symposium on Electrode Processes,* E. Yeager, ed., Wiley, New York, 1959, p. 209.
[68]X. Wu and W. Zhang, *J. Electroanal. Chem.* **383,** (1995) 1.

[69]T. J. VanderNoot, *J. Electroanal. Chem.* **300** (1991) 199.
[70]R. D. Armstrong and R. E. Firman, *J. Electroanal. Chem.* **45** (1973) 3.
[71]D. A. Harrington, *J. Electroanal. Chem.* **403** (1996) 11.
[72]M. Fleischmann, S. Pons, and J. Daschbach, *J. Electroanal. Chem.* **317** (1991) 1.
[73]M. Fleischmann, S. Pons, D. R. Rolison, and P. P. Schmidt, eds., *Ultramicroelectrodes,* Datatech Systems, Inc., Morganton, NC, 1987, Chap. 2.
[74]T. Jacobsen and K. West, *Electrochim. Acta* **30** (1995) 255.
[75]M. Fleischmann and S. Pons, *J. Electroanal. Chem.* **250** (1988) 277.
[76]R. de Levie and A. A. Husovsky, *J. Electroanal. Chem.* **22** (1969) 29.
[77]D. E. Smith, *Anal. Chem.* **35** (1963) 610.
[78]J. H. Sluyters, *Rec. Trav. Chim.* **79** (1960) 1092.
[79]M. Sluyters-Rehbach and J. H. Sluyters, *J. Electroanal. Chem.* **4** (1970) 1.
[80]K. Darowicki, *Electrochim. Acta* **40** (1995) 767.
[81]K. Darowicki, *Electrochim. Acta* **42** (1997) 1073.
[82]J.-P. Diard, B. Le Gorrec, and C. Montella, *Electrochim. Acta.* **42,** (1997) 1053.
[84]C.-N. Cao, *Electrochim. Acta* **35** (1990) 831.
[84]L. Bai and B. E. Conway, *Electrochim. Acta* **38** (1993) 1803.
[85]J.-P. Diard, B. Le Gorrec, and C. Montella, *J. Electroanal. Chem.* **326** (1992) 13.
[86]F.Berthier, J.-P. Diard, and C. Montella, *J. Electrochem. Soc.* **410** (1996) 247.
[87]A. Lasia and A. Rami, *J. Electroanal. Chem.* **294** (1990) 123.
[88]F. Berthier, J.-P. Diard, L. Pronzato, and E. Walter, in *Proceedings of the 10th IFAC Symposium on System Identification.* Copenhagen, 1994.
[89]F. Berthier, J.-P. Diard, C. Montella, L. Pronzato, and E. Walter, *J. Chim. Phys.* **90** (1993) 2069.
[90]F. Berthier, J.-P. Diard, P. Landaud, and C. Montella, *J. Electroanal. Chem.* **362** (1993) 13.
[91]F. Berthier, J.-P. Diard, L. Pronzato, and E. Walter, *Automatica* **32** (1996) 973.
[92]R. D. Armstrong and M. Henderson, *J. Electroanal. Chem.* **39** (1972) 81.
[93]R. D. Armstrong, R. E. Firman, and H. R. Thirsk, *Farad. Discuss. Chem. Soc.* **56** (1973) 244.
[94]C.-N. Cao, *Electrochim. Acta* **35** (1990) 837.
[95]J.-P. Diard, B. Le Gorrec, C. Montella, and C. Montero-Ocampo, *J. Electronal. Chem.* **352** (1993) 1.
[96]L. Bai and B. E. Conway, *J. Electrochem. Soc.* **137** (1990) 3737.
[97]D. A. Harrington, *J. Electroanal. Chem.* **449** (1998) 9, 29.
[98]R. C. Salvarezza and A. J. Arvia, in *Modern Aspects of Electrochemistry,* Vol. 28, B. E. Conway, J. O'M. Bockris, and R. E. White, eds., Vol. 30, Plenum, New York, p. 289.
[99]K. S. Cole and R. H. Cole, *J. Chem. Phys.* **9** (1941) 341.
[100] G. J. Brug, A. L. G. van den Eeden, M. Sluyters-Rehbach, and J. H. Sluyters, *J. Electroanal. Chem.* **176** (1984) 275.
[101]T. Pajkossy, *J. Electroanal. Chem.* **364** (1994) 111.
[102]Z. A. Rotenberg and N. V. Nekrasove, *Sov. Electrochem.* **25** (1989) 651.
[103]U. Rammlet and G. Reinhard, *Corr. Sci.* **27** (1987) 373.
[104]U. Rammlet and G. Reinhard, *Electrochim. Acta* **35** (1990) 1045.
[105]P. K. Wrona, A. Lasia, M. Lessard, and H. Ménard, *Electrochim. Acta* **37** (1992) 1283.
[106]T. J. VanderNoot, *J. Electroanal. Chem.* **386** (1995) 57.
[107]T. Pajkossy, T. Wandlowski, and D. M. Kolb, *J. Electroanal. Chem.* **414** (1996) 209.
[108]R. Devaux, A. M. de Becdelievre, C. Duret-Thual, and M. Keddam, *Electrochim. Acta* **38** (1993) 1615.
[109]Z. Stoynov, *Electrochim. Acta* **35** (1990) 1493.
[110]B. B. Mandelbrot, *The Fractal Geometry of Nature,* W. H. Freeman, San Francisco, 1982.
[111]R. de Levie, *J. Electroanal. Chem.* **281** (1990) 1.

[112]H. von Koch, *Ark. Mat. Astron. Fys.* **1** (1904) 681.
[113]L. Nyikos and T. Pajkossy, *Electrochim. Acta* **30** (1985) 1533.
[114]T. Pajkossy, *J. Electroanal. Chem.* **300** (1991) 1.
[115]A. Le Méhauté and G. Crépy, *Solid State Ionics* **9/10** (1983) 17; A. Le Méhauté, G. Crépy, and A. Hurd, *C. R. Acad. Sci.* Paris **306** (1988) 117.
[116]L. Nyikos and T. Pajkossy, *J. Electrochem. Soc.* **133** (1986) 2061.
[117]L. Nyikos and T. Pajkossy, *Electrochim. Acta* **31** (1986) 1347.
[118]T. Pajkossy and L. Nyikos, *Electrochim. Acta* **34** (1989) 171.
[119]A. P. Borossy, L. Nyikos, and T. Pajkossy, *Electrochim. Acta* **36** (1991) 163.
[120]L. Nyikos and T. Pajkossy, *Electrochim. Acta* **35** (1990) 1567.
[121]A. Sakharova, L. Nyikos, and T. Pajkossy, *Electrochim. Acta* **37** (1992) 973.
[122]T. Pajkossy, *Heterogen. Chem. Rev.* **2** (1995) 143.
[123]M. Keddam and H. Takenouti, *Electrochim. Acta* **33** (1988) 445.
[124]T. Pajkossy and L. Nyikos, *J. Electroanal. Chem.* **332** (1992) 55.
[125]R. de Levie, *J. Electroanal. Chem.* **261** (1989) 1.
[126]W. Mulder, *J. Electroanal. Chem.* **326** (1992) 231.
[127]J. C. Wang, *Electrochim. Acta* **33** (1987) 707.
[128]S. H. Liu, *Phys. Rev. Lett.* **55** (1985) 529.
[129]T. Kaplan, S. H. Liu, and L. J. Gray, *Phys. Rev.* **34** (1986) 4870.
[130]T. Kaplan, L. J. Gray, and S. H. Liu, *Phys. Rev. B* **35** (1987) 5379.
[131]B. Sapoval, *Solid State Ionics* **23** (1987) 253.
[132]B. Sapoval, J.-N. Chazalviel, and J. Peyrière, *Solid State Ionics* **28/30** (1988) 1441.
[133]B. Sapoval, J.-N. Chazalviel, and J. Peyrière, *Phys. Rev. A* **38** (1988) 5867.
[134]D. W. Davidson and R. H. Cole, *J. Chem. Phys.* **19** (1951) 1484.
[135]A. Rami and A. Lasia, *J. Appl. Electrochem.* **22** (1992) 376.
[136]L. Chen and A. Lasia, *J. Electrochem. Soc.* **139** (1992) 3458.
[137]P. Los, A. Rami, and A. Lasia, *J. Appl. Electrochem.* **23** (1993) 135.
[138]E. Chassaing, B. Sapoval, G. Daccord, and R. Lenormand, *J. Electroanal. Chem.* **279** (1990) 67.
[139]T. Pajkossy and L. Nyikos, *Electrochim. Acta* **34** (1989) 181.
[140]R. de Levie and A. Vogt, *J. Electroanal. Chem.* **278** (1990) 25; **281** (1990) 23.
[141]A. N. Frumkin, *Zh. Fiz. Khim.* **23** (1949) 1477.
[142]O. S. Ksenzhek, *Russ. J. Phys. Chem.* **36** (1962) 331.
[143]A. Winsel, *Z. Electrochem.* **66** (1962) 287.
[144]F. A. Posey, *J. Electrochem. Soc.* **111** (1962) 1173.
[145]J. M. Bisang, K. Jüttner, and G. Kreysa, *Electrochim. Acta* **39** (1994) 1297.
[146]R. de Levie, in, *Advances in E1ectrochemistry and Electrochemical Engineering,* P. Delahay ed., Vol. 6, Interscience, New York, 1967, p. 329.
[147]P. Los, A. Lasia, H. Ménard, and L. Brossard, *J. Electroanal. Chem.* **360** (1993) 101.
[148]K. Scott, *J. Appl. Electrochem.* **13** (1983) 709.
[149]A. Lasia, *J. Electroanal. Chem.* **397** (1995) 27.
[150]J. S. Newman and C.W. Tobias, *J. Electrochem. Soc.* **109** (1962) 1183.
[151]L. G. Austin and H. Lerner, *Electrochim. Acta* **9** (1964) 1469.
[152]S. K. Rangarajan, *J. Electroanal. Chem.* **22** (1969) 89.
[153]M. Keddam, C. Rakomotavo, and H. Takenouti, *J. Appl. Electrochem.* **14** (1984) 437.
[154]C. Cachet and R. Wiart, *J. Electroanal. Chem.* **195** (1985) 21.
[155]I. D. Raistrick, *Electrochim. Acta* **35** (1990) 1579.
[156]A. Lasia, *J. Electroanal. Chem.* **428,** (1997) 155.
[157]R. de Levie, *Electrochim. Acta* **10** (1965) 113.
[158]J. Gunning, *J. Electroanal. Chem.* **392** (1995) 1.
[159]H. Keiser, K. D. Beccu, and M. A. Gutjahr, *Electrochim. Acta* **21** (1976) 539.

[160] K. Eloot, F. Debuyck, M. Moors, and A. P. van Peteghem, *J. Appl. Electrochem.* **25** (1995) 326, 334.
[161] T. C. Halsey and M. Leibig, *Electrochim. Acta* **36** (1991) 1699.
[162] M. Leibig and T. Halsey, *J. Electroanal. Chem.* **358** (1993) 77.
[163] G. Inzelt and G. Láng, *J. Electroanal. Chem.* **378** (1994) 39.
[164] H. A. Kramers, *Phys. Zeit.* **30** (1929) 52.
[165] R. de L. Kronig, *J. Opt. Soc. Am.* **12** (1926) 547.
[166] H. W. Bode, *Network Analysis and Feedback Amplifier Design,* Van Nostrand, New York, 1945.
[167] D. D. Macdonald and M. Urquidi-Macdonald, *J. Electrochem. Soc.* **132** (1985) 2316.
[168] M. Urquidi-Macdonald, S. Real, and D. D. Macdonald, *J. Electrochem. Soc.* **133** (1896) 2018.
[169] M. Urquidi-Macdonald, S. Real, and D. D. Macdonald, *Electrochim. Acta* **35** (1990) 1559.
[170] J. M. Esteban and M. E. Orazem, *J. Electrochem. Soc.* **138** (1991) 67.
[171] M. E. Orazem, J. M. Esteban, and O. C. Moghissi, *Corrosion,* **47** (1991) 248.
[172] D. D. Macdonald and M. Uurquidi-Macdonald, *J. Electrochem. Soc.* **137** (1990) 515.
[173] M. Urquidi-Macdonald and D.D. Macdonald, *J. Electrochem. Soc.* **137** (1990) 3306.
[174] D. Townley, *J. Electrochem. Soc.* **137** (1990) 3305.
[175] P. Agarwal, M. E. Orazem, and L. H. Garcia-Rubio, in *Electrochemical Impedance: Analysis and Interpretation,* J. R. Scully, D. C. Silverman, and M. W. Kending, eds., ASTM STP 1188, American Society for Testing and Materials, Philadelphia, 1993, p. 115.
[176] C. Gabrielli, M. Keddam, and H. Takenouti, in *Electrochemical Impedance: Analysis and Interpretation,* J. R. Scully, D. C. Silverman, and M. W. Kending, eds., ASTM STP 1188, American Society for Testing and Materials, Philadelphia, 1993, p. 140.
[177] B. J. Dougherty and S. I. Smedley, in *Electrochemical Impedance: Analysis and Interpretation,* J. R. Scully, D. C. Silverman, and M. W. Kending, eds., ASTM STP 1188, American Society for Testing and Materials, Philadelphia, 1993, p. 154.
[178] R. V. Churchill and J. W. Brown, *Complex Variables and Applications,* McGraw-Hill, New York, 1990.
[179] M. Kendig and F. Mansfeld, *Corrosion* **39** (1983) 466.
[180] C. Haili, M.Sc. Thesis, University of California, Berkeley, 1987.
[181] P. Agarwal, M. E. Orazem, and L. H. Garcia-Rubio, *J. Electrochem. Soc.* **139** (1992) 1917.
[182] P. Agarwal and M. E. Orazem, *J. Electrochem. Soc.* **142** (1995) 4159.
[183] B. A. Boukamp and J. R. Macdonald, *Solid State Ionics* **74** (1994) 85.
[184] B. A. Boukamp, *J. Electrochem. Soc.* **142** (1995) 1885.
[185] J. R. Macdonald, *Electrochim. Acta* **38** (1993) 1883.
[186] G. Láng, L. Kocsis, and G. Inzelt, *Electrochim. Acta* **38** (1993) 1047.
[187] J.-P. Diard, P. Landaud, J.-M. Le Canut, B. Le Gorrec, and C. Montella, *Electrochim. Acta* **39** (1994) 2585.
[188] J. Max, *Méthodes et techniques de traitement du signal,* 4th ed., Masson, Paris, 1985.
[189] J. S. Bendat and A. G. Piersol, *Measurements and Analysis of Random Data,* Wiley, New York, 1966.
[190] G. T. Burstein and C. Liu, *Electrochim. Acta* **39** (1994) 873.
[191] Z. B. Stoynov and B. S. Savova-Stoynov, *J. Electroanal. Chem.* **183** (1985) 133.
[192] B. Savova-Stoynov and Z. B. Stoynov, *Electrochim. Acta* **37** (1992) 2353.
[193] Z. B. Stoynov, *Electrochim. Acta* **37** (1992) 2357.
[194] Z. Stoynov, *Electrochim. Acta* **38** (1993) 1919.
[195] M. E. Orazem, P. Agarwal, A. N. Jansen, P. T. Wojcik, and L. H. Garcia-Rubio, *Electrochim. Acta* **38** (1993) 1903.
[196] M. E. Orazem, P. Agarwal, and L. H. Garcia-Rubio, *J. Electroanal. Chem.* **378** (1994) 51.
[197] Z. B. Stoynov and B. Savova-Stoynova, *J. Electroanal. Chem.* **209** (1986) 11.

[198] Z. Stoynov, *Electrochim. Acta* **34** (1989) 1187.
[199] Z. Stoynov, *Electrochim. Acta* **35** (1990) 1493.
[200] P. Zoltowski, *J. Electroanal. Chem.* **375** (1994) 45.
[201] P. Zoltowski, *Polish J. Chem.* **68** (1994) 1171.
[202] J. R. Macdonald, J. Schoonman, and A. P. Lehnen, *J. Electroanal. Chem.* **131** (1982) 77.
[203] B. A. Boukamp, *Solid State Ionics* **20** (1986) 31.
[204] R. H. Milocco, *J. Electroanal. Chem.* **273** (1989) 243.
[205] W. H. Press, S. A. Teukolsky, W. V. Vetterling, and B. P. Flannery, *Numerical Recipes. The Art of Scientific Computing,* Cambridge University Press, Cambridge, UK, 1992.
[206] P. R. Bevington, *Data Reduction and Error Analysis for the Physical Sciences,* McGraw-Hill, New York, 1969.
[207] J. R. Macdonald, *J. Electroanal. Chem.* **307** (1991) 1.
[208] P. Zoltowski, *J. Electroanal. Chem.* **178** (1984) 11.
[209] P. Agarwal, O. D. Crisalle, M. E. Orazem, and L. H. Garcia-Rubio, *J. Electrochem. Soc.* **142** (1995) 4149.
[210] P. Agarwal, M. E. Orazem, and L. H. Garcia-Rubio, *Electrochim. Acta* **41** (1996) 1017.
[211] Equivalent Circuit Analysis Technology, Sirotech Ltd., Ness-Ziona, Israel, 1994.
[212] Y.-T. Tsai and D. W. Whitmore, *Solid State Ionics* **7** (1982) 129.
[213] M. W. Kendig, E. M. Meyer, G. Lindberg, and F. Mansfeld, *Corr. Sci.* **23** (1983) 1007.
[214] J.-P. Diard, B. Le Gorrec, and C. Montella, *J. Electroanal. Chem.* **205** (1986) 77.
[215] G. W. Walter, D. N. Nguyen, and M. A. D. Madurasinghe, *Electrochim. Acta* **37** (1992) 245.
[216] A. S. Barański and A. Szulborska, *Electrochim. Acta* **41** (1996) 985.
[217] A. S. Barański and A. Moyana, *Langmuir* **12** (1996) 3295.
[218] A. S. Barański and W. Lu, *J. Electroanal. Chem.* **260** (1989) 1.
[219] G. Schöne and W. Wiesbeck, *J. Electroanal. Chem.* **229** (1987) 407.
[220] C. Gabrielli, M. Keddam, and J. F. Lizee, *J. Electroanal. Chem.* **163** (1984) 419.
[221] H. Göhr, M. Mirnik, and C. A. Shiller, *J. Electroanal. Chem.* **180** (1984) 273.
[222] S. A. G. R. Karunathilaka, R. Barton, M. Hughes, and N. A. Hampson, *J. Appl. Electrochem.* **15** (1985) 251.
[223] S. Chechirlian, P. Eichner, M. Keddam, H. Takenouti, and H. Mazille, *Electrochim. Acta* **35** (1990) 1125.
[224] A. Lasia and P. Los, unpublished data, 1991.
[225] W. Botter, Jr., D. M. Soares, and O. Teschke, *J. Electroanal. Chem.* **267** (1989) 279.
[226] S. Fletcher and M. D. Horne, *J. Electroanal. Chem.* **297** (1991) 297.

3

Establishing the Link Between Multistep Electrochemical Reaction Mechanisms and Experimental Tafel Slopes

Mark C. Lefebvre

Department of Chemistry, University of Ottawa, Ottawa, Ontario, Canada KlN 6N5

I. INTRODUCTION

The aim of mechanistic studies of chemical reactions is to determine reaction pathway(s), identifying if possible the rate-determining step (rds) and the species involved in it. This involves (1) evaluation of the reaction orders of the various participating reactants, taking into account any chemisorption effects when the process is heterogeneous; (2) characterization of reaction intermediates and their adsorption behavior, and in addition in the case of electrochemical reactions, "double-layer" effects; (3) measurement of steady-state potential versus logarithmic current relations (known as Tafel plots after the phenomenological relationship

Modern Aspects of Electrochemistry, Number 32, edited by B. E. Conway *et al.* Kluwer Academic / Plenum Publishers, New York, 1999.

established by Tafel in 1905), and (4) the determination, where possible, of the stoichiometric number[1] (ν) of the reaction. In the case of a reaction involving only a single electron-transfer step, the derived Tafel slopes may be directly related to characteristics of the transition state determining the reaction rate of the process, specifically β, its symmetry factor, or what may also be thought of as its electrochemical Brønsted factor.[2] When a reaction involves transfer of more than one electron, it is usual for these to be transferred in discrete steps (i.e., associated with distinct transition states), in which case the polarization behavior and transfer coefficients derived from measured Tafel slopes can give information relevant to reaction mechanisms under certain conditions.

In the electrochemical benchmark monograph by Bockris and Reddy (B&R) (Ref. 3, p. 1001), these authors developed, based upon the quasi-equilibrium approximation, transfer coefficients, αs, in terms of mechanistic parameters. Their analysis demonstrated how such αs, obtained from experimental polarization curves, can give information directly, enabling elucidation of reaction mechanisms. Their transfer coefficients are written as

$$\alpha_c = \frac{\gamma_p}{\nu} + z_{\text{rds}}\beta \tag{1a}$$

$$\alpha_a = \frac{\gamma_f}{\nu} + z_{\text{rds}}(1-\beta) \tag{1b}$$

and the pertinent quantities are the numbers of electrons transferred prior to, during, and following a rate-determining step (rds). These are represented by the symbols γ_p, z_{rds}, and γ_f, respectively, which indicate the number of times the rds occurs (i.e., the stoichiometric number, ν) for one overall act of the process. The quantity β is the barrier symmetry factor for the transition state of the rate-limiting step. It is commonly supposed that these coefficients have a straightforward relation to the important mechanistic parameters [via Eqs. (1a) and (1b)] and hence they have been cited in many experimental works.

This chapter originates from work we have been conducting on the cathodic plating reaction of aluminum from nonaqueous solutions, a process that involves three electrons and therefore must be a multistep reaction. A particular bath for this purpose is the well-known etheric

hydride bath which is based on mixtures of $AlCl_3$ and $LiAlH_4$ in tetrahydrofuran.[4] Elsewhere[5] we have described experiments that lead to an elucidation of the mechanisms of the aluminum plating reaction from such baths. In addition, we reviewed previous work in which attempts to determine the mechanism of Al deposition from this bath were described. However, among those reports there was no consensus in the conclusions on the mechanism, although all were based on essentially the same experimental data. In these cases, the bases upon which the various reaction mechanisms were proposed were transfer coefficients derived from polarization experiments involving Eqs. (1a) and (1b). In the reviewed work,[6–9] these were seemingly used without regard to the limitations of their application. This confusion is due, in the present author's opinion, to an incomplete understanding of how the transfer coefficients and rate-determining steps to which they refer link particulars of electrochemical reaction mechanisms to the experimentally observable Tafel slopes and other aspects of the kinetic behavior.

This problem prompted a closer examination and ultimately a rederivation of the theory describing the link between mechanistic features in generalized sequential reaction schemes and the values of experimentally accessible transfer coefficients upon which the conclusions on mechanism were based. We endeavor here to develop this link, which is built upon the "quasi-equilibrium approximation" for dealing with the kinetics of multistep reactions, clearly and concisely, giving attention to the limits of its application. We hence justify its significance in relation to determination of the reaction mechanism.

In addition to the multiple electron-transfer steps that are formally involved in deposition of metal phases from multiply charged cations, or in their formation by anodic dissolution of a bulk metal phase, a variety of gas or other molecular- generation reactions require two electron-transfer steps (e.g., in the processes of electrochemical formation or reduction of F_2, Cl_2, Br_2, and I_2, and ethane in the Kolbe reaction from acetate). Four electron transfers are required in the important process of O_2 reduction while the extensively studied H_2 formation or oxidation reactions involve two electron-transfers.

The relation of the number of electrons required in the overall reactions and the intermediates adsorbed or produced in solution, to the observed and theoretical Tafel slopes b (the derivative of the electrode potential with respect to ln[current-density]) has formed a major aspect of

the field of electrode kinetics and studies of electrochemical mechanisms.[10] In particular, the evolution of transfer coefficients (α) and barrier symmetry factors (β) in interpretations of Tafel b values has been an important, if sometimes controversial, aspect of electrode kinetics.

Usually the kinetics of a multistep electrochemical reaction, as also for analogous regular chemical reactions, can be treated in two complementary ways.

1. The first is by means of the assumption that the formation and decomposition of a particular transition state limits the rate of the overall reaction and that any steps prior to the rate-determining step characterized by that transition state are at *quasi-equilibrium.* This allows the concentrations of any intermediates involved in the rds to be expressed as a function of potential [$f(V)$] and hence a kinetic expression for the potential dependence of the rds can be formulated in terms of its Tafel slope (b) and transfer coefficient (α), formally defined as $b = dV/d \ln i \equiv RT/\alpha F$.

In the case of a single-step reaction such as the reduction of Fe^{3+} to Fe^{2+} (in the absence of diffusion control), no assumptions are required about a rate-determining step in the usual sense (although microscopically, for such redox reactions in solution, consideration can be given to solvent reorganization[11] in the formation of the transition state associated with electron transfer). Correspondingly, no intermediate (except the transition state itself!) need be considered in the reaction mechanism scheme.

2. The second way of treating kinetics is by means of the "steady-state" condition, that is, the rates of all steps prior to and including the rds are proceeding at the *same* rate at a given potential and constant current density. Then a differential expression for the rates of formation and consumption of an intermediate (in a multistep process) can be written for a given potential and the net derivative equated to 0 for the supposed steady state.

Usually such expressions are more cumbersome than those derivable by the "quasi-equilibrium" method (especially for a step involving recombination of an intermediate, e.g., $2H \rightarrow H_2$), but reduce to the same expressions when simplifications are made (e.g., that rate constants for steps prior to the rds are at least 100 times smaller than that of the rds).

Some complications can arise when rate constants for reverse directions of a step are much smaller than that for the forward direction of the given process. This of course then leads to a large quasi-equilibrium constant, $>> 1$, for the step concerned. For steps in an electrode reaction

that involve electron transfer, the (electrochemical) rate constants are normally sensitively dependent (exponentially) on the electrode potential adjusted in the experiment.

1. Structure of this Chapter

The approach to the kinetic formulations to be developed here will start from the transition state or absolute reaction rate theory of chemical kinetics, [12] followed by analysis of the effect of an applied potential on electrochemical kinetics built up through the well-known Butler–Volmer (BV) equation,[13,14] which was originally written for a one-electron reaction. As discussed earlier for multistep electrochemical mechanisms, it is necessary to assume a rate-limiting step (rds) within the scheme and make a quasi-equilibrium approximation to define the potential dependence of rates for electrons transferred prior to, during, and following this rds. Thus, the BV equation can be extended to simple multistep cases including, significantly, the case of an overall reaction limited by a step having a stoichiometric number greater than 1. The circumstances under which $v > 1$ can arise will be described in detail later.

The following derivations are based on fundamental principles and will clearly illustrate how the potential dependence of electrochemical reaction rates, characterized by experimentally determinable transfer coefficients, arises in generalized reaction schemes, and the constraints that the required limiting assumptions impose upon this potential dependence. This approach is required because the simple transfer coefficients of B&R are really only of use for assigning mechanisms if they are properly applied; this is actually not so trivial a point given the above-mentioned confusion that has arisen in the kinetic analysis of, e.g., the Al electrodeposition reaction.[5] Hence, attention will be given in the following material to completeness.

The first half of this chapter covers basic concepts concerning the potential dependence of rates of electrochemical charge-transfer reactions, which will be familiar to specialists in the field. However, this material is included for the more general reader in order to provide a basis for following the more convoluted analysis required for dealing with complex, multistep electron-transfer reactions that are treated in the later part of this article in some detail.

II. CHEMICAL KINETICS

The kinetic treatment of electrochemical reactions is based on that for regular chemical reactions but with the inclusion of electrical energy terms. We first consider the progress of a simple chemical transformation

$$\text{A-B} + \text{C} \rightleftharpoons \text{A} + \text{B-C} \tag{2}$$

which can be regarded as involving a transition state defined by an activated complex (‡) of high energy, having a configuration intermediate between that of the reactant and the product, and thus Eq. (2) can be written as

$$\text{A-B} + \text{C} \rightleftharpoons \text{A·B·C}^{\ddagger} \rightleftharpoons \text{A} + \text{B-C} \tag{3}$$

It is generally assumed that the same transition-state describes the reaction in the reverse direction and that this is a thermodynamic requirement for a process at equilibrium [as is written Eq. (3)].

The energy required to attain the transition state is the energy difference between the activated complex, $\text{A·B·C}^{\ddagger}$, and the minima (zero-point energies) of the reactants for the forward reaction direction or of the products for the reverse direction where the Gibbs energies of these are described by their respective standard chemical potentials ($\boldsymbol{\mu}_i^{\circ}$). The standard forward activation energy barrier, $\Delta G_{\rightarrow}^{\circ\ddagger}$ is then

$$\mu^{\circ}_{\text{A·B·C}^{\ddagger}} - (\mu^{\circ}_{\text{A–B}} + \mu^{\circ}_{\text{C}}) = \Delta G^{\circ\ddagger}_{\rightarrow} \tag{4}$$

From the transition-state model, or the theory of absolute reaction rates (Ref. 15, p. 89), the forward rate constant, $k_{\rightarrow}$, for a reaction, the rate of which is determined by a potential barrier $\Delta G^{\circ\ddagger}_{\rightarrow}$, will be given by Eq. (5):

$$k_{\rightarrow} = \frac{k_B T}{h} \exp\left[-\frac{\Delta G^{\circ\ddagger}_{\rightarrow}}{RT}\right] \tag{5}$$

where k_B is the Boltzmann constant, h is Planck's constant, T is the temperature (in K) and R is the gas constant. The transmission coefficient, κ, which is usually formally included, has been assumed to be equal to 1.

Following from this, the rate of the reaction (in mol s^{-1}) in the cathodic direction, v, depends upon the number of molecules entering the transition state per second and the rate constant for the tranformation, $k_{\rightarrow}$, as

$$\upsilon_{\rightarrow} = [\mathrm{A{\cdot}B{\cdot}C^{\ddagger}}]k_{\rightarrow} \tag{6}$$

Note that although the use of activities is preferred for bulk species in kinetic expressions for electrochemical reactions, owing to the demonstrated ability of the Debye–Huckel limiting law to predict trends in reaction rate for ionic processes,[16,17] the molarity of the transition-state complex is formally used in Eq. (6) since this species is ephemeral. It is usually neither convenient nor possible to measure this species concentration, but if it is assumed that the passage of the $\mathrm{A{\cdot}B{\cdot}C^{\ddagger}}$ complex over the activation barrier determines the rate of the reaction, the formation of the complex from the reactants (or products for the reverse reaction) can be considered to be a "quasi"-equilibrium process, for which a quasi-equilibrium constant, $K^{\ddagger}_{\rightarrow}$, can be defined. For a forward direction of reaction (3), this constant would be

$$K^{\ddagger}_{\rightarrow} = \frac{[\mathrm{A{\cdot}B{\cdot}C^{\ddagger}}]}{a_{\mathrm{A-B}} \cdot a_{\mathrm{C}}} \tag{7}$$

where the as are activities of the solution species A-B and C.

The activated complex concentration, from a rearranged Eq. (7), can be substituted in the rate equation [Eq. (6)] to give Eq. (8) for the rate of the forward reaction:

$$\upsilon_{\rightarrow} = a_{\mathrm{A-B}} a_{\mathrm{C}} K^{\ddagger}_{\rightarrow} k_{\rightarrow} \tag{8}$$

where $k_{\rightarrow}$ is the rate constant from Eq. (5) and $K^{\ddagger}_{\rightarrow}$ the forward quasi-equilibrium constant from Eq. (7). For simplicity, $K^{\ddagger}_{\rightarrow}$ will be dropped and assumed to be part of $k_{\rightarrow}$.

III. SIMPLE ONE-STEP, ONE-ELECTRON ELECTROCHEMICAL KINETICS

1. Introduction

The transition-state theory is easily applied to the kinetics of electrochemical reactions that involve electrons as reactants supplied from the Fermi level of a substrate electrode. The simplest one-electron process is a one-electron reaction involving solution species [e.g., $\mathrm{Fe(CN)_6^{3-/4-}}$]. An illustrative example of an electrochemical reaction that parallels the

present author's interests is, say, the electrodeposition of a species A from a solution complex A^+-L^-, onto a conductive electrode substrate M:

$$M(e^-) + A^+\text{-}L^- \rightleftharpoons M\text{-}A + L^- \tag{9}$$

Note that it must be assumed that no other reactions are occurring.

2. Energetics of the Electrochemical Transition State at Equilibrium

In order to describe the energetic course of reaction (9), it is useful to introduce the potential-energy (PE) representation of the progress of the reactant species along a reaction coordinate,[18] as shown in Fig. 1. This is the single axis along which the bonds for both the reactant, A^+-L^-, and product, M-A, vibrate. The transition state for the reaction is defined by that region where the reactant and product PE surfaces intersect. This is usually at a point (or region) where both reactant and product bonds are stretched (or activated), or, for aquo or other complex ions, in some way are configurationally modified to higher energy states. An assumption that permits mathematical treatment of the PE curves is that the positions along

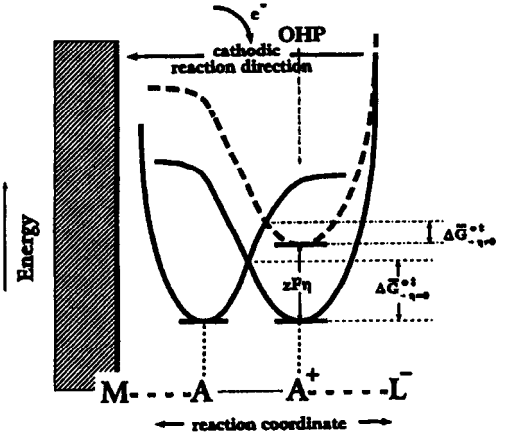

Figure 1. Potential-energy diagram showing the course of an electrochemical reaction and the effect of an applied overpotential (solid curve [$\eta = 0$], dashed curve [$\eta \neq 0$]). The magnitude of the cathodic activation barriers in the presence, $\Delta\bar{G}^{o\ddagger}_{\eta\neq 0}$, and absence, $\Delta\bar{G}^{o\ddagger}_{\eta=0}$, of the applied η are drawn, as is the magnitude of the applied $zF\eta$. Zero-point energies not distinguished.

the reaction coordinate of the substrate (M) and ligand (L^-) of the complex ion A^+-L^- are considered to be frozen in place, the latter just outside the outer Helmholtz plane (the reaction plane) of the substrate (see Fig. 1). The course of the reaction is then described by the movement of A or A^+ along the reaction coordinate. This representation is a simplification of the real geometric progress of a reaction, idealized as a process taking place in one dimension. In reality, the activation process may often require a multidimensional representation (e.g., when desolvation of an ion is involved). Note also that, owing to the difference between heterogeneous and homogeneous reactions, a PE surface describing the (product) bond with the metal substrate would be an average of all different bonding situations arising from various influences of near-neighbor atoms and conditions of solvation at the crystallographic faces the metal that may be present at its surface.

The energies of the component species of this system may be described by their electrochemical potentials, $\bar{\mu}$s (the overbars indicate the "electrochemical" quantities[19,20]), which, for a species *i*, would be

$$\bar{\mu}_i = \mu_i^\circ + RT \ln[a_i] + z_i F \phi_i \tag{10}$$

Note that $\bar{\mu}_i$, Eq. 10, includes the species' standard chemical potential, an activity term, and an electrical energy term. The electrical term is composed of the electrical work required to bring the molar charge $z_i F$ on a given ionic species from infinity into the species' phase, and ϕ_i is the standard inner potential or work function of the phase in question (e.g., that of the metal, ϕ_M, or of a particular ion in solution, ϕ_S) (Ref. 21, p. 20).

The rate of the reaction described by Fig. 1 (in either direction) depends upon the height of the energy barrier (for that direction) where for the forward, reductive reaction direction the barrier height is given by $\Delta\bar{G}^{\circ\ddagger}_{\rightarrow}$

$$\Delta\bar{G}^{\circ\ddagger}_{\rightarrow} = \bar{\mu}^\circ_{[M\cdot A\cdot L^-]^\ddagger} - (\bar{\mu}^\circ_{A^+\text{-}L^-} + \bar{\mu}^\circ_{M(e^-)}) \tag{11}$$

which is the energy of the transition state relative to that of the reactants. Analogously, $\Delta\bar{G}^{\circ\ddagger}_{\leftarrow}$ would define the energy barrier for the reverse, oxidative direction of reaction (see Eq. 9). Generally, of course, $\Delta\bar{G}^{\circ\ddagger}_{\rightarrow} - \Delta\bar{G}^{\circ\ddagger}_{\leftarrow}$ is equal to the standard Gibbs energy change in the overall reaction. The rate constant for the forward reaction would be (cf. Eq. 5)

$$\bar{k}_{\rightarrow} = \frac{k_B T}{h} \exp\left[-\frac{\Delta\bar{G}^{\circ\ddagger}_{\rightarrow}}{RT} \right] \tag{12}$$

It is important to note that the height of the electrochemical barrier is variable under the influence of the electric field in the interfacial region; this is the result of applying an externally adjustable potential difference, *E,* at the electrode/solution interface. The applied *E* can modify the electrical component of the $\bar{\mu}$ of reacting electrons, at any one temperature, and this indirectly results in changes in the electrical energy experienced by ions in their progress along the reaction coordinate. Applied potentials can be controlled, with even the simplest instrumentation, to an accuracy of about 1 mV (96 J mol^{-1}), resulting in an easily measured energy change with respect to electrons (if reaction kinetics do indeed limit the observed current); herein lies the great advantage of studying the kinetics of electrochemical over chemical processes.

The potential difference between metal and solution, $\phi_M - \phi_S$, is the total electrical driving force across the reaction interface, which for the condition of equilibrium can be defined as $\phi_{M,rev} - \phi_{S,rev}$. The fact is, however, that the transition-state complex will exist at some unknown position along the reaction coordinate across the double layer (see Fig. 1) between the substrate and the bulk of solution and hence it does not experience the entirety of this potential difference, but only a fraction that corresponds to an intermediate potential $\phi_{\ddagger}$. It is convenient to assume that the potential difference at this point, $\phi_{\ddagger,rev} - \phi_{S,rev}$, is some constant fraction, β, of the total interfacial potential difference, that is, $\beta(\phi_{M,rev} - \phi_{S,rev})$, where $\beta zF(\phi_{M,rev} - \phi_{S,rev})$ would be the energy (in J mol^{-1}) associated with transfer of *zF* coulombs across the metal/solution interface under standard conditions.

Up to this point, we have considered potentials associated with a single metal/solution interface (i.e., ϕ_M, ϕ_S, and $\phi_{\ddagger}$). It is, of course, not possible to measure directly either the absolute potentials or differences between them. Potential is only experimentally measurable or controllable relative to that of another electrode of defined, invariant potential (i.e., a nonpolarizable reference electrode). Apart from defining the applied potential and enabling it to be measured, a reference electrode is required in order to complete the circuit and maintain electrical neutrality with zero current flow throughout the potential-measuring circuit of the cell.

The symbol E_e°, the standard equilibrium potential, now replaces $\phi_{M,rev} - \phi_{S,rev}$, indicating that it is measured against an appropriate reference electrode and where the activities of all involved species are (hypothetically) equal to 1 (i.e., standard conditions). Practical electrochemical

cells are, however, usually nonstandard, and this requires the introduction of the Nernstian reversible potential, E_r, which is related to E_e^o by the well-known Nernst equation[22]:

$$E_r = E_e^o + \frac{RT}{zF} \ln \left[\frac{a_O}{a_R} \right] \tag{13}$$

for an equilibrium: $R \rightarrow O + ze$.

With this in mind, a forward equilibrium rate constant for the electrodeposition reaction Eq. (9) under nonstandard conditions is

$$\bar{k}_{\rightarrow} = \frac{k_B T}{h} \exp \left[- \frac{\Delta G_{\rightarrow}^{o\ddagger}}{RT} \right] \exp \left[- \frac{\beta z F E_r}{RT} \right] \tag{14}$$

in which the chemical and electrical terms are separated [see Eq. (5)] but when combined, will become $\Delta \bar{G}_{\rightarrow}^{o\ddagger}$. The potential that the transition-state complex experiences at its position in the double layer has been defined by a fraction β of that across the entire interface (i.e., E_r), although note that experimentally, consideration must be given to the structure of the double layer and in fact β operates only on that part of the potential across the Helmholtz layer and not on any part of the diffuse layer (see Section III.5).

3. Electrochemical Reaction under Polarization

If it is assumed that the chemical component of the electrochemical potentials of all species (including the transition-state complex) is potential independent, applied potentials add linearly across the reaction interface, giving, likewise, a linear change in the energy of electrons involved in the interfacial reaction. When applying a potential, it is useful to introduce this E relative to that of the reversible potential of the reaction under study, E_r, the latter being the potential of the interfacial reaction at equilibrium. In this way, the overpotential, η, is defined as the difference between these two potentials, viz., $\eta = E - E_r$, and defines the electrical driving force that can be applied to a given reaction, say, Eq. (9). If βE_r defines the potential at the position of the transition-state complex, then that same fraction of $(E - E_r)$ will modify its energy (i.e., $\beta zF(E - E_r)$] when an external potential is applied. Note that at the electronic mechanistic level, it is the change in the Fermi-level energy of electrons through the change in electrode potential that is the principal origin of the effects of electrode potential on electron charge-transfer rates in electrochemical

reactions. However, little attention has been given to the effect of the interfacial double-layer field, $d\phi/dx$, on the state of reacting molecules or ions except for the case of solvent molecule orientation in the double layer[23] and its possible effect[24] on the temperature dependence of β (for gas-evolving reactions).

The amount by which an applied η will decrease the cathodic energy barrier is $\beta zF\eta$, which gives a potential-dependent cathodic rate constant of

$$\bar{k}_{\rightarrow} = \frac{k_B T}{h} \exp\left[-\frac{\Delta G^{o\ddagger}_{\rightarrow}}{RT}\right] \exp\left[-\frac{\beta zF\eta}{RT}\right] \tag{15}$$

An applied potential, E, equal to E_r, corresponds to a situation where η is equal to 0 and hence to equilibrium conditions, in which case the rates of forward and reverse reactions are equal. Considering the PE surface representation of the reaction coordinate in Fig. 1, equilibrium corresponds to the PE surface consisting of the two solid curves (indicated by $\eta = 0$) in which the barrier height is the same in both reaction directions.[a] The situation of E being more negative[b] than E_r (i.e., being of higher electrical energy) corresponds to a negative overpotential that gives rise to a negative surface excess charge for cases where the corresponding reversible potential is at or already negative to the potential-of-zero charge (pcz) of the electrode metal.

This application of a negative overpotential will shift upward (perfectly vertically, it is assumed[26]) the zero-point energy level of the reactant PE surface [i.e., for reaction Eq. (9)], that of A^+-L^-, by $zF\eta$ with respect to that of the product PE surface. This $\eta < 0$, higher energy curve (dashed

[a] Confusion has sometimes arisen in the literature pertaining to potential-energy surface (or section) diagrams for the representation of β and the corresponding Gibbs energy quantities. Strictly speaking, β operates as a fraction of the Gibbs energy change associated with a change in electrode potential, leading to the Tafel equation: $\Delta G^{\ddagger}_{\eta} = \Delta G^{\ddagger}_{\eta=0} \pm \beta zF\eta$. This effect is equivalent to that represented on a PE diagram only if the entropy change in the process is 0 or is unaffected by potential change. A further complication is that for equilibrium conditions and relations to i_o (and for quasi-equilibrium conditions), it is the electrochemical Gibbs energy quantities, $\overline{G}$, that are equal across the reaction process, and not the energies or enthalpies of the states involved.

[b] As a point of clarification, the convention of the International Union of Pure and Applied Chemistry (IUPAC) is followed here where a *negative* applied potential *raises* the energy of the electrons in the electrode and drives *reduction* in the forward direction[25] Correspondingly, resulting currents are written negatively.

line) is shown in Fig. 1. Note that in this particular example it is the A^+-L^- curve that shifts since it is on the same side of the electrochemical reaction Eq. (9) as the electrons, written as $M(e^-)$. As noted earlier, in the usual analysis no change of shape of this curve is envisaged, although this may be a not entirely satisfactory assumption. Although the reactant curve in Fig. 1 was shifted by $zF\eta$, it is evident that the cathodic barrier height, $\Delta G^{o\ddagger}_{\rightarrow}$, will be changed by only a fraction, β, of that. This introduces an alternative, physical interpretation of β, which is conceptually different from the previous consideration of the electrical characteristics of the transition-state complex, that is, $\phi_{\ddagger} - \phi_S = \beta(\phi_M - \phi_S)$ in relation to its position[27] along the reaction coordinate in the double-layer field.

4. The Symmetry Factor

β is termed the *symmetry factor* and is a means of describing the fraction of an applied overpotential that influences the activation energy and hence the rate of an electrochemical reaction. For most electrochemical reactions, β is usually taken to be equal to about 1/2, an assumption justified for a "symmetrical" energy barrier, which means that for a negative applied η, one half of the applied η decreases the cathodic (Gibbs) energy barrier while the other half, $1 - \beta$, *increases* the anodic (Gibbs) energy barrier. Electrochemists have been grappling with a physical representation of β since the very beginning of electrochemical kinetics. Although it is central to electrochemistry, there has not been considerable discussion in the literature;[28] currently there is no single physical model that is generally accepted.

One of the earliest models was that of Butler,[27] in which β was considered to represent the relationship between the potential-distance profile across the electrical double layer and the position of the transition-state complex relative to the "locations" of the initial and final states of the reaction. A model by Hush[29] considered β to be the (fractional) charge on the ion in the transition state. Marcus' treatment of electrochemical electron-transfer reactions has β as a multicomponent term that is dependent upon the reorganization of the medium necessary to attain the transition state.[11,30] If the electrochemical transition state is represented as intersecting classical[26] PE surfaces along the reaction coordinate (as introduced in the previous section), β gives a measure of the relative slopes of reactant and product PE surfaces, making it a geometric factor; this is the origin of its being termed the *symmetry factor.* β, in this case, has the

same kind of significance as the Brønsted factor in linear Gibbs energy relationships, for example, for homogeneous acid-base reactions.[17] Note again, however, the formal confusion between β representing effects in a PE vs. a Gibbs energy diagram.

The value of β, according to the PE surface representation adopted in this work, can be put on a more quantitative footing by analyzing the relationship between overpotential and the variation of, say, the cathodic activation energy [i.e., $zF\eta$ and $(\Delta\bar{G}^{o\ddagger}_{\eta\neq0} - \Delta\bar{G}^{o\ddagger}_{\eta=0})$ or $\Delta_\eta\Delta\bar{G}^{o\ddagger}_{\rightarrow}$; such analysis generally relies on linearization of the PE surfaces near the transition-state region, such as in Fig. 2, in which the reactant surfaces in the absence and presence of an applied overpotential are the solid and dashed curves, respectively. Also shown are the respective cathodic barrier heights; owing to their varying points of reference, these quantities (as represented by the lengths of the drawn lines in Fig. 2) have been redrawn in the inset box and aligned to illustrate the fraction β of the applied overpotential that ends up modifying the height of the cathodic energy barrier. On the basis of the necessary simplifying assumptions that their slopes do not change with η and that

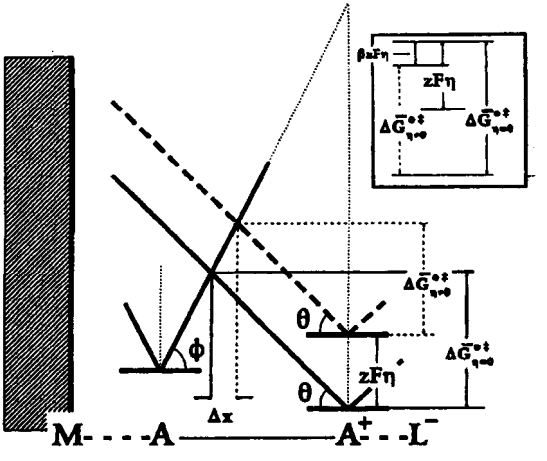

Figure 2. A linearized potential-energy diagram showing the course of an electrochemical reaction. The reactant curves in the absence and presence of an applied overpotential (solid curve [η = 0], dashed curve [η ≠ 0]) are shown. The magnitude of the cathodic activation barriers in the presence, $\Delta\bar{G}^{o\ddagger}_{\eta\neq0}$, and absence, $\Delta\bar{G}^{o\ddagger}_{\eta=0}$, of the applied η are shown and redrawn in the inset box to scale in such a way as to compare their difference due to the applied $zF\eta$.

the relative reaction coordinate positions of these curves do not move, simple, if a little involved, trigonometry (see Ref. 3, p. 922) can express β in terms of the reactant and product PE curves:

$$\Delta_\eta \Delta G^{\ddagger}_{\rightarrow} = \left(\frac{\tan\theta}{\tan\phi + \tan\theta} \right) zF\eta \tag{16}$$

where the term in parentheses is β, θ is the angle the reactant (the ion in the outer Helmholtz plane, OHP) PE surface makes with the reaction coordinate axis (see Fig. 2), and ϕ is that for the product adsorbed on the substrate surface. In Fig. 2, the PE surface of the product is deliberately shown as more acute (or conversely less obtuse) in aspect than the reactant surface and hence represents a stronger bond than that of the reactant, corresponding to $\beta < 1/2$ for this example.

There has been considerable discussion in the literature concerning the possible potential dependence of β. Whether there is support for a potential-independent β seems to depend on the system involved; for instance, β is known to vary little over a wide overvoltage range for the hydrogen evolution reaction on Hg or Pb (see Ref. 31 and references therein) and for the oxygen evolution reaction on various oxidized metal surfaces, while for the reduction of nitrocompounds in nonaqueous solutions, a significant change with potential is observed (Ref. 32, p. 276). Note that if the PE surfaces (defining the transition state) were to intersect near the zero-point energy of one of the curves, a change of β with overpotential would be anticipated on the basis of this model since the slope near the base of a PE surface changes quite significantly. This is demonstrated in Fig. 3 by the tangent lines for the intersection of the PE curves that are progressively closer to one of their zero-point energy levels. The limit of this effect is when the PE curves cross at the zero-point energy level and corresponding vibrational amplitude [e.g., in cases approaching either the barrierless or activationless kinetic conditions; (Ref. 32, p. 278)]. Note that it is often difficult to observe this effect experimentally since, for the high applied potentials necessary, diffusion of the reaction species in solution usually becomes rate-limiting instead. In addition, it is conceivable that the changing electric field present at the electrified interface could affect the position of charged species with respect to the OHP. For the purpose of the present discussion, however, β is assumed to be potential independent and symmetric (i.e., equal to 1/2), which is noted for many reactions.

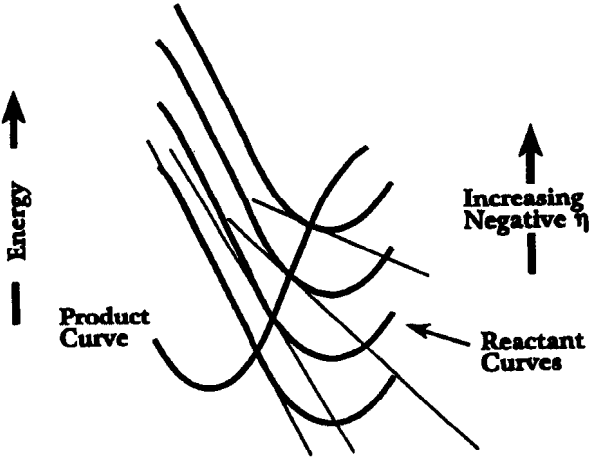

Figure 3. Potential-energy diagram demonstrating the effect of PE surface curvature. The intersection of product and reactant curves progressively nearer to the zero-point energy of the reactant curve gives considerably different slopes (drawn lines) and hence βs.

5. Double-Layer Considerations

The potential difference across the electrode/solution interface is "dropped" by the accumulation of ions of opposite charge in the solution immediately adjacent to the electrode surface in the electrochemical double layer. The spatial distribution of ions gives a potential profile across the double layer into the solution over a distance that is dependent upon the electrolyte concentration. Given this position-dependent potential profile, it is possible that species undergoing electrochemical reaction, which are assumed to reside in the outer Helmholtz plane of the electrical double layer adjacent to the substrate electrode (otherwise known as the plane of closest approach of nonspecifically adsorbed ions), may not actually be at ϕ_S and hence would not experience the full electrical field corresponding to the electrode/solution potential difference. The result of this is that only a part of the measurable applied η affects the Gibbs energy of activation of the process. The potential at the OHP with respect to solution, ϕ_S, is denoted[c] ψ_1 and is known as the potential of the (inner limit

[c]This is the symbol used in the Russian literature; ϕ_d or ϕ_2 have been employed elsewhere.

of the) diffuse layer and is actually the part of the applied potential that does not affect the reactant in the OHP. Thus the ultimate electrical driving force of an applied overpotential η at the OHP becomes modified to $\beta(\eta - \psi_1)$. However, as long as ψ_1 is small, which is usually the case when solutions contain an inactive supporting electrolyte of concentration 0.1 to 1.0 M, or remains constant, it does not affect the actual potential dependence of the interfacial reaction and η can then be used in the kinetic equations without alteration.

6. Rate Equation

The rate $\upsilon_{\rightarrow}$ of the forward, reductive direction of reaction Eq. (9) is the product of the activities of reactants [from the concentration of the activated complex $[M{\cdot}A{\cdot}L^-]^{\ddagger}$ as per Eq. (7)] and the rate constant describing the energy barrier, $\overline{k}_{\rightarrow}$ [Eq. (15)], which is composed of a potential-independent $k_{\rightarrow}$ [likened to Eq. (5)] and a potential-dependent term. The rate of the deposition reaction, having units of mol s^{-1} cm^{-2} (the reaction cross-section area of the substrate electrode), is

$$\upsilon_{\rightarrow} = a_{A^+-L^-} k_{\rightarrow} \exp\left[-\frac{zF\beta\eta}{RT} \right] = \frac{I_{\rightarrow}}{zFA} \tag{17}$$

where $a_{A^+-L^-}$ is the activity of A^+-L^- in solution (i.e., diffusion is assumed not to be limiting), $k_{\rightarrow}$ is the heterogeneous rate constant, $I_{\rightarrow}$ is the current for the reduction reaction, and A is the accessible electrode area.

The reaction rate in the reverse direction is given, analogously, by Eq. (18):

$$\upsilon_{\leftarrow} = a_{M-A} a_{L^-} k_{\leftarrow} \exp\left[\frac{zF(1-\beta)\eta}{RT} \right] = \frac{I_{\leftarrow}}{zFA} \tag{18}$$

Combining the forward and reverse rates [Eqs. (17) and (18)] gives Eq. (19) for the net current:

$$\begin{aligned} I_{net} &= -I_{\rightarrow} + I_{\leftarrow} \\ &= zFA \left(-a_{A^+-L^-} k_{\rightarrow} \exp\left[-\frac{zF\beta\eta}{RT} \right] \right. \\ &\quad \left. + a_{M-A} a_{L^-} k_{\leftarrow} \exp\left[\frac{zF(1-\beta)\eta}{RT} \right] \right) \end{aligned} \tag{19}$$

Note that this equation is constructed so that the cathodic reaction contributes a negative current that follows the usual electrochemical convention (see footnote b).

At equilibrium ($\eta = 0$), $I_{net} = 0$, but an exchange current continues to pass reversibly in both directions of reaction. The exchange current density is a direct measure of the kinetic facility of an electrochemical reaction through a particular transition state and is given by

$$i_0 = zFa_{A^+-L^-}k_{\rightarrow} = zFa_{M-A}a_{L^-}k_{\leftarrow} \tag{20}$$

writing i for I/A. This i_0 may be introduced into Eq. (19) to give the simplified Eq. (21), which is the well-known Butler–Volmer (BV) relation[13,14]

$$i_{net} = i_0\left(\exp\left[\frac{zF(1-\beta)\eta}{RT}\right] - \exp\left[-\frac{zF\beta\eta}{RT}\right]\right) \tag{21}$$

Equation (21) essentially states that the cathodic and anodic slopes of log i vs. η curves (when the reaction is under kinetic control) in potential regions where one or other of the reaction branches is negligible (i.e., the Tafel regions), is going to be proportional to $z\beta$ and $z(1-\beta)$, respectively, for a single-step, z-electron reaction (i.e., including hypothetically the unlikely case of more than one electron being transferred in the transition state). These factors are called the *transfer coefficients* and can be essential tools for deriving reaction mechanisms in multistep electron-transfer processes (i.e., where $z > 1$), as will be demonstrated in the next section.

IV. SEQUENCE OF CONSECUTIVE ELECTROCHEMICAL REACTIONS INVOLVING A SINGLE RATE-DETERMINING STEP

1. Reaction Schemes and Intermediates

We now proceed to the main topic of this chapter and examine the situation for an electrochemical reaction that involves multiple consecutive electron-transfer steps of the kind referred to in a general way in the introduction. A hypothetical reaction sequence involving n consecutive electron-transfer reduction steps is given in Scheme 1. The A_is are stable species that can be reactants or products and the I_is are reaction intermediates of lower stability. The z_is indicate the number of electrons trans-

Step						
	1.	A_1	+	$z_1 e^-$	$\rightleftharpoons$	I_2
	2.	I_2	+	$z_2 e^-$	$\rightleftharpoons$	I_3
	.	.....				
	rds-1.	I_{rds-1}	+	$z_{rds-1} e^-$	$\rightleftharpoons$	I_{rds}
	rds.	I_{rds}	+	$z_{rds} e^-$	$\rightleftharpoons$	I_{rds+1}
	rds + 1.	I_{rds+1}	+	$z_{rds+1} e^-$	$\rightleftharpoons$	I_{rds+2}
	.	.....				
	n.	I_n	+	$z_n e^-$	$\rightleftharpoons$	A_{n+1}

Scheme 1. Consecutive electrochemical reaction scheme

ferred in each step and can have values of 0, 1, 2, etc.; they are used as a means of including the possibility of chemical steps ($z_i = 0$) and single and multielectron steps, respectively, as discrete reaction steps in the mechanism, although it should be noted that the number of electrons transferred in a given step (i.e., z_i) is usually assumed ≤ 1. This assumption arises from the absolute rate theory of electron transfer of Marcus (Ref. 11 and references therein), in which it is argued that the energy requirements for medium reorganization associated with electron transfer would favor incremental transfer of charge. z, used previously in the Equation (21) (which is for the single-step reaction) for the number of electrons transferred in the rds, is now the sum total of all electrons transferred for a single turnover of the entire reaction, while z_{rds} is the number specifically transferred in the rds, that is, the usually assumed value of 1. The A_is and I_is can be uncharged, or positively or negatively charged (the charge balance among these is omitted in Scheme 1 for simplicity). Although there are limits to the charge these species can have and hence how many electron-transfer steps are possible, n steps are assumed in the scheme to illustrate the origin of the potential dependence that is relevant to determination of mechanism in this discussion.

Each step will have individual rate constants for its forward and reverse reaction directions; for instance, for step i (see Scheme 1), these will be $\vec{k}_i$ and $\vec{k}_{-i}$, respectively. The activities of the reactants and products of the reaction are defined in terms of their solution activities, a_{A_i}s. The reaction intermediates, however, remain in the immediate vicinity of the electrode substrate surface and do not possess "solution" activities per se, since they are often unstable and ephemeral; thus they are normally

defined by surface activities, $a_{I_i}^{S}$s (mol cm^{-3}).[d] The volume that describes the surface activity is defined by a solution thickness on the order of that of the double layer itself, and a particular species' bulk solubility would define the upper limit of its concentration (if that could be estimated).

It is the potential dependence of the surface activities of these intermediates created in electron-transfer steps that gives rise to characteristic variations in the Tafel slopes with the reaction mechanism. Note, however, that if the intermediates are adsorbed onto the electrode surface, only in the case of low coverages will a simplified treatment be possible; otherwise, potential-dependent surface coverage terms, θ_is, are required (see Sections 2 and 4 for further discussion).

Scheme 1, as written, is considered to be closed between steps 2 and $n - 1$; that is, reactants enter the reaction at step 1 and products exit at step n. If it is recognized that only the surface activities of reaction intermediates are potential dependent and hence affect the "electron" reaction order, Scheme 1 can be easily extended to permit the entrance of further reactants or products (the latter being reactants for the reverse reaction) in intermediate steps as well. These would be represented simply by their solution activities and hence would be potential independent.

2. Underlying Assumptions

In order to derive rate expressions for multistep mechanisms such as those in Scheme 1, the following assumptions are usually made:

1. Only one of the steps is rate-limiting (the rate-determining step, rds), which generally requires that the rate constant of this reaction step be at least 100 times smaller than those of all other prior steps.
2. The same step is also rate limiting in the reverse direction (a condition arising from reversibility of the reaction).
3. Intermediates, if adsorbed on the surface of the electrode substrate, are at low coverages (note, however, that when coverages of intermediates do approach saturation, potential-dependent rates can still arise if an electrochemical desorption type of step is involved; then $b \simeq 118$ mV dec^{-1} at 298 K for β taken as 0.5).

[d]The activities of intermediates at the substrate surface are designated by a superscript "s" to distinguish them from those of solution species.

4. The kinetics of all the other steps do not deviate significantly from either steady-state or quasi-equilibrium conditions (see later discussion).
5. The nature of the mechanistic scheme does not change with potential.

In reality, this last point often does not hold since the PE surfaces for initial reactant, final product, and all the intermediates will shift relative to one another; then some other step in the scheme could become rate-limiting. There is also the possibility of the emergence of alternative parallel steps that could lead to a different mechanism (although it should be mentioned that mass transport can often become controlling before such alternative pathways are experimentally recognized).

If however, the above assumptions do hold, as they often will near the reversible potential, the net rate of the overall reaction (measured as current density) will be determined by the rate of the rds. The equation for the net rate, i_{net}, of the overall reaction is then [cf. Eq. (19)]:

$$i_{\text{net}} = -zFk_{\text{rds}}a^{s}_{I_{\text{rds}}} \exp[-z_{\text{rds}}\beta f\eta] + zFk_{-\text{rds}}a^{s}_{I_{\text{rds}+1}} \exp[z_{\text{rds}}(1-\beta)f\eta] \quad (22)$$

where $k_{-\text{rds}}$ and k_{rds} are the heterogeneous rate constants corresponding to the PE barrier of the rds at equilibrium ($\eta = 0$), z_{rds} is the number of electrons transferred in the rds, z is the total number transferred per turnover of the overall reaction, $a^{S}_{I_{\text{rds}+1}}$ and $a^{S}_{I_{\text{rds}}}$ are the surface activities of the species involved in this step, and for simplicity, the constants $F/(RT)$ have been replaced by f.

The potential dependence of i_{net} in this expression [Eq. (22)] might initially appear to be defined solely by the exponential terms in either branch, but if in fact I_{rds} and $I_{\text{rds}+1}$ are reaction intermediates, under certain conditions their surface activities are also potential dependent. In order to clarify this, the next step is to develop expressions for the potential dependence of the surface activities of intermediates.

3. Steady-State and Quasi-Equilibrium Treatments

The standard method for evaluating the concentration dependence of reaction intermediates in chemical kinetics is to use the steady-state assumption (see Ref. 15, p. 89 and references therein, and the introductory paragraphs in Section I), which may also be employed to determine the potential dependence of the activities of reaction intermediates in electro-

chemical kinetics. It is assumed for any reaction that following a short induction time after initiation of the process, the effective concentrations of all intermediates reach values that remain constant in time and therefore are in a steady state, which means that the rates of their formation and disappearance will be equal, with the result that the rates of change of their effective concentrations will be 0. This situation allows the following evaluation for say, $a^S_{I_2}$, the activity of the first intermediate of Scheme 1:

$$\frac{da^S_{I_2}}{dt} = k_1 a_{A_1} \exp[-z_1 \beta f\eta] + k_{-2} a^S_{I_3} \exp[z_2(1-\beta) f\eta]$$

$$- k_{-1} a^S_{I_2} \exp[z_1(1-\beta) f\eta] - k_2 a^S_{I_2} \exp[-z_2 \beta f\eta] = 0 \qquad (23)$$

which occurs since v_1 (the rate of the forward direction of step 1 in Scheme 1) and v_{-2} (that of the reverse direction of step 2) produce the intermediate I_2 and v_{-1} and v_2 consume it. Solving for the surface activity of I_2 gives Eq. (24):

$$a^S_{I_2} = \frac{k_1 a_{A_1} \exp[-z_1 \beta f\eta] + k_{-2} a^S_{I_3} \exp[z_2(1-\beta) f\eta]}{k_{-1} \exp[z_1(1-\beta) f\eta] + k_2 \exp[-z_2 \beta f\eta]} \qquad (24)$$

This is clearly a complicated expression that will become simplified only upon making (in some cases, arbitrary) assumptions about the relative magnitudes of some of the rate constants and hence neglecting some terms (see Ref. 33 for an example of this worked out fully). Such steady-state expressions could be written for the surface activities of all intermediates involved in the reaction scheme. If they were substituted one into the other, they could progressively lead to an expression, albeit quite complicated, defining the complete potential dependence of the surface activity of I_{rds}.

In order to avoid such complicated expressions, the quasi-equilibrium method is used, although the above steady-state approach can become reduced to the same result if various limiting assumptions about relative values of rate constants, referred to earlier, are introduced. This approach assumes a rate-limiting step so that all other steps are supposed to have much larger rate constants (in both directions) and hence are all in virtual or "quasi"-equilibrium. Bockris[34] applied a similar treatment in a less general way to the kinetics of various pathways of the oxygen evolution reaction. With the application of a negative overpotential that drives the forward, supposed reductive direction of the reaction, each of the steps prior to the rds (which are hence limited by it) will be at quasi-equilibrium,

while those following it will not be limited by the rds and will simply run to products without influencing the rate in that direction.

The steps after the rds (as they are written in Scheme 1, i.e., as reductions) will be rate limited by the rds only in the reverse, oxidative reaction direction. The effect of these steps following the rds will be observed for applied positive "overpotentials." In the case of oxidation the steps following the rds will be in quasi-equilibrium and those preceding the rds will now run (backward) to reactants without influencing the rate in the reverse direction. Ignoring the opposite reaction direction is a convenient simplication that, as we will see (Section IV.6) does not seriously affect the validity of the quasi-equilibrium treatment.

At this point, the surface activities of the "reactant" and "product" intermediates of the rds in Eq. (22) have unknown potential dependencies, but these can usually be evaluated by use of the quasi-equilibrium method. For the cathodic, forward direction, this potential dependence may be built up progressively in terms of the initial reactant of the reaction scheme, that is, A_1. Thus the rate of step 1 (in Scheme 1) is limited by the rds and according to the above assumptions is considered to be in quasi-equilibrium. Therefore the rates (as current density) of the forward and reverse reactions of this step may be equated as

$$z_1 F k_1 a_{A_1} \exp[-z_1 \beta f\eta] = i_1 = z_1 F k_{-1} a_{I_2}^S \exp[z_1(1-\beta) f\eta] \qquad (25)$$

Note that we are considering the current for this individual step and thus z_1 (probably unity) is used in the preexponentials instead of z; this latter finds application when the overall reaction is considered [i.e., as in Eq. (22)]. Equation (25) is rearranged to extract the surface activity of the intermediate I_2 in terms of the bulk solution activity of A_1 and for simplicity K_1 is substituted for k_1/k_{-1}. This gives Eq. (26), a Nernst equation-like expression for the quasi-equilibrium of step 1:

$$a_{I_2}^S = a_{A_1} K_1 \exp[-z_1 f\eta] \qquad (26)$$

in which β and the preexponentials in Eq. (25) have become cancelled in the rearrangement. [Obviously, for any quasi-equilibrium expression of this kind, the β_a and β_c factors must be assumed to be linked (i.e., $\beta_a = 1 - \beta_c$) in order for them to disappear].

Next, the rates of the forward and reverse reactions in step 2 may be similarly equated and the activity of the next intermediate, I_3, solved for, as in Eq. (27):

$$a_{I_3}^S = a_{I_2}^S K_2 \exp[-z_2 f\eta] \tag{27}$$

into which the surface activity for I_2 may be substituted from Eq. (26), giving

$$a_{I_3}^S = a_{A_1} K_1 K_2 \exp[-(z_1 + z_2) f\eta] \tag{28}$$

which is an expression for the surface activity of the intermediate I_3 in terms of the (known and potential independent) bulk solution activity of the initial reactant of the overall reaction.

This procedure may be carried through stepwise for all reaction steps that are in quasi-equilibrium up to the rds, and this then gives the general expression, Eq. (29):

$$a_{I_{rds}}^S = a_{A_1} \left(\prod_{k=1}^{rds-1} K_k \right) \exp\left[-\left(\sum_{k=1}^{rds-1} z_k \right) f\eta \right] \tag{29}$$

The argument of the exponential term of Eq. (29) shows the overall potential dependence of the cathodic reaction rate that arises from all the quasi-equilibrium electron transfers occurring prior to the rds. The z_is must all be integers and thus each previously transferred electron adds "1" to the η-dependence factor.

A general equation for the surface activity of the intermediate that is the product of the rds, I_{rds+1} (which would be the reactant for the reverse, oxidation reaction) can be similarly developed for the reverse, anodic direction of reaction. In the case of the oxidation reaction, however, it would be built backward from the ultimate product of the reaction (as written in Scheme 1), A_{n+1}, and would be

$$a_{I_{rds+1}}^S = a_{A_{n+1}} \left[\prod_{k=rds+1}^{n} \frac{1}{K_k} \right] \exp\left[\left[\sum_{k=rds+1}^{n} r_k \right] f\eta \right] \tag{30}$$

4. Rate Equation for Consecutive Electrochemical Reactions

The rate equation for the reaction described by Scheme 1 is derived by substituting the (potential-dependent) expressions for the activities I_{rds} and I_{rds+1} [Eqs. (29) and (30), respectively] into the rate equation for the rds

[Eq. (22)]. This then gives Eq. (31), the equation for the net overall rate for a multistep electrochemical reaction having a single rds:

$$i_{\text{net}} = zF\left(-a_{\text{A}_1}k_{\text{rds}}\left[\prod_{k=1}^{\text{rds}-1} K_k\right]\right)\exp\left[-(\gamma_p + z_{\text{rds}}\beta)f\eta\right] + a_{\text{A}_{n+1}}k_{-\text{rds}}\left[\prod_{k=(\text{rds}+1)}^{n}\frac{1}{K_k}\right]\exp\left\{[\gamma_f + z_{\text{rds}}(1-\beta)]f\eta\right\} \tag{31}$$

The first term in Eq. (31) is the cathodic term, negative by convention (see footnote *b*), that contains the activity of the initial reactant, A_1. For simplification, γ_p, which is the total number of electrons transferred **p**rior to the rds, has replaced the summation term in the argument of the exponential of Eq. (29). The second term in Eq. (31) is the anodic direction term, giving a positive current contribution, which contains the activity of the overall product of the reaction, A_{n+1}, and γ_f is the number of electrons transferred **f**ollowing the rds.

Grouping potential-independent terms into an exchange current density and collecting the arguments of the exponentials simplifies the rate equation to

$$i_{\text{net}} = i_{\text{o}}[\exp(\alpha_a f\eta) - \exp(-\alpha_c f\eta)] \tag{32}$$

This is obviously a BV type of equation [see Eq. (20)], but where β and $(1 - \beta)$ in that equation have become replaced, respectively, by transfer coefficients which are

$$\alpha_c = \gamma_p + z_{\text{rds}}\beta \tag{33a}$$

for the cathodic direction of reaction and

$$\alpha_a = \gamma_f + z_{\text{rds}}(1-\beta) \tag{33b}$$

for the anodic reaction direction. The first terms (on the rhs) in Eqs. (33a) and (33b) are the contributions from quasi-equilibrium, nonrate-limiting or non-rds steps, while the second terms are the contributions from the rds. Recall that preceding and following electron transfers in a reaction mechanism add integers to the transfer coefficients for the rds. Note, however, that the addition of integers is valid only when the effective surface concentrations of the intermediates are below their solubility

limits or, in the case of reactions involving adsorbed intermediates, when the total surface coverage by intermediates is sufficiently small to allow the approximation $(1 - \theta_{I_2} - \theta_{I_3} \ldots) \rightarrow 1$ (see below, Section IV.5). Other limitations apply with respect to the relative magnitudes of the rate constants of the steps involved in a reaction sequence and these will be examined in Section IV.6.

5. Adsorption of Intermediates

In the special but not uncommon situation where the intermediates of a reaction are adsorbed onto the surface of the electrode substrate,[e] the activities of the intermediates in the surface region, as they are used in the present derivation, would have to be replaced with surface coverage fractions (θ_is) since in this case the available electrode substrate area limits the extent of the reaction. If the electrode were to become completely covered by one or more of the intermediates (as with the application of a larger driving force η), the potential dependence of the rate (i.e., the Tafel slope, b) would no longer include the contribution that would otherwise arise for the non-rds coverage-limited reaction steps.

In this case, the quasi-equilibrium expression for step 1 of Scheme 1 would be [compare to Eq. (25)] modified to

$$z_1 F k_1 a_{A_1}[1 - (\theta_{I_2} + \theta_{I_3} + \ldots)] \exp(-z_1 \beta f\eta) = z_1 F k_{-1} \theta_{I_2} \exp(z_1(1-\beta) f\eta) \tag{34}$$

where rearrangement would give

$$\theta_{I_2} = a_{A_1}[1 - (\theta_{I_2} + \theta_{I_3} + \ldots)] K_1 \exp(-z_1 f\eta) \tag{35}$$

Ordinarily, electrochemical adsorption isotherms would have to be written (e.g., a Frumkin-like isotherm) as given in, for example, Eq. (36), which includes a lateral interaction parameter, g:

$$\frac{\theta_{I_2}}{1 - \sum \theta_i} = a_{A_1} K_1 \exp\left(g \cdot \sum \theta_i\right) \cdot \exp(f\eta) \tag{36}$$

where g expresses the way in which increased coverage changes a given species adsorption energy and it might be expected that there would be as

[e] An important example of this is in the hydrogen evolution reaction (Ref. 21, p. 170).

many g parameters as there are individual types of interactions between adsorbed species. However, it is possible to envisage a communal basis of interactions among the assembly of adsorbed intermediate species, as proposed by Conway and Gileadi.[35] Only in the limiting case where the total electrode coverage, $\Sigma\theta_i$, is low [i.e., where $1 - \Sigma\theta_i \rightarrow 1$ and perhaps also $g = 0$, but not necessarily], could the potential dependence be elaborated as developed in for example, Eqs. (29) and (30), in which surface activities were used.

If saturation coverage were to prevail (i.e., $\Sigma\theta_i \rightarrow 1$, for instance, at elevated potentials), the coverage and hence the measured rate contribution of the step would become potential independent. It is therefore important to identify such limiting situations by complementary experimental techniques[36] such as ac impedance spectroscopy[37,38] or recording of potential-decay transients[39–41] in order to avoid erroneous conclusions about mechanisms. These two procedures serve to identify and characterize any pseudo-capacitance associated with the potential dependence of coverage by intermediates when their θ_i values become larger than about 0.1. As a final point, the $\theta = 1$ condition generally does not arise in multistep reactions because usually there is a following desorption step that prevents this, except, of course, in underpotential deposition, where no continuous faradaic reaction in time takes place.

6. Validity of the Quasi-Equilibrium Approximation

The quasi-equilibrium approximation offers a considerable simplication of the usual steady-state approach for the solution of reaction mechanism problems. It relies on the assignment of an rds with the assumption [assumption (i), Section IV.2] that the rate constants of this step are at least 100 times smaller than all other steps. This assumption cannot of course be applied to all electrochemical reactions without prior knowledge that it is indeed valid. Even when this assumption is acceptable, there are limits to the overpotential range over which mechanistically significant Tafel slopes can be derived using this approximate method. In order to make clear these limits and the effect that various combinations of rate constants can have on a simple multistep reaction scheme, Tafel plots will be simulated using the steady-state treatment. Of critical importance in this regard are the relative magnitudes of the rds and non-rds rate constants.

Consider a reaction mechanism similar to Scheme 1, but involving only three consecutive electron-transfer steps. If, as an example, we take

the second, middle step as rate-limiting, the rate equation for this three-step reaction is

$$i_{\text{net}} = -3Fk_2 a_{\text{I}_2}^S \exp[-\beta f\eta] + 3Fk_{-2} a_{\text{I}_3}^S \exp[(1-\beta) f\eta] \tag{37}$$

It should be recognized that the activities of the two reaction intermediates, I_2 and I_3 in Eq. (37), are potential dependent. If we assume that the reaction is in a steady-state and for the time being ignore the solubility limits of these intermediates, steady-state expressions for these potential-dependent activities can be developed [i.e., as per Eqs. (23) and (24)]. In this particular example, $\exp[\beta f\eta]$ may be factored out and cancelled from both numerator and denominator of the steady-state expression for I_2 and $\exp[(1-\beta) f\eta]$ for that for I_3, giving respectively

$$a_{\text{I}_2}^S = \frac{k_1 a_{\text{A}_1} + k_{-2} a_{\text{I}_3}^S \exp[f\eta]}{k_{-1} \exp[f\eta] + k_2} \tag{38}$$

and

$$a_{\text{I}_3}^S = \frac{k_2 a_{\text{I}_2}^S \exp[-f\eta] + k_{-3} a_{\text{A}_4}}{k_{-2} + k_3 \exp[-f\eta]} \tag{39}$$

If we substitute these steady-state expressions for the activities of the two intermediates into the rate equation for the rds [Eq. (37)], we then have

$$i_{\text{net}} = -3Fk_2 \left[\frac{k_1 a_{\text{A}_1} + k_{-2} a_{\text{I}_3}^S \exp[f\eta]}{k_{-1} \exp[f\eta] + k_2} \right] \exp[-\beta f\eta]$$

$$+ 3Fk_{-2} \left[\frac{k_2 a_{\text{I}_2}^S \exp[-f\eta] + k_{-3} a_{\text{A}_4}}{k_{-2} + k_3 \exp[-f\eta]} \right] \exp[(1-\beta) f\eta] \tag{40}$$

and this will describe the steady-state polarization behavior for this reaction. Note that there remain in these expressions two intermediate activities (for I_3 and I_2) in the cathodic and anodic terms, respectively. These activities are for species on the "other side" of the rds and will have to be assumed not to influence the rates of the respective terms (see later discussion).

For this particular reaction (assuming $\beta = 0.5$), where one electron is transferred both before and after the rds, the quasi-equilibrium approach examined earlier (Seciton IV.4) would predict transfer coefficients [from

Eqs. (33a) and (33b)] of $\alpha_c = \alpha_a = 1.5$, which should give (at room temperature) Tafel slopes for both cathodic and anodic branches of about |39| mV dec^{-1}. The fact is, however, that the limiting conditions under which the quasi-equilibrium treatment applies are not necessarily met for all multistep reactions and, perhaps surprisingly in cases where they are met, the treatment might give mechanistically significant results only over a relatively narrow (and low) overpotential range. In order to clarify this, we will examine the effect that various sets of rate constants (k_i and k_{-i}) for steps 1–3 of this hypothetical reaction have on the form of the semilogarithmic polarization curves calculated from Eq. (40).

For simplicity in this simulation, the solubility or coverage limits of the activities of the rds intermediates which are calculated by either Eq. (38) or (39), have been ignored and the calculated (potential-dependent) effective concentrations have been allowed to vary freely and can reach unrealistically large values. Although this is an oversimplication, it provides a better demonstration of how variations in the relative magnitudes of the rate constants can affect the appearance of the Tafel relations.

To elaborate, in Fig. 4 is shown simulated [by Eq. (40)] Tafel plots demonstrating the effect of varying k_2, the forward rate constant of the rds, with respect to k_1. All other quantities are held constant in this simulation. The effective concentrations a_{A_1} and a_{A_4} have been set equal to 0.5 mol dm^{-3}, the rate constants k_{-1}, k_3, and k_{-3} have all been set to 1×10^{-4} cm s^{-1} and k_{-2} (i.e., k_{-rds}) to 1×10^{-6} cm s^{-1}. k_2 and k_1 are the only rate constants that vary in this simulation where the ratio, k_1/k_2, (i.e., prior step relative to the rds) changes from 10^0 to 10^6. Note that k_1 does not actually change independently since the principle of microscopic reversibility and detailed balance (Ref. 15, p. 285) requires that the following equality must hold:

$$\frac{k_1 k_2 k_3}{k_{-1} k_{-2} k_{-3}} \frac{a_{A_1}}{a_{A_4}} = 1 \tag{41}$$

With all other quanitities set, k_1 must vary as k_2 does to satisfy this equality [Eq. (41)].

In most of the simulated curves in Fig. 4 two linear regions in both the cathodic and anodic branches can be clearly seen that have slopes of |39| and |118| mV dec^{-1} (at 298 K), whereas the quasi-equilibrium treatment would have predicted only a single linear Tafel region of slope |39| mV dec^{-1} for this mechanism. When the k_1/k_2 ratio increases, varying from 10^0 (solid line) to

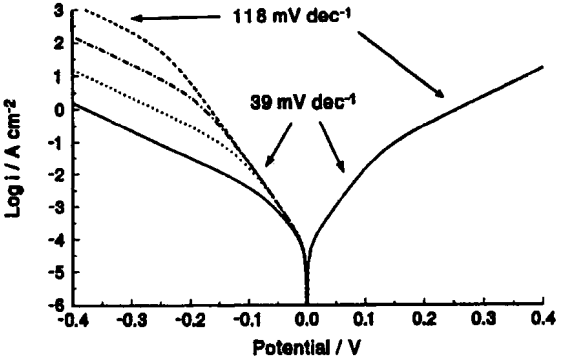

Figure 4. Simulated Tafel plots [from Eq. (40)] for a reaction involving three consecutive electron-transfer steps. The effective concentrations a_{A_1} and a_{A_4} have been set to 0.5 mol dm^{-3}; the rate constants k_{-1}, k_3, and k_{-3} to 10^{-4} cm s^{-1}; and k_{-2} (i.e., k_{-rds}) to 10^{-6} cm s^{-1}. k_2 has values of 10^{-5} (solid), 10^{-6} (dots), 10^{-7} (dot-dash), and 10^{-8} (dash) cm s^{-1} and therefore, according to Eq. (41), k_1 has values of 10^{-5}, 10^{-4}, 10^{-3}, and 10^{-2} cm s^{-1}, respectively, corresponding to k_1/k_2 ratios of 10^0 (solid), 10^2 (dots), 10^4 (dot-dash), and 10^6 (dash) cm s^{-1}.

10^6 (dashed line) in Fig. 4, the effect is an increase in the length of the (mechanistically significant) cathodic region of slope |39| mV dec^{-1}. This illustrates the importance of considering the relative magnitudes of the rate constants of reaction steps and the criterion for the use of Tafel slopes for mechanism elucidation. Note that the first (solid) curve, which shows no region of (cathodic) slope –39 mV dec^{-1}, does not actually correspond to a situation where step 2 is rate-limiting. All curves in Fig. 4 become superimposed at higher positive potentials here, since the values of k_{-3} and k_{-2} have been held constant, their ratio, k_{-2}/k_{-3}, in this case being 100.

The transition from –39 to –118 mV dec^{-1} in the curves in Fig. 4 occurs as increasing overpotential [either negative in the case of Eq. (38) or positive for Eq. (39)] makes negligible the exponential terms relative to the potential-independent terms in these equations [Eqs. (38) and (39)]. Recall that the numerators of the steady-state expressions, Eqs. (38) and (39), contain activity terms for intermediate species on the "other side" of the rds, i.e., a_{I_3} and a_{I_2}, respectively. It was found, however, in these simulations that the values for these activities, whether calculated by an approximation or ignored, had little effect on the ultimate potential dependence calculated by the steady-state expressions [Eqs. (38) and (39)].

Figure 5 shows simulated polarization curves [by Eq. (40)] that demonstrate the effect of varying the relative magnitudes of forward and reverse rate constants of the *non-rds* reaction steps with respect to those for the rds. For the curves in Fig. 5(a), the following values are set: $k_2 = k_{-2} = 1 \times 10^{-6}$ (rds) and $k_1 = k_{-3} = 1 \times 10^{-3}$ (where these rate constants are for the "intermediate-forming" directions of non-rds reaction steps). k_{-1} and k_3 are varied, but remain equal to one another owing to the equality of Eq. (41). The result is that the predicted Tafel plots have longer mechanistically significant regions (i.e., of slope |39| mV dec^{-1}) with an increasing ratio of the rate constants of the "intermediate-consuming" rds steps, either k_{-1}/k_2 or k_3/k_{-2} for the respective cathodic and anodic Tafel branches (as for Fig. 4). The plots all become superimposed at higher overpotential, having common slopes of |118| mV dec^{-1}. This characteristic for these simulated curves arises from the fact that the sums of $k_2 \cdot k_1$ and $k_{-2} \cdot k_{-3}$ for cathodic and anodic branches, respectively, have been set constant in this simulation.

In Fig. 5(b) the rds and [in contrast to the simulated curves in Fig. 5(a)] intermediate-consuming reaction directions of the non-rds steps are set with $k_2 = k_{-2} = 1 \times 10^{-6}$ and $k_{-1} = k_3 = 1 \times 10^{-4}$. In this case, the rate constants of both intermediate-forming (non-rds) reaction steps vary. It is seen in Fig. 5(b) that all simulated curves have the same lengths of mechanistically significant slope [defined by the ratios, k_{-1}/k_2 or $k_3/k_{-2}[10^{-2}]$ which are set constant], but that the curves are shifted vertically along the log i axis as $k_2 \cdot k_1$ or $k_{-2} \cdot k_{-3}$ vary.

Essentially, it is the changing (with overpotential) of the effective concentration of the intermediates involved in the rds that gives rise to a decrease in the usual one-electron Tafel slope of |118| mV dec^{-1}. Practically speaking, however, the potential dependence of these effective concentrations would be restricted to the solubility limits for these intermediate species or, in the case of surface reactions involving adsorbed intermediates, to saturation (or complete coverage) conditions, which in both cases would result in prior electron-transfer reactions becoming potential independent and invisible to scrutiny by polarization experiments. This fact imposes a further restriction on the appropriate region from which mechanistically significant Tafel slopes should be evaluated. As a further consideration, it must also be assumed that during experimental measurements, the activities of species that define the reversible potential of the reaction (i.e., via the Nernst equation [Eq. (13)]) do not change significantly; otherwise, unless this change could be determined and E_r corrected, the overpotential values would be incorrect.

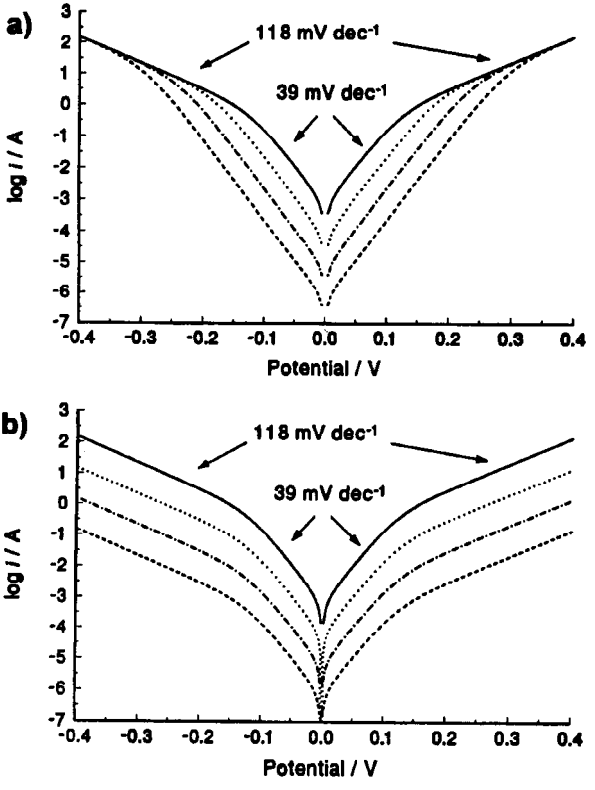

Figure 5. Simulated Tafel plots [from Eq. (40)] for a reaction involving three consecutive electron-transfer steps, showing the effect of variation of rate constants for (a) intermediate-consuming and (b) intermediate-creating nonrds steps. (a) Rate constants: $k_2 = k_{-2} = 10^{-6}$ cm s^{-1} (i.e., the rds) and $k_1 = k_{-3} = 10^{-3}$ cm s^{-1} for $k_3 = k_{-1}$ values of 10^{-4} (solid), 10^{-3} (dots), 10^{-2} (dot-dash), and 10^{-1} (dash) cm s^{-1}. (b) Rate constants: $k_2 = k_{-2} = 1 \times 10^{-6}$ cm s^{-1} (i.e., the rds) and $k_{-1} = k_3 = 1 \times 10^{-4}$ cm s^{-1} for $k_1 = k_{-3}$ values of 10^{-3} (solid), 10^{-4} (dots), 10^{-5} (dot-dash), and 10^{-6} (dash) cm s^{-1}.

Clearly, without prior knowledge of the mechanism of a given reaction, it is difficult to identify mechanistically significant Tafel slopes when the rate-determining step does not have rate constants at least 100 times smaller than those of all other reaction steps.

V. MODIFICATIONS TO THE CONSECUTIVE ELECTROCHEMICAL REACTION

1. General Remarks

The rate expression for the multistep consecutive electron-transfer reaction of Scheme 1 [i.e., Eq. (31)] is able to relate complex consecutive electron-transfer reaction mechanisms to experimental potential vs. logarithmic current-density relations. When β is assumed to be 1/2, the Tafel slopes ($1/\alpha f$) predicted by this relation can only have values less than or equal to 118 mV dec^{-1} (at 25 °C) for electron-transfer limited reactions, since electrons transferred in non-rds steps will add integers (to β) in the expected α values and therefore decrease the Tafel slope below 118 mV dec^{-1}. For instance, the usual cathodic Tafel slope of 118 mV dec^{-1} for a one- electron transfer over a symmetric barrier is decreased to 39 mV dec^{-1} for one preceding quasi-equilibrium electron transfer and to 24 mV dec^{-1} for two, etc., and the anodic Tafel slopes are similarly decreased for one and two "following" (where the reaction steps are still written as reductions, as in Scheme 1) electron transfers, respectively. It should be noted that the Tafel slopes that are determined by α values involving $\gamma + \beta$ differ substantially and discontinuously from the value for $\alpha = \beta \simeq 1/2$, and therefore should be easily distinguishable.

The effect of the occurrence, within a generalized reaction scheme, of chemical steps, multielectron transfers, or an rds that is a dissociation or combination step (i.e., one that involves a change of stoichiometric coefficients) will be examined as well as mechanisms where the rds (and hence the overall reaction) has a stoichiometric number greater than 1. This latter case is more complicated than these others and, since it is the only mechanistic situation[f] in a consecutive reaction scheme that can give

[f] A situation of a different kind that can lead to b values > 118 mV dec^{-1} arises when electron transfer takes place across a barrier-layer oxide film (e.g., of TiO_2 or ZrO_2). Then β operates only on the fraction of the metal solution p.d. that arises across the double layer on the solution side of the oxide film.

rise to Tafel slopes greater than 118 mV dec^{-1} (under a specific set of circumstances), it will be discussed separately in a section that follows.

2. Chemical Steps

If a step within the general mechanism does not involve an electron transfer, its involvement in determining the potential dependence of the rate will depend on whether it occurs as the rds. If some step, *c,* limited by the rds, is a chemical step, its quasi-equilibrium expression will be

$$a_{\mathrm{I}_c} k_c = a_{\mathrm{I}_{c+1}} k_{-c} \tag{42}$$

which when rearranged gives

$$a_{\mathrm{I}_{c+1}} = a_{\mathrm{I}_c} K_c \tag{43}$$

This term is obviously independent of potential and so its effect is only a trivial one, which is that K_c is multiplied in among all the other quasi-equilibrium constants (ΠK_is). Note that reaction order in Eq. (42) could be >1.

However, if the rds itself is a chemical step, the transition state does not involve electron transfer and hence β plays no part in the net rate, i.e.

$$i_{\mathrm{net}} = zF(-a_{\mathrm{I}_{\mathrm{rds}}} k_{\mathrm{rds}} + a_{\mathrm{I}_{\mathrm{rds}+1}} k_{-\mathrm{rds}}) \tag{44}$$

In this case, the potential dependence of the net rate manifests itself indirectly through that of the surface activities of the intermediates, $\mathrm{I}_{\mathrm{rds}}$ and $\mathrm{I}_{\mathrm{rds}+1}$, if their prior formation involves electron-transfer reactions. This situation is described by the transfer coefficients developed previously [Eqs. (33a) and (33b)], where z_{rds} in these would be 0.

3. Multielectron Transfers

A multielectron transfer in one step (unlikely as these are considered to be), if rate-limiting, would modify the transfer coefficients [Eqs. (33a) and (33b)] by multiplying the potential dependence of the rds [the β parts of Eqs. (33a) and (33b)] by the number of electrons involved in this transfer, z_{rds}. If it does not arise during the rds, such a multielectron-transfer step would simply contribute to (and disappear into) γ_p or γ_f.

4. Combination or Dissociation as a Rate-Limiting Step

When an electrochemical combination or dissociation step is rate-limiting for a given reaction sequence, a unique potential dependence of the non-rds steps arises owing to the difference in stoichiometric coefficients[g] between reactant and product of the rds. The simplest examples that can be envisaged are (1) where ω equivalents of some reactant combine to form a single product in an electrochemical reduction reaction (e.g., $2H^+ + 2e^- \rightarrow H_2$) or (2) for the case where a single reactant splits into ω equivalents of some product (e.g., $Cl_2 + 2e^- \rightarrow 2Cl^-$).

Considering a hypothetical reaction in which a dissociation (in the cathodic reduction direction) step is rate-limiting, the equation for the net rate for a reaction, the rds of which involves the dissociation of 1 into ω entities, would be written as

$$i_{\text{net}} = zF\{-a^S_{\text{I}_{\text{rds}}} k_{\text{rds}} \exp[-z_{\text{rds}}\beta f\eta] + (a^S_{\text{I}_{\text{rds}+1}})^{\omega} k_{-\text{rds}} \exp[z_{\text{rds}}(1-\beta) f\eta]\} \quad (45)$$

Note that the change in stoichiometric coefficients in this rate-limiting step (i.e., from 1 to ω) affects only the potential dependence of the surface activity of the product, $\text{I}_{\text{rds}+1}$, which, in fact, is raised to the ω^{th} power in Eq. (45). If the potential dependence of the activities of the intermediates is expanded by the usual quasi-equilibrium approach [Eqs. (27)–(31)], the net rate equation for a reaction, the rds of which is a dissociation step, is

$$i_{\text{net}} = zF\left(-a_{\text{A}_1} k_{\text{rds}} \left[\prod_{k=1}^{\text{rds}-1} K_k\right] \exp[-(\gamma_{E-P} + z_{\text{rds}}\beta) f\eta] + a^{\omega}_{\text{A}_{n+1}} k_{-\text{rds}} \left[\prod_{k=\text{rds}+1}^{n} \frac{1}{K_k}\right]^{\omega} \exp[(\omega\gamma_{E-F} + z_{\text{rds}}(1-\beta)) f\eta]\right) \quad (46)$$

[g] For clarification, note that the term stoichiometric *coefficients,* ω, refers to the numbers of reactant and product equivalents involved in a given step while the stoichiometric *number, v,* is the number of repetitions or acts of a given reaction step necessary to achieve an overall multistep reaction. Although a relative change of ω in a step usually necessitates that all following steps (in the case of a dissociation) occur $v = \omega$ times, the distinction between ω and *v* should be emphasized since a mechanism having a rds with a stoichiometric number greater than 1 has a unique effect on the theoretical transfer coefficients, as will be discussed in Section VI.

where γ_{E-P} and γ_{E-F}[h] are the numbers of electrons transferred in elementary electron-transfer steps prior to and following the rds, respectively, and those following affect only the reverse, oxidation rate term.

It is at this point that we depart from the terminology used by Bockris and Reddy (Ref. 3, p. 1007) in their often-cited and generalized discussion of transfer coefficients [Eqs. (1a) and (1b)] (i.e., γ_p and γ_f) and introduce the related terms γ_{E-P} and γ_{E-F}. The difference between these sets of electron-number parameters is that in the latter, an electron transferred in a step that occurs, say, *v* times (i.e., it has a stoichiometric number *v* greater than 1) is counted only *once* and not the *v* times it actually has to occur for one turnover of the overall reaction. This added "complication" of the electron accounting has the advantage of showing more clearly how stoichiometric coefficients and numbers enter into experimentally obtainable transfer coefficients and hence can demonstrate one of the links between mechanism and experiment.

The transfer coefficients for an rds that is a dissocation (reductive or chemical) step are therefore

$$\alpha_c = \gamma_{E-P} + z_{\text{rds}}\beta \tag{47a}$$

and

$$\alpha_a = \omega\gamma_{E-F} + z_{\text{rds}}(1-\beta) \tag{47b}$$

while those for an rds that is a combination (reductive or chemical) step are

$$\alpha_c = \omega\gamma_{E-P} + z_{\text{rds}}\beta \tag{48a}$$

and

$$\alpha_a = \gamma_{E-F} + z_{\text{rds}}(1-\beta) \tag{48b}$$

[h] The subscript terminology means: γ elementary-following, previous, and stoichiometric as will be seen later. The seemingly minor difference between the terminologies has importance for later conclusions. Further, an "elementary" step is a reaction step that involves a single transition state.

VI. TAFEL SLOPES GREATER THAN 118 mV dec^{-1}

1. Introduction

The theoretical transfer coefficients derived from the hypothetical reaction mechanisms considered so far, Eqs. (33a) and (33b), (47a) and (47b), and (48a) and (48b), can predict, for an assumed value of $\beta = 1/2$ (at room temperature), Tafel slopes that are either less than 118 mV dec^{-1} or infinite (where this latter would correspond to the case of a chemical rds with no prior quasi-equilibrium electron-transfer steps). They cannot, however, explain the Tafel slopes significantly greater than 118 mV dec^{-1} that are sometimes observed.

Tafel slopes that are not infinite but are substantially greater than 118 mV dec^{-1} can be explained by: (1) an arbitrary and trivial assumption that $\beta < 1/2$; (2) the effect (footnote f) of barrier-layer films such as oxide on ZrO_2 or $TiO_2$42–44 (but this is usually only in the case of anodic reactions, particularly those involving valve-metal barrier oxide films); and (3) an electrochemical reaction mechanism where the rds is a chemical step *and* has a stoichiometric number, v, greater than 2 [refer to Eq. (1)]. This latter possibility will be developed in the next section in terms of a general multistep reaction mechanism.

2. Stoichiometric Number

The stoichiometric number, v, of a given reaction step is defined as the number of times that step must occur for one turnover of the whole reaction. The overall stoichiometric number of a reaction is specifically the number of times the rds has to occur. This is an important quantity with respect to mechanism elucidation and was originally defined by Horiuti for the hydrogen reaction.[45,46] According to the stoichiometric number concept of Horiuti,[45] v_i for each reaction step will multiply the Gibbs energy change (or as it is also called, its electrochemical affinity) for that step, Δg_i, and the affinity, ΔG, for the overall reaction is

$$\Delta G = \sum_{i=1}^{n} \nu_i \Delta g_i \tag{49}$$

In this derivation, since it is assumed that a single step, the rds, limits the rate of the overall reaction, all other steps must be in quasi-equilib-

rium, which means that there are no Gibbs energy changes associated with them. Thus the overall Gibbs energy change (ΔG) for the reaction is defined by that of the rds. Therefore the stoichiometric number of the rds, ν_{rds}, or what has come to be termed simply ν, may be determined from Eq. (50):

$$\frac{\upsilon_{\rightarrow}}{\upsilon_{\leftarrow}} = \exp\left[-\frac{\Delta G}{\nu_{rds}}/RT\right] \tag{50}$$

Equation (50) forms the basis upon which ν can be evaluated (e.g. (1) by the radioactive tracer method[46–48] to evaluate simultaneously $\upsilon_{\rightarrow}$ and $\upsilon_{\leftarrow}$), (2) by comparing i values at appropriate potentials for different reactant activities; (3) coupling information from high and low overpotential regions of steady-state polarization curves[49–51] (extrapolated i_0 and charge-transfer resistance, R_{CT}, respectively); (4) or by back-reaction correction analysis.[52] The first two methods involve determination of ν at any single potential while the latter two procedures must assume that the same mechanism (and hence ν) applies at different potentials (at which individual measurements are required) and that the reverse reaction occurs by the same path and has the same transition state and thus rate-determining step [for both forward (cathodic) and reverse reactions].

The third method listed above is based upon the relation

$$\nu = i_0 z f \frac{d\eta}{di_{low}} \tag{51}$$

initially developed by Parsons,[51] and which was originally deduced by Horiuti[45] for the special case of the hydrogen evolution reaction. This approach to the determination of ν relies on the assumption that the same reaction mechanism prevails at both low and high overpotentials from which R_{CT} and i_0 are measured, respectively. Equation (51) is generally considered to be correct, but it should also be mentioned that aspects Parsons' development have been questioned as involving the fortuitous cancellation of some ill-defined (Ref. 21, p. 262) and invalid[53] terms.

The stoichiometric number concept does not, however, demonstrate in a simple way how ν becomes incorporated into and affects the theoretical rate expressions that describe polarization behavior for multistep reactions that involve a stoichiometric number. This has been one of the problems in understanding its significance. In the theoretical evaluation of transfer coefficients based upon the quasi-equilibrium treatment of Bockris and Reddy (B&R) in their monograph (Ref. 3, p. 1005), ν forms

a parameter of the experimentally accessible transfer coefficients [as shown earlier; see Eqs. (1a) and (1b)].

At first glance, the non-rds terms of these transfer coefficients [i.e., the first on the lhs of Eqs. (1a) and (1b)] seem to be able to give fractional contributions (i.e., 0 to 1) for *both* anodic and cathodic transfer coefficients simultaneously due to ν in these terms [e.g., if $z_{rds} = 0$ (hence for a chemical step)] and $\nu > \gamma_p$ and γ_f. This, as we will demonstrate, is in fact not possible. In order to prove this and to establish the appropriate use of these transfer coefficients, they will be derived here for the two general types of reaction mechanism that require use of a stoichoimetric number (Schemes 2 and 3 below).

3. Reaction Mechanisms Involving a Stoichiometric Number Greater than 1

In the closed reaction sequences considered in this work, stoichiometric numbers greater than 1 can arise *only* in order to satisfy a material balance for a reaction step preceding or following the rds that creates or consumes ν intermediates in a single transition state.

The first of these cases, represented by Scheme 2, is the situation where some facile and therefore nonrate-limiting dissociation step (either reductive or chemical) occurs before the rds and produces, from a unit

Step							
	1.	A_1	+	$z_1 e^-$	$\rightleftharpoons$	I_2	Group I
	.	.....					
	i − 1.	I_{i-1}	+	$z_{i-1} e^-$	$\rightleftharpoons$	I_i	
	i.	I_i	+	$z_i e^-$	$\rightleftharpoons$	νI_{i+1}	
	i+1.	$\nu[I_{i+1}$	+	$z_{i+1} e^-$	$\rightleftharpoons$	$I_{i+2}]$	Group II
	.	.....					
	rds.	$\nu[I_{rds}$	+	$z_{rds} e^-$	$\rightleftharpoons$	$I_{rds+1}]$	
	.	.....					
	j.	$\nu[I_j$	+	$z_j e^-$	$\rightleftharpoons$	$I_{j+1}]$	Group III
	.	.....					
	n.	$\nu[I_n$	+	$z_n e^-$]	$\rightleftharpoons$	A_{n+1}	

Scheme 2. Consecutive electrochemical reaction scheme involving a dissociation step occurring before the rds

reactant, v identical intermediate equivalents; this is step i in Scheme 2. These v intermediates must react in respective subsequent steps, including the rds, v times, corresponding to a stoichiometric number > 1 for the reaction.

In the second case (Scheme 3), some nonrate-limiting step occurring after the rds in the reaction sequence combines v intermediate equivalents into a unit product I_{j+1} in a reduction or chemical step and this is step j in Scheme 3. The v equivalents that must react and combine in step j require that all prior steps, including the rds, be repeated v times to supply this step with its reagent (the intermediate formed in the previous step).

If it is assumed that the rate of the overall reaction is controlled by the transition state of the rds, then the net rate expression will be

$$i_{\text{net}} = zF(-a^S_{I_{\text{rds}}} k_{\text{rds}} \exp[-z_{\text{rds}}\beta f\eta] + a^S_{I_{\text{rds}}} k_{-\text{rds}} \exp[z_{\text{rds}}(1-\beta)f\eta]) \tag{52}$$

The potential-dependent exponential term is also independent of v. This may be explained if we recall that the effect of an applied overpotential in electrochemical kinetics is to modify the relative energies of reactant and product curves through a change in the Fermi level energy and, by extension, that of the transition state for the elementary (recall footnote h) reaction step. The potential dependence of the energy of the transition state is sensitive to the number of electrons transferred in it, but not the v times that it must occur per turnover of the overall reaction; thus the exponential in Eq. (52) is independent of v.

Step	1.	$\nu[A_1 + z_1 e^- \rightleftharpoons I_2]$
	.	. . . . .
	i.	$\nu[I_i + z_i e^- \rightleftharpoons I_{i+1}]$
		. . . . .
	rds.	$\nu[I_{\text{rds}} + z_{\text{rds}} e^- \rightleftharpoons I_{\text{rds}+1}]$
	.	. . . . .
	j.	$\nu I_j + z_j e^- \rightleftharpoons I_{j+1}$
	.	. . . . .
	n.	$I_n + z_n e^- \rightleftharpoons A_{n+1}$

Scheme 3. Consecutive electrochemical reaction scheme involving a combination step occurring after the rds

4. Prior Dissociation, Forward Reaction Direction

We consider Scheme 2, that is, a prior dissociation giving an rds with a stoichiometric number v. The surface activities of the intermediate species participating in the rds will again be potential dependent and, taking into consideration the usual quasi-equilibrium assumptions, can be evaluated, as has been shown earlier (Section IV.3). In order to see clearly the development of the potential dependence of the activities or coverages of the rds intermediates, it is useful to split the reaction steps into three groups and to focus on the dissociation step and rds separately. For the prior dissociation scheme, the groups (shown in Scheme 2) are Group I, up to step i, the dissociation step; Group II, from the dissociation step to the rds; and Group III, all steps following the rds (which are important only when the reverse reaction is considered). The dissociation reaction step can be thought of as that step that gives rise to the necessity that subsequent steps occur more than once (a reductive combination step can be conceived in this way as well). We will call such a step the *stoichiometry-determining* step. This separation of the reaction steps helps to identify clearly and specifically where and how v becomes a part of the potential dependence of the reaction rate and ultimately the transfer coefficients.

Thus to expand the potential dependence of the surface activity of the reactant (which is an intermediate) of the rds, and ultimately that of the forward, reductive reaction direction, we again build up progressively from the initial reactants. The potential dependence of Group I reaction steps would be exactly that which was evaluated previously (Section IV) for the simple consecutive reaction sequence, since there is no change in molecularity between [or stoichiometric coefficients (see footnote g) of] reactant and product for any of these reaction steps. Thus the potential dependence of the activity of the reactant of the dissociation step i is given by Eq. (29) (but where "$i-1$" is used as the limit for the summation and product in that equation), i.e.

$$a_{\mathrm{I}_i}^{S} = a_{\mathrm{A}_1}\left[\prod_{k=1}^{i-1} K_k\right]\exp\left\{-\left[\sum_{k=1}^{i-1} z_k\right] f\eta\right\} \tag{53}$$

Assuming the quasi-equilibrium approximation, the surface activity of the product of the dissociation step (step i) is defined by equating the rates of the forward and reverse directions of that reaction step:

$$z_i F a^S_{\mathrm{I}_i} k_i \exp[-z_i \beta f\eta] = z_i F (a^S_{\mathrm{I}_{i+1}})^{\nu} k_{-i} \exp[z_i(1-\beta) f\eta] \tag{54}$$

which upon rearrangement gives

$$(a^S_{\mathrm{I}_{i+1}})^{\nu} = a^S_{\mathrm{I}_i} K_i \exp[-z_i f\eta] \tag{55}$$

Substituting for the activity of I_i [Eq. (53)] (i.e., for steps up to the dissociation in step i), and taking the ν^{th} root gives Eq. (56)

$$a^S_{\mathrm{I}_{i+1}} = a^{1/\nu}_{\mathrm{A}_1} \left[\prod_{k=1}^{i-1} K_k \right]^{1/\nu} K_i^{1/\nu} \exp\left\{ -\left[\sum_{k=1}^{i-1} z_k + z_i \right] \frac{f\eta}{\nu} \right\} \tag{56}$$

To continue, we now consider Group II reaction steps (i.e., those between the dissociation step and the rds). The quasi-equilibrium expression for the first of these, step $i + 1$, is

$$\nu z_{i+1} F a^S_{\mathrm{I}_{i+1}} k_{i+1} \exp[-z_{i+1} \beta f\eta] = \nu z_{i+1} F a^S_{\mathrm{I}_{i+2}} k_{-i+1} \exp[z_{i+1}(1-\beta) f\eta] \tag{57}$$

When this relation is rearranged to solve for the surface activity of the product of this step, the stoichiometric number will cancel. Although this step and in fact all others in Group II individually occur ν times, their potential dependence evidently does not involve ν, and hence the expression for the Group II reaction steps, steps $i + 1$ through rds $- 1$, will [analogously to Eq. (29)] be given by

$$a^S_{\mathrm{I}_{\mathrm{rds}}} = a^S_{\mathrm{I}_{i+1}} \left[\prod_{k=i+1}^{\mathrm{rds}-1} K_k \right] \exp\left[-\left[\sum_{k=i+1}^{\mathrm{rds}-1} z_k \right] f\eta \right] \tag{58}$$

Then, if we substitute for the surface activity of I_{i+1} from Eq. (56), Eq. (59) is the result:

$$a^S_{\mathrm{I}_{\mathrm{rds}}} = a^{1/\nu}_{\mathrm{A}_1} \left[\prod_{k=1}^{i} K_k \right]^{1/\nu} \left[\prod_{k=i+1}^{\mathrm{rds}-1} K_k \right] \exp\left[-\left[\frac{1}{\nu} \sum_{k=1}^{i} r_k + \sum_{k=i+1}^{\mathrm{rds}-1} r_k \right] f\eta \right] \tag{59}$$

which is the potential dependence of activities of all intermediates affecting the rate of the forward, reductive, direction of the reaction.

If we identify where ν arises in Eq. (59), it is clear that Group I steps (see Scheme 2) and the dissociation step contribute in a power of $1/\nu$ that of Group II steps [i.e., those between the dissociation and the rds (steps

$i + 1$ to rds–1)] and thus parts of both the preexponential and the exponential (potential-dependent) terms in Eq. (59) are dependent on v while others are independent of v.

5. Prior Dissociation, Reverse Reaction Direction

Considering now the reverse, anodic direction of the same reaction, Scheme 2, the surface-region activity of the cathodic product of the rds, I_{rds+1} (which is now the reactant for the reverse anodic reaction) will be potential dependent if it is an intermediate. The Group III steps, now all those following the rds, are all repeated v times,[i] but when their quasi-equilibrium expressions are derived and the surface activity of I_{rds+1} is built up, they will all be independent of v, just as was the case for Group II reaction steps in the forward direction [Eq. (58) and the related text]. Thus v has no bearing on the potential dependence of these steps (steps rds + 1 to n) and hence the expression for the activity of the reaction intermediate I_{rds+1} is simply [see Eq. (29)]

$$a^{S}_{I_{rds+1}} = a_{A_{n+1}} \left[\prod_{k=rds+1}^{n} \frac{1}{K_k} \right] \exp\left[\left[\sum_{k=rds+1}^{n} z_k \right] f\eta \right] \tag{60}$$

When Eqs. (59) and (60) are substituted into the overall [Eq. (54)], the result is

$$i_{net} = zF \left(-a_{A_1} k_{rds} \left[\prod_{k=1}^{i} K_k \right]^{1/\nu} \left[\prod_{k=i+1}^{rds-1} K_k \right] \times \exp\left[-\left(\frac{\gamma_{E-S}}{\nu} + (\gamma_{E-P} - \gamma_{E-S}) + z_{rds}\beta \right) f\eta \right] + a_{A_{n+1}} k_{-rds} \left[\prod_{k=rds+1}^{n} \frac{1}{K_k} \right] \exp[(\gamma_{E-F} + z_{rds}(1-\beta)) f\eta] \right) \tag{61}$$

[i]It is assumed that the v intermediates formed in the preceding dissociation do not recombine in the same reaction.

which is the net rate equation for a reaction whose rds has a stoichiometric number of ν arising on account of a previous dissociation step.

The resulting transfer coefficients are

$$\alpha_c = \frac{\gamma_{E-S}}{\nu} + (\gamma_{E-P} - \gamma_{E-S}) + z_{\text{rds}}\beta \tag{62a}$$

$$\alpha_a = \gamma_{E-F} + z_{\text{rds}}(1 - \beta) \tag{62b}$$

where γ_{E-F}, γ_{E-P}, and γ_{E-S} have replaced the summation terms in the exponentials of Eq. (61) and are the total numbers of electrons transferred in elementary (footnote g) electron-transfer steps following the rds, prior to the rds, and those up to and including the stoichiometry-determining step in the case of a previous dissociation. Note that the number of elementary electrons transferred between the dissociation step and the rds is given by $\gamma_{E-P} - \gamma_{E-S}$ in Eq. (61) and hence α_c [Eq. (62a)], but that the actual number of electrons transferred in these steps in ν times that, namely, $\nu(\gamma_{E-P} - \gamma_{E-S})$. The added coefficient, γ_{E-S}, is used in order to maintain links to both the familiar terminology of B&R [Eqs. (1a) and (1b)] and the stoichiometry-determining step. These points, it is hoped, will reinforce the connection between mechanistic situations and these kinetic derivations.

6. Following Combination Step

The second case, represented by Scheme 3, involves a combination (chemical or reductive) step following the rds (e.g., in step j), and will also give rise to a stoichiometric number, ν, for the rds. The transfer coefficients for this case, following a derivation similar to that given above, are

$$\alpha_c = \gamma_{E-P} + z_{\text{rds}}\beta \tag{63a}$$

$$\alpha_a = \frac{\gamma_{E-S}}{\nu} + (\gamma_{E-F} - \gamma_{E-S}) + z_{\text{rds}}(1 - \beta) \tag{63b}$$

where in this case γ_{E-S} is the number of electrons transferred in elementary steps after the stoichiometry-determining step for a combination step following (in the forward reaction direction) the rds.

7. Electron Number Coefficients

The preceding/following electron-number coefficients (γ) used here are slightly different and less general than those employed by B&R (namely, γ_p and γ_f) in their transfer coefficient analysis [Eq. (1)]. They are, however, related and for a preceding dissociation, the expressions that link them are

$$\gamma_p = \gamma_{E-S} + \nu \cdot (\gamma_{E-P} - \gamma_{E-S}) \tag{64a}$$

$$\gamma_f = \nu \cdot \gamma_{E-F} \tag{64b}$$

Substitution of these γ_p and γ_f expressions into the B&R transfer coefficients [Eq. (1)] immediately demonstrates the equivalence of the derivations. Although, practically speaking, it is difficult to imagine examples where the stoichiometry-determining step would be far separated from the rds, we believe that the expanded transfer coefficients derived here are expressed in a fashion that is more directly relevant to their use in determining mechanism.

The present notation, while requiring a distinction between combination and dissociation cases, shows clearly and specifically how the type of mechanism involved determines the transfer coefficients. In addition, substituting $\nu = 1$ into either of the above coefficients [Eq. (62) or (63)] reduces them to those for a simple consecutive electrochemical reaction, Eqs. (33a) and (33b).

One important point of clarification of the B&R relations has arisen from the treatment here. If we consider a reaction scheme where a stoichiometric number arises as a result of a preceding dissociation, the non-rds contribution to the anodic transfer coefficient for such a reaction would be γ_f/ν [Eq. (1a)] in B&R's terminology, but γ_{E-F} [Eq. (62b)] according to the terminology used here. It would seem from a first glance at the B&R transfer coefficients that the non-rds steps following the rds could contribute a fraction to α_a if $\nu > \gamma_f$. The non-rds part of the anodic transfer coefficient from the present derivation clearly demonstrates that the contribution of γ_{E-F} to α_a can only be of whole numbers (i.e., not fractional) since only integral numbers of electrons can be transferred in electrochemical steps. In addition, the non-rds contribution to the cathodic

[i]It is assumed that the ν intermediates formed in the preceding dissociation do not recombine in the same reaction.

transfer coefficients for, say, the prior dissociation example [Eq. (62a)] will only be fractional if $v > \gamma_{E-S}$ and $\gamma_{E-P} - \gamma_{E-S}$ is 0.

Thus, the conclusion is that for a preceding dissociation or a following combination, either of the non-rds terms, γ_p/v or γ_f/v, can be fractional, but the other *must* be a whole number. This is an important point that is not otherwise apparent. In fact, we have found[5] that just such an error has been made in an analysis of the mechanism of the reaction of aluminum electroplating from a hydride bath. This error was found to be due entirely to the mistaken assumption that both anodic and cathodic non-rds terms (i.e., γ_p/v and γ_f/v), of B&R's theoretical transfer coefficients [Eqs. (1a) and (1b)] could simultaneously give fractional contributions and so account for the transfer coefficients that had been derived from experimental Tafel plots.

VII. APPLICATION TO THE PROCESSES OF ALUMINUM DEPOSITION AND DISSOLUTION

The thoughts developed here on the link between reaction mechanism and experimental transfer coefficients have been used to assign[5] a mechanism for Al electrodeposition and dissolution reactions from a thf-hydride bath. An analysis of results from that work has served to clarify the confusing literature that has also given attention to the kinetics and mechanism of Al deposition from a hydride bath.[6–9]

The hydride bath for Al deposition is a complex mixture of chlorohydridoaluminates. The aluminate species that are present in the hydride baths result from ligand mixing of the components, $AlCl_3$ and $LiAlH_4$, in thf. The distribution of hydridochloroaluminate species formed in this reaction depends on the molar ratio of $AlCl_3$ to AlH_4^- ions introduced into the donor etheric solvent. Two mechanistically significant compositional regimes may be identified: Cl^--rich, where $AlCl_3$ is in greater proportion than $LiAlH_4$, and, conversely, H^--rich, where AlH_4^- is in excess.

In the Cl^--rich bath type, experimental transfer coefficients were $\alpha_c = \alpha_a \simeq 0.5 \pm 0.05$, while in the H^--rich baths the values were $\alpha_c \simeq 0.3 \pm 0.05$ and $\alpha_a \simeq 0.65 \pm 0.05$. The stoichiometric number for the process was calculated by coupling the charge-transfer resistance with the extrapolated exchange current density from low and high overpotential regions, respectively,[5] and by back-reaction correction.[5–7] It was determined to be 3 by both methods and for all bath compositions. It has been suggested[6,7] that

the transfer coefficients in the H^--rich baths corresponded to a mechanism in which the rds was a chemical step having a stoichiometric number of 3 preceded by one quasi-equilibrium electron transfer step and followed by two (which govern the anodic reaction). This information, referring to Eq. (1), would give 1/3 + 0 and 2/3 + 0 for α_c and α_a, respectively, closely corresponding to the experimental values given above.

At first this would appear to be a reasonable conclusion, but upon reevaluation of how a stoichiometric number becomes incorporated into the transfer coefficients, this mechanism cannot be correct since it has been shown in this review (Section VI) that it is impossible for both non-rds electron-number coefficients to be fractional. So, although one of those could be fractional, giving, say, $\alpha_c \simeq 1/3$, the other non-rds contribution would have to be a whole number integer. With this in mind, it is evident that the experimentally derived transfer coefficients for the Al reaction, given that they are all near to about 1/2 for both bath types, must describe the transition state of the rds.

An interpretation of reaction mechanisms from Tafel slopes depends on the potential dependence of the surface activity or coverage, θ_i, of adsorbed reaction intermediates combined with that of any coupled electron-transfer step through its β. For cases where the θ_is tend to 1 and thence become potential independent, the Tafel *b* value can be ~118 mV (i.e., $\beta \simeq 0.5$), a value that can also apply to an initial one-electron charge transfer not involving an intermediate, as we have considered in Section IV.5. It is therefore possible that non-rds electron-transfer reactions could be involved in a given mechanism, but that they are at saturation conditions in the overpotential region in which the Tafel slopes for the reaction are derived. This would, of course, give an erroneous mechanism assignment if such a saturation condition could not be otherwise identified. When situations such as this may apply (as is possible with the Al deposition and dissolution reactions involving three electrons), further information is desirable (e.g., from impedance spectroscopy), especially when a pseudocapacitance[35] (related to $d\theta/d\eta$) may be involved. It was found previously[5] that pseudocapacitances associated with Al reaction intermediates were absent and this indicates that Al deposition and dissolution involves neither prior nor following (for the reverse reaction direction) electron transfers. This conclusion confirmed and validated the Tafel slope measurements and resulting mechanistic analyses that would otherwise have required taking into account an electrosorption isotherm for an adsorbed intermediate.

It might be thought that the mechanism for Al deposition would involve three consecutive one-electron transfer steps, which conceptually would be the most obvious pathway; then cathodic αs having values of *ca.* 0.5 (β), 1.5 (1 + β), or 2.5 (2 + β), would be expected with the corresponding pseudo-capacitances arising for Al(+I) and Al(+II) interediate species in the second or third steps, respectively. In addition, v values would be one for *each* of the three steps if they were individually rate determining. None of these expectations is consistent with the experimental kinetic data.

The facts that (1) there were no electron-transfer steps prior to or following (for the reverse anodic reaction direction) the rate-determining step; (2) α values were statistically near 1/2 in all cases; and (3) v was determined to be 3 for all bath compositions, suggest that the Al deposition reaction must be represented as

$$3[AlX_3 + e^- \rightarrow M - AlX_2 + X^-] \tag{65a}$$

$$3M - AlX_2 \rightleftharpoons M - Al + 2AlX_3 \tag{65b}$$

which is a reaction involving a thrice occurring electron transfer as rds followed by a facile chemical disproportionation of three Al(+II) intermediates. The disproportionation process [reaction Eq. (65b)] must itself be complex and would hardly be expected to take place in one step. However, since it supposedly follows step (65a), with the latter being rate-limiting, its kinetics and mechanism are veiled from electrochemical observation. At sufficiently high negative potentials, the second (chemical) step would eventually lead to a limiting current, as also would this step in the reverse direction at large anodic polarizations since it is independent of potential.

The variation of the transfer coefficients for the Al deposition reaction from the hydride bath from $\alpha_c = \alpha_a = 1/2$ in Cl^--rich baths to $\alpha_c = 1/3$ and $\alpha_a = 2/3$ in H^--rich baths has been explained[5] by a change in β between the different bath types and not a difference of mechanism, as has been suggested elsewhere.[6,7] The change in β has been attributed to the different chloro hydrido aluminate species that are involved in the electrode process in the different bath types, where the distribution of these species has been shown to vary among these bath types,[54] by means of NMR measurements.

VIII. CONCLUSIONS

The measurement of Tafel slopes is an important means for elucidating electrochemical reaction mechanisms, and the keys to their analysis are the resulting transfer coefficients. The ability to gain insight into a mechanism from the experimentally obtained αs arises from the potential dependence of the activities of reaction intermediates formed by electron-transfer steps before a rate-determining step (in either reaction direction).

The theoretical αs of B&R [Eqs. (1a) and (1b)] have been applied in many investigations of multistep electrochemical reactions. This is largely due to the straightforward means by which the particulars of reaction mechanisms (i.e., parameters such as γ_p, γ_f, and v) contribute to the experimentally accessible αs. The relationship between experimental αs and the mechanism parameters is only appropriate, however, if the assumptions upon which the link between them has been established are indeed valid. The trouble is that these assumptions, which are the basis of the quasi-equilibrium treatment, impose limits upon the ability to deduce a mechanism from evaluation of experimental αs. During the course of recent efforts[5] to unravel the confusing literature surrounding the electrochemical kinetic work on the aluminum deposition reaction from an etheric hydride bath, the elements of a number of these underlying assumptions have been carefully considered. It is felt that this reexamination would be useful to others attempting to analyze electrochemical mechanisms through polarization measurements on multistep reactions.

The quasi-equilibrium approximation relies on the assumption that there is a single rate-determining step, the forward and reverse rate constants of which are at least 100 times smaller than those of all other reaction steps in the kinetic scheme. It is then assumed that all steps other than the rds are always at equilibrium and hence the forward and reverse reaction rates of each non-rds step may be equated. This gives simple potential relations describing the varying activity of reaction intermediates in terms of the stable solution species (of known and potential-independent activity) that are the initial reactants or final products of the reaction. The variation of the activities of reaction intermediates is, however, restricted by either the hypothetical solubility limit of these species or, in the case of surface-confined reactions and adsorbed intermediates, the availability of surface sites. In both these cases, saturation or complete coverage conditions would result in a loss of the expected

potential dependence for non-rds electron transfers. This would require the use of other complementary experimental methods to ascertain the existence of non-rds electron transfers in a particular reaction.

It has been shown that the relative magnitudes of rate constants for the rds and those for non-rds reaction steps can affect the appearance of Tafel plots and could result in misleadingly high Tafel slope values or unexpected inflection points in Tafel plots.

In this chapter, transfer coefficients have been developed that describe a number of mechanistic possibilities (Section V). The stoichiometric number of a reaction emerges as an important parameter that may be determined by a number of methods. The only reason an electrochemical reaction pathway would show v values > 1 would be to satisfy the material balance for either a reductive (or chemical) dissociation step occurring before a rds as per Scheme 2 or a reductive (or chemical) combination step occurring after a rds as per Scheme 3 (recall that in these schemes reaction steps are written as a series of consecutive reductions, among which may be a chemical step). By considering the types of reaction steps that can give rise to $v > 1$ within a generalized scheme, an important restriction has

Table 1
Summary of Derived Transfer Coefficients

Mechanism details	α_a	α_c
A *single* electrochemical reaction step	$z(1-\beta)$	$z\beta$
Multiple electrochemical reaction steps	$\gamma_f + z_{rds}(1-\beta)$	$\gamma_p + z_{rds}\beta$
Multiple electrons transferred in rds:	z_{rds} greater than 1	
Chemical step is rds:	z_{rds} equal 0	
Change of *stoichiometric coefficients* within rds when:		
rds is a dissociation	$\omega\gamma_{E-F} + z_{rds}(1-\beta)$	$\gamma_{E-P} + z_{rds}\beta$
rds is a combination	$\gamma_{E-F} + z_{rds}(1-\beta)$	$\omega\gamma_{E-P} + z_{rds}\beta$
Stoichiometric number of rds, v, greater than 1 arising from:		
A prior dissociation	$\gamma_{E-F} + z_{rds}(1-\beta)$	$\gamma_{E-S}/\nu + (\gamma_{E-P} - \gamma_{E-S}) + z_{rds}\beta$
or a following combination	$\gamma_{E-S}/\nu + (\gamma_{E-F} - \gamma_{E-S}) + z_{rds}(1-\beta)$	$\gamma_{E-P} + z_{rds}\beta$

been demonstrated for the values that the non-rds terms within the theoretical transfer coefficients can take; that is, γ_p/ν or γ_f/ν can be fractional, but if one is fractional, the other *must* be a whole number. We have introduced further mechanistic parameters for the theoretical transfer coefficients that demonstrate this point and these are collected in Table 1.

ACKNOWLEDGMENTS

Grateful acknowledgement is made to the Natural Sciences and Engineering Research Council of Canada and to Alcan International for support of this work under the aegis of the NSERC/Alcan Industrial Research Chair at the University of Ottawa (incumbent, Professor B. E. Conway). Thanks are also due to Professor Conway for useful discussions during the preparation of this review.

REFERENCES

[1] J. Horiuti, *J. Catal.* **1** (1962) 199.
[2] A. N. Frumkin, *Zeit. Phys. Chem.* **160** (1932) 116.
[3] J. O'M. Bockris and A. K. N. Reddy, *Modern Electrochemistry,* 6th ed., Plenum, New York, 1977.
[4] N. Ishibashi, Y. Hanamura, M. Yoshio, and T. Seiyama, *Denki Kagaku* **37** (1969) 73.
[5] M. C. Lefebvre and B. E. Conway, *J. Electroanal. Chem.,* 1999.
[6] M. Galova, D. Kladeskova, and I. Lux, *Surf. Tech.* **13** (1981) 315.
[7] J. Eckert and M. Galova, *Electrochim. Acta* **26** (1981) 1169.
[8] M. W. M. Graef, *J. Electrochem. Soc.* **132** (1985) 1038.
[9] W. A. Badawy, B. A. Sabrah, and N. H. Y. Hilal, *J. Appl. Electrochem.* **17** (1987) 357.
[10] J. O'M. Bockris, *Modem Aspects of Electrochemistry,* J. O'M. Bockris, ed., Plenum, New York, 1954, Chapter 4.
[11] R. A. Marcus, *Can. J. Chem.* **37** (1959) 155.
[12] S. Glasstone, K. J. Laidler, and H. Eyring, *The Theory of Rate Processes,* McGraw-Hill, New York, 1941.
[13] J. A. V. Butler, *Trans. Farad. Soc.* **19** (1924) 729, 734.
[14] T. Erdey-Gruz and M. Volmer, *Z. Physik. Chem.* **150A** (1930) 203.
[15] K. J. Laidler, *Chemical Kinetics,* Harper and Row, New York, 1987, p. 89.
[16] V. K. La Mer, *Chem. Rev.* **10** (1932) 179.
[17] R. P. Bell, *Acid-Base Catalysis,* Oxford, London, 1949, Chapter 2.
[18] H. Eyring and M. Polanyi, in *Selected Readings in Chemical Kinetics,* M. H. Back and K. J. Laidler, eds., Pergamon, Oxford, 1967.
[19] J. A. V. Butler, *Proc. Roy. Soc. (Lond.)* **A112** (1926) 129.
[20] E. A. Guggenheim, *J. Phys. Chem.* **33** (1929) 842; **34** (1930) 1540.
[21] B. E. Conway, *Theory and Principles of Electrode Processes,* Ronald Press, New York, 1965. (Contribution from E. Gileadi, pp. 262–271 in this volume).
[22] A. J. Bard and L. R. Faulkner, *Electrochemical Methods: Fundamentals and Applications,* Wiley, New York, 1980, p. 91.

[23] M. A. V. Devanathan, J. O'M. Bockris, and K. Muller, *Proc. Roy. Soc. London* **A274** (1963) 55.
[24] B. E. Conway, in *Modern Aspects of Electrochemistry,* B. E. Conway, R. E. White, and J. O'M. Bockris, eds., No. 16, Plenum, New York, 1985, p. 181.
[25] R. Parsons, *Pure Appl. Chem.* **52** (1979) 233.
[26] J. Horiuti and M. Polanyi, *Acta Physicochim.* **2** (1935) 505.
[27] J. A. V. Butler, *Trans. Farad. Soc.* **16** (1924) 729,734.
[28] H. H. Bauer, *J. Electroanal. Chem.* **16** (1968) 419.
[29] N. S. Hush, *J. Chem. Phys.* **28** (1958) 962.
[30] R. A. Marcus, *Biochim. Biophys. Acta* **811**(1985) 265.
[31] L. I. Krishtalik, *Charge Transfer Reactions in Electrochemical and Chemical Processes,* Consultants Bureau (Plenum), New York, 1986, p. 4.
[32] J. O'M. Bockris and S. U. M. Khan, *Surface Electrochemistry,* Plenum, New York, 1993.
[33] L. I. Krishtalik, in *Comprehensive Treatise of Electrochemistry,* B. E. Conway, J. O'M. Bockris, E. Yeager, S. U. M. Khan, and R. E. White, eds., Plenum, New York, 1983, p. 131.
[34] J. O'M. Bockris, *J. Chem. Phys.* **24** (1956) 817.
[35] B. E. Conway and E. Gileadi, *Trans. Faraday Soc.* **58** (1962) 2493.
[36] B. E. Conway and B. V. Tilak, *Adv. Catalysis* **38** (1992) 1.
[37] R. D. Armstrong and M. Henderson, *J. Electroanal. Chem.* **39** (1972) 81.
[38] L. Bai, D. A. Harrington, and B. E. Conway, *Electrochim. Acta* **32** (1987) 1713.
[39] D. A. Harrington and B. E. Conway, *J. Electroanal. Chem.* **21** (1986) 745.
[40] B. E. Conway and L. Bai, *Faraday Trans.* **81** (1985) 1841.
[41] B. E. Conway and Gu Ping, *Faraday Trans.* **86** (1990) 923.
[42] A. C. Makrides, *J. Electrochem. Soc.* **111** (1964) 392.
[43] A. C. Makrides, *J. Electrochem. Soc.* **111** (1964) 400.
[44] R. E. Meyer, *J. Electrochem. Soc.* **107** (1960) 847.
[45] J. Horiuti, *J. Res. Inst. Catal., Hokkaido* **1** (1948) 8.
[46] J. Horiuti and M. Ikusima, *Proc. Imper. Acad. Tokyo* **15** (1939) 39.
[47] M. Enyo and T. Yokoyama, *J. Res. Inst. Catal., Hokkaido* **17** (1969) 1.
[48] M. Enyo and T. Yokoyama, *Electrochim. Acta* **12** (1967) 1631.
[49] J. Horiuti and A. Matsuda, *J. Res. Inst. Catal., Hokkaido* 7 (1959) 19.
[50] J. O'M. Bockris and E. C. Potter, *J. Chem. Phys.* **20** (1952) 614.
[51] R. Parsons, *Trans. Farad. Soc.* **47** (1951) 1332.
[52] P. L. Allen and A. Hickling, *Trans. Farad. Soc.* **53** (1957) 1626.
[53] M. Enyo and T. Yokoyama, *Electrochim. Acta* **16** (1971) 223.
[54] M. C. Lefebvre and B. E. Conway, *J. Electroanal. Chem.,* **448** (1998) 217.

4

Electro-Osmotic Dewatering of Clays, Soils, and Suspensions

Ashok K. Vijh

Institut de recherche d'Hydro-Québec,
Varennes, Québec, Canada J3X 1S1

I. INTRODUCTION

There is a large range of industries that produce suspensions of fine particles in water: the disposal of very large quantities of such dilute suspensions requires procedures for concentrating and consolidating them to produce sediments of "spadeable" consistency. Mechanical methods of removing water from concentrated suspensions or sludges are energetically inefficient and inadequate because hydraulic flow falls off drastically with decreasing pore size so that after the initial stages of dewatering, subsequent dewatering becomes progressively harder to achieve. Thus, energetically efficient and cost-effective handling and dewatering of "fines" is a major industrial problem.[1–6] This chapter reviews electro-

Modern Aspects of Electrochemistry, Number 32, edited by B. E. Conway *et al.* Kluwer Academic / Plenum Publishers, New York, 1999.

chemical approaches that provide promising avenues to solutions of this problem. Although an attempt is made to outline industrial applications, the main emphasis is on the conceptual theoretical basis of this methodology.

The fundamental electrochemical approach of interest in this context is the electro-osmotic dewatering (EOD) of clays,[7–12] the phenomenology of which is described in the next section. It is pertinent to indicate here, however, the breadth of possible applications of EOD in solving the problems of industries and environmental degradation.[1–2]

There are very large quantities of "fines" produced by many metallurgical and mineral processes: treatment of ores, tailings, and extracted metals; clay and sand washing in diamond mining; phosphate extraction; brown coal and peat dewatering; oil sands treatment; fly ash disposal; and electroplating and metal finishing.[1–6] All of these yield to dewatering by EOD.

In the chemical industry, EOD can find applications in industries connected with paints, pigments, and pharmaceuticals; textiles; papermaking–pulp products and residues. In the food industry, an enormous range of EOD processes can be used, as may be seen in most issues of the journal *Drying Technology.* Perhaps the largest potential of EOD is in environmental protection: treatment of agricultural and animal wastes, sewage, water purification residues, radioactive and hazardous wastes, and dredged materials. Also, there are many electrochemical and electrical processes conceptually related to EOD or utilizing EOD as one of their components that are being commercially developed for the removal of contaminants from soils or from toxic solid waste dumps: the attractiveness of these processes lies in the fact that they can provide *in situ* soil decontamination at a reasonable cost.

An important geotechnical application of EOD is in the stabilization of soils in areas and locations where mud slides, wet soil slippage, quicksand, etc. can cause safety hazards: such catastrophes become possible after prolonged rains and floods, particularly in areas where mine residues were dumped (in the years past) to create artificial land for buildings, etc. Such a dangerous landslide occurred, for example, in St.-Jean-de-Vienney, near the city of Jonquière in the province of Quebec, Canada, some years ago, with terrible loss of life and property. These landslides are caused by an excess of water in the fine soil capillaries, making it behave like a sludge; EOD can provide a means to dewater very large tracts of soil in an *in situ* operation.

II. AN OUTLINE OF ELECTRO-OSMOTIC DEWATERING

Mechanical dewatering methods based on gravitational settling, filtration, centrifugation, or hydraulic flow, achieved by applied pressure or vacuum techniques, become ineffective in dewatering suspensions of particles smaller than approximately 10 μm in diameter. If the water is initially removed by mechanical methods, the particles move closer together, thus decreasing the size of pores through which the water must flow and drastically diminishing the rate of water removal[9]; electro-osmotic dewatering becomes the ideal method for the *further* removal of water trapped in the rather compacted fine clays because its mechanism is based on the electrostatic effects operating in the electrochemical double layers formed at the clay particle/water (actually, very dilute electrolyte) interfaces in these wet clays.

EOD is carried out by applying an electric field between two electrodes submerged in wet clay, using a voltage imposed from an external power supply.[9–12] One may conduct EOD either under continuous dc[12] or with periodic power interruption,[8] when a dc power supply is used to drive the EOD. Of particular interest is combined field dewatering in which some combination of applied external pressure and EOD is used to remove water from a sludge or a comparable matrix of water trapped in colloidal suspensions. A schematic representation of EOD, with and without applied pressure, is shown in Fig. 1 (after Yoshida[12]).

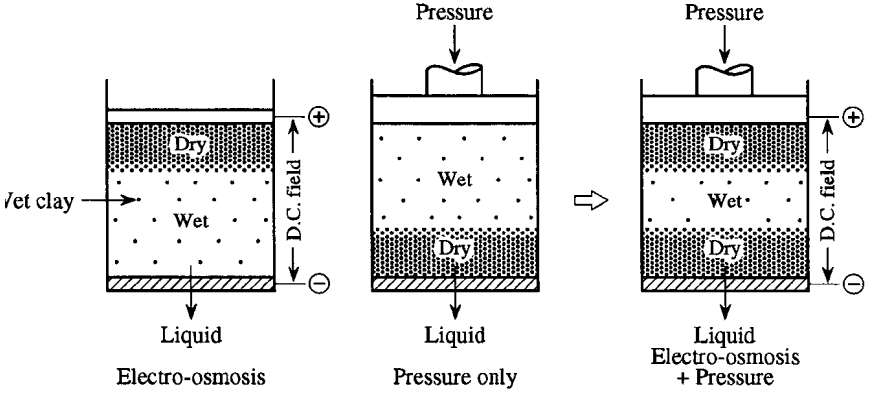

Figure 1. A schematic diagram of dewatering of clay by the combined processes of electro-osmosis and pressure.[12]

EOD is based on the electrically induced flow (namely, electro-osmosis) of water trapped between the clay particles (Fig. 2). Such electrically induced flow is possible because of the presence of the electrochemical double layer at the clay/water interface; in this double layer (Fig. 2), the charges on the clay surface are electrically balanced by the opposite charges in the water; this water is actually an electrolyte because of the presence of some salts, hydronium or hydroxyl ions, etc. The structure and potential gradients of such a double layer are shown in Fig. 3 by analogy with a metal/electrolyte interface.[10]

In this situation, the solid clay particles are the immobile phase and the electro-osmotic flow causes the water to move as a "plug,"[10] the entire velocity gradient being concentrated at the solid surface in a layer that is the same order of thickness as that of the diffuse double layer (Fig. 3). In concentrated solutions, the thickness of the diffuse double layer is quite small (<1 nm) whereas in very dilute solutions (which are indeed represented by the water in the clays), the diffuse double layer can assume much

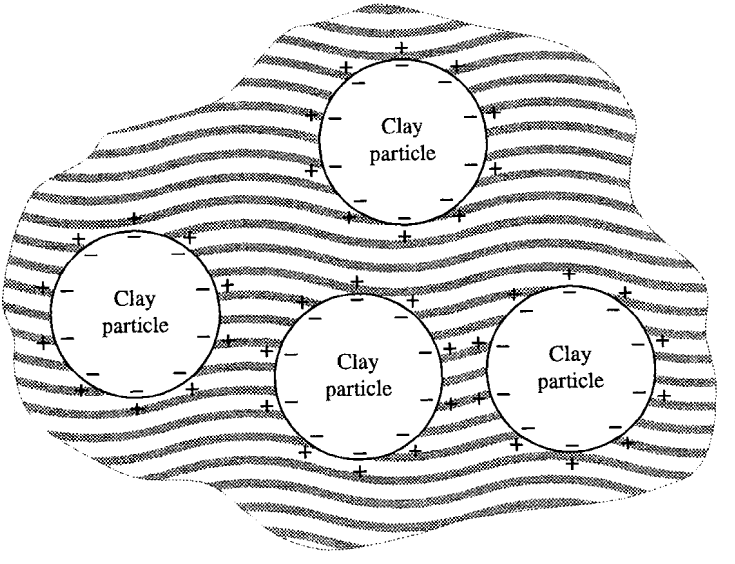

Figure 2. A schematic diagram of clay particles with water (electrolyte) trapped between them. The electrochemical double layer is indicated for each negatively charged clay particle with positive ions (in water) poised against the negative charge.[10]

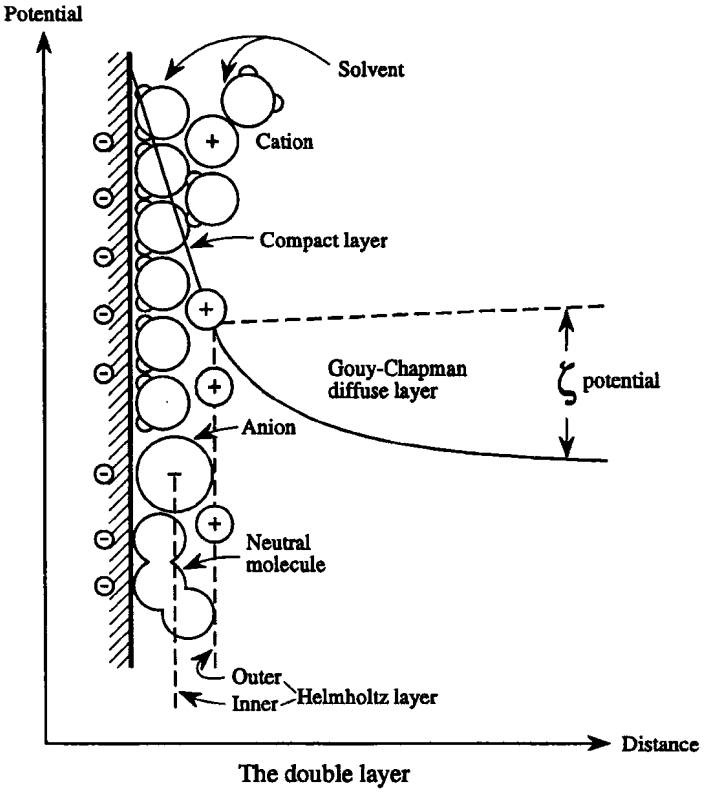

Figure 3. A small portion of the electrochemical double layer at the clay/water (electrolyte) interface is shown to depict the microscopic structure and the potential drops involved, by analogy with the metal/electrolyte interface.[10] (Diagram from Conway, Theory and Principles of Electrode Processes, p. 26, Ronald Press, New York, 1965).

larger values (~10^2–10^3 nm), depending on the concentration of ions in the water. The electro-osmotic movement of water between the clay particles is exactly similar to electro-osmotic flow in a capillary pore[13] (Fig. 4): the thin layer of charged fluid (i.e., water containing some ions) next to the clay particle wall moves like a single ion (hence the analogy of a plug) under the action of the electric field and in a direction parallel to it.[10] The electrochemical double layer originates from the requirements of charge neutrality in which the charge on the clay surface must be balanced against the opposite charge in the water (or any other fluid in a more general case).[13]

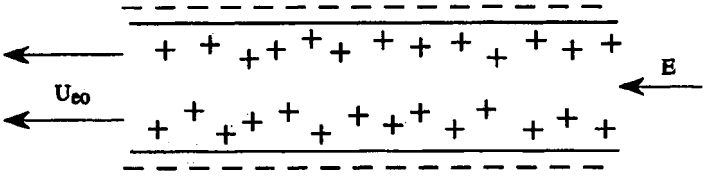

Figure 4. A schematic diagram of the electro-osmotic flow of medium (e.g., an electrolyte) in a capillary caused by the flow of counter-ions as a "plug," under the influence of the applied electric field, E; U_{eo} is the convective liquid velocity from electro-osmosis.[10,13]

III. PHENOMENOLOGICAL EQUATIONS

The methods of irreversible thermodynamics are useful in providing a quantitative approach to the phenomenon of electro-osmotic dewatering and its connection to other electrokinetic effects. The main ideas were developed by Overbeek[14] and reviewed by DeGroot[15]; these ideas were applied by many workers to a number of problems,[16–18] following the earlier papers of Overbeek and co-workers[19,20] on the treatment of electrokinetic phenomena in terms of irreversible thermodynamics. Recently we have shown[23] that this approach can also be applied to EOD, as follows.

Consider the clay or sludge with the trapped water (actually an electrolyte since it contains dissolved ions) as a sort of porous diaphragm (Fig. 1). When an electric field or a pressure, or both, are applied across this diaphragm, dewatering occurs. We examine here the case of simultaneous application of pressure and the electrical field.

Nonequilibrium treatment[14,18] of EOD under these conditions yields the following rate equations for the simultaneous transport of matter (i.e., water) and electricity (i.e., current), assuming that the diaphragm is uniform:

$$J = L_{22}\Delta P + L_{21}\,\Delta V$$

$$I = L_{11}\Delta V + L_{12}\Delta P \tag{1}$$

where J and I are, respectively, the total volume flux and electric current due to both hydrostatic pressure difference, ΔP, and electric potential difference, ΔV. The coefficients L_{22}, L_{21}, and L_{12} characterize the hydrodynamic and electro-osmotic flows, and streaming current, respectively, while the conductance of the diaphragm is given by the coefficient L_{11}. If

the relationship between $(J)_{\Delta V=0}$ and ΔP is linear, L_{22} can be obtained from the slope of the straight line that results from plotting $(J)_{\Delta V=0}$ against ΔP, and the value of L_{21} can be obtained from the slope of a plot of $(J)_{\Delta P=0}$ against ΔV. A linear relationship between $(J)_{\Delta V=0}$ and ΔP and between $(J)_{\Delta P=0}$ and ΔV shows that the flow regime is laminar.

Similarly, a plot of $(I)_{\Delta P=0}$ against ΔV can give L_{11}, whereas a plot of $(I)_{\Delta V=0}$ against ΔP should give L_{12}. Thus all four coefficients namely, L_{22}, L_{21}, L_{11}, and L_{12} can be determined.

Noting that Onsager's relation is[14]

$$L_{12} = L_{21}$$

one may deduce that the above system is completely described by three constants (or coefficients): L_{11}, L_{22}, and $L_{12} = L_{21}$. As mentioned above, L_{11} is the electric conductance of the diaphragm, L_{22} the hydrodynamic conductance of the diaphragm, and $L_{21} = L_{12}$ are the electrokinetic effects.

The coefficient L_{21} can be interpreted in the usual way in terms of the zeta potential as[14]

$$L_{21} = \frac{\varepsilon\zeta}{4\pi\eta} \cdot \frac{A_{cs}}{l} \tag{2}$$

where ε is the dielectric constant of the liquid (water) in the pores, ζ represents the zeta potential; η is the viscosity of the liquid (water) in pores, A_{cs} is the effective cross section through the diaphragm, and l is the geometric distance between the anode and the cathode in the experimental cell.

If one conducts EOD without the externally applied pressure (i.e., $\Delta P = 0$), the total volume flux of water J is given by Eq. (1) as

$$J = L_{21}\Delta V = L_{12}\Delta V \tag{3}$$

By combining Eqs. (3) and (2) we obtain

$$J = \frac{\varepsilon\zeta A_{cs}\Delta V}{4\pi\eta l} = \frac{\varepsilon\zeta A_{cs}E}{4\pi\eta} \tag{4}$$

where E is the electric field gradient ($\Delta V/l$, l being the thickness of the diaphragm).

It should be noted that Eq. (4) is exactly the same as that derived for electro-osmotic volume flux on the basis of electrocapillary phenomena,

that is, from kinetic considerations (21). The dimensional analysis of the various quantities in these equations is given in the Appendix.

1. Components of Current and Flux During Electro-Osmotic Dewatering with or without Pressure

There is a great deal of confusion surrounding the dewatering efficiency in terms of the significance of the measured electric current and the related problem of liters per ampere-hour (or liters per watt-hour at constant voltage). It has been remarked that "experimental efficiencies translate to high and obviously untenable amounts of water per ion."[22] The nature of the current and the flux in terms of its various components has been recently elucidated,[23] as follows.

(i) Electrochemical/Electrical Current

This is the current measured by the ammeter when an electrical field E drives the EOD. At zero pressure difference, the electrical conductance of the clay diaphragm is given by the coefficient L_{11} as

$$L_{11} = \left(\frac{I}{lE}\right)_{P=0} \tag{5}$$

where I is the measured current, E is the applied field gradient across a diaphragm of length l, and P is the hydrostatic pressure. This current is that carried by the ions, which are then discharged at the anode and the cathode, and is not synonymous with the total current responsible for the water removal in EOD; it is, in fact, incidental (see equations and text on pp. 216 and 217 of Ref. 10) to EOD and in any practical situation constitutes only a small fraction of the total current, as pointed out previously.[10]

(ii) Hydrodynamic Flux

This is given by the coefficient L_{22} as[14]

$$L_{22} = \left(\frac{J}{\Delta P}\right)_{E=0} \tag{6}$$

This is the hydrodynamic volume flux at zero applied field, that is, the fraction of dewatering caused by the applied pressure alone.

(iii) Electro-osmotic Current

This is the main driving force in the EOD and is given by Eq. (4) as[14]

$$J = \frac{\varepsilon \zeta A_{cs} E}{4\pi\eta} \tag{4}$$

All quantities in Eq. (4) have been defined above. This electro-osmotic current in the absence of the applied electric field is driven only by the zeta potentials and is given by the electrokinetic coefficient as [see Eq. (2)][14]

$$L_{21} = L_{12} = \frac{\varepsilon \zeta A_{cs}}{4\pi\eta l} \tag{2}$$

In order to obtain the electro-osmotic current in the absence of an applied field [Eq. (2)], one may use two identical *inert* electrodes (i.e., not sustaining electrode reactions such as corrosion, or oxidation or redox reactions), which must be connected to each other externally to complete the circuit in order to allow the electro-osmotic current, driven by the zeta potential alone, to occur. Identical electrodes (ideally, gold electrodes but more practically, inert graphite or stainless steel electrodes) are required to eliminate (ideally, but more practically to minimize) the galvanic battery effects and the associated electrode reactions. The total water removal during combined pressure and electro-osmotic dewatering is thus given by

$$\text{total water removal} = [\text{electrical} + \text{hydrodynamic} + \text{electro-osmotic}] \text{ components}$$

In other words, the water removal by EOD is given for unit voltage and pressure difference by

$$\text{EOD} = L_{11} + L_{22} + L_{21} \tag{7}$$

The total current, at unit voltage and pressure, is given through Eq. (1) by

$$I = L_{11} + L_{12} \tag{8}$$

This current is composed of two parts: an electrochemical and an electro-osmotic part.

From Eq. (8), it is easy to see the explanation of a persistent puzzle in the EOD literature that "experimental efficiencies translate to high and obviously untenable amounts of water per ion"[22]: the measured current accounts only for L_{11}, whereas most of the water is removed by L_{21} (electro-osmosis) and, in the presence of applied hydrostatic pressure, by L_{22}.

It should be added that L_{12} represents the streaming current, which is equal to the electro-osmotic current L_{21}: the streaming current is the converse of the electro-osmotic current.

2. Connection of Electra-Osmosis to Other Electrokinetic Effects

Although the focus in the electro-dewatering literature is only on the electro-osmotic dewatering caused by an applied electric field (with or without applied pressure) as described in the preceding section, it is of general scientific interest to indicate that Eq. (1) here, and the various coefficients it contains, provide the conceptual basis for the complete range of electrokinetic phenomena. We summarize below these cases following Overbeek, [14] De Groot,[15] Mazur and Overbeek,[20] Sanfeld,[18] and Van Rysselberghe.[24]

From the phenomenological Eq. (1) and the Onsager relation, one may obtain four effects that can be studied experimentally:

1. At zero electrical current, one obtains the streaming potential

$$(\Delta V/\Delta p)_{I=0} = -L_{12}/L_{11} \tag{9}$$

2. At uniform pressure, we have the electro-osmotic effect

$$(J/I)_{\Delta p=0} = L_{21}/L_{11} \tag{10}$$

3. When the flux J is 0, one gets the electro-osmotic pressure

$$(\Delta p/\Delta V)_{J=0} = -L_{21}/L_{22} \tag{11}$$

and

4. At uniform electrical potential, the streaming current appears

$$(I/J)_{\Delta V=0} = L_{12}/L_{22} \tag{12}$$

On application of the Onsager relation, $L_{12} = L_{21}$, these four effects give the connection between the osmotic and the streaming effects:

$$(\Delta V/\Delta p)_{I=0} = -(J/I)_{\Delta p=0} \tag{13}$$

$$(\Delta p/\Delta V)_{J=0} = -(I/J)_{\Delta V=0} \tag{14}$$

Equation (13), known as Saxen's relation, has also been established by applying kinetic considerations, which are, however, only possible if some simplified model is invoked in which the diaphragm is identified as equivalent to a capillary of uniform section. The importance of the thermodynamic approach is that it holds whatever the nature of the diaphragm or the porous plug.

Although an irreversible thermodynamic approach provides a quantitative framework for the EOD phenomenon, it does not elucidate the mechanistic details of the physical and chemical events that take place in electro-osmotic dewatering; in other words, *it is phenomenological and not mechanistic in content.*

An electrochemical approach based on the considerations of double layers at the clay-water interface provides a more transparent approach for understanding the physical and chemical events occurring during electro-osmotic dewatering; in particular, it shows more clearly how various parameters (applied voltage, pH profiles, zeta potential, electrode reactions, etc.) known to influence the EOD process come into play. The framework for the electrochemical interpretation of the EOD phenomenon is summarized in the next section.

IV. THE ELECTROCHEMICAL APPROACH TO ELECTRO-OSMOTIC DEWATERING: HELMHOLTZ–SMOLUCHOWSKI RELATION

The theoretical approach generally used[1–12] in electro-osmotic dewatering is an electrochemical one in which the Helmholtz–Smoluchowski relation is used to relate the electro-osmotic convective liquid velocity to such parameters as the viscosity and permittivity of the solution, the zeta potential of the clay surface, and the strength of the applied field. Also, electrode kinetic effects are taken into account where the data point to the involvement of electrochemical reactions at the electrodes during the EOD process.[10] In combined pressure–electro-osmotic dewatering (CPEOD), the effect of pressure is interpreted in an empirical, ad-hoc manner without any attempt to develop a comprehensive theoretical framework that combines the two driving forces, namely, the pressure and the electric field.[12]

It should be emphasized that EOD is most attractive when the water is trapped between *fine* clay particles (i.e., small "pores" or water transport channels) and cannot be further removed efficiently by the application of pressure or vacuum, etc. If the ionic concentration of the trapped water is low, the thickness of the electrochemical double layer[10,13] can become comparable to or even exceed the pore size, thus requiring corrections to the zeta potential approach based on the simple Helmholtz–Smoluchowski equation; such corrections cannot, however, be carried out accurately despite many attempts.[14]

Quantitatively, the convective liquid velocity from electro-osmosis, U_{eo}, is given by

$$U_{eo} = -\frac{\varepsilon\zeta E}{4\pi\eta} = -\frac{\varepsilon\zeta}{4\pi\eta}\cdot\frac{V}{l} \tag{15}$$

Here E is the applied field driving the electro-osmosis and is equal to the voltage V divided by l, the thickness of the porous diaphragm, assuming a uniform distribution of field: other terms have been defined in connection with Eq. (2).

The zeta potential is the potential difference between the plane of shear (or slipping plane) and the bulk solution. From Eq. (15), it is clear that for a given situation of water (electrolyte) in clay, the U_{eo} is proportional to the zeta potential and to the applied field strength. Also, in a real situation of EOD, it is necessary to use the length-averaged value of the zeta potential in order to take into account the effect of the axially variable zeta potential on the electro-osmotic velocity.[8] Further, since both the zeta potential and the electric field depend on the ionic concentration and pH of the fluid (water in the present case), variations in electro-osmotic velocity can be expected as the dewatering experiment progresses in time.

It should be noted from Eq. (15) that for EOD to occur, the passage of electric current is not required, if ideally one could develop high E (V cm^{-1}) without the passage of significant electrical current. However, in practice, the clay-water medium has a given resistance, R, so that

$$I = \frac{V}{R} = \frac{E}{R}\,(\text{for clay thickness} = 1\ \text{cm}) \tag{16}$$

It is the passage of this current that is associated with the electrochemical reactions at the two electrodes inserted in the clay for applying the potential gradient (i.e., field) necessary for the electro-osmotic flow to

occur. The electrode reactions at the anode and cathode induced by the passage of this current result in a number of effects. For example, there are changes in pH near the electrodes which give rise to concentration gradients in the bulk of the clay, causing changes in zeta values near the electrodes. This results in reduced electro-osmotic flow, as described by Rabie *et al.*,[8] among others. There can also be elctrolytic gassing.

Following Rabie *et al.*,[8] we note that the initial pH of their water in the clay (i.e., the electrolyte) was around 9, that is, slightly alkaline. When the dc power was turned on, there was the usual electrolysis reaction, giving rise to evolution of H_2 at the cathode and O_2 at the anode, as follows:

$$\text{cathode}: 2H_2O + 2e \rightarrow H_2 + 2OH^- \tag{17}$$

$$\text{anode}: 2OH^- \rightarrow 1/2\ O_2 + H_2O + 2e^- \tag{18}$$

$$\text{overall cell reaction}: H_2O \underset{\text{(fuel cell)}}{\overset{\text{electrolysis}}{\rightleftharpoons}} H_2 + 1/2\ O_2 \tag{19}$$

As the electrolysis proceeds, the magnitude of the zeta potential of the clay (e.g., bentonite) near the anode decreases because of the decrease in pH caused by reaction (18), that is, evolution of O_2. Near the cathode, the pH remains high during electrolysis and changes little. The result is that there is a gradient of zeta potential across the clay after electrolysis (i.e., EOD) has proceeded for several minutes: there is a low zeta potential near the anode and a high one near the cathode. The low zeta potential value at the anode causes, through the logic of Eq. (15) the diminution (even cessation) of the dewatering process.

It has been observed that for electroosmosis in a system such as

anode | clay (electrolyte) | cathode

the measured open-circuit potentials, which were also close to the threshold voltages for starting the EOD (i.e., electrolysis), were between 1.8 and 2.3 V. These values were interpreted in terms of potential-pH diagrams for the platinum/water systems.[8] Such an interpretation is invalid in principle in that the potential-pH diagrams formally apply to equilibrium conditions where irreversible electrolysis events (including the electrode oxidation) are not involved, in contrast to the present case of electrochemical reactions on the electrodes driven by the passage of a current.

The most straightforward interpretation of the open-circuit potentials (OCP) is as follows[10]:

$$\mathrm{OCP} = E^{\circ}_{\mathrm{H_2/O_2}} + \eta_{\mathrm{anode}} + \eta_{\mathrm{cathode}} + IR + \frac{RT}{F}\,\mathrm{pH} \tag{20}$$

where $E^{\circ}_{\mathrm{H_2/O_2}}$ is the reversible potential difference between the hydrogen and oxygen electrodes (= 1.23 V); η_{anode} is the anodic overpotential during EOD and its minimum expected value will be ~0.3 V for conditions of detectable oxygen evolution; η_{cathode} is the cathodic overpotential during EOD and its minimum expected value will be ~0.1 V for conditions of detectable hydrogen evolution; IR is the resistive drop in the clay (note: its value during open-circuit measurement with a high-input impedance voltmeter will be 0 V; however, during electrolysis involving the passage of high currents, the IR would become significant, e.g., ~1–3 V); and (RT/F)pH is the voltage drop between the anode and the cathode due to the pH gradient in the clay; at the end of dewatering, Rabie *et al.* observed this to be around 8 pH units (i.e., 0.472 V).

If one adds all the above potential drops, the estimate of the OCP value is ~2.1 V, which is very close to the observed value. The *absolute* minimum value expected for the OCP is that found in the absence of significant battery effects (hence vanishingly small η_{anode} and η_{cathode} values) and would be ~1.7 V.[10] This was indeed observed by Rabie *et al.*[8]

It should be noted that the total volume flux, J, in Eq. (1) is related to the convective liquid velocity, U_{eo} of Eq. (15) by

$$J = U_{eo} A_{cs} \tag{21}$$

where A_{cs} is the effective cross section through the diaphragm [see Eq. (2)]. By substituting Eq. (15) in Eq. (21),

$$J = -\frac{\zeta\varepsilon}{4\pi\eta} \cdot \frac{A_{cs}}{l} \cdot V \tag{22}$$

Since, by definition, $L_{21}\,\dfrac{J}{V}$, one may write [see Eq. (2)]

$$L_{21} = \frac{J}{V} = -\frac{\zeta\varepsilon}{4\pi\eta} \cdot \frac{A_{cs}}{l} \tag{2}$$

Thus the phenomenological description in terms of irreversible thermodynamics connects very well with the electrochemical kinetic approach.

V. ELECTRO-OSMOTIC DEWATERING: SOME EXPERIMENTAL ASPECTS

As mentioned in Section III.2 in the context of phenomenological equations, electro-osmosis is related to several electrokinetic phenomena that occur in a charged porous medium (such as wet clay) when there are couplings (see Fig. 1) between hydraulic (i.e., pressure) and electrical driving forces and flows. Based on the driving forces causing the relative movement between the solid and the liquid phases, the observed phenomena can be broadly classified into two groups as in Table 1, which is taken from Yeung,[25] who adapted it from Abramson.[26] *Electro-osmosis* and *electrophoresis* constitute the first group in which the liquid or the solid phase, respectively, moves relative to the other under an applied voltage.

Streaming potential and *migration* or *sedimentation potential* comprise the second group and here the liquid or the solid phase moves relative to the other under the influence of a hydraulic or gravitational force, respectively, thus inducing an electrical potential difference across the medium. These four complementary electrokinetic phenomena are shown schematically in Fig. 5, which is taken from Yeung,[25] and Yeung and Mitchell.[27]

Table 1
Classification of Electrokinetic Phenomena

Phenomenon	Description	Cause
Electro-osmosis	Movement of a liquid phase through a stationary solid phase	An externally applied electrical gradient
Streaming potential	Formation of a potential difference across the upstream and the downstream ends of a stationary solid phase	Movement of a liquid phase through a stationary solid phase induced by an externally applied hydraulic gradient
Electrophoresis	Movement of charged particles dispersed in a stationary liquid phase	An externally applied electrical gradient
Migration or sedimentation potential	Generation of a potential difference along the migration direction of a solid phase in a stationary liquid phase	Movement of a solid phase through a stationary liquid phase induced by the gravitational field

Source: Abramson[26] as cited by Yeung.[25]

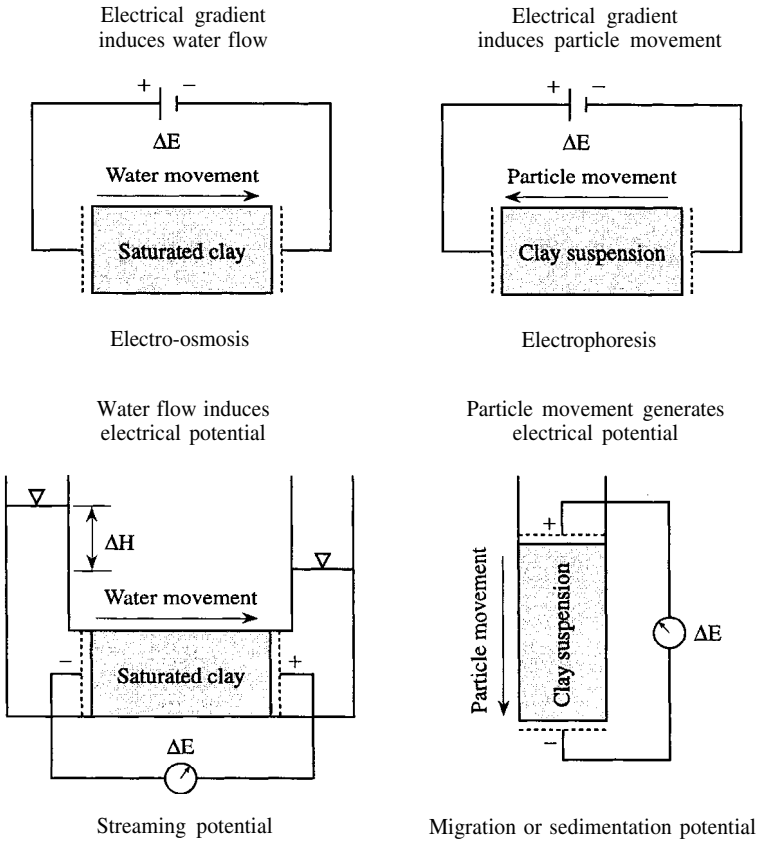

Figure 5. A schematic summary of the electrokinetic phenomena in clay. (After Yeung and Mitchell,[27] as reviewed by Yeung.[25])

In electro-osmosis (Fig. 5), when an externally applied electric field gradient operates across the wet clay, water is moved from the anode (the positive electrode) to the cathode (the negative electrode); that is, there is a movement of the liquid phase through the stationary solid phase (a clay, soil, capillary, or porous plug, etc.) in response to an applied electric field, as shown schematically in Fig. 6, taken from Probstein.[28]

One possible EOD configuration, as applied to multistage dewatering of sludge, is shown in Fig. 7, taken from Yoshida[12]; sludge is poured in at the top and water flows out at the bottom. Of course, practical, commercial electro-osmotic systems, although similar in principle to that illustrated in the schematic of Fig. 7, are much more complicated and have been described in the literature[4,25,28–31] and references cited there.

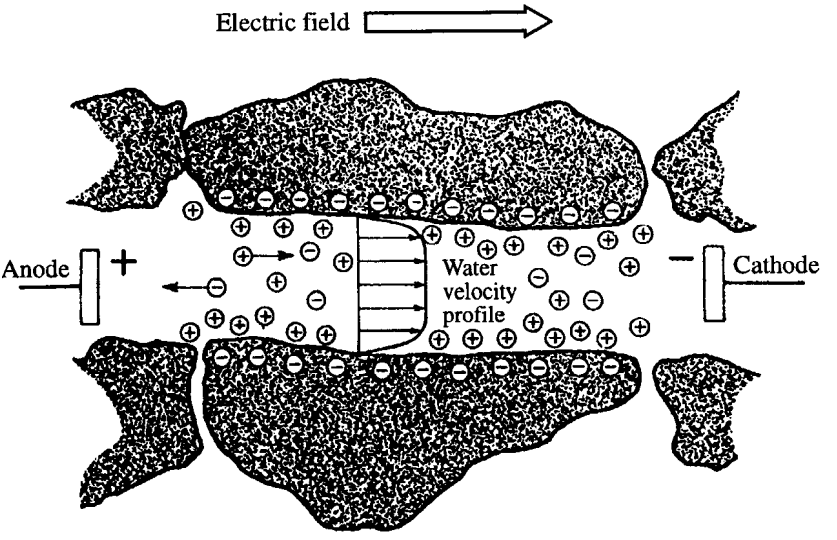

Figure 6. Schematic depiction of electro-osmotic flow in a porous charged medium. (After Probstein.[28])

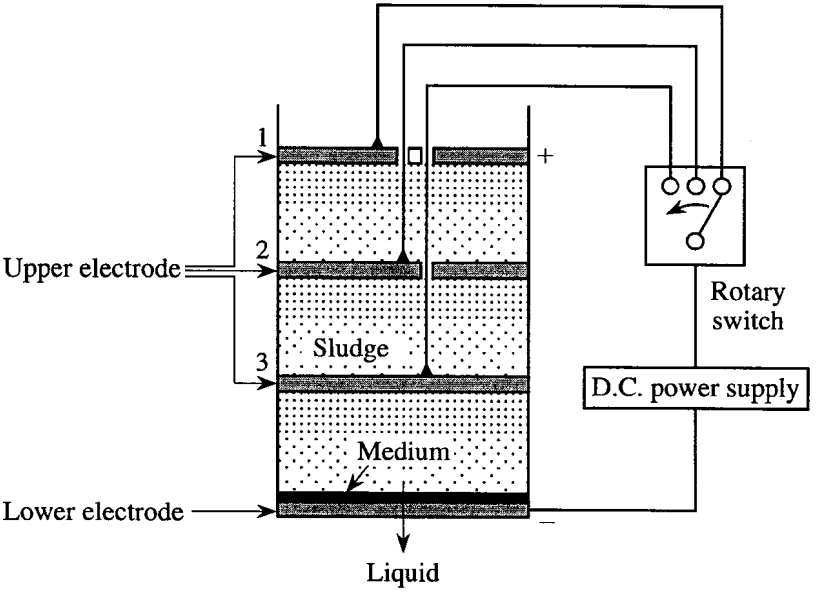

Figure 7. A three-stage upper electrode-type electro-osmotic dewatering apparatus. (After Yoshida.[12]) The upper electrode is the anode whereas the lower electrode is the cathode.

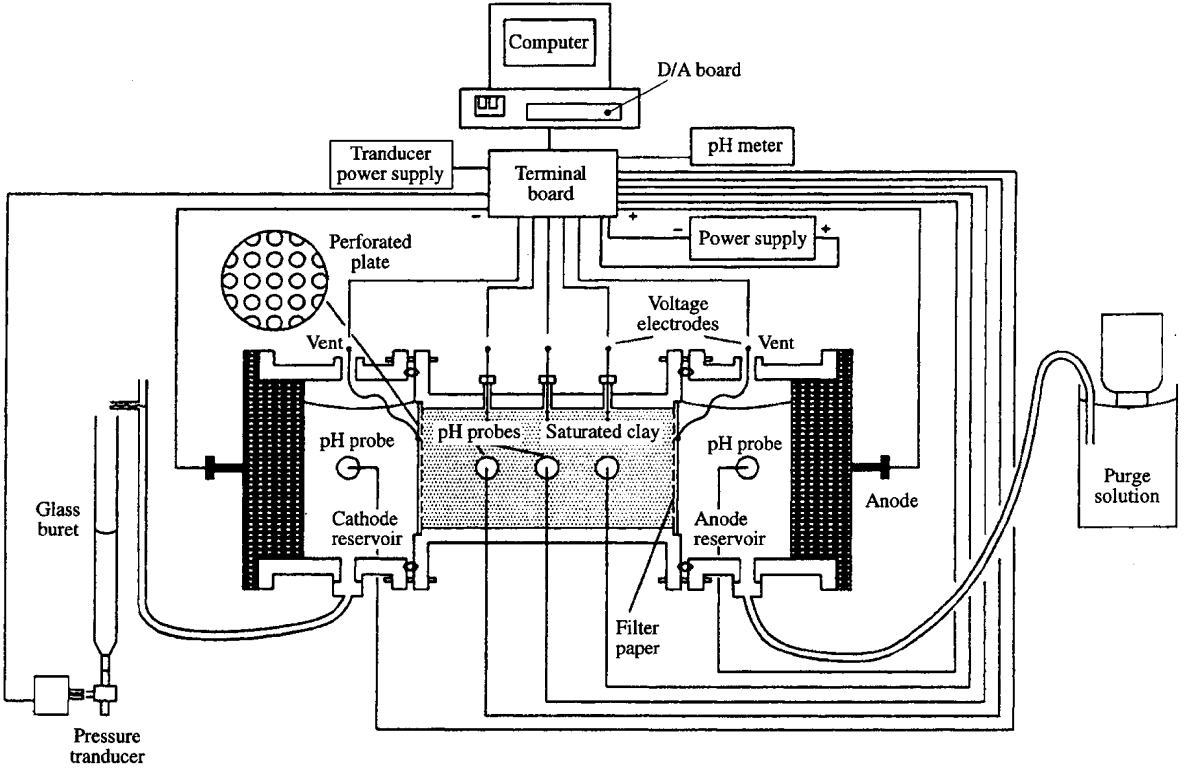

Figure 8. Diagram of an experimental setup for laboratory studies of electro-osmotic flushing technique to remove heavy metals from clays. It is basically an electro-osmotic dewatering setup with the addition of a continuous flow of purge solution at the anode and removal of contaminated water at the cathode.[33]

Of great interest to electrochemists is a practical laboratory setup for conducting EOD studies as, for example, in the work by Yeung and co-workers,[25,32] Mujumdar *et al.*,[8,9,33] and many other investigators.[1–7,29–31,34] A diagram of a typical experimental setup for laboratory studies on electro-osmotic dewatering is shown in Fig. 8, which is taken from Chen[33] and the laboratory of Mujumdar and Weber at McGill University; here EOD is being used to flush out heavy metals from the clay (see Section VI below).

In regard to the experimental results of laboratory or field investigations of EOD, a large number of parametric studies are available in which the effects of the following factors on EOD have been examined[1–6,8,9,12,28–33]: voltage, current magnitude and type (i.e., interrupted or continuous dc, etc.), salts, acids, flocculants, clay types, clay conductivity, the presence of various exchangeable cations, various electrode materials, and the presence or absence of hydraulic pressure or vacuum accompanying the EOD process. Most of these studies are empirical and of the "recipe type" and usually pertain to a given set of experimental conditions, without leading to a set of generalizations amenable to the construction of a comprehensive parametric theory that could lead to clear-cut predictions. A few important points, however, can be deduced from these studies, as indicated by a few observations for some typical experimental cases[1–6,8,9]:

1. The higher the externally applied voltage, the faster the dewatering in an EOD experiment.
2. Dewatering at a given voltage slows down when 45–50 wt% solids is reached in the sludge or clay being dewatered.[1]
3. The current efficiency is highest for the initial part of dewatering at every voltage[1]; its value of about 5–6 ml/mA is found[1] to be independent of the applied voltage.
4. The energy requirement (mWh/ml), even at maximum current efficiency, is proportional to the applied voltage.[1]
5. The step sequence 1 V, 2 V, 4 V, 10 V, 50 V (or some other similar step sequence) in which the initial part of dewatering is captured (a high current efficiency region) at each voltage before stepping up to the higher voltage, uses about five times less electrical energy for dewatering than a voltage fixed at 50.[1]
6. No significant differences in the dewatering, for example, of sodium kaolinite, were observed with mild steel, copper, or carbon electrodes.[1] With aluminum electrodes, however, the

application of high voltages is required to obtain even modest EOD[3] effectiveness.

7. Salt or acid concentrations up to 10^{-2} M usually allow dewatering to proceed at lower voltages, compared with suspensions in pure water, presumably by lowering the resistance of the clay.[2] At higher electrolyte concentrations (0.1 M), electro-osmotic dewatering became limited, and significant electrode polarization and electrode reactions were observed.[2]
8. Flocculants (nonionic) usually diminish the current efficiencies and increase the energy requirements for the EOD.
9. For high rates of EOD and for high current efficiencies, it is necessary to maintain a high value of the zeta-potential, for example, by causing the continued existence of a high pH at the anode and a low pH at the cathode.[8]
10. The cationic component of the clay has a paramount effect on the EOD. For example, for Na-kaolinite, EOD takes place at low (1–2 V) voltages, whereas for Ca-kaolinite, detectable dewatering occurs only above 10 V; for Al-kaolinite, 25 V was needed just to *initiate* the dewatering, with appreciable continuing dewatering being observed only when 150–250 V were applied.
11. When a highly electropositive anode (e.g., Mg) is used in conjunction with a very electronegative anode (e.g., Au), electro-osmotic dewatering occurs without an externally applied voltage, owing to the battery effect; this is called galvani dewatering.[1]
12. In dc electro-osmotic dewatering, current interruption followed by short-circuiting removed 20–40% more water than continuous dc or interruption with an open circuit, for otherwise equal energy consumption.[8]
13. The electro-osmotic transport of water during EOD leads to very high energy efficiencies; for example, the observed efficiencies of 5.6 ml/mAh (1.55 ml/C) are equivalent to 8300 moles of water per Faraday of electricity,[1] so that EOD is extremely cost effective.

The above-mentioned experimental observations encapsulate the main empirical facts established in a large number of studies on EOD. Several of these observations present features that have been analyzed in some detail as described in the following section.

1. Electro-Osmotic Dewatering under Interrupted Direct Current Conditions

Following earlier work by Lockhart and Hart,[35] Rabie *et al.*,[8] have reported some work on the EOD of clay suspensions under interrupted dc voltage; their main observations are as follows:

1. When the power was on, the passage of dc current caused electrode reactions at the anode and the cathode. Changes in pH caused by the electrode reactions affect the rate of water removal by changing the zeta potential.
2. If during the current interruption periods the electrodes were short-circuited, the water removed was 20–40% more than that obtained either with continuous dc or with interruption with an open-circuit period, for equal energy consumption.
3. When the power was on, the current was positive, that is, it flowed through the clay–water column from the anode to cathode; during the short-circuit, however, the current flowed in the opposite direction.
4. The open-circuit potentials of the electrode/clay (electrolyte)/electrode system were found to be between 1.8 and 2.3 V. It was concluded that these values arise from the electrochemistry of the system rather than from dewatering. However, the interpretation of these open-circuit potentials as arising from the hydroxides and oxides on the platinum anode, the pH effects, etc., is not electrochemically valid, as shown in Section IV [see Eq. (20)].
5. When the dc power is interrupted and the electrodes are short-circuited, a transient current is observed that is opposite in sign to that seen during dc power application. The short-circuit current was correctly interpreted by Rabie *et al.*[8] as resulting from "discharge of an electrochemical cell," thus reversing reactions (17) to (19), with the accompanying elimination of the zeta potential gradient and the restoration of the zeta potential near the anode to a high value approaching that at the start of the electrolysis. In effect, a short-circuit current more or less tends to restore the original conditions of the experiment, enabling one to restart the dewatering by switching on the dc power.

This discovery of Rabie *et al.,*[8] namely, that increasing the zeta potential near the anode by short-circuiting the electrodes after a dc power interruption, and thus restarting the electrolysis process (and thence dewatering), has provided the electrochemical clues for making other proposals for increasing the energetic efficiency of the EOD process.[10] These are described below.

(i) Fuel-Cell Effect

The fuel-cell effect is the proper name one could give to the discovery by Rabie *et al.,*[8] described above. As they correctly concluded, the electrolysis reactions (17) to (19) that occur when the dc power is on are (temporarily) reversed during short-circuiting; this would create a fuel-cell situation: Reaction (19) would be reversed so that the overall reaction would be the electrochemical combustion of H_2 and O_2 to produce H_2O [see the reverse of reaction (19)] with the provision of power; hence the observation of a current (of the opposite sign) during short-circuiting. This is essentially an H_2-O_2 primary battery effect, corresponding to fuel-cell behavior.

(ii) Forced Polarity Reversal

This "fuel-cell" effect, it may be suggested, could be more dramatically realized by *reversing* the dc power polarity for a few seconds; this should lead to a high zeta potential near the anode and cause the recommencement of EOD when the normal polarity for dewatering is restored.

(iii) High Overvoltage Electrodes

In principle, it would be possible to apply high voltage gradients to effect EOD in such a manner that the rates of the electrode reactions (and hence the currents) are minimized at the anode and cathode. This can be done by using highly polarizable, noncatalytic electrode materials. For cathodes, metals such as Zn, Sn, Pb, In, Cd, and Hg (as an amalgam) are excellent candidates for minimizing the rate of the hydrogen evolution reaction.[8] For anodes, non-noble metals, alloys, carbides, silicides, etc. can be found for minimizing the rates of the oxygen evolution reaction (e.g., titanium coated by nonstoichiometric oxides to make its surface conducting).[35] By minimizing the rates of electrode reactions, for a given

(high) applied voltage gradient, the diminution of zeta potential at the anode is delayed, thus postponing the cessation of dewatering.

(iv) Maintaining High Zeta Potential

In principle, in a system such as that studied by Rabie *et al.,* it would be possible to saturate the clay (or soil) with a low volume of concentrated NaOH (or KOH) solution that continues to maintain high pH and hence high values of the zeta potential near the anode even during prolonged electrolysis. This would tend to avoid cessation of dewatering after several minutes of EOD, as observed by Rabie *et al.*[8]

(v) Depolarization of the Anodic Reaction

It would appear that the depletion of OH near the anode could be stopped (and thus changes in pH and zeta potential prevented) during EOD by depolarizing the reaction (18) by another competing, parallel reaction such as the following:

$$Fe^{2+} \rightarrow Fe^{3+} + e^{-} \tag{23}$$

$$2Cl^{-} \rightarrow Cl_2 + 2e^{-} \tag{24}$$

However, the presence of extraneous ions such as Fe^{2+} or Cl^{-}, either in clays or soils, may not be acceptable for environmental reasons, not to mention their probable adsorption by clays. The idea of a depolarization reaction leaves open, however, the possibility of a suitable reaction (other than O_2 evolution) at the anode, for example, some organic oxidation such as that of $HCOO^{-}$ or CH_3COO^{-} or CH_3OH or C_6H_5OH. This may also provide a method of using anodic oxidation to clean soils contaminated by organics.

2. Electro-Osmotic Dewatering under Galvanic Conditions

Lockhart has observed[1] that "by combining an electropositive magnesium anode with an electronegative gold cathode, substantial Galvanic dewatering of sodium kaolinite was achieved *without* an external power supply. Even better Galvanic dewatering was obtained for copper kaolinite, a clay having an easily discharged cation."

His statement that the need for an external power supply is eliminated because of the electricity-producing battery effect between the Mg anode and an Au cathode (connected, of course, through a conducting "electrolyte" in the clay pores) is correct. However, a more important effect[3] that would seem to operate in this arrangement is that a high zeta potential is maintained by ensuring a high pH at the anode and a low pH at the cathode, owing to the following reactions:

Anode:

$$Mg + H_2O \rightarrow MgO + H_2 \uparrow \tag{25}$$

$$MgO + H_2O \rightarrow Mg(OH)_2 \tag{26}$$

Cathode:

$$Cu^{2+} + 2e \rightarrow Cu \tag{27}$$

Both MgO and $Mg(OH)_2$ are highly basic[16,17] and tend to maintain a high pH at the anode; deposition of Cu^{2+} at the cathode, suggested by Lockhart,[3] ensures that H_3O^+ is not depleted near the cathode. Hence this Galvanic dewatering creates the conditions for continued maintenance of the high zeta potential so necessary for continued dewatering.

3. Dewatering Efficiency in Terms of Liters per Ampere-Hour (or Liters per Watt-Hour at Constant Voltage)

Although the dewatering efficiency $[l(\mathrm{A\,h})^{-1}]$ is of great practical significance, its fundamental conceptual significance is less clear. As pointed out previously,[10] EOD involves the electro-osmotic flow of water (electrolyte) through the clay as if the whole water were behaving as a single "ion" or a charged "plug" driven by electrostatic effects arising from the electrochemical double layers at the clay/water (electrolyte) interface. Thus this current is not a faradaic current (as, e.g., carried by each ion) but an electro-osmotic current, although the faradaic current is a fraction of the total current and constitutes that part which is carried by the ions discharging at the electrodes. Ideally [see Eq. (15) and the related discussion], the passage of faradaic electric current (and hence the discharge of ions on the electrodes) is not required for the EOD to occur by purely electro-osmotic effects. In practice, however, the electrolytic effects[36] (and thus the faradaic current) can and do arise for the reasons described previously.[10]

If one examines [37] the large-scale field trials of electro-dewatering conducted by Lockhart,[4] high rates of dewatering were perhaps sustained because the ionic concentrations were low, with very large values for the widths of the diffuse double layers (~10^{2}–10^{-3}nm). This would lead to repulsions between the double layers[38] with "opening up" (electrostatically speaking) of the clay pores, thus creating the conditions for the electro-osmotic flow of a large "single ion" or "plug." The fact that high levels of dewatering could be sustained for 2 months indicates that conditions for the maintenance of the high zeta potential continued to operate during that period. It is clear that conceptually, one cannot simply try to relate the observed EOD rates to the measured currents since these currents represent only the faradaic component; it is realized, however, that for practical, industrial problems, it is precisely this efficiency that is of interest. This problem, of course, is the basis of the observation that "experimental efficiencies translate to high and obviously untenable amounts of water per ion."[1] A more detailed analysis of the components of the currents and fluxes observed during EOD has been given recently[23] and is presented here in Section III.1.

4. High Voltages Needed for Dewatering Al-Kaolinite and the Aluminum Electrode Effect

Another interesting observation made by Lockhart[3] is as follows: "For Na-kaolinite, . . . most of the electro-osmotic dewatering took place at low voltages (1 V and 2 V) whereas for Ca-kaolinite no significant dewatering occurred until 10 V was reached. For Al-kaolinite, 25 V was needed to initiate water flow and only at 150–250 V was an appreciable degree of dewatering achieved." He realized[3] that "the situation for Al clay is more complex—even though high voltages are necessary for dewatering, the currents are low but their dewatering efficiencies are reasonable; also the pH of the water is neutral which implies that reaction ($Al^{3+} + 3e \rightarrow Al$) is unlikely. Either the aluminum is present as a (less electropositive) complex ion that does react according to ($Al^{n+} + ne \rightarrow Al$) or reaction ($2H_2O + 2e \rightarrow H_2 + 2OH^-$) occurs but the OH^- then combines with the Al^{3+} ions." Note that the electrodeposition of Al from Al^{3+} in aqueous solution is thermodynamically impossible.

By taking the latter suggestion of Lockhart,[3]: we [38]conclude that $Al(OH)_3$ is indeed initially formed. This Al(OH)3 can exhibit the equilibrium reaction[39]

$$Al(OH)_3 = AlO_2^- + H_2O + H^+ \quad (28)$$

The AlO_2^- can then get discharged on the carbon-covered steel anode (when the voltage is applied), giving rise to an aluminum oxide layer:

$$M + 2AlO_2^- + H_2O \rightarrow M - Al_2O_3 + 2\,OH^- \quad (29)$$

This then sets the stage for the anodic growth of a barrier-type insulating aluminum oxide layer[36] on the electrode (anode), represented by M in Eq. (29). The reaction in Eq. (29) is an illustrative one and is written only to suggest that a complex aluminum ion with a negative charge (e.g., any oxygenated complex anionic species such as oxides, hydroxides, oxyhalides, or a mixture thereof) is needed to initiate the formation of a barrier layer, which will then require the application of high voltages for appreciable dewatering: this will also explain the low currents.[36] In the picture suggested here, most of the voltage used for dewatering operates (once the barrier oxide has been formed) in fact across the insulating layer[36] and is not "available" to assist dewatering.

Similar effects would also be expected with Ca^{2+}, but to a much lesser extent because (1) anodic oxide growth on a "Ca anode" (actually a CaO layer on the anode) reaches only a few volts since the oxide is not truly of the barrier type; (2) the highly ionic CaO undergoes dissolution concomitant to the growth process; (3) the CaO is not expected to be without a large number of cracks and imperfections, which are much more deleterious to the integrity of the oxide than the self-healing "microfissures" usually found in Al_2O_3 and other barrier-type oxides. The evidence for the involvement of insulating Al_2O_3 is quite clear when C/C electrodes are compared with Al/Al electrodes (Ref. 5, Table 5) since very high voltages are observed for the latter electrodes, a case typically associated with anodic oxide growth on Al.[36] Furthermore, no other plausible mechanism exists for explaining these high voltage buildups in dewatering when aluminum is involved as an anode either directly (e.g., as the electrode) or indirectly (i.e., deposition of AlO_2^- to give an Al_2O_3 layer anode).

5. Electro-Osmotic Dewatering at Low Applied Voltages

Another fact that needs comment is the observation by Lockhart[1] that EOD can be achieved even by the application of 1 V to the

Anode | Clay (water) | Cathode

system. In terms of our analysis[10] [see Eq. (21)], this would be possible if very low differences of reversible electrode potentials as well as overpotentials existed between the anode and the cathode. An example would be

$$\mathrm{Cu} \underset{\text{Cathode reaction}}{\overset{\text{Anode reaction}}{\rightleftharpoons}} \mathrm{Cu^{+} + e^{-}} \tag{30}$$

A variety of other plausible electrode reactions could be invoked (some perhaps arising from trace impurities in the clay/water system or corrosion reactions at the electrodes) to account for the existence of EOD at low applied voltages, (e.g., 1 V).

It is important to note again that the current observed during EOD is not a faradaic current (as, for example, carried by each ion), but an electro-osmotic current in which the water trapped in the clay moves as a plug, just as in a capillary. This is the reason why high faradaic power efficiencies are observed compared with normal electrolysis in which the discharge of ions at the anode and the cathode is the only manner of eliminating water, namely, by electrolysis to H_2 and O_2. The EOD involves the electro-osmotic flow of the water (electrolyte) through the clay as if the whole water were behaving as a single "ion" or a charged "plug" driven by the electrostatic effects arising from the electrochemical double layers at the clay/water (electrolyte) interface.

6. Components of Voltage in an Electro-Osmotic Cell

When either an externally applied voltage or a galvanically created voltage is applied to an electro-osmotic cell, a number of potential drops develop within the cell which together constitute the total voltage. A simple extension of Eq. (20) will give the components of the voltage V, as follows:

$$V = E^{\circ}_{\mathrm{H_2/O_2}} + \eta_{\text{anode}} + \eta_{\text{cathode}} + \frac{RT}{F}\,\mathrm{pH} + IR + V_{\text{oxide}} + V_{\text{cake}} \tag{31}$$

On comparison with Eq. (20), which defines various quantities at open circuit (i.e., in the absence of the passage of an externally applied current, although short-circuiting on open circuit will cause the flow of some current owing to the fuel-cell type of effects discussed earlier), it

should be noted that the various quantities on the right-hand side of Eq. (32) refer to the passage of appreciable currents so that η_{anode}, $\eta_{cathode}$, and *IR* defined earlier would now attain relatively high magnitudes. V_{oxide} is the potential drop across the barrier oxide when an anode such as Al, Ta, Nb, W, Zr, Hf, or Bi is used, since these anodes develop highly insulating thick oxides during passage of an electrolytic current.[36] V_{cake} is the voltage drop across the dry anodic "cake" that usually forms (with any anode, including those that do not form insulating oxides) on the anode owing to the extreme dewatering and dryness of the clay in the vicinity of the anode, once EOD has been proceeding for some time, especially at high current. This drying effect is caused by a combination of electro-osmotic dewatering and the resistive, I^2R, heating effect.

In a more detailed analysis, one must decompose $E^{\circ}_{H_2/O_2}$ for water electrolysis (or for any other overall cell reaction operating in a given situation) into component values for the cathodic and anodic half-cell reactions; each half-cell potential can then be shown to consist of a detailed potential profile (Helmholtz double layer, diffuse double layer, etc.) at the metal/electrolyte interface, in the usual way. Furthermore, the various quantities in Eq. (31), especially *IR* and (*RT*/*F*) pH, can further show temporal variations with the passage of current over a significant period of time.

It is thus clear that in most of the empirical studies on EOD, one talks of "voltage across the cell" or some variation thereof (e.g., field, i.e., voltage divided by the length of the clay column in the cell) as if it were a single quantity. It is, in fact, a quite complex quantity constituted of several components [see Eq. (31)] and this should be taken into account, as far as possible, in interpreting the results from EOD experiments.

VI. APPLICATIONS OF ELECTRO-OSMOTIC DEWATERING

Although several applications of EOD were already mentioned in Section I, it is appropriate here to outline the ways in which EOD provides solutions to industrial problems.

In geotechnical engineering work,[11,40] electro-osmotic technology is used in stabilizing embankments, dewatering foundation sites, strengthening steeply cut slopes, and increasing the capacity of steel friction piles.

In the field of environmental engineering, electro-osmotic dewatering can be used to remove organic contaminants or toxic heavy metals from

fine-grained soils. This is carried out by an electro-osmotic contaminant-flushing technique, which has been used, for example, to remove benzene, toluene, trichloroethylene, and *m*-xylene from saturated kaolin clay by Bruell *et al.* [40,41] Contaminants are flushed from the soil by injecting clean water (or purge solution) at pipe anodes inserted in the clay; pore water is displaced and contaminated water is removed at pipe cathodes (Figs. 6–8). Similarly, toxic heavy metal cations such as Pb^{2+} and Cd^{2+} have been removed from soils by Probstein and co-workers[7,28,34,42] and Chen *et al.* [33] (Fig. 8).

Removal of water from mine tailings and residues has been carried out by Lockhart and co-workers. [1–6] Laboratory experiments on electro-osmotic dewatering of vegetable sludge, such as that produced in the food processing industry, have been reported by Chen *et al.*[43] Yeung[25] has provided a good summary of the wide range of applications of electro-osmotic dewatering. The application of this technique to field tests for the electrochemical remediation of polluted soils[44,45] or to the residues of the mining industry [4] has shown spectacular results.

NOTE ADDED IN PROOF

Some aspects of the theoretical interpretations presented here have been further developed and published recently[46–48]; the theory of EOD has also been applied to the electrochemical treatment of cancerous tumors. [49,50]

VII. APPENDIX

The form of Eq. (1) in the text implies that the dimensions of the problem (e.g., the length and cross section of a channel delimiting the flow) are included in the coefficients L_{ij}. A dimensional analysis of relationship (13) in the SI unit system yields

$$[J/I] = [V/P] = (\mathrm{m}^2\cdot\mathrm{kg}\cdot\mathrm{s}^{-3}\cdot\mathrm{A}^{-1})/(\mathrm{kg}\cdot\mathrm{m}^{-1}\cdot\mathrm{s}^{-2}) = \mathrm{A}/(\mathrm{m}^3\cdot\mathrm{s}^{-1}), \qquad (32)$$

where I is a total current in amperes and J is a total volume flow in cubic meters per second (square brackets indicate that only dimension of the variable is considered). Furthermore, the dimension of the coefficient L_{21} from Eq. (1) for J, assuming $\Delta P = 0$, is

$$[L_{21}] = (m^3 \cdot s^{-1})/(m^2 \cdot kg \cdot s^{-3} \cdot A^{-1}) = A/(kg \cdot m^{-1} \cdot s^{-2}); \quad (33)$$

The same result is obtained for L_{12} using Eq. (1) for I and assuming $\Delta V = 0$, in accordance with Onsager's relation. Similarly we obtain

$$[L_{11}] = A/V = A^2/(m^2 \cdot kg \cdot s^{-3}) = S \quad (34)$$

and

$$[L_{22}] = m^4 \cdot s/kg \quad (35)$$

In the homogeneous case, or when considering a sufficiently small elementary volume, the flow and current are directly proportional to the area of the channel (perpendicular to the flow) and indirectly proportional to the length (parallel to the flow). Thus relationship (2) defines the coefficient L_{21} in terms of material properties and parameters of the volume in question (area and length). It differs from Overbeek's relationship,[14] where the length is omitted. Again, dimensional analysis of Eq. (2) yields expression (33).

It is often convenient, in particular when we are dealing with nonhomogeneous problems, to write Eq. (1) for specific quantities related to unit volume. Then relationship (1) reads

$$j = l_{22} \frac{dP}{dx} + l_{21} \frac{dV}{dx}$$

and

$$i = l_{11} \frac{dV}{dx} + l_{21} \frac{dP}{dx} \quad (36)$$

Here $[j] = m^{-3} \cdot s{-}1/m^2$ and $[i] = A/m^2$ are the flux per unit area and the current density, respectively; l_{11} is the specific conductance in siemens per meter, l_{22} is the specific hydrodynamic conductance ($m^3 \cdot s/kg$) and $l_{12} = \epsilon\zeta/(4\pi\eta)$ is the specific electrokinetic coefficient ($As^2 \cdot kg^{-1}$).

Note: A useful reference for the dimensions of the quantities used here is *A Physicist's Desk Reference,* H. L. Anderson, ed., American Institute of Physics, New York (1989).

ACKNOWLEDGMENTS

I would like to thank Prof. Arun J. Mujumdar of McGill University, Montréal, for initially bringing this topic to my attention. Thanks are also

due to H. Chen, M. Weber, and A. J. Mujumdar for giving me the opportunity to contribute some electrochemical aspects to the ongoing work on electro-osmotic dewatering at McGill University.

Grateful acknowledgment is also made to Dr. J. Novak of the Hydro-Quebec Institute of Research for collaboration on some theoretical aspects. I also thank Dr. Guy Bélanger for his encouragement of this work at our institute.

REFERENCES

[1] N. C. Lockhart, *Colloids Surfaces* **6** (1983) 229.
[2] N. C. Lockhart, *Colloids Surfaces* **6** (1983) 239.
[3] N. C. Lockhart, *Colloids Surfaces* **6** (1983) 253.
[4] N. C. Lockhart, *MINFO-NSW Mining and Exploration Quarterly* (Australia) **11** (1986) 52.
[5] N. C. Lockhart and G. H. Hart, *Drying Technology* **6** (1988) 415.
[6] N. C. Lockhart, *Drying Technology* **10** (1992) 839.
[7] R. F. Probstein and R. E. Hicks, *Science* **260** (1993) 498.
[8] H. R. Rabie, A. S. Mujumdar, and M. E. Weber, *Sep. Tech.* **4** (1994) 38.
[9] S. Ju, M. E. Weber, and A. S. Mujumdar, *Sep. Tech.* **1**(1991) 214.
[10] A. K. Vijh, *Drying Technology* **13** (1995) 215.
[11] L. Casagrande, *Geotechnique* **1**(3) (1949) 159; *J. Boston Soc. Civ. Eng. Sect., ASCE,* **69** (2) (1983) 255.
[12] H. Yoshida, *Drying Technology* **11** (1993) 787.
[13] D. H. Everett, *Basic Principles of Colloid Science,* Royal Society of Chemistry, London (1988).
[14] J. Th. G. Overbeek, *J. Colloid Sci.* **8** (1953) 420.
[15] S. R. De Groot, *Thermodynamics of Irreversible Processes,* North-Holland, Amsterdam (1966).
[16] R. L. Blokhra and Ch. Prakash, *J. Membrane Sci.* **70** (1992) 1.
[17] R. P. Rastogi and R. Shabd, *J. Phys. Chem.* **81** (1977) 1953.
[18] A. Sanfeld, in *Physical Chemistry: An Advanced Treatise,* Vol. 1, W. Jost, ed., Academic Press, New York, 1971 p. 239.
[19] J. Th. G. Overbeek and P. W. O. Wijga, *Rec. Trav. Chim.* **65** (1946) 556.
[20] P. Mazur and J. Th. G. Overbeek, *Rec. Trav. Chim.* **70** (1951) 83.
[21] D. N. Staicopolus, in *The Encyclopedia of Electrochemistry,* C. A. Hampel, ed., Reinhold, New York, 1964, p. 384.
[22] N. C. Lockhart, *Drying Technology,* **14** (1996) 1487.
[23] A. K. Vijh and J. Novak, *Drying Technology* **15** (1997) 699.
[24] P. Van Rysselberghe, *Thermodynamics of Irreversible Processes,* Hermann, Paris, 1963, p. 93.
[25] A. T. Yeung, *Advances in Porous Media* **2** (1994) 309.
[26] H. A. Abramson, *Electrokinetic Phenomena and Their Application in Biology and Medicine,* Am. Chem. Soc. Monograph Series, Chemical Catalog, New York (1934), as cited in Ref. 25.
[27] A. T. Yeung and J. K. Mitchell, *Géotechnique* **43** (1) (1993) 121.
[28] R. F. Probstein, *Physicochemical Hydrodynamics: An Introduction,* Butterworths, London (1989).

[29]J. G. Sunderland, *J. App. Electrochem* **17** (1987) 889.
[30]J. G. Sunderland, *J. App. Electrochem* **17** (1987) 1048.
[31]J. G. Sunderland, *J. App. Electrochem* **17** (1987) 1171.
[32]A. T. Yeung, S. M. Sadek, and J. K. Mitchell, *Geotech. Test. J. ASTM* **15** (3) (1992) 207.
[33]H. Chen, M. Weber, and A. J. Mujumdar, to be published; H. Chen, M.S. thesis, Chemical Engineering Dept., McGill University, Montréal, 1997.
[34]A. P. Shapiro, P. C. Renaud, and R. F. Probstein, *Physico-Chemical Hydrodynamics* **11** (1989) 785.
[35]N. C. Lockhart and G. H. Hart, *Drying Technology* **6** (1988) 415.
[36]A. K. Vijh, *Electrochemistry of Metals and Semiconductors,* Marcel Dekker, New York, 1973.
[37]N. C. Lockhart, *Drying Technology* **14** (1996) 1487.
[38]A. K. Vijh, *Drying Technology* **15** (1997) 225.
[39]M. Pourbaix, *Lectures on Electrochemical Corrosion,* Plenum, New York, 1973.
[40]B. A. Segall and C. J. Bruell, *J. Environ. Eng., ASCE* **118** (1) (1992) 84.
[41]C. J. Bruell, B. A. Segall, and M. T. Walsh, *J. Envir. Engr., ASCE* **118** (1) (1992) 68.
[42]G. Denisov, R. E. Hicks, and R. F. Probstein, *J. Colloid Interf. Sci.* **178** (1996) 309.
[43]H. Chen, A. S. Mujumdar, and G. S. V. Raghavan, *Drying Technology* **14** (1996) 2435.
[44]J. Trombley, *Environ. Sci. Technol.* **28** (6) (1994) 289A.
[45]Y. B. Acar, E. E. Ozsu, A. N. Alshawabkeh, M. F. Rabbi, and R. J. Grale, *Chemtech* **26** (4) (1996) 40.
[46]A. K. Vijh, *Drying Technology* **17** (1999) 555.
[47]A. K. Vijh, *Drying Technology* **17** (1999) 565.
[48]A. K. Vijh, *Drying Technology* **17** (1999) 575.
[49]A. K. Vijh, *Drying Technology* **17** (1999) 585.
[50]A. K. Vijh, *J. Mater. Sci.: Materials in Medicine,* in the press (1999).

5

The Effect of Magnetic Fields on Electrochemical Processes

Thomas Z. Fahidy

Department of Chemical Engineering, University of Waterloo, Waterloo, Ontario, Canada N2L 3G1

I. INTRODUCTION

The title of this chapter invites a question to be asked immediately: Why should magnetic fields exert any effect at all on an electrochemical process? A simplistic but powerful answer is provided by a fundamental law of electromagnetics (often called the right-hand rule), which states that coupled electric and magnetic fields generate motion; electric motors operate according to this principle. Electrolytes are no exception to this rule, as depicted qualitatively in Fig. 1. The four photographs show progressively turbulent surface motion in a cell

Modern Aspects of Electrochemistry, Number 32, edited by B. E. Conway *et al.* Kluwer Academic / Plenum Publishers, New York, 1999.

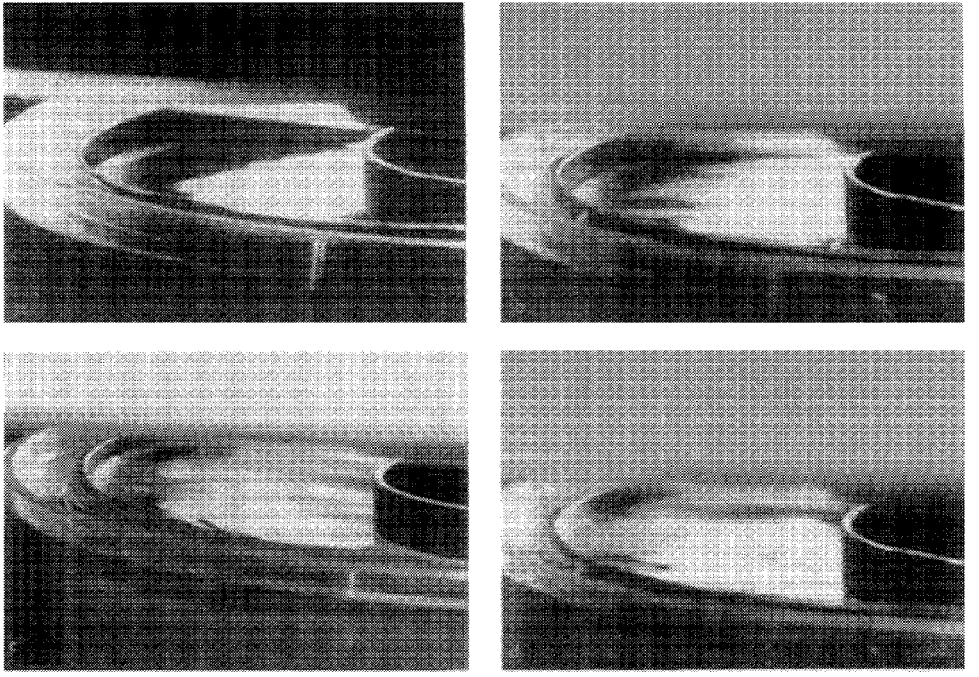

Figure 1. Illustration of motion generated in an aqueous acidified $CuSO_4$ solution, exposed to a vertical magnetic gradient field and a radial electric field. (a) At a low magnetic field strength (MFS), the electrolyte surface is flat. (b) With a gradual increase in MFS, the surface becomes increasingly undulatory. (c) At a sufficiently high MFS, the surface-wave amplitude is large enough to cause spilling over the outer cell wall. (d) Back of the cell (S. Mohanta and T. Z. Fahidy, 1977, unpublished results.)

containing an aqueous $CuSO_4/H_2SO_4$ solution between two concentric cylindrical copper electrodes. The electric field produces a modest current and the magnetic field strength is progressively increased. If the vertically imposed magnetic field were uniform, the flow would be circular and essentially laminar; in a nonuniform (gradient) field, turbulent wavy motion is easily generated. This is, in essence, the thrust of magnetic field imposition, although its theoretical and empirical aspects span a wide spectrum of its appearance, importance, and utilization.

Since the first recorded interest[1] in the effects of magnetic field on electrolyte solutions, a large number of researchers have contributed to this complex and challenging field. Earlier studies were primarily focused on relating an apparent electrolyte resistivity to the strength of imposed magnetic fields, as shown in a thorough survey by Olivier[2]; in a typical paper,[3] a "twisting" effect on ionic paths was offered as an explanation for the minimal conductance values observed. This period was followed by an intensive investigation of the Hall effect in electrolytes, convective diffusion under magnetic influence, and the effect of magnetic fields on electrode-process kinetics. More recent investigations probed into surface-structural effects and the utility of imposing a magnetic field on electrolytic cells in the production of various chemical compounds. Two review papers[4,5] summarize major aspects of research in this area. The wealth of information also available in the non-English-language literature (e.g., Refs. 6 and 7) has not yet found wide recognition, to the author's knowledge.

This chapter provides an overview of knowledge accumulated in certain key directions of this research domain, but without any claim to completeness (which would be a difficult task to achieve). The general aim is to leave the reader with a view of what has been accomplished over a few decades, and with an appreciation of the major challenges that are still facing investigators of magnetic field effects. Theoretical frameworks of analysis are also included, with caveats about their limited quantitative applicability to experimental observations. It is hoped that this material will also spur the reader to examine particular areas of the pertinent literature in depth.

II. MAGNETIC FIELD EFFECTS ON ELECTROLYTE BEHAVIOR

1. The Hall Effect in Electrolytes

As indicated in an earlier review,[4] the Hall effect has been the subject of numerous investigations. The Hall constant R_H is defined by the classical electric field equation

$$\mathbf{E} = \mathbf{j}/\sigma - R_H(\mathbf{j} \times \mathbf{B}) \tag{1}$$

where **E** is the electric field vector, **j** is the current-density vector, **B** is the magnetic flux-density vector, and σ is the bulk electrolyte conductivity. The Hall constant can be related to ionic mobilities[2] and characteristic ionic coefficients in terms of the ionic kinetic energy (Section VII; typically between 40 and 54 zeptojoules per ion, in the case of monovalent ions). In a somewhat similar formulation, Meton and Gerard[8] found the order of magnitude of the Hall constant to be between 10^{-7} and 10^{-6} $m^3 A^{-1} s^{-1}$ for certain monovalent ions. In a conceptually different approach, Friedmann[9] applied advanced concepts of statistical mechanics and, specifically, a Brownian motion-based model of ionic mobility. Model-predicted values of Hall conductance show good agreement with values obtained from the kinetic theory of slightly ionized plasmas.[10,11] In considering electrohydrodynamic forces acting on ions moving in a magnetic field, Hubbard and Wolynes[12] have shown that this force, acting in the opposite direction, can be about one-third of the Lorentz force. Conceptual disagreements notwithstanding, the Hall conductance in aqueous electrolytes is about eight to nine orders of magnitude smaller than the bulk conductance.

2. Diffusivity

In an analysis of the diffusion equations in magnetic fields, Dumarque *et al.*[13] introduced a diffusivity tensor and an effectiveness parameter related to the difference between diffusivity in the presence and in the absence of a magnetic field. In a less general, but somewhat more amenable approach to numerical estimations, Lielmezs and Musbally[14] derived a magnetic correction factor called the *arithmetic mean average fractional integral diffusion coefficient*

$$k_M = \langle (D_M - D_0)/D_0 \rangle \quad (2)$$

where D_M is the diffusivity of the electrolyte in the presence and D_0 in the absence of the magnetic field. In a comprehensive experimental program, Lielmezs and co-workers obtained k_M values experimentally and found that their variation with temperature, electrolyte concentration, and magnetic field strength is normally less than 1%,[15,16] although a value of k_M = 6.13% has also been observed in aqueous KCl solutions.[17] In general, the k_M versus concentration curve has a local minimum at a fixed magnetic field strength whose existence cannot be explained by a simple theory of electromagnetism. The experimentally observed values of k_M are somewhat larger than values predicted via the Lielmezsd–Musbally equation[14]

$$k_M = [\mathbf{v}_1 \times \mathbf{B} - \mathbf{v}_2 \times \mathbf{B}]/[\mu_{ss}\, \mathbf{grad}(c_s)] \quad (3)$$

where $\mathbf{v}_1$ and $\mathbf{v}_2$ are the ionic average drift velocity vectors in interacting diffusion flow, and μ_{ss} is the derivative of the chemical potential of the electrolyte with respect to electrolyte concentration, c_s.

3. Viscosity

The existence of a local minimum at an intermediate magnetic field strength has been shown for the viscosity of water[18] (about a 3.5% drop with respect to the H = 0 value at a magnetic field strength of $H \approx 370$ A m^{-1}; $H = B/\mu$ and μ is the magnetic permeability of water), in aqueous KCl,[19] manganese nitrate,[20] and nickel nitrate[21] solutions. In water, increases in viscosity have been reported from 0.06% (B = 0.5 tesla, T) to 0.27% [B = 1.2 T] in the 10–50°C temperature range.[22] The variation of viscosity in combined alternating electric and constant magnetic fields with electric-field frequency has also been suggested[23] on the basis of the concept of "volume viscosity" in ultrasonic absorption and velocity studies in certain fluids.[24] The variation of viscosity with magnetic field strength cannot, however, be predicted from the fundamental relationships of physics.

4. Properties of Chemical Equilibrium

The thermodynamics of magnetic systems have a solid theoretical foundation; for example, in the case of ideal gases, the conventional pressure-volume-temperature (PVT) basis is replaced by the magnetic field-

magnetization-temperature (HMT) basis.[25] Nevertheless, there is little information available on the variation of equilibrium composition in electrolytes with the magnetic field strength. The recent work by Yamaguchi *et al.* on chemical equilibrium between metals and hydrogen[26–28] may be considered as a "pathfinder" for much needed research in this area. Under the influence of a magnetic field, a portion of the magnetostatic energy of $LaCo_5H_x$ hydride is converted into the chemical potential of hydrogen in the hydride. The equilibrium hydrogen pressure (EHP) ratio is expressed as

$$[\text{EHP when } B \neq 0]/[\text{EHP when } B = 0] = \exp(2\,B\Delta M_s/RT) \qquad (4)$$

where ΔM_s[= 8.7 J(T mol hydrogen)$^{-1}$ at 343.2 K] denotes the change in saturation magnetization per 1/2 mol of desorbed hydrogen gas. Under magnetization up to 14 T and constant hydrogen pressure at 313.2 K, the hydrogen content changes from $x = 1.88$ to $x = 0.96$ in the hydride. If similar data for ionic equilibria in electrolyte solutions were readily available, the current understanding of magnetic field effects would be significantly enhanced.

5. Magnetic Properties

Ions in solution are either paramagnetic (i.e., they develop a magnetic moment parallel to an imposed magnetic field), or diamagnetic (i.e., they develop a magnetic moment opposed to the imposed magnetic field). The magnetic force tends to repel diamagnetic ions in a nonhomogeneous magnetic field from the strong-field region, the latter attracting, in a relative sense, paramagnetic ions. A fingerprint of this property is the volume susceptibility, κ, related to the relative permeability of the medium as $\mu_r = 1 + \kappa$, where μ_r is the ratio of the absolute permeability of the medium to $\mu_o = 4\pi \times 10^{-7}$ H m^{-1}, the absolute permeability of a vacuum. The mass susceptibility (i.e., the volume susceptibility divided by the density) is a similar fingerprint. Magnetic moments are commonly expressed in Bohr magneton units: one Bohr magneton $\equiv \mu_B = 9.2732$ yJ. m^2(Wb)$^{-1}$.

The range of mass susceptibilities is 10^{-9} to 10^{-7} (per kilogram, at 20°C); typical experimental values of magnetic moments are 1.9 (Cu^{2+}); 3.2 (Ni^{2+})[29]; 5.0 (Co^{2+}); 5.2 (Fe^{2+}) and 5.9 (Fe^{3+}) Bohr magnetons.[30] In a gradient of field, the magnetic force acting on a compound with the dissociation constant K_d in an aqueous electrolyte may be written as

$$\mathbf{f}_M = (\mu_o\chi/2cK_d)\ \mathbf{grad}(\mathbf{H}^2) \tag{5}$$

where χ is the susceptibility of the solution, c is the electrolyte concentration, and **H** is the magnetic field strength vector. In experiments using aqueous sodium carbonate solutions placed in solenoidal magnetic fields,[31] an ionic separation ratio of 0.42 was found for sodium ions when f_M was about 5 fN. While susceptibility effects are of a small magnitude, they can generate ionic movement (ion separation) under carefully designed experimental conditions (Section IX.2).

The smallness of the susceptibility effect is equally evident in an early study [4,32] of magnetically modified reaction equilibria, where the expression for the equilibrium constant

$$-\ln(K) = (1/RT)\ \Sigma_i\nu_1(\mu_i^0 - [\mu_i^0\chi_iH^2/2]) \tag{6}$$

carries a magnetic correction term of a 10^{-5} order of magnitude. Here v_i are the stoichiometric coefficients, μ_i^0 are the standard chemical potentials, and χ_i are the magnetic susceptibilities of the reacting species.

III. MAGNETIC FIELD EFFECTS ON SURFACE MORPHOLOGY

1. Cathode Deposits

The beneficial effect of magnetic fields on surface quality has been amply demonstrated by a number of investigations.[33–38] O'Brien and co-workers [39–40] indicate the important effect of electrode configuration on the denseness and uniformity of zinc deposits; in pulsed electric fields, microturbulence generated by polarity reversal contributes to evenness of deposit. The variety of micro- and macroscopic deposit structures has been illustrated by Chiba and co-workers,[41,42] Young,[43] and Ismail *et al.*[44] in nonuniform magnetic fields. Recent investigations[45] indicate that very compact Zn deposits can be obtained in a $B = 8$ T field, in contrast to the open-ramified fractal growth patterns observed in the absence of a magnetic field. Similar results were obtained in the magnetically assisted electropolymerization of pyrrole,[46,47] in which the fractal structure progressively disappears as the magnetic field strength is increased. The fractal dimension at a fixed value of B depends on the thickness of the solution in the experimental cell. Cathodic deposition from aqueous silver

nitrate solutions in high magnetic fields is accompanied by a dense radial growth of silver metal "leaves."[48]

2. Deposits Formed in Anodic Dissolution

Secondary and tertiary processes accompanying anodic dissolution often result in products that may be deposited (at least temporarily) on the anode surface. Oscillatory current behavior arising from deposition and redissolution cycles has been extensively studied via nonlinear dynamics and chaos theory,[49,50] although experimental results obtained in magnetic fields combined with electric fields are essentially confined to copper.[51,52] Oscillation can be suppressed by imposition of a magnetic field, and this finding suggests the possibility of magnetic field control of anodic corrosion[53] under appropriate conditions. The exact role of the magnetic field is not understood at present, and the interpretation of this effect in terms of a modified Brusselator model of chemical reactions is rather tentative.[54] (See also Chapter 1 in this volume.)

IV. THE MAGNETIC FIELD EFFECT ON ELECTRODE REACTION KINETICS

The expression "electrode reaction kinetics" implies in a strict sense the governance of an electrode process by charge transfer. Under such conditions, the classic Butler–Volmer equation, or the more phenomenological Tafel equation, describes the electrode process within an appropriate range of the electrode potential. In practice, the "hybrid" range, where control is shared between charge transfer and diffusion, is also included with a tacit understanding that charge transfer is considered to be dominant. There is good reason, therefore, to distinguish between studies of the relationships between the magnetic field strength and electrode-kinetic parameters (i.e., the exchange current density, i_o, and the transfer coefficient α) and (rather simplistic) analyses of experimental current-voltage curves.

In the latter category, no magnetic field effect at low voltages has been reported in the electrolysis of, for example, cupric sulfate solutions[55] when charge transfer is fully controlling. However, it has also been shown that in a mixed-control regime, the magnetic field results in local maxima for the relative increase in current that are sensitive to the field strength, in

contrast to current observed in the absence of a magnetic field.[56] In the former category, Kelly[57] proposed a modified Butler–Volmer relationship on the basis of experiments with Ti electrodes in sulfuric acid solutions, where the conventional exponential term included a magnetically induced potential difference.

A study involving iron amalgams in acidic and alkaline media[58] indicates a magnetic field effect on the Tafel slope, probably due to a complex interaction of the magnetic field with amalgam formation, diffusion, and hydrogen evolution. Experimental results obtained with cupric sulfate solutions show no magnetic field effect on the transfer coefficient of the cathodic process.[59] The small effect on the exchange current density may most probably be ascribed to a magnetically induced widening of the Tafel region as well as deposit structural effects.

More recent findings by Waskaas[60–62] using iron electrodes in ferric chloride solutions tend to indicate that anode and cathode polarization curves depend on the magnetic field strength, but this effect is not purely kinetic, since it involves bulk-to-diffusion layer transfer of ferric ions.

To counteract the (vexing) convection effects on kinetic experiments, Aogaki and co-workers, having developed a special electrode assembly to separate mass transport and kinetic effects, report[63] a marked decrease in the exchange current density (about 25%) in magnetic fields imposed on a copper deposition cell. Virtually no effect on the transfer coefficient ($\alpha \approx 0.44$) was observed. Experimental results obtained in nickel–phosphorus alloy deposition,[63] cupric ion reduction in ethylenediamine solutions,[64] and the electrolytic reduction of acetophenone[65] are further demonstrations of the interaction of the magnetic fields with polarization characteristics, and point to the difficulty of fully eliminating the effect of convection and/or diffusion on electrode kinetics.

V. THE MAGNETIC FIELD EFFECT ON IONIC MASS TRANSPORT

The quantitatively most tangible effect of magnetic field imposition has been found in the area of ionic mass transport. There is abundant experimental evidence[4,5] in the earlier literature for increasing mass transport rates under the influence of magnetic fields, although opposite observations have also been made under specific conditions.[66] From an empirical

point of view, the effect on mass transport rates is conveniently expressed via the power regression written for the limiting current density as

$$i_L = i_L^0 + mB^p \tag{7}$$

where the zero superscript refers to the absence of a magnetic field, and the numerical value of the p-exponent varies according to the magnetic and electric field configuration. There has been a strong tendency to correlate (for theoretical reasons, but with some statistical bias) current density versus magnetic flux density data with a priori set values of p = 1/3, 1/4, and 1/2, but such regression relationships may be statistically indistinguishable by model discrimination techniques.[67] Recent results on the cathodic reduction of oxygen in metalloporphyrins,[68] the cathodic reduction of acetophenone,[65] and the electropolymerization of aniline [69] are further illustrations of the magnetic enhancement of mass transport.

A useful tool in studying mass transport in magnetic fields has been the electrohydrodynamic impedance technique based on the frequency response of limiting currents observed in the presence of sinusoidally excited magnetic fields.[70] The variation of magnetohydrodynamic (MHD) impedance with frequency is a clearly detectable function of the magnetic flux density at low frequencies. Complex-plane analysis allows the identification of three distinct frequency ranges for the evaluation of the magnetic field effect. Natural convective transport can also be distinguished from the forced flow generated by imposition of a magnetic field. A notable advantage of the impedance technique over rotating disk-based studies lies in the practical possibility of using very small cells without mechanical means of rotation. The technique has also shown promise for the analysis of thermoelectrochemical impedances obtained by frequency response analysis of thermally perturbed electrolytic systems.[71]

Surface wave formation and stationary vortex formation are particularly effective demonstrations of convection enhancement via magnetic fields. A theoretical prediction[72] for aqueous electrolytes was corroborated by experimental evidence[73] produced in a concentric cylindrical cell using copper electrodes and aqueous cupric sulfate electrolytes. Similar observations were reported by Gak and co-workers.[7] Self-sustained oscillations induced by nonhomogeneous periodic and aperiodic magnetic fields have been demonstrated in photographs showing contiguous six- and seven-vortex "cluster" domains in the experimental apparatus.[7,74,75] A laser-based visualization technique[76] was successfully used to detect vortices

carrying a highly dispersed gas–solid suspension generated by magnetically assisted anodic dissolution of copper.

VI. MAGNETIC FIELD EFFECTS IN ENVIRONMENTAL ELECTROCHEMISTRY

1. Areas of Importance

In this context, the basic question is whether magnetic fields can efficiently be employed to strengthen electrochemical means of environmental protection. A recent survey[77] of areas of application suggests that there is much potential for properly exploited magnetic field interaction with various physical parameters of electrolytes. A case in point is water employed in injection oil recovery, where the variation of hardness, dissolved oxygen content, alkalinity, viscosity, pH, and suspended-particle content with magnetic field strength[18] is a key factor in the efficiency of the process. Magnetic filtration and coagulation is the currently most evident field of application, including metal recovery from industrial waste.[78] Water degasification, capillary flow control, filtration, precipitation, and crystallization in magnetic fields are potentially promising applications.

2. Magnetic Field Effects on Corrosion Rates

Yee and Bradford[79] properly state that "it is still uncertain whether enhancement, retardation, or both are the result of magnetic electrochemical interactions," on the basis of pertinent literature. Their own observations of corrosion of steel indicate that the extent of magnetically induced enhancement of corrosion is determined by the electric field strength. Cyclic polarization of steel specimens in aqueous sodium chloride solutions reveals that localized corrosion is not influenced by magnetic fields unless the nonmagnetic corrosion rates themselves are a priori high. As may be expected, the electric–magnetic field configuration, as well as the geometric orientation of the specimens with respect to the fields, plays a significant role in the extent of corrosion. More recent findings by Chiba *et al.*[80] indicate an increase in corrosion inhibition of aluminum in NaCl solutions with an increase in the magnetic field strength, accompanied by a decrease in the corrosion potential. It appears that, under the influence of the magnetic field, the thickness of the inhibitive oxide film increases

at a fixed chloride concentration. A representative list [77] of experimental observations about the accelerating, decelerating, or indifferent effects of the magnetic field provides ample encouragement for thorough systematic studies to be done in the future.

3. Miscellaneous Aspects

Several investigations have been devoted to the influence of magnetic fields on natural bodies of water (e.g., groundwater, spring water, water in capillary flow).[7] An outgrowth of experimental observations is the dynamics of thin water layers, where horizontal bulk motion can be decelerated due to friction at the surface of the thin laminary layer. The imposition of a magnetic field results in various vortex forms shown by visualization experiments, on account of MHD forces.[81]

The role of magnetic fields in various agricultural and geological areas has also been well documented[7]; a short list[77] outlines sources of representative experimental investigations. One particularly interesting set of observations[82] emphasizes the importance of reliable magnetic field measurements in the detection of underground water locations and the movement of large expanses of water.

VII. MICROSCALE BEHAVIOR: APPLICATION OF BOLTZMANN EQUATION-BASED TRANSPORT MODELS

The classical Boltzmann equation

$$\partial f_i/\partial t + \mathbf{c}_i \cdot \mathbf{grad}_r(f_i) + (Q_i/m_i)[\mathbf{E} + \mathbf{c} \times \mathbf{B}]\mathbf{grad}_c(f_i) = (\partial f_i/\partial t)_{\text{coll}} \tag{8}$$

represents electromagnetic interaction under general conditions on a particle i of mass m_i carrying the electric charge Q_i . $\mathbf{r}$ and $\mathbf{c}$ describe the geometric and concentration space, respectively, and f_i is the distribution function of the particle. The right-hand side of Eq. (8) is the collision term. Assuming that the particles undergo only binary collisions, thus allowing application of the Chapman–Enskog approximation,[83] Tronel–Peyroz [84] and Olivier[2] derived the ionic current density distribution in terms of the Γ and Γ' characteristics defined as

$$\Gamma \equiv [\text{erfc}(R) + (4R/\sqrt{\pi})\exp(-R^2) + (1/2 + R^2/3)]^{-1} \tag{9}$$

and

$$\Gamma' \equiv R^4/[3/2 + R^2 + \{3\sqrt{\pi}\ \mathrm{erfc}(R)/4R \exp(-R^2)] + 5/2 \quad (10)$$

where

$$R^2 = W/kT \quad (11)$$

and W is the kinetic energy of ionic species i. For a given ion, Γ and Γ' are strongly temperature dependent [in the case of potassium ions, e.g., $W \cong 29.7$ kJ mol^{-1}; $\Gamma = 5486.2$ at 293.16 K, and 3977.6 at 302.16 K]. At 25°C, the value of Γ varies for common univalent ions between 3000 and 11,000. This approach was employed to estimate concentration and temperature distributions, and induced potential differences in electrolytic cells subjected to electric and magnetic fields.[2] The ratio of computed to experimental variations in pH in the case of aqueous hydrochloric acid is rather large (2 for 0.001 mol dm^{-3} and 3.8 for 0.01 mol dm^{-3}), but is well within one order of magnitude. In the case of aqueous KCl solutions, the ratio of differences in the logarithm of chloride ion concentrations is 1.74 (0.1 mol dm^{-3}) and 1.78 (0.02 mol dm^{-3}).

The estimation of temperature variations depends rather strongly on the temperature dependence of K_w , the dissociation constant of water, and agreement with measured values is not uniform. In the case of HCl solutions, the discrepancy is minimal at concentrations below, for example, 0.02 mol dm^{-3} at $B = 450$ mT, but is not negligible at $B = 640$ mT. In the case of NaOH solutions, the discrepancy is minimal even at 0.025 mol dm^{-3} when $B = 450$ mT. In NaBr solutions, the discrepancy is large even in a 0.005 mol dm^{-3} solution.

Application of the theory to potential differences observed under steady-state conditions, when the direction of the magnetic field is reversed, has quantitatively been more successful. The predicted potential difference is given[2] by

$$\Delta V \approx -2E_x BYe[(\tau a/m)_a + (\tau a/m)_c] \quad (12)$$

where E_x is the electric potential field along the cell, Y is the cell width, e is the charge of an electron (0.16 aC), τ is the characteristic relaxation time for an ion, a is ionic activity, and m is the ionic mass. The subscripts a and c refer to anion and cation, respectively. The ratio of predicted and measured values of ΔV in certain HCl, KCl, and NaCl solutions, ranging between 0.8 and 1.22, provides good support for the approach, which

yields a relatively simple relationship for the estimation of the Hall coefficient (Section I):

$$R_H = [\mu_c^2 \Gamma_c - \mu_a^2 \Gamma_a] / n_0 F (\mu_c + \mu_a)^2 \tag{13}$$

in terms of the ionic (bulk) mobilities μ_a and μ_c, the ionic Γ characteristics, and the bulk electrolyte concentration n_0.

VIII. APPLICATION OF THE MODEL OF SLIGHTLY IONIZED PLASMAS

In this approach, electrolyte solutions are considered as a mixture of fast charge carriers, slow (or normal) charge carriers, and neutral species (e.g., solvent), providing an analogy to slightly ionized plasmas carrying electrons, ions, and neutral atoms with widely different transport properties. The tensorial nature of mobility, hence conductivity, in plasma theory readily translates into this framework, applying Cambel's formulation [85] of constitutive plasma equations to a plasma-oriented continuum model of electrolytes subjected to combined electric and magnetic fields.[86] Using experimentally determined Hall coefficients, the computed charge density of fast carriers in aqueous solutions of cupric sulfate disagrees only by one order of magnitude with predictions of a "competing" MHD model.[87]

The plasma-oriented approach is also useful in estimating the interaction area between fast and slow charge carriers, by an appropriate adaptation of the concept of collision cross sections to electrolytes. As an illustration, the apparent cross-section radius of 181 nm in the case of a 0.005-mol dm^{-3} solution subjected to a 1 mT magnetic field compares favorably with the 134 nm computed from the classical Rosenbluth formula [85] applying to electron–ion collisions.

IX. MACROSCALE BEHAVIOR: APPLICATION OF MHD THEORY

1. Basic Notions

The flow of fluids under the influence of magnetic and electric fields can be readily analyzed via classical MHD theory.[88–91] In its application to aqueous electrolytes, compressibility and viscous effects may usually be neglected in the equation of motion. The magnetic Reynolds number

(Re_m) is essentially of the same order of magnitude as the ratio of the induced magnetic field strength to the imposed magnetic field strength. The equation of motion is augmented by the MHD force density term $\mathbf{j} \times \mathbf{B}$, and Ohm's law by the $\sigma(\mathbf{v} \quad \mathbf{B})$ term, where σ is the bulk electrolyte conductivity. Of particular importance is the vorticity equation

$$D[\omega/\rho]/Dt - [\omega/\rho]\mathbf{grad}(\mathbf{v}) = [1/\rho]\mathbf{curl}(\mathbf{j} \times \mathbf{B}/\rho) \tag{14}$$

which allows a theoretical exploration of the vortex generation or vortex suppression capabilities of imposed magnetic fields. MHD theory has become a widely applied tool of analysis and the interpretation of various magnetoelectrolytic phenomena in the current literature.

2. The Application of MHD Theory to Mass Transport

In applying Eq. (14) to mass transport-controlled electrolytic processes, an important step is the estimation of the effect of the imposed magnetic field strength on properties of the diffusion boundary layer. Since electrolyte density is space-variant in this layer, the right-hand side of Eq. (14) is nonzero, even if the low-Re_m approximation [i.e., $\mathbf{curl}(\mathbf{j} \quad \mathbf{B}) = 0$] is invoked. This is clearly shown by the expanded form

$$\mathbf{curl}(\mathbf{j} \times \mathbf{B}/\rho) = [1/\rho]\mathbf{curl}(\mathbf{j} \times \mathbf{B}) - [1/\rho^2)(\mathbf{j} \times \mathbf{B}) \times \mathbf{grad}(\rho) \tag{15}$$

since $\mathbf{grad}(\rho)$ is nonzero in the diffusion layer. On this basis, the vorticity equation predicts vortex generation in the diffusion layer under appropriate conditions and this finding offers one plausible explanation for the experimentally observed enhancement of cathodic mass transport rates. [92] A somewhat different but equally valid interpretation is a decrease in the mean diffusion-layer thickness due to an increasing presence of the convective component of the convective diffusion process.

The latter interpretation was successfully used to analyze natural convection at vertical plate electrodes by including a magnetic field-related term in the classical convective diffusion equation.[93,94] The beneficial effect of the magnetic field on mass transport may be estimated from the ratio of the limiting current density in a magnetic field to that in its absence, called the *augmentation factor* f_A :

$$f_A = 1.455/[F_1(\beta, \gamma)\mathrm{Sc}^{1/4}]; \mathrm{Sc} >> 1 \tag{16}$$

where Sc is the electrolyte Schmidt number and F_1 is a function of two important parameters in the classical theory[95] of natural convection. The

latter carries a correction for the presence of the magnetic field by the term $\psi(B) = (i_L B/\rho g \alpha)$, where α is the densification coefficient of the electrolyte. Furthermore,

$$\beta = 1.0924[\{0.333 + 0.5\psi(B)\}^3/\mathrm{Sc}]^{1/4} \tag{17}$$

and

$$\gamma = -6[1 + \psi(B)] \tag{18}$$

In a cupric sulfate/sulfuric acid cell with vertical copper electrodes

$$F_1(\beta, \gamma) = 0.0882/\beta^{1/3} - 1.212 \times 10^{-4}[\gamma/\beta^{5/3}] \tag{19}$$

Comparison with experimental values[94] of the limiting current density indicates a maximum of 7% relative error when Eq. (19) is employed for estimation, within an imposed magnetic flux density range of 0.3–1.05 T. Interferograms obtained in a thorough experimental study of electrodeposition offer good qualitative support for the MHD approach, although the temporal development of concentration-gradient patterns is highly complex.[96]

An attempt to solve the somewhat simplified set of MHD model equations directly from the concentration field and current flow[97] met with limited success for certain electrode and field configurations, where the predicted and experimental values of current density agree at best within one order of magnitude. Care must be exercised in assigning the role of the convection propagator, inasmuch as magnetic fields can also induce convection due to the nonuniform magnetic susceptibility of the participating ions,[98] provided that MHD-related mass transport can be suppressed or minimized, as in a recent study by Kim and Fahidy.[96]

MHD-based models have been widely used in various magnetically assisted electrolyte flow investigations.[7,74,75] An application of the pumping effect of combined electric and magnetic fields led to the development of MHD-pump electrode cells,[99] where the concentration distribution, modeled by the classical convective diffusion equation

$$v_x(\partial c/\partial x) + v_y(\partial c/\partial y) = D(\partial^2 c/\partial y^2) \tag{20}$$

in the diffusion layer, was solved by considering the magnetic field effect as an interaction with the bulk electrolyte flow rate. The resulting equation for the limiting current density:

$$i_L = kB^{1/3} - k'B^{-1} \tag{21}$$

reduces to the simpler form $i_L = kB^{1/3}$ if the pressure drop over the flow cell is negligible (k depends on the physical parameters of the cell and the electrolyte). In a viscous flow in a narrow channel,[100] i_L is proportional to $B^{1/2}$; in both pump-cell configurations, agreement between theory and experimental results is excellent.

The prediction of oscillatory flow rates in self-induced MHD-generated oscillations (Section V) is equally possible from basic MHD principles.[74,101] The mean velocity along the circular path located halfway between two concentric cylindrical electrodes may be written as

$$V_m = [I\mathrm{Br}_0]/[16\pi h\eta]f(K) \tag{22}$$

where

$$f(K) = [K^4 - 2\{K\ln(K)\}^2 + 1]/[(K-1)^2(K+1)];\ K = R_o/r_o \tag{23}$$

is the shape factor, I is the current, R_o is the outer cylinder radius, r_o is the inner cylinder radius, h is the cell height, and η is the electrolyte viscosity. Under sinusoidal electric and magnetic fields of $I_o \sin(\omega t)$ and $B_o \sin(\omega t)$, respectively, the expression for the mean velocity becomes

$$V_m = [I\mathrm{Br}_o]/32\pi h\eta]f(K)[1 - \cos(2\omega t)] \tag{24}$$

hence hydrodynamic oscillation occurs at twice the frequency of the field excitation. Equation (24) predicts velocity wave amplitudes between 0.6 and 1.2 cm s^{-1} (0.5 mol dm^{-3} $CuSO_4$; H = 400–800 A m^{-1}; current below 600 mA; K = 6), which fall within the order of magnitude of experimental observations.

3. Magnetoelectrolytic Mass Transport in a Magnetic Field Gradient

MHD theory readily predicts (at least in a qualitative sense) the beneficial effect of *gradient* fields on electrolytic mass transport. Conditions of 3D-*gradient* fields can easily be generated for instance in large-scale electrolytic cells by inclined electrodes[102,103] and a solenoidal-type winding of cables carrying electric current. In Cartesian coordinates, the magnitude of the magnetic flux density at an arbitrary (x, y, z) coordinate position in the cell is given by the modulus equation

$$B = [B_x^2 + B_y^2 + B_z^2]^{1/2} \tag{25}$$

where the subscripted variables denote the flux-density vector components in the indicated spatial directions. In the simplest case where the electric field is uniform and unidimensional in the y-direction, the MHD body force density, $\mathbf{j} \quad \mathbf{B}$, has two nonzero components, $\mathbf{e}_x j_y B_z$ and $-\mathbf{e}_z j_y B_x$, and the forcing function on the right-hand side of Eq. (14) has four nonzero terms with the magnitude

$$|\mathbf{curl}\,(\mathbf{j} \times \mathbf{B})| = j_y[(\partial B_x/\partial y)^2 + \{\partial B_x/\partial x + \partial B_z/\partial z\}^2 + (\partial B_z/\partial y)^2]^{1/2} \tag{26}$$

It follows that strong localized vortex motion may be generated by even slightly nonuniform fields, and the convective component of the convective diffusion equation (Eq. 20) becomes predominant. In fact, a convincing argument may be put forward in favor of replacing Eq. 20 by the general vector equation

$$\mathbf{v}.\mathbf{grad}(c) = D\ \mathbf{div}\ \mathbf{grad}(c) \tag{27}$$

where the velocity vector must be obtained from the general equation of motion

$$\rho D\mathbf{v}/Dt + \mathbf{grad}\,(p) = \mathbf{j} \times \mathbf{B} + \eta\ \mathbf{div}\ \mathbf{grad}(\mathbf{v}) + \rho\mathbf{F} \tag{28}$$

if compressibility is ignored. $\mathbf{F}$ is an external force vector, for example, gravity in the case of natural convection. The solution of Eqs. (27) and (28) is generally impossible since not all auxiliary conditions are known, in addition to the usual mathematical encumbrances associated with 3D differential equations. This reality poses at present the major limitation for extensive MHD-based modeling.

An alternative view, based on the energetic aspects of MHD flows,[88] leads to the same result. The rate of electromagnetic energy input into an electrolyte under an electric field $\mathbf{E}$ is

$$\mathbf{E} \cdot \mathbf{j} = |\mathbf{j}^2|/\sigma - \mathbf{j} \cdot (\mathbf{v} \times \mathbf{B}) \tag{29}$$

where the first term on the right-hand side represents ohmic dissipation (i.e., the joule effect), and the second term, describing electromagnetic energy conversion, indicates that kinetic energy is created, producing convective motion due to the magnetic field.

4. Profitability of Magnetoelectrolytic Processes: The MHD View

In a first approximation, the profitability of an electrolytic process may be estimated by the profit-rate relationship[4]

$$P = [\gamma C_p - (EC_e/\lambda)]I \tag{30}$$

where P is the rate of profit generation, γ is the electrochemical equivalent of the electrode reaction product, C_p is the market value of the product, C_e is the unit cost of electricity, and γ is the specific area (electrode area per unit cell volume). If the magnitude of current I is increased by an imposed magnetic field, then $P_M > P$, if P_M is the rate of profit generation under the influence of a magnetic field, provided that the magnitude of the electric field is *not* increased by the generation of secondary electric fields opposing ionic motion to the electrode. It is hazardous, therefore, to make sweeping statements about the relative technological merits of magnetically assisted electrolysis, all the more so because experimental data collected in large-scale magnetoelectrolytic cells are scarce.

X. FINAL REMARKS

In spite of the continual growth of information on multifaceted phenomena in electrolytic systems under the influence of magnetic fields, the *exact* role of magnetism in modifying microscopic as well as macroscopic behavior is not completely understood. Consequently, there exists at present no overall mathematical framework or model that can explain various magnetic field effects within a single cohesive physical or mathematical paradigm. For this reason alone, further research on magnetic field effects on electrolytes remains a challenging and worthwhile endeavor.

ACKNOWLEDGMENTS

The efforts of the author and his collaborators in this research area have been supported over a span of 30 years mainly by the Natural Sciences and Engineering Research Council of Canada (NSERC). The author takes this opportunity to express his special thanks to this organization.

REFERENCES

[1] M. Faraday, *Diary,* Vol. IV, pp. 288, 7706–21, Bell and Sons, London, 1933.
[2] A. Olivier, Thesis Doctorat d'Etat, Reims, France, 1979.
[3] N. F. Starostenko, *Zhurn. Fiz Khim.* **27** (1053) 95.
[4] T.Z. Fahidy, *J. Appl. Electrochem.* **13** (1983) 553.

5 R. A. Tacken and L. J. J. Janssen, *J. Appl. Electrochem.* **25** (1995) 1.
6 E. Ya. Blum, Y. A. Mikhailov, and R. Ya. Ozols, *Teplo- i Massoobmen v Magnitnom Polye* ("Heat and Mass Transfer in a Magnetic Field"), Zinatne, Riga, Latvia, 1980.
7 N. F. Bondarenko and E. Z. Gak, *Elekromagnitye Yevlenya v Prirodnykh Vodakh* ("Electromagnetic Phenomena in Natural Waters"), Gidrometeizdat, St. Petersburg, 1984.
8 M. Meton and P. Gerard, *Chem. Phys. Lett.* **44** (1976) 582.
9 H. L. Friedmann, *J. Phys. Chem.* **69** (1965) 2617.
10 S. Mohanta and T. Z. Fahidy, *Electrochim. Acta* **19** (1974) 227.
11 S. Mohanta and T. Z. Fahidy, *Electrochim. Acta* **21** (1976) 25.
12 J. B. Hubbard and P. G. Wolynes, *J. Chem. Phys.* **75** (1981) 3051.
13 P. Dumarque, P. Humeau, and F. Penot, *Electrochim. Acta* **18** (1973) 447.
14 J. Lielmezs and G. M. Musbally, *Electrochim. Acta* **17** (1962) 1609.
15 J. Lielmezs and H. Aleman, *Thermochim. Acta* **9** (1974) 247.
16 J. Lielmezs and H. Aleman, *Electrochim. Acta* **21** (1976) 273.
17 J. Lielmezs, H. Aleman, and J. M. Musbally, *Z. Phys. Chem.* **90** (1974) 8.
18 A. N. Kutzenko, *Neftepromysl. Delo* **8** (1974) 43.
19 J. Lielmezs and H. Aleman, *Thermochim. Acta* **18** (1977) 315.
20 J. Lielmezs and H. Aleman, *Thermochim. Acta* **20** (1977) 219.
21 J. Lielmezs and H. Aleman, *Thermochim. Acta* **21** (1977) 233.
22 J. Lielmezs and H. Aleman, *Thermochim. Acta* **21** (1977) 225.
23 E. Z. Gak and G. P. Komarov, *Soviet Physics-Technical Physics* **16** (1972) 1578.
24 T. A. Litovitz and C. M. Davis, in *Physical Acoustics,* Vol. 2, Part A, W. P. Parsons, ed., Academic Press, New York, 1965.
25 R. L. Carlin, *Magnetochemistry,* Springer-Verlag, New York, 1986, Chapter 3.
26 M. Yamagouchi, H. Nomura, T. Ohta, and T. Goto, *Phys. Lett. A* **126** (1987) 133.
27 M. Yamagouchi, I. Yamamoto, T. Goto, and S. Miura, *Phys. Lett. A* **134** (1989) 504.
28 I. Yamamoto, M. Yamagouchi, M. Fujino, T. Goto, and S. Miura, *Physica B* **216** (1996) 399.
29 G. W. C. Kaye and T. H. Laby, *Tables of Physical and Chemical Constants,* Longmans, London, 13th ed., 1966, p. 107.
30 L. Pauling, *General Chemistry,* Dover, New York, 1970, Table XIV- 1, p. 933.
31 L. I. Matskevich and A. A. Rumyantsev, *Izvest. Ser. Estestv. Nauk* **7** (1979) 31.
32 K. J. Hansen, *Z. Naturforsch. A* **9**(11) (1954) 919.
33 S. Mohanta and T. Z. Fahidy, *Can. J. Chem. Eng.* **50** (1972) 248.
34 G. Dash and W. W. King, *J. Electrochem. Soc.* **119** (1972) 51.
35 R. M. Bozorth, *Phys. Rev.* **26** (1925) 390.
36 I. Ohno, *Electrodep. Surf. Treat.* **3** (1975) 213.
37 P. Fricoteaux, A. Olivier, and R. Delmas, *J. Electrochem. Soc.* **139** (1992) 1096.
38 M. I. Ismail and T. Z. Fahidy, *Metall(Berlin)* **39** (1984) 118.
39 R. N. O'Brien and K. S. V. Santhanam, *Can. J. Chem.* **65** (1987) 2009.
40 R. N. O'Brien and K. S. V. Santhanam, *J. Appl. Electrochem.* **20** (1990) 781.
41 A. Chiba, K. Kitamura, and T. Ogawa, *Surf. Coat. Tech.* **27** (1986) 83.
42 A. Chiba, T. Niimi, H. Kitayama, and T. Ogawa, *Surf. Coat. Tech.* **29** (1986) 347.
43 L. Yang, *J. Electrochem. Soc.* **101** (1954) 456.
44 M. I. Ismail and T. Z. Fahidy, *Metall(Berlin)* **34** (1980) 729.
45 I. Mogi, *Physica B* **216** (1996) 396.
46 I. Mogi and M. Kamiko, *Dengi Kagaku* **64** (1996) 842.
47 I. Mogi and M. Kamiko, *Bull. Chem. Soc. Japan* **69** (1996) 1889.
48 I. Mogi, S. Okubo, and Y. Nakagawa, *J. Phys. Soc. Japan* **60** (1991) 3200.
49 J. L. Hudson and T. T. Tzotsis, *Chem. Eng. Sci.* **49** (1994) 1493.
50 T. Z. Fahidy and Z. H. Gu, in *Modern Aspects of Electrochemistry,* No. 27, R. E. White, J. O'M. Bockris, and B. E. Conway, eds., Plenum, New York, 1995, p. 383.

[51] Z. H. Gu, J. Chen, A. Olivier, and T. Z. Fahidy, *J. Electrochem. Soc.* **140** (1993) 408.
[52] Z. H. Gu, A. Olivier, and T. Z. Fahidy, *Electrochim. Acta* **35** (1990) 933.
[53] Z. H. Gu, J. Chen, and T. Z. Fahidy, *Electrochim. Acta* **38** (1993) 2631.
[54] Z. H. Gu, J. Chen, and T. Z. Fahidy, *Electrochim. Acta* **37** (1992) 2637.
[55] E. Z. Gak, E. Y. Rokhinson, and N. F. Bondarenko, *Elektronnaya Obrab. Mater.* **76** (1974) 62.
[56] E. Z. Gak, E. Y. Rokhinson, and N. F. Bondarenko, *Elektrokhimiya* **11** (1975) 528.
[57] J. K. Kelly, *J. Electrochem. Soc.* **124** (1977) 987.
[58] L. N. Sviridova and V. N. Korshunov, *Elektrokhimiya* **14** (1978) 99.
[59] P. Fricoteaux, *Electrodeposition Du Cuivre Sous Champs Magnétique (Rapport du Stage),* Université de Paris VI, France, 1987–88.
[60] M. Waskaas, *Acta Chem. Scand.* **50** (1996) 516.
[61] M. Waskaas, *Acta Chem. Scand.* **50** (1996) 521.
[62] M. Waskaas, *Acta Chem. Scand.* **50** (1996) 525.
[63] H. Zang and G. Zhang, *Cailiao Baoku* **24** (1991) 17.
[64] K. Leinertas, *Chemija* **3** (1991) 77.
[65] S. R. Ragsdale, J. Lee, X. Gao, and H. S. White, *J. Phys. Chem.* **100** (1996) 5913.
[66] T. Z. Fahidy and T. S. Rutherford, *J. Appl. Electrochem.* **10** (1980) 481.
[67] T. Z. Fahidy, *Electrochim. Acta* **35** (1990) 929.
[68] O. Ikeda and C. Iwakura, *Chem. Express* **6** (1991) 455.
[69] L. Cai, S. Yao, and S. Zhou, *Dianhuaxue* **1** (1995) 159.
[70] O. Aaboubi, J. P. Chopart, J. Douglade, A. Olivier, C. Gabrielli, and B. Tribollet, *J. Electrochem. Soc.* **137** (1990) 1796.
[71] A. Olivier, E. Merienne, J. P. Chopart, and O. Aaboubi, *Electrochim. Acta* **37** (1992) 1945.
[72] T. Z. Fahidy, *Electrochim. Acta* **21** (1976) 21.
[73] S. Mohanta and T. Z. Fahidy, *J. Appl. Electrochem.* **6** (1976) 211.
[74] E. Z. Gak, *Inzh.-Fiz. Zhurn.* **43** (1982) 140.
[75] N. F. Bondarenko and M. E. Gak, *Fiz. Atmosfyeri i Okeana* **20** (1984) 640.
[76] Z. H. Gu and T. Z. Fahidy, *Int. J. Eng. Fluid Mech.* **1** (1988) 1.
[77] T. Z. Fahidy, in *Environmental Oriented Electrochemistry, Studies in Environmental Science 59,* C. A. C. Sequeira, ed., Elsevier, Amsterdam, 1994, p. 601.
[78] C. S. Brooks, *Metal Recovery from Industrial Wastes,* Lewis Publishers, Chelsea, MI, 1991.
[79] S.-S. W. Yee and S. A. Bradford, in *Corrosion of Electronic and Magnetic Materials,* ASTM STP 1148, P. J. Peterson, ed., American Society for Testing and Materials, Philadelphia, PA, 1992, p. 10.
[80] A. Chiba, K. Kawazu, O. Nakono, T. Tamura, S. Yoshihara, and E. Sato, *Corr. Sci.* **36** (1994) 539.
[81] N. F. Bondarenko, *Fizika Dvizheniya Podzennikh Vod* ("Physics of Groundwater Motion"), Gidrometeoizdat, St. Petersburg, Russia, 1973.
[82] R. W. Haupt, J. R. Martin, and J. R. Greenfeld, *Trans. Am. Geophys. Union* **62** (1981) 1053.
[83] S. Chapman and T. G. Cowling, *The Mathematical Theory of Nonuniform Gases,* Cambridge Univ. Press, Cambridge, UK, 1939.
[84] E. Tronel-Peyroz, Thesis Doctorat d'Etat, Reims, France, 1978.
[85] A. B. Cambel, *Plasma Physics and Magnetofluid Mechanics,* McGraw-Hill, New York, 1963.
[86] T. Z. Fahidy, *Electrochim. Acta* **23** (1978) 549.
[87] R. Sundermann and T. Z. Fahidy, *J. Appl. Electrochem.* **6** (1976) 89.
[88] J. A. Shercliff, *A Textbook of Magnetohydrodynamics,* Pergamon Press, Oxford, 1965.
[89] V. C. A. Ferraro and C. Plumpton, *An Introduction to Magneto-Fluid Mechanics,* Oxford Univ. Press, Oxford, 1966.

[90]P. C. Kendall and C. Plumpton, *Magnetohydrodynamics with Hydrodynamics,* Pergamon Press, Oxford, 1964.
[91]A. Jeffrey, *Magnetohydrodynamics,* Academic Press, New York, 1966.
[92]T. Z. Fahidy, *Electrochim. Acta* **18** (1973) 607.
[93]T. Z. Fahidy, *Chem. Eng. J.* **7** (1974) 21.
[94]T. Z. Fahidy, *Chem. Eng. J.* **17** (1979) 245.
[95]V. G. Levich, *Physicochemical Hydrodynamics,* Prentice-Hall, Englewood Cliffs, NJ, 1962, p. 127.
[96]R. N. O'Brien and K. S. V. Santanam, *J. Electrochem. Soc.* **129** (1982) 1266.
[97]K. Kim and T. Z. Fahidy, *J. Electrochem. Soc.* **142** (1995) 4196.
[98]R. N. O'Brien and K. S. V. Santanam, *J. Appl. Electrochem.* **27** (1997) 573.
[99]R. Aogaki, K. Fueki, and T. Mukaibo, *Denki Kagaku,* **43** (1975) 509.
[100]R. Aogaki, K. Fueki, and T. Mukaibo, *Denki Kagaku* **44** (1976) 89.
[101]E. Z. Gak, *Elektrokhimiya* **12** (1976) 664.
[102]M. I. Ismail and T. Z. Fahidy, *Can. J. Chem. Eng.* **57** (1979) 734.
[103]M. I. Ismail and T. Z. Fahidy, *Can. J. Chem. Eng.* **58** (1980) 505.

6

Analysis of Mass Transfer and Fluid Flow for Electrochemical Processes

J. Deliang Yang,* Vijay Modi,† and Alan C. West*

* *Department of Chemical Engineering and Applied Chemistry Columbia University, New York, NY 10027*

† *Department of Mechanical Engineering, Columbia University, New York, NY 10027*

I. INTRODUCTION

Current-distribution simulations are valuable for the design and analysis of electrochemical processes.[1,2] For example, such simulations are ubiquitous in the battery and fuel-cell literature.[2,3] They are used for electrochemical metallization processes not only in reactor design but also in wafer design.[4–6] A great deal of effort has also been put into the development of analog solvers for cathodic protection systems.[7]

Figure 1 shows a schematic diagram of the information required as input into a current-distribution solver for metallization processes. The input labeled "homogeneous chemistry" refers to chemical interactions,

Modern Aspects of Electrochemistry, Number 32, edited by B. E. Conway *et al.* Kluwer Academic / Plenum Publishers, New York, 1999.

such as the formation of complexed forms of cupric ions in electroless deposition baths,[8] throughout the electrolyte. It is commonly assumed that such reactions are equilibrated (Ref. 1, Chapter 19). The input labeled "physical properties" refers to diffusion coefficients, electrolyte conductivity, etc. "Electrode kinetics" refers to governing laws and rate constants for the correlation of rates of interfacial reactions with variables such as electrode potential or surface composition.

Various approximations for the fluid flow can be made. Commonly, the flow is simply considered to be sufficient to render concentration variations insignificant. It is assumed in Fig. 1 that the initial substrate is a perfect conductor, so that the "terminal effect"[9,10] does not need to be considered. It is also assumed that the entire process is isothermal. Depending on the complexity of the model, the amount of information required can vary greatly. For example, for a primary or secondary current distribution, where variations in concentration are ignored, the flow need

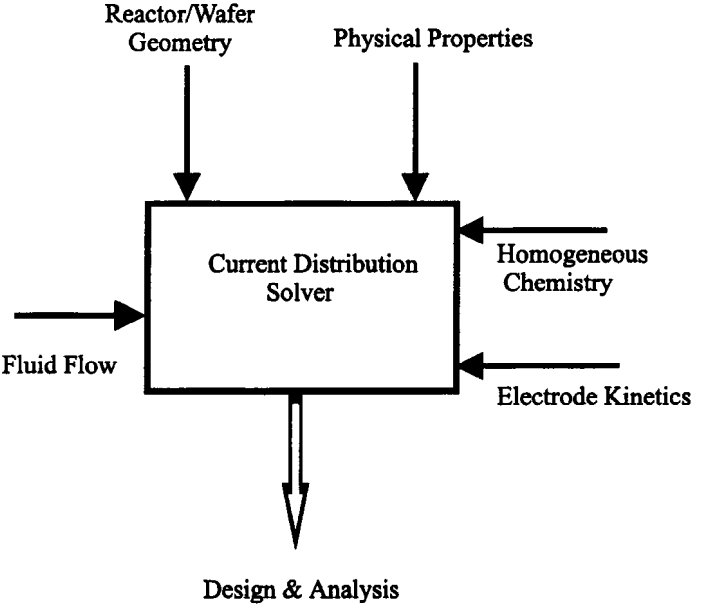

Figure 1. Schematic diagram illustrating the input or assumptions required for the development of a current-distribution solver for metallization processes. It is assumed that the substrate is a perfect conductor.

not be described. For more general models, the major uncertainties in the input to the solver arise from descriptions of the fluid flow and the electrode kinetics, especially when polarization measurements cannot be well described in terms of a Butler–Volmer-type relationship. Assuming that the fluid flow is laminar and that the flow and electrode kinetics are well characterized, it should be feasible to develop an effective current-distribution solver.

In the 1980s, a large number of laboratories developed Laplace equation solvers for use in current-distribution simulations.[5,11] These procedures are normally based on boundary-element methods (BEM), finite-difference methods (FDM), or finite-element methods (FEM). For Laplace's equation, it is not clear that any particular method has an overwhelming advantage over the others. It is, however, clear that a large number of current distributions cannot be described by Laplace's equation.

As Newman[1,12] outlines, current distribution is governed by Laplace's equation when it can be described by an electrical potential in the absence of concentration variations or by diffusion of a single species in the absence of convection and electrical migration. For certain restrictive conditions, current-distribution problems involving both diffusion and electrical migration in the absence of convection are governed by Laplace's equation if the quasi-potential is introduced.[13–15] Except when solid or extremely viscous electrolytes are used, it is difficult to achieve a stagnant electrolyte situation because of natural convection. Nevertheless, for some geometries and for simple, boundary-layer flows, a stagnant diffusion-layer approximation may be adequate.

In the majority of the Laplace equation solutions, the electrical potential, subject to appropriate boundary conditions, is determined. These primary or secondary current-distribution problems may appear to be particularly relevant for electrodeposition, where useful deposit properties are obtained at small fractions of the limiting current. However, the fact that industry has paid considerable attention to fluid flow in reactor design suggests that flow effects can be important, even at a relatively small fraction of the limiting current density.[16–19]

For example, practical electrodeposition processes use additives that are present in very small concentrations to control deposit microstructure. Consumption of the additives at an electrode surface is likely to lead to concentration variations that may affect current distribution. Even in an

additive-free bath, alloy deposition may involve significant concentration variations for the dilute reactants.[20–22] In addition, the occurrence of side reactions, which may be mass-transfer controlled, can influence the distribution of deposition rate through ohmic potential drop or by changing, for example, the solution's pH.[20–25] Such phenomena may be difficult to incorporate rigorously into a current-distribution solver based on Laplace's equation.

The approach developed by Newman for the treatment of both mass-transfer and electric-field effects in boundary-layer flows has had considerable success.[1,26] However, many flows of practical interest have separation and recirculation regions, features not amenable to a boundary-layer analysis. Fortunately, there has been significant progress in the heat-transfer and other communities in computational fluid dynamics (CFD), providing numerical methods applicable to problems important to electrochemistry. The pioneers in using CFD for electrochemical applications are Alkire and co-workers, who have been largely interested in flow effects in localized corrosion. The literature is briefly reviewed in the next section.

Along with continued progress in CFD, computational power continues to decrease in cost. CFD will thus become increasingly common for the design and analysis of electrochemical-metallization processes, especially for high-end applications, where feature dimensions are small, requiring precise control of growth processes. This chapter highlights some of the issues involved in choosing numerical approaches for mass-transfer and fluid-flow calculations. For example, a research group must decide between a commercial or an in-house CFD code. We also discuss problems not frequently encountered in the mainstream CFD literature, but common to researchers in the field of electrochemical metallization.

Finally, we would like to emphasize the importance of experimental verification of numerical simulations. Verification of CFD results is particularly important. A discussion of a variety of experimental methods for studying fluid flow can be found in Goldstein.[27] Of particular interest for electrochemical applications is the work of Hanratty and co-workers, who have extensively used redox couples at limiting-current densities to characterize shear at solid walls. Much of this work has been reviewed recently.[28,29]

II. LITERATURE REVIEW

The CFD and mass-transfer literature is vast. In this survey, we only highlight papers related to applications in electrochemistry. This review is by no means exhaustive; some important papers are undoubtedly omitted. In order to answer questions concerning flow relevant to a specific geometry, consideration of the entire literature may be fruitful. We have found the heat-transfer literature to be of particular relevance, although Schmidt and Prandtl numbers in an aqueous phase normally differ significantly.[30] Furthermore, flows may be quite geometry dependent, and extracting quantitative information from a similar but not identical situation may be problematic.

When the governing model is given by the convection-diffusion equation (no electrical migration effects are considered), well-established numerical methods can be used directly in electrochemical cell design. When using commercial software, it should be remembered that the code has probably been benchmarked for applications different from those found in metallization, where spatial distributions of flux at high Schmidt numbers may be of more interest than the spatial average flux. Freitas[31] has recently provided a comparison of several commercial CFD codes. Many of these codes are based on a finite-volume method (FVM) or a finite-element method. West *et al.*[32,33] have discussed the application of FVM to electrochemical systems. A similar treatment is provided below.

With a few exceptions, the fluid flow must be simulated before the mass-transfer simulations can be rigorously performed. Nevertheless, here are several important situations, such as that at a rotating disk electrode, where the fluid flow is known analytically or from an exact, numerical solution. Thus there exists a body of work that was done before CFD was a readily available tool (for example, see Refs. 34–37). In many of these studies, a boundary-layer analysis, based on a Lighthill transformation (Ref. 1, Chapter 17), is employed.

There have been fewer studies in electrochemistry where the flow is known but the boundary-layer approach is inapplicable. One example has been recently analyzed and compared with experiment. In this case, mass transfer to a line electrode[38] or an array of line electrodes[39] in the presence of an oscillatory shear flow was treated. A finite-volume approach was used for the numerical analysis and a ferri/ferrocyanide redox couple was used to measure the mass-transfer rate. The studies show that boundary-

layer analysis is useful for shear flows that switch direction, but only if the frequency is sufficiently low.

The resolution of concentration fields in geometries relevant to industry normally requires numerical computation of the fluid flow. For example, mass transfer in the wake region behind a bluff body has been studied extensively.[38,40–43] Such flows may be of interest, for example, for the Romankiw paddle cell.[16–19] Numerical simulations, confirmed with experimental observations, indicate that the presence of a bluff body promotes eddies that increase the mass-transfer rate to a downstream wall. Recently, Yang *et al.*[44] investigated the mass-transfer phenomena downstream of a circular cylinder in a confined channel. The fluid velocity fields were computed using an FEM with unstructured grids, and the concentration field was computed using an FVM with an orthogonal mesh independent of that used for the fluid flow calculation. The fluid velocity was interpolated linearly from that calculated by the FEM.

Convective mass transport from small cavities is relevant to through-mask electrodeposition and to localized corrosion and has hence received much attention. In localized corrosion, mass transport is important for determination of the local environment inside an active pit. For through-mask deposition, an understanding of mass transport may be important for design of mixing methods or for analysis of measured deposit profiles. The electrodeposition in circular or rectangular cavities formed by a photoresist has been studied by Kondo *et al.*[45]; it was found that the shapes of deposited bumps can be explained by calculations of vortex evolution and penetration flow.

Studies on the effect of hydrodynamics on localized corrosion and electrochemical etching processes have been reviewed by West *et al.*[46] Much of the work has been performed by Alkire and co-workers.[47–52] They have used FIDAP,[53] a commercial FEM code, to investigate the influence of fluid flow on geometries relevant to etching and to pitting corrosion. In most cases, Stokes' flow was considered. The Stokes' flow approximation is frequently valid inside the cavity because its characteristic dimension is small. However, the flow outside the cavity may not be in the Stokes flow regime. Since it is the external fluid motion that induces flow inside the cavity, under many (especially unsteady) situations, the use of the Stokes flow approximation may be problematic. Some of the work of Alkire and co-workers has been extended by Shin and Economou,[54,55] who simulated the shape evolution of corrosion pits. Natural convection was also considered in their study.

Many other studies related to transport to and from cavities can be found in the heat-transfer literature. Fully developed shear flow in a channel passing over the top of a cavity has been studied by O'Hern *et al.*[56] and Chen.[57] A similar study was performed by Chang *et al.*[58] for aspect ratios greater than 1. Multiple recirculation eddies were found; the characteristic velocity of each eddy was found to decrease as the bottom of the cavity was approached. Ghaddar *et al.*[59,60] investigated the flow pattern inside a cavity when the channel flow was destabilized by upstream cavities. It was found that the resulting unsteady flow enhanced the heat-transfer rate to the bottom surfaces of downstream cavities.

Jordan and Tobias[61] used CFD in a study of flow effects in a trench with a triangular cross section. Such a geometry simulates a scratch and is used to study leveling agents. Chen *et al.*[62] extended this work by coupling shape-change calculations with CFD. Here, the influence of leveling agents on electrodeposition into hemicylindrical cavities in the presence of a shear flow was calculated. The stream function–vorticity form of the Navier–Stokes equations was simulated. Structured, orthogonal grids generated with GridPro[63] were used. Numerical results were compared with more approximate simulations based on stagnant-diffusion layer models. Prudence was required in the development of the shape-change algorithm.

Additional applications of CFD to electrochemical systems can be found in the work of Moreno *et al.*,[64] who used FIDAP to study mass transfer of an impinging jet confined between parallel plates. Lee *et al.*[65] used a different commercial CFD software, microCOMPACT,[66] to aid the design of fountain-plating cells. Applications to bump plating were emphasized. Hourng and Chang[67] numerically calculated the fluid flow and the potential field of a typical electrochemical drilling process. They used a Poisson equation to transform the irregular physical domain to a rectangular computational domain.

As discussed in the introduction, many current-distribution problems are not described by a simple, convection-diffusion equation or by Laplace's equations. Alavyoon *et al.*[68] provided an example in which the coupled concentration and potential fields were solved throughout the entire computational domain, along with natural convection flow fields. The equations were solved by evaluating the nonlinear terms at the previous time step. Gu *et al.*[69] provided an additional study that coupled charge and mass transfer to natural convection. This work is related to

lead-acid batteries and used three benchmark cases for validation of the code.

Harb and Alkire[51] have modified FIDAP to solve for a tertiary current distribution in a pit. However, few details of the numerical procedure were given. Sani used a Galerkin FEM with a front-tracking, adaptive mesh technique to create a model for certain problems in electrochemical plating and free-surface fluid mechanics.[70] The model includes the effect of convection, diffusion, and migration. Yang and West[71] numerically and experimentally characterized the current distribution on a line electrode with varying concentrations of supporting electrolyte. Since the electroneutrality tightly coupled the electrical potential and the concentration fields, the discretized sets of algebraic equations at each node point were solved simultaneously.

The simulation of convective effects on current distributions in the presence of turbulent fluid flow has not been treated extensively, even though turbulence is common in many practical applications. Wang *et al.*[72] provided a literature review of some of the previous work. They also presented simulation results for a two-equation kinetic energy-dissipation turbulence model.[73,74] The model equations were solved numerically using the SIMPLE[75] algorithm.

III. COMPUTATIONAL FLUID DYNAMICS

We limit our discussion here to laminar flows governed by the steady or unsteady, incompressible Navier–Stokes equations. In addition, we restrict ourselves to flows where the solution to the energy or the concentration equation does not influence the flow field, a circumstance not uncommon to isothermal constant viscosity liquid flows of relevance for many electrochemical systems. The incompressible, constant-property, Navier–Stokes equations are given below, with summation over repeated indices:

$$\frac{\partial u_i}{\partial x_i} = 0 \tag{1}$$

$$\frac{\partial u_i}{\partial t} + u_j \frac{\partial u_i}{\partial x_j} = \frac{\partial}{\partial x_j}\left[\nu\left(\frac{\partial u_i}{\partial x_j} + \frac{\partial u_j}{\partial x_i}\right)\right] - \frac{1}{\rho}\frac{\partial p}{\partial x_i} \tag{2}$$

While these equations continue to hold for incompressible turbulent flows, the range of length scales (i.e., length scales of the smallest eddies to those of the physical dimensions of domains) encountered in a turbulent flow requires a prohibitively large number of grid points.[76] Moreover, a three-dimensional, time-accurate calculation with time steps small enough to resolve the smallest scale motion is needed, even though the flow may be steady and two-dimensional in a time-averaged sense. Incidentally, an approach of this type to resolve turbulent flow is called *direct numerical simulation* (DNS). Currently, DNS remains solely a research tool, owing to the prohibitive computational costs associated with simulating even the simplest geometries at relatively low turbulent Reynolds numbers. The primary means for solving turbulent flows at present is through their time-averaged form, known as the Reynolds-averaged Navier–Stokes (RANS) equations. The averaging process leads to new terms that are interpreted as "apparent" stress gradients and are usually expressed in terms of mean variables through turbulence models.

Having decided to limit ourselves to laminar flow, we have a word of caution. Unless one has existing knowledge from theory, experiment, or otherwise, there is no easy way to ascertain that a given flow (determined by the geometry and the boundary and initial conditions) will indeed be laminar, or steady, or two-dimensional. Usually for a given domain, as the characteristic flow speed is increased, there may exist one or more critical Reynolds numbers at which a steady laminar flow may become unsteady periodic, an unsteady periodic flow may become turbulent, and/or 3D structures may appear in an otherwise nominally 2D domain. Such critical Reynolds numbers vary greatly with geometry. Hence, DNS may be the only tool for determining the range of applicability of a laminar flow calculation in the absence of experimental data.

1. CFD Algorithms

Equations (1) and (2) are said to be in primitive (u_x, u_y, u_z, p) variable form. While there are other forms that rely on derived variables, such as stream function vorticity, vorticity–velocity potential, and dual-potential methods, we restrict ourselves to the primitive variable form because of their popularity and ease of interpretation. For a discussion of these methods, as well as for further details of most aspects of CFD discussed here, see Refs. 73, 74, and 77.

The governing equations (1) and (2) are of a mixed parabolic-elliptic nature. A key feature of incompressible flow is that that the time derivative of pressure vanishes from the equations. Hence the equations do not transmit any pressure history directly, and it is as if a new pressure field is established at each step. This situation does not arise for compressible flow where, owing to the presence of the time derivative of the pressure term in the continuity equation, one can solve the coupled hyperbolic system by advancing in time. In the absence of such a term, the algebraic system of equations becomes singular. This is also why attempts to solve the incompressible flow problem as a low Mach-number, compressible-flow problem lead to ill-conditioned algebraic systems with poor algorithmic efficiency and accuracy. For a detailed discussion of these issues, see Ref. 74, p. 642.

The above problems are essentially numerical in nature since no observable changes occur in the flow physics as the Mach number is reduced from, say, 0.3 to 0.01, while holding all other parameters the same. In fact, one of the solution techniques for incompressible flow relies on adding an artificial time term that vanishes at convergence to a steady state, allowing steady-state solutions to be obtained efficiently. A similar approach can also be used to obtain time-accurate solutions by ensuring that the artificial time term vanishes upon convergence at each physical time step. The coefficient of the artificial time term is chosen to eliminate the ill-conditioning of the algebraic system. Methods that rely on such an approach treat all dependent variables as simultaneous unknowns and the coupled hyperbolic system is solved by advancing in time. These methods are called *artificial compressibility methods.* The steady-state version of the method was proposed by Chorin.[78] Since then, successful time-accurate solutions have been obtained by Merkle and Athavale[79] and Chen and Pletcher,[80] among others; see Ref. 74, p. 664.

The second class of methods, which seem to be more popular among the commercial CFD codes, relies on the pressure-correction approach. Here, the velocity components are solved in an uncoupled manner without using the continuity equation as a constraint. An equation for pressure or a change in pressure (hence the term "pressure correction") is derived that will alter the velocity field so as to better satisfy the continuity equation. The precise formulation and the iterative procedures may differ as long as iterative application of the momentum and the pressure-correction equations produces a solution that satisfies both the momentum and the continuity equations. Algorithms that differ in this fashion are employed

in the marker-and-cell (MAC) method of Harlow and Welch,[81] the SIMPLE or SIMPLER methods of Patankary,[75] and the PISO method of Issa.[82]

Despite many advances in algorithms and techniques aimed at accurate solution, convergence acceleration, reduction in storage requirements, and more recently, parallelization, there still remains considerable uncertainty about the precise numerical accuracy of an approach and about its applicability to a wide range of physical problems. For the case of laminar flow, where there are no uncertainties that are due to the choice of a turbulence model, the most significant source of uncertainty (and debate) arises out of the choice of spatial discretization for the convective term in the momentum equation. The two most popular choices are either upwind differencing (along with other versions that revert to upwind at high grid Reynolds numbers) or central differencing. While the former is nominally (for uniform grids) only a first-order scheme, it is not obvious that the latter scheme, which is nominally second order, is necessarily better. This is because of the need to add and manually adjust parameters that control artificial dissipation in central difference schemes in order to damp spurious oscillations. There are a variety of such means to add artificial dissipation.

The use of a particular differencing scheme is, however, intimately tied in with the grid that is used, for two reasons. The first is that the actual physical and mathematical properties of the equations of motion (or, for that matter, scalar transport) suggest that upwinding is indeed the appropriate approach as grid Reynolds (or Peclet) numbers (Re_{grid}) become much greater than 2 (say, 10). For values of Re_{grid} less than 2, central differencing is not only appropriate but is also stable (i.e., does not lead to spurious oscillations). Note that the computational demands of using sufficiently refined grids, so as to ensure that Re_{grid} is everywhere less than 2, are often severe enough to preclude the use of central differencing.

The second reason is that most theoretical arguments for use of either central or upwind schemes rely on one-dimensional considerations, where by default the grid is aligned with the flow. This is not the case in two or three dimensions where, except for boundary-layer-type flows, it is difficult to ensure that the grid is everywhere aligned with the flow. De Vahl Davis and Mallison (Ref. 83, p. 108) have shown that when the flow is oblique to grid lines, upwind schemes are dissipative and this "false diffusion" can be minimized either by grid refinement or by realigning the grid lines with the flow. A current assessment of artificial dissipation models for central differencing is given by Lin and Sotiropoulos.[84]

Given the inconclusive nature of this debate, our recommendation is that regardless of what scheme is utilized, studies that progressively refine the grid until the computed results are grid independent are a necessary but not sufficient ingredient of any CFD analysis. Moreover, as far as possible, an attempt should be made to ensure that grid lines are aligned with the flow.

A variety of explicit (Dufort–Frankel, Lax–Wendroff, Runge–Kutta) and implicit (approximate factorization, LU–SGS) or hybrid schemes have been employed for integration in time. Because of the complexity of the incompressible Navier–Stokes equations, stability analyses to determine critical time steps are difficult. As a general rule, the allowable time step for an explicit method is proportional to the ratio of the smallest grid size to the largest convective velocity (or the wave propagation speed for an artificial compressibility method).

As viscous regions become thinner or physical features of the problem become smaller, demanding finer grids, or as convective velocities become large, implicit methods become particularly attractive because of their lack of a severe time-step constraint. However, even for an implicit method, in practice, the time step cannot be made arbitrarily larger, and a larger time step is frequently attained at significant additional computational costs. For engineers, who are likely to use existing research or commercial codes, a heuristic choice that is usually made is to set the implicit time step to a small multiple of the explicit time step. Frequently, time steps are continuously increased until further increases lead to a nonconvergent solution.

2. Grid Generation

The choice of an appropriate grid becomes a critical issue for a variety of reasons. There are two somewhat separate issues involved. One is the overall layout. If the geometry is regular (e.g., rectangular), then the choice of grid lines that follow coordinate lines is straightforward, producing what is called a *structured, orthogonal grid.* It is structured because the number of grid points per grid line is constant, making it easy to identify the neighboring grid points immediately and easy to address the grid points in a computer program. It is orthogonal because grid lines intersect each other at right angles, so that all surface (e.g., surfaces of control volumes produced by the grid points) vectors have only one non-zero

component. This feature makes it much easier to evaluate fluxes across each face.

However, the need to obtain numerical solutions most often arises in studies of complex geometries. Hence the ability to model complex geometries is one of the key aspects of CFD. Consequently, orthogonality is sacrificed. In fact, most finite-volume-based commercial codes use boundary-fitted, nonorthogonal, structured grids. The advantage of such grids is that they can be adapted to any geometry, and since grid lines follow boundaries, boundary conditions are easily implemented. While a structured grid is desirable, as discussed earlier, it does limit geometric flexibility, sometimes producing grids with severe nonorthogonality. While nonorthogonality is essential for describing complex geometries, it almost always leads to loss of accuracy. This difficulty has largely been alleviated by the development of algorithms that allow block-structured grids, where the domain is subdivided into blocks (the block-connectivity information must now be stored), with the grid being structured and nearer to orthogonality within each block. Most FEM commercial codes use unstructured grids, sacrificing simplicity of data structure for virtually unlimited control of element shape.

Once the type of grid is selected, the second important issue is the number of grid points that must be used in each direction and in each block, for block-structured grids. As discussed earlier, accuracy as well as stability are intimately dependent upon the grid size. The need for refined grids arising from these requirements must be balanced by the increased computational costs that are, at least, proportional to the number of grid points. Also, the allowable time step, and hence computational time, depends on the ratio of grid size to convective velocity.

Most users of CFD are likely to use either a built-in grid generation module within their CFD code or a separate grid-generation software package. In the latter case, a file that contains the coordinates of all grid point locations is produced. If the grid is block structured or unstructured, connectivity information for blocks or elements, respectively, is also included. Grid generation for CFD is a field by itself with entire books (e.g., Ref. 85) written on the subject. A more accessible review is also provided by some of the recent books on CFD.[73,74] An overview of structured grid generation is provided by Eiseman.[86]

It is not possible here to review the variety of existing techniques for grid generation. Instead, some rules of thumb governing the choice of grids are discussed. Perhaps the single most important consideration in

modeling fluid flow is the existence of boundary layers. For example, for a flow over a stationary flat plate, the streamwise velocity is nearly uniform, except in the vicinity of the wall, where the velocity must rapidly reduce to its no-slip value. The thickness of this boundary layer depends upon the flow velocity and the distance from the leading edge. The dramatic variation in velocity occurs in the direction normal to the wall, whereas the changes in the direction along the wall are more gradual. One way to handle such a case is to stretch the grid in the normal direction with a stretching factor, of, say, 1.1. This means that the size of each consecutive grid in the normal direction is 1.1 times the previous one. One of the many heuristic criteria that describe grid quality is that stretching factors should not exceed 1.15. Note that if a stretching factor of 1.15 is applied to 100 consecutive gird lines, the largest grid is more than a million times larger than the smallest one.

It may also be necessary to cluster grids in flow regions, where one may anticipate separation (e.g., downstream of bluff bodies) or recirculation regions (e.g., in cavities or downstream of separation points). Hence, physical features of the geometry as well as the flow physics influence the clustering of grids in selected regions of the flow domain. The art and science of clustering grids in such regions is usually achieved by evaluating some measures based upon tentative flow solutions. This procedure is called *adaptive* grid generation. Note that fine grids near a wall, where velocities are low, are not as detrimental to time-step size as fine grids in a uniform flow region, where velocities are much larger.

Moreover, when changes in one coordinate direction (e.g., along the wall) are considerably slower than in the other (normal to the wall), grid lines in the streamwise direction can be spaced further apart than those in the normal direction. This produces grids with a high aspect ratio, that is, the ratio of the larger dimension to the smaller. While aspect ratios can be high if one is certain of the flow behavior, one must be careful not to deviate significantly from unity in separation and recirculation regions. One should be particularly aware of the unusually high aspect ratios that can be produced when grid stretching is utilized. The elimination of high-aspect-ratio grids is perhaps the most significant advantage that unstructured grids offer.

One usually begins with a computation on a coarse grid in order to ensure that the geometry, boundary conditions, initial conditions and fluid properties are properly implemented. A preliminary flow solution is obtained in this fashion. Coarse-grid solutions, combined with any other

a priori knowledge of the flow physics, are utilized to progressively refine, stretch, and cluster the grid to capture the flow physics accurately.

Frequently, the goal of an engineering CFD assignment may be to study a host of different cases with parameter or geometry variations. The only means of minimizing inaccuracy in such situations is to carry out a detailed analysis of at least one test case, preferably the one that is considered most stringent (e.g., has the largest gradients in flow). A detailed analysis would involve ensuring that any further grid refinement; reduction in time step; and reduction in stretching, aspect ratio, and nonorthogonality do not alter the essential physics. A recent study of three-dimensional, incompressible laminar (Re = 790) flow in a 90º bend has demonstrated that this is no easy task and that even if they are carried out in painstaking detail, such efforts may still be inconclusive.[84] For this classic test case, for which detailed experimental data exist,[87] it was found that even the finest mesh with an excess of 700,000 points was not sufficient to establish grid-independent solutions. This note of apparent pessimism is only meant as a warning and is not intended to discourage the use of CFD.

IV. MASS TRANSFER

Except when natural convection is considered, the analysis of mass transfer can be determined after the flow field is obtained. Here, we thus assume that fluid velocity fields are known. Since Schmidt numbers in aqueous electrolytes are typically on the order of 1000 and can be much larger, the accurate resolution of concentration fields may require much finer meshes than those for the flow fields. It thus may be advantageous to develop methodologies that permit the use of different grids for the concentration fields.

Flexibility in solving for concentration fields may also be important because the fields may be coupled through an electrical potential or through homogeneous chemical reactions.[1] Such problems often involve the solution of coupled, nonlinear differential equations that may not be easily amenable to commercial solvers. For models involving only one spatial dimension, Newman's BAND(J) subroutine,[1,88,89] a block tridiagonal matrix algorithm (TDMA), has been widely used. A finite-difference method using central-difference discretization is typically used to generate the coupled algebraic equations resolved by the block TDMA. Numerical

methods that utilize this or similar algorithms can be developed to solve the discretized equations that result from two- or three-dimensional problems. Common algorithms are described, for example, by Ferziger, [90] Ferziger and Peric, [73] and Pantakar. [75]

Various methods can be used for the discretization of the governing equations, including FDM, FEM, and FVM. FDM is well known in electrochemistry and is derived by using truncated Taylor series for the approximation of derivatives. FVM, which is less well known in electrochemistry but is commonly employed for CFD, is discussed here.

1. Finite-Volume Methods

In finite-volume methods, the integral formulation of the conservation laws over a small physical control volume is discretized directly. FVM employs a conservative discretization, that is, each species is guaranteed to be conserved, even for coarse meshes. In contrast, many traditional FDMs are not conservative. For example, owing to the nonlinear nature of the constitutive flux equations of ionic species in an a priori unknown electric field, FDM is nonconservative, even when constant physical properties are assumed. [32]

In an FVM, the region of interest is subdivided, as in FEM, into a set of nonoverlapping cells that cover the entire domain. On each cell, the conservation laws are applied to determine the unknowns at a discrete point in the cell. These node points can be positioned anywhere in the cells. A typical choice would be a cell-centered node point, that is, the node point is at the geometric center of the cell. There is considerable freedom in the shape of the cell and the node positions. For example, cells can be quadrilateral or triangular and they can be structured or unstructured [77] In addition to the conservation of material and its geometric freedom, another important advantage of FVM is its flexibility in treating high-Peclet number problems.

Consider one-dimensional transport in the element shown in Fig. 2. The shell mass balance is written as

$$\{\text{Rate of accumulation}\} = \{\text{Rate of mass in}\} - \{\text{Rate of mass out}\} + \{\text{Rate of generation}\} \tag{3}$$

or, on a unit area base,

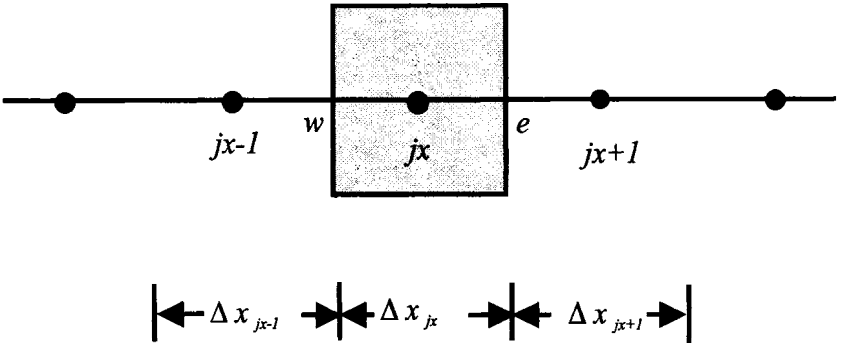

Figure 2. Schematic diagram of a one-dimensional control volume, with the west and east faces and the neighboring node points labeled.

$$\frac{\partial c_i(jx)}{\partial t}\Delta x_{jx} = N_{i,w} - N_{i,e} + R_i \Delta x_{jx} \tag{4}$$

where $N_{i,w}$ is the flux of species i at the "west" face of cell jx, $N_{i,e}$ is the flux at the "east" face, and R_i is the rate of generation of species i per unit volume. The cell has dimension Δx_{jx} in the x-direction and unit dimensions in the y- and z-directions. The flux of species i usually contains convective terms and diffusive terms:

$$N_{i,w} = \left\{ -D_i \frac{\partial c_i}{\partial x} + uc_i \right\}_w \tag{5}$$

$$N_{i,e} = \left\{ -D_i \frac{\partial c_i}{\partial x} + uc_i \right\}_e \tag{6}$$

Typically, after making the mass balance for a small element, the element spacing, Δx_{jx}, is allowed to become infinitesimally small to obtain a partial diffrential equation. In an FDM, the differential equation is discretized and the resulting algebraic equations are solved numerically.

In an FVM, the step where Δx_{jx} is assumed to be infinitesimally small is omitted. Instead, Eq. (4) is discretized. The flux expressions are discretized with an appropriate finite-difference approximation. In the limit as $\Delta x_{jx} \to 0$, FVM and FDM give identical results. If the flux is the same for a surface shared by adjacent cells, material is rigorously conserved. This

conservation is true regardless of the size of Δx_{jx}. Therefore, preliminary results can be obtained quickly with a coarse mesh without loss of material conservation.

2. Two-Dimensional Formulation on an Orthogonal Grid

A two-dimensional control volume is shown in Fig. 3. The control volume centered at the node point (*jx, jy*) is rectangular. A material balance for species *i* at node point (*jx, jy*) can be written as

$$\frac{\partial c_i(jx,jy)}{\partial t}\Delta x_{jx,jy}\Delta y_{jx,jy} = N_{i,w}\Delta y_{jx,jy} - N_{i,e}\Delta y_{jx,jy} + N_{i,s}\Delta x_{jx,jy} - N_{i,n}\Delta x_{jx,jy} + R_i\Delta x_{jx,jy}\Delta y_{jx,jy} \tag{7}$$

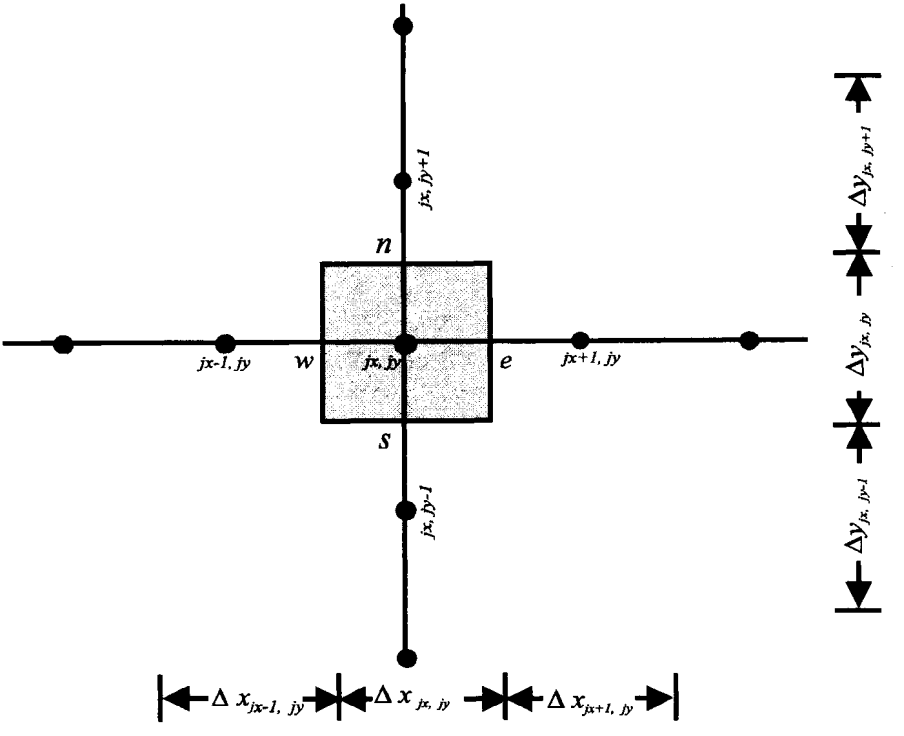

Figure 3. Schematic diagram of a two-dimensional control volume.

where $N_{i,w}$, $N_{i,e}$, $N_{i,s}$, and $N_{i,n}$ are the normal fluxes of species i at the west, east, south, and north faces of the cell (jx,jy), and R_i is the production rate per unit volume. The volume of the cell is $\Delta x_{jx,\,jy}\Delta y_{jx,\,jy}$, assuming that the cell has unit dimension in the z direction. In general, the flux of species i can be affected by all of the variables and their gradients. For example, along the west face the flux can be written as

$$N_{i,w} = \sum_k d_{i,k}^w \nabla c_k|_w + f_{i,k}^w c_k|_w \tag{8}$$

Analogous equations are written for fluxes along the other faces. Equation (8) is assumed to be linear. Commonly, in electrochemical systems, the constitutive relationship may be nonlinear. For example, assuming dilute-solution theory, the flux of species j is given by

$$N_j = -z_j D_j c_j \nabla\phi - D_j \nabla c_j + c_j \mathbf{u} \tag{9}$$

Since the electrical potential is an unknown, the first term on the right-hand side is nonlinear. However, a numerical method to be employed is likely to linearize that term around a guess so that for a given iteration, the flux relationship (in deviation form) is given by Eq. (8).

To obtain an algebraic approximation to Eq. (7), the for fluxes expressions on each face must be discretized. The optimal interpolation formula used to evaluate the variables c_k and their derivatives depends on the local Peclet number. Nevertheless, the formulas for the east and west faces will have the following forms:

$$c_k|_w = \alpha_w c_k(jx,jy) + (1-\alpha_w)c_k(jx-1,jy) \tag{10}$$

$$c_k|_e = \alpha_e c_k(jx+1,jy) + (1-\alpha_e)c_k(jx,jy) \tag{11}$$

$$\nabla c_k|_w = \beta_w[c_k(jx,jy) - c_k(jx-1,jy)] \tag{12}$$

$$\nabla c_k|_e = \beta_e[c_k(jx+1,jy) - c_k(jx,jy)] \tag{13}$$

Similar expressions would be utilized along the north and south faces. For a low Peclet number, a linear interpolation is most appropriate. For this case,

$$\alpha_w = \frac{\Delta x_{jx-1,jy}}{\Delta x_{jx-1,jy} + \Delta x_{jx,jy}};\ \alpha_e = \frac{\Delta x_{jx,jy}}{\Delta x_{jx,jy} + \Delta x_{jx+1,jy}} \tag{14}$$

and

$$\beta_w = \frac{2}{\Delta x_{jx-1,jy} + \Delta x_{jx,jy}}; \beta_e = \frac{2}{\Delta x_{jx,jy} + \Delta x_{jx+1,jy}};$$

When uniform meshes are used, $\alpha_w = \alpha_e = \alpha_s = \alpha_n = 1/2$, $\beta_w = \beta_e = 1/\Delta x$, and $\beta_s = \beta_n = 1/\Delta y$.

The high Schmidt numbers (i.e., the ratio of kinematic viscosity v to the relevant diffusion coefficient D, that arise in electrochemical systems) suggest that many convection-diffusion problems may be characterized by large Peclet numbers,

$$\mathrm{Pe} = \frac{u_{\mathrm{char}} L_{\mathrm{char}}}{D} \tag{15}$$

where u_{char} and L_{char} are the characteristic velocity and length, respectively. When the grid Peclet number

$$\mathrm{Pe}_{\mathrm{grid}} = \frac{u_{\mathrm{char}} \Delta x_{jx}}{D} > 2 \tag{16}$$

where Δx_{jx} is the grid size, the central-difference approximation causes oscillatory behavior in the concentration profile (which is physically unrealistic). This can be eliminated by use of an upwind scheme. In the upwind scheme, the variable in the convection term is assumed to have the value at the node point on the upwind side of the cell. Therefore β_w and β_e remain the same, but

$$\alpha_e = 0; \quad \alpha_w = 0 \text{ when the flow is from west to east} \tag{17}$$

and

$$\alpha_w = 1; \ \alpha_e = 1 \text{ when the flow is from east to west.}$$

The upwind scheme described here is first-order accurate in space while the central difference scheme is second-order accurate. Hence a central-difference scheme is preferred whenever possible. Since it is the grid Peclet number that decides the behavior of the numerical schemes, it is, in principle, possible to refine the grids until the grid Peclet is smaller than 2. This strategy, however, is often limited by the required computing time. With sufficiently fine meshes, the two schemes should give essen-

tially the same solution. The upwind scheme, however, gives physically realistic solutions even for coarse grids.

The order of accuracy of the upwind scheme can be improved by using a higher-order accurate scheme such as QUICK (quadratic upwind interpolation for convective kinematics).[77] The concentration at an interface is interpolated by means of a parabola instead of a straight line. The use of QUICK or similar methods may, however, complicate implementation of boundary conditions or lessen the convergence rate of the solution algorithm.

In order to treat geometries of arbitrary complexity, nonorthogonal grids are required. Even when an orthogonal mesh can be used, the ability to use nonuniform grids is normally required to allow sufficient grid density in the regions where concentration variations are the greatest. Various strategies outlined in the previous section can be adopted.

3. Validation of Simulations

In order to obtain confidence in the results of numerical simulations, numerical experiments are performed. These involve solving similar problems, for which theoretical or numerical treatments or high-quality experimental data are available. Ultimately, however, simulations of the problem of interest must be verified by increasing the grid density until the solution does not change when additional grid points are added. For an unsteady solution, convergence on time-step size must also be verified.

V. EXAMPLES OF APPLICATIONS

In order to highlight some possibilities and potential problems for current-distribution simulations, two examples from recent articles are discussed. The first example is concerned with copper deposition from a poorly supported electrolyte, but in well-defined, unsteady fluid flow, for which an analytical solution is available.[71] The second example refers to ferricyanide reduction in the presence of an unsteady flow, for which CFD was required to interpret experimental measurements.[44]

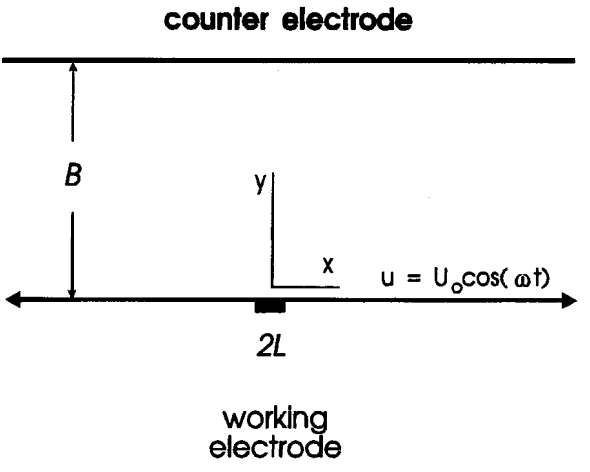

Figure 4. An oscillating-plate cell. The counter electrode is stationary, and the working electrode is flush mounted in an otherwise insulating plate that oscillates in its own plane.

1. Copper Deposition

A schematic of the electrochemical cell is shown in Fig. 4. A working electrode of length $2L$ is mounted on an otherwise insulating plate that oscillates in its own plane:

$$u_{\text{plate}} = U_o \cos(\omega t) \tag{18}$$

The counterelectrode is placed at a distance B from the working electrode. When $L/B \ll 1$, the solution domain is essentially semi-infinite.* Calculations were carried out on a finite domain. Numerical experiments were performed to determine the appropriate size of the truncated computational domain. The required size decreases with increasing Peclet number.

Deposition of copper at various fractions of the limiting current in the presence of either excess or a limited amount of sulfuric acid was studied. For the analysis of the latter conditions where electrical migration is

*For a convection-diffusion problem, where the electrical potential is not relevant to the prediction of current distribution, a semi-infinite domain poses no conceptual problems; however, the treatment of an electrical potential in a two-dimensional, semi-infinite domain is problematic. When comparing simulation with experiment, the potential drop between the outer edge of the computational domain and the actual position of the reference or counter-electrode must be estimated.

important, the sulfuric acid was assumed to be dissociated completely into sulfate and hydrogen ions.

Simulations assumed dilute-solution theory, so that the flux of species j is given by Eq. (9). If the origin is attached to the center of the electrode on the moving plate and if $L/B \ll 1$, the velocity parallel to the electrode can be approximated by

$$u_x = U_o \sqrt{\frac{\omega}{\nu}} y \cos(\omega t - \theta) \tag{19}$$

where θ is a constant.

It is assumed that no homogeneous reactions take place in the solution; hence the three (one each for Cu^{2+}, H^+, and SO_4^{2-}) material balance equations become

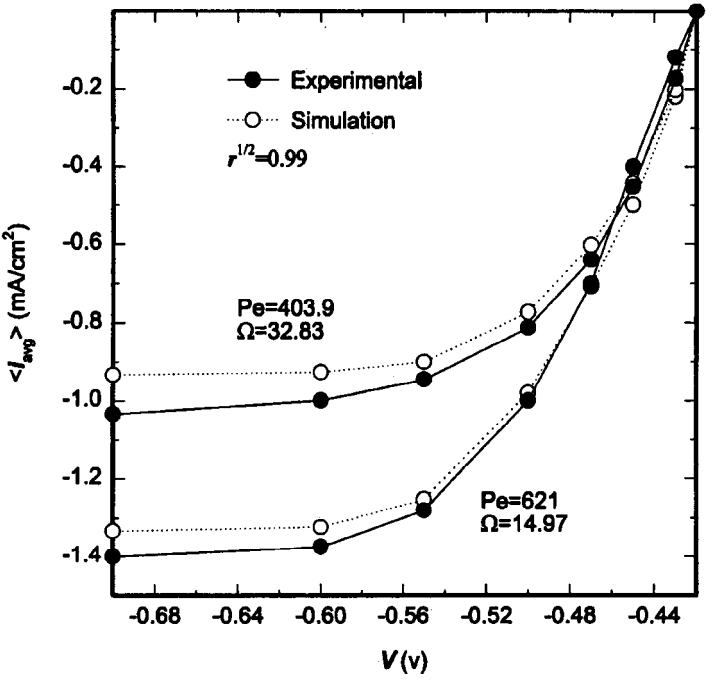

Figure 5. Simulated and measured polarization curves obtained for two flow conditions, in the presence of excess, supporting electrolyte. The bulk concentration was 3 mM $CuSO_4$ and 0.1 M H_2SO_4. The potential is relative to an Hg/Hg_2SO_4 reference electrode.

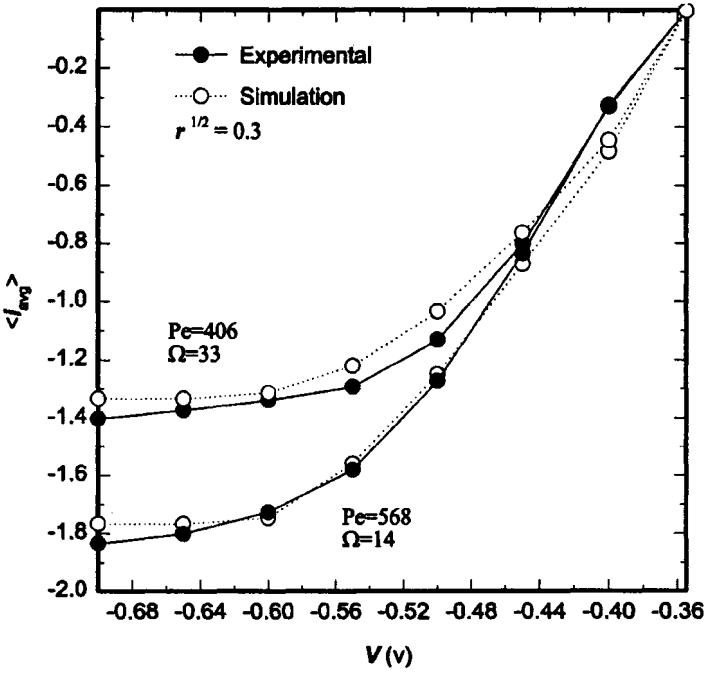

Figure 6. Simulated and measured polarization curves obtained for two flow conditions, in the presence of a small amount of supporting electrolyte. The bulk concentration was 3 mM $CuSO_4$ and 0.3 mM H_2SO_4. The potential is relative to an Hg/Hg_2SO_4 reference electrode.

$$\frac{\partial c_j}{\partial t} = -\nabla \cdot N_j \tag{20}$$

In order to determine the electrical potential, the electroneutrality constraint is also imposed:

$$\Sigma z_j c_j = 0 \tag{21}$$

The boundary conditions are described in more detail elsewhere. A zero-flux condition is imposed on the electrode for all species except the reactant Cu^{2+}. A Tafel relationship with a concentration-dependent exchange current density was used to describe the electrode kinetics.[91] The exchange current density was found from rotating disk experiments, and all other model parameters were taken from the literature. No parameters were adjusted for the simulations in the cell.

For most cases, the experimental and simulated time-varying current densities are in good agreement. Figures 5 and 6 compare measured and simulated polarization curves under different flow conditions. Here the dimensionless plate frequency is defined as $\Omega = \omega L^2/D_{Cu^{2+}}$, and $\mathrm{Pe} = \sqrt{\omega/\nu}U_o L^2/D_{Cu^{2+}}$. In these figures, each point is the time-average current density, and the ratio r is defined as $r = c_{H^+}/(2c_{SO_4^{2-}})$. The dimensionless concentration of Cu^{2+} is then given by electroneutrality.

Figure 5, where $\sqrt{r} = 0.99$, shows results for an excess supporting electrolyte; the results could be simulated with a standard convection-diffusion solver as well as the coupled-field solver outlined below. Discrepancies between experiment and simulation at the limiting current density are believed to be due to surface roughness. In contrast, Fig. 6, with $\sqrt{r} = 0.3$, shows results for a case where electrical migration is important and was treated in the manner described below.

Equations (9), (20), and (21), and the boundary conditions define a nonlinear and coupled system of partial differential equations, solved by an FVM. The equations were linearized around a guessed value. The guessed values were updated iteratively to convergence before executing the next time step. Since the electroneutrality constraint tightly couples the potential and concentration fields, the discretized sets of algebraic equations at each node point were solved simultaneously. Attempts were made to employ a sequential solver in which the electrical field was assumed for determination of the concentration of each species. In this way, the concentration fields appear decoupled and could be determined easily with a commercial, convection-diffusion solver. A robust method for converging upon the correct electrical field was, however, not found.

Both point-by-point and line-by-line overrelaxation methods were used to resolve the algebraic equations.[75,90] An overrelaxation parameter of 1.5–1.8 was typically used. The two methods required similar computational times. An upwind scheme was used for all variables for high-Pe problems, while a central-difference scheme was used for low Pe. For some high-Pe cases, a central-difference scheme was used for the potential, but no appreciable differences in the results were observed.

Numerical experiments were performed to determine the minimum computational domain and an adequate grid size. Uniform grids were used near the electrode. Beyond this region, nonuniform (compound-interest) grids, with a stretching factor of less than 1.2 in both directions, were used. When the electric field is large, a more finely resolved grid is required. The number of iterations to obtain a converged result was also found to

increase in the presence of large electric fields. The convergence rate was improved if a good initial, trial solution was given for the potential. However, convergence was obtained for almost any initial guess. A conclusion concerning the numerical method is that tertiary current-distribution solvers, which are time accurate and based on a control volume formulation, can be effectively implemented if the tight coupling between the electrical and concentration fields is exploited.

2. Mass Transfer during Unstable Flows Generated by a Blocking Cylinder

The second example is also concerned with estimation of mass-transfer rates in the presence of unsteady, laminar fluid flows. The present problem was investigated because an understanding of mass-transfer rates behind bluff bodies may enable the development of mixing methods for high-end metallization applications. This example is chosen here to highlight the complexity in flow fields that can appear in an ostensibly simple geometry.

For example, the vortex shedding phenomena downstream of a cylinder, which have been studied extensively, show very rich dynamic behavior. For a cylinder in a free stream, the flow is found to be steady for $\mathrm{Re} < 50$ and periodic for $50 < \mathrm{Re} < 194$. At higher flow rates, the appearance of three-dimensional vortices has been observed before the development of turbulence. A detailed review of vortex dynamics behind a cylinder is given by Williamson.[92]

Yang *et al.*[44] report an experimental and computational study of mass transfer to a channel wall downstream of a cylinder. The rate of mass transfer was recorded at various locations. Ferricyanide reduction at a mass-transfer-controlled rate from an electrolyte containing a large amount of KCl was used for the experimental measurements. A diagram of the cell is shown in Fig. 7. A cylinder of diameter d is placed a distance b from the bottom wall, and a working electrode of length $2L$ is placed at a distance x downstream of the center of the cylinder. The fluid flow can be characterized with a Reynolds number defined as

$$\mathrm{Re} = \frac{u_{\mathrm{avg}} d}{\nu} \tag{22}$$

where v is assumed to be 10^{-2} cm^2/s and u_{avg} is the average velocity.

The Reynolds numbers that were investigated ranged between 40 and 500. The primitive-variable forms of the continuity and momentum equa-

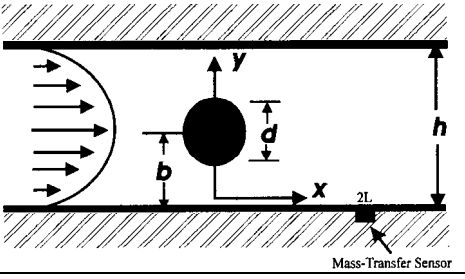

Figure 7. Schematic diagram of a flow channel of height h with a blocking cylinder of diameter d placed in the center ($b = h/2$). The working electrode (labeled mass-transfer sensor) is placed a distance x downsteam of the cylinder center. The counterelectrode (not shown) is located on the opposite wall of the channel.

tions were solved using an FEM detailed by Wasfy *et al.*[93] The standard Galerkin approximation, which reduces to a central-difference scheme, was used. The solution algorithm can be classified as being of an artificial compressibility type. The code had previously been validated against several steady as well as unsteady benchmark fluid flow problems.[78]

The electrode length, $2L$, is much smaller than the computational domain used in the fluid simulations. A separate mesh was therefore used for the mass-transfer calculations. Velocity components in the mass-transfer calculations were approximated by their first terms in a Taylor series expansion in distance y from the wall:

$$u_x = \beta(x,t)y \quad \text{and} \quad u_y = -\frac{1}{2}\frac{\partial \beta}{\partial x}y^2 \tag{23}$$

where $\beta(x,t) = \partial u_x/\partial y|_{y=0}$ was determined from the flow simulations. These velocity components satisfy the continuity equation as well as the no-slip boundary conditions.

With these approximations, the concentration field near the electrode is given by

$$\frac{\partial c}{\partial t} + \beta y \frac{\partial c}{\partial x} - \frac{1}{2}\frac{\partial \beta}{\partial x}y^2 \frac{\partial c}{\partial y} = D\left(\frac{\partial^2 c}{\partial x^2} + \frac{\partial^2 c}{\partial y^2}\right) \tag{24}$$

At the flow exit, the normal concentration gradient is set to 0. At the flow inlet and at large distances from the electrode, the concentration is set at the bulk value. The concentration is set to 0 on the electrode surface.

Temporal variations of the current density for Re = 110 are shown in Fig. 8. Only the quasi-steady results, after the initial time transient has disappeared, are shown. The blocking cylinder with $d/h = 0.25$ was placed at the channel center ($b/h = 0.5$). The current density is shown for a sensor

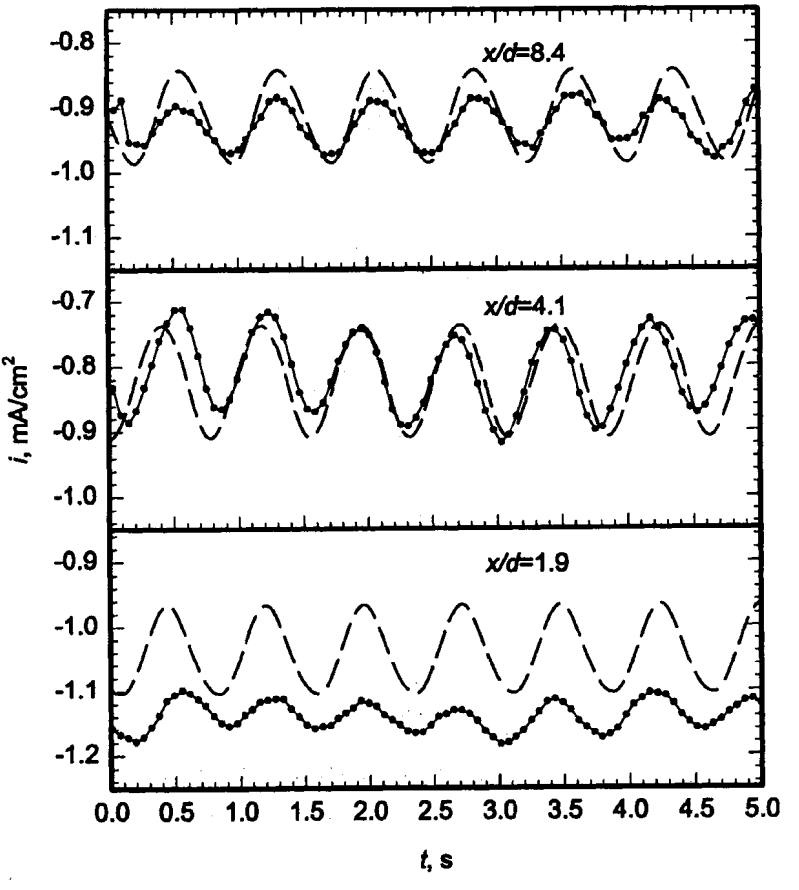

Figure 8. Simulated (dashed lines) and measured (solid lines) limiting current density as a function of time for three positions downsteam of the cylinder for $d/h = 0.25$. The experiments were obtained at Re = 110, and the simulations for Re = 100.

located at $x/d = 8.4$, 4.1, and 1.9. The simulated current densities for Re = 100 are also shown. Similar agreement was found for a large range of Reynolds numbers. The agreement in the average current density near the cylinder ($x/d = 1.9$) was generally found to be the worst.

Current densities were recorded as a function of time for a large number of flow rates. For Re < 50, the mass-transfer rate was steady. When Re > 200, more than one frequency of oscillation in mass-transfer rate was encountered. In the range 50 < Re < 200, only one dominant frequency was observed. The frequency of oscillation is a function of Re. The experimental and simulated frequencies as a function of Re for both $d/h = 0.25$ and $d/h = 0.5$ are in close agreement.

Both experiments and simulation indicate that the frequency is the same for all three positions. The oscillation amplitude increases with distance downstream of the cylinder and reaches a maximum near $x/d = 4.1$. Beyond this region, the amplitude decreases. For most simulations, there is reasonable agreement with experiment in frequency and in average current density. Simulations, however, tend to overpredict the amplitude of the temporal oscillations in the current density (*see* Chapter 1).

The discrepancy in average current density at $x/d = 1.9$ is believed to be due to the sharp variation of the shear with position in the cylinder region. Figure 9 shows the simulated spatial variation of the time-averaged wall shear β_{avg} for Re = 100. The shear is at a maximum slightly downstream of the cylinder center. It decreases sharply to a minimum at around $x/d = 4.1$ and then increases to a nearly constant shear. The current density (also shown) has the same shape as the shear. The lowest mass-transfer rate is obtained at $x/d = 4.1$ while the highest rate was measured at $x/d = 1.9$. Stream lines indicate that the minimum in mass-transfer rate occurs at a position of recirculation. The location of the recirculation region varies with Reynolds numbers and moves upstream with increasing Re in the range of 50 to 200.

The numerical simulations were all carried out by making an assumption of a two-dimensional flow. The transition to three-dimensionality in the near wake of a cylinder has been observed to occur at a Reynolds number of about 200 in the absence of confining walls.[92] The study indicates that where the flow remains two-dimensional, numerical simulations provide a good description of mass transfer. However, the simulations apparently do not give the precise spatial variation of shear with the Reynolds number. The reasons for this are not known with certainty; the

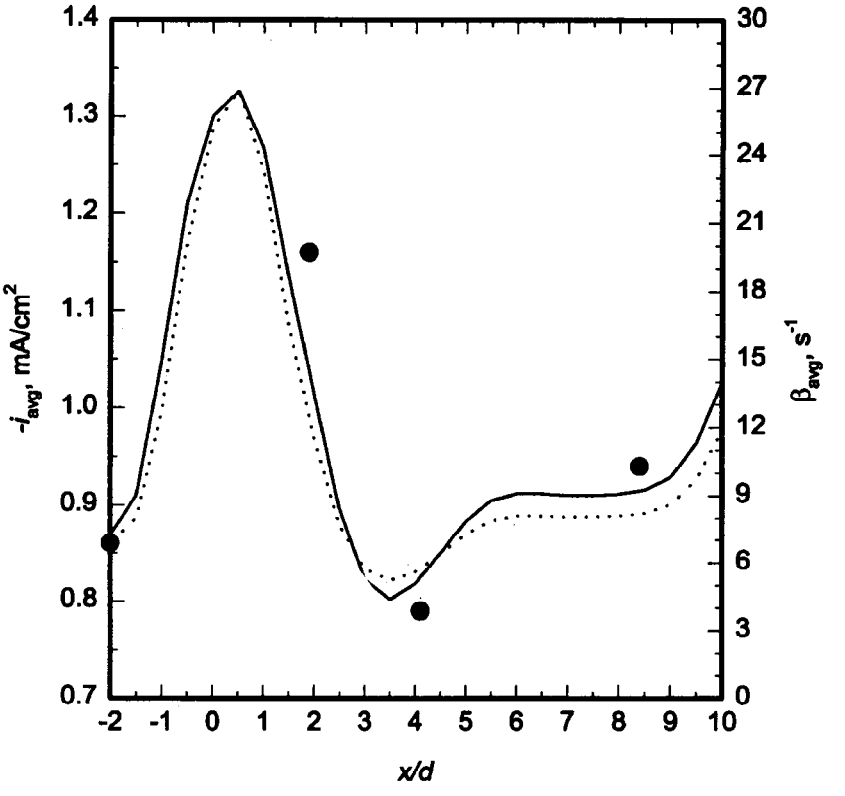

Figure 9. Simulated spatial variation of the time-averaged current density (solid line) and wall shear (dotted line) downstream of a cylinder at Re = 100. For comparison, experimental current densities (symbols) for Re = 110 are shown.

discrepancies, however, indicate the need for experimental studies, especially when the current distribution strongly depends on CFD.

VI. SUMMARY

Numerical analyses of fluid flow and mass transfer in electrochemical systems will become more common. It may be difficult, however, to utilize currently available commercial solvers for mass transfer, especially when

concentration fields are coupled through an electrical field or through homogeneous chemical reactions. The large Schmidt numbers that are important in electrochemistry may also imply that mass-transfer calculations require much finer computational grids than fluid-flow simulation. Nevertheless, commercial fluid-flow solvers will often be adopted. Attention must be paid to experimental verification of the simulations.

The focus of this review has been on mass transfer in laminar, single-phase flows. Significant work is necessary for the rigorous analysis of current distribution in turbulent flows. Progress is also required for the analysis of current distribution in multiphase flows, especially in porous media relevant to fuel cell or battery applications.

ACKNOWLEDGMENTS

Much of this work was supported by the National Science Foundation under grant No. CTS-93-15991. We would also like to thank Mr. Scott Calabrese Barton for helpful comments concerning the manuscript.

Notation

c	variable or concentration
d	diameter of a cylinder
d^w	coefficient of a linearized diffusive term at the west face
D	diffusion coefficient
f^w	coefficient of a linearized convective term at the west face
h	height of a channel
L	characteristic length
N	flux or number of dependent variables
p	pressure, Pa
Pe	Peclet number
R	rate of generation per unit volume
Re	Reynolds number
t	time
u	velocity
x, y, z	cartesian coordinates
z_i	charge of species i

Greek symbols

α_w convective term interpolation variable at the west face
β_w diffusive term interpolation variable at the west face
β shear at a wall
Δ indicates deviation variable
ϕ dimensionless potential
ω oscillation frequency
Ω dimensionless frequency of plate oscillation

Subscript/superscript

e east face of a control volume
grid characteristic dimension is the grid size
i, j equation or species number
jx, jy spatial index in the x- and y-direction
k variable number
w west face of a control volume
x, y, z cartesian coordinates

REFERENCES

[1] J. S. Newman, *Electrochemical Systems,* 2nd ed., Prentice-Hall, Englewood Cliffs, NJ, 1991.
[2] G. Prentice, *Electrochemical Engineering Principles,* Englewood Cliffs, NJ, 1991.
[3] J. Newman and W. Tiedemann, *A. I. Ch. E. J.* **21** (1975) 25.
[4] S. Mehdizadeh, J. Dukovic, P. C. Andricacos, L. T. Romankiw, and H. Y. Cheh, *J. Electrochem. Soc.* **137** (1990) 110.
[5] J. O. Dukovic, *IBM J. Res. Develop.* **34** (1990) 693.
[6] J. O. Dukovic, in *Advances in Electrochemical Science and Engineering,* H. Gerischer and C. W. Tobias, eds., Vol. 3, VCH Publishers, New York, 1994, p. 117.
[7] K. Nisancioglu, in *Modern Aspects of Electrochemistry,* Vol. 23, B. E. Conway, J. O'M. Bockris, and R. E. White, eds., Plenum, New York, 1992, p. 149.
[8] G. O. Mallory and J. B. Hajdu, eds., *Electroless Plating. Fundamentals and Applications,* American Electroplaters and Surface Finishers, Orlando, FL, 1990.
[9] C. W. Tobias and R. Wijsman, *J. Electrochem. Soc.* **100** (1953) 459.
[10] M. Matlosz, P.-H. Valloton, A. C. West, and D. Landolt, *J. Electrochem. Soc.* **139** (1992) 752.
[11] A. C. West and J. Newman, in *Modern Aspects of Electrochemistry,* Vol. 23, B. E. Conway, J. O'M. Bockris, and R. E. White, eds., Plenum, New York, 1992, p. 101.
[12] J. Newman, in *Electroanalytical Chemistry,* A. J. Bard, ed., Marcel Dekker, New York, 1973, p. 187.
[13] D. R. Baker, M. W. Verbrugge, and J. Newman, *J. Electroanal. Chem.* **314** (1991) 23.
[14] D. R. Baker, *SIAM J. Appl. Math.* **53** (1993) 419.

[15]B. Pillay and J. Newman, *J. Electrochem. Soc.* **140** (1993) 414.
[16]J. V. Powers and L. T. Romankiw, "Electroplating Cell Including Means to Agitate the Electrolyte in Laminar Flows," U.S. Patent No. 3,652,442 (1972).
[17]L. T. Romankiw, P. E. Acosta, and J. V. Powers, in *Electrochemical Society Meeting,* Abstract No. 287, Electrochemical Society, Pennington, NJ, 1997.
[18]D. T. Schwartz, B. G. Higgins, and P. Stroeve, *J. Electrochem. Soc.* **140** (1993) 414.
[19]D. E. Rice, D. Sundstrom, M. F. McEarchen, L. A. Klumb, and J. B. Talbot,*J. Electrochem. Soc.* **135** (1988) 2777.
[20]P. C. Andricacos and L. T. Romankiw, in *Advances in Electrochemical Science and Engineering,* H. Gerischer and C. W. Tobias, eds., Vol. 3, VCH Publishers, New York, 1994, p. 227.
[21]P. C. Andricacos, C. Arana, J. Tabib, J. Dukovic, and L. T. Romankiw, *J. Electrochem. Soc.* **136** (1989) 1336.
[22]K. H. Wong, P. C. Andricacos, and L. T. Romankiw, in *Magnetic Materials, Processes and Devices,* L. T. Romankiw and D. A. Herman, eds., Vol. PV 90-8, Electrochemical Society Proceedings Series, Pennington, NJ, 1995, p. 387.
[23]S. Hessami and C. W. Tobias, *J. Electrochem. Soc.* **136** (1989) 3611.
[24]H. Dahms and I. M. Croll, *J. Electrochem. Soc.* **112** (1965) 771.
[25]W. C. Grande and J. B. Talbot, *J. Electrochem. Soc.* **140** (1993) 675.
[26]J. Newman, *Ind. Eng. Chem.* **60** (1968) 12.
[27]R. H. Goldstein, ed., *Fluid Mechanics Measurements,* 2nd ed., Taylor and Francis, Washington, DC, 1996.
[28]T. J. Hanratty, *J. Applied Electrochem.* **21** (1991) 1038.
[29]T. J. Hanratty and J. A. Campbell, in *Fluid Mechanics Measurements,* R. H. Goldstein, ed., 2nd ed., Taylor and Francis, Washington, DC, 1996, p. 575.
[30]R. B. Bird, W. E. Stewart, and E. N. Lightfoot, *Transport Phenomena,* Wiley, New York, 1960.
[31]J. Freitas, *J. Fluids Eng.* **117** (1995) 208.
[32]A. C. West, D. Yang, and B. DeBecker, in *Fundamentals of Electrochemical Process Design: A Tutorial,* J. B. Talbot and J. Fenton, eds., Electrochemical Society, Pennington, NJ, 1995.
[33]A. C. West and T. F. Fuller, *J. Appl. Electrochem.* **26** (1996) 557.
[34]R. Alkire and A. A. Miraferi, *J. Electrochem. Soc.* **120** (1973) 1507.
[35]R. Alkire and A. A. Miraferi, *J. Electrochem. Soc.* **124** (1977) 1043.
[36]R. Alkire and A. A. Miraferi, *J. Electrochem. Soc.* **124** (1977) 1214.
[37]M. Pesco and H. Y. Cheh, *J. Electrochem. Soc.* **136** (1989) 399.
[38]D. G. Thomas, *A.I.Ch.E. J.* **11** (1965) 848.
[39]D. G. Thomas, *A.I.Ch.E. J.* **12** (1966) 124.
[40]S. Isaacson and A. A. Sonin, *Ind. Eng. Chem. Process Des. Develop.* **15** (1976) 313.
[41]A. A. Sonin and M. S. Isaacson, *Ind. Eng. Chem. Process Des. Develop.* **13** (1974) 241.
[42]S. Zheng and W. M. Worek, *Int. J. Heat Mass Transfer* **39** (1996) 97.
[43]P. Berger and K.-F. F.-L. Hau, *Int. J. Heat Mass Transfer* **22** (1979) 1645.
[44]J. D. Yang, A. Shehata, V. Modi, and A. C. West, *Int. J. Heat Mass Transfer* **40** (1997) 4263.
[45]K. Kondo, K. Fukui, K. Uno, and K. Shinohara, *J. Electrochem. Soc.* **143** (1996) 1880.
[46]A. C. West, C. Madore, M. Matlosz, and D. Landolt, *J. Electrochem. Soc.* **139** (1992) 499.
[47]R. Alkire, T. Bergh, and R. L. Sani, *J. Electrochem. Soc.* **125** (1978) 1981.
[48]R. C. Alkire, D. B. Reiser, and R. L. Sani, *J. Electrochem. Soc.* **131** (1984) 2795.
[49]R. C. Alkire and H. Deligianni, *J. Electrochem. Soc.* **135** (1988) 1093.
[50]R. C. Alkire, H. Deligianni, and J.-B. Ju, *J. Electrochem. Soc.* **137** (1990) 818.
[51]J. N. Harb and R. Alkire, *J. Electrochem. Soc.* **138** (1991) 3568.
[52]M. Georgiadou and R. Alkire, *J. Electrochem. Soc.* **141** (1994) 679.

[53]M. Engelman, *FIDAP Users' Manual,* Fluid Dynamics International, Evanston, IL, 1997.
[54]C. B. Shin and D. J. Economou, *J. Electrochem. Soc.* **136** (1989) 1997.
[55]C. B. Shin and D. J. Economou, *J. Electrochem. Soc.* **138** (1991) 527.
[56]J. O'Hern, J. R. Torczynski, T. K. Blanchat, T. Y. Chu, and A. L. Tassin, in *Laser Anemometry 1994 Advances and Applications,* ASME, Fluids Engineering Division, DED, Vol. 191, American Society of Mechanical Engineers, New York, 1994, p. 135.
[57]P. H. Chen, *J. Chinese Inst. Eng.* **19** (1996) 273.
[58]H. N. Chang, H. W. Ryu, D. H. Park, and J. K. Park, *Int. J. Heat Mass Transfer* **30** (1984) 2137.
[59]N. K. Ghaddar, M. Magen, B. B. Mikic, and A. T. Patera, *J. Fluid Mech.* **163** (1986) 99.
[60]N. K. Ghaddar, M. Magen, B. B. Mikic, and A. T. Patera, *J. Fluid Mech.* **168** (1986) 541.
[61]K. G. Jordan and C. W. Tobias, *J. Electrochem. Soc.* **138** (1991) 1933.
[62]Q. Chen, V. Modi, and A. C. West, "The Influence of Fluid Flow on Leveling Performance," *J. Appl. Electrochem.,* Vol. 28 (1998) 579.
[63]GridPro/az3000, *User's Guide and Reference Manual,* Program Development Corporation, White Plains, NY, 1996.
[64]O. A. Moreno, R. H. Katyl, J. D. Jones, and P. A. Moschak, *IBM J. Res. Develop.* **37** (1993) 43.
[65]T. Y. Tom Lee, B. Lytle, and B. Hileman, in *Advances in Electronic Packaging,* ASME, EEP, Vol. 10-1, American Society of Mechanical Engineers, New York, 1995.
[66]MicroCOMPACT Users' Manual, Innovative Research, Inc., Minneapolis, MN, 1992.
[67]L. W. Hourng and C. S. Chang, *J. Appl. Electrochem.* **24** (1994) 1170.
[68]F. Alavyoon, *Electrochim. Acta* **37** (1992) 334.
[70]R. L. Sani, in *Advances in Finite Element Analysis in Fluid Dynamics,* ASME, FED-Vol. **123** (1991) 47.
[71]J. D. Yang and A. C. West, *AICHE J.* **43** (1997) 811.
[72]Y. Wang, J. Postlethwaite, and D. J. Bergstrom, *J. Appl. Electrochem.* **26** (1996) 471.
[73]J. H. Ferziger and M. Peric, *Computational Methods for Fluid Dynamics,* Springer, New York, 1996.
[74]J. C. Tannehill, D. A. Anderson, and R. H. Pletcher, *Computational Fluid Mechanics & Heat Transfer,* Taylor and Francis, New York, 1997.
[75]S. V. Patankar, *Numerical Heat Transfer and Fluid Flow,* Taylor and Francis, New York, 1980.
[76]D. C. Wilcox, *Turbulence Modeling for CFD,* DCW Industries, La Canada, 1993.
[77]C. Hirsch, *Numerical Computation of Internal and External Flows,* Wiley, New York, 1988.
[78]A. J. Chorin, *J. Computational Physics* **2** (1967) 12.
[79]L. Merkle and M. Athavale, in *AIAA,* paper 87-1137-CP, Honolulu, 1987.
[80]K. H. Chen and R. H. Pletcher, *AIAA J.* **31** (1993) 901.
[81]H. Harlow and J. E. Welch, *Physics of Fluids* **8** (1965) 2182.
[82]R. I. Issa, *J. Computational Physics* **62** (1985) 40.
[83] G. De Vahl Davis and G. D. Mallison, in S. V. Patankar, *Numerical Heat Transfer and Fluid Flow,* Taylor and Francis, New York, 1980.
[84]B. Lin and F. Sotiropoulos, *ASME J. Fluids Eng.* **119** (1997) 119.
[85]J. F. Thompson, Z. U. A. Warsi, and C. W. Martin, *Numerical Grid Generation-Foundations and Applications,* Elsevier, New York, 1985.
[86]P. Eiseman, "Automatic Structured Grid Generation," in *CFD Review,* M. Hafez and K. Oshima, eds., Wiley, New York, 1995,54.
[87]J. A. C. Humphrey, A. M. K. Taylor, and J. H. Whitelaw, *J. Fluid Mechanics* **83** (1977) 509.
[88]J. Newman, *Ind. Eng. Chem. Fund.* **7** (1968) 514.
[89]R. E. White, *Ind. Eng. Chem. Fund.* **17** (1978) 367.

[90]J. H. Ferziger, *Numerical Methods for Engineering Applications,* Wiley, New York, 1981.
[91]E. Mattson and J. O'M. Bockris, *Trans. Faraday Soc.* **55** (1959) 1586.
[92]K. Williamson, *Ann. Rev. Fluid Mechanics* **28** (1996) 477.
[93]T. Wasfy, A. C. West, and V. Modi, "Parallel Finite Element Computation of Unsteady Incompressible Flows," *Int. J. Numerical Methods in Fluids,* Vol. 26 (1998) 17.

This page intentionally left blank

Cumulative Author Index for Numbers 1–32

This page intentionally left blank

Cumulative Title Index for Numbers 1–32

Index